Synthesis, Redox and Spectroscopic Properties of Nindigo and a Variety of Nindigo Coordination Compounds

by

Graeme Nawn
M.Phil., University of Bath, 2008
M.Chem., University of Bath, 2006

A Dissertation Submitted in Partial Fulfillment
of the Requirements for the Degree of

DOCTOR OF PHILOSOPHY

In the Department of Chemistry

Supervisory Committee

Synthesis, Redox and Spectroscopic Properties of Nindigo and a Variety of Nindigo Coordination Compounds

by

Graeme Nawn
M.Phil., University of Bath, 2008
M.Chem., University of Bath, 2006

Supervisory Committee

Dr. Robin G. Hicks, (Department of Chemistry)
Supervisor

Dr. Thomas M. Fyles, (Department of Chemistry)
Departmental Member

Dr. Lisa Rosenberg, (Department of Chemistry)
Departmental Member

Dr. Al Boraston, (Department of Biochemistry)
Outside Member

Supervisory Committee

Dr. Robin G. Hicks, (Department of Chemistry)
Supervisor

Dr. Thomas M. Fyles, (Department of Chemistry)
Departmental Member

Dr. Lisa Rosenberg, (Department of Chemistry)
Departmental Member

Dr. Al Boraston, (Department of Biochemistry)
Outside Member

Abstract

Ligand design plays an important role in the development and control of new coordination compounds. A new ligand architecture, Nindigo, has previously been reported and this study represents an expansion of that research to gain better insights into the attributes of this multifunctional ligand family.

Mono- and bis-palladium chelates of Nindigo have been synthesized with resulting electrochemical measurements allowing for the reversible redox-active nature of the ligand set to be identified. The electronic absorption properties of these complexes were also studied. The presence of the palladium centre was found to drastically perturb the ligand centered π-π* transition resulting in significant red shifts in the absorption spectra with respect to free Nindigo.

The main group coordination chemistry of Nindigo was explored by generating mono- and bis-BF_2 Nindigo chelates. The electrochemical and spectral properties of these compounds were investigated with both families displaying weak emission in the NIR region. The bis-BF_2 chelates were found to be sensitive in nature and decompose to the mono-BF_2 chelates. In addition, heteroleptic complexes of mono-BF_2 Nindigo chelates with palladium were also synthesized. The redox chemistry as well as the electronic absorption characteristics of these compounds provides a conceptual bridge between the two homologues.

Homoleptic zinc and copper complexes of mono-BF_2 Nindigo chelates have been synthesized. The zinc derivative serves as an “innocent” system where all redox and spectral properties are ligand

centered and the oxidation states of both the metal and surrounding ligands can be assigned. The copper complexes exhibit more diverse chemistry with the redox and electronic absorption properties differing dramatically from the zinc system. A combination of EPR, XPS and computational analysis suggests the copper systems to be non-innocent in nature.

In addition to the bis-bidentate anionic Nindigo ligand system, the fully oxidized neutral analogue has also been synthesized. DehydroNindigo exhibits significantly different chemical behaviour from Nindigo. Bridged ruthenium dimers have been synthesized that are obtained as two isomers, cis and trans (with respect to the bridging ligand). Both isomers exhibit rich electrochemical behaviour. The mixed valence states of both species are found, electrochemically, to be extremely stable with respect to disproportionation.

Table of Contents

List of Tables

List of Schemes

List of Figures

List of Numbered Compound

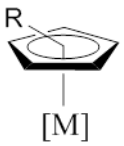

1.1

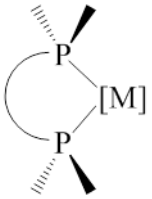

1.2

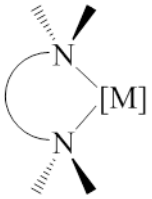

1.3

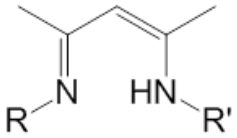

1.4

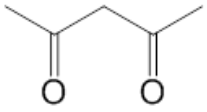

1.5

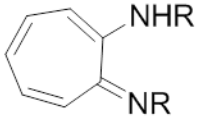

1.6

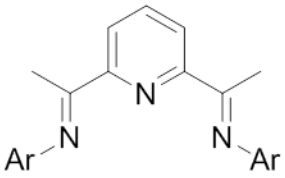

1.7

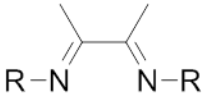

1.8

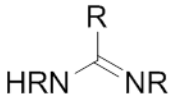

1.9

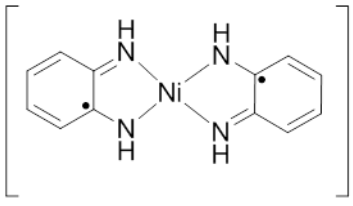

1.10

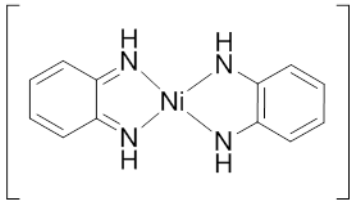

1.11

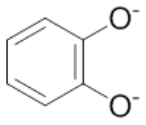

1.12

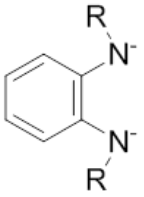

1.13

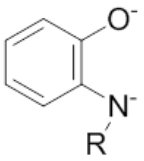

1.14

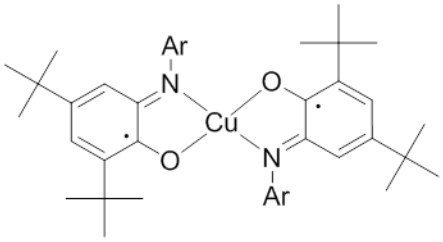

1.15

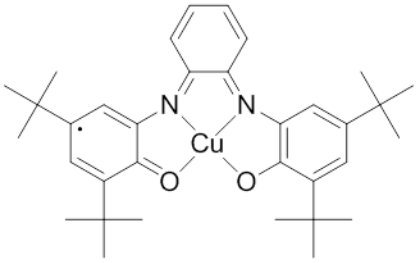

1.16

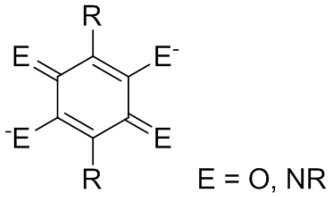

E = O, NR

1.17

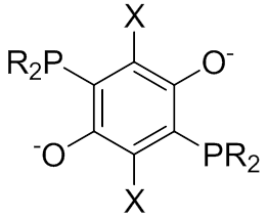

1.18

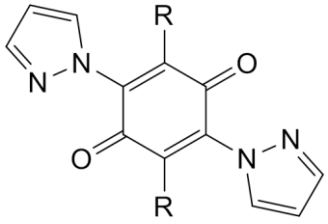

1.19

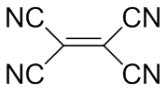

1.20a

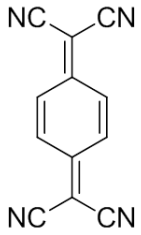

1.20b

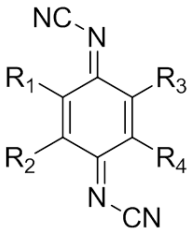

1.21

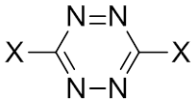

1.22

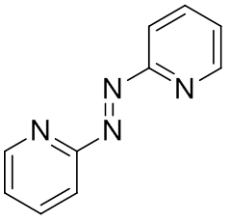

1.23

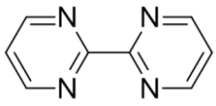

1.24

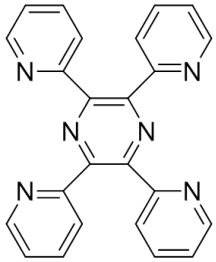

1.25

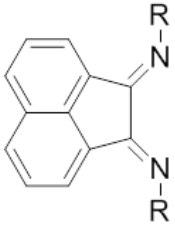

1.26

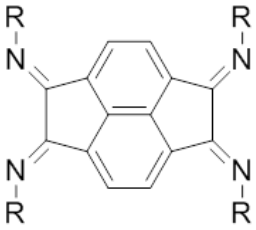

1.27

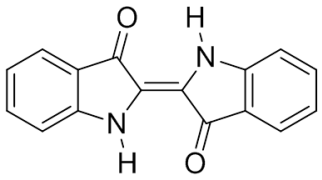

1.28

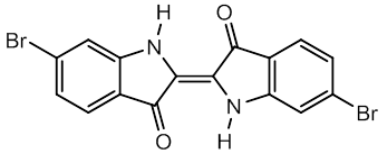

1.29

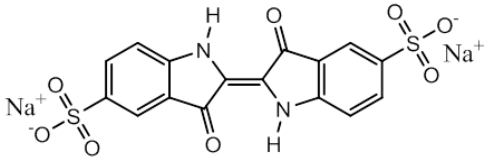

1.30

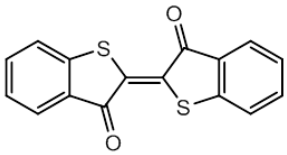

1.31

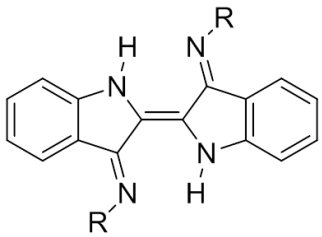

1.32

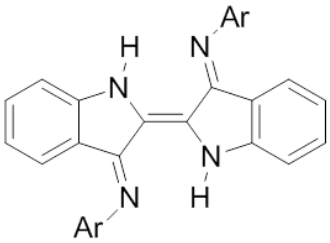

1.32a Ar = phenyl (Phen) **1.32b** Ar = pTolyl (pTol)
1.32c Ar = 2,6-dimethylphenyl (Dmp) **1.32d** Ar = 2,6-diisoproplyphenyl (Dipp)
1.32e Ar = 2-t-butylphenyl (2tButylPhen) **1.32f** Ar = pChlorophenyl (pClPhen)
1.32g Ar = 2-biphenyl (Biphen) **1.32h** Ar = mesityl (Mes)
1.32i Ar = t-Butyl (tButyl) **1.32j** Ar = pMethoxyphenyl (pMeOPhen)

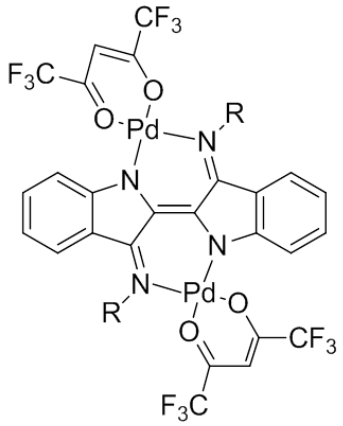

1.33a R = phen
1.33b R = *p*-tolyl
1.33f R = *p*-chlorophenyl
1.33i R = *t*-butyl
1.33j R = *p*-methoxyphenyl

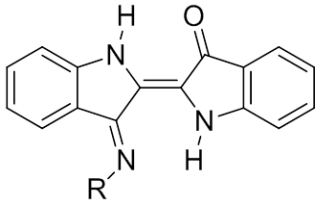

2.1a R = mes
2.1b R = dmp
2.1c R = dipp

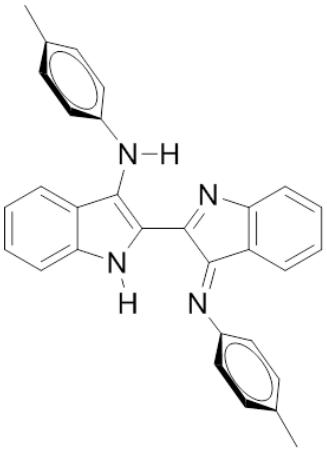

1.32b'

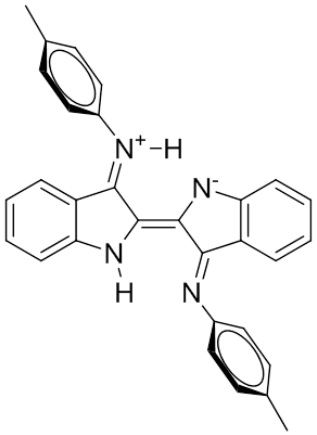

1.32b''

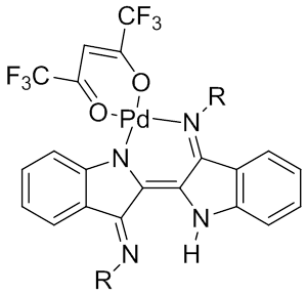

2.3

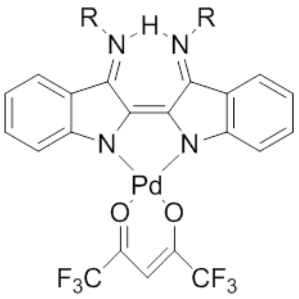

2.2c R = Dmp
2.2d R = Dipp
2.2h R = Mes

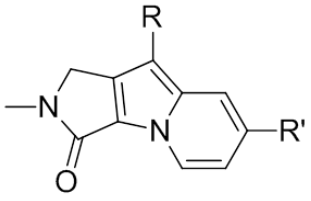

3.1

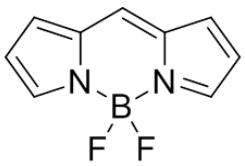

3.2

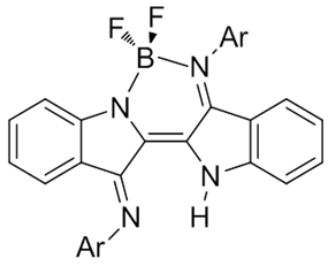

3.3a Ar = Phen
3.3b Ar = pTol
3.3c Ar = Dmp
3.3d Ar = Dipp
3.3e Ar = 2tButylPhen
3.3f Ar = pClPhen

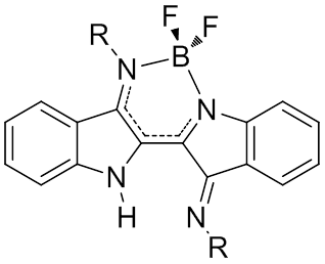

3.4

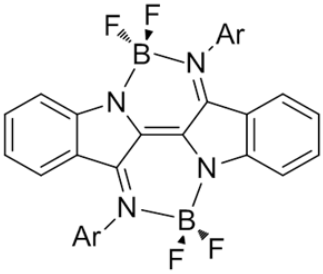

3.5a Ar = Phen
3.5b Ar = pTol
3.5c Ar = Dmp
3.5d Ar = Dipp
3.5f Ar = pClPhen

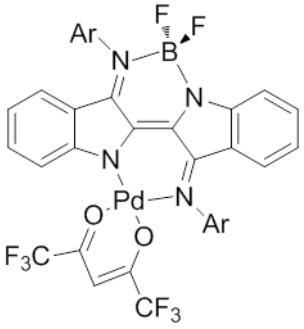

3.6a Ar = Phen, **3.6b** Ar = pTol
3.6c Ar = Dmp, **3.6d** Ar = Dipp
3.6f Ar = pClPhen

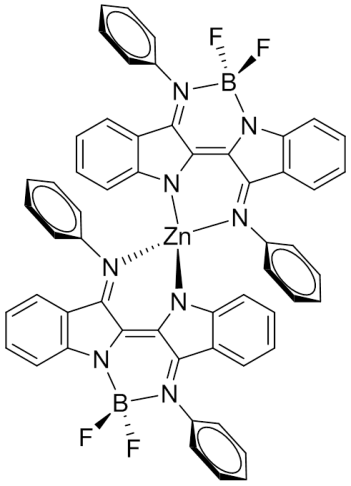

4.1

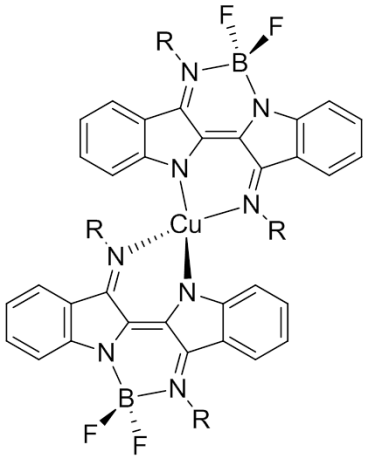

4.2a R = Phen
4.2c R = Dmp

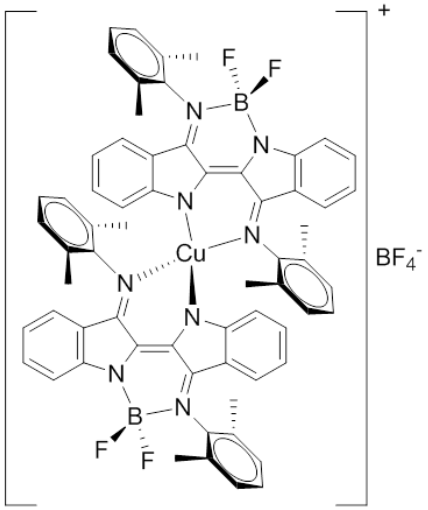

[4.2c]$^{+}$

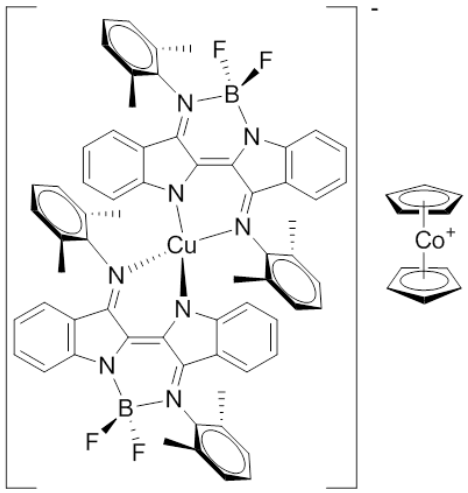

[4.2c]$^{-}$

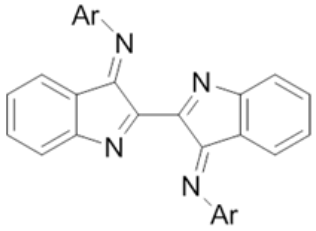

5.1a Ar = phenyl
5.1b Ar = pTolyl
5.1c Ar = 2,6-dimethylphenyl
5.1h Ar = mes

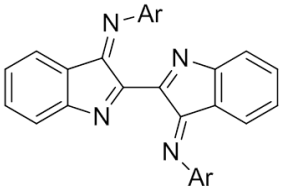

5.1'

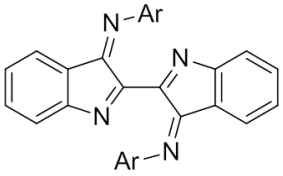

5.1"

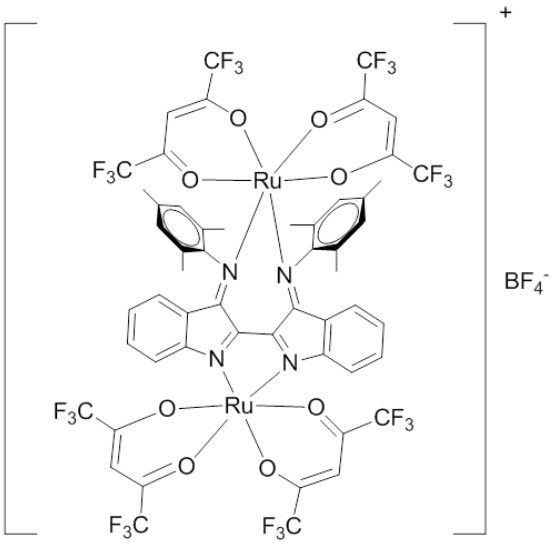

[5.2h-cis]$^{+}$

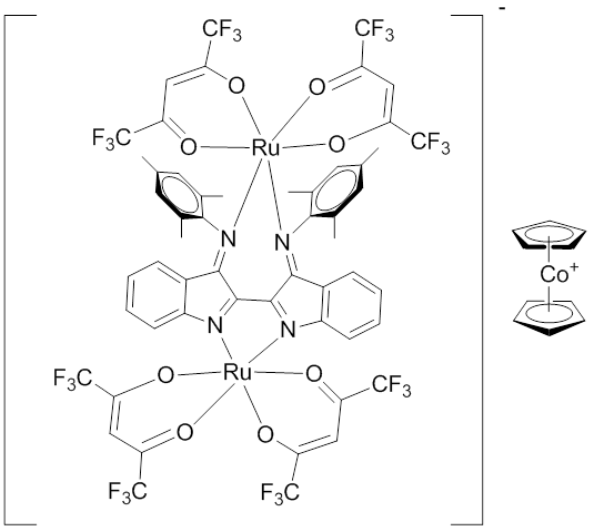

[5.2h-cis]$^{-}$

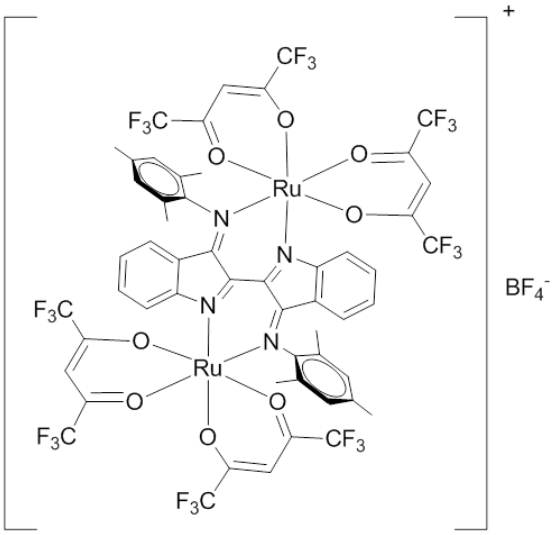

[5.2h-trans]$^{+}$

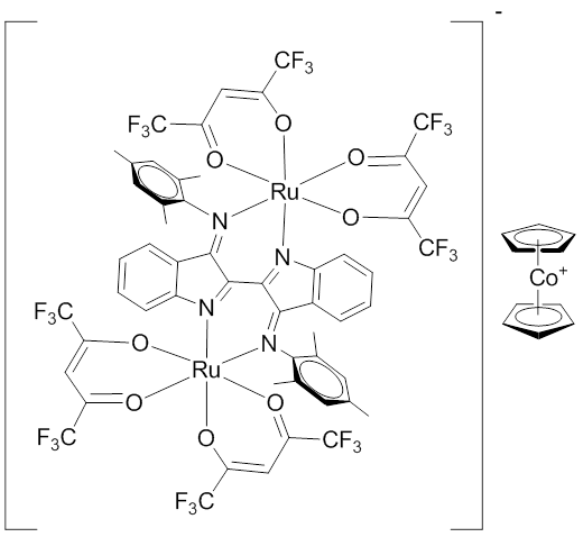

[5.2h-trans]$^{-}$

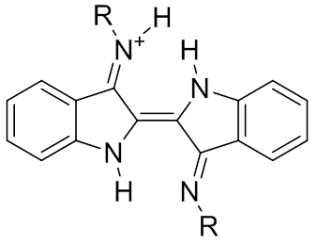

6.1

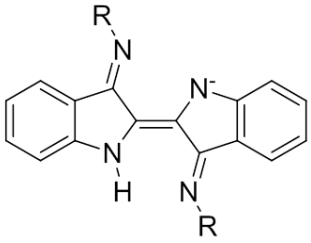

6.2

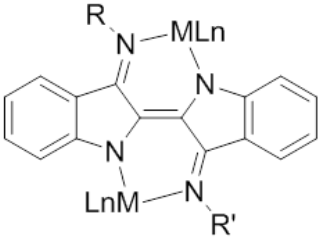

6.3

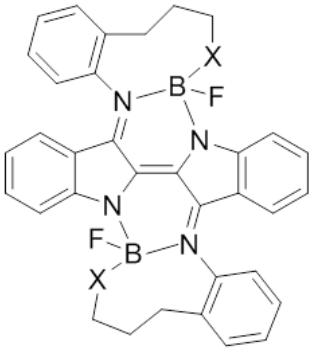

6.4

List of Abbreviations

1D	one-dimensional
2D	two-dimensional
3D	three-dimensional
A	absorbance
A.U or a.u	absorbance units
Å	angstroms
acac	acetylacetonoate
Ar	aromatic group
Bipy	2,2'-bipyridyl
BODIPY	4,4-difluoro-4-bora-3a,4a-diaza-s-indacene
nBu	n-Butyl
^{o}C	degrees Celsius
C	carbon atom
ca.	approximately
CH_2Cl_2	dichloromethane
cm	centimeter
cm^{-1}	wavenumber
Cp	cyclopentadienyl
CT	charge-transfer
$Cu(OAc)_2.2H_2O$	copper(II)acetate dihydrate
CV	cyclic voltammetry
d	doublet
^{o}	degrees

DABCO	1,4-diazabicyclo[2.2.2]octane
DCM	dichloromethane
DIPEA	N,N-diisopropylethylamine
δ	parts per million (chemical shift, NMR)
Δ	heat or difference or denotes chirality
DFT	density functional theory
DMSO	dimethylsulfoxide
DPPH	1,1-diphenl-2-picrylhydrazyl
D_2O	deuterium oxide
ε	molar extinction coefficient
e^-	electron
EI	electron impact
emu	electromagnetic units
EPR	electron paramagnetic resonance
eq	equivalents
Et_3N	triethylamine
eV	electron volt(s)
E^{cell}	electrode potential
E_{ox}	oxidation potential
E_{red}	reduction potential
Et	ethyl
Fc	ferrocene
Fc^+	ferrocenium
FMO	frontier molecular orbital(s)
g	g-factor

G	Gauss
GalOA	galactose oxidase
GHz	gigahertz
H_2O	water
hfac	1,1,1,5,5,5-hexafluoroacetylacetonoate
HRMS	high resolution mass spectrometry
HOMO	highest occupied molecular orbital
Hz	hertz
i or ^{i}	ipso
IET	intramolecular electron transfer
IR	infrared
IVCT	inter-valence charge-transfer
J	coupling constant (NMR)
K	Kelvin
kcal	kilocalorie
K_c	comproporptionation constant
λ	wavelength
λ_{max}	wavelength of maximam electronic absorption
Λ	denotes chirality
LLCT	ligand-to-ligand charge transfer
LMCT	ligand-to-metal charge-transfer
LUMO	lowest unoccupied molecular orbital
m	multiplet (NMR)
M	molarity
Me	methyl

MeCN	acetonitrile
μ	denotes bridging ligation
μA	microamps
μg	microgram
MB	mono-BF_2 Nindigo chelate
MeOH	methanol
mg	milligram
MHz	megahertz
min	minute(s)
MLCT	metal-to-ligand charge-transfer
mol	mole
mol^{-1}	per mole
mmol	millimole
MS	mass spectrometry
mV	millivolt
MV	mixed valence
m/z	mass per unit charge
N	nitrogen donor
NacNac	diketimine
NaOH	Sodium hydroxide
nBuOH	n-butanol
NIR	near infrared
nm	nanometer (10^{-9} m)
NMR	nuclear magnetic resonance
O	oxygen donor

Oxi	oxidation
O or ^{o}	ortho
p	para
Ph	phenyl
ppm	parts per million
q	quartet (NMR)
RAL	redox-active ligands(s)
Red	reduction
s	singlet (NMR)
s^{-}	per second
SOMO	singly occupied molecular orbital
t	triplet (NMR) or time
t	tertiary
T	temperature
TCNE	tetracyanoethylene
TCNQ	tetracyanoquinodimethane
THF	tetrahydrofuran
TLC	thin layer chromatography
UV	ultraviolet
V	volt
vis	visible
vs.	versus
VT	valence tautomerizm
XPS	X-ray photoelectron spectroscopy
$Zn(OAc)_2.2H_2O$	zinc(II)acetate dihydrate

Acknowledgments

Firstly I would like to acknowledge the efforts of my supervisor Dr Robin Hicks for guidance, support and patience. He gave me the freedom to develop as a synthetic chemist and was instrumental in building my confidence in communicating chemistry to others. I would also like to thank the Hicks-Frank household for numerous splendid social events and loaning me Zelly to walk on occasion.

Thank you also to Hicks group members past and present for personal and professional support as well as sharing synthetic ideas. Many thanks to Dr Steve MacKinnon, Dr Tyler Trefz, Dr Kevin Anderson, Bart Nowak, Cooper Johnston, Corey Sanz, Gennevieve Boice, Emma Nichols-Allison. Also, a big thank you to Aman Bains, Mark Zsombor and Aiko Kurimoto. In addition I would like to acknowledge the various undergraduate students that contributed to this work; Kate Waldie, Bryan Robertson and Brenden Peters.

I would like to thank the many staff and faculty of the chemistry department that have all contributed to making my time at UVic both enjoyable and academically fruitful.

Finally I would like to thank my team mate Meg. You have taught me so many things and I am blessed to have you in my corner.

Dedication

For you, Mum.

……. If you can meet with Triumph and Disaster
And treat those two impostors just the same…..

- R. Kipling

Chapter 1: Introduction

1.1 Ligand design

The world of coordination chemistry is symbiotic in such a way that for any chemical action to occur effectively it requires the mutual participation of both metal centre and ligand set that surrounds it. For this reason the use of ligand design to control the properties of coordination complexes pervades chemistry. There are a variety of ligand attributes that can be manipulated in order to control the reactivity at the metal centre. The steric nature, hapticity, denticity and hemi-lability of the ligand can be tuned to govern the availability of free sites, whilst electron donating and withdrawing groups can be selectively positioned to alter the electronic properties of the coordination complex. Amongst the first to achieve great success in tuning both the electronic and steric properties of coordination compounds were the cyclopentadienyl **(1.1)**, polydentate phosphines **(1.2)** and polydentate amines and pyridines **(1.3)**.

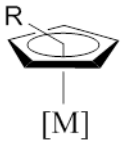

1.1

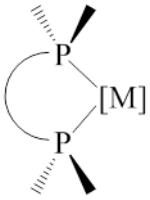

1.2

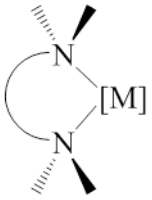

1.3

Varieties of the above ligand groups can be seen throughout many aspects of inorganic and organometallic chemistry where they facilitate catalytic reactions at metal centres as well as numerous organic transformations.

1.1.1 N-Donor ancillary ligands

One of the more recent successful examples of ligand design was the emergence of the ancillary ligand, β-diketiminate, commonly known as NacNac (**1.4**).[1,2] This chelating ligand is the N-analogue of the acetylacetonate, acac, (**1.5**) ligand set. The conversion of the carbonyl moieties to imines introduces a point for tuning and controlling the properties of resulting complexes. As a result, a diverse range of coordination compounds incorporating NacNac have been explored.

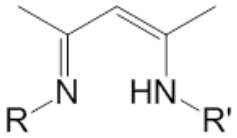

1.4

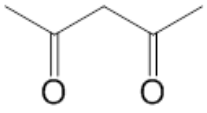

1.5

Other π-conjugated polydentate ancillary ligands that are based on the isolobal replacement of O by NR include, but are not limited to, aminotoponiminates[3] (**1.6**), diimino pyridines[4,5] (**1.7**), α-dimines[6,7] **(1.8)** and amidinates[8,9] (**1.9**). The attractiveness of these ligand families stems from straightforward syntheses and the ability to tune the N-substituent.

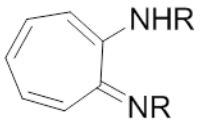

1.6

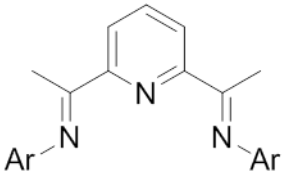

1.7

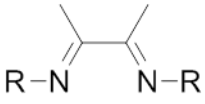

1.8

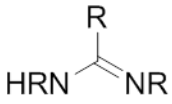

1.9

1.2 Redox-active ligands (RALs)

Although ligands undoubtedly facilitate the chemistry of coordination compounds, in general they are spectators with respect to any chemical transformations. Owing to the redox potentials of the metal centre being more accessible than that of the surrounding ligand set, the electron transfer role is

traditionally filled by the metal. A lot of chemical transformations involve two-electron chemistry, this requires metal centres that are able to change oxidation state by two. This attribute is generally reserved for precious metals (iridium, ruthenium, rhodium, osmium *et al*) and is why they can often be found at the heart of numerous catalysts. However, if the potentials of the ligand set and the metal centre can come close in energy, there is the possibility that the ligand can participate in redox changes itself. Ligand sets that are able to give and receive electrons, known as redox-active ligands (RALs), are now being investigated for their potential use in coordination compounds of earth abundant metals to perform catalytic and stoichiometric reactions.

Understanding the nature of the oxidation states of atoms, especially metal centres, is central to understanding the chemistry of molecules. The oxidation state concept, as illustrated by numerous textbooks, is frequently used and generally accepted to generate formal oxidation states. However, the concept is often disputed when it comes to physical (spectrochemical) oxidation states.[10,11] In the mid 1960's Christian Klixbüll Jørgenson described ligands as suspect (later non-innocent) after establishing non-integer oxidation state values for a series of complexes.[11,12] Early pioneers in RAL chemistry suffered from the lack of analytical tools available to the modern chemist and as a result there was much debate over the assignment of oxidation states. One of the complexes at the centre of the early debates was a nickel (II) bisiminoquinone species. Two electronic structures were proposed, one a diradical (**1.10**) and the other involving the combination of a neutral and dianionic ligand set (**1.11**).[13-15]

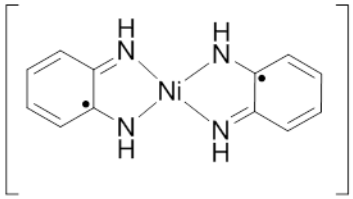

1.10

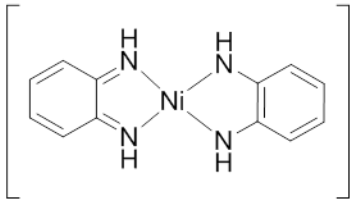

1.11

As characterization methods become more advanced a clearer picture of the oxidation states of redox-active systems developed. The methods involved in elucidating the nature of redox events (spectroscopic, structural, magnetic and theoretical modeling)[16] have been deemed so elegant that their use has been branded "art" by those involved.[17] RALs mimic the abilities of transition metals in two important ways. They adopt more than one oxidation state and support an open-shelled configuration

in one or more of these accessible oxidation states. One of the early RAL groups and still one of the most studied are the *o*-quinones[18] (**1.12**), their nitrogen[19] (**1.13**) and their mixed donor analogues[20] (**1.14**).

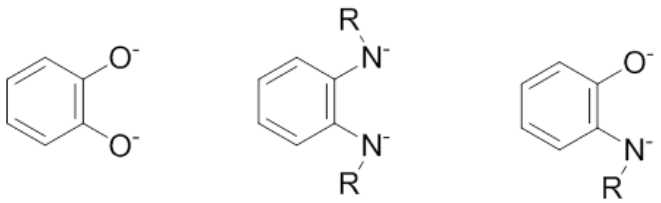

1.12 **1.13** **1.14**

It is the ability of these ligand sets to exist in a variety of oxidation states that resulted in a menagerie of complexes being synthesized and the conventional oxidation state assignment protocols being challenged (**Figure 1.1**).

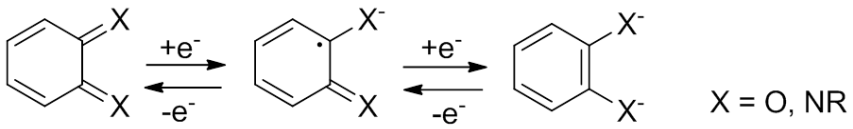

Figure 1.1: The three oxidation states of *o*-benzoquinone type molecules (neutral quinone, monoanionic semiquinonate, and the dianionic catecholate)

RALs have also been found to exist in several domains of bioinorganic chemistry with perhaps the best understood example being galactose oxidase (**Figure 1.2**). The two-electron redox chemistry required for the oxidation of an alcohol to an aldehyde arises from the cooperation of both the copper centre and the coordinated phenoxyl ligand.[11,21]

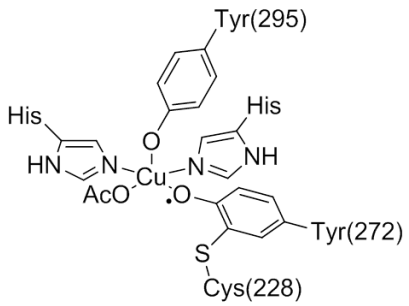

Figure 1.2: The active site of galactose oxidase (GalOA)

Several synthetic mimics for GalOA have been developed incorporating a variety of RALs.[22] Two examples are shown below involving *ortho*-iminosemiquinonate[23] (**1.15**) and Salen type ligands[24] (**1.16**).

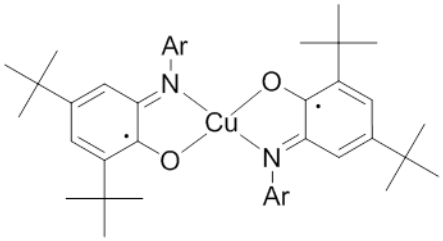

1.15

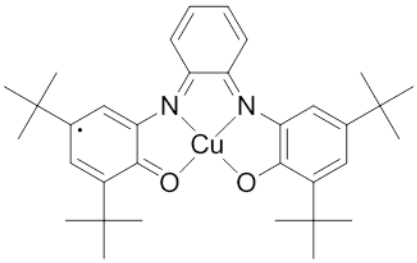

1.16

More recently, complexes containing RALs have been shown to facilitate catalytic and stoichiometric reactions including bond forming reactions, disproportionations, hydrosilylations, and water and alcohol oxidations.[25-31] The RAL acts as a reservoir that stores/shuttles electrons to and from the active site when needed. In some cases the RAL is the sole supplier of electrons with the metal centre acting as a static anchor where the substrates can come together (**Figure 1.3**).[32,33]

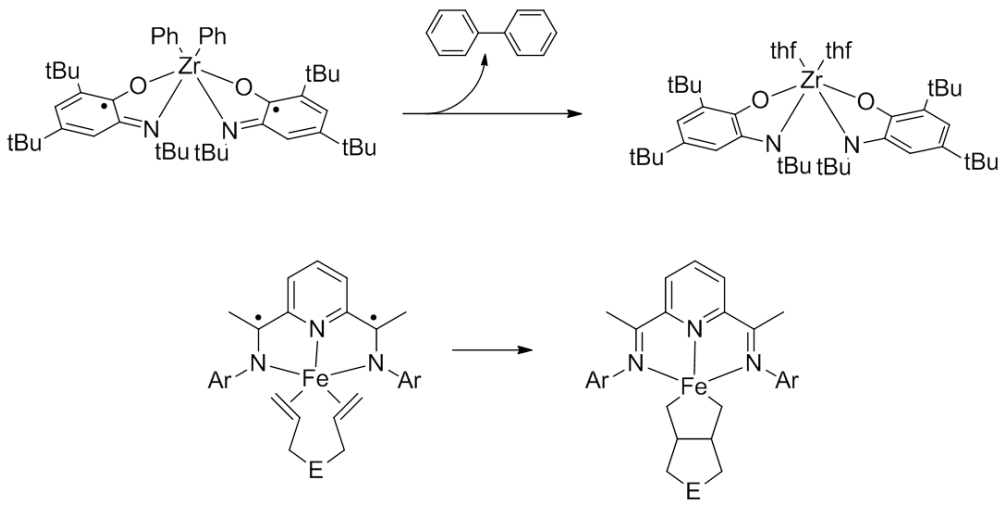

Figure 1.3: Ligand based redox chemistry facilitating 'molecular reductive elimination' (top) and cycloaddition (bottom) reactions

1.2.1 Redox-active bridging ligands

Whilst RALs that bind to a single metal centre have become somewhat prevalent, RALs that are able to bridge between more than one metal are less common. Of the somewhat sparse examples in the literature, those based on the benzoquinoid family of molecules are again the most common (**1.17**.[34-36] Despite the popularity of phosphorous containing moieties in ancillary ligation, examples of coordination compounds involving phosphorous based redox-active bridging ligands are limited to just one family, bis(phosphinyl)hydroquinone (**1.18**), with the use of this ligand in bimetallic complexes limited to just three examples.[37,38] Polymeric bis(pyrazole)quinone (**1.19**) chains involving copper centres have also been studied, in this case for their 1D magnetic properties.[39] The redox-activity of all three ligand sets arises from the readily accessible catecholate, semiquinonate and quinone redox states.

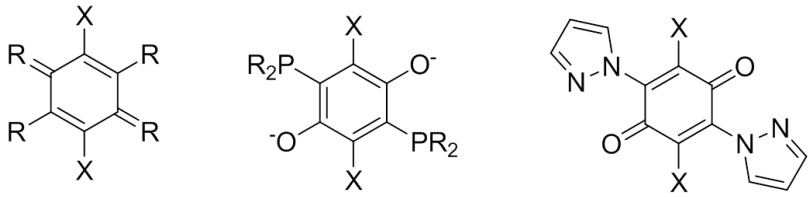

1.17 **1.18** **1.19**

Another example of a conjugated redox-active bridging ligand system is the polynitriles. Ligands based on tetracyanoethylene (**1.20a**) and tetracyanoquinonedimethane (**1.20b**) have been shown to exhibit redox-active behavior as well as a variety of 1D, 2D and 3D networks that display interesting conducting properties.[40,41] Related to **1.20** are systems based on N,N'-dicyanobenzoquinonedimines (**1.21**). Selected complexes of **1.21** exhibit high conductivities with significant tolerance of functionality allowing for high levels of control.[42] The redox-activity in these systems arises from the numerous cyano groups present in conjugation. This gives rise to low energy π* orbitals and renders the ligand sets highly electron accepting and thus stable radical anions and dianions are accessible.

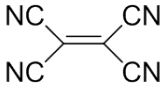

1.20a

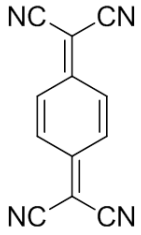

1.20b

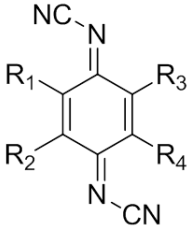

1.21

Tetrazines (**1.22**) have also been shown to effectively bridge metals and, depending on the nature of the 3,6-substituents (X), the degree of nucleation can be controlled.[43] 2,2'-azobypyridine (**1.23**) and related 'S-frame' azo containing functions have also been probed as redox-active bridging ligands.[44] Both **1.22** and **1.23** are strongly electron accepting and can be reduced to give radical anionic and dianionic ligand redox states.

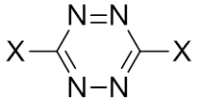

1.22

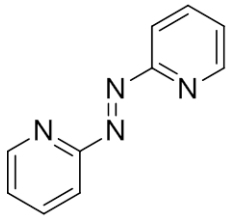

1.23

Finally, bipyrimidines (**1.24**) and multidentate pyrazine derivatives (**1.25**) have been shown to effectively bridge metal centres. These ligand sets are able to undergo reversible one-electron reductions to generate radical anions.

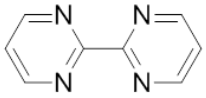

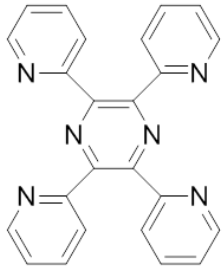

1.24 **1.25**

All of the above examples (and RALs in general) possess extended π-delocalization. This aids in both accessing and stabilizing various redox states. However, in most cases these ligands lack the potential for derivitization and so cannot be easily tuned. Examples of tunable multidentate bridging RAL systems are rare. One such example is bis(imino)acenapthene (TIP) (**1.27**).[45,46] This is the bifunctional analogue of the redox-active capping ligand, BIAN (**1.26)**. Control of the resulting coordination compounds properties can be gained by varying the N-substituents. **1.27** can undergo two reversible one-electron reductions at both imine functionalities with the resulting dianion exhibiting significant delocalization over both diazabutadiene moieties.

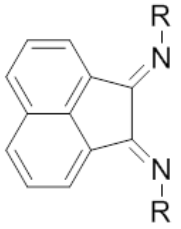

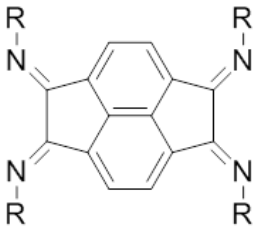

1.26 **1.27**

1.3 Indigo

One of the earliest known dyes, the use of indigo (**1.28**)[47] dates back millennia where it was used all over the globe for its intense colour.[48] Indigo was originally extracted indirectly from the leaves of plants belonging to the genus *indigofera*. Owing to the difficulty in obtaining indigo in any substantial

quantities and the difficulties with manipulating it to dye fabrics, it was such a luxury that it was often referred to as blue gold.

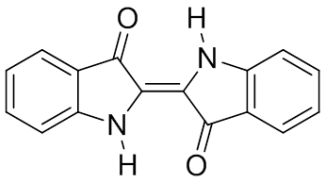

1.28

Despite its wealth of history, the structure of indigo was not established until 1883 by Nobel laureate Adolf Von Baeyer.[49] (Its *trans* configuration was not determined until 1928)[50]. The structural elucidation resulted in a boom of synthetic procedures to produce indigo on a commercial scale. Some 38,000 tonnes of indigo are now produced *per annum* with the primary use being to dye denim.[51,52]

Compared to similar sized conjugated molecules, indigo exhibits unusually long wavelength absorption. A variety of calculations on indigo have established that the chromophore consists of two donor groups (NH) and two acceptor group (C=O) in a doubly cross conjugated arrangement (**Figure 1.4**).[53-57] The donor groups raise the energy of the HOMO and acceptor groups lower the energy of the LUMO resulting in the low energy transition.[57,58]

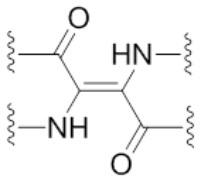

Figure 1.4: The fundamental "H-chromophore" of Indigo

In general indigo is seen as blue in colour. However, it exhibits different colours depending on its phase and solid state morphology (gas phase λ_{max} = 540 nm, crystalline λ_{max} = 675 nm, amorphous λ_{max} = 650 nm)[59,60]. In addition, the planarity of the molecule gives rise to aggregation effects in solution that

alters the colour of the dye under certain conditions. At high concentrations or low temperatures indigo undergoes J-type aggregation resulting in a red shift of λ_{max} from 603 nm to 700 nm (**Figure 1.5**).[61]

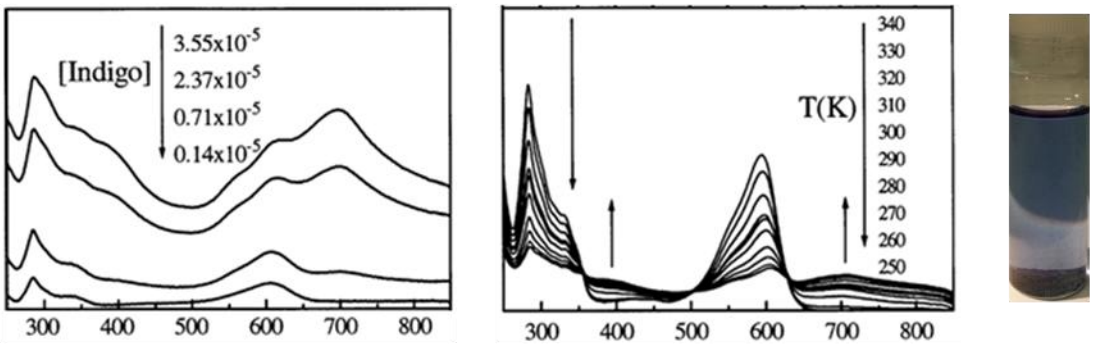

Figure 1.5: UV/vis/NIR spectra of indigo at varying concentrations (left) and varying temperature (right) (reprinted with permission from *Molecules*)[61] along with a photo of a saturated solution of indigo in DCM

In solution, indigo exhibits positive solvatochromism resulting in colour variance from violet to blue. This is as a result of the ground state being neutral with the excited state being a combination of charge separated resonance structures (**Figure 1.6**).[59]

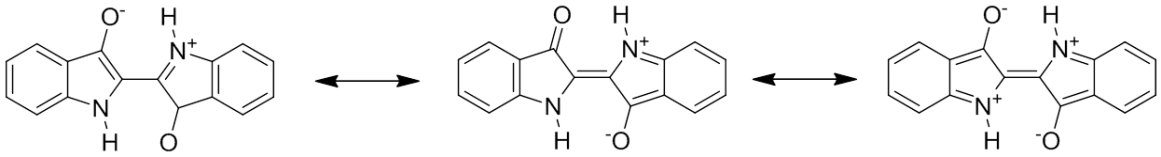

Figure 1.6: Resonance contributions to the indigo excited state

Other highly coloured indigo derivatives exist that possess various functional groups on the peripheral rings. Tyrian purple (**1.29**) contains bromines on the benzannulated rings and the water soluble indigo carmine (**1.30**) possesses sulfonate groups. These additional subsituents somewhat perturb the electronic spectra resulting in the compounds displaying different colours. Derivatives with different donor units also exist resulting in dramatic colour changes. Thioindigo (**1.31**) contains two

sulfur atoms in place of the NH groups and is deep red in colour. The inherent problem with all simple indigo derivatives is their extreme lack of solubility. Whilst this may be desirable for their pigment based applications, this insolubility is a hindrance for performing coordination chemistry.

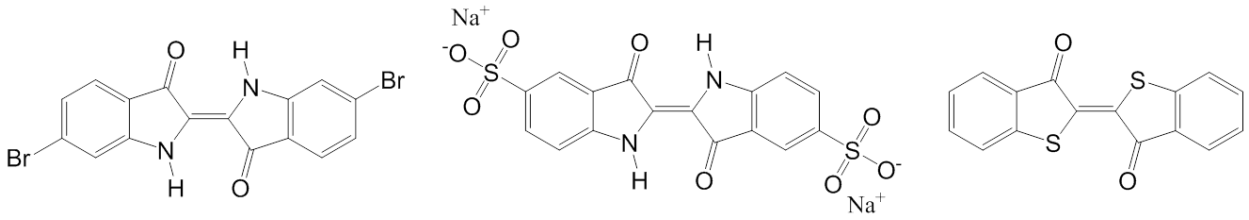

1.29 **1.30** **1.31**

In order to address the solubility issue, numerous bulkier indigoid compounds have been synthesized (**Figure 1.7**). Whilst various new derivatives have been shown to have improved solubility, their syntheses are not straightforward and require multi step reactions. [62-64]

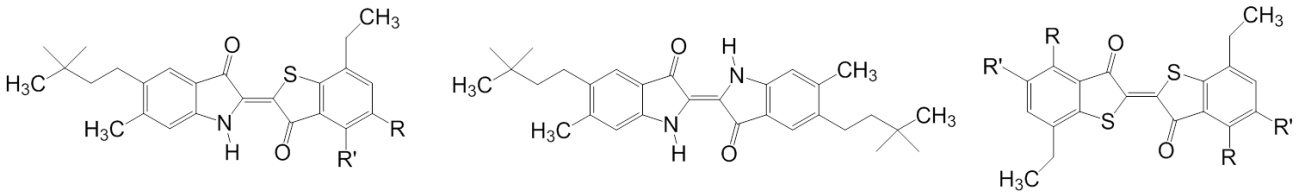

Figure 1.7: Bulkier indigoid derivatives

1.3.1 Coordination chemistry of indigo

Despite possessing some inherently attractive features structurally - with a bis-bidentate chelating motif - and economically - with its relative inexpense and commercial availability, the use of indigo, and closely related molecules, in coordination chemistry has been limited to just a handful of examples. In the early 20th century a variety indigo chelate complexes of copper, nickel, zinc and cobalt were reported, but owing to a lack of characterization techniques their structures were left somewhat in

doubt.[65-70] It was not until the latter part of the century that palladium and platinum complexes of indigo were conclusively synthesized (**Figure 1.8**).[71-72] Whilst these compounds were fully characterized, their capacity to undergo chemistry was not investigated. This was likely because they maintain the same high degree of insolubility as their parent indigoids. This issue was addressed by employing saturated indigo derivatives e.g. octahydroindigo. The fundamental chromophore is preserved but the resulting complexes possess slightly more freedom and thus do not adopt a planar geometry.[73]

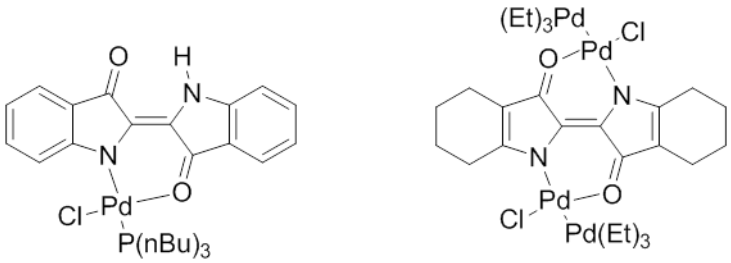

Figure 1.8: Early indigo based coordination complexes, Indigo[Pd(nBuP)$_3$Cl] (left) and octahydroindigo[Pd(Cl)PEt$_3$]$_2$ (right)

The coordination chemistry of indigo remained largely undeveloped until its incorporation into an elaborate hexarhenium cluster reported in 2008.[74] This exotic molecule was later shown to possess rich redox behaviour and NIR absorption , both of which are ligand centered in origin (**Figure 1.9**).[75]

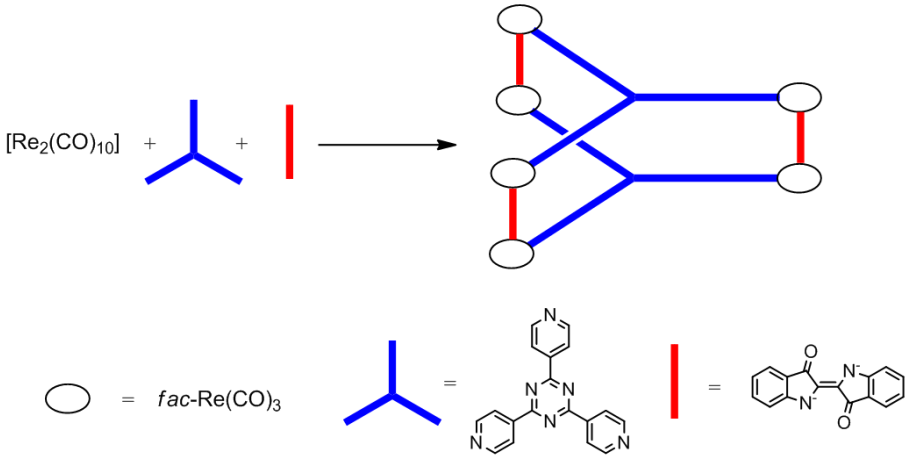

Figure 1.9: Rhenium indigo cluster

1.3.2 Previous Nindigo research

The inherent insolubility and lack of facile routes to derivitization renders indigo challenging to exploit as a bridging ligand. Much in the same way as NacNac was developed as an extension to acac, one could envision the same conversion of indigo to the N-analogue (Nindigo), **1.32**. The resulting molecule seemed to be a potentially attractive bridging ligand where the N-subsituents could improve solubility as well as offer a handle for tuning the attributes of resulting coordination compounds.

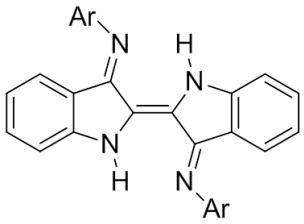

1.32

The first reported synthesis of indigo diimines was in 1909.[76] The simplest of all previous syntheses, indigo was heated in neat aniline in the presence of boric acid, the latter perhaps acting as both a drying and activating agent to promote the forward condensation reaction. However, this synthesis has since been brought into disrepute due to problems with reproducing the data.[77] Alternative pathways have involved the thermal oligomerisation of aryl isocyanides[78] and reactions of bis-imidoylchlorides of oxalic acid with powdered magnesium (reducing agent) under ultrasonic conditions.[77,79] The poor yields combined with complex syntheses and limited substrate scope renders these methodologies of limited use in ligand design.

Unactivated ketones have been reported to be activated by $TiCl_4$ during the formation of N-sulfonylimines (**Scheme 1.1**).[80] The $TiCl_4$ was thought to act as both a Lewis acid activator and drying agent with an auxiliary base employed to mop up the generated HCl. The use of $TiCl_4$ was subsequently shown to aid the conversion of the carbonyl groups of anthraquinone to imines (**Scheme 1.2**).

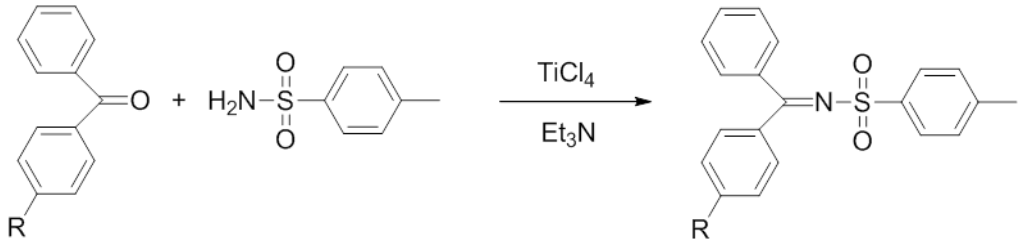

Scheme 1.1: Formation of N-sulfonylimines using $TiCl_4$

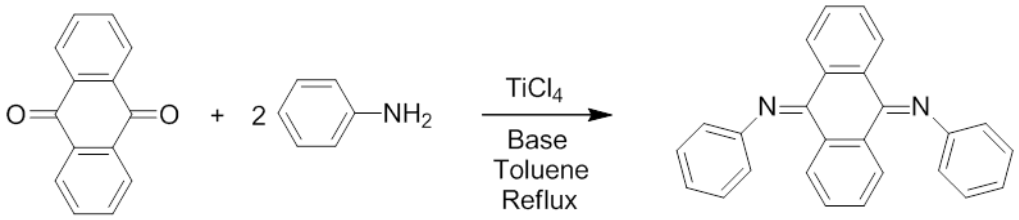

Scheme 1.2: Converting the carbonyl groups of anthraquinone to imines using $TiCl_4$

During the synthesis of anthraquinonediimine it was found that the order of reagent addition effects the yield of the product.[81] Combining $TiCl_4$ with the aniline in the presence of the base before addition of the substrate was shown to be the most efficient method. It is postulated that the $TiCl_4$ and aniline come together to form a titanium imido type intermediate. This highly nucleophilic species subsequently reacts with the anthraquinone substrate to form the diimine (**Figure 1.10**).

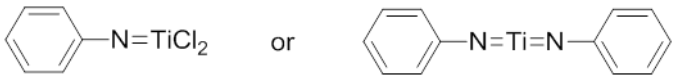

Figure 1.10: Postulated reactive intermediates during reaction

The nature of the base was also found to have an effect on the course of the reaction. When triethylamine (and other bases possessing α-hydrogen atoms) were employed, a black tarry side product was observed. This was not present when non-α-hydrogen containing bases or hindered bases were

used e.g. DABCO. It is thought that a redox reaction occurs to form a radical cation with subsequent α-hydrogen loss leading to a stabilized imonium ion (**Figure 1.11**).[82] Bicylic bases do not have the option of stabilizing the iminium ion as the resulting bridgehead olefin would be in direct violation of Bredt's rule.[83]

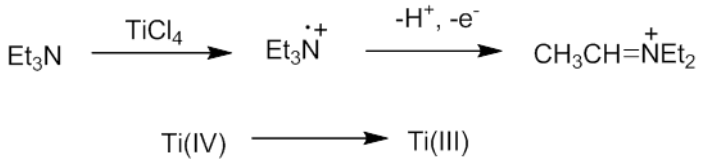

Figure 1.11: Postulated redox side reaction that occurs when the base contains unhindered α-hydrogen atoms

Using similar conditions a modest library of Nindigo ligands were synthesized in yields that are dependent upon the nature of the aniline used.[84] Anilines possessing electron withdrawing groups resulting in the isolation of Nindigo in lower yields (**Scheme 1.3**). With the exception of **1.31i**, the reaction is limited to aromatic groups.

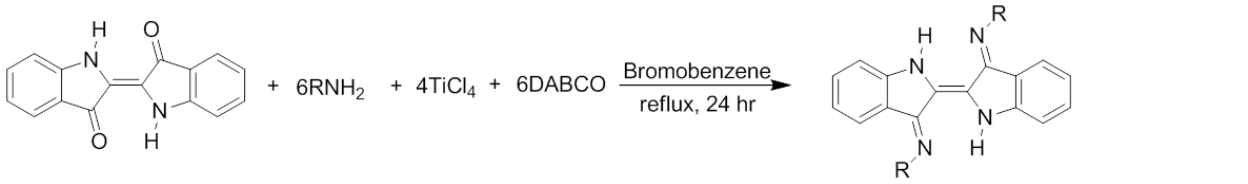

1.32b R = p-tolyl (pTol) [67%]
1.32f R = pchlorophenyl (pClPhen) [63%]
1.32h R = mesityl (Mes) [42%]
1.32i R = tButyl (tbutyl) [60%]
1.32j R = pmethoxyphenyl (pMeOPhen) [64%]

Scheme 1.3: General conditions used for Nindigo synthesis

All derivatives of **1.32** showed improved solubility in a range of solvents with respect to indigo. The high intensity, low energy absorption is maintained with the colours of DCM solutions ranging from blue to purple depending on the N-aryl subsituents (**Figure 1.12**).

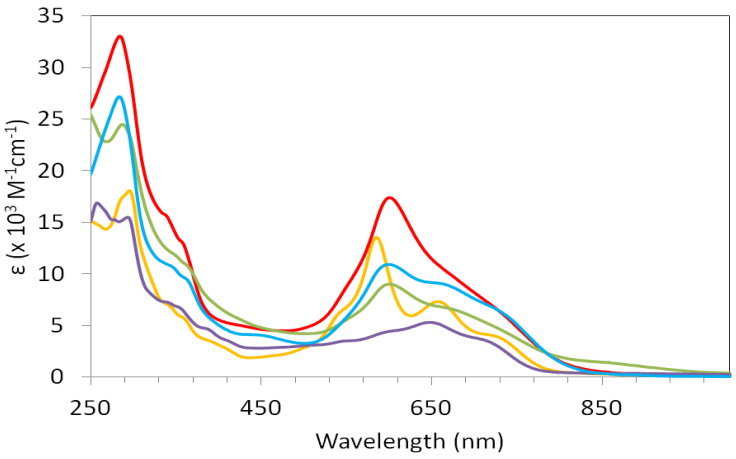

Figure 1.12: UV/vis/NIR spectra of **1.32b** (blue), **1.32f** (green), **1.32h** (orange), **1.32i** (purple), **1.32j** (red). Spectra obtained in DCM at a concentration of 1.25 x 10^{-5} M

The ability of Nindigo to act as a bridging ligand was probed by reactions with palladium bis(hexafluoroacetylacetonoate). This generated bis-Pd(hfac) chelates of Nindigo (**Scheme 1.4**). [85,86]

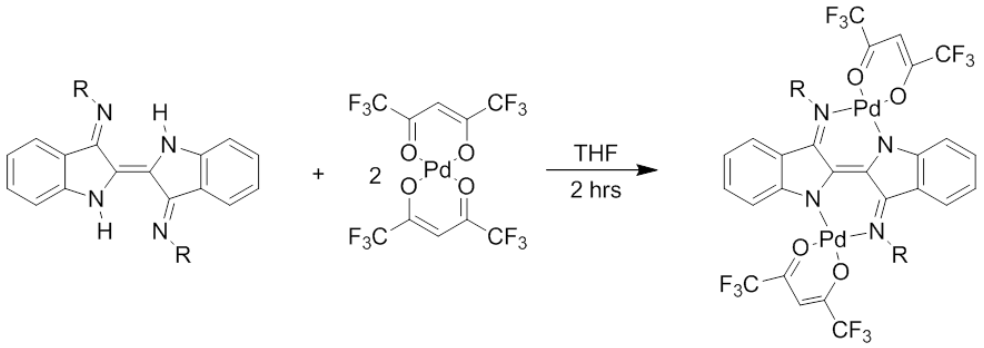

1.33a R = phen [60%]
1.33b R = *p*-tolyl [68%]
1.33f R = *p*-chlorophenyl [57%]
1.33i R = *t*-butyl [15%]
1.33j R = *p*-methoxyphenyl [58%]

Scheme 1.4: General conditions used for the synthesis of bis-Pd(hfac) chelates of Nindigo

The solubility traits of the resulting complexes were found to match those of the parent Nindigos. The absorption spectra of the complexes were found to undergo a significant red shift with respect to the free Nindigo (**1.33b** λ_{max} = 912 nm, **1.32b** λ_{max} = 600 nm) **(Figure 1.13)**.

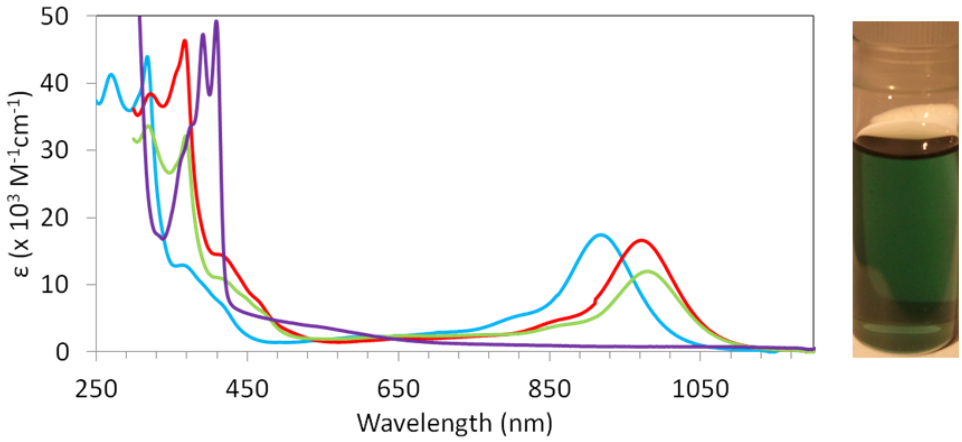

Figure 1.13: UV/vis/NIR spectra for previously synthesized **1.33b** (blue), **1.33f** (green), **1.33i** (purple), **1.33j** (red). Spectra obtained in DCM at a concentration of 1.25 x 10^{-5} M. Photograph of **1.33b** in DCM solution (right) (all photographed solutions are approximately 0.1 µg/mL in DCM unless otherwise stated).

Palladium bis(hexafluoroacetylacetonate) was employed as the metal precursor because the resulting complexes would then consist of square planar palladium (II) centres. The benefit of this is the d^8 configuration not only renders the palladium centre redox inert,[87,88] but it simplifies characterization as the complexes are diamagnetic.

Cyclic voltammetry experiments were conducted to probe the ligand redox-activity. All derivatives were found to be electrochemically active with some derivatives exhibiting both reversible oxidation and reduction processes (**Figure 1.14**).

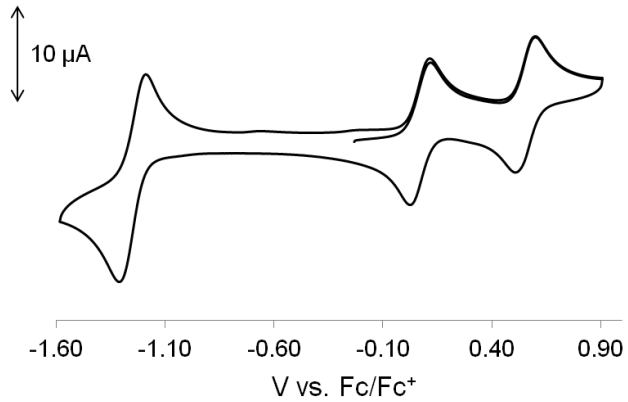

Figure 1.14: Example cyclic voltammogram of **1.33a**

1.4 Thesis objectives

Earlier work by Oakley established the potential of Nindigo as a new bridging ligand system with an attractive range of properties.[84] The work presented in this thesis represents a significant expansion of the chemistry of Nindigo. Specifically, the redox-activity and spectral properties have been explored through a variety of coordination compounds with a few to probing any changes that may arise from chelation of either transition metal or main group elements.

Chapter 2 highlights improvements made to the synthesis of Nindigo and diversifies the Nindigo library. The concept of Nindigo tautomerism is explored as well as the *trans*/*cis* isomerization observed for palladium chelates of bulky Nindigo derivatives.

Chapter 3 focuses on main group coordination compounds of Nindigo. Nindigo compounds containing one and two boron moieties have been synthesized to further probe the electronic nature of the Nindigo ligand as well as to probe the potential for NIR fluorescence. Mixed boron/palladium chelates are also described and their chemistry compared with that of the homonuclear (bis-BF_2 and bis-Pd(hfac)) derivatives.

Chapter 4 presents further exploration of mono-boron chelates of Nindigo; specifically, homoleptic zinc and copper complexes are discussed and their electronic properties probed for the potential metal-ligand non-innocence.

Chapter 5 introduces the fully oxidized Nindigo derivative, DehydroNindigo. Ruthenium dimers of dehydroNindigo have been synthesized and their mixed valence states examined.

Chapter 6 provides a global summary of the progress made regarding Nindigo chemistry as well as discussion of the possible future directions for Nindigo.

Chapter 2: Synthesis and characterization of Nindigo derivatives

2.1 Introduction

As discussed in chapter 1, the focus of this work is on exploring the versatility of indigo diimines (Nindigos) with respect to redox-activity, colour and coordination chemistry. Prior to the research undertaken in the Hicks group, the synthesis of Nindigos had been limited to a handful of examples. These will be briefly discussed along with further exploration and development of the Nindigo chemistry established by Oakley – specifically, ligand synthesis and palladium coordination chemistry.

2.2 Synthesis and characterization of indigo monoimines and indigo diimines (Nindigos)

2.2.1 Synthesis

Oakley was successful in establishing a synthetic pathway for the conversion of indigo to Nindigo. However, the forcing conditions and long reaction times necessary provided motivation to seek a milder more efficient synthesis. Initial attempts to convert the carbonyl moieties of indigo into imine functionalities via acid catalyzed condensation reactions were unsuccessful. It was thought that the water by-product was encouraging the reverse condensation reaction. The use of a Dean Stark apparatus to remove the water and thus drive the equilibrium towards imine formation was also unsuccessful and no water was ever observed. In order to move the synthesis forward two ideas were explored;

1) Employ a Lewis acid to activate the carbonyl groups of indigo with the hope of making them more susceptible to nucleophilic attack.
2) Use a thermodynamic driving force to promote the imine formation and shut down the back reaction.

A variety of Lewis acids have been shown to be effective in promoting imine formation of weakly electrophilic and nucleophilic substrates.[89] However, under similar conditions these procedures were not successful in the conversion of indigo to Nindigo and no reaction was observed (**Scheme 2.1**).

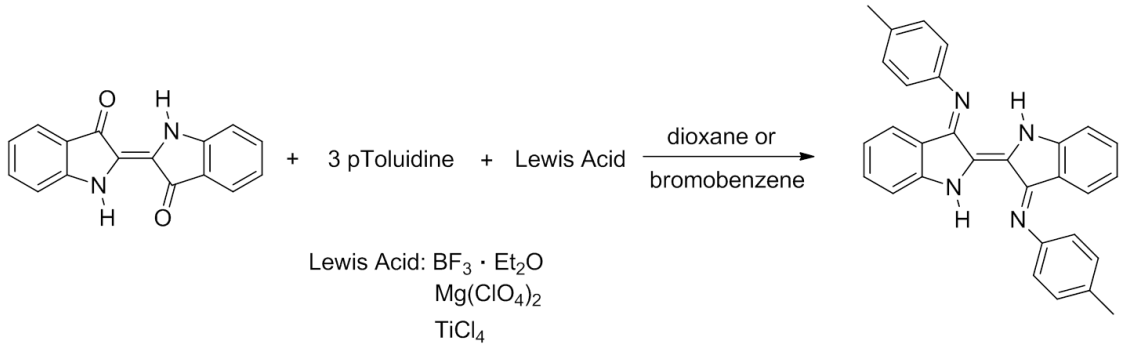

Scheme 2.1: Attempted Nindigo formation employing a variety of Lewis Acids

The use of silylamines was explored in the hopes of driving the conversion thermodynamically via the formation of Si-O bonds in the silyl ether by-product (**Scheme 2.2**).

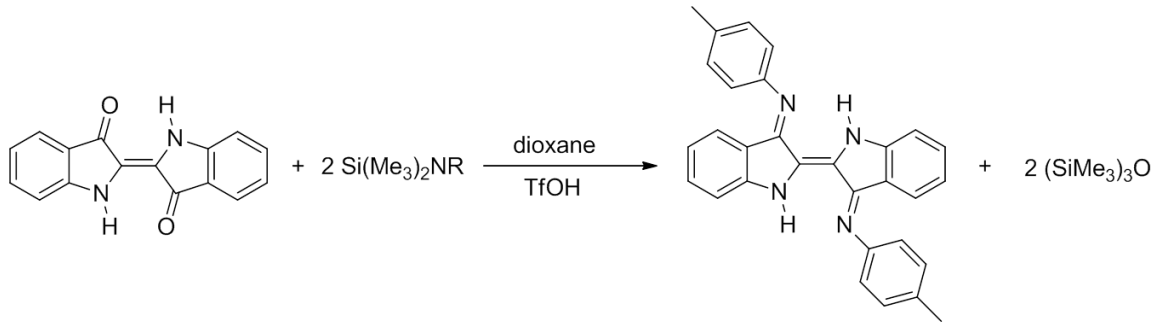

Scheme 2.2: Attempted Nindigo synthesis employing silylamines

Unfortunately this strategy was also unsuccessful and it was decided to continue with the reaction conditions previously established by Oakley. Due to the high insolubility of indigo in most solvents, reactions were initially attempted in dioxane after conducting solubility tests. The reagent stoichiometries were as previously reported (2.5 eq aniline, 1.5 eq of $TiCl_4$ and 6 equivalents of DABCO with the reaction left to reflux for 15 hours).[85,86] Initial reactions incorporating 2,6-dimethylaniline and 2,6-diisopropylaniline proceeded to yield dark purple solids (**2.1c** and **2.1d**), typical of those Nindigos previously synthesized. However, the ^1H NMR spectra of these compounds did not exhibit the number and pattern of signals expected for bis-imine formation (**Figure 2.1**).

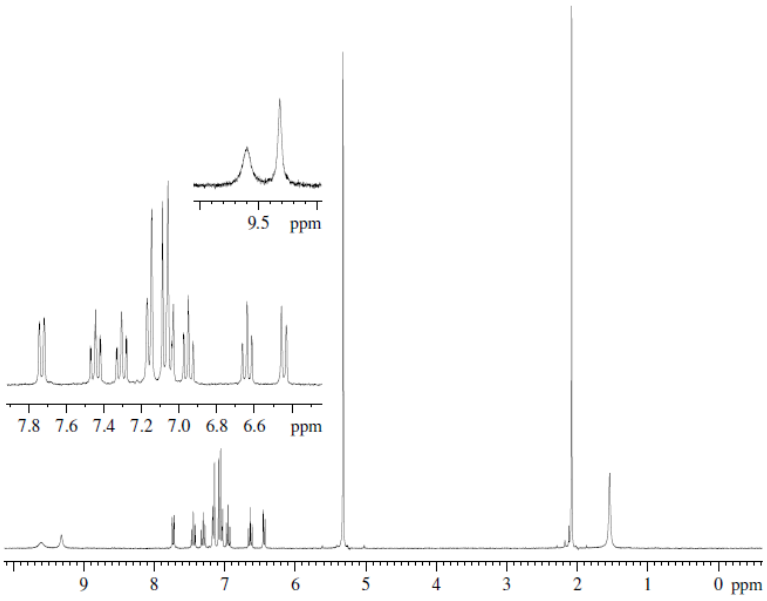

Figure 2.1: ^{1}H NMR spectrum of **2.1c** (Sample run in CD_2Cl_2)

For **2.1c** the downfield region exhibits two one-proton singlets at 9.60 ppm and 9.32 ppm. This suggests the two indole type hydrogen atom environments are inequivalent. There are 8 aromatic signals corresponding to 11 different hydrogen atom environments. The aliphatic singlet (2.10 ppm) corresponds to only 6 protons rather than the expected 12 for the bis-imine (**1.32c**). This suggests the reaction proceeded with the condensation of only one aniline unit leaving one carbonyl remaining (**Scheme 2.3**). The monoimine formation of a substrate containing two carbonyl moieties has been previously observed with napthoquinone.[90] The authors attribute the monoimine formation to a conjugation extension of the first carbonyl upon derivitization thus reducing the reactivity of the second carbonyl.

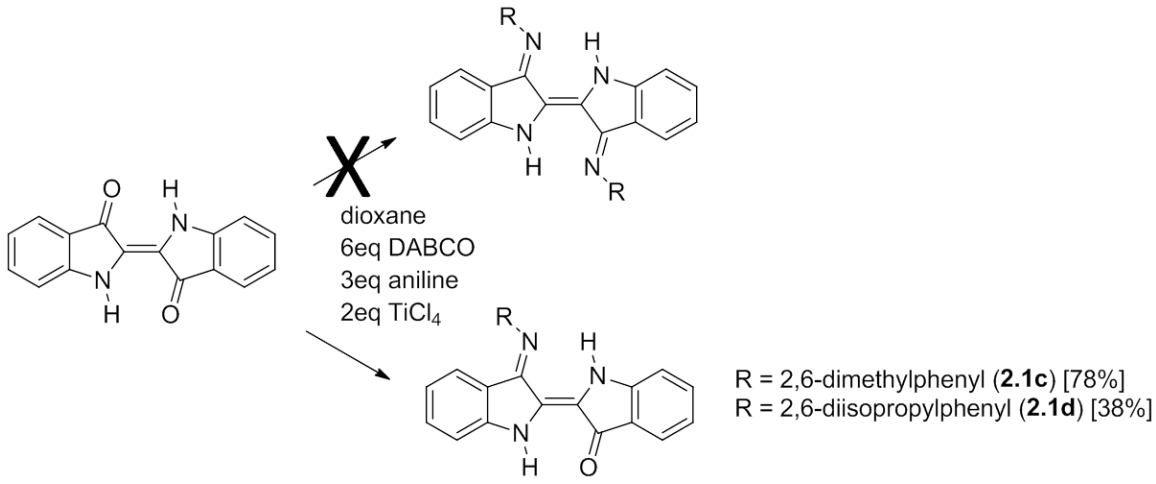

Scheme 2.3: Reactions of indigo with anilines to yield indigo-monoimines

The connectivity of **2.1c** was confirmed by single crystal X-ray crystallography where it is clear only one carbonyl moiety has been converted to an imine. The aromatic N-substituent is twisted with respect to the Nindigo core by 85.5^{o} and hereafter called N-aryl twist. This is defined by the angle between the mean plane consisting of the C4N2 Nindigo core (C12, C11, C21, C22, N11 and N21) and the plane of the N-aryl ring (N22 and the 6 carbon atoms of the benzene ring) (**Figure 2.2**).

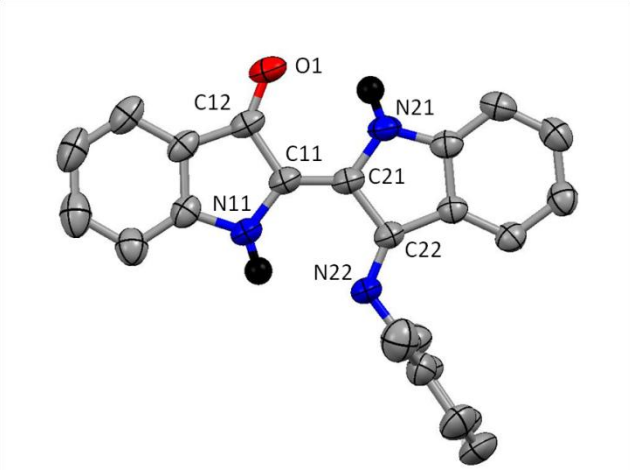

Figure 2.2: X-ray crystal structure of **2.1c**. Thermal ellipsoids at the 50% probability level with all hydrogen atoms, with exception of the indole type hydrogen atoms, removed for clarity

Within the central conjugate core of **2.1c** all single bonds are slightly shorter and all double bonds are slightly longer than typical. This reflects the delocalized nature of the core (**Table 2.1**).

Atoms	Length (Å)
C11-C21	1.354(2)
C11-N11	1.3897(19)
C21-N21	1.3753(18)
C11-C12	1.4786(19)
C21-C22	1.4765(19)
C12-O1	1.2392(17)
C22-N22	1.2905(18)

Table 2.1: Selected bond lengths for **2.1c**

The indigo-monoimines exhibit a marked increase in solubility with respect to indigo. The electronic spectra of **2.1c** and **2.1d** exhibit a λ_{max} of 594 nm with a hypsochromic shoulder at *ca.* 552 nm (**Figure 2.3**). They are intensely coloured with molar extinction coefficients in the order of 30.0 x 10^3 M^{-1} cm^{-1}. The molecules follow Beer's law within a concentration range of 1.0 x 10^{-4} - 1.0 x 10^{-6} M suggesting that the molecules remain monomeric in solution. The lack of aggregation (in contrast to indigo) is likely due to the orthogonal aromatic substituent preventing π-π stacking (**Figure 2.2**).

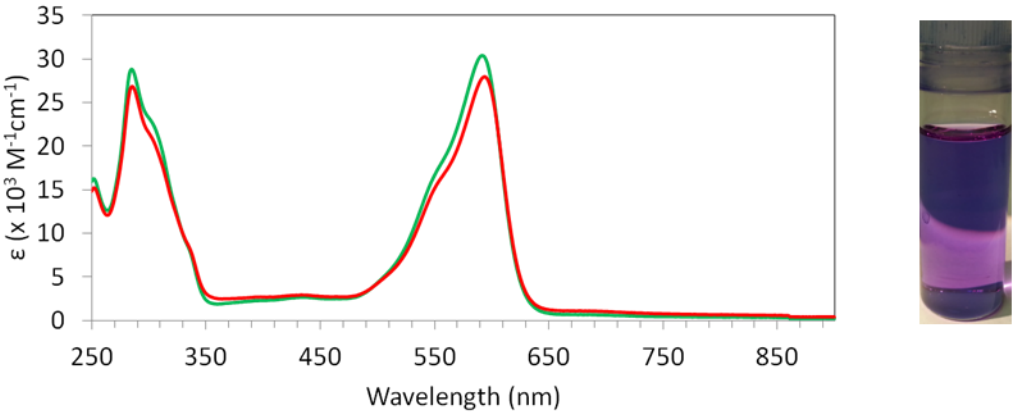

Figure 2.3: UV/vis/NIR spectra of **2.1c** (green) and **2.1d** (red) Spectra obtained in DCM at a concentration of 1.25 x 10^{-5} M. Photograph of **2.1d** in DCM solution (right)

Although derivatives of **2.1** are interesting molecules in their own right, the primary focus of this project was on the chemistry of Nindigos and so further investigations of **2.1** were not pursued.

The incomplete conversion is not well understood and conditions were altered to try to force bis-imine formation (**Scheme 2.4**).

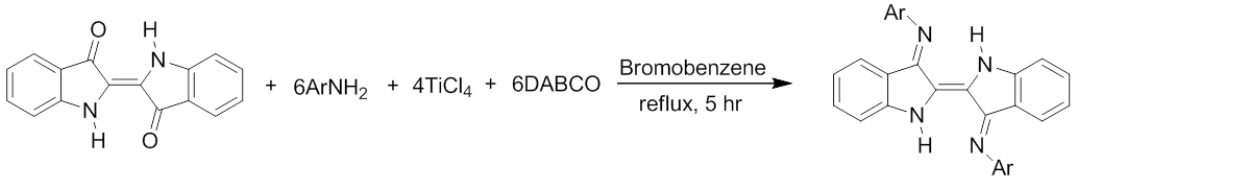

1.32a Ar = phenyl (Phen) [66%]
1.32b Ar = pTolyl (pTol) [67%]
1.32c Ar = 2,6-dimethylphenyl (Dmp) [75%]
1.32d Ar = 2,6-diisoproplyphenyl (Dipp) [23%]
1.32e Ar = 2-t-butylphenyl (2tButylPhen) [60%]
1.32g Ar = 2-biphenyl (Biphen) [7%]

Scheme 2.4: Reaction conditions for Nindigo synthesis

Using the conditions shown in scheme 2.4, the Nindigo family has been expanded and diversified. Yields range from *ca*. 80% to less than 5% and are still found to be dependent on the nature of the aniline. The lower yielding syntheses involve anilines that contain strong electron withdrawing groups that likely render the nitrogen atom less nucleophilic. The order of reagent addition was found to play a significant role on how the reaction proceeds. This was most evident in the formation of **1.32b** where yields were improved from less than 30% to greater than 70% by adding the $TiCl_4$ last rather than the indigo in typical syntheses (**Table 2.2**).

	order of addition				
Nindigo	Indigo	Aniline	$TiCl_4$	Dabco	Yield (%)
1.32b	4	2	3	1	70
1.32c	1	2	4	3	75
1.32d	1	2	4	3	24
1.32e	4	2	3	1	60
1.32g	1	2	4	3	7

Table 2.2: Optimized order of reagent addition for a selection of Nindigo derivatives

The fact that somewhat forcing conditions are required to facilitate what is, on paper, a simple condensation reaction, is likely due to the low reactivity of the carbonyl group. Specifically, the carbonyl is present as a ketone (as opposed to an aldehyde) and possesses cross conjugation that allows for vinylogous amide resonance with the neighbouring nitrogen atom (**Figure 2.4**).

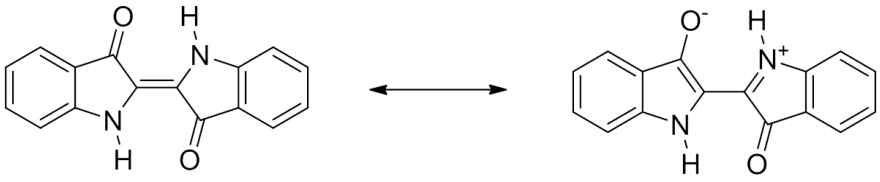

Figure 2.4: Vinylogous amide resonance in indigo

All Nindigos exhibit ^{1}H NMR spectra that resemble those previously reported.[77,79] **1.32c** is shown as a representative example below (**Figure 2.5**). The most diagnostic regions are the broad downfield singlet attributed to the two equivalent indole type hydrogen atoms, and the 12 hydrogen singlet in the aliphatic region for the 4 equivalent methyl groups.

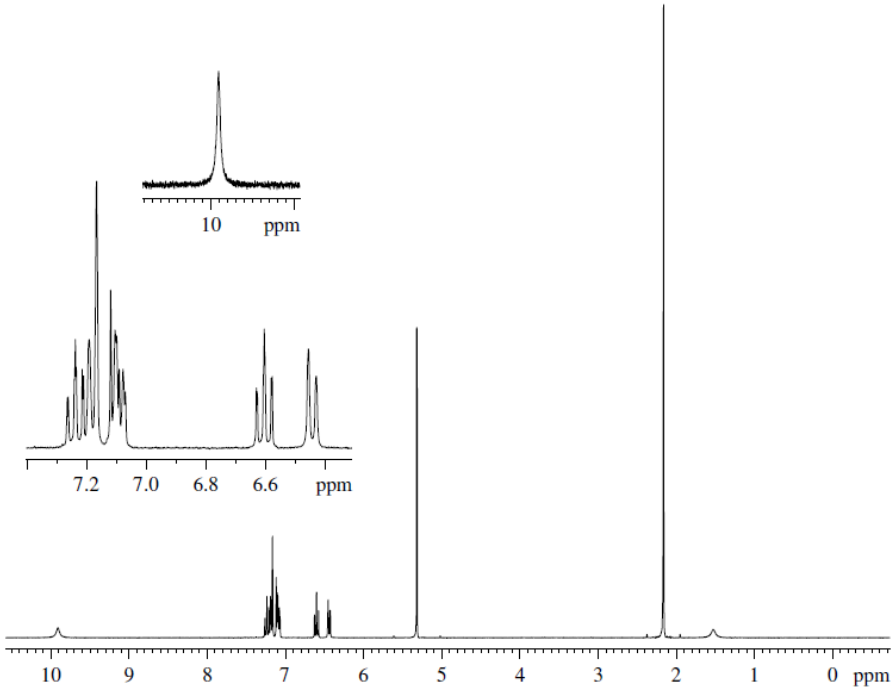

Figure 2.5: ^{1}H NMR of **1.32c** (Sample run in CD_2Cl_2)

Although the NMR spectra suggest that the molecules are symmetrical in nature, due to the *trans/cis* isomerisation that is known for various indigoid systems (where the NH groups are replaced by oxygen, selenium or sulfur)[92-94] the possibility that the Nindigo structure exists as the *cis* isomer as opposed to the *trans* isomer cannot be ruled out by NMR data alone (**Figure 2.6**).

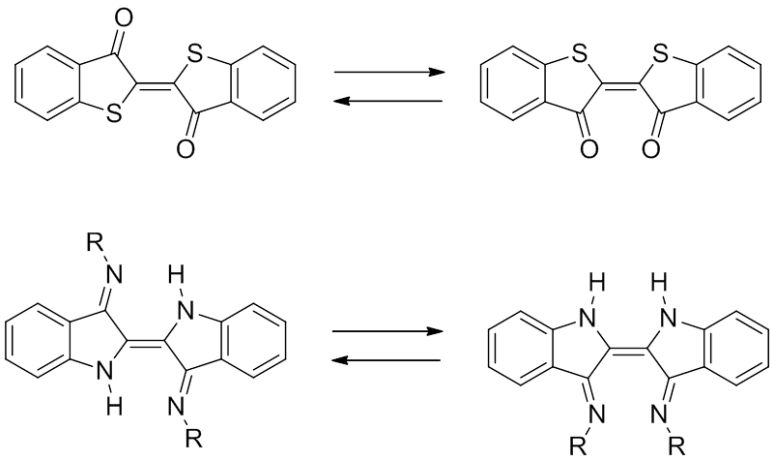

Figure 2.6: *Trans/cis* Isomerisation of Thioindigo (top) and Nindigo (bottom)

However, the *trans* geometry was confirmed by single crystal X-ray diffraction (**Figure 2.7**). This finding is perhaps unsurprising given the potential for intramolecular hydrogen bonding between the indole type hydrogen and the imine nitrogen that could serve to lock the geometry of the molecule. Similar hydrogen bonding in indigo (NH---O) is postulated to be the reason why indigo also does not undergo t*rans/cis* isomerization.[92] The central C1-C1' bond length in **1.32h** is 1.366 Å. This is longer than a typical C=C double bond. The C1-N1 and C1-C2 single bonds are longer than typical single bonds involving sp^2 carbons. The imine bonds, C2-N2 also show deviations and are slightly longer than typical imine C=N bonds (**Table 2.3**).

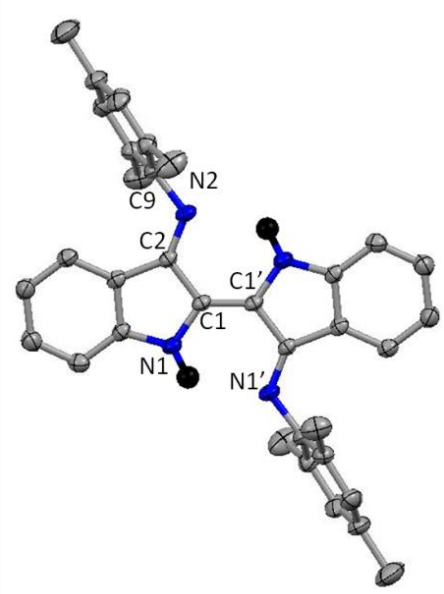

Figure 2.7: X-ray crystal structure of **1.32h**. Thermal ellipsoids at the 50 % probability level and all hydrogen atoms, with exception of the indole type hydrogen atoms, removed for clarity

Atoms	Length (Å)	Typical Length (Å)
C1-C1'	1.415(2)	1.33
C1-C2	1.397(2)	1.47
C1-N1	1.501(2)	1.40
C2-N2	1.3904(18)	1.28

Table 2.3: Selected bond lengths for **1.32h** and typical equivalent bond lengths from the literature

These bond deviations are not unexpected given the donor-acceptor nature of the Nindigo manifold. The core can therefore be more appropriately viewed as partially delocalized rather than the Kekulé structures depicted in (**Figure 2.6**). The N-aryl rings of **1.32h** lie nearly orthogonal to the plane of the Nindigo core, likley as a result of steric interactions between the *ortho* alkyl groups and the benzannulated aromatic periphery.

Although Nindigos display better solubility characteristics than indigo, obtaining high quality ^{13}C NMR spectra is still a challenge. Despite clean NMR and HRMS spectra, elemental analyses were

inconsistent with carbon abundance generally lower than expected. This suggests incomplete combustion. As an example, combustion analysis for **1.32a** is shown in appendix D along with the corresponding NMR and HRMS spectra. This phenomenon was also observed for the Nindigo and Nindigo type molecules reported previously by other groups.[77,79,91]

Given that Nindigos posses a donor-acceptor configuration about the central core reminiscent to that of indigo, it would be expected that the fundamental choromophore would also be similar to that of the indigo H-chromophore resulting in a low energy π-π* transition (**Figure 2.8**).

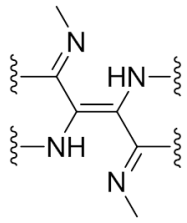

Figure 2.8: Fundamental chromophore of Nindigo

Like derivatives of **2.1**, Nindigos display significantly improved solubility with respect to indigo. They exhibit solubility is in solvents such as DCM, acetone, toluene, THF and ethyl acetate but are typically insoluble in very apolar solvents. The electronic absorption spectra of **2.1c** and **1.32c** are qualitatively very similar, both exhibiting strongest visible absorptions at *ca.* 590 nm. However, there are additional lower energy transitions (< 650 nm) present in **1.32c** are not present in for **2.1c** (**Figure 2.9**).

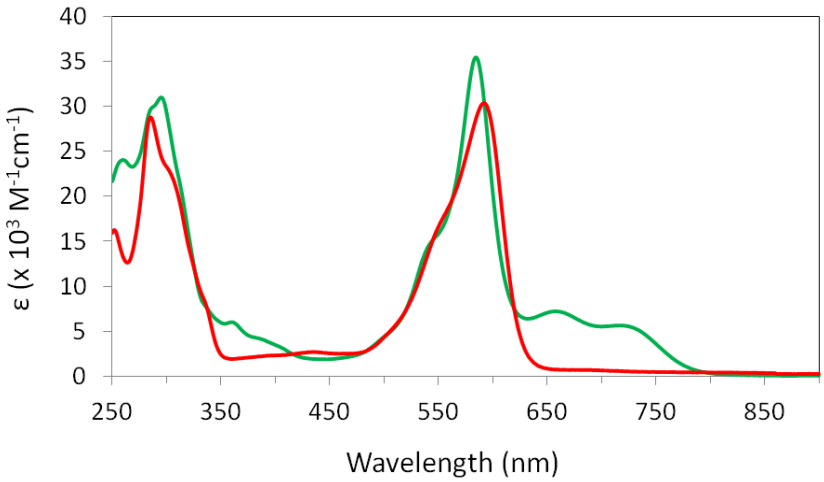

Figure 2.9: A comparison of UV/vis/NIR spectra for **2.1c** (green) and **1.32c** (red). Spectra obtained in DCM at a concentration of 1.25 x 10^{-5} M

Derivatives of **1.32** exhibit similar absorption profiles, with the position of the strongest transition and presence of multiple shoulders common to all derivatives (**Table 2.4**). There are however, differences observed for the intensity of the transitions (**Figure 2.10**). Nindigos that possess *ortho* substituents on the N-aryl rings (**1.32c** and **1.32d**) exhibit a more intense transition (ε ≈ 33.5 x 10^3 M^{-1} cm^{-1}) than those Nindigos that contain N-aryl rings that are *ortho* unsubstituted, **1.32a** and **1.32b** (ε ≈ 11.5 x 10^3 M^{-1} cm^{-1}). The Nindigo with one N-aryl *ortho* susbstituent, **1.32e**, has an absorption that is intermediate between the two (20.4 x 10^3 M^{-1} cm^{-1}). The shape of the absorption profile is followed for all derivatives. Two shoulders are observed that are red shifted from the main transition and one shoulder is oberved that is blue shifted. Initially it was postulated that, similar to indigo, these lower energy transitions may result from solution aggregation. However, variable concentration experiments ruled out aggregation effects. All derivatives were found to obey Beer's law within a concentration range from 1.0 x 10^{-4} - 10^{-6} M. Alternatively these low energy shoulders may come as a result of tautomerisation (see later). The intensity of the lower energy transitions appears unaffected by varying N-aryl substitution.

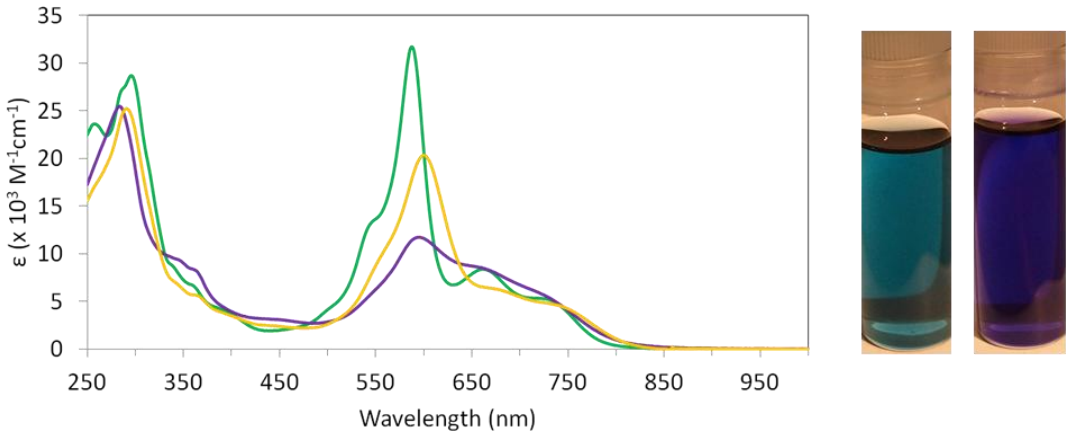

Figure 2.10: UV/vis/NIR spectra of **1.32a** (purple), **1.32d** (green) and **1.32e** (orange). Spectra obtained in DCM at a concentration of 1.25 x 10^{-5} M. Photographs of solutions of **1.32a** (left) and **1.32d** (right)

Nindigo	λ_{max} (nm)	ε (x 10^3 M^{-1} cm^{-1})
1.32a	597	12.0
1.32b	598	10.9
1.32c	584	35.5
1.32d	588	31.7
1.32e	600	20.4
1.32f	601	9.0
1.32g	604	10.7

Table 2.4: UV/vis/NIR data from a variety of Nindigos

Derivatives of **1.32** exhibit weak solvatochromism with λ_{max} ranging from 580 nm - 588 nm. The wavelength of the lower energy absorption bands are also only slightly affected by the solvent conditions. However, unlike the strongest absorbtion bands, the intensity of the lower energy transisitions are not consistant in differing solvents (**Figure 2.11**).

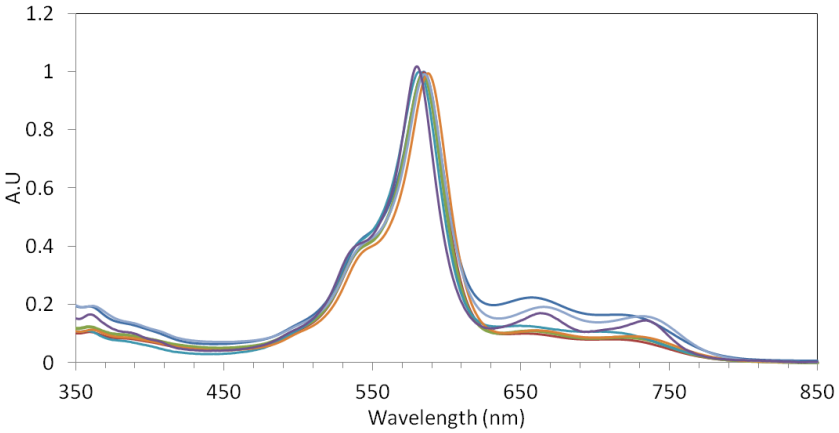

Figure 2.11: Normalized UV/vis/NIR spectra of **1.32c** DCM (dark blue), acetone (red), THF (orange), toluene (light blue), ethyl acetate (green), acetonitrile (grey), hexane (purple). Spectra obtained at a concentration approximately 1.25 x 10^{-5} M

Electrochemically, all Nindigo derivatives exhibit irreversible multi-electron redox behaviour. Two irreversible oxidations are observed at *ca.* +0.10 V and *ca.* +0.69 V (vs. Fc/Fc^+ in DCM) respectively. The irreversibility of these processes is likely due to proton loss resulting from an increase in acidity upon oxidation. Multiple irreversible reduction processes are also present at *ca.* -0.60 V and -1.4 V (**Figure 2.12**).

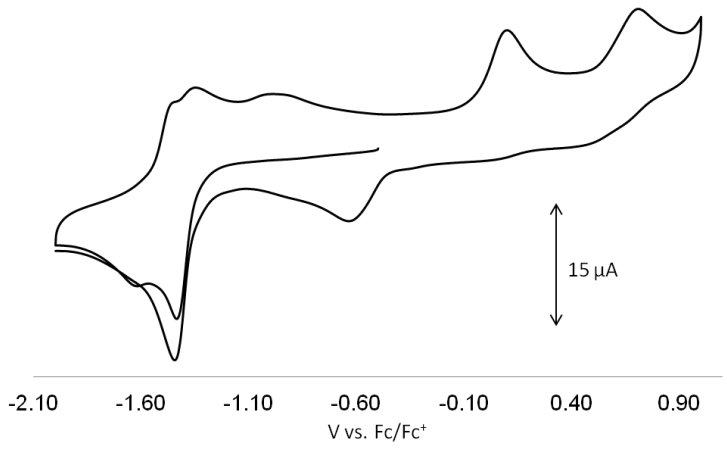

Figure 2.12: Cyclic voltammogram of **1.32b** showing two irreversible oxidations and numerous reduction processes (DCM solution, 0.1 mM Bu_4NBF_4 electrolyte and scan rate = 100 mVs^{-1})

Whilst the Nindigo synthesis has been advanced and the ligand architecture diversified, in some instances the products obtained from the reaction mixture are not those of the anticipated structure type (**1.32**). The ^{1}H NMR spectrum of the compound isolated during a typical synthesis to obtain **1.32b** is shown below (**Figure 2.13**).

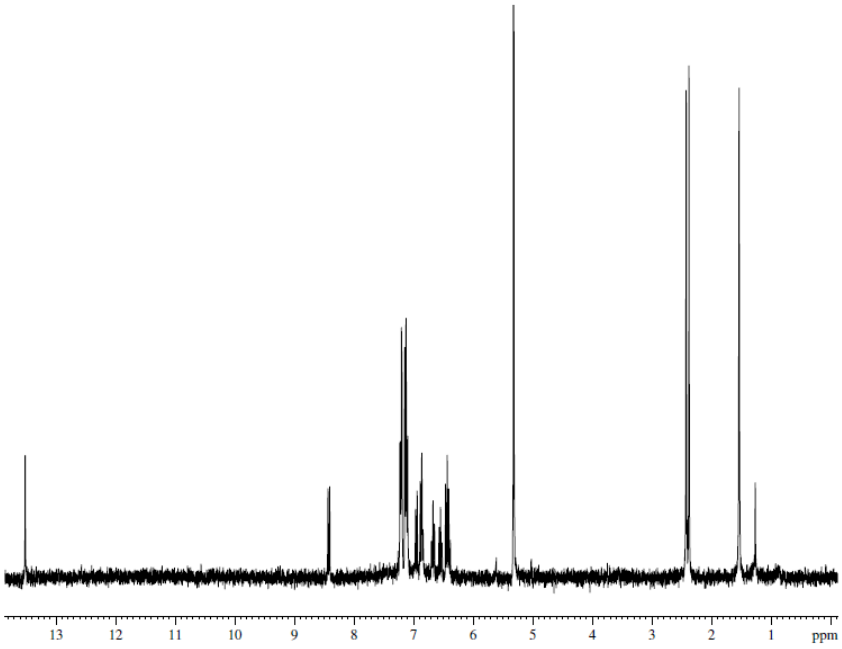

Figure 2.13: ^{1}H NMR spectrum of the different product isolated from an attempted synthesis of **1.32b**. (Sample run in CD_2Cl_2)

Two resonances are observed for the *para* methyl groups at 2.39 ppm and 2.41 ppm indicating that they are chemically inequivalent. More signals are observed in the aromatic region than what are observed for **1.32b**. This suggests that the molecule possesses a lower symmetry configuration. The indole type proton resonance at 9.90 ppm for **1.32b** is not present; instead a significantly deshielded singlet at 13.50 ppm is observed. This suggests that the structure does not possess the bis-indole type motif. There is one proton signal unaccounted for by integration and no changes to the spectrum are observed following the introduction of D_2O to the NMR sample. X-ray crystallography confirmed the molecule to be that of a tautomer, **1.32b'** (**Figure 2.14**). Secondary amine hydrogen atoms similar to that of H22 are sometimes not observed by ^{1}H NMR in similar systems which could explain the missing signal.[95]

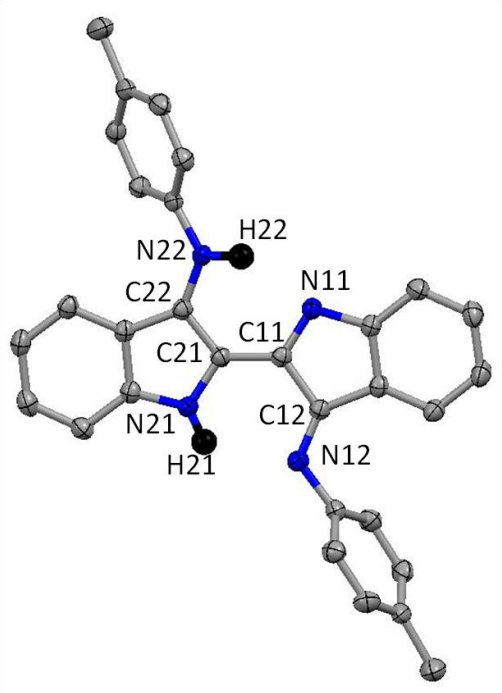

Figure 2.14: X-ray crystal structure of **1.32b'**. Thermal ellipsoids at the 50% probability level with all peripheral and aromatic hydrogen atoms removed for clarity

The most striking distinction between the structure of **1.32b'** and those of type **1.32** is that the two hydrogen atoms that are located on the indole type nitrogen atoms in **1.32**, are now located on the same side of the molecule. One hydrogen atom resides on the indole type nitrogen with the other now residing on the exocyclic nitrogen atom (N22). Another significant difference is the carbon-carbon bond length that connects the two halves of the molecule. C11-C21 is significantly longer (1.415 Å) in comparison to the equivalent bond in **1.32h** (1.366Å). This suggests it contains more single bond character. The non-centrosymmetric nature of **1.32b'** results in the C22-N22 bond being significantly longer (1.3666 Å) than its counterpart on the opposing side of the molecule (C12-N12 1.2815 Å). This is indicative of N22 being more of a secondary amine in nature as opposed to an imine (**Table 2.5**). The two halves of the molecule remain coplanar and the *trans* geometry is retained. This is possibly due to packing effects and/or intramolecular hydrogen bonding. The N-aryl twist of *p*-tolyl moiety on the 3-aminoindole half of **1.32b'** is 51.9^{o} with its counterpart on the dehydroindolimine side twisted by 73.0^{o}. The inequivalence of the two halves of the molecule in conjunction with bond lengths that are between that of formal single and double bond lengths suggests a combination of the resonance structures, **1.32b'** and **1.32b''**, to be an accurate representation of this tautomer.

Atoms	Length (Å)
C11-C21	1.415(2)
C21-C22	1.397(2)
C11-C12	1.501(2)
C21-N21	1.3904(18)
C11-N11	1.3208(18)
C22-N22	1.3666(18)
C12-N12	1.2815(18)

Table 2.5: Selected bond lengths for **1.32b'**

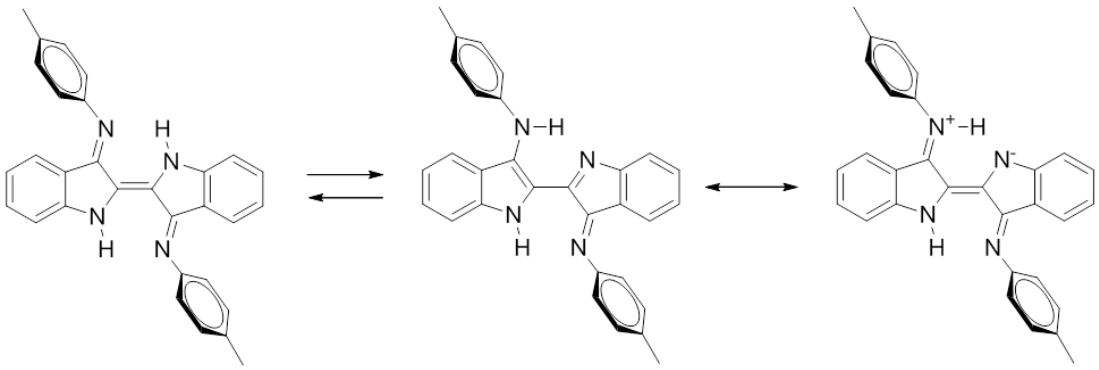

1.32b **1.32b'** **1.32b''**

The majority of the previously published syntheses of indigo diimines all describe ^{1}H NMR spectra that are indicative of the centrosymmetric tautomer.[77,79] However, before our interest in indigo-dimines, there had been only one crystal structure reported. Interestingly the connectivity was also found to be that of the non-centrosymmetric tautomer (**Figure 2.15**).[78] Bond lengths and angles of this previously reported structure are consistent with those observed in **1.32b'**.

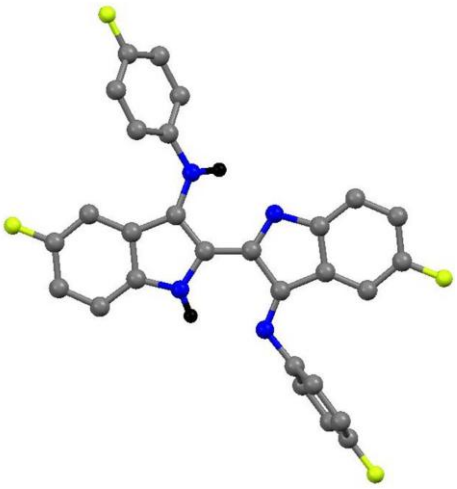

Figure 2.15: X-ray crystal structure of a non-centrosymmetric para-fluorinated indigodiimine (generated from deposited coordinates) with all peripheral and aromatic hydrogen atoms removed for clarity[78]

Tautomerisation of the simplest indigo diimine, where the N-substituent is a hydrogen atom, has been studied previously (**Figure 2.16**).[96,97] IR spectroscopic measurements found that the molecule exists solely in the asymmetric form in both solution and the solid state. The room temperature ^{1}H NMR spectrum exhibited resonances that seemed to match those expected for the symmetric tautomer. However, at lower temperatures the spectrum deconvolutes and the inequivalent proton environments for the various tautomers can be observed. This suggests that the room temperature spectrum is a weighted average of the tautomers and that the tautomerisation occurs rapidly on the NMR timescale. Computationally the non-centrosymmetric tautomer was found to be more stable than the symmetric form by 2.1 kcal mol^{-1}. This is attributed to the presence of an aromatic indole that is not present in the centrosymmetric structure. However, the magnitude of the difference may not be significant enough to categorically support this favouritism.[97]

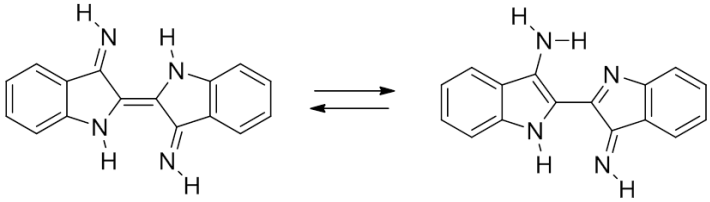

Figure 2.16: Tautomerisation of indigo diimine

The tautomerism of **1.32b** can be shown spectroscopically by significant changes in the solution absorption profile. Compared with the **1.32b**, **1.32b'** exhibits an equal intensity but lower energy transition (λ_{max} = 841 nm, ε = 9.19 x 10^3 M^{-1} cm^{-1}) (**Figure 2.17**).

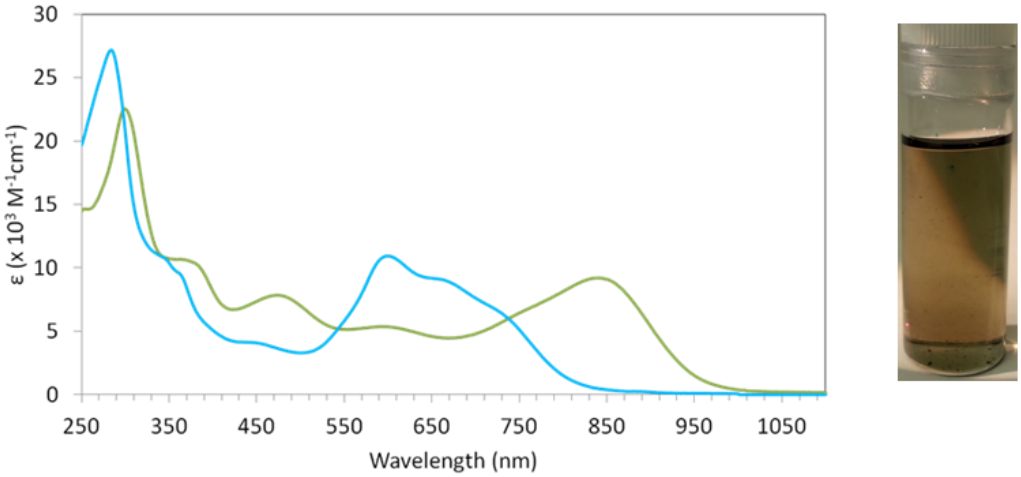

Figure 2.17: UV/vis/NIR spectra of **1.32b** (blue) and **1.32b'** (green). Spectra obtained from DCM at a concentration of 1.25 x 10^{-5} M. Photograph of a solution of **1.32b'** (right)

Depending on the nature of the solvent, **1.32b'** converts to **1.32b** over time in solution at room temperature. A 1.25 x 10^{-5} M dichloromethane solution **1.32b'** takes 16 days to fully convert to **1.32b** as monitored by electronic spectroscopy (**Figure 2.18**).

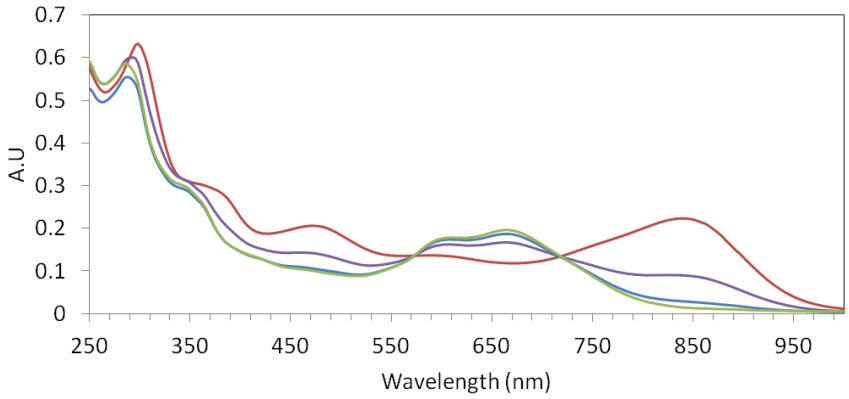

Figure 2.18: Electron spectra showing the conversion of **1.32b'** to **1.32b** over 16 days in DCM (Red = zero days, purple = four days, blue = 8 days, green = 16 days).

Conversely, in more polar solvents the conversion does not occur. In DMSO **1.32b'** persists with no evidence of the centrosymmetric derivative present whatsoever (**Figure 2.19**).

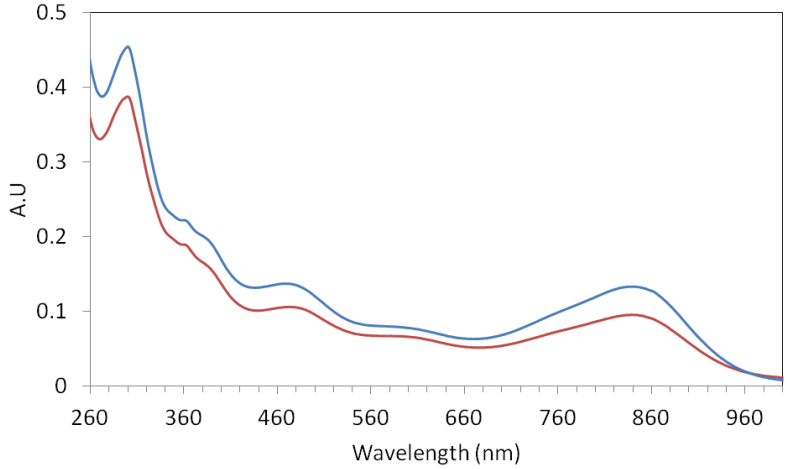

Figure 2.19: UV/vis/NIR spectra showing the persistence of **1.32b'** over 16 days in DMSO (blue = zero days, red = 16 days).

The presence of tautomerism during the synthesis of Nindigos seems to be substrate dependent and appears to be more prevalent for the bulkier derivatives (**1.32c** and **1.32d**) where, in some cases, the tautomer is the sole product.

Subsequent chemistry can be somewhat hampered by having the Nindigo in the non-centrosymmetric tautomeric form. For this reason the asymmetric derivatives were always converted to their symmetric counterparts. The most facile way to achieve 100% conversion is by refluxing in nBuOH for an hour, cooling and filtering. This leaves the product exclusively in its symmetrical form. Refluxing in other alcohols (ethanol or methanol) did not facilitate the conversion suggesting the tautomerisation is sensitive to both temperature and solvent.

2.3 Palladium complexes of Nindigo

2.3.1 Synthesis

The general conditions previously reported (**scheme 1.4**)[85] were followed but the solvent was changed from THF to DCM and improvements made to the work up. This resulted in increased yields. Reactions were found to proceed instantaneously as observed by colour changes from blue or purple (depending on the Nindigo derivative) to deep green. The complexes were isolated as dark green powders with yields ranging from 30% - 60%. One notable development in the palladium chelate chemistry of Nindigo concerns palladium complexes of the bulkier Nindigos (**1.32c, 1.32d** and **1.32h**). Initially Oakley reported that these reactions yielded intractable mixtures; current studies reveal that the anticipated bis-Pd(hfac) (**1.33**) is not obtained, but rather a mono-Pd(hfac) complex **2.2** is isolated.

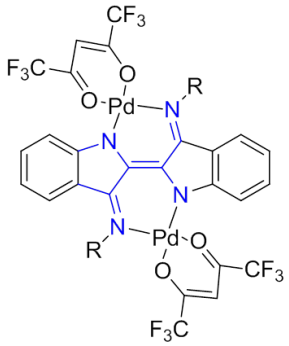

R = Aromatic without ortho substituents

1.33

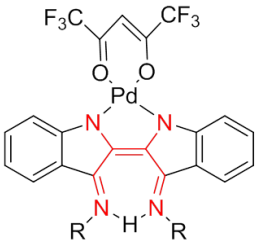

R = Aromatic with ortho substituents

2.2

The formation of derivatives of **2.2** is observed even when excess $Pd(hfac)_2$ is used. Conditions have been optimized to produce these complexes in decent yields (**Scheme 2.5**).

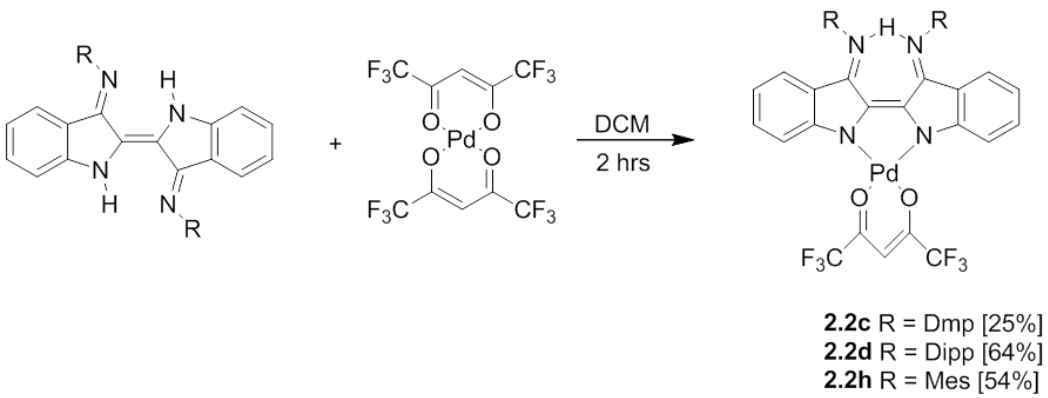

Scheme 2.5: MonoPalladium chelates of Nindigo as a result of *trans/cis* isomerization

The chelation of one Pd(hfac) unit was confirmed by ^{1}H NMR and the spectrum for **2.2c** is shown below as a representative example (**Figure 2.20**). A single proton singlet corresponding to one hfac unit is observed at 6.4 ppm. The single aliphatic signal at 2.2 ppm for 12 equivalent methyl protons rules out the possible *trans* monopalladium complex, **2.3**.

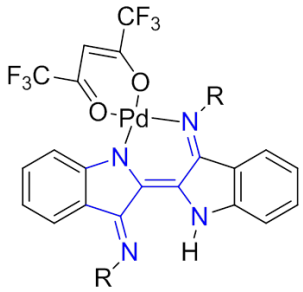

2.3

Further evidence supporting the symmetric nature of the molecule comes from the presence of only 8 proton environments as opposed to the expected 15 should the structure be of the form **2.3**. The presence of a significantly deshielded proton at 12.3 ppm is assigned to the NH proton bridging between to imines. The final piece of spectroscopic evidence that supports the symmetric nature of the molecule comes from the ^{19}F NMR spectrum where only one fluorine signal is observed. Should the molecule be of the form **2.3** two signals would be expected from the two fluorine environments rendered inequivalent by symmetry. It should be noted that minor quantities of bis-Pd(hfac) chelates of **1.32c** can be detected by ^{1}H and ^{19}F NMR. This suggests that the Pd(hfac) substrate may be able to coordinate to bulkier Nindigo derivatives in the imine/amide bonding mode.

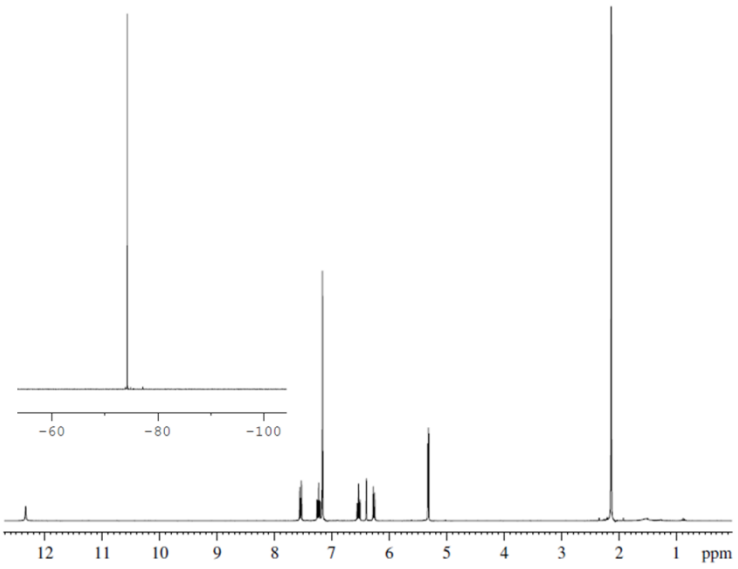

Figure 2.20: ^{1}H NMR and ^{19}F NMR (inset) of the monopalladium chelate of **2.2c** (sample run in CD_2Cl_2)

The connectivity of structure **2.2c** was confirmed by single crystal X-ray crystallography (**Figure 2.21**). The bond lengths within the Nindigo core (**Table 2.6**) are all comparable to the corresponding bond lengths of the bis-Pd(hfac) complexes of type **1.33**. This is consistent with the fact that, despite the structural reorganization, the donor-acceptor substitution pattern about the central C-C bond remains. In the solid state the complex is rendered asymmetric as the NH proton is associated with one of the imines more than the other. This results in slight bond deviations for each half of the molecule. For example one imine (C22-N22) is 1.33 Å and the other (C12-N12) is 1.31 Å. The asymmetry is not observed in solution as the proton likely undergoes rapid exchange between the two nitrogen atoms. The imine/amine nitrogen atoms (N22 and N12) are separated by 2.82(3) Å. This is comparable to that of the chelating nitrogen atoms in the bis-Pd(hfac) derivatives that are separated by *ca.* 2.83 Å. Chelation of the palladium via the two indole type nitrogen atoms results in a contraction of the molecule with the two halves of the ligand deviating off the long central molecular axis. This type of binding also results in an overall distorted square planar geometry about the palladium with an acute N-Pd-N bite angle of *ca.* 80^{o} compared with the N-Pd-N angles of 88^{o} - 92^{o} in the bis-Pd(hfac) analogues. In both the monopalladium and bis-Pd(hfac) complexes the PdN bonds are all approximately 1.99 Å in length.

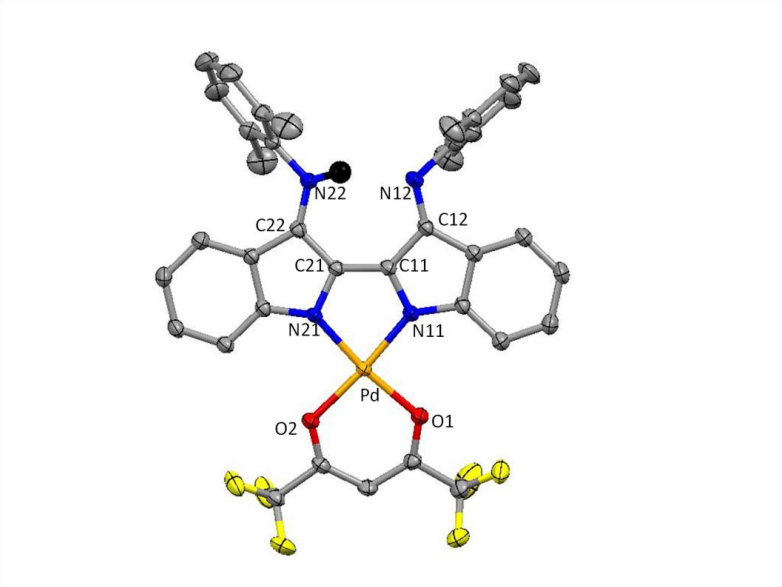

Figure 2.21: X-ray crystal structure of **2.2c**. Thermal ellipsoids at the 50% probability level with all hydrogen atoms, except for the acidic proton that is retained for charge balance, removed for clarity

Atoms	Length (Å)	Atoms	Angle (deg)
C11-C21	1.389 (2)	N11-Pd-O1	92.58 (6)
C11-C12	1.468 (2)	N21-Pd-O2	94.34 (5)
C21-C22	1.441 (2)	O1-Pd-O2	92.16 (5)
C12-N12	1.310 (2)	N11-Pd-N21	80.73 (6)
C22-N22	1.327 (2)		
N11-Pd	1.9823 (15)		
N21-Pd	1.9911 (15)		
Pd-O1	2.0182 (13)		
Pd-O2	2.0267 (12)		

Table 2.6: Selected bond lengths and angles for **2.2c**

The N-aryl rings in **2.2c** are twisted by 74^{o} and 81^{o} respectively, and the palladium lies out of the plane of the chelating Nindigo core (NCCCN) by 0.30 Å. The Nindigo core itself remains planar unlike in the bis-Pd(hfac) derivatives where significant buckling results in a saddle type geometry (**Figure 2.22**).

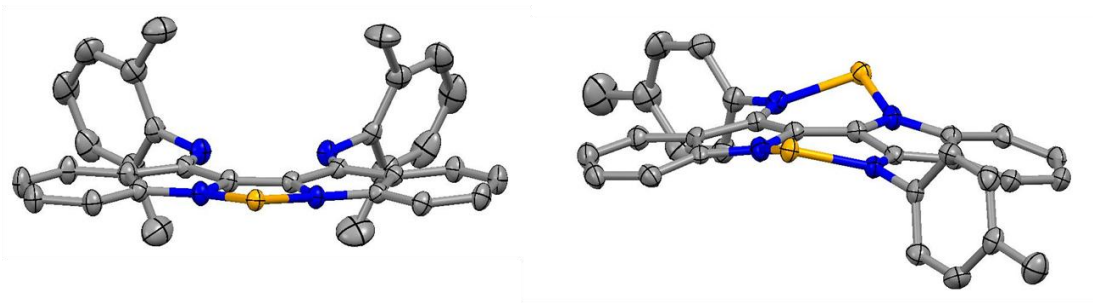

Figure 2.22: X-ray structures of **2.2c** (left) and **1.33b** (right) viewed across the central carbon-carbon bond. All hydrogen atoms and hfac units removed for clarity

Complexes of type **2.2** exhibit similar solubility traits to their corresponding Nindigo ligands. The electronic spectra display λ_{max} of *ca*. 830 nm with a hypsochromic shoulder at *ca*. 730 nm. Molar extinction coefficients for the 830 nm band are on the order of 16.0 x 10^3 M^{-1} cm^{-1} and the intensity and position of the absorption do not deviate between the different bulky derivatives (**Figure 2.23**). Similar to derivatives of **1.33**, derivatives of **2.2** exhibit a significant red shift from their parent Nindigos. The bathochromic shift is not quite as large as those observed for **1.33** (*ca.* 234 nm vs. 316 nm).

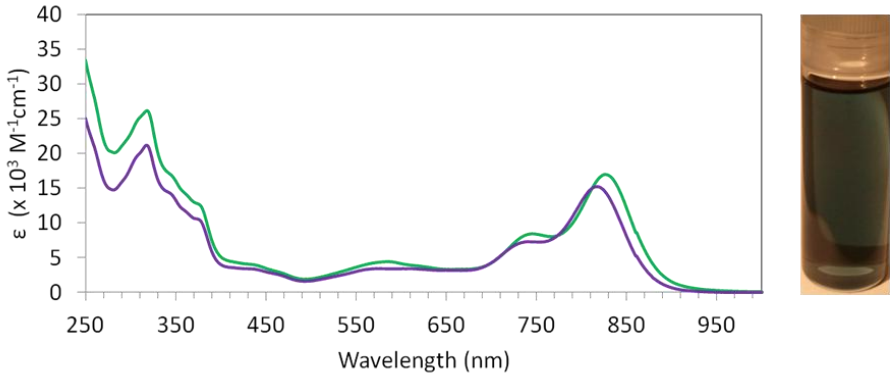

Figure 2.23: UV/vis/NIR spectra for **2.2c** (purple) and **2.2d** (red). Spectra obtained in DCM at a concentration of 1.25 x 10^{-5} M. Photograph of **2.2c** (right)

The previously reported bis-Pd(hfac) Nindigo complexes were found to exhibit two reversible one-electron oxidations (*ca.* +0.08 V, +0.57 V) and a single true two-electron reduction (*ca.* -1.21 V). Derivatives of **2.2** show two reversible one-electron oxidation events and two one-electron reduction

processes, the first of which is reversible (**Figure 2.24**). Derivatives of **2.2** are slightly more difficult to oxidize than those of **1.33** but oxidations still occur at mild potentials (**Table 2.7**).

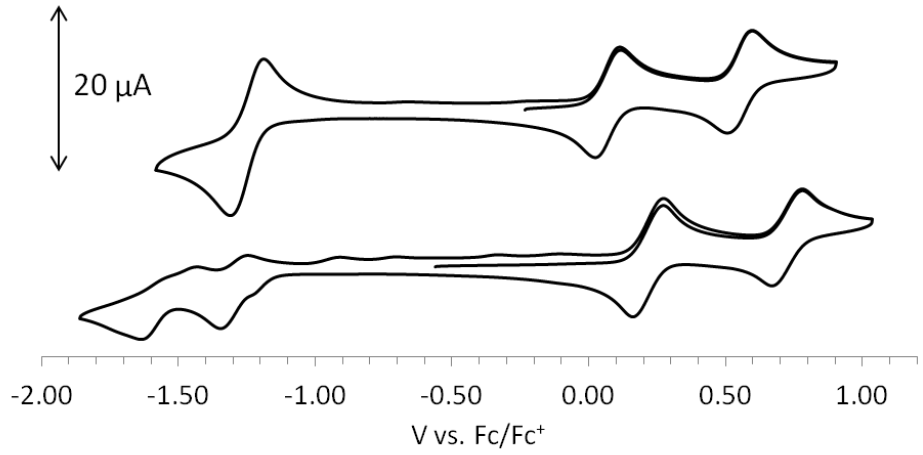

Figure 2.24: Cyclic voltammogram for **2.2c** (bottom) and **1.33a** (top) (DCM solution, 0.1 mM Bu_4NBF_4 electrolyte and scan rate = 100 mVs^{-1})

Derivative	Reduction (V)	Oxidation (V)
2.2c	-1.30[b]	+0.20[a], +0.80[a]
1.33a	-1.21[c]	+0.08, +0.57

Table 2.7: Electrochemical data for **2.2c** and **1.33a** ([a] = pseudo reversible, [b] = irreversible, [c] = net two electron process)

2.4 Summary

The previously reported conversion of the carbonyl moieties on indigo to imines via a $TiCl_4$ mediated condensation reaction resulted in a modest library of Nindigo derivatives.[85] This synthesis has since been improved and the library expanded and diversified.[86] The N-Aryl substituents give Nindigo derivatives better solubility characteristics than indigo whilst maintaining a similar low energy, high intensity visible absorption band. The position of which is generally independent of the N-aryl substituent ($\lambda_{max} \approx 600$ nm). For the less bulky members (**1.32a**, **1.32b**, **1.32f** and **1.32j**) molar extinction coefficients are approximately 10.0 x 10^3 M^{-1} cm^{-1} with the bulkier derivatives (**1.32c** and **1.32d**) exhibiting more intense transitions of approximately 34.0 x 10^3 M^{-1} cm^{-1}. In some instances Nindigos are obtained as their non-centrosymmetric tautomers and these can be converted to the centrosymmetric derivatives by refluxing in nBuOH. However, interconversion between the two has not yet been achieved. Whilst there is some precedence for the tautomerisation of indigo-diimines in the few previous reported Nindigo diimine syntheses,[96,97] the apparent large barrier for tautomerisation is not well understood.

Bis-Pd(hfac) chelates of Nindigo (**1.33**) enabled the reversible redox-activity of the ligand family to be established. In most cases two reversible one-electron oxidations and a reversible true two-electron reduction process are observed. In addition to the redox-activity, the ligand centered π-π* transition (identified computationally) of the palladium chelates undergoes a significant bathochromic shift with respect to their parent Nindigos. Attempted syntheses of palladium chelates involving bulkier Nindigo derivatives (**1.32c**, **1.32d** and **1.32h**) did not result in the bis-Pd(hfac) chelates but rather mono-nuclear chelates (**2.2**). The palladium atom in derivatives of **2.2** is bound by the two indolide type nitrogen atoms as a result of trans-cis isomerisation about the central carbon carbon double bond. This new geometry in conjunction with mono-chelation results in observed electrochemical differences between **2.2** and **1.32**. Derivatives of **2.2** still exhibit reversible one-electron oxidations but they occur at higher potentials than those observed for **1.33**. The true two-electron reduction process observed for **1.33** is now two distinct one-electron reductions, the first of which is reversible. Derivatives of **2.2** exhibit substituent independent, intense, low energy absorption bands ($\lambda_{max} \approx 830$ nm, $\varepsilon \approx 20.0 \times 10^3$ M^{-1} cm^{-1}) that are red-shifted with respect to Nindigo. They are however, not shifted to the same magnitude as the bis-Pd(hfac) chelates.

2.5 Experimental

2.5.1 Methods and materials

All reactions and manipulations were carried out under an argon atmosphere using standard Schlenk or glovebox techniques unless otherwise stated. All reagents were purchased from Aldrich and used as received unless stated in which case they were purified or dried under appropriate conditions.[98] Palladium bis(hexafluoroacetylaceonate) was synthesized according to the literature.[99] NMR spectra were recorded on 300, 360 or 500 mHz instruments at room temperature unless stated otherwise. Electronic spectra were recorded on a Perkin-Elmer Lambda 1050 at room temperature unless otherwise stated. Cyclic voltammetry experiments were performed with a Bioanalytical Systems CV50 voltammetric analyzer. Typical electrochemical cells consisted of a three-electrode setup including a glassy carbon working electrode, platinum counter electrode, and a silver wire as quasi-reference electrode. Dichloromethane solutions of analyte (1 mM) and electrolyte (0.1 mM $Bu_4^+NBF_4^-$) were referenced against an internal standard (0.1 M ferrocene). Accurate mass determination was performed at the UVic Genome BC Proteomics Centre on a Thermo Scientific LTQ Velos Orbitrap instrument. Samples (mg/mL) were diluted by a factor of 10-100 and injected by liquid infusion through a nano ESI source. X-ray diffraction data was collected on a Bruker PLATFORM/SMART 1000 CCD with a graphite-monochromatacized Mo-Kα radiation (λ = 0.71073 Å) by Dr. Robert McDonald (University of Alberta) or Dr. Brian O. Patrick (University of British Columbia). Experimental details for all computations can be found in Appendix G.

Indigo mono-2,6-dimethylphenylimine, 2.1c: DABCO (1.43 g, 12.7 mmol) and 2,6-dimethylaniline (770 mg, 6.36 mmol) were dissolved in dioxane (80 mL) and heated to 70°C. To this solution was added $TiCl_4$ (1 M in toluene, 4.24 mmol, 4.24 mL) under a nitrogen atmosphere with rapid stirring. After complete addition, indigo (529 mg, 2.12 mmol) was added and the reaction mixture heated to reflux for 24 hours. The reaction mixture was filtered whilst hot and washed with ether until the washings ran clear. The solvent was then removed in vacuo before the crude residue was refluxed in nBuOH. The suspension was then filtered leaving a dark purple powder (604 mg, 78 %). X-ray quality crystals were grown via slow evaporation of DCM from a concentrated solution. ^{1}H NMR (300 mHz, CD_2Cl_2, 293 K): δ = 2.1 (s, 6H), 6.4 (d 1H, *J* = 7.8 Hz), 6.6, (dodod, 1H, *J* = 7.6 Hz, 0.8 Hz), 7.0 (dodod, 1H, *J*

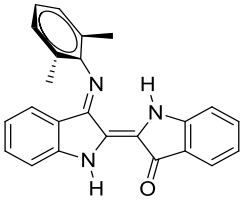

= 7.4 Hz, 0.6 Hz), 7.1 (m, 3H), 7.2 (d, 2H, *J* = 7.4 Hz), 7.3 (dodod, 1H, *J* = 7.7 Hz, 7.7 Hz, 1.2 Hz), 7.5 (dodod, 1H, *J* = 8.4 Hz, 7.8 Hz, 1.3 Hz), 7.7 (d, 1H, *J* = 7.7 Hz), 9.3 (s, 1H), 9.6 (s, 1H). ^{13}C NMR (500 mHz, CD_2Cl_2, 293 K): δ = 18.3, 112.0, 112.7, 118.7, 120.1, 120.5, 121.3, 121.3, 124.3, 124.6, 125.7, 126.2, 127.7, 128.9, 133.8, 135.2, 149.2, 149.7, 151.6, 162.2, 186.7. UV/vis/NIR (CH_2Cl_2), λ_{max}/nm (ε, $M^{-1}cm^{-1}$): 285 (28,800), 303 (20,900), 553 (15,800), 592 (30,400). HRMS, *m/z:* calcd for $(M-H)^+$ $C_{24}H_{20}N_3$ 365.1606; found 366.1611 Anal. Calcd. for $C_{24}H_{19}N_3$: C, 78.88; H, 5.12; N, 11.43. Found: C, 78.88; H, 5.24; N, 11.50

Indigo mono-2,6-diisopropylphenylimine, 2.1d: DABCO (2.02 g, 18.0 mmol) and 2,6-diisopropylaniline

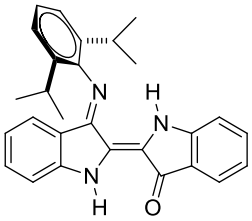

(1.60 g, 9.00 mmol) were dissolved in dioxane (100 mL) and heated to 70°C. To this solution was added $TiCl_4$ (1 M in toluene, 6.0 mmol, 6.0 mL) under a nitrogen atmosphere with rapid stirring. After complete addition, indigo (792 mg, 3.0 mmol) was added and reaction mixture heated to reflux for 24 hours. The reaction mixture was filtered whilst hot and washed with ether until the washings became clear. The solvent was removed in vacuo before the crude product was refluxed in *n*BuOH. The suspension was allowed to cool before being filtered resulting in a dark purple powder (480 mg, 38 %). ^{1}H NMR (300 MHz, CD_2Cl_2, 293K): δ = 1.0 (d, 6H, *J* = 6.8 Hz), 1.2 (d, 6H, *J* = 6.9 Hz), 2.9 (septet, 2H, *J* = 6.8 Hz), 6.4 (dot, 1H, *J* = 7.3 Hz, 1.0 Hz), 6.6 (tod, 1H, *J* = 7.5 Hz, 0.9 Hz), 7.0 (tod, 1H, *J* = 7.4 Hz, 0.8 Hz), 7.0 (tod, 2H, *J* = 8.7 Hz, 0.7 Hz), 7.3 (m, 4H), 7.5 (dodod, 1H, *J* =7.7 Hz, 7.6 Hz, 1.4 Hz)), 7.7 (dod, 1H, *J* = 8.5 Hz, 1.0 Hz), 9.3 (s, 1H), 9.6 (s, 1H). ^{13}C NMR (500 MHz, CD_2Cl_2, 293K): δ = 23.6, 23.8, 29.0, 112.1, 112.8, 118.6, 120.2, 120.6, 121.0, 121.4, 124.1, 124.4, 125.3, 126.5, 127.7, 133.8, 135.2, 136.5, 147.6, 149.4, 151.6, 162.8, 186.6. UV/vis/NIR (CH_2Cl_2), λ_{max} /nm (ε, $M^{-1}cm^{-1}$): 286 (26,900),304 (22,500), 551 (16,900), 594 (28,000), HRMS, *m/z*: calcd for $(M-H)^+$ $C_{28}H_{28}N_3O$ 421.2232; found 422.2241

Indigo bis(*para*-tolylimine), 1.32b: To a bromobenzene (250 mL) solution of DABCO (24.0 g, 214 mmol)

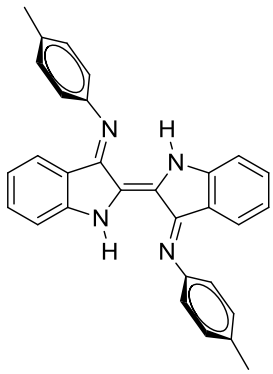

and *p*-toluidine (9.55 g, 89.2 mmol) was added $TiCl_4$ (1 M in toluene, 53.5 mmol, 53.5 mL) at 70 °C under nitrogen with rapid stirring. After complete addition, indigo (9.55 g, 35.7 mmol) was added and reaction mixture heated to reflux for 24 hours. The reaction mixture was filtered whilst hot and washed with ether until the washings became clear. The solvent was removed in vacuo and the crude product was refluxed in *n*BuOH and left to cool to room temperature before being put in a freezer for 2 days. The resulting mixture was filtered and washed with hexanes to give a dark blue

powder (10.5 g, 67%). ^{1}H NMR (300 MHz, CD_2Cl_2, 293K): δ = 2.4 (s, 6H, C*H*$_3$), 6.8 (m, 2H), 7.0 (t, 1H, *J* = 0.9 Hz), 7.0 (t, 1H, *J* = 1.0 Hz), 7.1 (2H, t, *J* = 1.0 Hz), 7.1 (2H, t, *J* = 1.0 Hz), 7.3 (m, 8H), 9.9 (s, 2H). ^{13}C NMR (500 MHz, CD_2Cl_2, 293K): δ = 20.9, 115.4, 118.9, 120.0, 120.9, 124.9, 129.9, 124.9, 130.6, 134.2, 144.4. UV/vis/NIR (CH_2Cl_2), λ_{max} /nm (ε, $M^{-1}cm^{-1}$): 283 (27,100), 362 (9,540), 603 (10,900), 660 (9,090). HRMS, *m/z*: calcd for $(M-H)^+$ $C_{30}H_{25}N_4$ 441.2079; found 441.2068

3-ptolylamino-2-(3-ptolylimino-2-dehydroindolyl)-1H-indole, 1.32b': A reliable preparation of this derivative has as yet not been obtained. The compound is sometimes obtained from attempted syntheses of **1.32b**. X-ray quality crystals were grown from slow evaporation of DCM. ^{1}H NMR (300 MHz, CD_2Cl_2, 293K): δ = 2.4 (s, 3H, C*H*$_3$), 2.4 (s, 3H, CH_3), 6.4 (t, 2H, *J* = 8.3 Hz), 6.5 (t, 1H, *J* = 8.2 Hz), 6.7 (t, 1H, *J* = 8.2 Hz), 6.9 (d, 2H, *J* = 8.0 Hz), 6.9 (d, 1H, *J* = 8.0 Hz), 7.1 (m, 8H), 8.5 (d, 1H, *J* = 8.3 Hz), 13.5 (s, 1H). ^{13}C NMR (500 MHz, CD_2Cl_2, 293K): δ =21.3, 21.4, 117.9, 118.2, 119.4, 120.0, 120.1, 120.2, 121.4, 121.6, 123.3, 123.8, 125.8, 130.2, 130.5, 131.4, 133.1, 135.6, 136.1, 140.0, 144.1, 147.7, 151.1, 155.4, 157.2, 157.9. UV/vis/NIR (CH_2Cl_2), λ_{max} /nm (ε, $M^{-1}cm^{-1}$): 298 (22,000), 380 (10,400), 660 (5,360), 842 (9,190). HRMS, *m/z*: calcd for $(M-H)^+$ $C_{30}H_{25}N_4$ 441.2079; found 441.2068

Indigo bis(2,6-dimethylphenylimine), 1.32c: Dimethylaniline (5.78 g, 47.7mmol), indigo (5.00 g, 19.1 mmol) and DABCO (12.83 g, 114.4 mmol) were combined in bromobenzene (150 mL). The mixture was stirred under argon and heated to approximately 80^{o}C. $TiCl_4$ (1M in toluene, 28.6 mL, 28.6 mmol) was added slowly and the mixture stirred at reflux for 24 hours. The mixture was then filtered hot and the solids washed with diethyl ether until the washings ran clear. The solvent was removed in vacuo and the crude product was washed with water. It was then taken up in hot *n*BuOH and left to cool to room temperature before being put in a freezer for 2 days. The resulting mixture was filtered to give a dark purple powder (6.64 g 75 %). ^{1}H NMR (300 MHz, CD_2Cl_2, 293K): δ = 2.2 (s, 12H), 6.4 (d, 2H, *J* = 7.9 Hz), 6.5 (dodod, 2H, *J* = 1.0 Hz, 7.6 Hz, 8.0 Hz), 7.1 (m, 4H), 7.2 (m, 6H), 9.90 (s, 2H). ^{13}C NMR (500 MHz, CD_2Cl_2, 293K): δ = 18.5, 113.5, 119.5, 120.7, 124.8, 125.0, 128.6, 128.8, 132.2, 147.7, 149.3, 158.4. UV/vis/NIR (CH_2Cl_2), λ_{max} /nm (ε, $M^{-1}cm^{-1}$): 258 (24,000), 285 (28,900), 295 (31,000), 362 (5,980), 542 (14,700), 584 (35,500), 658 (7,250),

730 (5,380). HRMS, *m/z*: calcd for $(M-H)^+$ $C_{32}H_{29}N_4$ 469.2387; found 469.2390. Anal. Calcd. for $C_{32}H_{29}N_4$: C, 82.02; H, 6.02; N, 11.96. Found: C, 80.40; H, 6.02; N, 11.58

Indigo bis(2,6-diisopropylphenylimine), 1.32d: To a bromobenzene (225 mL) solution of DABCO (15.39 g, 137.2 mmol) and 2,6-diisopropylaniline (5.33 g, 57.2 mmol) was added $TiCl_4$ (1M in toluene, 34.3 mmol, 34.3 mL) under nitrogen at 70 ^oC with rapid stirring. After complete addition, indigo (6.00 g, 22.9 mmol) was added and the reaction mixture heated to reflux for 24 hours. The reaction mixture was filtered whilst hot and washed with ether until the washings became clear. The solvent was removed in vacuo and the crude product washed with water before being taken up in hot *n*BuOH. This suspension was then left to cool to room temperature before being put in a freezer for 2 days. The resulting mixture was filtered to give a purple powder (3.10 g, 23 %). ^1H NMR (300 MHz, CD_2Cl_2, 293K): δ = 1.0 (d, 12H, *J* = 6.9 Hz), 1.2 (d, 12H, *J* = 6.9 Hz), 3.1 (septet, 4H, *J* = 6.9 Hz), 6.4 (d, 2H, *J* = 7.7 Hz), 6.6 (dodod, 2H, *J* = 0.9 Hz, 7.5 Hz, 7.9 Hz), 7.1 (d, 2H, *J* = 8.1Hz), 7.2 (dodod, 2H, *J* = 0.9 Hz, 7.9 Hz, 8.1 Hz), 7.28 (s, 6H), 9.9 (s, 2H). ^{13}C NMR (500 MHz, CD_2Cl_2, 293K): δ = 23.6, 24.1, 29.0, 113.5, 119.3, 120.2, 124.0, 125.7, 125.8, 128.5, 132.1, 139.2, 145.5, 150.2, 159.1. UV/vis/NIR (CH_2Cl_2), λ_{max} /nm (ε, $M^{-1}cm^{-1}$): 259 (23,600), 285 (26,300), 296 (28,700), 362 (6,530), 542 (12,700), 588 (31,700), 661 (8,400), 730 (5,230). HRMS, *m/z*: calcd for $(M-H)^+$ $C_{40}H_{45}N_4$ 581.3644; found 581.3618. Anal. Calcd. for $C_{40}H_{45}N_4$: C, 82.42; H, 7.68; N, 9.40. Found: C, 82.72; H, 7.64; N, 9.65

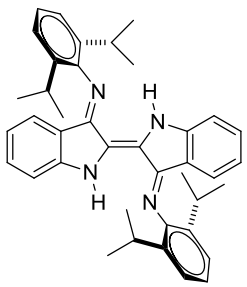

Indigo bis(2-*tert*-butylphenylimine), 1.32e: DABCO (3.88 g, 34.6 mmol) and 2-tertbutylaniline (14.4 mmol, 2.15 g) were dissolved in bromobenzene at 75^oC. To this solution was added $TiCl_4$ (1M in toluene, 8.65 mmol, 8.65 mL) under nitrogen with rapid stirring. After complete addition of $TiCl_4$, indigo (1.51 g, 5.76 mmol) was added and the reaction mixture heated to reflux for 24 hours. The reaction mixture was filtered whilst hot and washed with ether until the washings became clear. The solvent was removed in vacuo and the crude product was taken up in DCM and extracted with saturated $NaHCO_3$ solution. It was then taken up in hot *n*BuOH and left to cool to room temperature before being put in a freezer for 2 days. The resulting mixture was filtered to give a dark powder (1.82 g, 60 %). ^1H NMR (300 MHz, CD_2Cl_2, 293K): δ = 1.5 (s, 18H), 6.4 (m, 4H), 7.0 (m, 2H), 7.1 (d, 2H, *J* = 8.1 Hz), 7.2 (m, 6H), 7.6 (m, 2H), 10.0 (s, 2H) . ^{13}C NMR (500

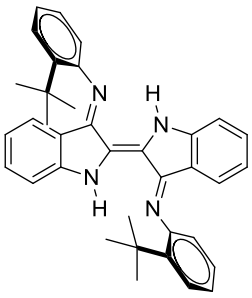

MHz, CD_2Cl_2, 293K): δ = 30.5, 35.7, 113.9, 119.0, 120.4, 122.1, 125.2, 125.9, 127.2, 127.3, 130.9, 131.5, 141.4, 148.0, 150.3, 155.9. UV/vis/NIR (CH_2Cl_2), λ_{max} /nm (ε, $M^{-1}cm^{-1}$): 291 (25,300), 362 (5,720), 600 (20,400), 679 (6,270), 748 (4,360). HRMS, *m/z*: calcd for $(M-H)^+$ $C_{36}H_{37}N_4$ 525.3047; found 525.3375

Indigo bis(2-biphenylimine), 1.32g: To a bromobenzene (140 mL) solution of DABCO (4.78 g, 42.6 mmol), 2-aminobiphenylaniline (3.00 g, 17.7 mmol) and indigo (7.10 mmol, 1.86 g) was added $TiCl_4$ (1M in toluene, 16 mmol, 16 mL) under nitrogen at 70 °C with rapid stirring. The reaction mixture was brought to reflux and left to stir for 24 hours. The reaction mixture was filtered whilst hot and washed with ether until the washings became clear. The solvent was removed in vacuo and the crude product was taken up in DCM and extracted with saturated $NaHCO_3$(aq). The solvent was removed and the solid dissolved in chloroform and run through an activated basic alumina plug. The solvent was removed yielding a dark solid (247 mg, 7 %). ^{1}H NMR (300 MHz, CD_2Cl_2, 293K): δ = 6.8 (t, 2H), 7.0 (d, 2H), 7.1 (d, 2H, *J* = 8.1 Hz), 7.3 (m, 14H), 7.5 (m, 6H), 9.7(s, 2H). ^{13}C NMR (500 MHz, CD_2Cl_2, 293K): δ = 115.1, 119.3, 119.6, 121.1, 124.8, 125.1, 127.6, 128.5, 128.5, 129.8, 131.0, 133.6, 139.8, 150.0. UV/vis/NIR (CH_2Cl_2), λ_{max} /nm (ε, $M^{-1}cm^{-1}$): 291 (25,700), 604 (10,700), 748 (5,300), 860 (2,000). HRMS, *m/z*: calcd for $(M-H)^+$ $C_{40}H_{29}N_4$ 565.2392; found 565.2770

cis-Indigo bis(2,6-dimethylphenylimine)palladium(hexafluoroacetylacetonoate), 2.2c: Under an argon atmosphere, **1.32c** (249 mg, 531 mmol) was dissolved in DCM (25 mL). To this solution was added drop wise a solution of $Pd(hfac)_2$ (1 eq, 276 mg) in DCM (75 mL) and the reaction was left to stir overnight. The reaction mixture was then extracted 3 times with water before the organic layer was dried and the solvent removed resulting in isolation of a dark solid 300 mg (85% mono-Pd(hfac) and 15% bis-Pd(hfac) by ^{1}H NMR). The crude solid was recrystalized from a DCM / hexanes mixture to give the mono-chelate as a dark powder (100 mg, 25 %). X-ray quality crystals were grown by layering MeOH on a saturated DCM solution. ^{1}H NMR (300 MHz, CD_2Cl_2, 293K): δ = 2.1 (s, 12H), 6.3 (d, 2H, *J* = 7.9 Hz), 6.4 (s, 1H), 6.5 (tod, 2H, *J* = 8.1 Hz, *J* = 0.9 Hz), 7.2 (s, 6H), 7.2 (2H, tod, *J* = 7.8 Hz, *J* = 1.2 Hz), 7.5 (d, 2H, *J* = 8.5 Hz), 12.3 (1H, s). ^{13}C NMR (500 MHz, CD_2Cl_2, 293K): δ = 18.5, 93.0, 114.4, 117.4 (q, CF_3, *J* = 252.0 Hz¸ only the central two signals of the quartet are visible), 119.5, 119.6, 120.0, 125.0, 127.0, 129.1, 131.7, 133.6, 142.7, 144.3, 154.2, 156.4, 175.0 (q, CO, *J* = 35.5 Hz). ^{19}F{^{1}H} NMR (300 MHz, CD_2Cl_2, 293 K): δ = -74.2 (s). UV/vis/NIR (CH_2Cl_2), λ_{max}

/nm (ε, $M^{-1}cm^{-1}$): 318 (21,200), 346 (14,000), 381 (9,420), 436 (3,350), 471 (2,270), 583 (3,380), 745 (7,260), 818 (15,200). HRMS, *m/z*: calcd for (M^+) $C_{37}H_{28}N_4F_6O_2Pd$ 778.1168 ; found 778.1157

μ-Indigo bis(2,6-dimethylphenylimine)bispalladium(hexafluoroacetylacetonoate), 1.33c:

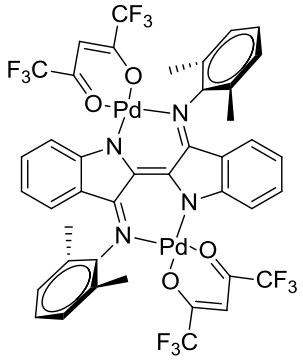

Characterisation extrapolated from the crude mixture of **2.2c** and **1.33c**. ^1H NMR (300 MHz, CD_2Cl_2, 293K): δ = 2.3 (s), 6.2 (s), 6.4 (s), 6.8 (t, *J* = 7.1 Hz), 7.4 (d), 7.5 (d, *J* = 8.2 Hz). $^{19}F\{^1H\}$ NMR (300 MHz, CD_2Cl_2, 293 K): δ = -74.4 (s), -75.5 (s).

cis-Indigo bis(2,6-dimethylphenylimine)palladium(hexafluoroacetylacetonoate), 2.2d: Under an argon atmosphere, **1.32d** (215 mg, 0.370 mmol) was dissolved in dry DCM (25 mL). A solution of $Pd(hfac)_2$ (1 eq, 193 mg) in dry DCM (50 mL) was added drop wise and the resulting reaction mixture was left to stir for 1 hour. The crude reaction mixture was then aqueously extracted three times before the organic layer was dried and the solvent removed. The crude solid obtained was recrystalized from a DCM/PET ether mixture resulting in isolation of a dark powder (211 mg, 64 %). X-ray quality crystals were grown by layering MeOH on a saturated DCM solution.

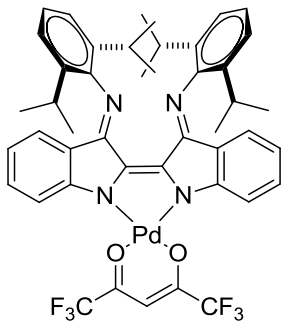

^1H NMR (300 MHz, CD_2Cl_2, 293K): δ = 1.0 (d, 12H, *J* = 6.8 Hz), 1.1 (d, 12H, *J* = 6.8 Hz), 3.1 (septet, 4H, *J* = 6.9 Hz), 6.2 (d, 2H, *J* = 8.0 Hz), 6.4 (s, 1H), 6.5 (2H, t, *J* = 7.6 Hz), 7.3 (m, 8H), 7.5 (d, 2H, *J* = 8.5 Hz), 11.8 (s, 1H). ^{13}C NMR (500 MHz, CD_2Cl_2, 293K): not well enough resolved to allow for full assignment. $^{19}F\{^1H\}$ NMR (300 MHz, CD_2Cl_2, 293 K): δ = -74.3 (s) . UV/vis/NIR (CH_2Cl_2), λ_{max} /nm (ε, $M^{-1}cm^{-1}$): 318 (28,100), 346 (16,800), 381 (11,600), 436 (4,020), 471 (2,680), 584 (4,450), 746 (8,460), 827 (17,000). HRMS, *m/z*: calcd for M^+ $C_{45}H_{42}N_4F_6O_2Pd$ 890.2420; found 890.2409

Chapter 3: Synthesis and properties of mono- and bis-BF_2 chelates of Nindigo, and heteronuclear boron-palladium Nindigo chelates

3.1 Introduction

Materials that absorb (and emit) in the near-infrared region (NIR) are used in a wide variety of applications including light harvesting for photovoltaics[100,101], organic light emitting diodes[102,103], fluorescence sensing,[104] anti-forgery dyes,[105] photo dynamic therapy[106,107] and heat absorbing polymers and paints[108]. The well established classes of NIR absorbing compounds (cyanines, squarines and azo dyes) each have their own strengths and weaknesses and considerable effort has been invested into evolving known chromophores to optimize spectral and practical properties. One common strategy for achieving low energy absorption involves extending the conjugation about the chromophore. As a result, common templates involve large flat molecules with diffuse π-systems such as porphyrins, tetrabenzoporphyrins, porphyrazines and phthalocyanines (**Figure 3.1**).[109,110]

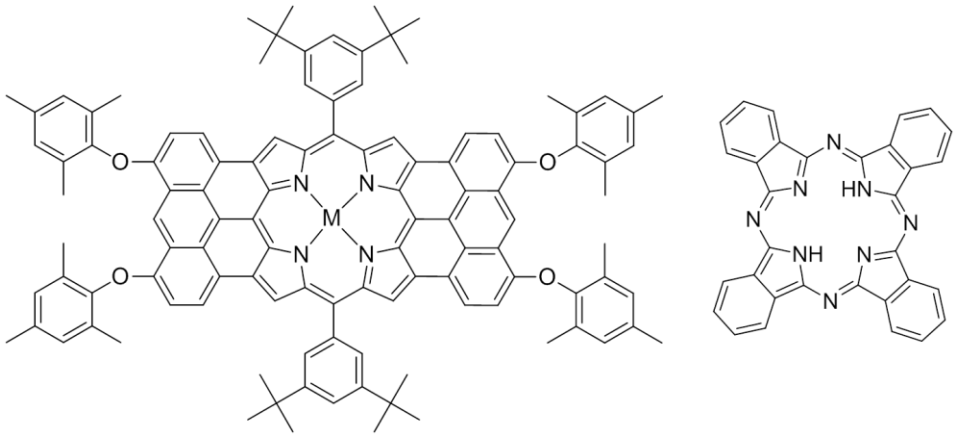

Figure 3.1: Representative examples of NIR chromophores based on N-donor macrocycles[109,110]

Understanding the electronic structure of a molecule is instrumental to manipulating its chromophore. Computer aided molecular design has enabled rational tuning of the frontier molecular orbitals (FMOs) by identifying the ideal position for installing electron donating and withdrawing groups to have the greatest perturbation on the molecules electronic structure.[109] This strategy was shown to

work with great success for Seoul fluor (**3.1**), where the absorption profile could be predictably tuned to span the entire visible region by manipulating the substitution at just two positions (R and R').[111]

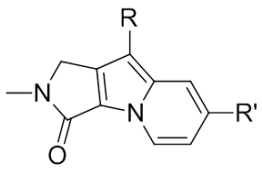

3.1

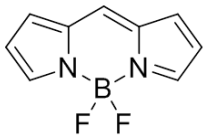

3.2

Perhaps the most well known and studied dyes are those based on the BODIPY (4,4-difluoro-4-bora-3a,4a-diaza-s-indacene) manifold, **3.2**. Although BODIPY dyes generally exhibit desirable high quantum yield emission, they suffer from small Stokes shifts and were initially limited to high energy transitions (below 600 nm). However, **3.2** can be tailored in a number of different ways such as ring fusion,[112-117] substitution of the fluorine atoms,[118,119] and by the introduction of heteroatoms directly into the BODIPY skeleton[120-124] (**Figure 3.2**). These diverse derivitization methods, used in conjunction with rational design, have led to lower energy transitions being realized.[112,113,125-127]

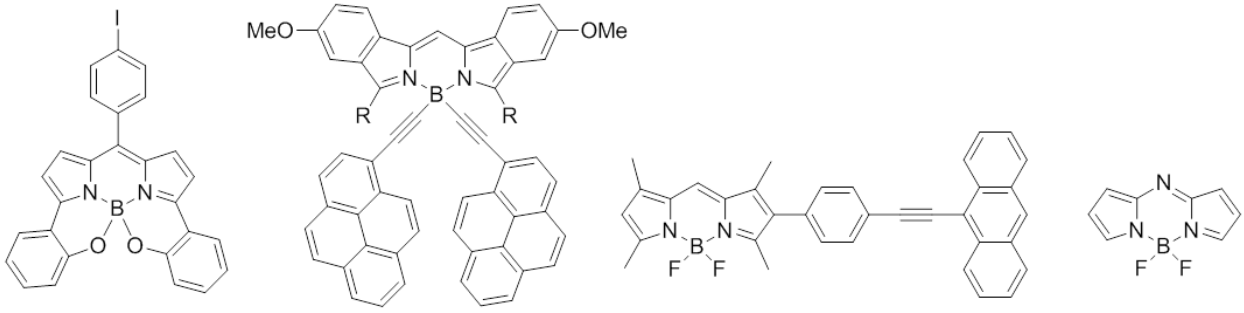

Figure 3.2: A variety of tuned BODIPY type structures

With the exception of aza-BODIPY (far right in above figure), the core of all the above molecules is comprised of a C3N2 unit. This same binding motif can be found in a variety of other NIR absorbing compounds (**Figure 3.3**).

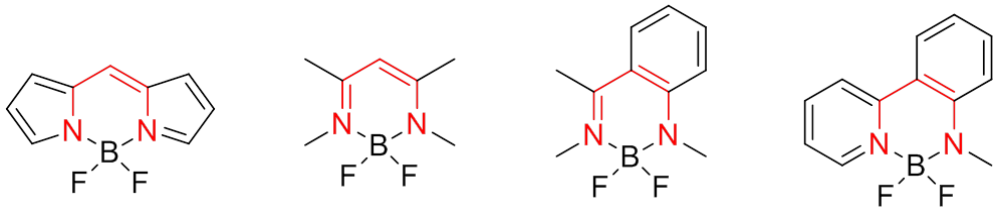

Figure 3.3: Various C3N2 based NIR absorbing systems[128,131,140]

Due to the strong low energy transition exhibited by Nindigo (*cf.* chapter 2) and the fact that boron chelation has been shown to red shift the electronic absorptions of similar chromophoric systems, BF_2 chelates of Nindigo were investigated. The resulting coordination compounds exhibit binding that is reminiscent of that of an asymmetrical BODIPY like structure. (**Figure 3.4**).

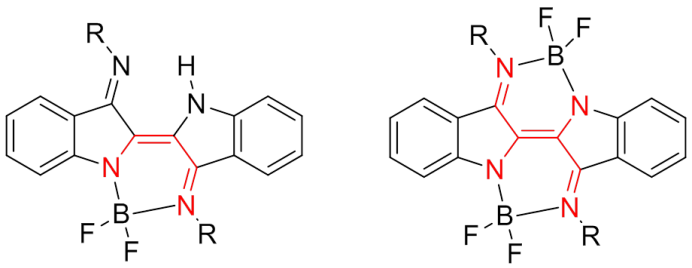

Figure 3.4: The common C3N2 binding motif found in a variety of BODIPY derivatives highlighted for Nindigo in red

3.2 Synthesis of boron chelates of Nindigo

Initial forays into boron chelates of Nindigo employed typical conditions for BF_2 chelation from the literature.[128] In the presence of a base (Et_3N), Nindigo was combined with boron trifluoride diethyletherate in a donor solvent (THF) (**Scheme 3.1**). Dark blue solids of complexes **3.3** containing one BF_2 unit bound by Nindigo were obtained in good yields ranging from 50% - 70%.[129]

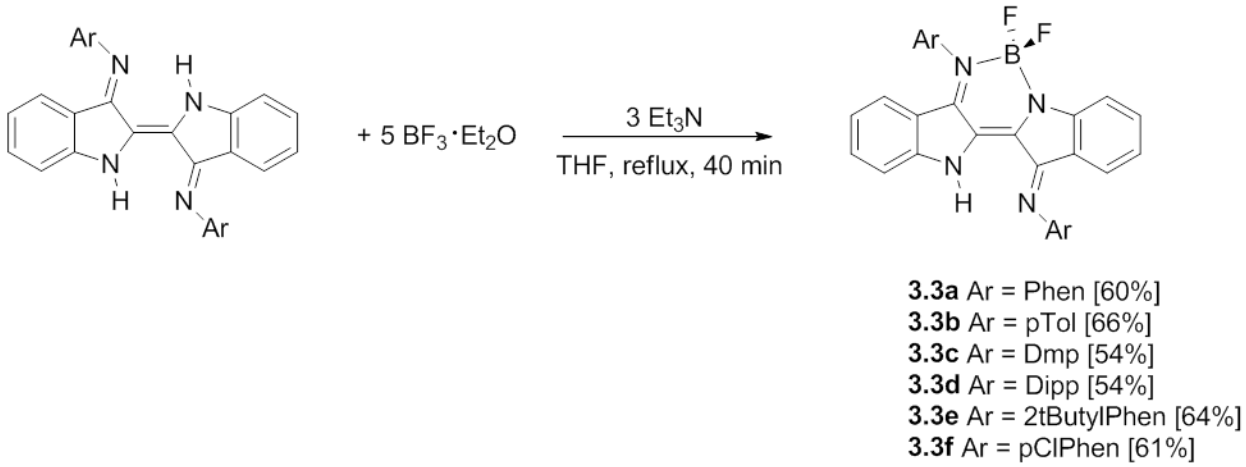

Scheme 3.1: Conditions used for the synthesis of **3.3**

Given derivatives of **3.3** possess a number of abundant spin active nuclei (^{1}H, ^{19}F, and ^{11}B) they can be characterized by variety of NMR spectroscopic methods. A complete spectral analysis for **3.3d** is provided here as a representative example with discussion of other derivatives included as warranted.

The ^{1}H NMR spectrum of **3.3d** exhibits the expected number of signals for an asymmetric molecule of type **3.3** (**Figure 3.5**). The isopropyl methyl groups are present as four six-proton doublets with the two inequivalent methine proton septets occurring at 3.2 ppm and 2.9 ppm respectively. The sole remaining indole type hydrogen atom is shifted slightly upfield (9.0 ppm) with respect to **1.32d** (9.6 ppm) and remains exchangeable in D_2O. The protons from the N-aromatic substituents and the Nindigo core are present in the expected integration. Unlike their parent Nindigos, there is no evidence of tautomerism for any derivatives of **3.3**.

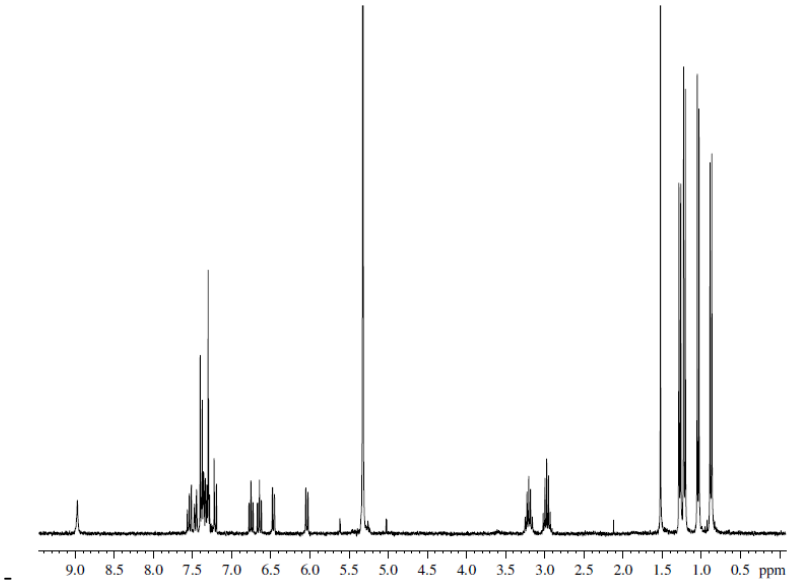

Figure 3.5: ^{1}H NMR spectrum of **3.3d** (Sample run in CD_2Cl_2)

The ^{19}F NMR spectrum displays a quartet centered at -125.7 ppm with a coupling constant of 30 Hz resulting from coupling to the ^{11}B nucleus (the smaller multiplet buried beneath the dominant signal is a result of coupling to the 20% abundant spin active ^{10}B nuclei). The ^{11}B NMR spectrum exhibits a triplet centered at 1.9 ppm, as a result of coupling to the two equivalent fluorine nuclei (**Figure 3.6**).

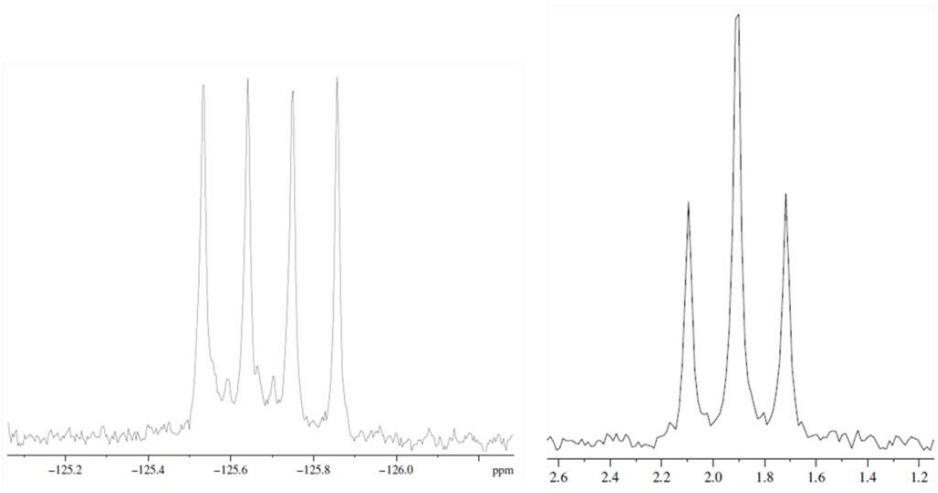

Figure 3.6: ^{19}F (left) and ^{11}B (right) spectra of **3.3d** (Samples run in CD_2Cl_2)

Converting the only Nindigo derivative that possesses mono-*ortho* substitution on the N-aryl ring, **1.32e**, to **3.3e,** results in two signals in the ^{19}F spectrum and a doublet of doublets in the ^{11}B spectrum (**Figure 3.7**). These spectral features suggest that the bulky t-butyl groups hinder the rotation of the N-aryl ring rendering the two fluorine atoms in **3.3e** chemically inequivalent. Like their parent Nindigos, derivatives of **3.3** appear to undergo incomplete combustion therefore obtaining reliable elemental analyses has proven problematic.

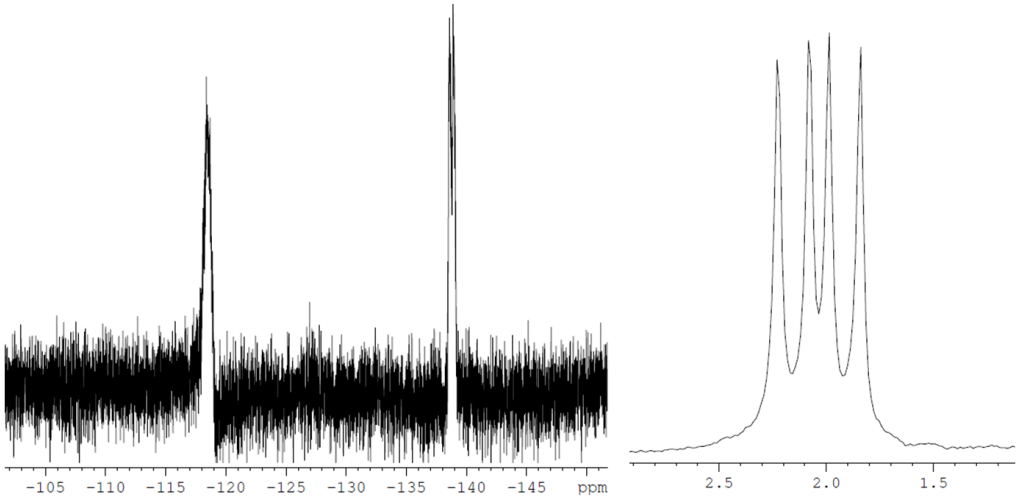

Figure 3.7: ^{19}F (left) and ^{11}B (right) NMR spectra for **3.3e** (Samples run in CD_2Cl_2)

Single crystal X-ray structures of a variety of **3.3** derivatives have been obtained and the structure of each compound is as expected from NMR spectroscopy. **3.3b** will be discussed in detail as a representative example (**Figure 3.8**) with discussion of other derivatives included as warranted.

The boron atom adopts a pseudo-tetrahedral geometry and is displaced out of the plane of the Nindigo chelate (NCCCN) by 0.35 Å. The boron-nitrogen (BN) bond between the anionic indolide nitrogen and the boron atom (1.54 Å) is shorter than that of the imine BN bond (1.57 Å). This is reminiscent of the bonding environments observed in similar anilido-imine and anilido-pyridine ligand systems bound to a BF_2 unit.[128,130,131] The N-aryl units are highly twisted relative to the plane of the Nindigo core by 55^o and 57^o respectively. Torsion angles are largest for those derivatives possessing *ortho*-substituents on the N-aryl rings (**3.3c**, **3.3d** and **3.3e**,) where they approach being truly orthogonal

(80-90^{o}). Derivatives without *ortho*-substitution (**3.3a**, **3.3b**, and **3.3f**) have more freedom to rotate. This is reflected by N-aryl twisting that spans a larger range (43-90^{o}). The long axis, encompassing the central carbon-carbon bond, of **3.3b** remains flat. This holds true for all derivatives with the exception of **3.3e** where there is some buckling observed (**Figure 3.9**). In some respects the bond metrics of **3.3b** are similar to those of its parent Nindigo, **1.32b**. A number of carbon-carbon and carbon-nitrogen bonds deviate from true single and double bond lengths suggested by the canonical valence bond representation shown in **Scheme 3.1**. However, due to the asymmetry of the molecule there are some noticeable differences in bond lengths. The boron bound imine (C22-N22) is considerably longer (1.42 Å) than the imine on the unbound side (C12-N12, 1.29 Å). The C21-C22 and C11-N11 bonds of the pseudo-six membered heterocycle are shorter (1.42 Å, 1.35 Å) than their counterparts (C11-C12 and C21-N21) on the unbound side (1.47 Å, 1.38 Å). These bond matrices infer a more pronounced delocalization about the boron bound side of the molecule. This suggests structure **3.4** to be a reasonable canonical representation for derivatives of **3.3**.

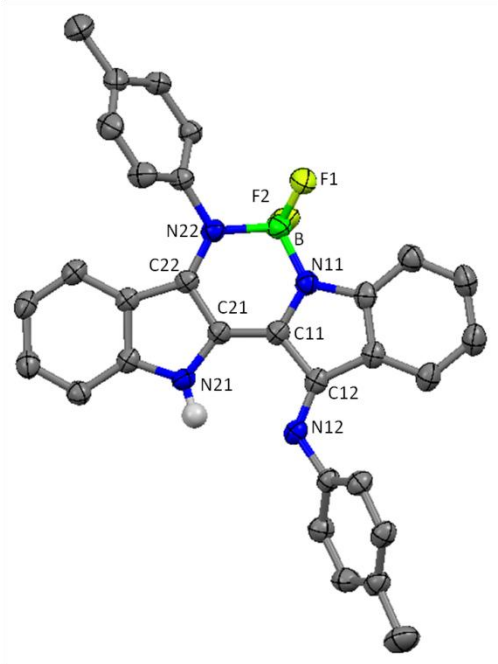

Figure 3.8: X-ray crystal structure of **3.3b**. Thermal ellipsoids at the 50% probability level with all hydrogen atoms, with the exception of the indole type hydrogen, removed for clarity

Atoms	Length (Å)	Atoms	Angle (deg)
C11-C21	1.374 (3)	N11-B-N22	107.92 (16)
C11-C12	1.469 (2)	N11-B-F1	111.32 (19)
C12-N12	1.287 (2)	N11-B-F2	109.08 (16)
C21-C22	1.423 (2)		
C22-N22	1.349 (2)		
C21-N21	1.376 (2)		
C11-N11	1.353 (2)		
N11-B	1.539 (3)		
N22-B	1.571 (3)		

Table 3.1: Selected bond lengths and angles for **3.3b**

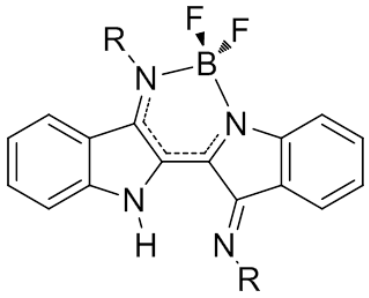

3.4

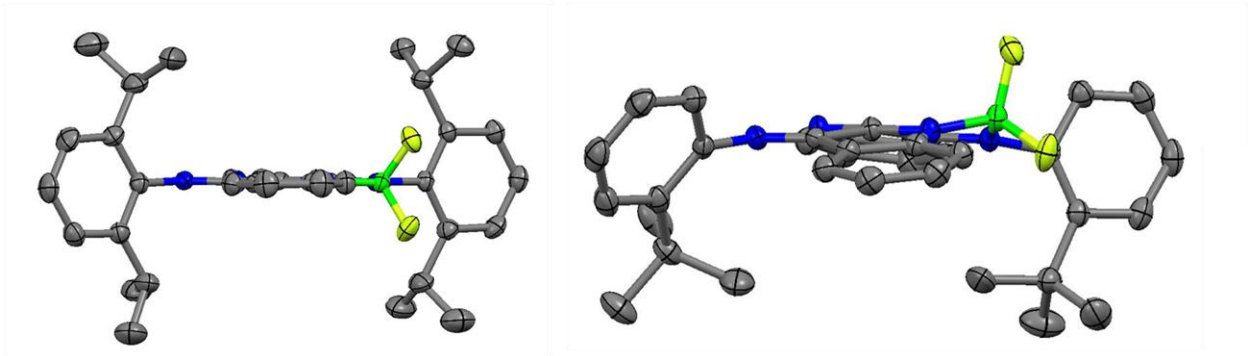

Figure 3.9: X-ray crystal structures of **3.3d** (left) and **3.3e** (right) viewed down the central carbon-carbon bond. Thermal ellipsoids at the 50% probability level and all hydrogen atoms removed for clarity

Similar to the bis-Pd(hfac) chelates of Nindigo, **1.33** (*cf.* chapter 2), boron occupation of a Nindigo cavity has a significant effect on the ligand centered chromophore (**Figure 3.10**). The resulting electronic absorption bands observed for **3.3** are red shifted ($\lambda_{max} \approx 650$ nm) with respect to free Nindigo ($\lambda_{max} \approx 590$ nm). The strongest transitions are either significantly more intense (for **3.3a** and **3.3b**) or maintain their high intensity (for **3.3c** and **3.3d**) with respect to their parent Nindigos. Molar extinction coefficients for all derivatives of **3.3** are in the order of 30.0 x 10^3 M^{-1} cm^{-1}. Both the energy and intensity of the main transition appear to be independent of the nature of the N-aryl substituent. Like their parent Nindigos, all derivatives of **3.3** follow Beer's law within a concentration range of 1.0 x 10^{-4}-10^{-6} M. The bathochromic shift upon coordination of a BF_2 unit is reminiscent of that observed for the boron chelation of N-methyltetrahydroindigo, where the λ_{max} shifts from 584 nm to 670 nm.[132]

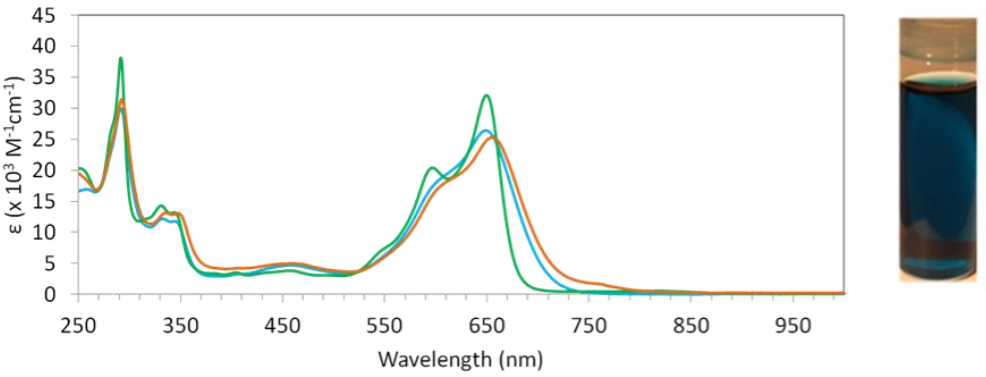

Figure 3.10: UV/vis/NIR absorption spectra for **3.3b** (blue), **3.3d** (green) and **3.3f** (brown). Spectra obtained in DCM at a concentration of 1.25 x 10^{-5} M. Photograph of a solution of **3.3c** (right)

Our previous work showed the Nindigo ligand system to be redox-active.[85,86] Cyclic voltammetry experiments were conducted on derivatives of **3.3**. Generally these compounds have one reversible oxidation at *ca.* +0.55 V, followed by a second irreversible oxidation process at potentials greater than +0.83 V. There are also two irreversible reduction processes present at lower potentials than -1.10 V (**Figure 3.11**).

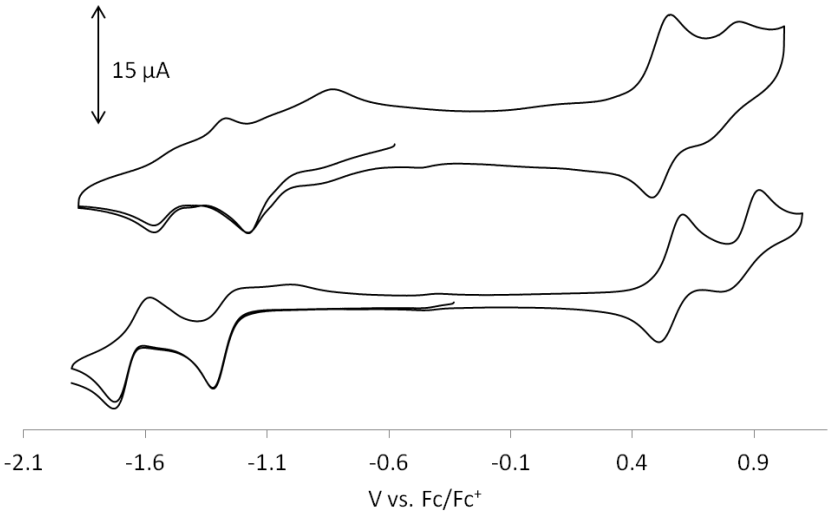

Figure 3.11: Cyclic voltammograms of **3.3a** (top) and **3.3c** (bottom) (DCM solution, 0.1 mM Bu_4NBF_4 electrolyte and scan rate = 100 mVs^{-1})

Derivative	Reduction (V)	Oxidation (V)
3.3a	-1.17[a], -1.56[a]	+0.53, +0.83[a]
3.3c	-1.32[a], -1.73[a]	+0.56, +0.92[a]

Table 3.2: Electrochemical data for mono-BF_2 Nindigo chelates **3.3a** and **3.3c** ([a] = irreversible)

Although **3.3** is a new example of a low energy absorbing, redox-active capping ligand, the primary goal of the main group chemistry of Nindigo was chelation of two BF_2 moieties. Initial attempts at obtaining the bis-BF_2 chelates of Nindigo (**3.5**) were thwarted by the hydrolytic sensitivity of the resulting compounds. Mixtures of mono- and bis-BF_2 chelates were often obtained with the bis-BF_2 chelates found by NMR to be the minor products (see below). In order to promote the formation of bis-BF_2 Nindigo chelates over mono-BF_2 chelates the reaction conditions were changed to be anhydrous. Further manipulation of the reaction conditions showed that the nature of both the base and solvent as well as the order of reagent addition plays a crucial role in the product ratios of **3.5** and **3.3** obtained. Increasing the steric bulk of the base from triethylamine to lutidine and finally to diispropylethylamine (Hünigs base) led to incremental increases in the proportion of **3.5**. Changing the solvent from THF to

toluene was also conducive to improving the ratio of **3.5** to **3.3**. Finally, adding the base last to a mixture of Nindigo and $BF_3{\cdot}Et_2O$ produced **3.5** in yields of greater than 70%. Derivatives of **3.5** are isolated as dark green solids (**Scheme 3.2**). All Nindigos were now able to be selectively converted to both **3.3** and **3.5** with the exception of **1.32e** (see below).[129]

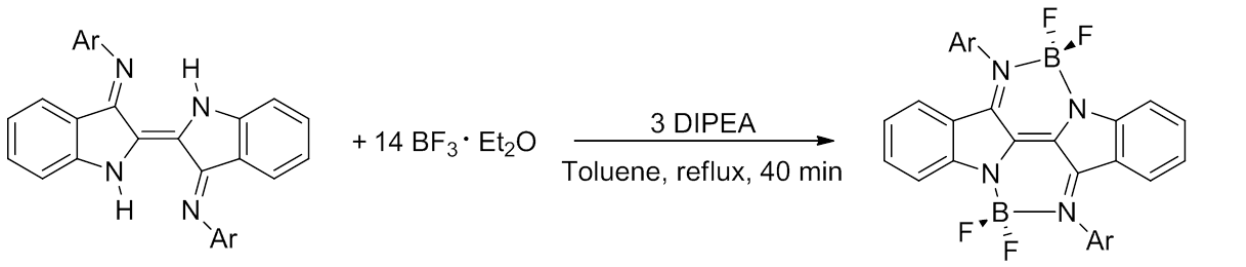

3.5a Ar = Phen [78%]
3.5b Ar = pTol [88%]
3.5c Ar = Dmp [84%]
3.5d Ar = Dipp [79%]
3.5f Ar = pClPhen [85%]

Scheme 3.2: Conditions employed to promote **3.5** as the major product

Derivatives of **3.5** exhibit the same solubility trends seen for Nindigo. The bulkier derivatives (**3.5b** and **3.5d**) exhibit reasonable solubility in a range of solvents and the less bulky derivatives (**3.5a**, **3.5b** and **3.5f**) prove to be less soluble. **3.5f** exhibits very limited solubility, which has hindered its full characterization. ^{1}H, ^{19}F and ^{11}B NMR spectroscopy can be used to readily distinguish between the derivatives of **3.3** and **3.5**. A full spectral analysis of **3.5c** is shown as a representative example. The ^{1}H NMR spectrum exhibits the number of signals expected for the structure depicted in scheme 3.2. There is only one aliphatic signal (2.3 ppm) corresponding to the 12 protons of the methyl groups that are rendered equivalent by the C_{2h} symmetry. There are no downfield signals (beyond 8.5 ppm) confirming double deprotonation of the indole type hydrogen atoms (**Figure 3.12**).

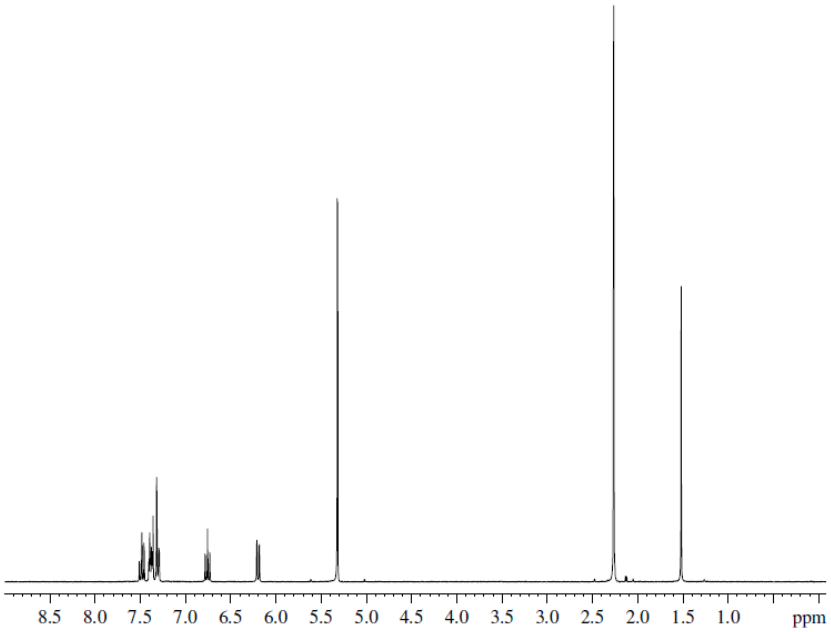

Figure 3.12: ^{1}H NMR spectrum of **3.5c** (Sample run in CD_2Cl_2)

The ^{19}F and ^{11}B spectra exhibit the same quartet and triplet multiplicities observed for **3.3c** along with the same 30 Hz coupling constants. However, the chemical shifts are slightly different (^{19}F = -131.0 and ^{11}B = -2.0 ppm for derivatives of **3.5**) (**Figure 3.13**).

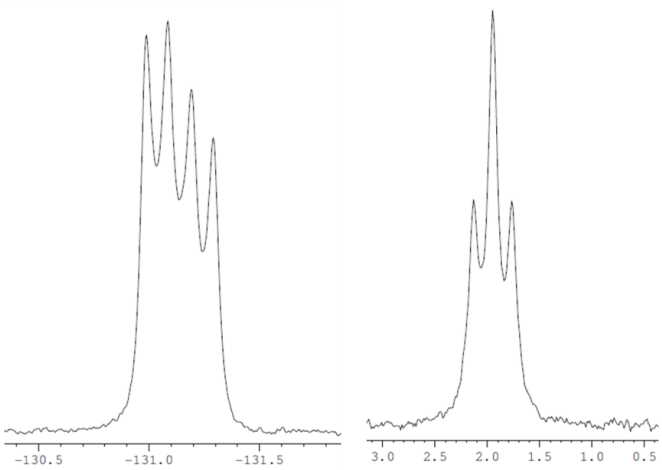

Figure 3.13: ^{19}F (left) and ^{11}B (right) NMR spectra of **3.5c** (Samples run in CD_2Cl_2)

Derivatives of **3.5** are all intensely coloured ($\varepsilon \approx 30.0 \times 10^3$ M^{-1} cm^{-1}) and exhibit lower energy transitions ($\lambda_{max} \approx 760$ nm) than both their parent Nindigo and their analogous mono-BF_2 Nindigo chelates (**Figure 3.14**). This suggests that occupancy of both binding cavities has a more significant effect on the HOMO-LUMO gap than single occupancy. This is reminiscent of the bathochromic shifts observed for mono- and bis-Pd(hfac) chelates of Nindigo (chapter 3).

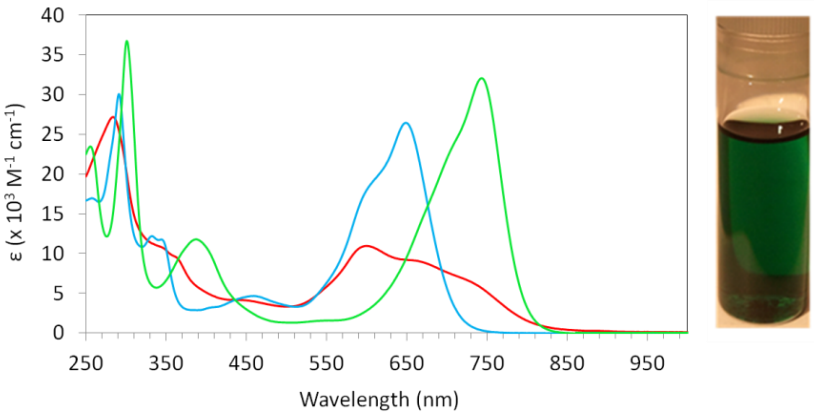

Figure 3.14: UV/vis/NIR spectra of **1.32b** (red), **3.3b** (blue) and **3.5b** (green). Spectra obtained in DCM at a concentration of 1.25×10^{-5} M. Photograph of a solution of **3.5d** (right)

Although stable in the solid state for extended periods of time (weeks), derivatives of **3.5** exhibit limited stability in solution and gradually decompose to their corresponding mono-BF_2 chelates. The decomposition can be monitored by NMR spectroscopy. During the decomposition a new peak appears in the ^{11}B NMR spectrum as a sharp singlet at *ca.* -1.0 ppm. Although the identity of this species is currently unknown, the lack of any coupling suggests the boron is no longer bound to any fluorine atoms. The sensitivity in solution of **3.5** has prevented any X-ray structures from being obtained. However, insights can be drawn from the solid state structures of **3.3** as to why derivatives of **3.5** may exhibit such sensitivity. Of particular significance is the interatomic distance between the imine and indolide type nitrogen atoms (refer to figure 3.7) (**Table 3.3**). The chelating side of **3.3** has N(imine)-N(indolide) separations of *ca*. 2.5 Å. This is comparable to similar BF_2 chelate systems and likely the ideal distance for boron binding.[130,131] The unbound side has N-N separations ranging from 2.93 Å, for *ortho* unsubstituted derivatives, to 3.05 Å for those possessing *ortho* substituents. The two separations are

smaller and larger respectively than the typical N-N separations found in Nindigo (≈ 2.8 Å) where the pair of N-N distances are equivalent by symmetry. It appears that in order to effectively accommodate one BF_2 unit, the binding cavity must bite inwards resulting in an expansion of the opposing cavity. The BN bond distances in derivatives of **3.5** are likely longer than those in **3.3** rendering them more sensitive and prone to cleavage. The largest expansion upon mono-BF_2 chelation is observed for **3.5e** and for this derivative no evidence of bis-BF_2 chelation was observed.

Derivative	N---N (boron bound) (Å)	N---N (unbound) (Å)
3.3a	2.504 (2)	2.989 (2)
3.3b	2.514 (3)	2.927 (3)
3.3c	2.498 (2)	3.015 (2)
3.3d	2.503 (2)	2.968 (2)
3.3e	2.485 (2)	3.047 (2)
3.3f	2.512 (2)	2.946 (2)

Table 3.3: Nitrogen-nitrogen distances of the bound and unbound cavities of derivatives of **3.3**

The rate of degradation of **3.5** was found to be dependent on the nature of the N-aryl substituent. The less bulky derivatives (**3.5a** and **3.5b**) exhibit longer lifetimes than their bulkier counterparts (**3c** and **3d**). The conversion of **3.5b** to **3.3b** was monitored by a time dependent ^{19}F NMR study (**Figure 3.15**). After 10 days **3.5b** was still the most abundant species but significant amounts of **3.3b** were also present. The decomposition of **3.5d** was followed by electronic spectroscopy (**Figure 3.15**). After 2 days in solution **3.3d** was found to be the dominant species with very little **3.5d** remaining. Multiple isosbestic points are observed during the decomposition, indicative of a clean conversion with respect to Nindigo.

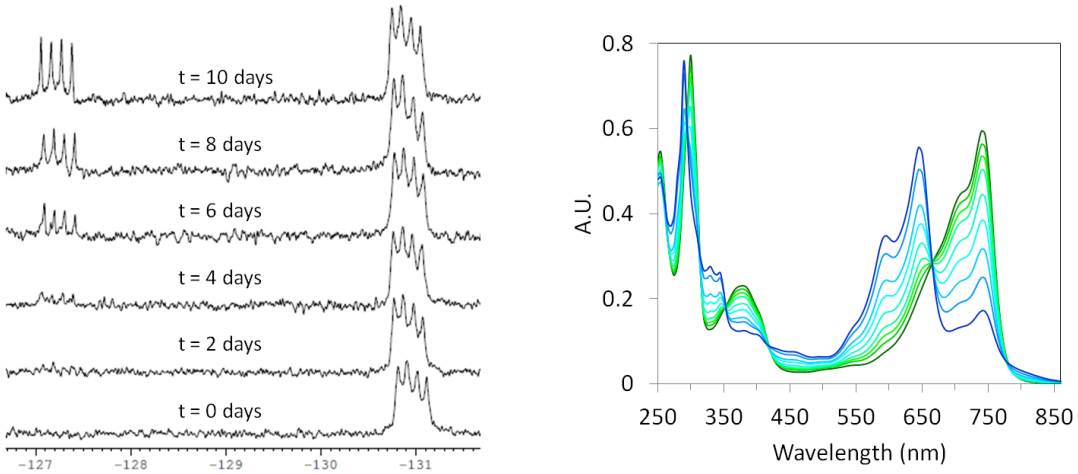

Figure 3.15: Time dependant ^{19}F NMR showing conversion of **3.5b** to **3.3b** in dry degassed CD_2Cl_2 at room temperature (left) and time dependent UV/vis/NIR spectroscopy showing the conversion of **3.5d** to **3.3d** in DCM over 90 hours

Just as occupation of both Nindigo cavities in bis-Pd(hfac) complexes (**1.33**) rendered all ligand based redox events fully reversible, bis-BF_2 chelation does likewise (**Figure 3.16**). All derivatives of **3.5** exhibit one fully reversible one-electron oxidation at *ca.* +0.80 V. All derivatives also exhibit two reversible one-electron reduction processes, the first of which appears between -0.67 V and -0.50 V with the second reduction occurring within a broader range of -1.07 V and -1.56 V.

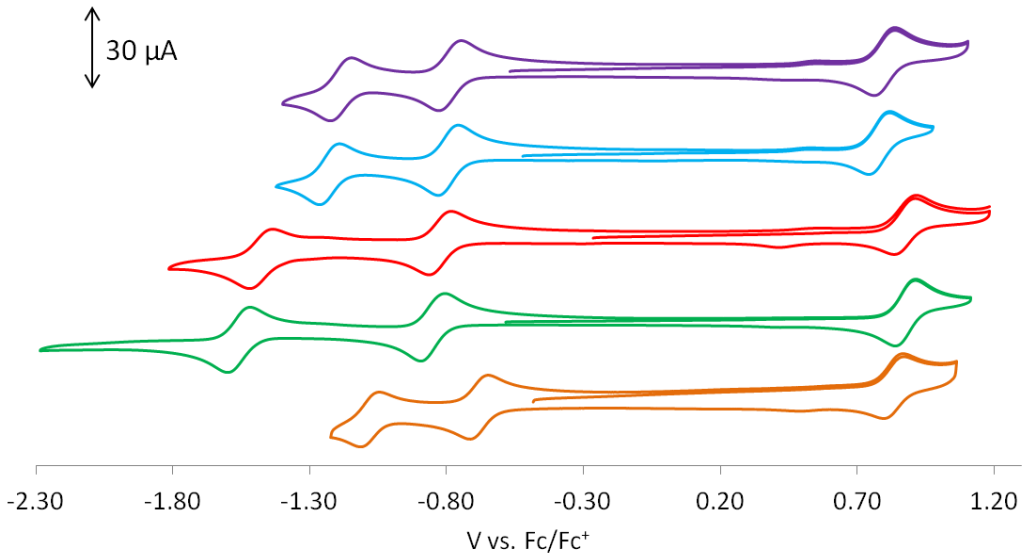

Figure 3.16: Cyclic voltammogram of **3.5a (**purple), **3.5b** (blue), **3.5c** (red), **3.5d** (green), **3.5f** (brown) (DCM solution, 0.1 mM Bu_4NBF_4 electrolyte and scan rate = 100 mVs^{-1})

The degree of separation between oxidation or reduction events provides information regarding the charge distribution of the generated radical ions.[116] The gap between reduction potentials (**Table 3.4**) ranges from 400 mV (for **3.5a**, **3.5b**, **3.5f**) to 710 mV (for **3.5c**, **3.5d**). This suggests the less bulky derivatives are able to delocalize the negative charge more effectively than the bulkier analogues.[116, 117] The differing redox potentials observed for derivatives of **3.5** can be attributed to a combination of both coulombic and steric factors. The two reductions of **3.5f** occur at more positive potentials than that of the closest derivative. This is likely due to the electron withdrawing nature of the chlorine atom on the N-aryl ring. This renders the Nindigo core with less electro dense and therefore easier to reduce. Surprisingly, **3.5f** is not the hardest to oxidize. The oxidation potentials of the bulkier derivatives (**3.5c** and **3.5d**) are approximately 0.10 V higher in energy than the other analogues that also do not possess electronicically active substituents. Another distinguishing feature of the bulkier derivatives is that their second reduction potentials are approximately 0.30 V lower in energy than the corresponding reduction potentials of **3.5a** and **3.5b**. The aliphatic nature of the substituents makes it unlikely that the differing potentials are a result of inductive effects. More likely the variation is a result of differing degrees of extended delocalization onto the N-aryl rings. As a result of steric interactions between the *ortho*-substituents and the hydrogen atoms of the benzannulated ring, the N-aryl rings in **3.5c** and **3.5d** are forced orthogonal with respect to the Nindigo core (**Figure 3.17**). For **3.5a** and **3.5b** there is less of a

steric barrier to rotation and this partial freedom permits some additional delocalization onto the N-aryl rings. This results in the anionic charge being less localized at the Nindigo core and therefore less columbic repulsion felt upon the addition of the second electron.

Derivative	Reduction (V)	Oxidation (V)
3.5a	-0.79, -1.19	+0.80
3.5b	-0.80, -1.22	+0.78
3.5c	-0.82, -1.48	+0.88
3.5d	-0.85, -1.56	+0.84
3.5f	-0.67, -1.07	+0.84

Table 3.4: Electrochemical data for derivatives of **3.5**

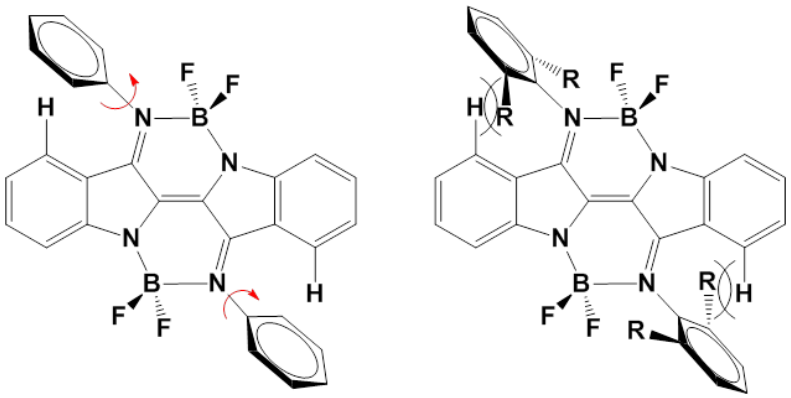

Figure 3.17: *ortho*-unsubstituted skeleton of **3.5** (left) and *ortho*-substituted skeleton of **3.5** (right) showing aryl twist hindering free rotation

Both **3.3** and **3.5** were subjected to computational studies though DFT calculations (all computations conducted by R.G. Hicks). Geometry optimizations were conducted using the B3LYP functional (6-31G* basis set). Structural parameters for **3.3a** and **3.5a** are shown as representative

examples (**Figure 3.18**). Calculated bond metrics for both derivatives are summarized along with bond lengths for **3.3a** obtained crystallographically.

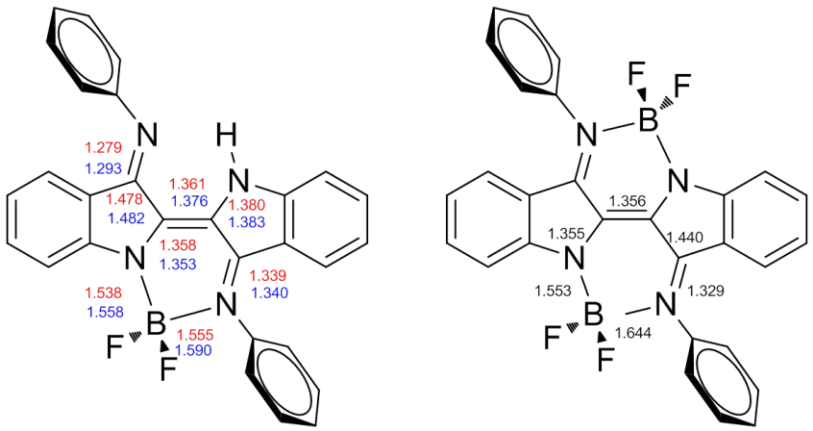

Figure 3.18: Calculated bond lengths for **3.3a** (left red) and experimental bond lengths for **3.3a** (left blue). Calculated bond lengths for **3.5a** (right)

There is good agreement between calculated and experimental bond lengths for the delocalized skeleton of **3.3a** with all CC and CN bond distances within 0.01 Å. However, there is larger disagreement between the experimental and calculated distances for the BN bonds. Both the B-N(indolide) and B-N(imine) bonds are calculated to be longer than those found experimentally by 0.02 Å and 0.03 Å respectively. The calculated bond lengths for **3.5a** are comparable to that of **3.3a** with the exception that the B-N(imine) is predicted to be relatively long, 1.644 Å. This may be another manifestation of the less than optimal chelating environments that Nindigo possesses for boron, leading to the instability of derivatives of **3.5**.

The frontier molecular orbitals (FMOs) of **3.3a** and **3.5a** are delocalized π-orbitals spanning the planar core of the Nindigo ligand with dominant contributions coming from the central CC, imine π-bonds and indole type nitrogen atoms. There is partial delocalization onto the benzannulated rings of the ligand core and the hindered rotation allows for only partial delocalization onto the N-aryl rings. This extended delocalisation could change the energies of the FMOs (**Figure 3.19**). The general features of the FMOs are reminiscent of indigo where the donor indole type nitrogen atom and acceptor carbonyl configuration have long been recognized as the reason behind the low energy transition. Time dependant DFT predicts transitions at 639 nm and 716 nm respectively, in good agreement with those

observed experimentally (649 nm and 744 nm). The relative energies of the HOMO and LUMO of **3.3a** and **3.5a** also correlate well with experimental results. Both the HOMO and LUMO of **3.5a** are lower in energy than **3.3a**. This is reflected by **3.5a** being electrochemically harder to oxidize but easier to reduce.

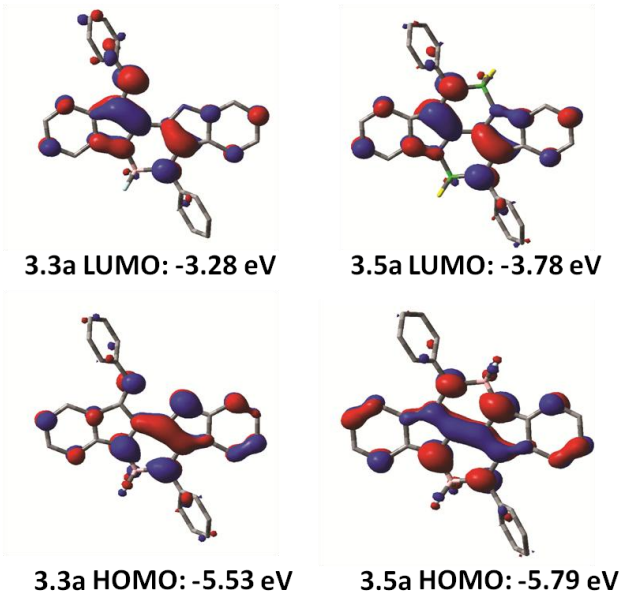

Figure 3.19: FMO contour plots and energies for **3.3a** and **3.5a**

The photophysical properties of **3.3** and **3.5** were examined in dilute CH_2Cl_2 solution (all emission studies conducted by M. Majewski at UBC). Preliminary studies indicate that both families exhibit weak emission in the NIR (**Figure 3.20**). Unlike the absorption maxima, there is substantial variation in the emission wavelengths within each series of compounds.

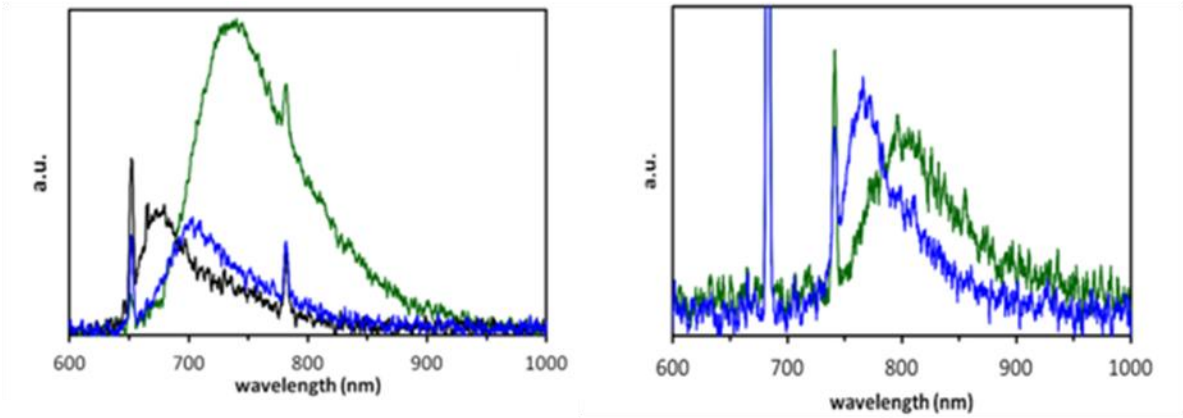

Figure 3.20: Emission spectra of selected derivatives of **3.3** (left, black = **3.3d**, blue = **3.3e**, green = **3.3a**) and **3.5** (right blue = **3.5d**, green = **3.5b**). The sharp peaks are due to the laser source

The Stokes shifts for derivatives of **3.3** ranges from 31-107 nm, whilst for derivatives of **3.5** the range is between 32-67 nm. Compounds with less sterically demanding substituents (**a, b**, and **f**) have the largest Stokes shifts. This suggests that the steric demands of the N-R group has important consequences for the nature of the excited state electronic structures of **3.3** and **3.5** (**Table 3.5**).

Derivative	λ_{abs} (nm)	ε_{max} (10^3 M^{-1} cm^{-1})	λ_{em} (nm)	Stokes shift (cm^{-1})
3.3a	649	21.1	750	2075
3.3b	649	29.9	756	2180
3.3c	646	39.7	687	924
3.3d	650	31.3	686	808
3.3e	654	25.7	712	1246
3.3f	655	25.3	762	2144
3.5a	744	26.0	800	941
3.5b	743	34.2	808	1083
3.5c	746	31.8	-	-
3.5d	742	24.4	774	557
3.5f	752	26.3	819	1088

Table 3.5: Absorption and emission data for **3.3** and **3.5**

3.3 Synthesis of heteronuclear boron-palladium Nindigo chelates

Reactions of **3.3** with 1 equivalent of $Pd(hfac)_2$ yields the corresponding heteronuclear complexes, **3.6**, in high yields (**Scheme 3.3**). The solubility characteristics of **3.6** are similar to those of the parent Nindigos, with the bulkier derivatives (**3.6c** and **3.6d**) exhibiting a higher degree of solubility than the less bulky derivatives (**3.6a, 3.6b** and **3.6f**). Unlike derivatives of **3.5**, the heteronuclear species are stable in solution showing no signs of decomposition over extended periods of time (days).[129]

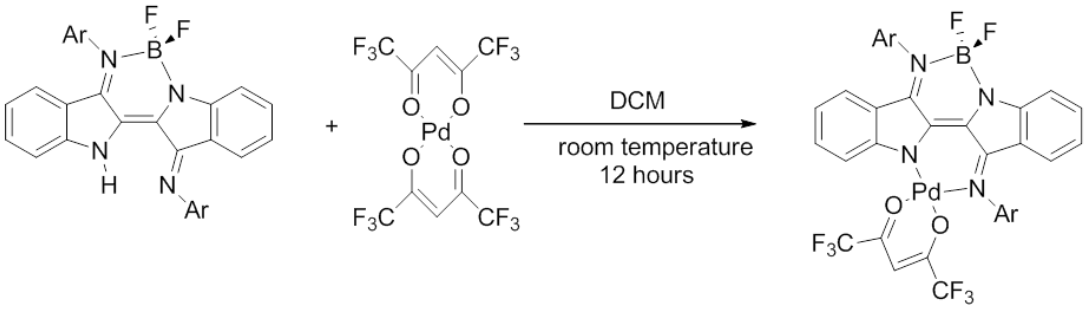

3.6a Ar = Phen [94%]
3.6b Ar = pTol [76%]
3.6c Ar = Dmp [77%]
3.6d Ar = Dipp [72%]
3.6f Ar = pClPhen [42%]

Scheme 3.3: Synthesis of palladium chelates of **3.3**

Derivatives of **3.6** all exhibit similar NMR spectra and **3.6b** will be discussed in detail as a representative example (**Figure 3.21)**. Similar to derivatives of **3.3**, the ^{1}H NMR reflects the asymmetry of the molecule with more signals being observed in comparison to the centrosymmetric derivatives, **1.32, 1.33** and **3.5**. The *para*-methyl groups are rendered inequivalent (2.50 ppm and 2.43 ppm) and the lack of any downfield signal, beyond 8.5 ppm, indicates the deprotonation of the indole type hydrogen atom of **3.3b**. The additional singlet for the hfac proton is observed at 6.26 ppm.

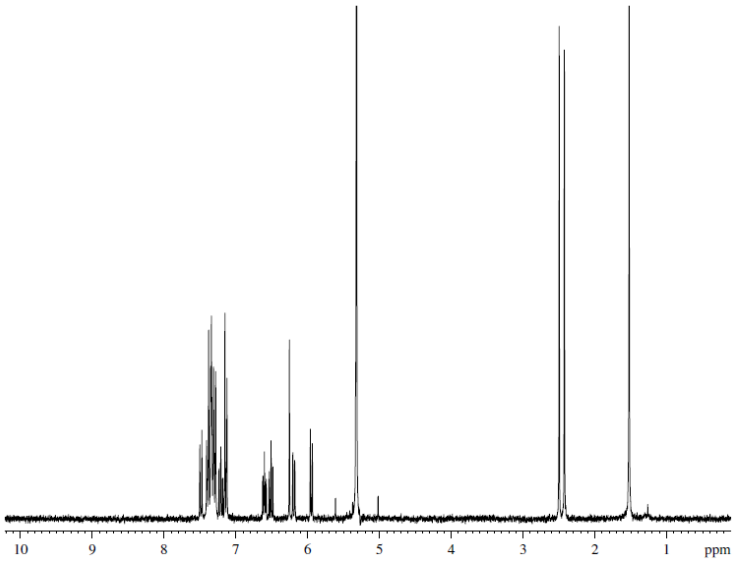

Figure 3.21: ^{1}H NMR spectrum of **3.6b** (Sample run in CD_2Cl_2)

A triplet is observed in the ^{11}B NMR spectrum at -1.48 ppm with the approximately 30 Hz coupling to the two equivalent fluorine nuclei maintained (**Figure 3.22**). The quartet in the ^{19}F NMR spectrum appears at -130.8 ppm along with two additional singlets at -73.4 ppm and -74.9 ppm respectively; the latter two signals corresponding to the two (inequivalent) CF_3 units of hfac (**Figure 3.22**).

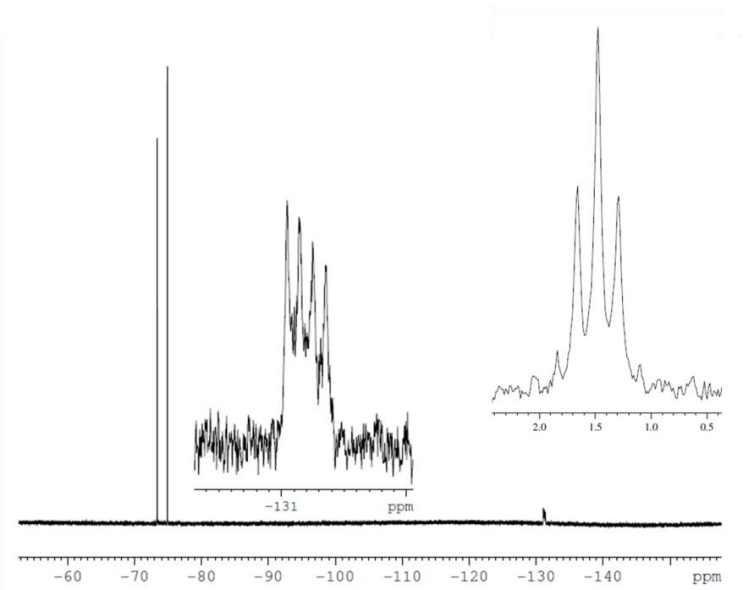

Figure 3.22: ^{19}F and ^{11}B spectra (inset right) of **3.6b** (Samples run in CD_2Cl_2)

X-ray crystal structures have been obtained for a number of derivatives of **3.6** with **3.6a** being discussed as a representative example (**Figure 3.23**). The boron atom remains approximately tetrahedral and resides within the chelating plane. The N(imine)-B and N(indolide)-B bonds remain very similar to those in **3.3** with the donor acceptor bond being slightly longer for **3.6a** (1.588 Å vs. 1.538 Å). Bonding on both sides of **3.6a** are intermediate in character between single and double bonds, whereas delocalization is more pronounced on the boron bound side of **3.3a** with localized bonding on the opposing side. This suggests that the delocalization in **3.6a** is more diffuse over the molecule than for **3.3a**. The intramolecular imine(N)-indolide(N) distances remain similar to those observed in **3.3**. This indicates little structural rearrangement is necessary to accommodate the Pd(hfac) unit. The palladium bound side of the molecule exhibits bond lengths that are similar to that of **1.33a** and the palladium atom deviates only slightly from being square planar with angles around the palladium ranging from 87.7^{o} to 92.6^{o} (**Table 3.6**). The palladium atom lies out of Nindigo C4N2 plane by 0.47 Å. The N-aryl twist on the boron bound side of the molecule is 81.4^{o} with that of the opposing side twisted by 77.4^{o}.

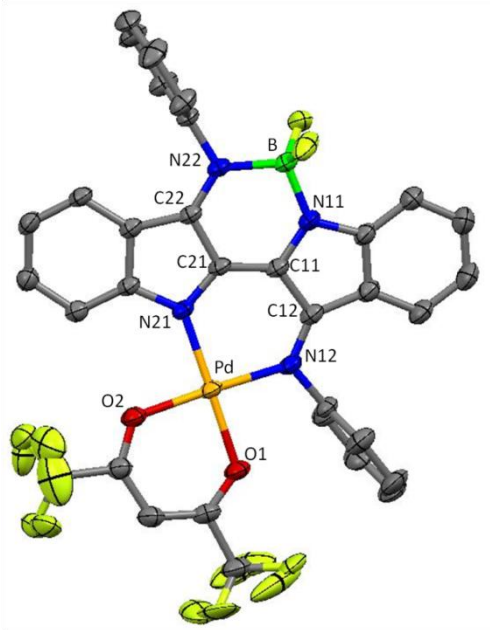

Figure 3.23: X-ray crystal structure of **3.6a**. Thermal ellipsoids at the 50% probability level and all hydrogen atoms removed for clarity

Atoms	Length (Å)	Atoms	Angles (deg)
C11-C21	1.365 (3)	N11-B-N22	107.6 (2)
C21-C22	1.449 (3)	N11-B-F7	110.5 (2)
C22-N22	1.323 (3)	N11-B-F8	111.7 (2)
C11-N11	1.366 (3)	F7-B-F8	109.5 (2)
C11-C12	1.449 (3)	N21-Pd-N12	92.57 (8)
C12-N12	1.314 (3)	N21-Pd-O2	89.65 (8)
C21-N21	1.358 (3)	O2-Pd-O1	90.39 (8)
N11-B	1.538 (3)	O1-Pd-N12	87.60 (8)
N22-B	1.588 (4)		
N21-Pd	1.9969 (19)		
N12-Pd	2.019 (2)		

Table 3.6: Selected bond lengths and angles for **3.6a**

Derivatives of **3.6** exhibit similar, but less severe, bowing of the Nindigo core compared to derivatives of **1.33** (**Figure 3.24**). The bowing can be quantified by measuring the angle defined by the planes of the benzannulated rings. The distortion is far less pronounced for **3.6a** (16.08^{o}) than that observed for the bis-palladium derivative **1.33b** (22.43^{o}). For the bulkiest heteronuclear derivative, **3.6d**, there is no bowing and the benzannulated rings are coplanar.

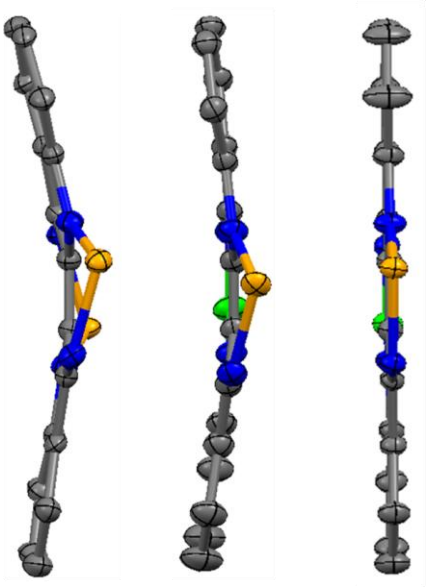

Figure 3.24: X-ray crystal structures of **1.33b** (left), **3.6a** (centre) and **3.6d** (right) showing core puckering (all hydrogen atoms, hfac units and N-aryl substituents removed for clarity)

Derivatives of **3.6** all exhibit strong low energy electronic absorptions ($\lambda_{max} \approx$ 830 nm, $\varepsilon \approx$ 20.0 x 10^3 M^{-1} cm^{-1}) with little difference observed upon varying the N-aryl substituent (**Figure 3.25**). The main visible transition is red shifted with respect to Nindigo and lies between that of **3.3** and **1.33**.

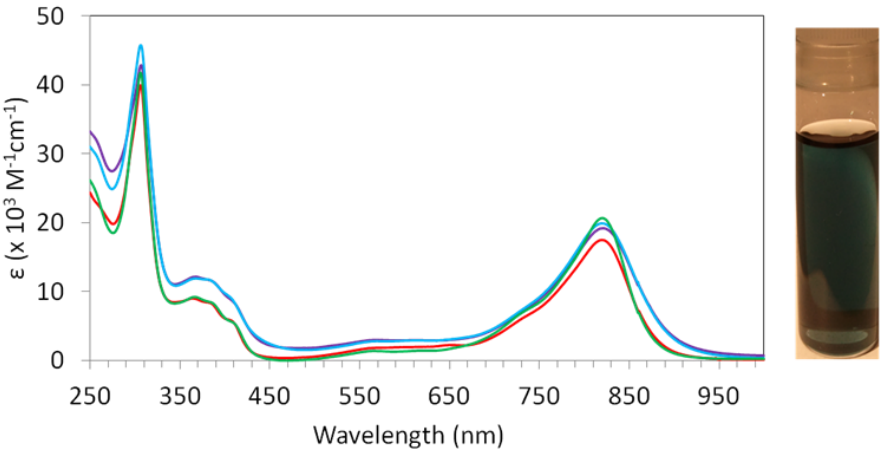

Figure 3.25: UV/vis/NIR spectra of **3.6a** (purple), **3.6b** (blue), **3.6c** (red) and **3.6d** (green). Spectra obtained in DCM at a concentration of 1.25 x 10^{-5} M. Photograph of a solution of **3.6a** (right)

The sequential red-shift of the π-π* transition with varying cavity occupation can be neatly demonstrated by comparing the electronic absorption profiles of all members of a single Nindigo derivative (**Figure 3.26**). The absorption energy spans a range of 316 nm and extends into the NIR region (**Table 3.7**).

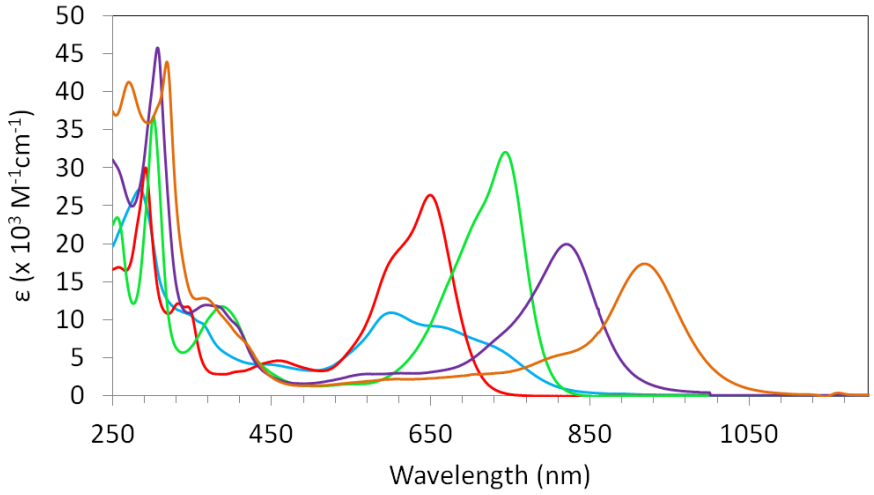

Figure 3.26: UV/vis/NIR spectra of the complete pTol family. **1.32b** (blue), **3.3b** (red), **3.5b** (green), **3.6b** (purple), **1.33b** (orange). All spectra obtained from DCM at a concentration of 1.25 x 10^{-5} M

pTol derivative	λ_{max} (nm)	ε (x 10^3 M^{-1} cm^{-1})
1.32b	603	11.0
3.3b	649	30.0
3.5b	743	34.0
3.6b	820	20.0
1.33b	919	17.0

Table 3.7: Electronic spectroscopy data for the homologues N-ptolyl Nindigo derivatives

Derivatives of **3.6** all exhibit multiple electrochemical processes. The *ortho*-unsubstituted derivatives (**3.6a**, **3.6b**, **3.6f**) all exhibit a reversible one-electron oxidation (*ca.* +0.45 V) accompanied by a second pseudo-reversible one-electron oxidation (*ca.* +0.88 V). They also possess two reversible one-electron reductions (*ca.* -1.08 V and -1.28 V). Derivatives with *otho*-N-aryl substituents (**3.6c**, **3.6d**)

display two reversible one-electron oxidations (*ca.* +0.50 V and +0.95 V), a single reversible one-electron reduction and an irreversible reduction event (*ca.* -1.10) (**Figure 3.27**).

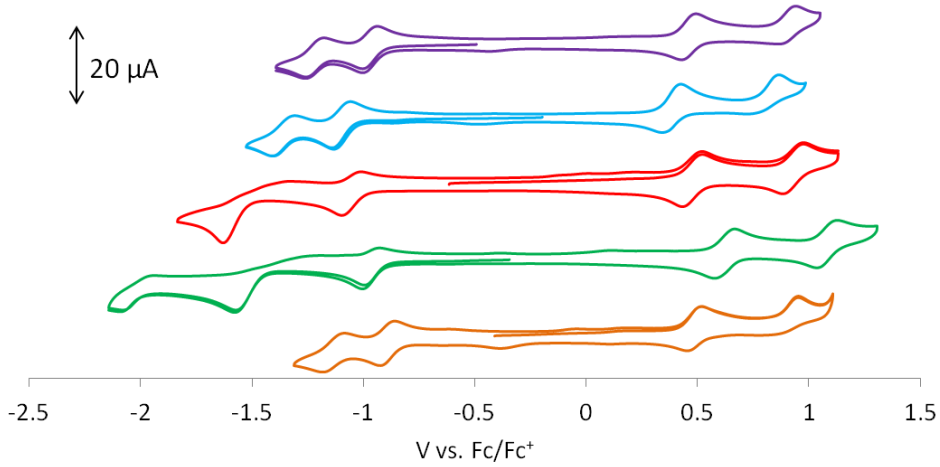

Figure 3.27: Cyclic voltammagrams for **3.6a** (purple), **3.6b** (blue), **3.6c** (red), **3.6d** (green) and **3.6f** (brown) (DCM solution, 0.1 mM Bu_4NBF_4 electrolyte and scan rate = 100 or 250 mVs^{-1})

3.6f is significantly easier to reduce (-0.87 V) than the nearest reducible derivative, **3.6a**. This characteristic was also observed for the analogous compounds of type **3.5**. Again, this is likely due to the electron withdrawing nature of the chlorine atom allowing for the negative charge to be more delocalized and thus less Coulombic repulsion felt upon the second reduction (**Table 3.8**).

Derivative	Reduction (V)	Oxidation (V)
3.6a	-1.23, -0.97	+0.45, +0.88[a]
3.6b	-1.32, -1.07	+0.47, +0.89[a]
3.6c	-1.02[b], -1.05	+0.47, +0.91
3.6d	-1.24[b], -1.09	+0.56, +1.02
3.6f	-1.11, -0.87	+0.51, +0.97[a]

Table 3.8: Electrochemical data for various derivatives of **3.6** ([a] quasi reversible, [b] irreversible)

The differing magnitude of the HOMO-LUMO gap of the various bis-chelates can be observed electrochemically as well as spectroscopically (**Figure 3.28**). Both the reduction and oxidation potentials are found to decrease with increasing palladium presence. The reduction potentials do so to a greater degree resulting in a decreasing E^{cell} value as the number of palladium atoms increases sequentially from 0 to 2. The apparent ease of oxidation with increasing palladium presence suggests that the palladium atom renders the Nindigo more electron rich. The second oxidation of **1.33a** actually occurs at a similar potential to that of the first oxidation of the **3.5a**. This suggests that the negative charge created upon oxidation is delocalized more effectively in **3.5a**, where as for **1.33a** it is more centrally localized. The inverse effect is observed for the reduction processes where **1.33a** is found to be harder to reduce than **3.5** and **3.6**. The gap between the first and second reductions is also affected by palladium presence; the bis-Pd(hfac) species exhibits a single two-electron reduction process whereas derivatives of **3.6a** have two one-electron reduction processes separated by 0.25 V and derivatives of **3.5a** have two one-electron processes separated by a larger 0.40 V.

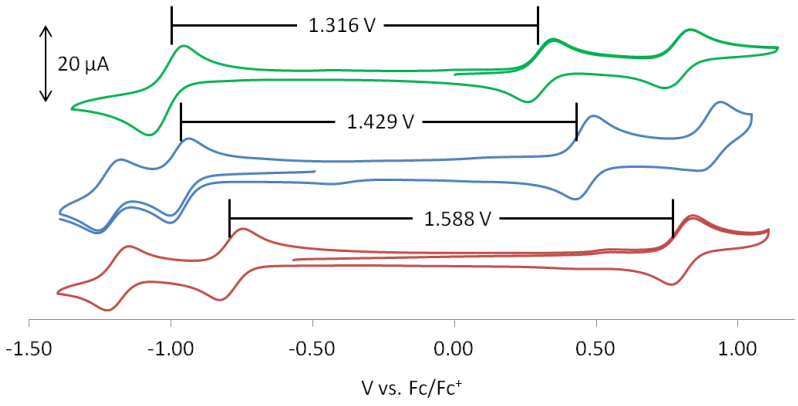

Figure 3.28: Cyclic voltammograms for **1.33a** (top), **3.6a** (blue) and **3.3a** (red) (DCM solution, 0.1 mM Bu_4NBF_4 electrolyte and scan rate = 100 mVs^{-1})

The relative energies of the HOMOs and LUMOs of the bis-chelates of **1.32a** predicted by DFT calculations corroborate the energies observed experimentally. **3.5a** is computationally found to have a HOMO-LUMO gap of 2.01 eV. Replacing a single boron atom with palladium (**3.6a**) results in a decrease to 1.92 eV with the bis-Pd(hfac) derivative (**1.33a**) predicted to have the lowest transition energy of 1.84 eV (**Figure 3.19**).

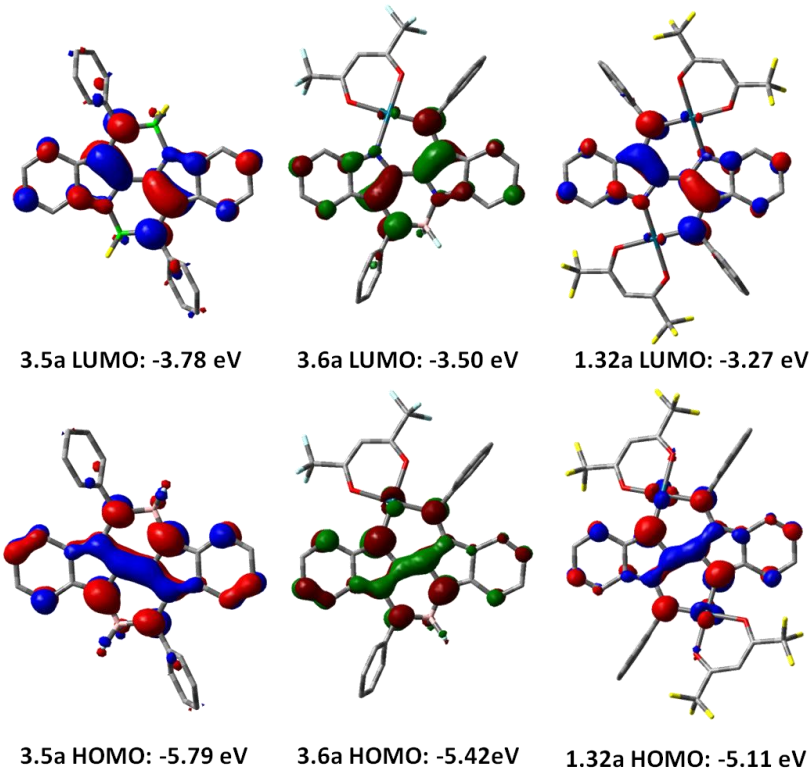

Figure 3.29: FMO contour plots and energies for **3.5a, 3.6a** and **1.33a**

3.4 Summary

Reactions of Nindigo derivatives with excess $BF_3.Et_2O$ in the presence of a base generates mixtures of mono- and bis-BF_2 Nindigo chelate complexes (**3.3a-f** and **3.5a-d, f**).[129] The product distribution was found to be governed not only by the order and nature of reagent addition, but also by the nature of the solvent employed. More hindered bases used in conjunction with higher boiling point solvents were found to favour the formation of the bis-BF_2 chelates. Derivatives of **3.3** display intense, long wavelength absorption maxima centered at *ca.* 650 nm with molar absobtivities of approximately 30.0 x 10^3 M^{-1} cm^{-1}. Derivatives of **3.5** also exhibit intense, low energy transitions (*ca.* 760 nm). Both these absorption bands are red shifted with respect to their parent Nindigos. Derivatives of **3.5** exhibit the greater bathochromic shift and for both families both the absorption intensity and maxima appear independent of the N-aryl substituent. The redox-activity of **3.3** shows a single reversible one-electron oxidation with all other redox events exhibiting irreversibility. Derivatives of **3.5** exhibit fully reversible redox behaviour. Electrochemical investigations reveal one reversible one-electron oxidation and two

reversible one-electron reduction processes. The potentials of the later, in particular, appear to be influenced by both the steric and electronic nature of the N-aryl substituents. Although isolable, derivatives of **3.5** decompose over time to the corresponding derivatives of **3.3**. This decomposition can be monitored by both UV/vis/NIR and NMR spectroscopy. Bis-BF_2 chelates incorporating the bulkier Nindigos (**3.5c** and **3.5d**) are more sensitive and decompose in solution at a quicker rate (hours) than their less bulky counterparts (**3.5a, 3.5b** and **3.5f**) where the bis-BF_2 chelates are still observed after days in solution.

The mono-BF_2 Nindigo chelates (**3.3**) were utilized to synthesize the first heteronuclear Nindigo complexes, **3.6**. These compounds are highly coloured with intense, low energy transitions ($\lambda_{max} \approx 830$ nm, $\varepsilon \approx 20.0 \times 10^3$ M^{-1} cm^{-1}) that appear independent on the nature of the N-aryl substituents. Derivatives of **3.6** exhibit two one-electron oxidation and two one-electron reduction processes. The reversibility of the redox events appears dependent on the steric nature of the N-aryl substituents. For the bulkier derivatives (**3.6c** and **3.6d**) both oxidations and the first reduction are reversible processes. For the less sterically hindered derivatives (**3.6a**, **3.6b** and **3.6f**) it is the two reductions and the first oxidation that exhibit reversibility. The spectroscopic and electrochemical attributes of **3.6** neatly bridge the gap between **1.33** and **3.5**. The HOMO-LUMO gap (represented by λ_{max} and E^{cell} values) is shown to decrease with increasing palladium presence, a trend that is further supported by computational analysis.

3.5 Experimental

3.5.1 Methods and materials

General procedures are outlined in Section 2.4.

[Indigo diphenylimine]difluoroboron, **3.3a:** A solution of **1.32a** (298 mg, 0.723 mmol) in toluene (100 mL) was brought to reflux under an argon atmosphere. Triethylamine (0.1 mL) was added and the reaction was left to stir for 20 minutes. $BF_3.Et_2O$ (5 eq, 3.6 mmol, 0.45 mL) was added and the reaction was left to stir at reflux for a further 20 minutes. The solvent was then removed and the solid obtained taken up in THF (40 mL). Water (10 mL) was added and the reaction was left to stir for 1.5 hours with mild heating. The THF was then removed under vacuum and the aqueous suspension extracted with DCM.

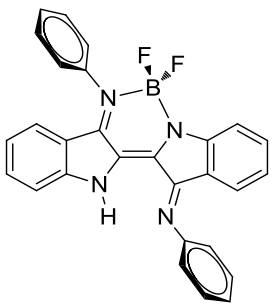

The organic layer was washed with brine before the solvent was removed. The resulting dark solid was washed with hexanes to give **3.3a** as a dark blue powder (200 mg, 60 %). X-ray quality crystals were grown from slow diffusion of acetonitrile into a saturated DCM solution. ^{1}H NMR (300 MHz, CD_2Cl_2, 293 K): δ 6.3 (d, 1H, *J* = 8.3 Hz), 6.7 (dodod, 1H, *J* = 8.2 Hz, 7.1 Hz, 1.0 Hz), 6.8 (tod, 1H, *J* = 7.2 Hz, 1.1 Hz), 6.9 (dod, 1H, *J* = 7.8 Hz, 0.8 Hz), 7.2 (dod, 2H, *J* = 8.5 Hz, 1.3 Hz), 7.2 (dot, 1H, *J* = 8.4 Hz, 0.8 Hz), 7.4 (m, 3H), 7.5 (m, 8H), 9.0 (s, 1H). ^{13}C NMR (500 MHz, CD_2Cl_2, 293 K), δ = 113.0, 116.0, 116.1, 117.5, 119.3, 119.8, 120.1, 123.1, 125.9, 126.1, 126.8, 127.9, 128.7, 130.1, 130.1, 133.5, 134.4, 142.7, 148.0, 151.3, 152.4, 152.9, 161.7. ^{19}F{^{1}H} NMR (300 MHz, CD_2Cl_2, 293 K): -127.1 (1:1:1:1 q, *J* = 30.6 Hz). ^{11}B{^{1}H} NMR (500 MHz, CD_2Cl_2, 293 K): δ = 1.9 (t, *J* = 30.6 Hz). UV/vis/NIR (CH_2Cl_2), λ_{max} / nm (ε, $M^{-1}\,cm^{-1}$): 291 (24,900), 332 (9,400), 344 (8,980), 457 (2,790), 499 (14,700), 649 (22,800). HRMS, *m/z:* calcd for $(M-H)^+$ $C_{28}H_{20}N_4BF_2$ 461.1785; found 461.1722

[Indigo bis(p-tolylimine)]difluoroboron, 3.3b: To a solution of **1.32b** (250 mg, 0.567 mmol) in toluene (100 mL) was added triethylamine (0.1 mL). The reaction mixture was taken to reflux under an argon atmosphere where upon $BF_3.Et_2O$ (5eq, 2.8 mmol, 0.35 mL) was added and the reaction left to stir at reflux for 20 minutes. The solvent was then removed and the solid obtained taken up in THF (40 mL). Water (10 mL) was added and the reaction was left to stir for 1.5 hours with mild heating. The THF was then removed and the aqueous suspension extracted with DCM. The organic layer was washed with brine and then the solvent was removed. The resulting solid was washed with hexanes to yield **3.3b** as a dark powder (183 mg, 66 %). ^{1}H NMR (300 MH, CD_2Cl_2, 293 K): δ = 2.4 (s, 3H), 2.5 (s, 3H), 6.4 (d, 1H, *J* = 8.2 Hz), 6.7 (tod, 1H, *J* = 8.1 Hz, 0.8 Hz), 6.8 (tod, 1H, *J* = 7.8 Hz, 0.7 Hz), 6.9 (d, 1H, *J* = 7.6 Hz), 7.0 (d, 2H, *J* = 7.6 Hz), 7.1 (d, 1H, *J* = 8.3 Hz), 7.3 (m, 8H), 7.5 (d, 1H, *J* = 8.0 Hz), 8.9 (s, 1H), ^{13}C NMR (500 MHz, CD_2Cl_2, 298 K): δ = 21.4, 21.6, 112.9, 116.0, 117.4, 119.5, 119.9, 120.0, 123.0, 126.0, 126.7, 127.5, 130.6, 130.6, 133.3, 134.2, 136.2, 137.5, 138.8, 139.1, 148.0, 148.6, 152.4, 153.0, 161.5. ^{19}F{^{1}H} NMR (300 MHz, CD_2Cl_2, 293 K): δ = -127.4 (1:1:1:1 q, *J* = 30.6 Hz). ^{11}B{^{1}H} NMR (500 MHz, CD_2Cl_2, 293 K): δ = 1.9 (t, *J* = 30.6 Hz). UV/vis/NIR (CH_2Cl_2, λ_{max} / nm (ε, $M^{-1}\,cm^{-1}$): 291 (30,000), 332 (12,300), 344 (11,800), 457 (4,670), 607 (19,000), 649 (26,400). HRMS,*m/z:* calcd for $(M-H)^+$ $C_{30}H_{24}N_4BF_2$ 489.2062; found 489.2043

[Indigo bis(2,6-dimethylphenylimine)]difluoroboron, 3.3c: A solution of **1.32c** (649 mg, 1.39 mmol) in

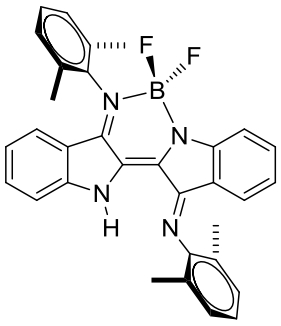

toluene (100 mL) was brought to reflux under an argon atmosphere. Triethylamine (0.2 mL) was added and the reaction left to stir for 25 minutes. $BF_3.Et_2O$ (5 eq, 7.0 mmol, 0.88 mL) was added and the reaction left to stir at reflux for a further 40 minutes. The solvent was removed and the residue taken up in THF (40 mL). Water (10 mL) was added and the reaction left to stir for 1.5 hours at room temperature. The THF was then removed and the remaining aqueous suspension was extracted with DCM. The organic layer was then washed with brine before the solvent was removed to yield a dark solid (388 mg, 54 %). ^{1}H NMR (300 MHz, CD_2Cl_2, 293 K): δ = 2.1 (s, 6H), 2.3 (s, 6H), 6.1 (d, 1H, *J* = 8.3 Hz), 6.5 (d, 1H, *J* = 7.5 Hz), 6.7 (dodod, 1H, *J* = 8.2 Hz, 7.1 Hz, 1.0 Hz), 6.8 (dodod, 1H, *J* = 8.1 Hz, 7.6 Hz, 1.0 Hz), 7.2 (m, 9H), 7.5 (d, 1H, *J* = 7.98 Hz), 9.0 (s, 1H). ^{13}C NMR (500 MHz, CD_2Cl_2, 293 K): δ = 18.4, 18.5, 112.9, 115.9, 120.7, 123.7, 124.9, 125.3, 125.8, 125.9, 128.7, 129.0, 129.5, 133.8, 134.6, 136.7, 148.1, 149.3. ^{19}F{^{1}H} NMR (300 MHz, CD_2Cl_2, 293 K): δ = -127.1 (1:1:1:1 q, *J* = 30.9 Hz). ^{11}B{^{1}H} NMR (500 MHz, CD_2Cl_2, 293 K): δ = 2.0 (t, *J* = 30.9 Hz). UV/vis/NIR (CH_2Cl_2), λ_{max} / nm (ε, $M^{-1}\,cm^{-1}$): 291 (36,140), 330 (13,000), 344 (12,100), 457 (3,360), 594 (19,200), 646 (29,800). HRMS, *m/z:* calc for $(M-H)^+$ $C_{32}H_{28}N_4BF_2$ 517.2344; found 517.2164

[Indigo bis(2,6-diisopropylphenylimine)]difluoroboron, 3.3d: A solution of **1.32d** (620 mg, 1.07 mmol)

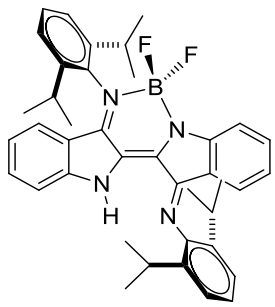

in toluene (100 mL) was brought to reflux under an argon atmosphere. Triethylamine (0.2 mL) was added and the reaction left to stir for 25 minutes. $BF_3.Et_2O$ (5 eq, 5.4 mmol, 0.66 mL) was added and the reaction left to stir at reflux for a further 40 minutes. The solvent was then removed and the residue taken up in THF (40 mL). Water (10 mL) was added and the reaction was left to stir for 1.5 hours at room temperature. The THF was then removed and the aqueous suspension was extracted with DCM. The organic layer was washed with brine before the solvent was removed to yield a dark powder (363 mg, 54 %). ^{1}H NMR (300 MHz, CD_2Cl_2, 293 K): δ = 0.9 (d, 6H, *J* = 6.9 Hz), 1.0 (d, 6H, *J* = 6.8 Hz), 1.2 (d, 6H, *J* = 6.8 Hz), 1.3 (d, 6H, *J* = 6.7 Hz), 3.0 (septet, 2H, *J* = 6.8 Hz), 3.2 (septet, 2H, *J* = 6.9 Hz), 6.0 (d, 1H, *J* = 8.3 Hz), 6.5 (d, 1H, *J* = 7.6 Hz), 6.6 (dodod, 1H, *J* = 8.2 Hz, 7.0 Hz, 1.0 Hz), 6.8 (dodod, 1H, *J* = 7.7 Hz, 7.7 Hz, 1.0 Hz), 7.2 (d, 1H *J* = 8.4 Hz), 7.3 (m, 7H), 7.4 (d, 1H, *J* = 3.1 Hz), 7.5 (t, 1H, *J* = 3.8 Hz), 9.0 (s, 1H). ^{13}C NMR (500 MHz, CD_2Cl_2, 293 K): δ = 23.2, 23.4, 24.2, 24.7, 28.6, 28.7, 112.5, 115.6, 119.7, 123.0, 123.8, 124.9, 125.5, 126.0, 126.2, 129.0, 133.3, 134.1, 135.7, 136.0, 146.5, 146.8, 148.0. ^{19}F{^{1}H} NMR (300 MHz,

CD_2Cl_2, 293 K): δ = -125.7 (1:1:1:1 q, *J* = 30.4 Hz). $^{11}B\{^1H\}$ NMR (500 MHz, CD_2Cl_2, 293 K): δ = 1.9 (t, *J* = 30.4 Hz). UV/vis/NIR (CH_2Cl_2), λ_{max} / nm (ε, M^{-1} cm^{-1}): 291 (38,100), 331 (14,299), 455 (3,810), 597 (20,400), 650 (32,100). HRMS, *m/z:* calc for $(M-H)^+$ $C_{40}H_{44}N_4BF_2$ 629.3614; found 629.3629

[Indigo bis(2-tert-butylphenylimine)]difluoroboron, 3.3e: A solution of **1.32e** (420 mg, 0.801 mmol) in toluene (100 mL) was brought to reflux under an argon atmosphere. Triethylamine (0.1 mL) was added and the reaction left to stir for 25 minutes. $BF_3.Et_2O$ (5 eq, 4.0 mmol, 0.49 mL) was added and the reaction left to stir at reflux for a further 40 minutes. The solvent was then removed and the residue taken up in THF (40 mL). Water (10 mL) was added and the reaction was left to stir for 1.5 hours at room temperature. The THF was then removed and the remaining mixture taken up in DCM and washed with Brine. The solvent was removed from the organic layer to yield a dark powder (275 mg, 64 %). ^1H NMR (300 MHz, CD_2Cl_2, 293 K): δ = 1.3 (s, 9H), 1.4 (s, 9H), 6.1 (d, 1H, *J* = 8.4 Hz), 6.7 (m, 2H), 6.8 (t, 1H, *J* = 7.1 Hz), 6.9 (d, 1H, *J* = 7.1 Hz), 7.2 (d, 1H, *J* = 8.3 Hz), 7.3 (m, 2H), 7.4 (m, 4H), 7.5 (m, 2H), 7.6 (m, 1H), 7.7 (dod, 1H, *J* = 8.1 Hz, 1.4 Hz), 9.1 (s, 1H). ^{13}C NMR (500 MHz, CD_2Cl_2, 293 K): δ = 30.1, 32.2, 32.2, 35.5, 36.9, 112.5, 115.6, 115.6, 116.6, 117.7, 116.6, 119.2, 119.9, 122.6, 125.8, 125.9, 126.7, 127.1, 127.3, 128.5, 130.6, 130.7, 133.1, 133.8, 138.2, 140.2, 146.4, 147.7, 150.1, 152.2, 154.1, 160.8. $^{19}F\{^1H\}$ NMR (300 MHz, CD_2Cl_2, 293 K): δ = -138.5, -118.6. $^{11}B\{^1H\}$ NMR (500 MHz, CD_2Cl_2, 293 K): δ = 2.0 (dod, *J* = 38.0 Hz, 23.5 Hz). UV/vis/NIR (CH_2Cl_2), λ_{max} / nm (ε, M^{-1} cm^{-1}): 292 (31,800), 333 (13,600), 346 (12,300), 457 (4,170), 610 (18,300), 654 (25,800). HRMS, *m/z:* calc for $(M-Na)^+$ $C_{36}H_{35}N_4BF_2$ 595.2828; found 595.2827

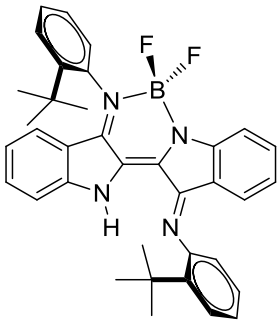

[Indigo bis(p-chloropropylphenylimine)]difluoroboron, 3.3f: A solution of **1.32f** (310 mg, 0.646 mmol) in toluene (100 mL) was brought to reflux under a nitrogen atmosphere. Hünigs base (2.5 eq, 1.6 mmol, 0.28 mL) was added and the reaction was left to stir for 25 minutes. $BF_3.Et_2O$ (14 eq, 9.0 mmol, 1.1 mL) was added and the reaction left was left to stir at reflux for a further 40 minutes. The solvent was removed and the residue taken up in THF (25 mL). Water (3 mL) was added and the reaction left to stir in air for 1 hour at room temperature. The THF was then removed and the remaining mixture taken up in DCM and washed with Brine. The solvent was removed from the organic layer to yield a dark powder (209 mg, 61 %). ^1H NMR (300 MHz, CD_2Cl_2, 293 K): δ = 6.5 (d, 1H, *J* = 8.3 Hz), 6.7 (dodod, 1H, *J* = 8.2 Hz, 7.1 Hz, 1.0 Hz), 6.8 (dodod, 1H, *J* = 8.1 Hz, 8.1 Hz, 1.1 Hz), 6.9 (d, 1H, *J*

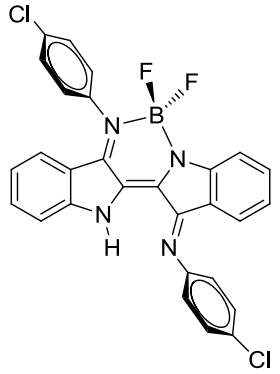

= 7.2 Hz), 7.1 (d, 2H, *J* = 8.7 Hz), 7.2 (d, 1H, *J* = 11.4 Hz), 7.4 (tot, 2H, *J* = 8.2 Hz, 1.7 Hz), 7.4 (m, 7H), 9.0 (s, 1H). ^{13}C NMR (500 MHz, CD_2Cl_2, 293 K): Spectrum not resolved enough to assign. $^{19}F\{^1H\}$ NMR (300 MHz, CD_2Cl_2, 293 K): δ = -127.1 (1:1:1:1 q, *J* = 32.5 Hz). $^{11}B\{^1H\}$ NMR (500 MHz, CD_2Cl_2, 293 K): δ = 1.8 (t, *J* = 32.5 Hz). UV/vis/NIR (CH_2Cl_2), λ_{max} / nm (ε, $M^{-1}\,cm^{-1}$): 292 (34,200), 335 (13,200), 348 (13,100), 460 (5,030), 603 (17,300), 655 (25,400). HRMS, *m/z:* calc for $(M\text{-}Na)^+$ $C_{28}H_{17}N_4BF_2$ 551.0794; found 551.0797253

μ-(Indigo diphenylamine)bis(difluoroboron), 3.5a: 1.32a (1.00 g, 2.43 mmol) was dissolved in 40 mL of

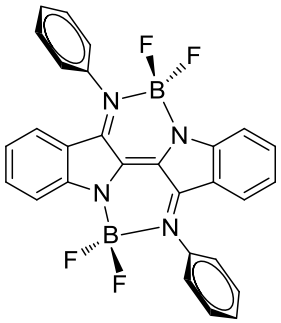

dry toluene and brought to reflux under a nitrogen atmosphere. Hünigs base (2.5 eq, 6.08 mmol, 1.06 mL) was added and reaction was left to stir for 20 minutes. $BF_3.Et_2O$ (14 eq, 34 mmol, 4.2 mL) was added slowly and the reflux maintained for a further 20 minutes. The solvent was then removed in vacuo and the brown residue washed with dry acetonitrile until the washings ran clear and a green powder was obtained (964 mg, 78 %). ^{1}H NMR (300 MHz, CD_2Cl_2, 293 K): δ = 6.5 (d, 2H, *J* = 8.1 Hz), 6.7 (dodod, 2H, *J* = 8.1 Hz, 6.4 Hz, 1.7 Hz), 7.4 (m, 4H), 7.5 (m, 10H). $^{19}F\{^1H\}$ NMR (300 MHz, CD_2Cl_2, 293 K): δ = -130.8 (1:1:1:1 q, *J* = 29.2 Hz). $^{11}B\{^1H\}$ NMR (500 MHz, CD_2Cl_2, 293 K): δ = 1.8 (t, *J* = 29.2 Hz). UV/vis/NIR (CH_2Cl_2), λ_{max} / nm (ε, $M^{-1}\,cm^{-1}$): 253 (22,000), 301 (34,800), 386 (12,100), 744 (26,000). HRMS, *m/z:* calc for $(M)^+$ $C_{28}H_{17}N_4{}^{10}B^{11}BF_4$ 507.16946; found 507.16900

μ-(Indigo bis(p-tolylimine)bis(difluoroboron), 3.5b: 1.32b (1.37 g, 3.10 mmol) was dissolved in 40 mL of

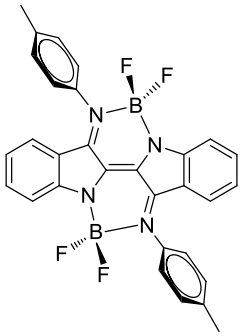

dry toluene and brought to reflux under a nitrogen atmosphere. Hünigs base (2.5 eq, 7.8 mmol, 1.9 mL) was added and the reaction was left to stir for 20 minutes. $BF_3.Et_2O$ (14 eq, 43 mmol, 5.4 mL) was added slowly and the reflux maintained for a further 20 minutes. The solvent was then removed in vacuo and the brown residue washed with dry acetonitrile until the washings ran clear and a green powder was obtained (1.47 g, 88 %). ^{1}H NMR (300 MHz, CD_2Cl_2, 293 K): δ = 2.5 (s, 6H), 6.6 (d, 2H, *J* = 8.1 Hz), 6.8 (dodod, 2H, *J* = 8.1 Hz, 8.1 Hz, 1.0 Hz), 7.4 (m, 12H). $^{19}F\{^1H\}$ NMR (300 MHz, CD_2Cl_2, 293 K): δ = -131.0 (1:1:1:1 q, *J* = 28.3 Hz). $^{11}B\{^1H\}$ NMR (500 MHz, CD_2Cl_2, 293 K): δ = 1.8 (t, *J* = 29.1 Hz). UV/vis/NIR (CH_2Cl_2), λ_{max} / nm (ε, $M^{-1}\,cm^{-1}$): 256 (23,500), 301 (36,700), 388 (11,800), 743 (34,200). HRMS, *m/z:* calc for $(M)^+$ $C_{30}H_{21}N_4{}^{10}B^{11}BF_4$ 535.20058; found 535.20030

μ-(Indigo bis(2,6-dimethylphenylimine)bis(difluoroboron), 3.5c: 1.32c (1.30 g, 2.77 mmol) was

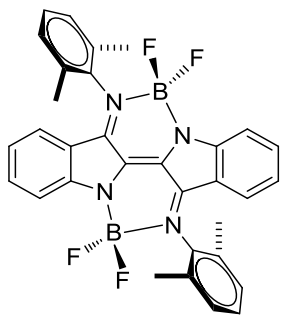

dissolved in 40 mL of dry toluene and brought to reflux under a nitrogen atmosphere. Hünigs base (2.5 eq, 6.9 mmol, 1.2 mL) was added and the reaction was left to stir for 20 minutes. $BF_3.Et_2O$ (14 eq, 38.78 mmol, 4.79 mL) was added slowly and the reflux maintained for a further 20 minutes. The solvent was then removed in vacuo and the brown residue washed with dry acetonitrile until the washings ran clear and a green powder was obtained (1.76 g, 84 %). ^{1}H NMR (300 MHz, CD_2Cl_2, 293 K): δ = 2.3 (s, 12H), 6.2 (d, 2H, *J* = 8.3), 6.8 (dodod, 2H, *J* = 8.2 Hz, 7.3 Hz, 1.3 Hz), 7.3 (m, 4H), 7.4 (m, 4H), 7.39 (dodod, t, 2H, *J* = 8.4 Hz, 7.2 Hz, 1.3 Hz). ^{19}F{^{1}H} NMR (300 MHz, CD_2Cl_2, 293 K): δ = -130.3 (1:1:1:1 q, *J* = 29.4 Hz). ^{11}B{^{1}H} NMR (500 MHz, CD_2Cl_2, 293 K): δ = 1.8 (t, *J* = 29.4Hz). UV/Vis/NIR (CH_2Cl_2), λ_{max} / nm (ε, $M^{-1}\,cm^{-1}$): 254 (30,700), 300 (30,000), 380 (8,480), 746 (31,800). HRMS, *m/z:* calc for $(M)^+$ $C_{32}H_{25}N_4{}^{10}B^{11}BF_4$ 563.23169; found 563.23160

μ-(Indigo bis(2,6-diisopropylphenylimine)bis(difluoroboron), 3.5d: 1.32d (1.30 g, 2.23 mmol) was

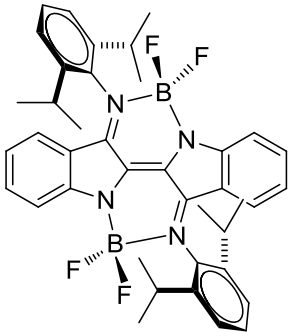

dissolved in 40 mL of dry toluene and brought to reflux under a nitrogen atmosphere. Hünigs base (2.5 eq, 5.58 mmol, 0.97 mL) was added and the reaction was left to stir for 20 minutes. $BF_3.Et_2O$ (14 eq, 31 mmol, 3.9 mL) was added slowly and the reflux maintained for a further 20 minutes. The solvent was then removed in vacuo and the brown residue washed with dry acetonitrile until the washings ran clear and a green powder was obtained (1.27 g, 79 %). ^{1}H NMR (300 MHz, CD_2Cl_2, 293 K): δ = 1.0 (d, 12H, *J* = 6.7 Hz), 1.3 (d, 12H, *J* = 6.7 Hz), 3.1 (septet, 4H, *J* = 6.8 Hz), 6.2 (d, 2H, *J* = 8.1 Hz), 6.7 (dodod, 2H, *J* = 8.1 Hz, 7.1 Hz, 1.0 Hz), 7.3 (m, 8H), 7.4 (t, 2H, 7.3 Hz). ^{19}F{^{1}H} NMR (300 MHz, CD_2Cl_2, 293 K): δ = -131.2 (1:1:1:1 q, *J* = 30.6 Hz). ^{11}B{^{1}H} NMR (500 MHz, CD_2Cl_2, 293 K): δ = 2.0 (m, *J* = 29.0Hz). UV/Vis/NIR (CH_2Cl_2), λ_{max} / nm (ε, $M^{-1}\,cm^{-1}$): 255 (19,200), 301 (33,500), 377 (9,320), 742 (24,400). HRMS, *m/z:* calc for $(M)^+$ $C_{40}H_{41}N_4{}^{10}B^{11}BF_4$ 675.35774; found 675.35680

μ-(Indigo bis(p-chlorophenylimine)bis(difluoroboron), 3.5f: 1.32f (353 mg, 0.735 mmol) was dissolved

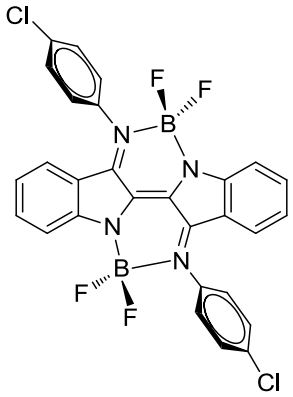

in 40 mL of dry toluene and brought to reflux under a nitrogen atmosphere. Hünigs base (2.5 eq, 1.8 mmol, 0.32 mL) was added and the reaction left to stir for 20 minutes. $BF_3.Et_2O$ (14 eq, 10 mmol, 1.3 mL) was added slowly and the reflux maintained for a further 20 minutes. The solvent was then removed in vacuo and the brown residue washed with dry acetonitrile until the washings ran clear and a green powder was obtained (360 mg, 85 %). ^{1}H NMR (300 MHz, CD_2Cl_2, 293 K): δ = 6.7 (d, 2H, *J* = 7.9 Hz), 6.8 (t, 2H, *J* = 8.1 Hz), 7.4 (d, 2H, *J* = 7.8 Hz), 7.5 (d, 6H, *J* = 8.6 Hz), 7.6 (d, 4H, *J* = 8.5 Hz). ^{13}C NMR (500 MHz, CD_2Cl_2, 293K): lack of solubility precludes carbon analysis. ^{19}F{^{1}H} NMR (300 MHz, CD_2Cl_2, 293 K): δ = -130.8. ^{11}B{^{1}H} NMR (500 MHz, CD_2Cl_2, 293 K): δ = 1.7. UV/Vis/NIR (CH_2Cl_2), λ_{max} / nm) (ε, M^{-1} cm^{-1}): 301 (29,400), 390 (11,800), 752 (26,300). HRMS, *m/z:* calc for $(M)^+$ $C_{28}H_{16}N_4{}^{10}B^{11}BF_4$ 576.08746; found 576.08743

μ-(Indigo bis(phenylimine)difluoroboron-palladium(hexafluoroacetyacetonoate), 3.6a: **3.3a** (170 mg,

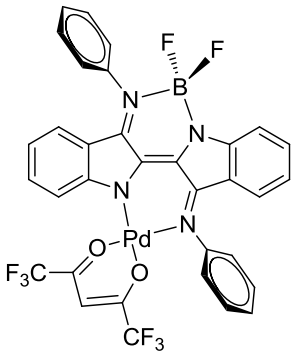

0.370 mmol) was dissolved in DCM (*ca*.15 mL). To this solution was added drop wise a solution of $Pd(hfac)_2$ (1eq, 192 mg) in DCM (*ca.* 35 mL) and the resultant solution was left to stir overnight. The crude reaction mixture was then extracted three times with water and once with brine before the organic layer was dried and the solvent removed to give a dark powder (270 mg, 94 %). X-ray quality crystals were grown by slow evaporation of a saturated THF solution. ^{1}H NMR (300 MHz, $CDCl_3$, 293 K): δ 5.8 (d, 1H, *J* = 8.1 Hz), 6.1 (d, 1H, *J* = 7.9 Hz), 6.2 (s, 1H), 6.5 (t, 1H, *J* =7.6 Hz), 6.5 (t, 1H, *J* = 7.9 Hz), 7.3 (m, 5H), 7.5 (m, 9H). ^{13}C NMR (500 MHz, CD_2Cl_2, 293 K): δ = 93.2, 115.7, 116.3 (q, CF_3, *J* = 284.1 Hz), 117.2, (q, CF_3, *J* = 285.6 Hz), 117.3, 119.4, 120.0, 120.2, 121.4, 125.5, 126.9, 127.1, 128.4, 128.5, 129.3, 130.2, 130.3, 132.6, 135.0, 135.6, 141.1, 145.9, 152.7, 157.6, 158.4, 159.0, 174.8 (q, CO, *J* 35.6 Hz), 175.7 (q, CO, *J* = 35.2 Hz). ^{19}F{^{1}H} (300 MHz, CD_2Cl_2, 293 K): δ = -130.5 (1:1:1:1 q, *J* = 29.2 Hz), -74.8, -73.4. ^{11}B{^{1}H} NMR (500 MHz, CD_2Cl_2, 293 K): δ = 1.50 (t, *J* = 29.2 Hz). UV/Vis/NIR (CH_2Cl_2), λ_{max} / nm (ε, M^{-1} cm^{-1}): 307 (42,900), 367 (12,200), 385 (11,600), 409 (8,620), 822 (19,200). HRMS, *m/z:* calcd for $(M)^+$ $C_{33}H_{19}N_4BF_8O_2Pd$ 722.0508; found 772.0512

μ-(Indigo bis(p-tolylimine)difluoroboron-palladium(hexafluoroacetyacetonoate), 3.6b: 3.3b (39 mg, 0.088 mmol) was dissolved in DCM (ca. 15 mL). To this solution was added drop wise a solution of $Pd(hfac)_2$ (1 eq, 41 mg) in DCM (*ca*. 35 mL) and the resultant solution was left to stir overnight. It was then extracted 3 times with water before the organic layer was dried and the solvent removed. The solid was dissolved in a minimal amount of DCM and run through a basic alumina column and dried to yield a dark powder (48 mg, 76 %). X-ray quality crystals were grown by slow diffusion of acetonitrile into a saturated DCM solution. ^{1}H NMR (300 MHz, CD_2Cl_2, 293K): δ = 2.4 (s, 3H), 2.5 (s, 3H), 6.0 (d, 1H, *J* = 8.2 Hz), 6.2 (d, 1H, *J* = 7.5 Hz), 6.3 (s, 1H), 6.5 (dodod, 1H, *J* = 7.2Hz , *J* = 7.2 Hz , *J* = 1.8 Hz), 6.6 (dodod, 1H, *J* = 7.2 Hz , *J* = 6.0 Hz , *J* = 1.8 Hz), 7.1 (d, 2H, 8.3 Hz), 7.2 (dodod, 1H, *J* = 8.7 Hz, *J* = 6.6, *J* = 1.4 Hz), 7.3 (m, 8H), 7.5 (d, 1H, *J* = 8.7 Hz). ^{13}C NMR (500 MHz, CD_2Cl_2, 293K): δ = 21.6, 93.2, 115.2, 115.6, 117.2, 119.5, 120.1, 121.3, 125.1, 126.5, 127.0, 127.2, 128.5, 130.7, 130.8, 132.5, 134.8, 135.5, 138.5, 138.8, 139.6, 143.3, 152.7, 158.5, 158.9, 157.5, 174.8 (q, CO, *J* = 34.6 Hz), 175.7 (q, CO, *J* = 35.0 Hz). ^{19}F{^{1}H} NMR (300 MHz, CD_2Cl_2, 293 K): δ = -130.8 (1:1:1:1 q, *J* = 29.4 Hz), -75.2,- 73.8. ^{11}B{^{1}H} NMR (500 MHz, CD_2Cl_2, 293 K): δ = 1.5 (t, *J* = 29.4 Hz). UV/vis/NIR (CH_2Cl_2), λ_{max} /nm (ε, $M^{-1}\,cm^{-1}$): 307 (45,700), 366 (11,900), 385 (11,600), 409 (8,760), 820 (19,900). HRMS, *m/z*: calcd for $(M)^+$ $C_{35}H_{23}N_4BF_8O_2Pd$ 800.0821 ; found 800.0827.

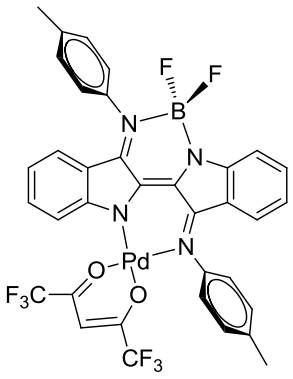

μ-(Indigo bis(2,6-dimethylphenylimine)difluoroboron-palladium(hexafluoroacetyacetonoate), 3.6c: 3.3c (44 mg, 0.085 mmol) was dissolved in DCM (15 mL). To this solution was added drop wise a solution of $Pd(hfac)_2$ (1 eq, 44 mg) in DCM (*ca*. 35 mL) and the resultant solution was left to stir overnight. It was then extracted 3 times with water before the organic layer was pumped dry. The crude solid was dissolved in a minimal amount of DCM and run through a basic alumina column before the solvent was removed to yield a dark powder (54 mg, 77 %). ^{1}H NMR (300 MHz, CD_2Cl_2, 293K): δ = 2.2 (s, 6H), 2.3 (s, 6H), 5.8 (d, 1H, *J* = 8.1 Hz), 5.9 (d, 1H, *J* = 8.2 Hz), 6.3 (s, 1H), 6.5 (t, 1H, *J* = 7.7 Hz), 6.1 (m, 1H), 7.3 (m, 9H), 7.6 (d, 1H, *J* = 8.7 Hz). ^{13}C NMR (500 MHz, CD_2Cl_2, 293K): δ = 18.4, 18.7, 93.3, 115.7, 117.2, 117.4, 119.7, 119.8, 120.7, 121.9, 125.8, 125.9, 128.2, 128.4, 129.0, 129.5, 129.6, 132.6, 132.8, 135.2, 135.5, 135.9, 139.0, 143.5, 152.8, 156.8, 158.8, 159.1, 174.9 (q, CO, *J* = 34.7 Hz), 176.0 (q, CO, *J* = 36.3 Hz) (The two CF3 quartets could not be resolved). ^{19}F{^{1}H} NMR (300 MHz, CD_2Cl_2, 293 K): δ = -73.7 (s), -75.3 (s), -130.7 (q, *J* = 29.9 Hz). ^{11}B{^{1}H} NMR (500 MHz, CD_2Cl_2, 293 K): δ = 1.7 (t, *J* =

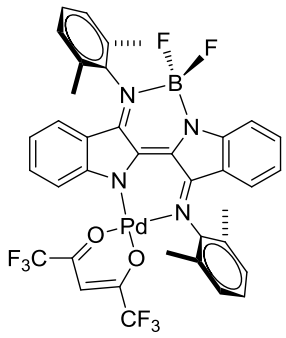

29.9 Hz). UV/vis/NIR (CH_2Cl_2), λ_{max} /nm (ε, $M^{-1}\,cm^{-1}$): 306 (40,000), 366 (8,970), 385 (8,270), 409 (5,620), 819 (17,500). HRMS, *m/z*: calcd for $(M)^+$ $C_{37}H_{27}N_4BF_8O_2Pd$ 828.1134 ; found 828.1140

μ-(Indigo bis(2,6-diisopropylphenylimine)difluoroboron-palladium(hexafluoroacetyacetonoate), 3.6d: 3.3d (82 mg, 0.13 mmol) was dissolved in DCM (15 mL). To this solution was added drop wise a solution of $Pd(hfac)_2$ (1 eq, 68 mg) in DCM (*ca*. 35 mL) and the resultant solution was left to stir overnight. It was then extracted 3 times with water before the organic layer was pumped dry. The solid was dissolved in a minimal amount of DCM and run through a basic alumina column before the solvent was removed to yield a dark powder (88 mg, 72 %). ^{1}H NMR (300 MHz, CD_2Cl_2, 293K): δ = 0.9 (d, 12H, *J* = 6.8 Hz), 1.0 (d, 12H, *J* = 6.8 Hz), 1.3 (d, 12H, *J* = 2.2Hz), 1.3 (d, 12H, *J* = 2.0Hz), 3.1 (septet, 2H, *J* = 6.7 Hz), 3.4 (septet, 2H, *J* = 6.8 Hz), 5.7 (d, 1H, *J* = 8.3 Hz), 5.9 (d, 1H, *J* = 8.3 Hz), 6.3 (s, 1H), 6.5 (t, 1H, *J* = 7.3 Hz), 6.6 (dodod, 1H, *J* = 8.3 Hz, *J* = 6.4 Hz, *J* = 1.8 Hz), 7.2 (dodod, 1H, *J* = 8.7 Hz, *J* = 7.2 Hz, *J* = 1.5 Hz), 7.4 (m, 6H), 7.6 (m, 2H), 7.7, d, 1H, *J* = 8.7 Hz). ^{13}C NMR (500 MHz, CD_2Cl_2, 293K): δ = 23.6, 24.1, 24.1, 24.8, 28.9, 93.1, 115.7, 116.8, 119.7, 119.8, 121.1, 125.0, 125.2, 126.6, 127.0, 128.9, 129.4, 134.7, 135.5, 135.6, 140.7, 142.3, 145.4, 152.2, 156.5, 156.6, 158.9, 159.0. ^{19}F{^{1}H} NMR (300 MHz, CD_2Cl_2, 293 K): δ = -129.0 (1:1:1:1 q, *J* = 29.3 Hz), -75.0, -73.5. ^{11}B{^{1}H} NMR (500 MHz, CD_2Cl_2, 293 K): δ = 1.5 (t, *J* = 29.3 Hz). UV/Vis/NIR (CH_2Cl_2), λ_{max} /nm (ε, $M^{-1}\,cm^{-1}$): 307 (41,600), 366 (9,230), 385 (8,440), 409 (5,550), 820 (20,700). HRMS, *m/z*: calcd for $(M)^+$ $C_{45}H_{43}N_4BF_8O_2Pd$ 940.2386 ; found 940.2386

μ-(Indigo bis(p-chlorophenylimine)difluoroboron-palladium(hexafluoroacetyacetonoate), 3.6f: 3.3f (21 mg, 0.04 mmol) was dissolved in DCM (*ca*. 5 mL). To this solution was added drop wise a solution of $Pd(hfac)_2$ (1 eq, 20 mg) in DCM (*ca*. 10 mL). and the resultant solution was left to stir overnight. It was then extracted 3 times with water before the organic layer was pumped dry to give a dark solid. The solid was washed with MeCN to yield a dark powder (14 mg, 42 %). ^{1}H NMR (300 MHz, $CDCl_3$ 293K): δ = 6.0 (d, 1H, *J* = 8.1 Hz), 6.2 (d, 1H, *J* = 8.2 Hz), 6.29 (s, 1H), 6.56 (t, 1H, *J* = 8.2 Hz), 6.66 (quintet, 1H, *J* = 4.1 Hz), 7.25 (m, 3H), 7.48 (m, 9H). ^{13}C NMR (500 MHz, CD_2Cl_2, 293K): δ = Lack of solubility precludes full spectral analysis. ^{19}F{^{1}H} NMR (300 MHz, CD_2Cl_2, 293 K): δ = -130.0 (1:1:1:1 q, *J* = 29.9 Hz), -74.8, -73.4. ^{11}B{^{1}H} NMR (500 MHz, CD_2Cl_2, 293 K): δ = 1.4 (t, *J* = 29.9 Hz). HRMS, *m/z*: calcd for $(M)^+$ $C_{33}H_{17}N_4BF_8O_2Pd$; 839.9729 found 839.9736

Chapter 4: Synthesis and properties of zinc and copper complexes of mono-BF_2 Nindigo chelates

4.1 Introduction

The combination of an electroactive metal with a redox-active ligand can lead to systems where the oxidation state of the metal and ligand cannot easily be assigned (*cf*. ligand non-innocence chapter 1). When the redox potentials of the metal and ligand are similar in energy but the charges on the two redox-active parties are localized, the possibility of valence tautomerism (VT) can arise. This is the process by which two nearly degenerate electronic states (valence tautomers) can interconvert as a result of reversible intramolecular electron transfer (IET). This phenomenon does not occur for all systems of the above type, due to the two criteria that must be satisfied.

1) The degree of covalency between the metal ion and electroactive ligand must be low
2) The energy of the frontier molecular orbitals (FMOs) of the metal and ligand must be similar

Not only do these two constraints need to be satisfied but VT has also been shown to be sensitive to other factors such as ancillary ligand,[133] counter ion,[134] light,[135] temperature,[136] pressure,[137] and matrix.[138] This sensitivity to conditions renders VT challenging to predict. The most studied valence tautomeric systems are based on quinone-type ligands incorporating cobalt as the metal centre. The redox-active nature of the ligand can also allow for cycles involving VT in a variety of oxidation states.[139] Examples of VT complexes involving other ligand architectures or other metal centres are less common. One such example, not involving a dioxolene-type ligand, is a triple-helicate copper (II) complex containing a redox-active N-heterocyclic ligand. This complex is shown to exhibit thermally driven valence tautomerism (**Figure 4.1**).[140]

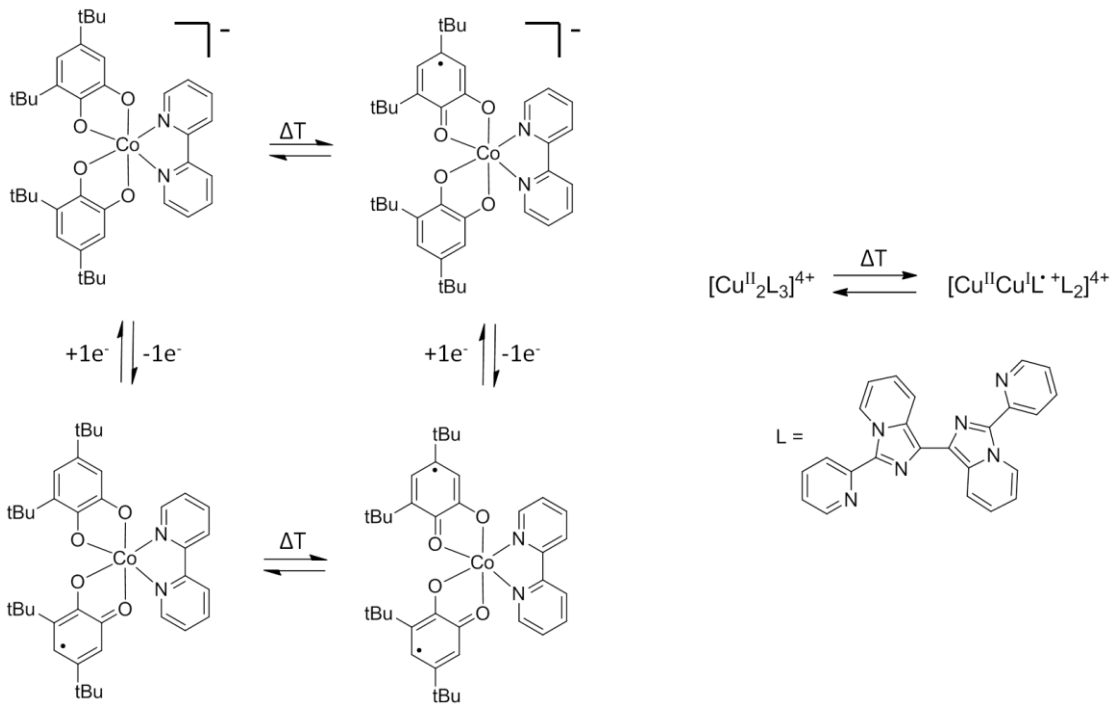

Figure 4.1: A unique cycle involving both valence tautomerism and redox-activity (left). An example of a valence tautomeric complex involving copper and a multidentate redox-active N-heterocyclic ligand (right)[139,140]

Molecules of type **3.3** have been shown to be effective redox-active capping ligands (*cf.* chapter 3). It was therefore decided to explore the chemistry that might result from their chelation to an electroactive metal centre. Copper was chosen as the resulting complex would contain Cu^{2+} which possesses an open shell configuration (d^9) and this could potentially lead to new chemistry not observed for the closed shell systems (*cf.* chapter 3). A zinc complex was also targeted as the resulting heteroleptic complex was hoped to adopt a similar geometry to that of the copper analogue. In addition, Zn(II) posses a closed shell configuration (d^{10}) likely rendering any redox events ligand centered. The zinc complex could therefore be used as an "innocent" complex for comparing the potentially non-innocent copper analogues.

4.2.1 Synthesis and characterization of ZnL_2 complex

Reacting two equivalents of **3.3a** with zinc acetate dihydrate in the presence of a base results in formation of the heteroleptic zinc complex **4.1** (**Scheme 4.1**). The complex is stable indefinitely in both the solid state and in solution and is soluble in a range of solvents.

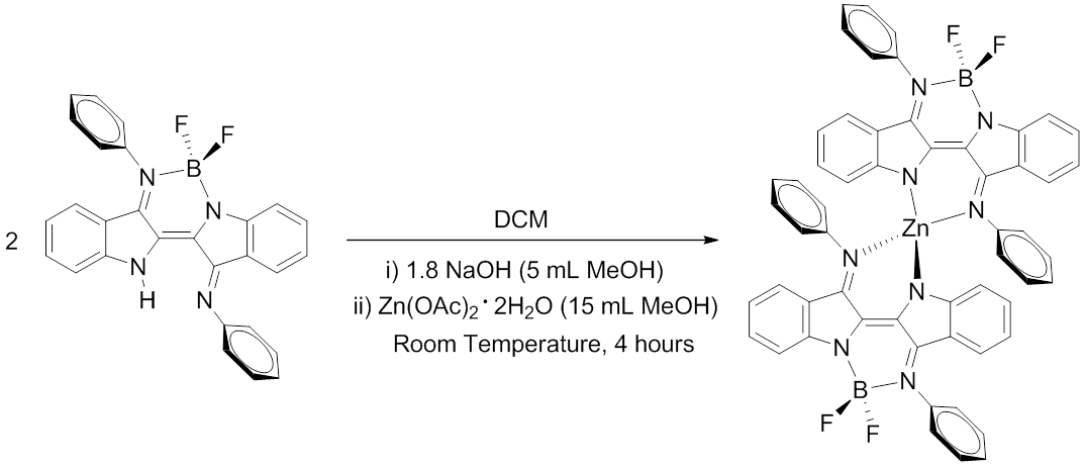

Scheme 4.1: Conditions for the synthesis of **4.1**

The ^{1}H and ^{13}C NMR spectroscopic data is consistent with the structure of **4.1**. The ^{19}F spectrum exhibits one quartet centered at -129.1 ppm with a coupling constant $^{1}J_{FB}$ = 29.9 Hz. The ^{11}B spectrum displays a triplet centered at 3.2 ppm with a $^{1}J_{BF}$ = 29.9 Hz. This is consistent with all fluorine atoms being equivalent, and likewise both boron atoms being equivalent, by symmetry (**Figure 4.2**).

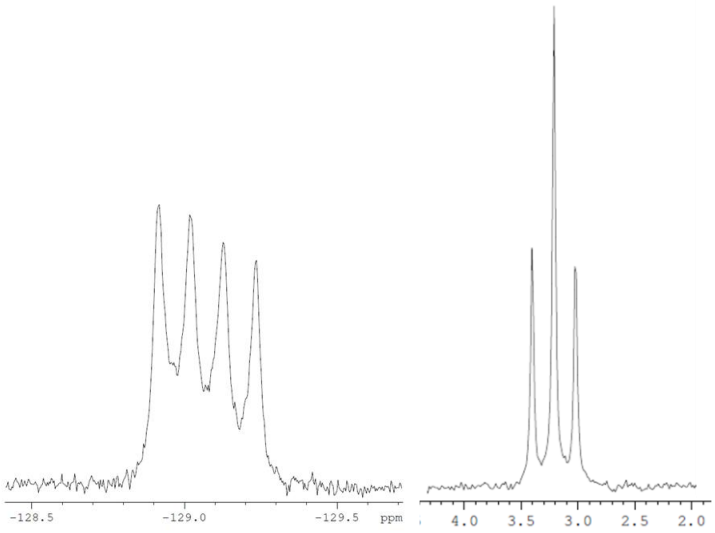

Figure 4.2: ^{19}F (left) and ^{11}B (right) NMR spectra for **4.1** (Samples run in CD_2Cl_2)

The structure of **4.1** was confirmed by single crystal X-ray diffraction (**Figure 4.3**). The two ligands on either side of the zinc atom are crystallographically equivalent. The zinc adopts a distorted tetrahedral geometry with bond angles ranging from 95.6° (for N11-Zn-N22) to 132.3° (N11-Zn-N11'). The zinc and boron atoms both lie within their C3N2 chelating planes. The core (C4N4) of each ligand remains close to planar with slight bowing of the benzannulated rings (9.43°). The intramolecular N(indolide) - N(imine) distances on both the boron side and the zinc side remain the same as those found on either side of **3.3a** (2.51(3) Å for the boron bound and 3.00(3) Å for the opposing side). This indicates that little structural reorganization is needed to chelate the zinc atom. The incorporation of zinc appears to increase the degree of delocalization over the entire core (C4N4) of Nindigo with respect to **3.3a**, where delocalization was more evident on the boron bound side of the molecule. This is reflected by both imine bonds being longer than typical imine bonds (1.33 Å and 1.31 Å) and the C21-C22 and C11-C12 bonds being equivalent in length (1.45 Å), and shorter than typical single bonds between sp^2 carbons (see Table 2.3). The N(indolide)-B and N(indolide)-Zn bonds are longer than the N(imine)-B and N(imine)-Zn bonds following the trend observed for derivatives of **3.6** (**Table 4.1**).

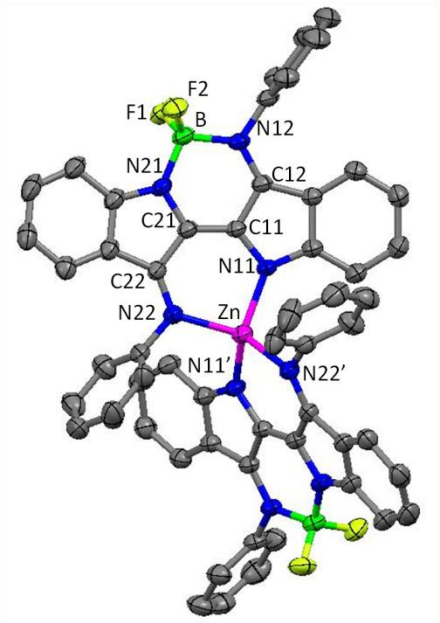

Figure 4.3: X-ray crystal structure of **4.1**. Ellipsoids at the 50% probability level with all hydrogen atoms removed for clarity

Atoms	Length (Å)	Atoms	Angles (deg)
C11-C21	1.370 (4)	N11-Zn-N22	95.71 (8)
C21-N21	1.368 (3)	N11-Zn-N22'	107.64 (8)
C11-C12	1.449 (3)	N11-Zn-N11'	132.25 (13)
C12-N12	1.331 (3)	N21-B-N12	107.69 (19)
C21-C22	1.457 (3)	N21-B-F1	110.6 (2)
C22-N22	1.307 (3)	N12-B-F1	109.2 (2)
C11-N11	1.376 (3)		
N22-Zn	2.076 (2)		
N11-Zn	1.965 (2)		
N21-B	1.544 (4)		
N12-B	1.558 (4)		

Table 4.1: Selected bond lengths and angles for **4.1**

Upon chelation of the zinc atom, the π-π* transition of the ligand chromophore undergoes a significant hypsochromic shift, exhibiting an absorption at 789 nm. This is blue-shifted by 33 nm from the π-π* transition observed for **3.6a** (λ_{max} = 822 nm) (**Figure 4.4**). The molar extinction coefficient of **4.1** (40.1 x 10^3 M^{-1} cm^{-1}) is approximately twice that of the **3.6a** (19.2 x 10^3 M^{-1} cm^{-1}). This is likely a

cumulative effect arising from the presence of two mono-BF_2 Nindigo chelate ligands being present, thus twice the number of chromophores.

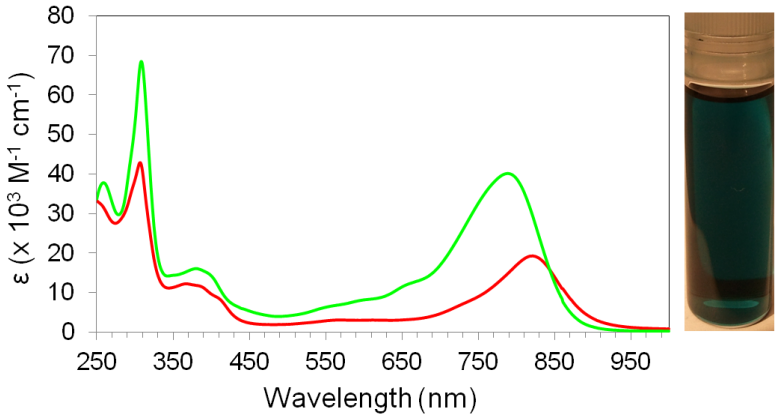

Figure 4.4: UV/vis/NIR spectra of **3.6a** (red) and **4.1** (green). Samples run at 1.25 x 10^{-5} M in DCM. Photograph of a solution of **4.1** (right)

Electrochemically, **4.1** exhibits numerous ligand based redox events. There are four reversible one-electron reductions and three one-electron oxidation events, two of which appear reversible (**Figure 4.5**). The four reductions occur as two sets of pairs. The first pair of reductions occur at -1.02 V and - 1.15 V with a gap of 334 mV to the next pair that occurs at -1.49 V and -1.63 V respectively. The first pair of reductions likely arises from the one-electron reduction of each ligand, giving rise to two radical anions. The second pair would then correspond to reduction of the radical anions to a pair of dianions. Oxidation events are less well defined. There are possibly two reversible one-electron oxidations at *ca* +0.47 V and an irreversible oxidation occurring at +0.70 V. The first two oxidations may result in formation of two radical cations, with the loss of a further electron resulting in dissociation of a fully reduced ligand (**Table 4.2**).

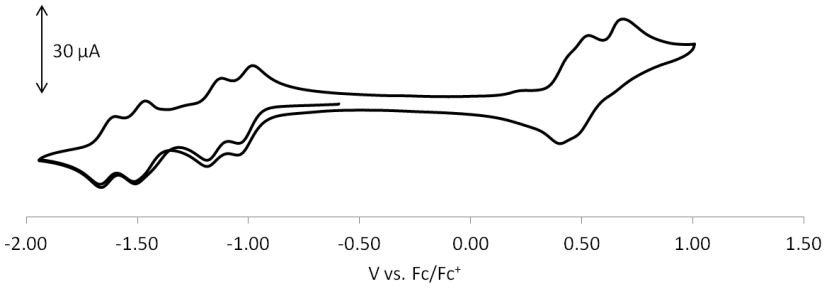

Figure 4.5: Cyclic voltammogram of **4.1** (DCM solution, 0.1 mM Bu_4NBF_4 electrolyte and scan rate = 100 mVs^{-1})

	Reduction (V)	Oxidation (V)
4.1	-1.63, -1.49, -1.15, -1.02	0.47[a], 0.69[b]

Table 4.2: Redox potentials for **4.1** ([a] = two coalesced oxidations, [b] = irreversible)

4.2.2 Synthesis and characterization of CuL_2 complexes

Reacting two equivalents of **3.3** with copper acetate dihydrate in the presence of a base results in the heteroleptic complexes **4.2** (**Scheme 4.2**). The complexes are stable in both the solid state and in solution and are soluble in a range of solvents. The paramagnetic nature of **4.2** precludes any quantitative ^{1}H NMR analysis. However, the expected number of proton signals for derivatives of **4.2** is observed, albeit significantly shifted and broadened (appendix D).

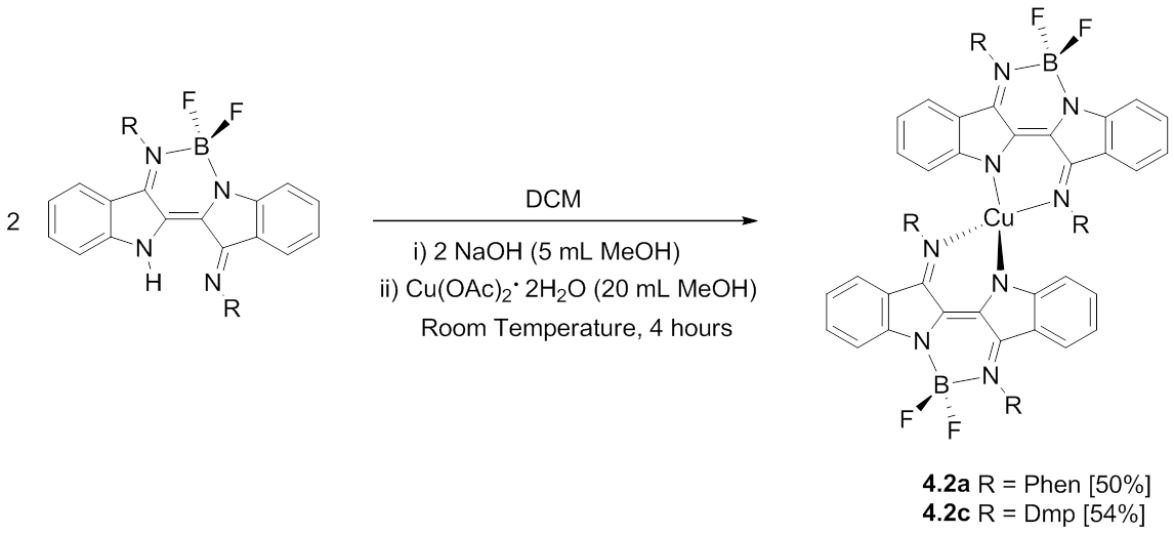

Scheme 4.2: General reaction conditions for the formation of **4.2**

The connectivity of **4.2a** and **4.2c** was confirmed by single crystal X-ray diffraction and **4.2c** will be discussed as a representative example (**Figure 4.6**). The copper adopts a pseudo-tetrahedral geometry, with angles about the copper ranging from 94.99° to 131.42°. These angular distortions are similar to those observed about the zinc in **4.1**. The equivalent bond lengths within each chelating ligand are within 0.01 Å from each other and within 0.01 Å of the corresponding bonds observed for **4.1**. This suggests the same degree of delocalization about the core is exhibited for both complexes. The intramolecular N-N separation on the boron side of **4.2c** is slightly expanded with respect to **4.1** (2.52(3) Å vs. 2.51(3) Å) and the N-N separation of the copper bound side is contracted with respect to the zinc side of **4.1** (2.96(2) Å vs. 3.00(3) Å). This may be a result of the Cu^{2+} ion being slightly smaller than the

Zn^{2+} ion, therefore a slightly greater contraction of the binding cavity is required to effectively bind to it (**Table 4.3**). The similarity in bond parameters of **4.1** and **4.2** suggests that the ligands in these complexes are both mono-anionic with +2 metal centres. However, the possibility of non-integral oxidation states i.e. ligand non-innocence, cannot be ruled out for derivatives of **4.2** by bond length analysis alone. The delocalization of the unpaired electron, present as a result of the open shell configuration of the copper, over the entire complex would likely only result in small bond length differences compared to that of the localized system, **4.1**.

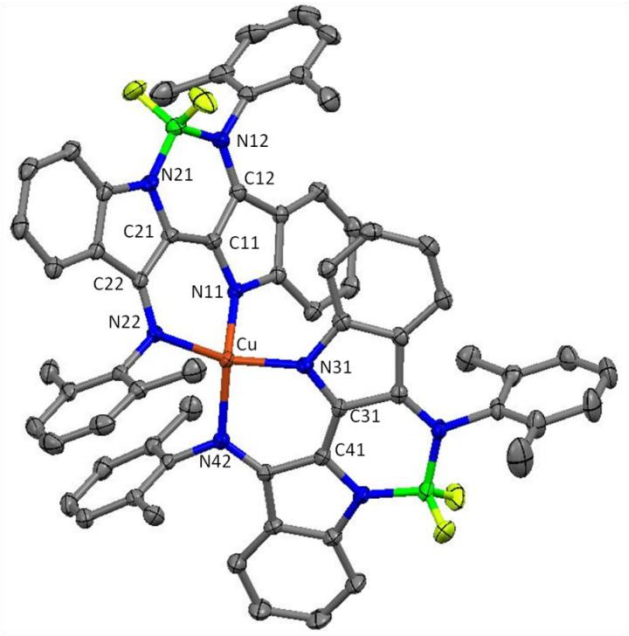

Figure 4.6: X-ray crystal structure of **4.2c**. Ellipsoids at the 50% probability level with all hydrogen atoms removed for clarity

Atoms	Lengths (Å)	Atoms	Angles (deg)
C11-C21	1.368 (3)	N11-Cu-N22	94.99 (7)
C21-N21	1.366 (3)	N11-Cu-N42	127.03 (7)
C11-C12	1.439 (3)	N11-Cu-N31	97.31 (7)
C12-N12	1.332 (3)	N22-Cu-N31	131.43 (7)
C21-C22	1.453 (3)	N22-Cu-N42	112.62 (7)
C22-N22	1.314 (3)	N31-Cu-N42	96.42 (7)
C11-N11	1.366 (3)	N21-B-N12	107.94 (18)
N22-Cu	2.0354 (17)	N21-B-F1	110.8 (2)
N11-Cu	1.9306 (17)	N12-B-F1	107.7 (2)
N21-B	1.539 (3)		
N12-B	1.583 (3)		

Table 4.3: Selected bond lengths and angles for **4.2a**

Compounds **4.2a** and **4.2c** exhibit qualitatively similar electronic absorption spectra to each other, but display significant differences to that of **4.1**. The electronic spectrum of **4.2a** is shown as a representative example (**Figure 4.7**). A major transition is observed at *ca.* 783 nm that is reminiscent of the lowest energy transition observed for **4.1** (789 nm). The absorption is however, not as intense, with a molar absorptivity of 22.8 x 10^3 M^{-1} cm^{-1} compared to 40.0 x 10^3 M^{-1} cm^{-1}. There is also a shoulder at slightly longer wavelengths (*ca.* 845 nm) present for **4.2a** that is not observed for **4.1**. There are also at least three additional bands between 537 - 666 nm of significant intensity (molar extinction coefficients greater than 15.0 x10^3 M^{-1} cm^{-1}) that are observed for **4.2a** but are not present for **4.1**.

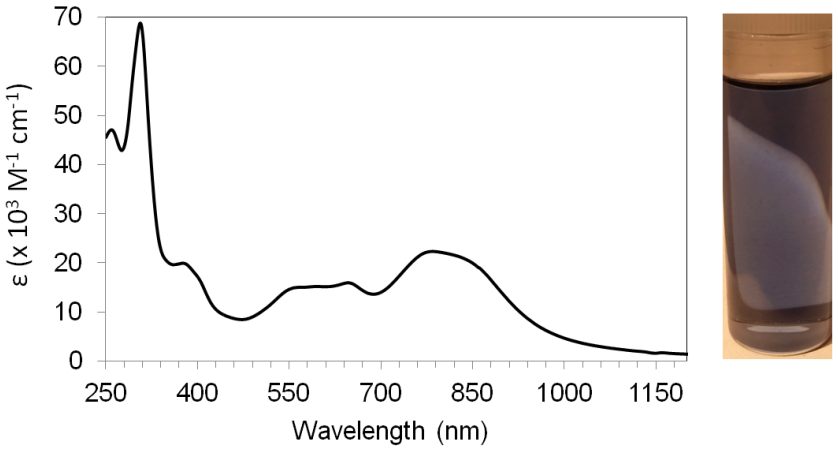

Figure 4.7: UV/vis/NIR spectrum of **4.2a**. Sample run at 1.25 x 10^{-5} M in DCM. Photograph of a solution of **4.2a** (right)

Two low energy transitions are observed for both **4.2a** and **4.2c** that are also not observed for **4.1.** For **4.2a** these transitions are observed at 1654 nm and 2056 nm with molar extinction coefficients of 1.5 x 10^3 M^{-1} cm^{-1} and 2.0 x 10^3 M^{-1} cm^{-1} respectively (**Figure 4.8**).

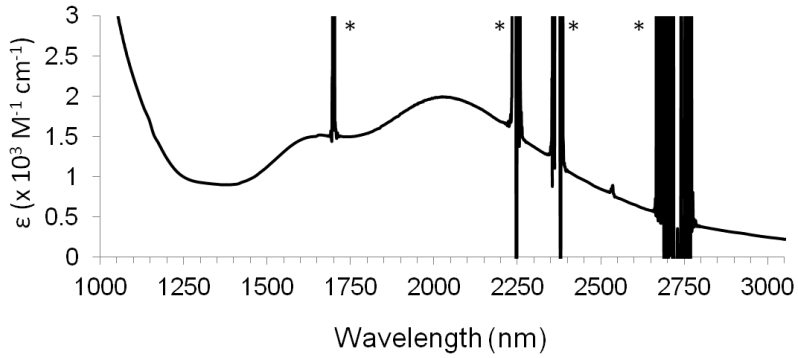

Figure 4.8: UV/vis/NIR spectrum of low energy transitions of **4.2a** (* artifacts of spectrometer)

Derivatives of **4.2** also exhibit significant electrochemical differences from that of **4.1**. Qualitatively the electrochemical behavior of **4.2a** and **4.2c** is similar, both exhibit 3 oxidation and 3 reduction processes (**Figure 4.9**). Both **4.2a** and **4.2c** display a mild reversible one-electron oxidation centered at +0.19 V for **4.2a** and +0.21 V for **4.2c**. They also both display a reversible one-electron reduction centered at -0.75 V for **4.2a** and -0.74 V for **4.2c**. Both these redox processes appear independent of the nature of the N-aryl substituent. The second and third oxidations of **4.2a** occur at

slightly milder potentials (+0.57 and +0.74) than the corresponding oxidations for **4.2c** (+0.79 V and +0.93 V). The second and third reductions of **4.2a** (-1.44 V and -1.64 V) also occur at milder potentials than those observed for **4.2c** (-1.58 V and -1.82 V) (**Table 4.4**).

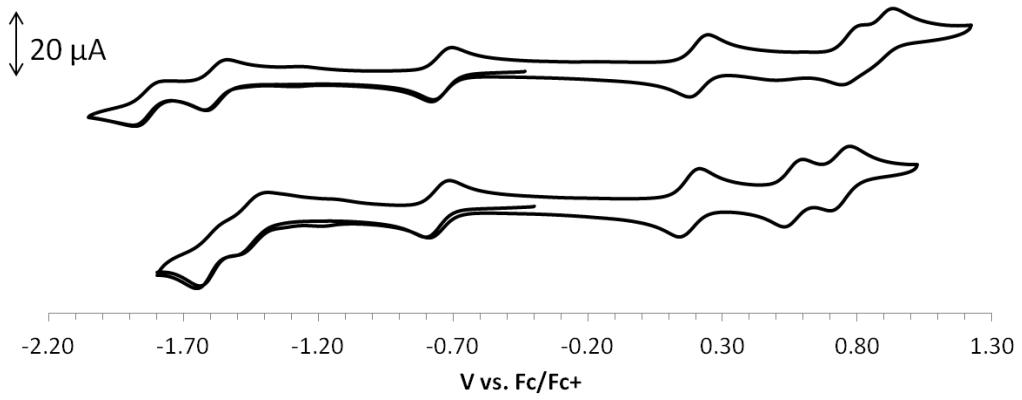

Figure 4.9: Cyclic voltammograms of **4.2c** (top) and **4.2a** (bottom) (DCM solution, 0.1 mM Bu_4NBF_4 electrolyte and scan rate = 100 mVs^{-1})

	Reductions (V)	Oxidations (V)
4.2a	-0.75, -1.44[b], -1.63[b]	0.19, 0.57, 0.74
4.2c	-0.74, -1.58, -1.82	0.21, 0.79, 0.93[a]

Table 4.4: Electrochemical data for **4.2a** and **4.2c** ([a] = irreversible, [b] = pseudo reversible)

X-ray photoelectron spectroscopy (XPS) was performed on **4.2a** and **4.2c**. The oxidation state of the copper in both derivatives was found to be the same (**Figure 4.10**). The $2p_{3/2}$ and $2p_{1/2}$ binding energies for both compounds are 932.4 eV and 952.4 eV respectively. These are closest to the binding energies obtained for the copper (I) standard, CuI, than the binding energies obtained for the standards containing copper (II). This data suggests that in both **4.2a** and **4.2c** the copper is cuprous in nature (**Table 4.5**).

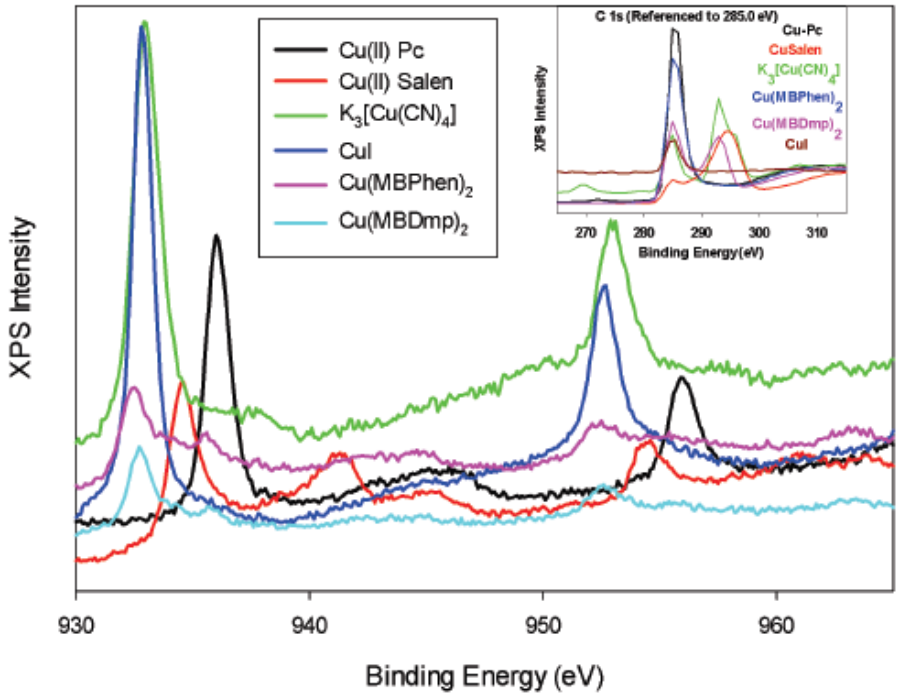

Figure 4.10: XPS data for **4.2a** (purple, labelled $Cu(MBPhen)_2$ in caption) and **4.2c** (blue, labelled $Cu(MBDmp)_2$ in caption) against a variety of Cu(I) and Cu(II) standards (all XPS experiments run by the group of T. Storr, Simon Fraser University)

Compound	Cu $2p_{3/2}$ binding energy (eV)	Cu $2p_{1/2}$ binding energy (eV)
4.2a	932.5	952.5
4.2c	932.7	952.5
CuI	932.8	952.6
Cu(II)-Pc	936.0	956.0

Table 4.5: Selected binding energy data for **4.2a** and **4.2c** as well as some selected standards

No signal was observed by room temperature solution state (DCM) EPR of **4.2a** and as a result solid state EPR was employed (**Figure 4.11**). The g-value of 2.08 is indicative of copper character in the SOMO with the broad spectrum suggesting delocalization of the unpaired spin onto the ligands. The broadness of the spectrum results in loss of the hyperfine couplings that would be expected should the unpaired electron in **4.2a** be delocalized.

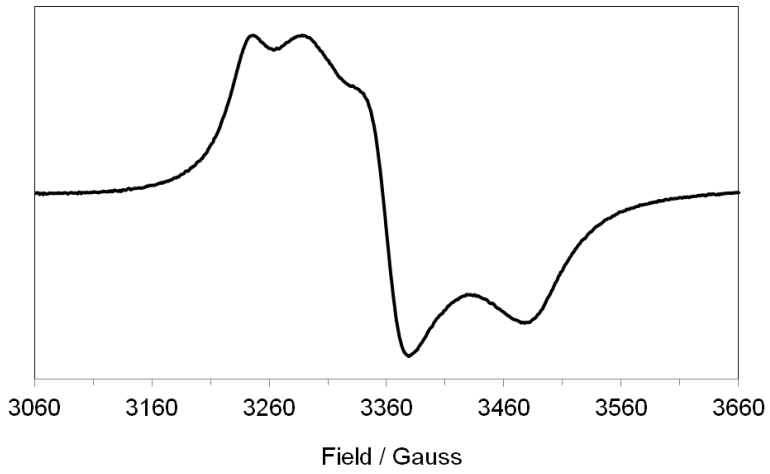

Figure 4.11: Solid state (powder sample at room temperature) EPR spectrum of **4.2a**

Computational analysis suggests that the unpaired electron in **4.2a** is fully delocalized, with equal amounts of spin density located on both ligands and the copper centre (*ca.* 33% on each) (**Figure 4.12**). This suggests that ligands of type **3.3**, when bound to copper, exhibit non-innocent behavior. The delocalization of the unpaired electron gives credence to the DFT calculated assignment of the low energy absorption bands (> 1600 nm) observed in the electronic spectra being LLCT in nature (Appendix G).

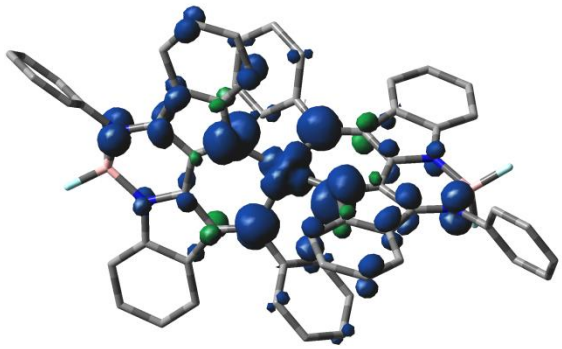

Figure 4.12: Spin density diagram for **4.2a**

Due to the open shell configuration of the copper, it could be convenient to assign the first redox events as metal centered oxidation (Cu^{2+} to Cu^{3+}) and reduction (Cu^{2+} to Cu^{+}) processes. However, given the redox-active nature of the surrounding ligand set, assigning these processes as purely metal centered may be an oversimplification. A variety of possible electronic structures can be envisioned where the unpaired electron is localized on the copper, either ligand, or delocalized with contributions from all resonance forms (**Figure 4.13**). In order to elucidate what is occurring during these redox events, a firmer understanding of the electronic nature of the neutral complex needs to be obtained.

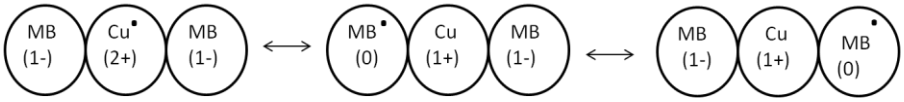

Figure 4.13: Schematic representation of the possible electronic structures of **4.2a**

4.3 Redox reactions of CuL_2 complexes

Reactions of **4.2c** with $AgBF_4$ in DCM generates the cationic complex, **[4.2c]$^+$**. The reversibility of the chemical oxidation, shown to be fully reversible under electrochemical conditions (**Figure 4.9**), was probed by reacting **[4.2c]$^+$** with ferrocene in order to reduce it back to the neutral species (**Scheme 4.3**).

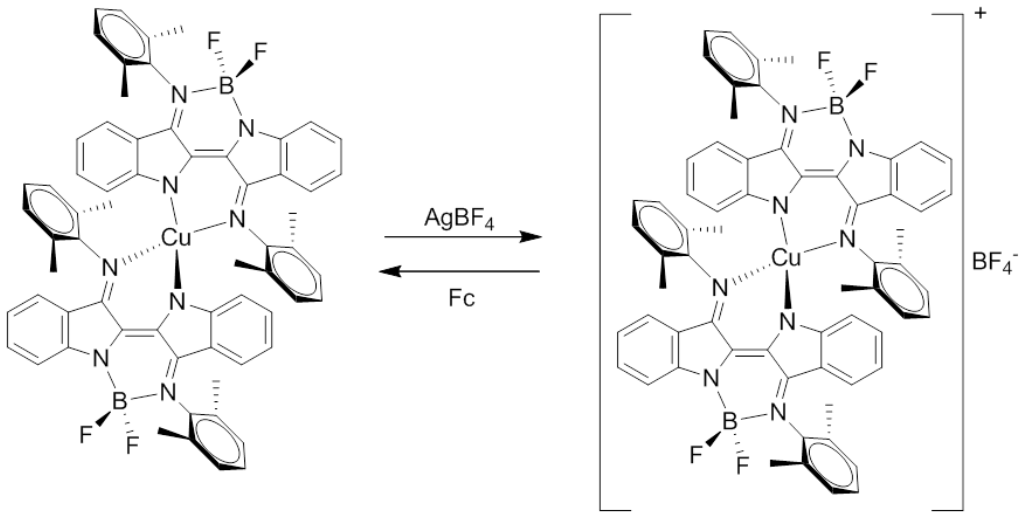

Scheme 4.3: Reversible chemical oxidation of **4.2c** to generate the cationic complex **[4.2c]$^+$**

The oxidation was monitored by electronic absorption spectroscopy. The absorption spectrum of **[4.2c]$^+$** shows significant differences from that of **4.2c**. The most striking difference is the presence of a very broad, intense, low energy transition centered at 1690 nm (ε = 10.0 x 10^3 M^{-1} cm^{-1}).There are also two new intense bands centered at 985 nm and 623 nm (ε = 11.0 x 10^3 M^{-1} cm^{-1} and 21.0 x 10^3 M^{-1} cm^{-1}). The reversibility of the chemical oxidation appears to proceed cleanly, with the original absorption spectrum of **4.2c** and that of the complex obtained by reduction of **[4.2c]$^+$** showing good agreement (**Figure 4.14**).

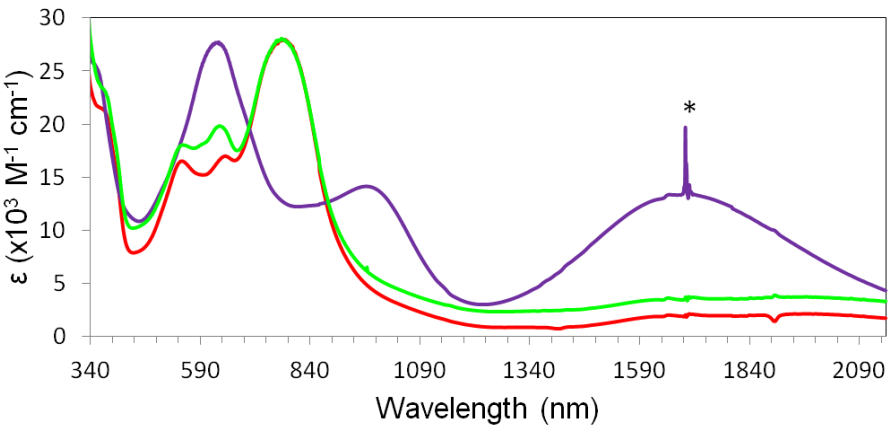

Figure 4.14: UV/vis/NIR spectra of **4.2c** (green), **[4.2c]**$^{+}$ (purple) and that obtained from the reduction of **[4.2c]**$^{+}$ (red) (*artifact from the spectrometer)

Reacting **4.2c** with cobaltocene in DCM generates the anionic complex, **[4.2c]**$^{-}$. The reversibility of this reaction was probed by reacting **[4.2c]**$^{-}$ with ferrocenium tetrafluoroborate to regenerate **4.2c** (**Scheme 4.4**).

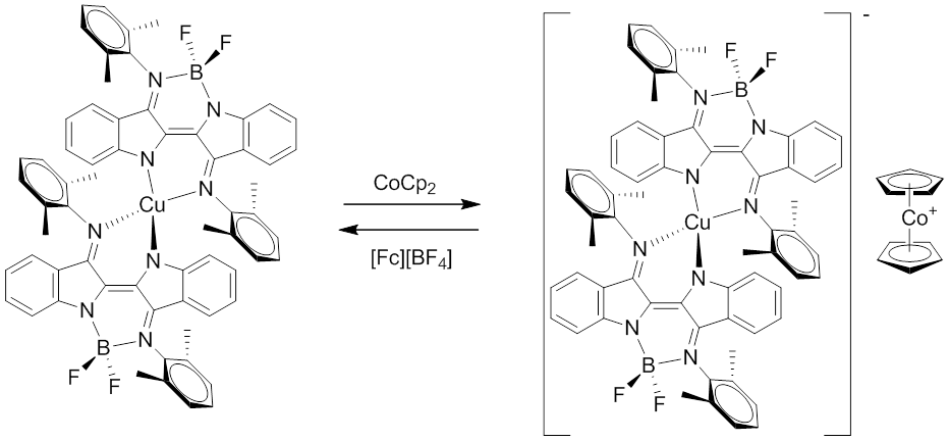

Scheme 4.4: Reversible chemical reduction of **4.2c** to generate the anionic complex **[4.2c]**$^{-}$

The absorption spectrum of **[4.2c]**$^{-}$ shows significant differences from that of **4.2c**. Unlike for **[4.2c]**$^{+}$, no intense low energy transitions (> 1600 nm) are observed (**Figure 4.15**). However, a low

energy band at *ca.* 1041 nm is present. There is good agreement between the absorption profile of **4.2c** and that obtained from the oxidation of **[4.2c]**$^{-}$ suggesting the chemical reduction is reversible.

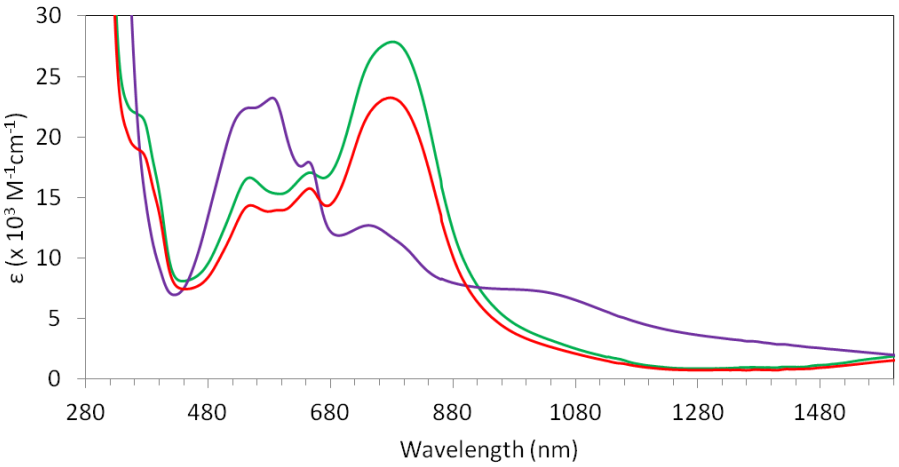

Figure 4.15: UV/vis/NIR spectra of **4.2c** (green), **[4.2c]**$^{-}$ (purple) and that obtained by oxidation of **[4.2c]**$^{-}$ (red)

The charged species, **[4.2c]**$^{+}$ and **[4.2c]**$^{-}$ were subjected to XPS studies in order to investigate how their electronic structure is affected by the chemical redox changes (**Figure 4.16**). Both the cation and anion exhibit binding energies that are different from those observed for **4.2c**. Both sets of doublets shift in the expected direction for the oxidised and reduced species with the copper remaining in the +1 oxidation state. The difference in binding energy of the cation and anion suggests that the MO's involved in the redox processes contain a certain degree of copper character (**Table 4.6**).

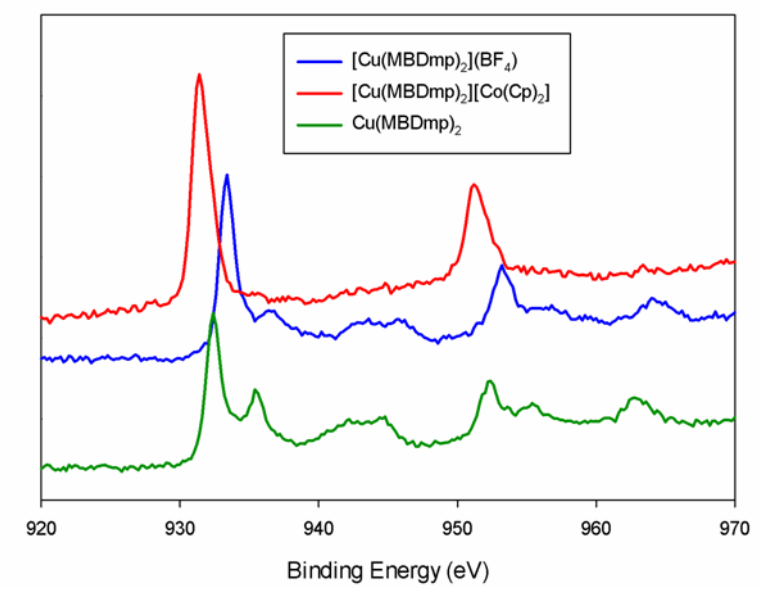

Figure 4.16: XPS data for **4.2c**, **[4.2c]**$^{+}$ and **[4.2c]**$^{-}$

Compound	Cu $2p_{3/2}$ binding energy (eV)	Cu $2p_{1/2}$ binding energy (eV)
[4.2c]$^{+}$	933.4	953.2
[4.2c]$^{-}$	931.4	951.2

Table 4.6: Binding energy data for **[4.2]**$^{+}$ and **[4.2c]**$^{-}$

Preliminary investigations into the possibility that **4.2c** can exhibit valence tautomerism were undertaken by conducting low temperature electronic spectroscopy experiments. The low temperature (77 K) absorption spectra of **4.2c** in DCM or toluene do not show any changes from those obtained at room temperature (294 K). This suggests that, under these conditions, valence tautomerism does not occur (**Figure 4.17**).

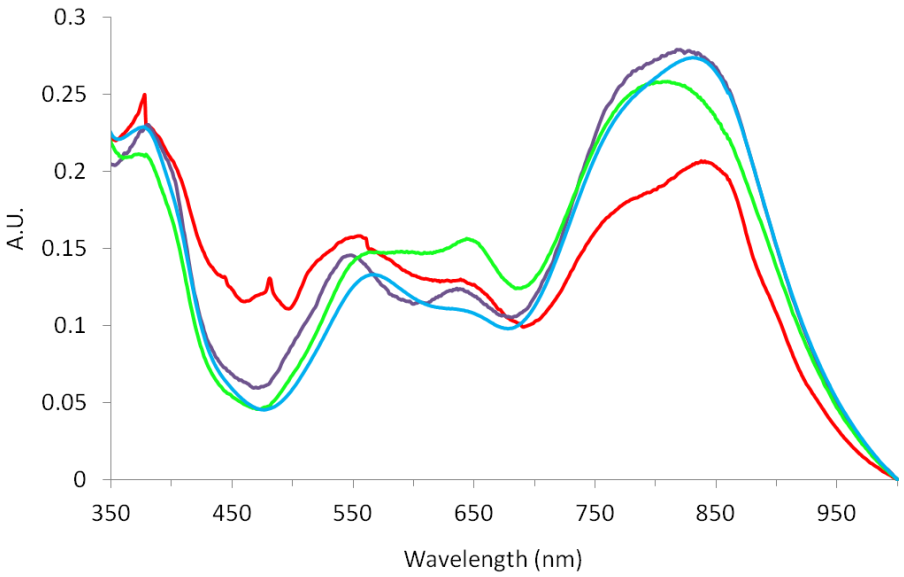

Figure 4.17: Low temperature (190 K) [toluene (red), DCM (green)] and room temperature [toluene (blue), DCM (purple)] UV/vis/NIR spectra for **4.2c**

4.4 Summary

The coordination chemistry of the redox-active capping ligand (**3.3**) was further investigated by synthesizing homoleptic zinc and copper complexes. X-ray crystallography of the zinc complex, **4.1**, found that the metal adopts a pseudo-tetrahedral geometry surrounded by two crystallographically equivalent ligand sets. Spectroscopically, **4.1** was found to exhibit a low energy, ligand centered transition at 789 nm with a molar extinction coefficient in excess of 40.0 x 10^3 M^{-1} cm^{-1}. Cyclic voltammetry experiments reveal multiple ligand centered redox processes. Two pairs of reversible one-electron reductions are observed. These are attributed to formation of two radical anionic ligands followed by further reduction generating two dianionic ligand sets. There are also three oxidation processes, the last of which appears irreversible. The characterisation data suggests **4.1** consists of a zinc(II) atom surrounded by two equivalent anionic ligands. Copper complexes, **4.2a** and **4.2c** display electronic absorption spectra that exhibit multiple visible transitions that are not present for **4.1.** These new transitions are likely a combination of π-π*and charge transfer bands, given the open shell electronic configuration of the copper. In addition, derivatives of **4.2** display two low energy transitions centered at 1669 nm and 2039 nm (for **4.2c**) that are thought, based on computations, to be LLCT in nature. This suggests that these complexes are not composed of purely copper(II) centres surrounded by

a pair of anionic ligands. Cyclic voltammetry experiments revealed redox behaviour that also differs significantly from the zinc system. Three oxidation and three reduction processes are observed, the first of each occurring at mild potentials (*ca.* +0.19 V and -0.75 V). Due to the electroactive nature of the metal centre is has, as yet, not been possible to assign these redox processes. Solid state EPR spectroscopy found **4.2a** to possess a g value of 2.08. This suggests that the unpaired electron resides on the metal, indicative of a copper(II) centre. However, XPS analysis suggests the copper to be +1 in nature based on 2p binding energy comparisons with known Cu(I) and Cu(II) standards. In addition, computations describe the unpaired electron in **4.2a** as being delocalized evenly over the entire complex (33.3 % on each ligand and 33.3 % on the metal centre). This somewhat contradictory characterisation data implies that these systems are non-innocent in nature. Chemical redox reactions, monitored spectroscopically, showed formation of the anion and cation to be chemically reversible. There are multiple new transitions observed for both **[4.2c]**$^{+}$ and **[4.2c]**$^{-}$ that are yet to be assigned. XPS analysis of the charged species found that the binding energy of the 2p electron is affected by the chemical redox. This suggests that there is some copper character involved in the redox orbitals of **4.2c**.

4.5 Experimental

4.5.1 General procedures

General procedures are as outlined in Section 2.4.

Zinc-bis(indigo bis(phenylimine)difluoroboron), 4.1 : To a solution of **3.3a** (740 mg, 1.61 mmol) in DCM (*ca*. 110 mL) was added a solution of NaOH (1.8 mmol, 70 mg) in methanol (*ca*. 5 mL). $Zn(OAc)_2.2H_2O$ (0.810 mmol, 178 mg) was dissolved in methanol (10 mL) and this solution was slowly added to the basic ligand solution. The mixture was stirred at room temperature in air for 4 hours before the solvent was removed. The crude solid was taken up in DCM and extracted with water and brine. The organic layer was pumped dry before being washed with Et_2O to yield a dark powder (477 mg, 60 %). X-ray quality crystals were grown by slow diffusion of acetonitrile into a saturated DCM solution. ^{1}H NMR (300 MHz, CD_2Cl_2, 293K): δ = 6.2 (d, 2H, *J* = 8.0 Hz), 6.5 (m, 4H), 6.6 (dodod, 2H, *J* = 8.1 Hz, *J* = 7.1 Hz, *J* = 1.1 Hz), 6.9 (m, 4H), 7.0 (m, 2H), 7.2 (dodod, 2H, *J* = 8.3 Hz, *J* = 7.0 Hz, 1.2 Hz), 7.5 (m, 10H), 7.6 (m, 10H).

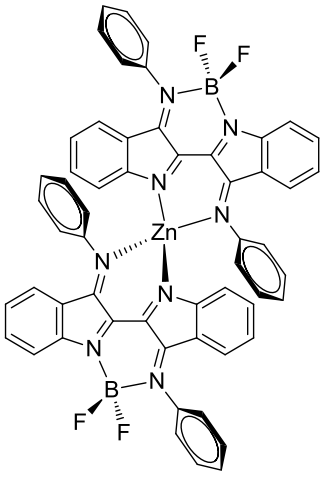

^{13}C NMR (500 MHz, CD_2Cl_2, 293K): δ = 165.6, 164.6, 160.5, 159.7, 156.3, 152.6, 147.4, 141.0, 135.2, 135.0, 132.9, 131.6, 130.4, 130.2, 129.8, 129.7, 128.7, 127.4, 127.0, 126.7, 126.7, 122.3, 122.1, 121.0, 119.2, 119.1, 116.7, 116.3, 115.4. $^{19}F\{^1H\}$ NMR (300 MHz, CD_2Cl_2, 293 K): δ = -129.1 (q, *J* = 29.9 Hz). $^{11}B\{^1H\}$ NMR (500 MHz, CD_2Cl_2, 293 K): δ = 3.4 (t, *J* = 29.9 Hz). UV/vis/NIR (CH_2Cl_2), λ_{max} /nm (ε, $M^{-1}cm^{-1}$): 259 (37,700), 308 (68,400), 379 (16,000), 789 (40,100). HRMS, *m/z*: calcd for $(M\text{-}Na)^+$ $C_{56}H_{36}N_8B_2F_4Zn$ 1005.2393; found 1005.2380. Anal. Calcd for $C_{56}H_{36}N_8B_2F_4ZnCu$: C, 68.36; H, 3.69; N, 11.39; Zn, 6.64. Found: C, 68.11, H, 3.57; N, 11.22; Zn, 6.64

Copper-bis(indigo bis(phenylimine)difluoroboron), 4.2a: To a solution of **3.3a** (810 mg, 1.76 mmol) in DCM (ca. 110 mL) was added a solution of NaOH (1.8 mmol, 70 mg) in methanol (ca. 5 mL). To this solution was added a suspension of $Cu(OAc)_2.2H_2O$ (0.880 mmol, 191 mg) in methanol (*ca*. 20 mL). The reaction was left to stir for 4 hours before the solvent was removed. The crude solid was taken up in DCM and extracted with water and brine. The organic layer was pumped dry followed by recrystalization from DCM/MeCN to yield dark purple crystals (872 mg, 50 %). X-ray quality crystals were grown by slow diffusion of acetonitrile into a saturated DCM solution. UV/vis/NIR (CH_2Cl_2), λ_{max} /nm (ε, $M^{-1}cm^{-1}$): 306 (69,300), 375 (20,400), 645 (16,400), 783 (22,800), 1654 (1,520), 2056 (1,980). HRMS, *m/z*: calcd for $(M)^+$ $C_{56}H_{36}N_8B_2F_4Cu$ 981.2499; found 981.2487. Anal. Calcd for $C_{56}H_{36}N_8B_2F_4Cu$: C, 68.49; H, 3.69; N, 11.39; Cu, 6.47. Found: C, 68.25, H, 3.45; N, 11.31; Cu.6.47

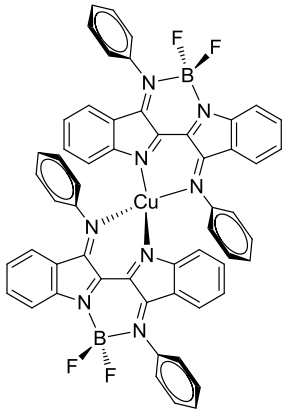

Copper-bis(indigo bis(2,6-dimethylphenylimine)difluoroboron), 4.2c: To a solution of **3.3c** (344 mg, 0.666 mmol, 2eq) in DCM (*ca*. 30mL) was added a solution of NaOH (26 mg, 0.67 mmol, 2 eq) in methanol (*ca*. 3 mL). To this was added a suspension of $Cu(OAc)_2.2H_2O$ (74mg, just over 1eq) in methanol (*ca*. 10 mL). The mixture was left to stir at room temperature in air for 2 hours. The reaction mixture was then extracted with water and the organic layer dried and the solvent removed to give a dark purple powder (408 mg, 54 %). X-ray quality crystals were grown by slow diffusion of acetonitrile into a saturated DCM solution. UV/vis/NIR (CH_2Cl_2), λ_{max} /nm (ε, $M^{-1}cm^{-1}$): 305 (86,100), 376 (20,500), 593 (17,100), 646 (20,600), 796 (27,500), 1666 (1,440), 1961 (1,600). HRMS, *m/z*: calcd for $(M\text{-}Bu)^+$ $C_{66}H_{58}N_8B_2F_4Cu$ 1093.37331; found 1093.37364.

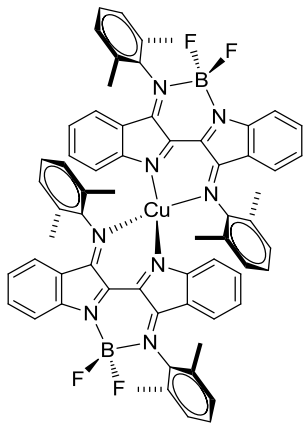

Anal. Calcd for $C_{60}H_{44}N_8B_2F_4Cu$: C, 70.24; H, 4.79; N, 10.24; Cu, 5.81. Found: C, 63.45, H, 4.46; N, 8.95; Cu, 4.93

Typical redox experiments:

[4.2c]$^+$: In a glovebox, **4.2c** (59 mg, 0.053 mmol) was dissolved in dry DCM (10 mL). Cobaltocene (10 mg, 0.053 mmol) was added and the reaction left to stir for 20 minutes. Ferrocenium tetrafluoroborate (14 mg, 0.053 mmol) was then added and the reaction was left for 20 minutes.

[4.2c]$^-$: In a glovebox, **4.2c** (58 mg, 0.051 mmol) was dissolved in dry DCM (10 mL). $AgBF_4$ (10 mg, 0.053 mmol) was added and the reaction left to stir for 20 minutes. Ferrocene (9.8 mg, 0.053 mmol) was then added and the reaction left to stir for 20 minutes.

Aliquots of the generated anions and cations were removed from the glovebox in a sure-sealed curvette in order to run the electronic absorption experiments. They were then returned to the stock solutions afterwards.

Chapter 5: Synthesis and properties of dehydroNindigo and bis-ruthenium-dehydroNindigo complexes

5.1 Dehydroindigodiimines

Reacting indigo with bromine in the presence of calcium hydroxide has been shown to produce the fully oxidized derivative, dehydroindigo (**Scheme 5.1**).[140-143] This molecule seems like a potential candidate for bridging ligation due to its neutral bis-bidentate bonding motif. However, despite the increased solubility exhibited by dehydroindigo, relative to indigo, no coordination chemistry has as yet been reported. The reason for this is likely that the isolation and purification of dehydroindigo is hampered by its propensity to return back to indigo.

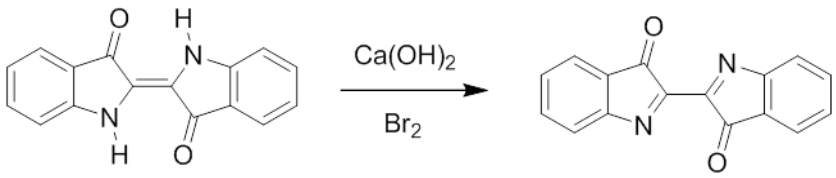

Scheme 5.1: Synthesis of dehydroindigo

The corresponding oxidation reaction of indigodiimines to yield dehydroindigodiimines was reported at the turn of the 20th century. Reactions of indigodiimine with lead oxide generated the fully oxidized species. Similar to dehydroindigo, this family of molecules possesses a bis-bidentate bonding motif and looks like a good candidate for bridging ligation. However, until this work no further chemistry of these molecules had been reported (**Scheme 5.2**).[145,146]

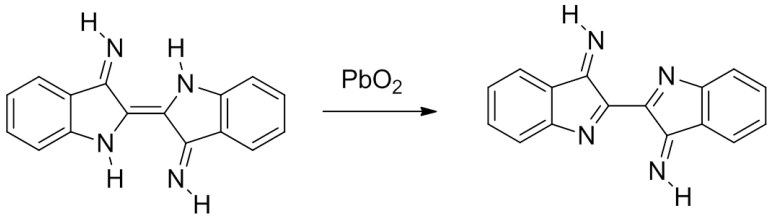

Scheme 5.2: Synthesis of dehydroindigodiimine[145,146]

In this chapter the synthesis of dehydroindigodiimines (dehydroNindigos) is presented and their coordination chemistry explored by studying bis-ruthenium chelates.

5.1.1 Synthesis of dehydroindigodiimines (DehydroNindigo)

Room temperature reactions of **1.33** in DCM with 2 equivalents of silver(I) oxide generate dehydroNindigo, **5.1**, in decent yields (**Scheme 5.3**). These compounds are isolated as red or brown powders that are stable indefinitely both in solution and the solid state. DehydroNindigos exhibit complete solubility in a variety of solvents and improved stability with respect to dehydroindigo.

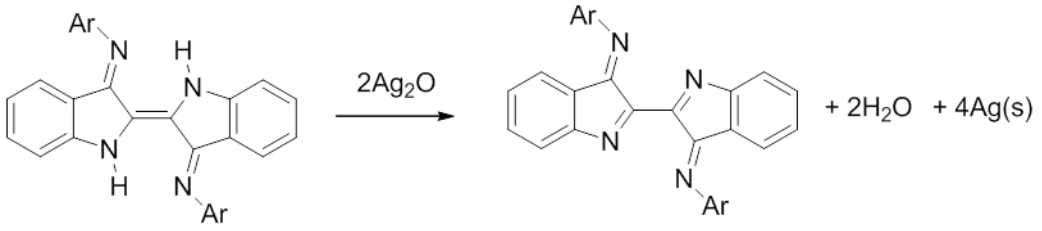

5.1a Ar = phenyl [50%]
5.1b Ar = pTolyl [75%]
5.1c Ar = 2,6-dimethylphenyl [50%]
5.1h Ar = mes [65%]

Scheme 5.3: Synthesis of dehydroNindigo (**5.1**)

^{1}H NMR spectra for derivatives **5.1c** and **5.1h** match those expected for the desired products. The spectrum for **5.1c** is shown below as a representative example (**Figure 5.1**). There are no downfield

signals (> 8.5 ppm), confirming the lack of indole type hydrogen atoms being present. There is a 12-proton singlet observed at 2.00 ppm suggesting that all methyl groups on the N-aromatic ring are in chemically identical environments.

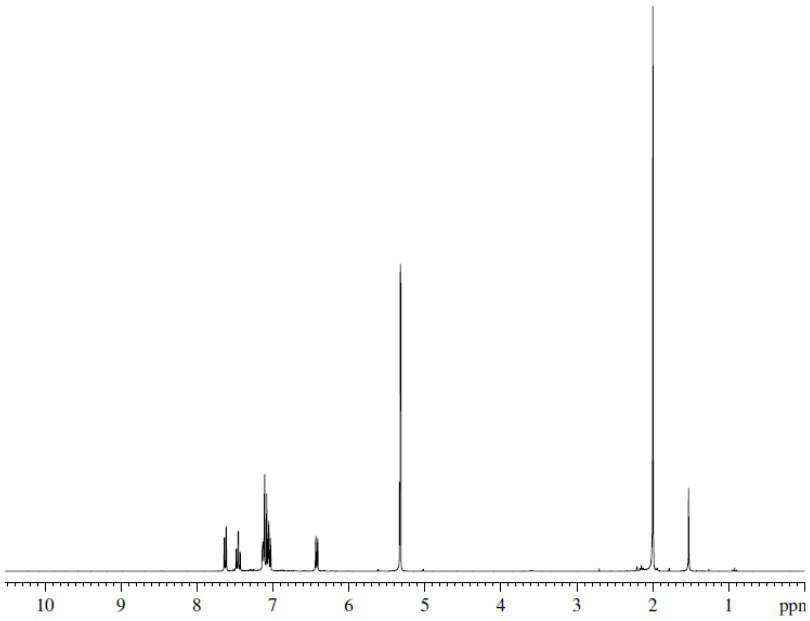

Figure 5.1: ^{1}H NMR spectrum for **5.1c** (Sample run in CD_2Cl_2)

For derivatives **5.1a** and **5.1b** there is an additional compound present in the product mixtures that can be observed by ^{1}H NMR. The aromatic region of the ^{1}H NMR spectrum for **5.1a** is shown as a representative example (**Figure 5.2**).

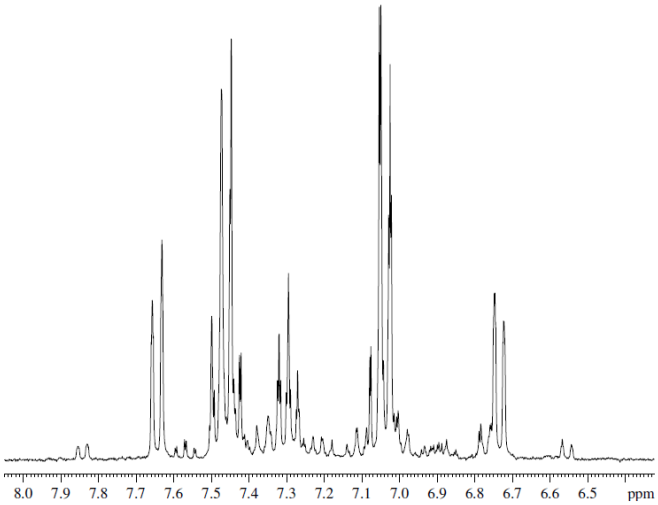

Figure 5.2: Aromatic region of the ^{1}H NMR spectrum for **5.1a**. (Sample run in CD_2Cl_2)

The minor impurity appears, by NMR spectroscopy, to be similar to, but as yet inseparable from **5.1a**. The potential for derivatives of **5.1** to undergo isomerisation to structures of type **5.1'** and **5.1''** cannot be ruled out.

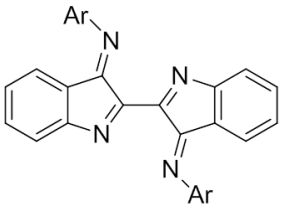

5.1

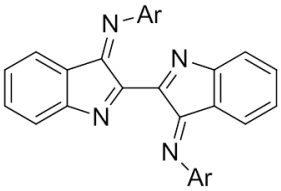

5.1'

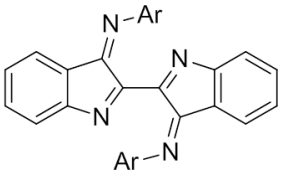

5.1''

The structure of **5.1a** was confirmed by single crystal X-ray diffraction (**Figure 5.3**). The extended conjugation about the C4N4 core present in derivatives of **1.33** is not present in **5.1a**. The two dehydroindole halves of **5.1a** are connected via a carbon-carbon bond (C1-C15, 1.47 Å) that is of typical length for a single bond between two sp^2 carbon atoms. This bond is significantly longer than that of the central carbon-carbon bond observed in Nindigo (*ca.* 1.37 Å). The C1-N1 bond (1.29 Å) is typical of a nitrogen-carbon double bond. The C1-C2 bond length (1.50 Å) is typical of a carbon-carbon single bond

between sp^2-sp^3 carbons and the C2-N2 bond length (1.28 Å) is typical of a formal imine bond.[147] The bond lengths of **5.1a** are comparable to those calculated for dehydroindigo (DHI)[144] and to that of the solid state structure of 2-t-butyl-3-ptolylimino-3H-indole (**Figure 5.4**),[155] the latter is reminiscent of one half of **5.1a** (**Table 5.1**). The single bond nature of the C1-C15 bond is also reflected by the lack of planarity that the molecule exhibits. The two dehydoindole halves are twisted relative to each other (about C1-C15), deviating by 65.6° from coplanarity. In the solid state both halves of the molecule remain *syn* over the C2-N2 bond with respect to the benzannulated rings.

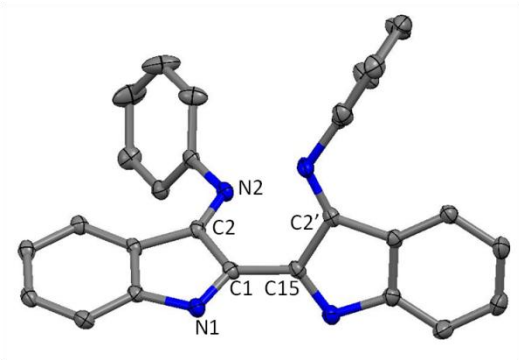

Figure 5.3: Single crystal X-ray structure of **5.1a**. Thermal ellipsoids set at the 50% probability level. All hydrogen atoms removed for clarity

Bond	5.1a (Å)	2-tbutyl-3-ptolylimino -3H-indole(Å)
C1-C15	1.4747(18)	-
C1-C2	1.5003(18)	1.515(3)
C1-N1	1.2933(17)	1.288(3)
C2-N2	1.2773(17)	1.273(3)

Table 5.1: Selected bond lengths for **5.1a** with equivalent bond lengths obtained from the solid state structure of 2-t-butyl-3-ptolylimino-3H-indole[148]

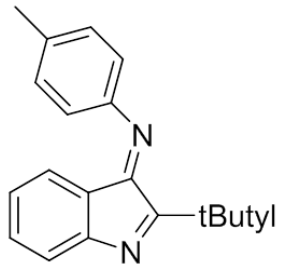

Figure 5.4: Structure of 2-t-butyl-3-ptolyl-3H-indole

The structural differences between dehydroNindigo and Nindigo are also reflected in the electronic absorption spectra (**Figure 5.5**). All derivatives of **5.1** exhibit very similar spectra and **5.1a** is shown below as a representative example. The longest wavelength absorption band of **5.1a** is centered at 433 nm with a molar absorptivity of 7.81 x 10^3 M^{-1} cm^{-1}. There is also a higher energy transition at 341 nm with a molar absorptivity of 9.58 x 10^3 M^{-1} cm^{-1}. These spectral features are reminiscent of indolone and dehydroindigo, where the most intense transition occurs at 456 nm with a higher energy band centered at 290 nm.[144,150] The formal single bond connecting the two halves of **5.1** prevents the cross conjugation that is present in **1.33**. This results in no low energy (> 500 nm) transitions being observed.

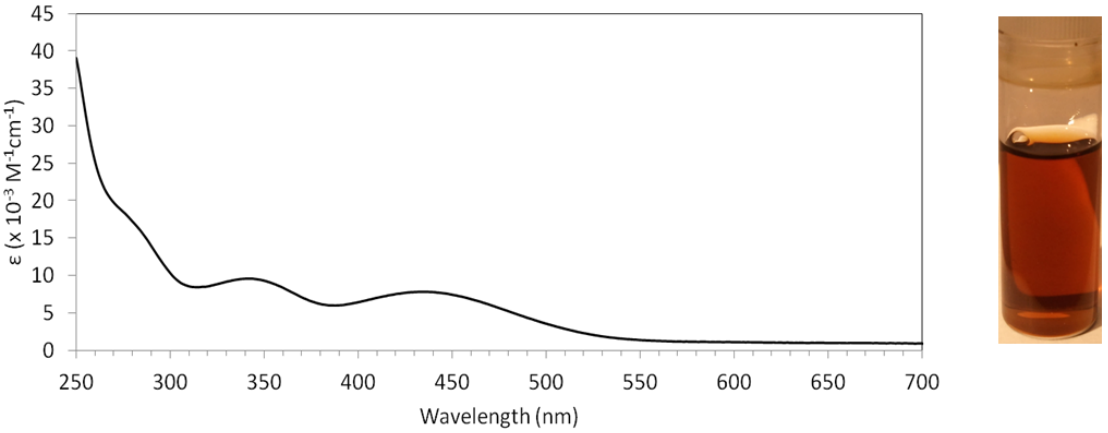

Figure 5.5: UV/vis/NIR spectrum of **5.1a**. Sample run in DCM at a concentration of 1.25 x 10^{-5} M. Photograph of a solution of **5.1a** (right)

The redox properties of derivatives of **5.1** were probed by running cyclic voltammetry experiments. Given that derivatives of **5.1** are the fully oxidized analogues of **1.33**, it is unsurprising that there are no oxidation processes observed**.** There are only irreversible reduction processes that occur at potentials lower than -1.00 V (**Figure 5.6**).

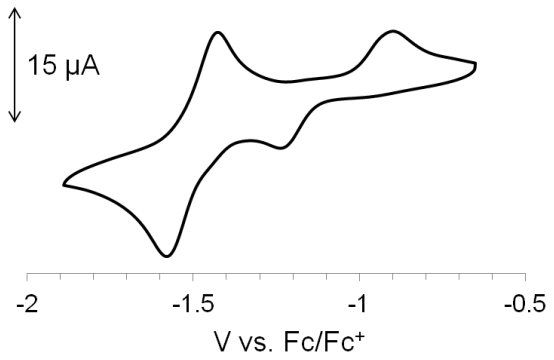

Figure 5.6: Cyclic voltammogram of **5.1a (**DCM solution, 0.1 mM Bu_4NBF_4 electrolyte and scan rate = 240 mVs^{-1}).

5.2 Synthesis of bis-ruthenium complexes of dehydroNindigo

Initial attempts to react **5.1** with 2 equivalents of $Ru(hfac)_2(MeCN)_2$ under an inert atmosphere in either hexanes, refluxing hexane or refluxing benzene, were unsuccessful in producing the target complex **5.2-trans** (the stereochemistry determined by the geometry about the central C11-C21 bond, see **figure 5.9**), and led only to recovery of both starting materials. Whilst this was not ideal, it does highlight the increased stability of **5.1** over dehydroindigo. Turning to a higher boiling solvent (toluene) led to successful consumption of **5.1** and what was thought to be the successful synthesis of **5.2-trans** (**Scheme 5.4**).

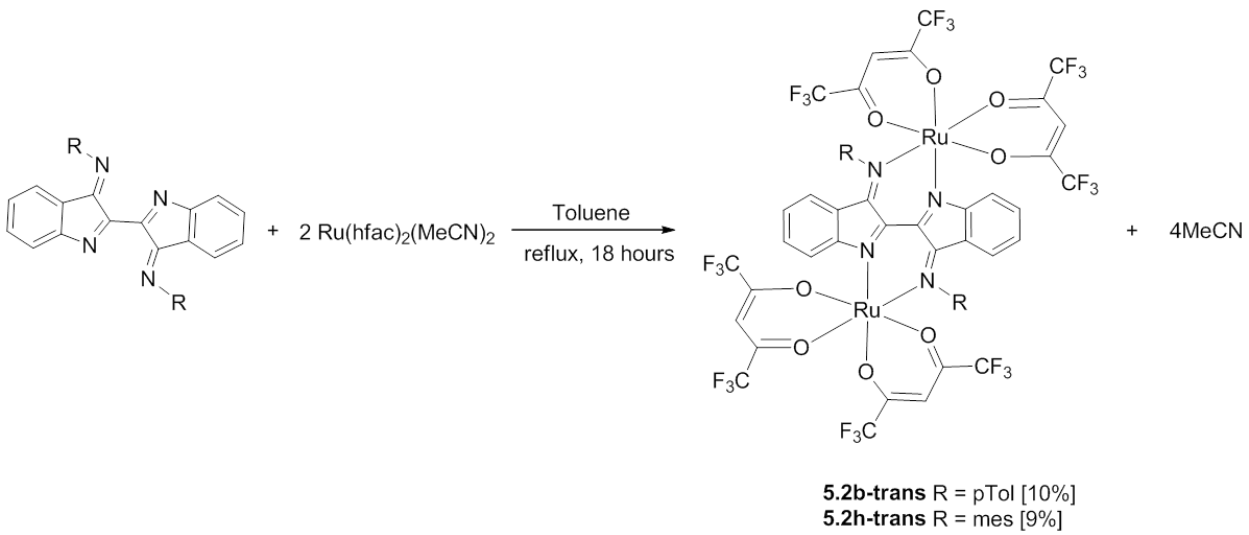

Scheme 5.4: General conditions employed in attempted synthesis of **5.2-trans**

However, TLC analysis of the dark solid obtained found **5.2b-trans** to be a two component mixture. Separation of the two compounds by column chromatography was challenging but successful. The ^{1}H NMR spectra of the two compounds isolated during the attempted synthesis of **5.2b-trans** suggests the two species are structurally similar (**Figure 5.7**). One aliphatic signal is observed for each compound at 2.43 ppm and 2.45 ppm. This suggests that the *para*-methyl groups of the N-aromatic substituents are in near chemically identical environments. Both spectra also exhibit two two-proton singlets at 5.84 ppm and 6.20 ppm for fraction one and 5.93 ppm and 6.35 ppm for fraction two. The integrals of these signals correspond to the four hydrogen atoms present in two inequivalent hfac environments. This allows tentative confirmation of bis-ruthenium chelation. The ^{19}F NMR spectra of both compounds are also similar with 4 independent fluorine environments observed for both fractions (**Figure 5.7**).

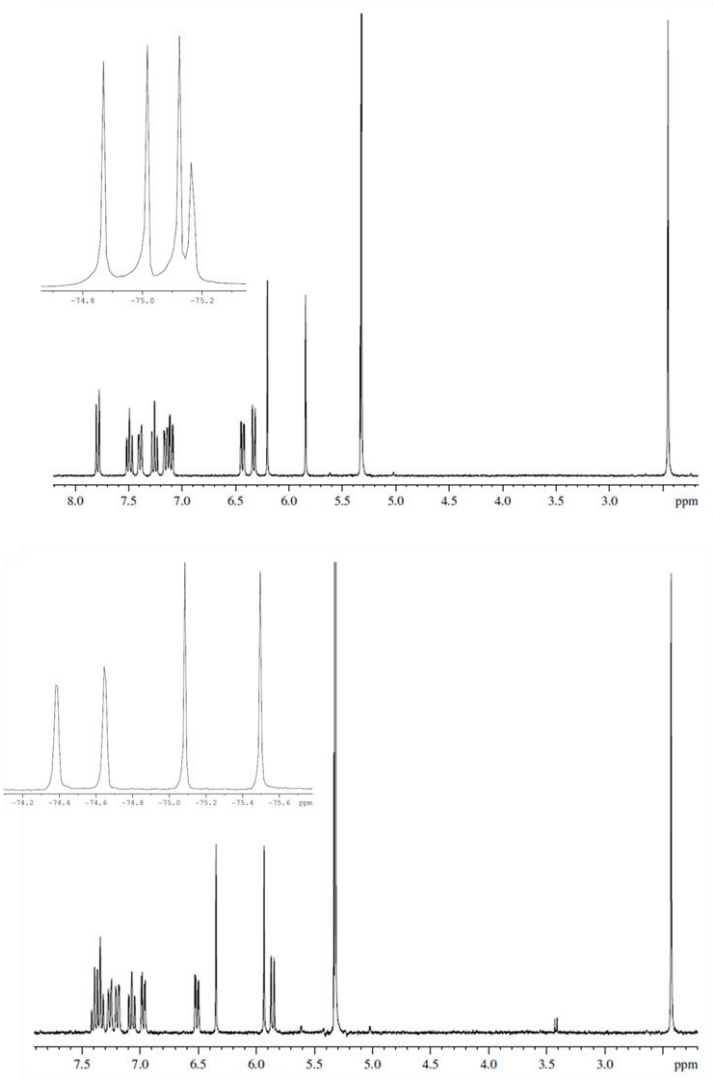

Figure 5.7: ^{1}H NMR data for attempted synthesis of **5.2b-trans**. Fraction one (top) with ^{19}F NMR (inset). ^{1}H NMR of fraction two (bottom) with ^{19}F NMR (inset). Samples run in CD_2Cl_2

Although the NMR spectra are useful for establishing the two products are similar and both exhibit a high degree of molecular symmetry, they do not confirm their identities. After mass spectrometry showed that both species possess the same mass, it seemed likely that the two compounds were structural isomers. Given the central carbon-carbon bond connecting the two halves of **5.1** is single bonding in nature; rotation about it could result in the formation of the *cis* isomer, **5.2-cis** as well as **5.2-trans**.

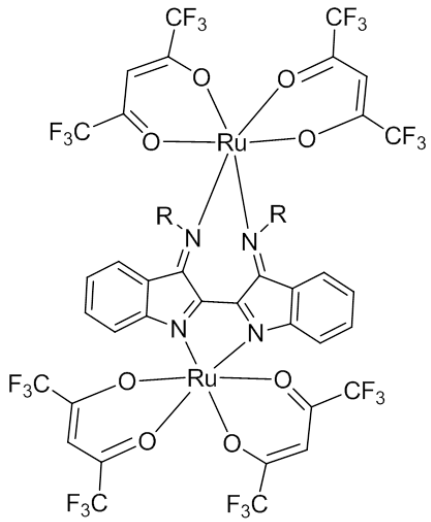

5.2b-cis R = pTol
5.2h-cis R = mes

The presence of the two isomers of **5.2b** was confirmed by X-ray crystallography. Surprisingly the minor product is that of the **5.2b-trans** (**Figure 5.8**). The product ratio was hoped to be encouraged to favour **5.2-trans** over **5.2-cis** by increasing the steric bulk of the dehydroNindigo employed. However, use of **5.1h** resulted in the same favouritism of c*is* over *trans*. Despite the possibility of both **5.2-trans** and **5.2-cis** existing as a pair of diastereomers (ΔΔ and ΔΛ), they are isolated as racemates of the ΛΛ and ΔΔ enantiomers of only one diastereomer. Bond parameters of the solid state structures of **5.2h-trans** and **5.2h-cis** were found to follow the observed trends for **5.2b-trans** and **5.2b-cis** and those of **5.2b-trans** and **5.2b-cis** are discussed below.

The two ruthenium atoms in **5.2b-trans** are present in a geometry that slightly deviates from octahedral with angles about Ru1 ranging from 88.9^{o} to 95.3^{o}. All equivalent bonds and angles on either side of the molecule are within 0.01Å and 0.1 degrees suggesting a pseudo-C_2 axis. Both benzannulated rings are bowed on the same side with respect to the central C4N4 core by 30.78^{o} and twisted about the long axis of the Nindigo core by 5.36^{o}. Upon complexation the central C21-C11 bond shortens considerably with respect to **5.1** (1.41 Å vs. 1.48 Å). This suggests an increase in the amount of double bond character. The C11-C12 and C12-N12 bonds increase in length upon chelation suggesting an increase in single bond character. The C11-N11 bond also lengthens from that of a double bond in **5.1**

(C1-N1 = 1.29Å) to a bond that exhibits more single bond character (1.33 Å). These bond deviations suggest that upon chelation the central core (C4N4) of **5.1** becomes more delocalized in nature with respect **5.1**. The degree of delocalization is however, not as high as that observed for derivatives of **1.33.** The bond parameters within the bridging ligand suggests that it maintains its fully oxidized form. Like all the other Nindigo type chelate compounds, the chelating (N)imine-Ru bond is longer than that of the chelating indole(N)-Ru bond (1.99 Å vs. 1.98 Å). The intramolecular separation of the chelating imine and indole nitrogen atoms is 2.80(3) Å. This is the same as the distance observed for free Nindigo. The N-aryl rings are twisted by 88.59^{o} and 83.78^{o} respectively from the dehydroNindigo core. The ruthenium atoms lie out of their NCCCN chelating planes by 0.78 Å and 0.81 Å and are separated by 6.06(4) Å (**Table 5.2**). This distance is comparable to the intramolecular separation of the two palladium atoms in **1.33b** (6.04 Å) and the intramolecular separation of the two ruthenium atoms in similar pyrazine bridged dimers.[151]

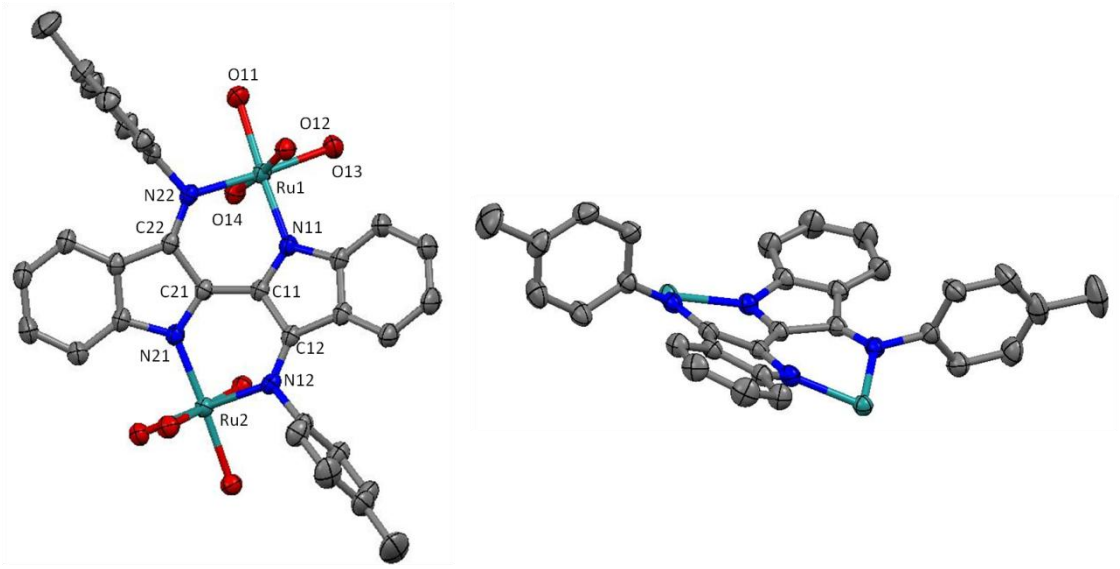

Figure 5.8: Single crystal X-ray structure of **5.2b-trans** (left) all hydrogen, fluorine and hfac carbon atoms removed for clarity. Alternate view of **5.2b-trans** (right) with all hydrogen and hfac atoms removed for clarity. Thermal ellipsoids set at the 50% probability level.

Atoms	Lengths (Å)	Atoms	Angles (deg)
C21-C11	1.409 (3)	N11-Ru1-N22	89.96 (8)
C21-C22	1.461 (3)	N11-Ru-O11	176.36 (8)
C11-C12	1.467 (3)	N11-Ru-O12	88.91 (8)
C21-N21	1.337 (3)	N11-Ru-O13	94.25 (8)
C11-N11	1.333(3)	N11-Ru-O14	95.32 (8)
C22-N22	1.304 (3)		
C12-N12	1.302 (3)		
N11-Ru1	1.981 (2)		
N22-Ru1	1.992 (2)		

Table 5.2: Selected bond lengths and angles for **5.2b-trans**

In **5.2b-cis** one ruthenium is chelated by the two indole nitrogen atoms with the other ruthenium chelated by the two imine nitrogen atoms (**Figure 5.9**). The ruthenium atom bound by the two indole nitrogen atoms (Ru1) lies within the NCCCN plane with angles around it ranging from 77.24^{o} to 99.61^{o}. Its counterpart (Ru2) lies out of the NCCCN plane by 0.98 Å with angles about it spanning a tighter range from 87.95^{o} to 98.62^{o}. The equivalent bond lengths of **5.2b-cis** and **5.2b-trans** are within 0.1 Å indicative of a similar degree of delocalization about the central C4N4 core. This again suggests that the fully oxidized nature of the bridging ligand is maintained upon chelation. The imine(N)-Ru2 bonds in **5.2b-cis** are slightly longer than the corresponding donor-acceptor bonds in **5.2b-cis** (2.01 Å vs 1.99 Å) as are the indole(N)-Ru1 bonds (1.99 Å vs. 1.98 Å). The chelating indole nitrogen atoms are separated by 2.49(3) Å with the chelating imine nitrogen atoms separated by 3.05(3) Å. These are shorter and longer respectively than the chelating nitrogen atom separation in **5.2b-trans** (2.81 Å). The two ruthenium atoms are separated by 6.10 Å with the N-aryl rings twisted by 78.6^{o} and 85.1^{o} respectively. Similar to **5.2b-trans**, the benzannulated rings bow out of the C4N4 plane by 30.06^{o}. They also deviate off the central axis(along the C11-C21 bond) of the Nindigo as one side contracts inwards to bind via the indole nitrogen atoms forcing the opposing cavity to expand (**Table 5.3**).

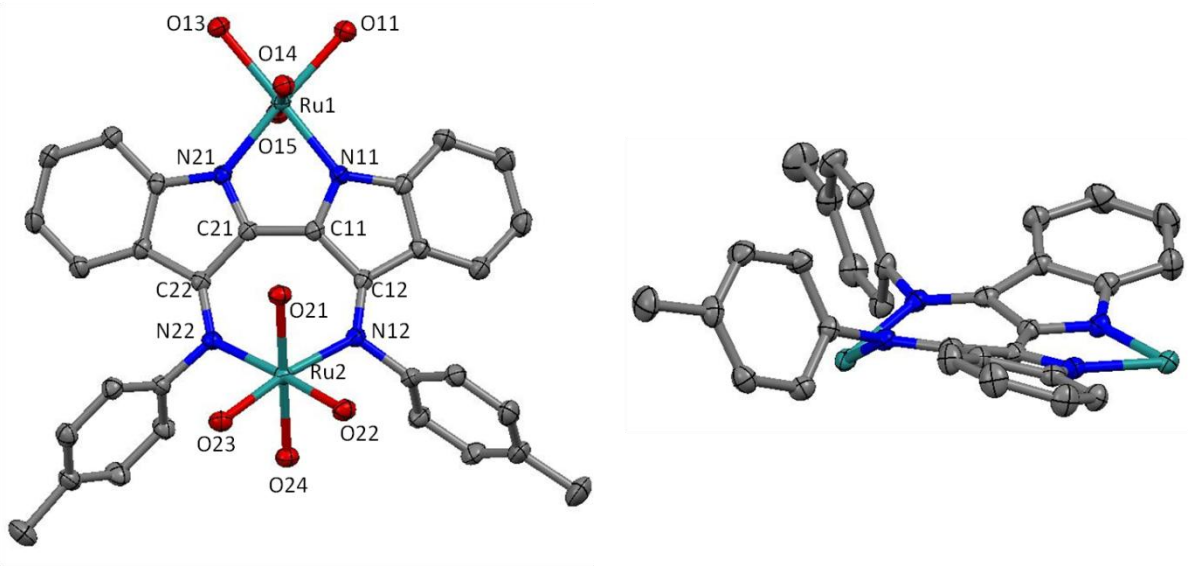

Figure 5.9: Single crystal X-ray structure of **5.2b-cis** (left) with all fluorine, hydrogen and hfac carbon removed for clarity. Alternative view of **5.2b-cis** (right) with all hydrogen and hfac atoms removed for clarity. Thermal ellipsoids set at the 50 % probability level

Atoms	Lengths (Å)	Atoms	Angles (deg)
C21-C11	1.415 (3)	N11-Ru1-N21	77.24 (7)
C21-C22	1.465 (3)	N11-Ru1-O11	99.61 (7)
C11-C12	1.464 (3)	N11-Ru1-O12	93.00 (7)
C11-N11	1.337 (3)	N11-Ru1-O13	178.51 (7)
C21-N21	1.334 (3)	N11-Ru1-O14	89.69 (7)
C12-N12	1.302 (3)	N12-Ru2-N22	98.62 (7)
C22-N22	1.313 (3)	N12-Ru2-O21	92.23 (7)
N11-Ru1	1.9805 (18)	N12-Ru2-O22	91.04 (7)
N21-Ru1	2.0030 (18)	N12-Ru2-O23	170.61 (7)
N12-Ru2	2.0154 (18)	N12-Ru-O24	87.95 (7)
N22-Ru2	2.0063 (18)		

Table 5.3: Selected bond lengths and angles for **5.2b-cis**

The electronic absorption spectra of the *trans* derivatives of **5.2** exhibit only minor differences from each other. Likewise, the spectra of the *cis* derivatives of **5.2** are quantitatively very similar. Data

for **5.2h-trans** and **5.2h-cis** will be discussed below. Both **5.2h-trans** and **5.2h-cis** display a number of similar transitions in the visible region with transitions between 420-680 nm being the most intense (ε > 10.0 x 10^3 M^{-1} cm^{-1}) (**Figure 5.10**). Given the ligand set in **5.2** maintains its fully oxidised form and as a result the extended cross conjugation observed for **1.33** is not possible, it is unlikely that the low energy absorptions (> 650 nm) are π-π* in nature and are more likely MLCT bands.

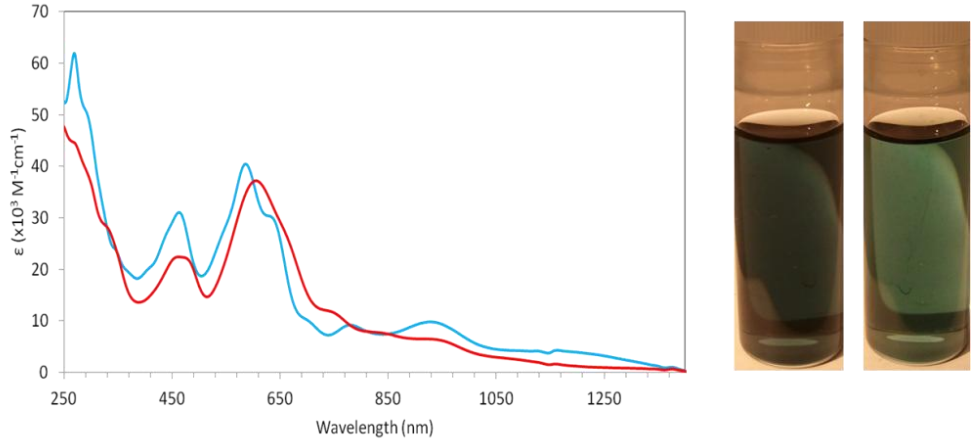

Figure 5.10: UV/vis/NIR spectra for **5.2h-trans** (blue) and **5.2h-cis** (red). Spectra obtained in DCM at a concentration of 1.25 x 10^{-5} M. Photograph of a solution of **5.2h-trans** (left) and **5.2h-cis** (right)

All derivatives of **5.2** are redox-active with the isomers of **5.2h** discussed below as representative examples. Both **5.2h-trans** and **5.2h-cis** display two reversible one-electron reduction events in their cyclic voltammogram spectra (**Figure 5.11**). The first reduction of **5.2h-trans** occurs at -0.81 V followed by a second reduction at -1.43 V. The corresponding reductions for **5.2h-cis** occur at similar potentials (-0.71 V and -1.36 V). Given the electron deficient nature of the ligand set, these reduction events are likely predominantly ligand centred. The first reduction corresponds to the formation of the radical anions, and the second reduction generates the dianions. Both complexes also exhibit one fully reversible one-electron oxidation (+0.66 V for **5.2h-trans** and +0.72 V for **5.2h-cis**) and a second oxidation event that occurs at the limit of the solvent window (+1.54 V for **5.2h-trans** and *ca.* +1.25 V for **5.2h-cis**). Given that dehydroNindigo is already fully oxidized, both oxidation events likely correspond to a pair of Ru(II/III) redox couples (**Table 5.4**). The first oxidation for each complex is

qualitatively similar differing by only 50 mV. The potentials of the second oxidation differ to a greater degree, approximately 300 mV.

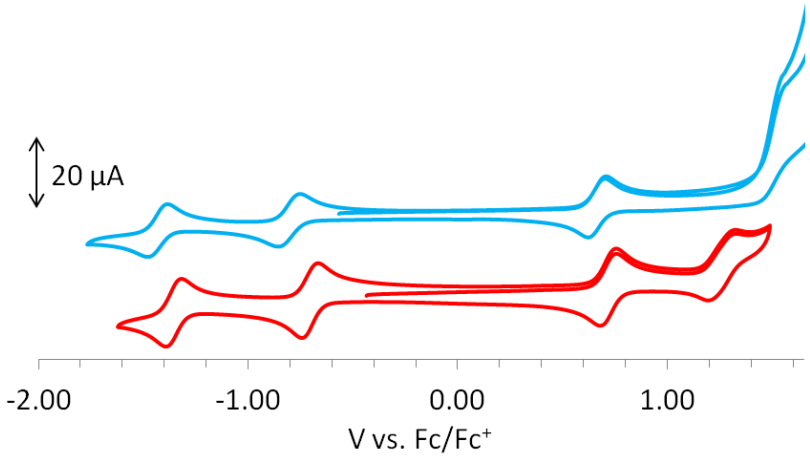

Figure 5.11: Cyclic voltammograms of **5.2h-trans** (top) and **5.2h-cis** (bottom). (DCM solution, 0.1 mM Bu_4NBF_4 electrolyte and scan rate = 100 mVs^{-1})

Isomer	Reduction (V)	Oxidation (V)
5.2h-trans	-1.43, -0.81	0.66, 1.54[a]
5.2h-cis	-1.36, -0.71	0.72, 1.25

Table 5.4: Electrochemical data for **5.2h-trans** and **5.2h-cis** ([a] estimated from anodic peak only)

The cationic complexes generated following the first oxidations of **5.2h-trans** and **5.2h-cis** contain two ruthenium atoms which, in a formal sense, exist in differing oxidation states (+2 and +3). This is known as mixed valency.[150-152] When two metals in a mixed valence compound are linked via a bridging ligand (as they are in **5.2**), they have the potential to interact (or communicate) with each other (**Figure 5.12**). This interaction can manifest itself electrochemically and spectroscopically.

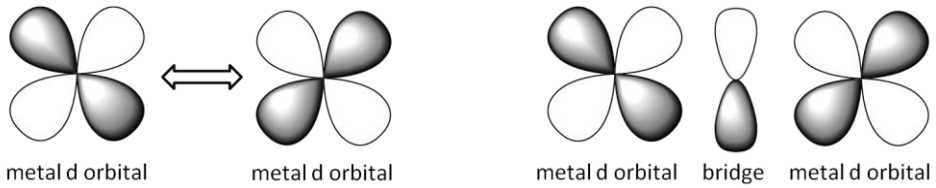

Figure 5.12: MO diagram showing no metal-metal communication (left) and metal-metal communication facilitated by a bridge (right)

The difference in potential between the two Ru (II/III) redox couples provides insight into the stability of the mixed valence compounds. The degree of stability can be quantified from an electrochemical parameter known as the comproportionation constant (K_c). This is calculated based on the equilibrium that exists between the mixed valence state and the two products of disproportionation (**Figure 5.13**).

$$K_c = \frac{[MV]^2}{[Red][Oxi]} = 10^{\Delta(E2-E1)/59mV} \quad \text{at 298 K}$$

$$Ru^n(\mu\text{-}L)Ru^n \underset{+e^-}{\overset{-e^-}{\rightleftharpoons}} Ru^n(\mu\text{-}L)Ru^{n+1} \underset{+e^-}{\overset{-e^-}{\rightleftharpoons}} Ru^{n+1}(\mu\text{-}L)Ru^{n+1}$$

Red (E_1) **MV** (E_2) **Oxi**

Figure 5.13: Equation showing comproportionation calculation (top) and schematic showing the redox processes involved (bottom)

The protypical mixed valence complex is a pyrazine bridged ruthenium dimer called the Creutz-Taube ion, **1.19**. This mixed valence species has been shown to exhibit a high degree of stability and has a ΔE of 390 mV corresponding to a K_c value of approximately 10^{7}.[153]

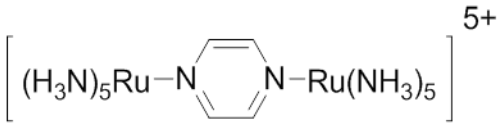

1.19

The difference between the two ruthenium redox couples in **5.2h-trans** is significantly larger than that observed for **5.2h-cis** (0.88 V and 0.54 V). This results in the comproportionation constant for **5.2h-trans** being 6 orders of magnitude larger than for **5.2h-cis** (*ca.* 10^{15} and 10^{9}). However, it should be noted that both comproportionation constants are indicative of highly stable mixed valence species.

The interaction between the two metal centres in mixed valence compounds is thought to occur through two different mechanisms that are dependent on the energy of the bridging ligands' molecular orbitals.[151] If the bridging ligands' LUMO is low lying and close in energy to the metal redox orbital then charge delocalization can occur via electron transfer. Alternatively, if the HOMO of the bridging ligand is similar in energy to that of the metal redox orbitals, charge delocalisation occurs via a hole transfer mechanism (**Figure 5.14**).

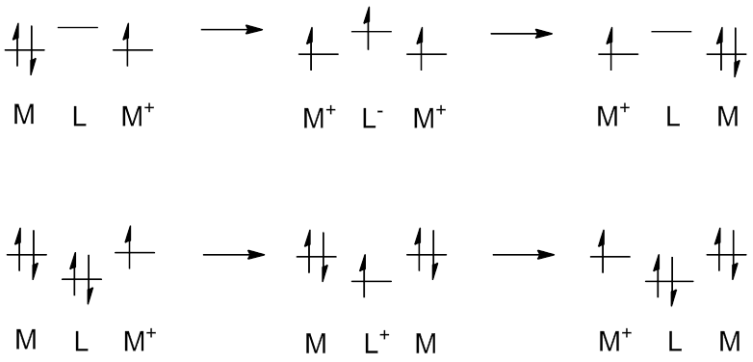

Figure 5.14: Electron transfer (top) and hole transfer (bottom) mechanism for valence exchange in a symmetrical dinuclear complex

Given that derivatives of the free ligand (**5.1**) are already fully oxidized, and therefore electron deficient, it seems likely that any communication between the two ruthenium atoms in the mixed valence state would be via an electron transfer process. The mild nature of the first ligand

centered reductions observed for derivatives of **5.2** is indicative of low lying LUMO's. Similar complexes where communication is thought to be via an electron transfer mechanism have ligand centered reduction potentials that are even lower than those observed for **5.2**.[154]

In order to probe the electronic structure of the mixed valence states, **5.2h-trans** and **5.2h-cis** were subjected to chemical oxidations. Reactions of **5.2h-trans** and **5.2h-cis** with nitrosium tetrafluoroborate yielded the corresponding mixed valence cations **[5.2h-trans]**$^{+}$ and **[5.2h-cis]**$^{+}$. The reversibility of the oxidations was tested by regenerating the neutral complexes by reacting the cations with ferrocene. One-electron chemical reductions were also conducted to probe the electronic nature of the anions. Reactions of **5.2h-trans** and **5.2h-cis** with cobaltocene yielded the anionic complexes **[5.2h-trans]**$^{-}$ and **[5.2h-cis]**$^{-}$. The reversibility of the reductions was probed by reacting the anionic complexes with ferrocenium tetrafluoroborate to regenerate the neutral complexes (**Scheme 5.5**). The chemical redox reactions were monitored by electronic absorption spectroscopy and all chemical reactions were found to exhibit good reversibility (appendix F).

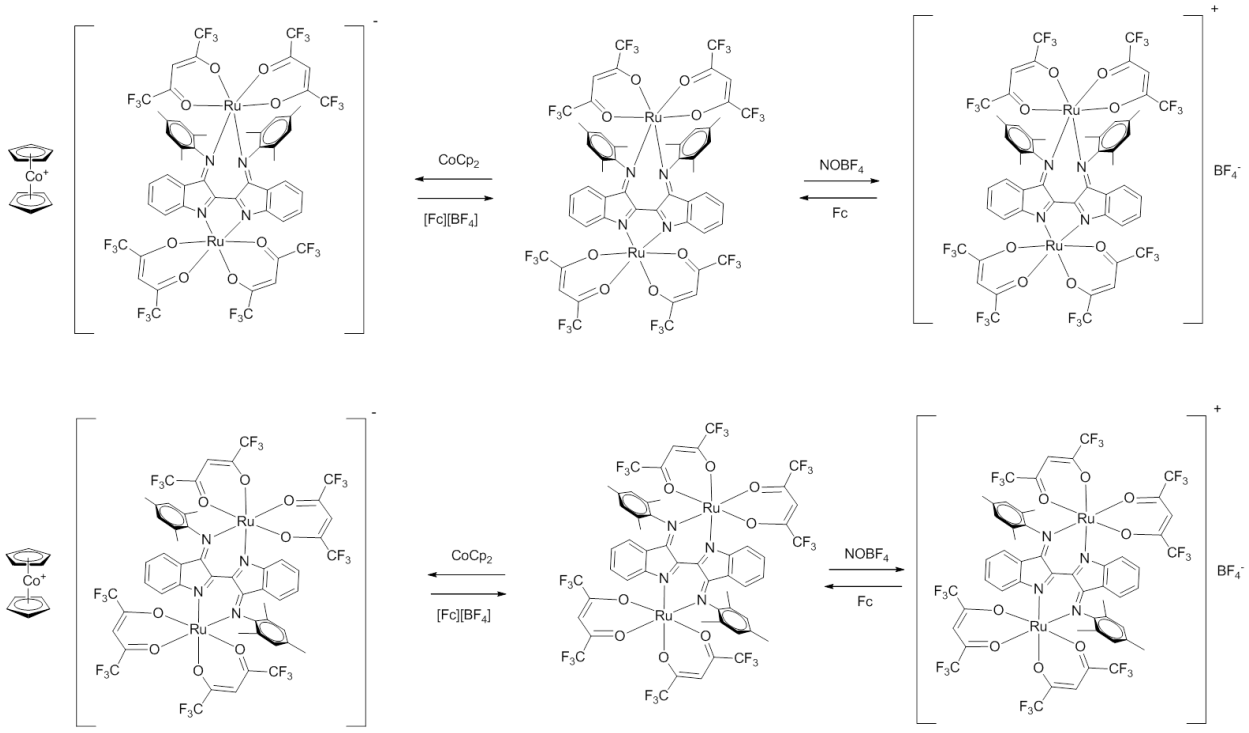

Scheme 5.5: Reversible chemical redox reactions of **5.2h-trans** (top) and **5.2h-cis** (bottom)

Upon oxidation of **5.2h-trans** to **[5.2h-trans]**$^{+}$ multiple new transitions are observed in the electronic absorption spectrum. Of note is the low intensity, low energy transition centered at 1388 nm that could be a new IVCT band, the latter of which being an indicator of metal-metal communication in mixed valence compounds.[153] In contrast to the array of new transitions observed for **[5.2h-trans]**$^{+}$**,** the spectrum observed for **[5.2h-cis]**$^{+}$ exhibits fewer new bands. There is a strong band that, similar to **[5.2h-trans]**$^{+}$, is blue shifted with respect to the neutral complex. There are however, no observable new low energy transitions (**Figure 5.15**).

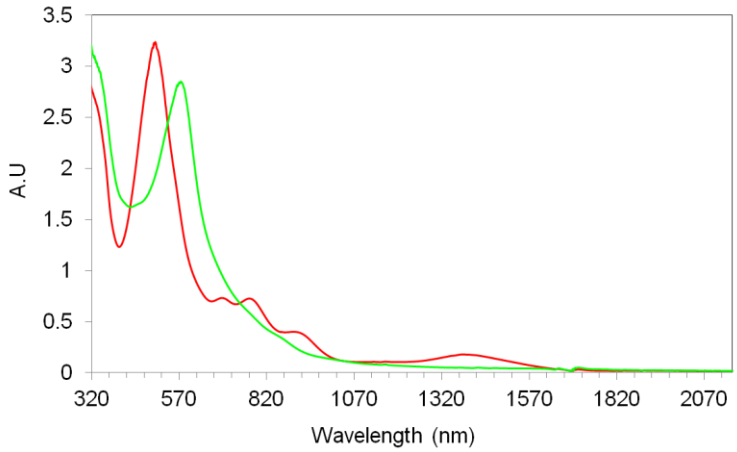

Figure 5.15: UV/vis/NIR spectra of **[5.2h-trans]**$^{+}$ (red) and **[5.2h-cis]**$^{+}$ (green)

The reduction of **5.2h-trans** to **[5.2h-trans]**$^{-}$ also results in a multitude of new transitions. There are at least three lower energy absorptions centered at *ca.* 2150 nm, 1450 nm and 1295 nm. The presence of new bands is likely a combination of a new π-π* transition as well as charge transfer processes. The reduction of **5.2h-cis** generates an electronic absorption spectrum that has a new lower energy transition at 1150 nm but does not show evidence of any broad, intense low energy transitions (> 1400 nm) that are observed for **[5.2h-trans]**$^{-}$ (**Figure 5.16**).

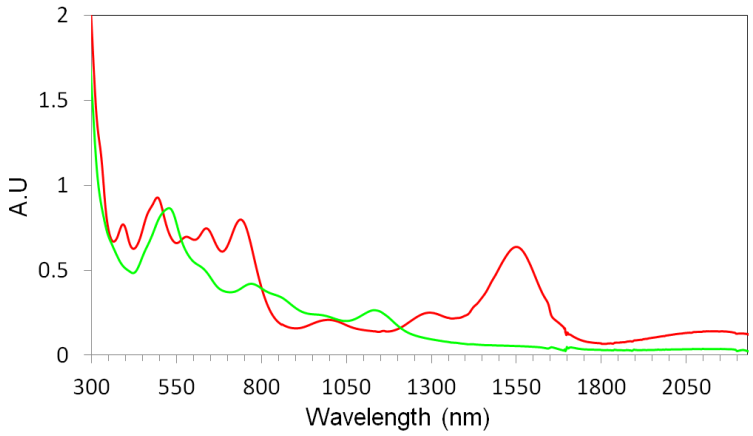

Figure 5.16: UV/vis/NIR spectra of **[5.2h-trans]**$^{-}$ (red) and **[5.2h-cis]**$^{-}$ (green)

5.3 Summary

Reactions of Nindigo with silver oxide yield the fully oxidized derivatives, dehydroNindigo (**5.1**). These new, neutral, bis-bidentate ligands exhibit greater solubility than their parent Nindigos and higher stability in comparison to that of the dehydroindigo analogue. Reactions of **5.1** with $Ru(hfac)_2(MeCN)_2$ generates two chemically similar and isolable compounds. These were found to be the dinuclear ruthenium dimers bridged by either *trans* (**5.2-trans**) or *cis* (**5.2-cis**) dehydroNindigo. The solid state structures of both compounds suggest the ligand maintains its fully oxidised form as bond parameters are comparable to that of the free ligand. Both **5.2-trans** and **5.2-cis** exhibit similar electronic absorption spectra that possess multiple bands in both the visible and NIR regions. Given the cross conjugation that gives rise to the low energy π-π* transitions observed for Nindigo derivatives is not present in DehydroNindigo, it is likely that these new transitions are CT in nature. Cyclic voltammetry experiments for both isomers reveals two reversible one-electron reductions that may be ligand centered in nature and two reversible one-electron oxidations that are likely metal centered. The difference in energy between the two Ru(II/III) redox couples for **5.2h-trans** is found to be larger than that of than for **5.2h-cis** (880 mV vs. 530 mV) and results in the former having a higher Kc value (*ca.* 10^{15} vs. 10^{9}) indicative of greater stability in the mixed valence state. The mixed valence cationic complexes of both ruthenium dimers were obtained following reactions with silver tetrafluoroborate. The electronic absorption spectrum of **[5.2h-trans]**$^{+}$ reveals a new low energy, low intensity transition (1388 nm) that may be a IVCT band which may suggests communication between the two ruthenium centres. The same band is

not observed in the absorption spectrum of **[5.2h-cis]$^{+}$**. The anionic complexes were also synthesized and *in situ* spectroscopic measurements reveal multiple new transitions for both derivatives. There are again differences between the two isomers, the most noticeable being the presence of a strong low energy band (1450 nm) and an additional broad band lower energy (2150 nm) for the trans derivative that are not observed for the cis derivative. These differences may suggest that the reduction processes of derivatives of **5.2** are not purely ligand centered in nature, and there may be differing amounts of ruthenium character in the FMO's of each isomeric complex.

5.4 Experimental

5.4.1 Methods and materials

General procedures are as outlined in Section 2.5.1 except for the following;

Reagents were purchased from Aldrich or gratefully received from Johnson Mathey and used as received. [Ru(hfac)$_3$][K] was synthesized according to the literature[155] and Ru(hfac)$_2$(MeCN)$_2$ was synthesized by literature procedures with slight alterations.[155,156]

DehydroPhenNindigo, 5.1a: 1.31a (200 mg, 0.243 mmol) was dissolved in dry DCM (*ca*. 80mL). Ag_2O (2 eq, 210 mg) was added and the reaction mixture was left to stir at room temperature for 24 hours. The solution was then filtered through celite before the solvent was removed in vacuo. The solid was taken up in a toluene (3 mL) hexane (6 mL) mixture and heated to reflux before being allowed to cool slowly resulting in isolation of red crystals (106 mg, 50 %). ^{1}H NMR (300 MHz, CD_2Cl_2, 293K): 6.7 (d, 2H, *J* = 7.2 Hz), 7.0 (dod, 4H, *J* = 7.9 Hz, 1.7 Hz), 7.3 (t, 2H, *J* = 8.0 Hz), 7.5 (m, 6H), 7.6 (d, 2H, *J* = 7.6 Hz). ^{13}C NMR (500 MHz, CD_2Cl_2, 293K): 118.2, 123.2, 126.0, 128.7, 129.8, 133.6, 150.8, 158.6, 163.4, 164.1 (full spectral analysis is hampered by the presence of the minor product. UV/vis/NIR (CH_2Cl_2), λ_{max} /nm (ε, $M^{-1}\,cm^{-1}$): 341 (9,580), 433 (7,810). HRMS, *m/z*: calcd for (M-Na)$^{+}$ $C_{28}H_{18}N_4$ 433.1421; found 433.1429.

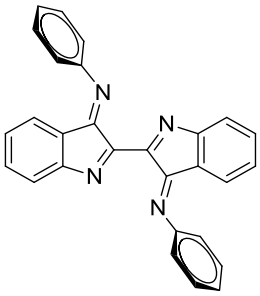

Minor product ^{1}H NMR (300 MHz, CD_2Cl_2, 293K): 6.6 (d), 7.6 (dodod), 7.8 (d). ^{13}C NMR (500 MHz, CD_2Cl_2, 293K): 119.2, 120.0, 120.6, 121.5, 122.6, 122.8, 122.9, 123.4, 125.6, 126.4, 126.5, 128.3, 129.3, 129.6, 133.5, 133.6, 149.7, 150.4, 156.8, 157.4, 158.7, 161.4, 166.8

DehydropTolNindigo, 5.1b: 1.31b (209 mg, 0.474 mmol) was dissolved in dry DCM (*ca*. 40mL). Ag_2O (2 eq, 220 mg) was added and the reaction mixture left to stir at room temperature for 24 hours. The solution was then filtered through celite before the solvent was removed to yield a red powder (155 mg, 75 %).^{1}H NMR (300 MHz, CD_2Cl_2, 293K): 2.4 (s, 6H), 6.9 (d, 2H, *J* = 7.6 Hz), 7.0 (d, 4H *J* = 7.9 Hz), 7.1 (dodod, 2H, *J* = 7.6 Hz, 7.5 Hz, 1.3 Hz), 7.3 (d, 4H, *J* = 7.9 Hz), 7.4 (dodod, 2H, *J* = 7.5 Hz, 7.3 Hz, 1.7 Hz), 7.6 (d, 2H, *J* = 7.7 Hz). ^{13}C NMR (500 MHz, CD_2Cl_2, 293K): 21.4, 118.7, 121.6, 123.3, 126.0, 128.8, 130.5, 133.6, 136.4, 148.2, 158.7, 163.6, 163.9. UV/vis/NIR (CH_2Cl_2), λ_{max} /nm (ε, M^{-1} cm^{-1}): 343 (9,510), 431 (7,680). HRMS, *m/z*: calcd for $(M-H)^+$ $C_{30}H_{22}N_4$ 439.1921; found 439.1923

Minor product ^{1}H NMR (300 MHz, CD_2Cl_2, 293K): 2.4 (s), 6.7 (t), 7.2 (d), 7.3 (m), 7.6 (dodod), 7.8 (d). ^{13}C NMR (500 MHz, CD_2Cl_2, 293K): 20.9, 21.7, 119.7, 120.9, 122.5, 122.7, 122.9, 125.4, 125.8, 128.1, 128.7, 129.1, 129.1, 129.5, 129.8, 130.1, 133.3, 133.4, 136.7, 137.2, 146.1, 147.0, 156.8, 157.5, 158.8, 161.4, 163.1, 167.1

DehydroDmpNindigo, 5.1c: 1.31c (100 mg, 0.227 mmol) was dissolved in dry DCM (*ca*. 40mL). Ag_2O (2 eq, 105 mg) was added and the reaction mixture left to stir at room temperature for 24 hours. The solution was then filtered through celite before the solvent was removed resulting in isolation of a red powder (53 mg, 50 %).^{1}H NMR (300 MHz, CD_2Cl_2, 293K): δ = 2.0 (s, 12H), 6.4 (d, 2H, *J* = 7.2 Hz), 7.1 (m, 8H), 7.5 (tod, 2H, *J* = 7.7 Hz, *J* = 1.1 Hz), 7.6 (d, 2H, *J* = 7.6 Hz). ^{13}C NMR (500 MHz, CD_2Cl_2, 293K): 17.9, 122.0, 122.8, 124.3, 124.9, 125.0, 128.6, 129.3, 133.7, 148.8, 157.9, 164.4, 165.1. UV/vis/NIR (CH_2Cl_2), λ_{max} /nm (ε, M^{-1} cm^{-1}): 333 (9,460), 425 (6,730). HRMS, *m/z*: calcd for $(M-H)^+$ $C_{32}H_{26}N_4$ 467.2236; found 467.2236

DehydroMesNindigo, 5.1h: 1.31h (120 mg, 0.242 mmol) was dissolved in dry DCM (*ca*. 80mL). Ag_2O (2 eq, 112 mg) was added and the reaction mixture left to stir at room temperature for 24 hours. The solution was then filtered through celite before the solvent was removed and resulting in isolation of a red powder (78 mg, 65 %).^{1}H NMR (300 MHz, CD_2Cl_2, 293K): 2.0 (s, 6H), 2.3 (s, 3H), 6.5 (d, 1H, *J* = 6.1 Hz), 6.9 (s, 2H), 7.07 (dodod, 1H, *J* = 7.6 Hz, 6.7 Hz, 0.9 Hz), 7.5 (dodod, 1H, 7.45 *J* = , 7.6 Hz, 8.3 Hz, 1.2 Hz), 7.6 (d, 1H, *J* = 7.6 Hz). ^{13}C NMR (500 MHz, CD_2Cl_2, 293K): 18.0, 21.1,

122.3, 122.9, 124.4, 125.2, 129.5, 133.8, 134.7, 146.7, 158.1, 164.7, 165.6. UV/vis/NIR (CH_2Cl_2), λ_{max} /nm (ε, M^{-1} cm^{-1}): 335 (9,220), 427 (6,650). HRMS, *m/z*: calcd for $(M\text{-}H)^+$ $C_{34}H_{30}N_4$ 495.25435; found 495.25223

Ruthenium-bis-hexafluoroacetylaceonoatebis-acetonitrile: $[Ru(hfac)_3]K$ (1.04 g, 1.37 mmol) was

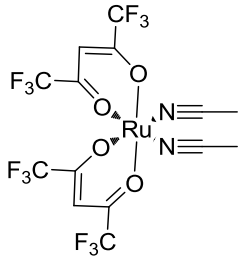

dissolved in MeCN (*ca.* 85 mL). To this was slowly added a solution of *p*-toluenesulfonic acid (5 eq, 6.85 mmol, 1.30 g) in MeCN (25 mL). Upon complete addition the reaction was left to reflux for one hour. The solvent was removed and the crude solid taken up in DCM and filtered before running through an alumina plug. The brown fraction was dried to give a dark powder (430 mg, 53 %). Characterization data matches that reported in the literature.[155,156]

DehydropTolNindigo[Ru(hfac)$_2$]$_2$ 5.2b-trans and **5.2b-cis**: **5.1b** (184 mg, 0.420 mmol) was dissolved in dry toluene (5 mL). This was transferred via cannula into a solution of $Ru(hfac)_2(MeCN)_2$ (2 eq, 0.840 mmol, 501 mg) in toluene (100 mL). The solution was left to stir at reflux for 18 hours before the solvent was removed. The dark residue was then passed through an alumina column (DCM 1 : 1 Hex). The green/blue fraction was collected and dried before being run through a silica column (DCM 1 : 10 Hex). Two fractions were collected (fraction 1 (**5.2b-trans**) = 62 mg, 10 %, fraction 2 (**5.3b-cis**) = 92 mg, 15 %). X-ray quality crystals of both compounds were grown by slow diffusion of acetonitrile into a saturated DCM solution.

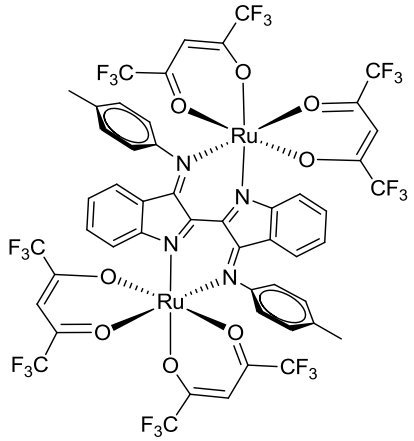

5.2b-trans: ^{1}H NMR (300 MHz, CD_2Cl_2, 293K): δ = 2.5 (s, 6H), 5.8 (s, 2H), 6.2 (s, 2H), 6.3 (d, 2H, *J* = 7.4 Hz), 6.4 (dod, 2H, *J* = 7.9 Hz, 2.2 Hz), 7.1 (dod, 2H, *J* = 8.1 Hz, 2.3 Hz), 7.1 (d, 2H, *J* = 8.2 Hz), 7.3 (t, 2H, *J* = 7.5 Hz), 7.4 (d, 2H, *J* = 8.2 Hz), 7.5 (t, 2H, *J* = 7.9 Hz), 7.8 (d, 2H, *J* = 8.2 Hz). ^{13}C NMR (500 MHz, CD_2Cl_2, 293K): δ = 21.5, 91.2, 91.3, 119.5, 119.7, 121.0, 123.2, 125.2, 139.3, 130.6, 131.3, 133.7, 139.3, 148.0, 152.0, 154.3, CF_3 and CO groups unresolved. $^{19}F\{^1H\}$ NMR (300 MHz, CD_2Cl_2, 293 K): δ = -74.9 (6F, s), -75.0 (6F, s), -75.1 (6F, s), -75.2 (6F, s). UV/vis/NIR (CH_2Cl_2), λ_{max} /nm (ε, $M^{-1}cm^{-1}$): 268 (52,800), 292 (46,000), 464 (27,600), 584, (35,100), 634 (25,700), 784 (8,110), 945 (8,540), 1190 (3,460). HRMS, *m/z*: calcd for $(M)^+$ $C_{50}H_{26}N_4O_8F_{24}Ru_2$ 1469.94544; found 1469.94856

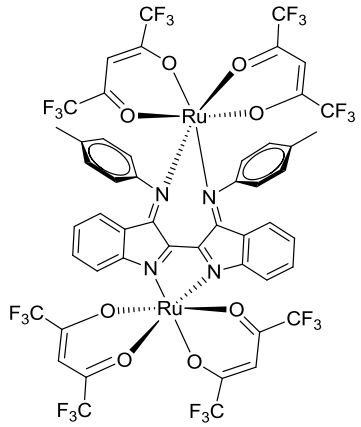

5.2b-cis: ^{1}H NMR (300 MHz, CD_2Cl_2, 293K): δ = 2.4 (s, 6H), 5.9 (d, 2H, *J* = 7.83 Hz), 5.9 (s, 2H), 6.4 (s, 2H), 6.5 (dod, 2H, *J* = 8.1 Hz, 2.4 Hz), 7.0 (dod, 2H, *J* = 8.1 Hz, 2.4 Hz), 7.1 (t, 2H, *J* = 7.6 Hz), 7.2 (d, 2H, *J* = 8.2 Hz), 7.3 (d, 2H, *J* = 8.2 Hz), 7.4 (m, 4H). ^{13}C NMR (500 MHz, CD_2Cl_2, 293K): δ = 21.0, 90.9, 91.9, 117.5, 121.1, 121.3, 121.5, 125.4, 129.3, 129.4, 129.8, 134.1, 138.8, 148.4, 158.0, 158.3, CF_3 and CO groups unresolved. ^{19}F{^{1}H} NMR (300 MHz, CD_2Cl_2, 293 K): δ = -74.4 (6F, s), -74.7 (6F, s), -75.1 (6F, s), -75.5 (6F, s,).UV/vis/NIR (CH_2Cl_2), λ_{max} /nm (ε, M^{-1} cm^{-1}): 279 (36,800), 336 (21,800), 457 (20,500), 477 (20,200), 637 (27,200), 736 (13,100), 884 (6,380). HRMS, *m/z*: calcd for $(M)^+$ $C_{50}H_{26}N_4O_8F_{24}Ru_2$ 1469.94544; found 1469.94816

DehydroMesNindigo[Ru(hfac)$_2$]$_2$ 5.2h-trans and **5.2h-cis: 5.1h** (700 mg, 1.42 mmol) was combined with $Ru(hfac)_2(MeCN)_2$ (2 eq, 2.83 mmol, 1.70 g) in toluene (100 mL). The solution was left to stir at reflux for 18 hours before the solvent was removed. The dark residue was then passed through an alumina column (DCM 1 : 1 Hex). The green/blue fraction was collected and dried before being run through a silica column (DCM 1 : 10 Hex). Two fractions were collected (fraction 1 (**5.2h-trans**) = 200 mg, 9 %, fraction 2 (**5.3h-cis**) = 500 mg, 23 %). X-ray quality crystals of both compounds were grown by slow diffusion of acetonitrile into a saturated DCM solution.

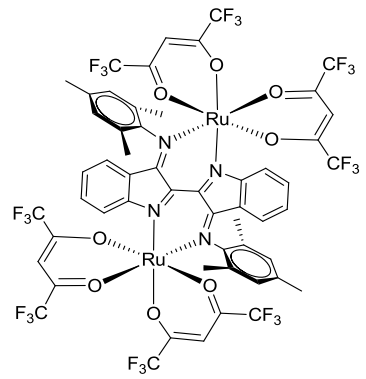

5.2h-trans: ^{1}H NMR (300 MHz, CD_2Cl_2, 293K): δ = 1.4 (s, 6H), 2.1 (s, 6H), 2.4 (s, 6H), 5.8 (s, 2H), 6.2 (s, 2H), 6.5 (d, 2H, *J* = 7.5 Hz), 6.8 (s, 2H), 7.1 (s, 2H), 7.3 (t, 2H, *J* = 7.9 Hz), 7.5 (t, 2H, *J* = 7.8 Hz), 7.8 (d, 2H, *J* = 8.2 Hz). ^{13}C NMR (500 MHz, CD_2Cl_2, 293K): δ =17.3, 17.4, 21.2, 90.8, 91.3, 116.0 (q, CF_3, *J* = 286.4 Hz), 116.6 (q, CF_3, *J* = 283.6 Hz), 117.4 (q, CF_3, *J* = 287.8 Hz), 119.5, 121.0, 124.1, 127.5, 129.8, 130.7, 130.3, 131.0, 133.9, 139.1, 145.9, 151.8, 154.5, 172.4, 173.5 (q, CO, *J* = 37.4 Hz), 173.6 (q, CO, *J* = 37.4 Hz), 177.6 (q, CO, *J* = 36.0 Hz) Complete carbon analysis is hampered by poor resolution. ^{19}F{^{1}H} NMR (300 MHz, CD_2Cl_2, 293 K): δ = -74.8 (6F, s), -74.9 (6F, s), -75.1 (6F, s), -75.2 (6F, s). UV/vis/NIR (CH_2Cl_2), λ_{max} /nm (ε, M^{-1} cm^{-1}): 269 (38,800), 298 (30,100), 412 (12,900), 586 (25,300), 632 (19,000), 776 (5,760), 929 (7,170). HRMS, *m/z*: calcd for $(M)^+$ $C_{54}H_{34}N_4O_8F_{24}Ru_2$ 1526.00802; found 1526.00802

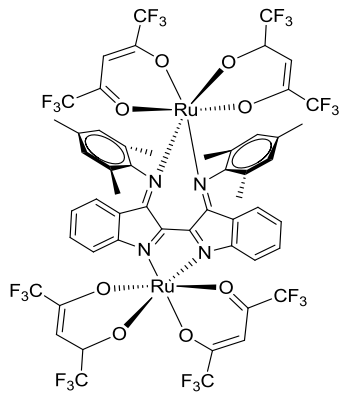

5.2h-cis: ^{1}H NMR (300 MHz, CD_2Cl_2, 293K): δ = 1.7 (s, 6H), 2.1 (s, 3H), 2.1 (s, 3H), 2.3 (s, 6H), 5.8 (d, 2H, *J* = 7.9 Hz), 5.9 (d, 2H, *J* = 2.8 Hz), 6.4 (d, 2H, 6.7 Hz), 6.9 (s, 2H), 7.0 (s, 2H), 7.1 (t, 2H, *J* = 7.8 Hz), 7.3 (d, 1H, *J* = 4.0 Hz), 7.3 (d, 1H, *J* = 3.7 Hz), 7.4 (t, 2H, *J* = 7.8 Hz). ^{13}C NMR (500 MHz, CD_2Cl_2, 293K): δ = 18.6, 21.1, 91.7, 92.4, 118.0, 121.5, 125.0, 125.9, 127.3, 127.4, 129.4, 129.5, 129.9, 130.6, 134.6, 139.0, 148.3, 154.3, 157.6, 175.0, complete carbon analysis is hampered by poor spectrum resolution. ^{19}F{^{1}H} NMR (300 MHz, CD_2Cl_2, 293 K): δ = -74.4 (6F, s), -74.8 (6F, s), -74.9 (3F, s), -75.0 (3F, s), -75.5 (6F, s). UV/vis/NIR (CH_2Cl_2), λ_{max} /nm (ε, $M^{-1}\,cm^{-1}$):272 (44,300), 336 (27,100), 464 (22,400), 618 (36,200), 762 (10,700), 918 (6,510). HRMS, *m/z*: calcd for $(M)^+$ $C_{54}H_{34}N_4O_8F_{24}Ru_2$ 1526.00802; found 1526.00802

Typical redox experiments:

Reductions: In a glovebox **5.2h-trans** or **5.2h-cis** (81 mg, 0.053 mmol) was dissolved in dry DCM (10 mL) generating a blue/green solution. Cobaltocene (10 mg, 0.053 mmol) was added and the reaction left to stir for 20 minutes during which time the reaction mixture took on a blue **[5.2h]**$^-$ or pink **[5.3h]**$^-$ colour. Ferrocenium tetrafluoroborate (14 mg, 0.053 mmol) was added and the reaction was left for 20 minutes resulting in a return to the original solution colours.

Oxidations: In a glovebox **5.2h-trans** or **5.2h-cis** (81 mg, 0.053 mmol) was dissolved in dry DCM (10 mL) generating a blue/green solution. $NOBF_4$ (6.2 mg, 0.053 mmol) was added and the reaction left to stir for 20 minutes during which time the reaction took on a purple colour for both derivatives. Ferrocene (9.8 mg, 0.053 mmol) was added and the reaction left to stir for 20 minutes resulting in a return to the original solution colours.

Chapter 6: Summary and Future Directions

The symbiotic nature of coordination compounds has rendered ligand design as one of the more important areas for chemistry development. Traditionally, ligand architectures have been utilized to gain better control of the resulting complexes through steric and/or electronic tuning. However, the emergence of redox-active ligand families, both bridging and capping, has enabled a wealth of new chemistry to be realized. One of the main driving forces behind redox-active ligand design is the potential for their use in catalysis. With the rising cost and diminished availability of the precious metals required for traditional catalysts, it would seem desirable to incorporate RALs with earth abundant metals to achieve the same catalytic processes for a fraction of the cost. In addition, coordination compounds of RALs have been shown to undergo a variety of novel chemistry that can be either metal or ligand centered and can result in new molecular structures.[1] The use of bridging redox-active ligands that are able to bring multiple metals together could be used to probe the chemistry of enzymes where multiple metal centres are connected together and work in cooperation to achieve specific chemistry. To date there are very few readily tunable bridging ligand families and only one that is redox-active (see chapter 1).[45,46] As well as redox-activity, another useful ligand attribute that is currently sought is low energy, high intensity absorption and/or emission. Applications of NIR chromophores are diverse with light harvesting, sensing and medicinal applications being just a handful of examples. Current NIR chromophoric compounds can be limited by complex syntheses, difficulties with tuning the spectral properties and stability issues (see chapter 3).

The work presented in this thesis introduces a new family of redox-active bridging ligand, Nindigo, which can be easily synthesized and tuned. In addition to redox-activity, Nindigo exhibits intense, low energy absorptions. The previously reported conversion of the carbonyl moieties on indigo to imines resulted in a modest library of Nindigo derivatives (see chapter 2).[85] This synthesis has since been improved and the library expanded and diversified.[86] The N-Aryl substituents not only render Nindigo more soluble than indigo, but introduces a point for derivitization and therefore a handle to control the resulting attributes. Similar to indigo, Nindigos exhibit a variety of irreversible redox events, established by electrochemical measurements. The donor acceptor motif about the central core of Nindigo is reminiscent of the H-chromophore of indigo,[53-58] albeit with imines in place of carbonyls. This results in Nindigos displaying low energy (λ_{max} 584 nm - 604 nm), high intensity nm (ε = 10.0 - 35.0 x 10^3 M^{-1} cm^{-1}) visible absorption bands.

Although the free ligand has been well studied, there are two phenomena that require further investigation. Firstly there are two transitions observed in the electronic absorption spectra for all derivatives that occur at slightly lower energy and with less intensity than the main absorption band. The current hypothesis is that intramolecular proton transfer could generate both a resonance stabilized cation (**6.1**) and anion (**6.2**) that may have similar chromophores both to each other and the parent Nindigo. This should be investigated by conducting UV/vis/NIR spectroscopy monitored acid/base reactions.

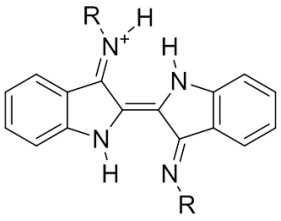

6.1

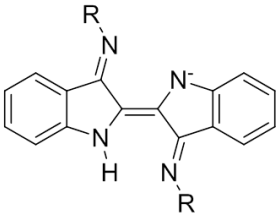

6.2

A second area for further investigation is the presence of the non-centrosymmetric tautomers that are sometimes synthesized. Whilst there is some literature precedence for tautomerisation in indigo-diimines, the large barrier for the process is not well understood and further work should be undertaken to probe the nature of this process.

Palladium chelates of Nindigo (**1.33**) enabled the reversible redox-activity of the Nindigo ligand family to be established.[84-85] Moreover, chelation of palladium was found to significantly shift the ligand centered π-π* transition to lower energy by approximately 320 nm into the NIR region ($\lambda_{max} \approx 910$ nm). When *ortho* N-aryl substituted Nindigos are involved, the expected binuclear complexes are generally not observed. Instead, the resulting complexes are mono-nuclear involving Nindigo that has isomerized from a *trans* to a *cis* geometry, **2.2**. The palladium is bound by the two deprotonated indolide type nitrogen atoms with a hydrogen atom shared between the two imines. Like the binuclear complexes, derivatives of **2.2** exhibit strong, low energy absorption bands ($\lambda_{max} \approx 830$ nm, $\varepsilon \approx 20.0 \times 10^3$ M^{-1} cm^{-1}) that are independent on the N-aryl substituents and ligand centered. The bathochromic shift is not as large as those observed for derivatives of **1.33**. The geometry and mono-chelation of **2.2** also has an effect on the electrochemical attributes of **2.2**. Like the bis-Pd(hfac) chelates, there are two reversible one-electron oxidation processes that, for derivatives of **2.2**, occur at slightly higher potentials. Unlike their binuclear counterparts the reduction processes are split into two one-electron reduction processes, the first of which is reversible.

Main group coordination compounds of Nindigo were investigated by synthesizing both mono- and bis-BF_2 Nindigo chelates (**3.3** and **3.5**).[129] Electronic spectra of both **3.3** and **3.5** display long wavelength transitions (λ_{max} ≈ 650 nm and 750 nm) of equal intensity (ε ≈ 30.0 x 10^3 M^{-1} cm^{-1}). Both **3.3** and **3.5** show weak fluorescence with derivatives of **3.5** emitting in the NIR region. The Stokes shifts range from 557 cm^{-1} - 2180 cm^{-1} which is comparable to similar BODIPY type systems.[112-128,131,140] Whilst derivatives of **3.3** exhibit predominantly irreversible redox events, derivatives of **3.5** exhibit fully reversible electrochemical behaviour. Two reversible one-electron reductions and one reversible one-electron oxidation are observed within the solvent window. The potential of these redox events seem to be influenced by both the steric and electronic nature of the N-aryl substituents. Hindered rotation and electron withdrawing groups are thought to affect the degree of delocalization of electron density onto the N-aryl rings altering the energy levels of the FMOs. Although derivatives of **3.5** can be isolated by manipulation of the reaction conditions, they exhibit sensitivity in solution and decompose over time to the corresponding derivatives of **3.3**. The decomposition can be monitored by both electronic and NMR spectroscopy where it was shown that the bulkier derivatives exhibit a greater sensitivity. Further work could be undertaken to manipulate Nindigo in an attempt to stabilize the bis-BF_2 derivatives and enable more in depth emission studies. Perhaps the incorporation of pendant side arms that contain donor atoms (X) may prevent or slow the decomposition of the bis-BF_2 species (**6.3**).

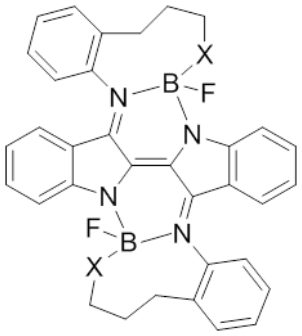

6.3

In addition to stabilizing the molecules, if there is to be any potential for their use in medical applications they need to be made soluble in aqueous media. One way of achieving this may be to incorporate sulfonate groups on the N-aryl rings or perhaps employ indigo carmine (**1.30**) as the starting material rather than indigo. The presence of sulfonate groups on the benzannulated rings renders this derivative water soluble.

Heteronuclear palladium - boron Nindigo chelates were synthesized (**3.6**) and both the spectral and electrochemical attributes of these derivatives neatly fit between those of the two homologues (**1.32** and **3.5**). The HOMO-LUMO gap of the ligand centered π-π* transition is shown, both spectrochemically and electrochemically, to decrease with increasing palladium presence. This trend is further supported by computational analysis.

The new redox-active capping ligands (**3.3**) were further investigated by synthesizing homoleptic zinc and copper complexes. X-ray crystallography of all complexes found the bonding, in particular the bond parameter of the ligand sets, to be quantitatively equivalent. Just like for all other bis-chelates of Nindigo the ligand centered π-π* transition of **4.1**, is red shifted with respect to the free ligand. The intensity of the transition is twice as strong as the free ligand, likely because there are now two ligand chromophores per one molecule. Cyclic voltammetry experiments of **4.1** reveal multiple reversible ligand centered redox processes. These consist of two apparent pairs of reversible one-electron reductions and three oxidation processes, the last of which is irreversible. The data suggests that **4.1** is composed of a formal zinc(II) metal centre surrounded by two equivalent monoanionic ligand sets. This complex therefore provides a model compound for comparing complexes that consist of electroactive metal centres where oxidation states may be less well defined. Examples of this are the copper complexes, **4.2a** and **4.2c**. The electronic absorption spectra of these complexes exhibit multiple visible transitions that are not present for **4.1**. In addition, these complexes also exhibit two much lower energy transitions that extend far into the NIR region. The spectral bands for these complexes likely consist of π-π*and a variety charge transfer bands (suggested computationally to be MLCT and LLCT in nature). Derivatives of **4.2** also exhibit different electrochemical behaviour compared to **4.1**. Three oxidation and three reduction processes are observed, the first of each occurring at mild potentials (*ca.* +0.19 V and -0.75 V). The spectroscopic and electrochemical parameters suggest that the bonding in derivatives of **4.2** is significantly different from the localized zinc analogue. Solid state EPR spectroscopy found **4.2a** to possess a g value of 2.08, indicative of a metal based radical and thus a copper(II) centre. However, this is contradicted by both XPS analysis that suggests the copper to be +1, and by computationally analysis that describes a system where the unpaired electron is evenly distributed over the entire complex. This somewhat contradictory characterisation data implies that these systems are non-innocent in nature. The oxidized and reduced complexes (**[4.2c]**$^{+}$ and **[4.2c]**$^{-}$) were synthesized and although these provided useful spectroscopic information regarding the oxidation states of the copper and surrounding ligand sets, further investigation is required to truly understand the copper systems. Additional experiments should also be undertaken not only to further probe the potential for valence tautomerism in both the

neutral and charged complexes of **4.2** but it would also be interesting to investigate the potential chemistry of transition metal complexes of the mono-BF_2 ligand in catalytic and stoichiometric reactions.

Another new ligand family derived from Nindigo is the fully oxidized analogue, dehydroNindigo (**5.1**). The chemistry of these neutral, bis-bidentate ligands was probed by synthesizing ligand bridged ruthenium dimers that are isolated as both *cis* and *trans* isomers. The dehydroNindigo in these species is thought to maintain its fully oxidized nature owning to bond parameters that are comparable to that of the free ligand. Both **5.2-trans** and **5.2-cis** exhibit qualitatively similar electronic absorption spectra that possess multiple low energy bands. Given that the extended conjugation within the Nindigo core is not present in dehydroNindigo, these transitions are likely CT in nature. Cyclic voltammetry experiments reveal two reversible one-electron reductions and two reversible one-electron oxidation processes. The electron deficient nature of the bridging ligand likely means the reduction processes are predominantly ligand centered with oxidation events being metal based. Both isomers are highly stable in their mixed valence state with comproportionation constants in the order of 10^{15} (for the trans isomers) and 10^{9} (for the cis derivatives). These values are higher than other similar mixed valence species where the metals are separated by *ca.* 6.1 Å across a conjugated bridge.[150-152] Both the one-electron oxidized and one-electron reduced cations and anions of each isomer were obtained. *In situ* electronic spectroscopy experiments highlighted some significant differences between the two isomers that might suggest differing degrees of ruthenium participation in the redox orbitals. Further spectroscopic, computation and EPR experiments should be run to further probe this. In addition, the potential for communication in the MV cations could be probed in order to classify the systems by the Robin-Day classification system.[157,158]

Finally, given that isolation of indigo-monoimines has been shown to be possible, perhaps the generation of mixed N-Aryl Nindigo (heteroNindigo) and coordination compounds thereof (**6.3**) could be achieved. This could potentially allow for tuning both sides of the ligand giving rise to novel controllable complexes.

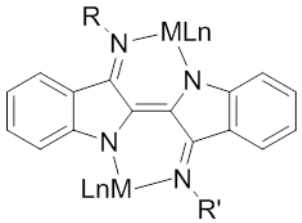

6.4

Although this work represents significant development in the multifunctional chemistry of Nindigo, this diverse ligand family is still very much in its infancy and there is broad scope for further studies and advancement. It is possible to envisage numerous potential applications for Nindigo and the related systems. This leaves the future looking ‘bright’ for this new multifunctional ligand family.

References

(1) L. Bourget-Merle, M. F. L.appert, J. R. Severn, *Chem. Rev.* **2002**, 102, 3031.

(2) S. G. McGeaghin, *Can. J. Chem.,* **1968**, 46, 1903.

(3) P. W. Roesky, *Chem. Soc. Rev.,* **2000**, 29, 335.

(4) Q. Knijnenburg, S. Gambarotta., P. H. M. Budzelaar, *Dalton Trans.,* **2006**, 5442.

(5) G. J. P. Britovsek, M. Bruce, V. C. Gibson, B. S. Kimberley, P. J. Maddox, S. Mastroianni, S. J. McTavish, C. Redshaw, G. A. Solan, S. Strömberg, A. J. P. White, D. J. Williams, *J. Am. Chem. Soc.,* **1999**, 121, 8728.

(6) S. D. Ittel, L. K. Johnson. *Chem. Rev.,* **2000**, 100, 1169.

(7) N. J. Hill, I. Vargas-Baca, A.H. Cowley, *Dalton Trans.,* **2009**, 240.

(8) F. T. Edelmann, *Coord. Chem. Rev.,* **1994**, 137, 403.

(9) M. P. Coles, *Dalton Trans.,* **2006**, 985.

(10) M. Jansen, U. Wedig, *Angew. Chem., Int. Ed.,* **2008**, 47, 10026.

(11) W. Kaim, B. Schwederski, *Coord.Chem. Rev.,* **2010**, 254, 1580.

(12) C. K. Jørgensen, *Coord. Chem. Rev.,* **1966**, 1, 164.

(13) M. D. Ward, J. A. McCleverty, *Chem. Soc., Dalton Trans.,* **2002**, 275.

(14) E. I. Steifel, J. H. Waters, E. Billig, H. B. Gray, *J. Am. Chem. Soc.,* **1965**, 87, 3016.

(15) A. L. Balch, R. H. Holm, *J. Am. Chem. Soc.,* **1966**, 88, 5201.

(16) P. J. Chirik, K. Wieghardt, *Science,* **2010**, 327, 794.

(17) P. Chaudhuri, C. N. Verani, E. Bill, E. Bothe, T. Weyhermuller, K. Wieghardt, *J. Am. Chem. Soc.*, **2001**, 123, 2213.

(18) C. G. Pierpont, *Coord.Chem. Rev.,* **2001**, 216-217, 99.

(19) H. Masui, A. B. P. Lever., P. R. Auburn, *Inorg. Chem,.* **1991**, 30, 2402.

(20) H. Chun, C. N. Verani., P. Chaudhuri, E. Bothe, E. Bill, T. Weyhermueller, K. Wieghardt, *Inorg. Chem.,* **2001**, 40, 4157.

(21) W. Kaim, B. Schwederski. *Pure Appl. Chem.,* **2004**, 76, 351.

(22) F. Thomas, *Eur. J. Inorg. Chem.,* **2007**, 2379.

(23) C. Mukherjee, U. Pieper, E. Bothe, V. Bachler, E. Bill, T. Weyhermueller, P. Chaudhuri, *Inorg. Chem.,* **2008**, 47, 8943.

(24) P. Chaudhuri, M. Hess, J. Mueller, K. Hildenbrandt, E. Bill, T. Weyhermueller, K. Wieghardt, *J. Am. Chem. Soc.,* **1999**, 121, 9599.

(25) R. A. Zarkesh, J. W. Zillwer., A. F. Heyduk, *Angew. Chem., Int. Ed.,* **2008**, 47, 4715.

(26) K. J. Blackmore, N. Lal, J. W. Ziller, A. F. Heyduk, *J. Am. Chem. Soc.,* **2008**, 130, 2728.

(27) A. M. Tondreau, E. Lobkovsky, P. J. Chirik, *Org. Let.,* **2008**, 10, 2789.

(28) A. L. Smith, L. A. Clapp, K. Hardcastle, J. D. Soper, *Polyhderon,* **2010**, 29, 164.

(29) J. L. Boyer, T. R. Cundari, N. J. DeYonker, T. B. Rauchfuss, S. R. Wilson, *Inorg. Chem.* **2009**, 48, 638.

(30) J. T. Muckerman, D. E. Polyansky, T. Wada, K. Tanaka, E. Fujita, *Inorg. Chem.,* **2008**, 47, 1787.

(31) T. Hino, T. Wada, T. Fujihara, K. Tanaka, *Chem. Lett.,* **2004**, 33, 1596.

(32) M. R. Haneline, A. F. Heyduk, *J. Am. Chem. Soc.,* **2006**, 128, 8410.

(33) M. W. Bouwkamp, A. C. Bowman, E. Lobkovsky, P. J. Chirik, *J. Am. Chem. Soc.,* **2006**, 128, 13340.

(34) S. Kitagawa, S. Kawata. *Coord. Chem. Rev.,* **2002**, *224*, 11.

(35) J-P. Taquet, O. Siri, P. Braunstein *Inorg. Chem.,* **2006**, *45*, 4668.

(36) S. Kar, B. Sakar., S. Ghumaan, D. Janardanan, J. van Slageren, J. Fiedler, V. G. Puranik, R. B. Sunoj, W. Kaim, G. K. Lahiri, *Chem. Eur. J.,* **2005**, 11, 4901.

(37) S. Ernst, P. Haenel, J. Jordanov., W. Kaim, V. Kasack, E. Roth, *J. Am. Chem. Soc.,* **1989**, 111, 1733.

(38) S. L. Caldwell, J. B. Gilroy, R. Jain, E. Crawford, B. O. Patrick, R. G. Hicks, *Can. J. Chem.,* **2008**, 86, 976.

(39) R. Dinnebier, H-W. Lerner, L. Ding, K. Shankland, W. I. F. David, R. W. Stephens, M. Wagner, *Z. Anorg. Allg. Chem.,* **2002**, 628, 310.

(40) N. Motokawa, H. Miyasaka, M. Yamashita, K. R. Dunbar, *Angew. Chem., Int. Ed.,* **2008**, 47, 7760.

(41) N. Lopez, H. Zhao, A. Ota, A. V. Prosvirin, E. W. Reinheimer, K. R. Dunbar, *Adv. Mater,.* **2010**, 22, 986.

(42) S. Huenig, E. Herberth, *Chem. Rev.,* **2004**, 104, 5535.

(43) W. Kaim, *Coord.Chem. Rev.,* **2002**, 230, 127.

(44) W. Kaim, *Coord. Chem. Rev.,* **2001**, 219-221, 463.

(45) K. V. Vasudevan, M. Findlater, A. H. Cowley, *Chem. Commun.,* **2008**, 1918.

(46) K. V. Vasudevan, I. Vargas-Baca., A. H. Cowley, *Angew. Chem. Int. Ed.,* **2009**, 48, 8369.

(47) E. S. B. Ferriera, A. N. Hulme, H. McNab, A. Quye, *Chem. Soc. Rev.,* **2004**, 33, 329.

(48) R. J. H. Clark, M. A. M. Daniels, R. Withnall *Endeavour,* **1993**, 17, 191.

(49) A. Baeyer, V. Dreswon, *Berichte der Deutschen Chemischen Gesellschaft,* **1882**, 2, 2856.

(50) L. Serrano-Andrés, B. O. Roos, *Chem. Eur. J.,* **1997**, 3, 717.

(51) M. I. G. M. Travasso, P. C. S. Santos, A. M. F Oliviera-Campos, M. M. M. Raposo, N. Prastipan, *Advances in colour science and technology,* **2003**, 6, 95.

(52) E. Steingruber, *Ullmann's Encyclopedia of Industrial Chemistry,* **2012**, 55.

(53) M. Klessinger, W. Luettke, *Tetrahedron,* **1963**, 19, 315.

(54) M. Klessinger, *Tetrahedron,* **1966**, 22, 3355.

(55) W. Luettke, M. Klessinger, *Chem. Ber.,* **1964**, 97, 2342.

(56) E. Wille, W. Luettke, *Liebigs Ann. Chem.,* **1980**, 2039.

(57) H. Bauer, K. Kowski, H. Kuhn, W. Luettke, P. Rademacher, *J. Mol. Struct.,* **1998**, 445, 277.

(58) E. Wille, W. Luettk, *Angew. Chem., Int. Ed.,* **1971**, 10, 803.

(59) R. M.Christie, *Biotechnic & Histochemistry,* **2007**, 82, 51.

(60) A. R. Monahan, J. E. Kuder, *J. Org. Chem.,* **1972**, 37, 4182.

(61) C. J. Cooksey, *Molecules,* **2001**, 6, 736.

(62) G. Voss, M. Gradzielski, J. Heinze, H. Reinke, C. Unverzagt, *Helv. Chim. Acta.,* **2003**, 86, 1982.

(63) H. Meier, W. Luettke, *Liebigs Ann. Chem.,* **1981**, 1303.

(64) K. Teijiro, *Reports of the Asahi Glass Foundation for Industrial Technology* **1989**, 55, 73.

(65) K. Kunz, O. Guenther, *Ber. Deutsch. Chem. Ges.* **1923**, 56B, 2027.

(66) K. Kunz, W. Stuehlinger, *Ber. Deutsch. Chem. Ges.,* **1925**, 58B, 1860.

(67) K. Kunz, *Ber. Deutsch. Chem. Ges.,* **1922**, 3688.

(68) R. Kuhn, H. Machemer, *Ber., Deutsch, Chem. Ges.,* **1927**, 61B, 118.

(69) L. F. Larkworthy, *Chem. Sci.,* **1961**, 4025

(70) K. Kunz, A. J. Kress, *Ber. Deutsch.Chem. Ges.,* **1927**, 60B, 367.

(71) W. Beck, C. Schmidt., R. Wienold, M. Stiemann, B. Wagner, *Angew. Chem. Int. Ed.,* **1989**, 28, 1529.

(72) A. Lenz, C. Schmidt., A. Lehmann, B. Wagner, W. Beck, Verlag der Zeitschrift fuer Naturforschung, **1996**, 474.

(73) C. Schmidt, H-U. Wagner, W. Beck, *Chem. Ber,.* **1992**, 125, 2347.

(74) J-Y Wu, P. Thanasekaran, C-C Tsai, T-W Tseng, G-H Lee, S-M Peng, K-L Lu *Dalton Trans.,* **2008**, 6110.

(75) D. Bhattacharya, C-H. Chang., Y-H. Cheng, L-L. Lai, H-Y. Lu, C-Y. Lin, K-L. Lu, *Chem. Eur. J.,* **2012**, 18, 5275.

(76) E. Grandmourgin, E. Dessoulavy, *Ber. Deutsch. Chem. Ges.,* **1909**, 42, 3636.

(77) C. Kuehn, R. Beckert, M. Friedrich, H. Goerls, *J. Heterocycl. Chem.,* **2006**, 43, 1569.

(78) J. C. A. Boeyens, L. M. Cook, Y. Ding, M. A. Fernandes, D. H. Reid, *Org. Biomol. Chem.,* **2003**, 1, 2168.

(79) M. Wenzel, F. Lehmann, R. Beckert, W. Guenther, H. Goerls, *Monatch. Chem.,* **1999**, 130, 1373.

(80) R. N. Ram, A. A. Khan, *Synth. Commun.,* **2001**, 31, 841.

(81) R. Carlson, U. Larson., L. Hansson, *Acta. Chem. Scan.,* **1992**, 46, 1211.

(82) H. K. Hall, J., A. B, Padias, P. A. Williams, J-M. Gosau, H. W. Boone, D-K. Park, *Macromolecules* **1995**, 28, 1.

(83) J. Bredt, *Justus Liebig's Annalen der chemie,* **1924**, 437, 1.

(84) S. R. Oakley, Master's Thesis, University of Victoria, **2008**

(85) S. R. Oakley, G. N., K. M. Waldie, T. M. McInnis, B. O. Patrick, R. G. Hicks, *Chem. Commun.,* **2010**, *46*, 6753.

(86) G. Nawn, K. M. Waldie, S. R. Oakley, B. D. Peters, D. Mandel, B. O. Patrick, R. MacDonald, R. G. Hicks, *Inorg. Chem.,* **2011**, 50, 9826.

(87) S-L. Kokatam, P. Chaudhuri., T. Weyhermueller, K. Wieghardt *Dalton Trans.,* **2007**, 373.

(88) D. Herebian, E. Bothe, F. Neese, T. Weyhermueller, K. Wieghardt, *J. Am. Chem. Soc.,* **2003**, 125, 9116.

(89) A. K. Chakraborti, S. Bhagat, S. Rudrawar, *Tetrahedron Lett.,* **2004**, 45, 7641.

(90) H.K. Hall, A. B. Padias, I. Yahagi, P. A. Williams, M. A. Bruck, X. Drujon, *Macromolecules,* **1995**, 28, 9

(91) W. Madelung, *Berichte,* **1913**, 2259.

(92) W. R. Brode, E. G. Pearson, G. M. Wyman, *J. Am. Chem. Soc.,* **1954**, 76, 1034.

(93) R. Pummerer, G. Marondel, *Justus Liebig's Annalen der chemie,* **1957**, 602, 228.

(94) R. Pummerer, G. Marondel, *Chem. Ber.,* **1960**, 93, 2852.

(95) L. Zhu, Y-M. Ye, L-X. Shao, *Tetrahedron,* **2012**, 68, 2414.

(96) H. Sieghold, W. Luettke, *Angew. Chem., Int. Ed.,* **1975**, 14, 52.

(97) J. D. Thoburn, W. Luettke, C. Benedict, H-H. Limbach, *J. Am. Chem. Soc.,* **1996**, 118, 12459.

(98) W. L. F. Armarego, C. L. L. Chai. *Purification of laboratory chemicals (5th edition),* **2003**.

(99) G. I. Zharkova, P. A. Stabnikov., S. A. Sysoev, I. K. Igumenov, *J. Struct. Chem.,* **2005**, 46, 320.

(100) S. Koleman, Y. Cakmak S. Erten-Ela, Y. Altay, J. Brendel, M. Thelakkat, E. U. Akkaya, *Org. Lett.,* **2010**, 12, 3812.

(101) P.Y Reddy, L. Giribabu, C. Lyness, H. J. Snaith, C. Vijaykumar, M. Chandrasekharam, M. Lakshmikantam, J-H. Yum, K. Kalyanasundaram, M. Graetzel, M.K. Nazeerunddin, *Angew. Chem., Int. Ed.,* **2007**, 46, 373.

(102) C. Borek, K. Hanson, P.I. Durovich, M.E. Thompson, K. Aznavour, R. Bau, Y. Sun, S.R. Forrest, J. Brooks, L. Michalski, J. Brown, *Angew. Chem., Int. Ed.,* **2007**, 46, 1109.

(103) J.A.G. Williams, S. Develay, D.L. Rochester, L. Murphy, *Coord. Chem. Rev.,* **2008**, 252, 2596.

(104) L. Fu, F-L. Jiang, D. Fortin, P.D. Harvey, Y. Liu, *Chem. Commun.,* **2011**, 47, 5503.

(105) M. Yousaf, M. Lazzouni, *Dyes and Pigments,* **1995**, 27, 297.

(106) D. E. J. D. J. Dolmans, D. Fukumura, R.K. Jain *Nat. Rev. Cancer,* **2003**, 3, 380.

(107) N. L. Fry, P. K. Masharak, *Acc. Chem. Res.,* **2010**, 44, 4, 289

(108) G. M. Fischer, E. Daltrozzo, A. Zumbusch *Angew. Chem., Int. Ed.,* **2011**, 50, 1406.

(109) N. Kobayashi, T. Furuyama., K. Satoh, *J. Am. Chem. Soc.,* **2011**, 133, 19642.

(110) N. K. S. Davis, A. L. Thompson, H. L. Anderson, *Org. Lett.,* **2010**, 12, 2124.

(111) E. Kim, M. Koh., B. J. Lim, S. B. Park, *J. Am. Chem. Soc.,* **2011**, 133, 6642.

(112) S. Goeb, R. Ziessel, *Org. Lett.,* **2007**, 9, 737.

(113) T. Okujima, Y. Tomimori, J. Nakamura, H. Yamada, H. Uno, N. Ono, *Tetrahedron,* **2010**, 66, 6895.

(114) K. Umezawa, A. Matsui, Y. Nakamura, D. Citterio, K. Suzuki, *Eur. J. Inorg. Chem.,* **2009**, 15, 1096.

(115) K. Umezawa, Y. Nakamura., H. Makino, D. Citterio, K. Suzuki, *J. Am. Chem. Soc.,* **2008**, 130, 1550.

(116) J. Chen, A. Burghart., A. Derecskei-Kovacs, K. Burgess, *J. Org. Chem.,* **2000**, 65, 2900.

(117) A.B. Descalzo, H-J. Xu., Z-L. Xue, K. Hoffmann, Z. Shen, M. G. Weller, X-Z. You, K. Rurack, *Org. Lett.,* **2008**, 10, 1581.

(118) Y. Kubo, Y. Minowa, T. Shoda, K. Takeshita, *Tetrahedron Lett.,* **2010**, 51, 1600.

(119) Y. Gabe, T. Ueno, Y. Urano, H. Kojima, T. Nagano, *Anal. Bioanal. Chem.,* **2006**, 386, 621.

(120) R. Gresser, M. Hummert., H. Hartmann, K. Leo, M. Riede, *Chem. Eur. J.,* **2011**, 17, 2939.

(121) V. F. Donyagina, S. Shimizu., N. Kobayashi, E. A. Lukyanets, *Tetrahedron Lett.,* **2008**, 49, 6152.

(122) Q. Bellier, S. Pégaz., C. Aronica, B. Le Guennic, C. Andraud, O. Maury, *Org. Lett.,* **2011**, 13, 22.

(123) W. Zhao, E. M. Carreira. *Chem. Eur. J.,* **2006**, 12, 7254.

(124) S. O. McDonnell, D. F. O'Shea, *Org. Lett.,* **2006**, 8, 3493.

(125) V.P. Yakubovskyi, M. P. Shandura., Y. P. Kovtun, *Eur. J. Inorg. Chem.,* **2009**, 3237.

(126) K. Rurack, M. Kollmannsberger, J. Daub, *New J. Chem.,* **2001**, 25, 289.

(127) O. Buyukcakir, O. A. Bozdemir, S. Kolemen, S. Erbas, E. U. Akkaya, *Org. Lett.,* **2009**, 11, 4644.

(128) J. F. Araneda, W. E. Piers., B. Heyne, M. Parvez, R. McDonald, *Angew. Chem., Int. Ed.,* **2001**, 50, 1.

(129) G. Nawn, S. R. Oakley., M. B. Majewski, R. McDonald, B. O. Patrick, R. G. Hicks, *Chem. Sci.,* **2013**, 4, 612.

(130) X. Liu, Y. Ren., H. Xia, X. Fan, Y. Mu, *Inorg. Chem. Acta,* **2010**, 363, 1441.

(131) Y. Ren, X. Liu., W. Gao, H. Xia, L. Ye, Y. Mu, *Eur. J. Inorg. Chem.,* **2007**, 1808.

(132) G. Pfeiffer, H. Bauer, *Liebigs Ann. Chem.,* **1980**, 564.

(133) A. Caneschi, A. Dei., D. Gateschi, V. Tangoulis, *Inorg. Chem.,* **2002**, 41, 3508.

(134) A. Caneschi, A. Dei., F.F, De Biani, P. Guetlich, V. Ksenofontov, G. Levchenko, A. Hoefer, F. Renz, *Chem. Eur. J.,* **2001**, 7, 3926.

(135) D. M. Adams, D. N. Hendrickson, *J. Am. Chem. Soc.,* **1996**, 118, 11515.

(136) C. G. Pierpont, *Coord. Chem. Rev.*, **2001**, 217, 99.

(137) C. Roux, D. M. Adams., J. P. Itie, A. Polian, D.N . Hendrickson, M. Verdaguer, *Inorg. Chem.,* **1996**,35, 2846.

(138) D. M. Adams, A. Dei, A. L. Rheingold, D. N. Hendrickson, *Angew. Chem., Int. Ed.,* **1993**, 32, 880.

(139) E. Evangelino, R. Ruiz-Molina, *C. R. Chimie,* **2008**, 11, 1137.

(140) N. Kundu, M. Maity, P. B. Chatterjee, S. J. Teat, A. Endo, M. Chaudhury, *J. Am. Chem. Soc.,* **2011**, 133, 20104.

(141) L. Kalb, *Ber. Deutsch. Chem. Ges.,* **1909**, 42, 2, 3642.

(142) L. Kalb, Ber. Deutsch. Chem. Ges., **1912**, 2136.

(143) L. Kalb, Ber. Deutsch. Chem. Ges., **1911**, 1455.

(144) R. Rondão, J. S. Seixas de Melo, V. D. B. Bonifácio, M. J. Melo, *J. Phys. Chem. A,* **2010**, 114, 1699.

(145) W. Madelung, *Liebigs Ann. Chem.,* **1914**, 405, 1, 58.

(146) E. Grandmourgin, E. Dessoulavy, *Berichte,* **1909**, 42, 4401.

(147) F. H. Allen, O. Kennard, D. G. Watson, L. Brammer, A. G. Orpen, *J. Chem. Soc. Perkins Trans. 2* ,**1987**, S1.

(148) P. Carloni, L. Greci, M. Iacussi, M. Rossetti, P. Cozzini, P. S. Garabotto, *J. Chem. Res.,* **1998**, 232.

(149) S-I. Takekuma, H. Takekuma, Y. Matsubara, K. Inaba, Z-I. Yoshida, *J. Am. Chem. Soc.,* **1994**, 116, 8849.

(150) P. Steel, *Acc. Chem. Res.,* **2005**, 38, 243.

(151) W. Kaim, A. Klein, M. Gloeckle, *Acc. Chem. Res.,* **2000**, 33, 755.

(152) W. Kaim, B. Sarkar, *Coord. Chem. Rev.,* **2007**, 251, 584.

(153) C. Creutz, H. Taube, *J. Am. Chem. Soc.,* **1969**, 91, 3988.

(154) S. Patra, B. Sarkar, S. Ghumaan, J. Fiedler, W. Kaim, G. Kumar, *Inorg. Chem.,* **2004**, 43, 6108.

(155) A. Endo, M. Kajitani, M. Mukaida, K. Shimizu, Gen. P. Sato, *Inorg. Chem. Acta,* **1988**, 150, 25.

(156) I. R. Baird, S. J. Rettig., B. R. James, K. A. Skov, *Can. J. Chem.,* **1999**, 77, 1821.

(157) M. B. Robin, P. Day. *Adv. Inorg. Chem. Radiochem.,* **1967**, 10, 247.

(158) K. D. Demadis, C. M. Hartshorn, T. J. Meyer, *Chem. Rev.,* **2001**, 101, 2655.

(159) M. J. Frisch *et al*, *Gaussian 09,* Revision B.1, Gaussian, Inc., Wallingford CT, **2009.**

(160) A. D. Becke, *Journal of Chemical Physics*, **1993**, 98, 5648; P. J. Stephens, F. J. Devlin, C. F. Chabalowski, M. J. Frisch, *Journal of Physical Chemistry*, **1994**, 98, 11623.

(161) C. T. Lee, W. T. Yang, R. G. Parr, *Physical Review B*, **1988**, 37, 785.

(162) A. Schafer, H. Horn, R. Ahlrichs, *Journal of Chemical Physics*, **1992**, 97, 2577.

(163) M. E. Casida, *Recent Advances in Density Functional Methods*, ed. D. P. Chong, World Scientific, Singapore, **1995**, 155; R. E. Stratmann, G. E. Scuseria, M. J. Frisch, *Journal of Chemical Physics*, **1998**, 109, 8218.

(164) V. Barone, M. Cossi, J. Tomasi, *Journal of Chemical Physics*, **1997**, 107, 3210; V. Barone, M. Cossi, J. Tomasi, *Journal of Computational Chemistry*, **1998**, 19, 404; S. Miertus, E. Scrocco, J. Tomasi, *Chemical Physics*, **1981**, 55, 117.

Appendix A: Crystallographic parameters

Table A- 1: Crystallographic parameters

	1.32b'	**2.1c**	**2.2c**
formula	C30H24N4	C24H19N3O	C37.5H29ClF6N4O2Pd
formula weight	440.53	365.42	823.50
crystal dimensions (mm)	0.82 × 0.13 × 0.06	0.33 × 0.29 × 0.20	0.38 × 0.32 × 0.23
crystal system	triclinic	monoclinic	triclinic
space group	*P* (No. 2)	*P*21/*n* (no. 14)	*P* (No. 2)
a (Å)	9.6208 (6)	14.1344 (10)	11.9753 (3)
b (Å)	10.5429 (6)	14.8496 (10)	12.5665 (4)
c (Å)	12.3563 (8)	17.8584 (12)	13.5421 (4)
α (deg)	110.7996 (8)		112.5730 (3)
β (deg)	100.8409 (8)	95.5371 (9)	93.9515 (3)
γ (deg)	100.8226 (8)		109.3867 (3)
V (Å3)	1105.61 (12)	3730.8 (4)	1729.42 (9)
Z	2	8	2
*r*calcd (g cm-3)	1.323	1.301	1.581
μ (mm-1)	0.079	0.081	0.687
temperature (°C)	–100	–100	–100
data collection 2*q* limit (deg)	51.34	52.82	55.14
total data collected	8298	29438	15527
independent reflections	4195 (*R*int = 0.0208)	7652 (*R*int = 0.0260)	7974 (*R*int = 0.0102)
data/restraints/parameters	4195 / 0 / 317	7652 / 0 / 509	7974 / 0 / 477
*R*1 [*F*o2 ³ 2*s*(*F*o2)]	0.0394	0.0393	0.0268
*wR*2 [all data]	0.105	0.1145	0.0739
CSD number	812586		

$^{f}R_1 = \Sigma||F_o| - |F_c||/\Sigma|F_o|$; $wR_2 = [\Sigma w(F_o^2 - F_c^2)^2/\Sigma w(F_o^4)]^{1/2}$.

Table A-1 continued: Crystallographic parameters

	2.2d	**3.3a**	**3.3b**
formula	C45H44F6N4O2Pd	C30H22BF2N5	C30H23BF2N4
formula weight	893.24	501.34	488.33
crystal dimensions (mm)	0.44 x 0.16 x 0.09	0.41 x 0.38 x 0.06	0.55x´ 0.35 x 0.03
crystal system	triclinic	triclinic	triclinic
space group	*P* (No. 2)	*P* (No. 2)	*P* (No. 2)
a (Å)	12.4188 (4)	11.9663 (7)	7.6722 (5)
b (Å)	13.3663 (4)	12.5933 (8)	12.8997 (9)
c (Å)	13.5280 (4)	19.2781 (12)	12.9358 (9)
α (deg)	66.8664 (3)	76.0890 (8)	74.6956 (8)
β (deg)	78.7331 (4)	85.2516 (9)	75.5868 (9)
γ (deg)	83.0717 (4)	62.9902 (7)	83.7805 (9)
V (Å3)	2022.80 (11)	2511.2 (3)	1194.73 (14)
Z	2	4	2
*r*calcd (g cm-3)	1.467	1.326	1.357
μ (mm-1)	0.53	0.09	0.092
temperature (°C)	–100	–100	–100
data collection 2*q* limit (deg)	54.98	51.68	51.56
total data collected	17961	18441	8999
independent reflections	9208 (*R*int = 0.0184)	18441 (*R*int = 0.0000)	4576 (*R*int = 0.0272)
data/restraints/parameters	9208 / 0 / 551	18441 / 0 / 688	4576 / 0 / 336
*R*1 [Fo2 ³ 2s(Fo2)]	0.0286	0.0562	0.0449
*wR*2 [all data]	0.0711	0.133	0.1186
CSD number	812594	805624	895625

$^{f}R_1 = \Sigma||F_o| - |F_c||/\Sigma|F_o|$; $wR_2 = [\Sigma w(F_o^2 - F_c^2)^2/\Sigma w(F_o^4)]^{1/2}$.

Table A-1 continued: Crystallographic parameters

	3.3c	**3.3d**	**3.3e**
formula	C32H27BF2N4	C40H43BF2N4	C36H35BF2N4
formula weight	516.39	628.59	572.49
crystal dimensions (mm)	0.61 × 0.24 × 0.21	0.53 × 0.18 × 0.15	0.38 × 0.12 × 0.09
crystal system	triclinic	triclinic	monoclinic
space group	*P* (No. 2)	*P* (No. 2)	*P*21/n (No. 14)
a (Å)	12.0332 (8)	10.7533 (7)	15.7903 (6)
b (Å)	14.8026 (10)	13.3999 (8)	11.9086 (5)
c (Å)	15.5572 (10)	24.5025 (15)	15.8933 (7)
α (deg)	89.0111 (8)	91.7881 (8)	
β (deg)	83.5450 (8)	95.0164 (8)	94.4690 (5)
γ (deg)	72.8575 (8)	100.2580 (8)	
V (Å3)	2630.8 (3)	3457.0 (4)	2979.5 (2)
Z	4	4	4
*r*calcd (g cm-3)	1.304	1.208	1.276
μ (mm-1)	0.087	0.078	0.084
temperature (°C)	–100	–100	–100
data collection 2*q* limit (deg)	52.72	51.5	53.04
total data collected	20842	23870	23713
independent reflections	10640 (*R*int = 0.0192)	23870 (*R*int = 0.0000)	6169 (*R*int = 0.0427)
data/restraints/parameters	10640 / 0 / 711	23870 / 0 / 848	6169 / 0 / 388
*R*1 [Fo2 ³ 2s(Fo2)]	0.0432	0.0597	0.0404
*wR*2 [all data]	0.1217	0.1575	0.1059
CSD number	895626	895627	895628

$^{f}R_1 = \Sigma||F_o| - |F_c||/\Sigma|F_o|$; $wR_2 = [\Sigma w(F_o^2 - F_c^2)^2/\Sigma w(F_o^4)]^{1/2}$.

Table A-1 continued: Crystallographic parameters

	3.3f	**3.6a**	**3.6c**
formula	C28.5H18BCl3F2N4	C35H23BF8N4O2.5Pd	C38H28.5BF8N4.5O2Pd
formula weight	571.63	808.78	849.36
crystal dimensions (mm)	0.36 x 0.21 x 0.07	0.49 x 0.12x 0.08	0.25 x 0.24 x 0.17
crystal system	monoclinic	triclinic	monoclinic
space group	*I*2/a (No. 15)	*P*i (No.2)	*Pc* (No. 7)
a (Å)	14.0731 (2)	11.3192 (8)	15.1584 (6)
b (Å)	11.5359 (2)	12.4363 (9)	11.8641 (4)
c (Å)	31.2056 (4)	13.4483 (10)	19.9033 (7)
α (deg)		83.4965 (8)	
β (deg)	93.7226 (5)	68.0361 (8)	105.0514 (4)
γ (deg)		64.4777 (8)	
V (Å3)	5055.41 (13)	1581.8 (2)	3456.6 (2)
Z	8	2	4
*r*calcd (g cm-3)	1.502	1.698	1.632
μ (mm-1)	3.643	0.677	0.623
temperature (°C)	–100	–100	–100
data collection 2*q* limit (deg)	140.14	55.36	55.02
total data collected	16710	14113	30380
independent reflections	4749 (*R*int = 0.0193)	7276 (*R*int = 0.0217)	15822 (*R*int = 0.0238)
data/restraints/parameters	4749 / 0 / 365	7276 / 0 / 543	15822 / 0 / 992
*R*1 [Fo2 ³ 2s(Fo2)]	0.0335	0.0356	0.0281
*wR*2 [all data]	0.1009	0.1012	0.0704
CSD number	895629		

$^{f}R_1 = \Sigma||F_o| - |F_c||/\Sigma|F_o|$; $wR_2 = [\Sigma w(F_o^2 - F_c^2)^2/\Sigma w(F_o^4)]^{1/2}$.

Table A-1 continued: Crystallographic parameters

	3.6d	**4.1**	**4.2a**
formula	C46H45BCl2F8N4O2Pd	C56H36B2F4N8Zn	C56H36B2Cl4CuF4N8
formula weight	1025.97	983.92	982.09
crystal dimensions (mm)	0.34 × 0.23 × 0.09	0.33 × 0.15 × 0.14	0.43 × 0.14 × 0.05
crystal system	triclinic	monoclinic	triclinic
space group	*P* (No. 2)	*I*2/a (No. 15)	*Pi (No. 2)*
a (Å)	9.4672 (3)	19.5211 (4)	8.81190 (10)
b (Å)	14.2029 (5)	9.4411 (2)	13.1797 (2)
c (Å)	17.3360 (6)	24.7912 (5)	20.4625 (3)
α (deg)	78.0317 (4)		79.5356 (7)
β (deg)	88.9814 (4)	100.7126 (7)	81.9245 (6)
γ (deg)	76.9012 (4)		85.6138 (5)
V (Å3)	2219.98 (13)	4489.40 (16)	2306.54 (6)
Z	2	4	2
*r*calcd (g cm-3)	1.535	1.456	1.414
μ (mm-1)	0.616	1.319	1.213
temperature (°C)	–100	–100	–100
data collection 2*q* limit (deg)	55.34	140.18	140.06
total data collected	19880	14769	15711
independent reflections	10238 (*R*int = 0.0165)	4242 (*R*int = 0.0123)	8235 (*R*int = 0.0257)
data/restraints/parameters	10238 / 0 / 577	4242 / 0 / 321	8235 / 0 / 640
*R*1 [Fo2 ³ 2s(Fo2)]	0.0433	0.0486	0.0404
*wR*2 [all data]	0.1293	0.1639	0.1162
CSD number			

$^{f}R_1 = \Sigma||F_o| - |F_c||/\Sigma|F_o|$; $wR_2 = [\Sigma w(F_o^2 - F_c^2)^2/\Sigma w(F_o^4)]^{1/2}$.

Table A-1 continued: Crystallographic parameters

	4.2c	**5.1a**	**5.2b-trans**
formula	C66H56B2Cl4CuF4N8	C28H18N4	C50H26F24N4O8Ru2
formula weight	1264.15	410.46	1468.89
crystal dimensions (mm)	0.36 x 0.09 x 0.09	0.05 x 0.15 x 0.27	0.41 x 0.26 x 0.26
crystal system	triclinic	monoclinic	triclinic
space group	*Pi (No. 2)*	$P2_{1/c}$ (No. 14)	*Pi* (No. 2)
a (Å)	8.4512 (3)	8.5038 (3)	13.3839 (6)
b (Å)	14.0955 (5)	22.0912 (7)	14.1124 (6)
c (Å)	25.1592 (8)	11.1934 (4)	16.4286 (7)
α (deg)	94.6574 (4)	90	95.5125 (5)
β (deg)	97.7943 (4)	91.511 (1)	91.2484 (5)
γ (deg)	91.8087 (4)	90	112.7365 (5)
V (Å3)	2956.82 (18)	2102.1 (1)	2842.8 (2)
Z	2	4	2
*r*calcd (g cm-3)	1.42	1.297	1.716
μ (mm-1)	0.613	0.78	0.665
temperature (°C)	–100	-100	–100
data collection 2*q* limit (deg)	53	59.9	55.14
total data collected	24264	28037	25342
independent reflections	12252 (*R*int = 0.0313)	5990 (Rint = 0.046)	12996 (*R*int = 0.0184)
data/restraints/parameters	12252 / 0 / 793	5990 / 0 / 289	12996 / 0 / 825
*R*1 [Fo2 ³ 2s(Fo2)]	0.04	0.047	0.0353
*wR*2 [all data]	0.1024	0.101	0.0983
CSD number		812589	

$^{f}R_1 = \Sigma||F_o| - |F_c||/\Sigma|F_o|$; $wR_2 = [\Sigma w(F_o^2 - F_c^2)^2/\Sigma w(F_o^4)]^{1/2}$.

Table A-1 continued: Crystallographic parameters

	5.2b-cis	**5.2h-trans**	**5.2h-cis**
Formula	C51H28Cl2F24N4O8Ru2	C54H34F24N4O8Ru2	$C_{54.5}H_{35}ClF_{24}N_4O_8Ru_2$
formula weight	1553.81	1524.99	1567.45
crystal dimensions (mm)	0.65 x 0.27 x 0.22	0.35 x 0.35 x 0.28	0.44 x 0.38 x 0.20
crystal system	monoclinic	monoclinic	triclininc
space group	*P*21/*c* (No. 14)	*P*21/*c* (No. 14)	*P1* (No. 2)
a (Å)	17.7541 (10)	17.6715 (7)	12.2069 (13)
b (Å)	17.8353 (10)	19.0495 (8)	15.1309 (16)
c (Å)	17.5154 (10)	17.3115 (7)	18.054 (2)
α (deg)			65.9839 (13)
β (deg)	91.0695 (7)	91.0741 (5)	83.4448 (15)
γ (deg)			83.2242 (14)
V (Å3)	5545.3 (5)	5826.6 (4)	3016.6
Z	4	4	2
*r*calcd (g cm-3)	1.861	1.738	1.726
μ (mm-1)	0.78	0.652	0.675
temperature (°C)	–100	–100	-100
data collection 2*q* limit (deg)	55.08	55.1	53.12
total data collected	49057	51425	43099
independent reflections	12749 (*R*int = 0.0204)	13432 (*R*int = 0.0229)	12475 (Rint = 0.0678)
data/restraints/parameters	12749 / 0 / 831	13432 / 0 / 862	12475 / 0 / 798
*R*1 [Fo2 ³ 2s(Fo2)]	0.0297	0.0318	0.0788
*wR*2 [all data]	0.09	0.0892	0.2243
CSD number			

$^f R_1 = \Sigma||F_o| - |F_c||/\Sigma|F_o|$; $wR_2 = [\Sigma w(F_o^2 - F_c^2)^2/\Sigma w(F_o^4)]^{1/2}$.

Appendix B: Complete listing of bond lengths and angles

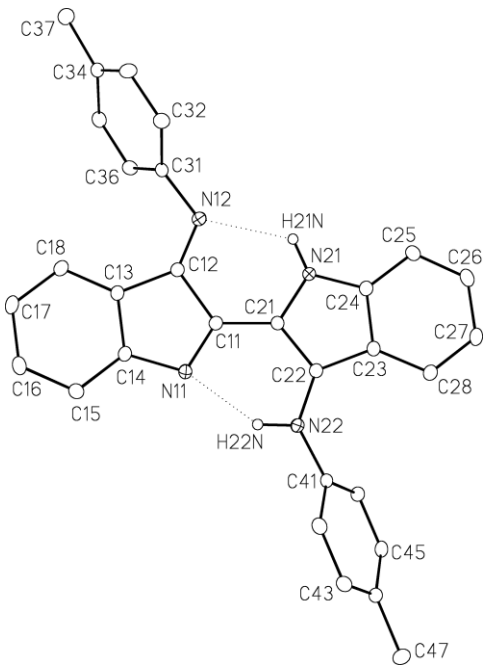

Figure B-1: ORTEP view of **1.32b'**. Thermal ellipsoids at the 50% probability level with all hydrogen atoms, with the exception of the N-H atoms, removed for clarity

Table B-1: Bond lengths (Å) and angles (^{o}) for **1.32b'** (α signifies non-bonded distances)

N11	N22	2.8025(18)*α*	C17	C18	1.390(2)
N11	C11	1.3208(18)	C21	C22	1.397(2)
N11	C14	1.4168(18)	C22	C23	1.439(2)
N11	H22N	2.040(18)*α*	C23	C24	1.417(2)
N12	N21	2.8299(18)*α*	C23	C28	1.408(2)
N12	C12	1.2815(18)	C24	C25	1.399(2)
N12	C31	1.4248(18)	C25	C26	1.377(2)
N12	H21N	2.223(18)*α*	C26	C27	1.400(2)
N21	H21N	0.886(18)	C27	C28	1.377(2)
N21	C21	1.3904(18)	C31	C32	1.387(2)
N21	C24	1.3592(19)	C31	C36	1.389(2)

N22	H22N	0.931(19)	C32	C33	1.382(2)
N22	C22	1.3666(18)	C33	C34	1.387(2)
N22	C41	1.4044(19)	C34	C35	1.393(2)
C11	C12	1.501(2)	C34	C37	1.500(2)
C11	C21	1.415(2)	C35	C36	1.382(2)
C12	C13	1.475(2)	C41	C42	1.393(2)
C13	C14	1.403(2)	C41	C46	1.391(2)
C13	C18	1.387(2)	C42	C43	1.380(2)
C14	C15	1.383(2)	C43	C44	1.389(2)
C15	C16	1.389(2)	C44	C45	1.390(2)
C16	C17	1.386(2)	C44	C47	1.512(2)
			C45	C46	1.384(2)

C11	N11	C14	106.15(12)	C22	C23	C28	135.16(14)
C12	N12	C31	120.24(13)	C24	C23	C28	118.77(13)
C21	N21	C24	109.01(12)	N21	C24	C23	109.29(13)
C21	N21	H21N	122.1(12)	N21	C24	C25	129.08(14)
C24	N21	H21N	128.6(12)	C23	C24	C25	121.60(14)
C22	N22	C41	128.64(13)	C24	C25	C26	117.96(14)
C22	N22	H22N	111.2(11)	C25	C26	C27	121.37(15)
C41	N22	H22N	119.6(11)	C26	C27	C28	121.13(14)
N11	C11	C12	112.26(12)	C23	C28	C27	119.17(14)
N11	C11	C21	122.93(13)	N12	C31	C32	119.54(13)
C12	C11	C21	124.81(13)	N12	C31	C36	120.76(13)
N12	C12	C11	121.64(13)	C32	C31	C36	119.50(14)
N12	C12	C13	134.79(14)	C31	C32	C33	119.73(14)
C11	C12	C13	103.45(12)	C32	C33	C34	121.87(15)
C12	C13	C14	104.97(12)	C33	C34	C35	117.48(14)
C12	C13	C18	134.62(14)	C33	C34	C37	121.92(15)
C14	C13	C18	120.36(13)	C35	C34	C37	120.55(15)
N11	C14	C13	113.16(12)	C34	C35	C36	121.52(14)
N11	C14	C15	125.63(13)	C31	C36	C35	119.87(14)
C13	C14	C15	121.21(13)	N22	C41	C42	118.56(13)
C14	C15	C16	117.81(14)	N22	C41	C46	122.60(13)
C15	C16	C17	121.49(15)	C42	C41	C46	118.66(13)
C16	C17	C18	120.68(14)	C41	C42	C43	120.51(14)
C13	C18	C17	118.45(14)	C42	C43	C44	121.29(14)
N21	C21	C11	123.81(13)	C43	C44	C45	117.87(14)
N21	C21	C22	108.67(12)	C43	C44	C47	120.95(15)
C11	C21	C22	127.52(13)	C45	C44	C47	121.17(15)

N22	C22	C21	121.29(13)	C44	C45	C46	121.41(14)
N22	C22	C23	131.34(13)	C41	C46	C45	120.25(14)
C21	C22	C23	107.05(12)	N12	H21N	N21	125.4(15)*a*
C22	C23	C24	105.98(13)	N11	H22N	N22	138.0(15)*a*

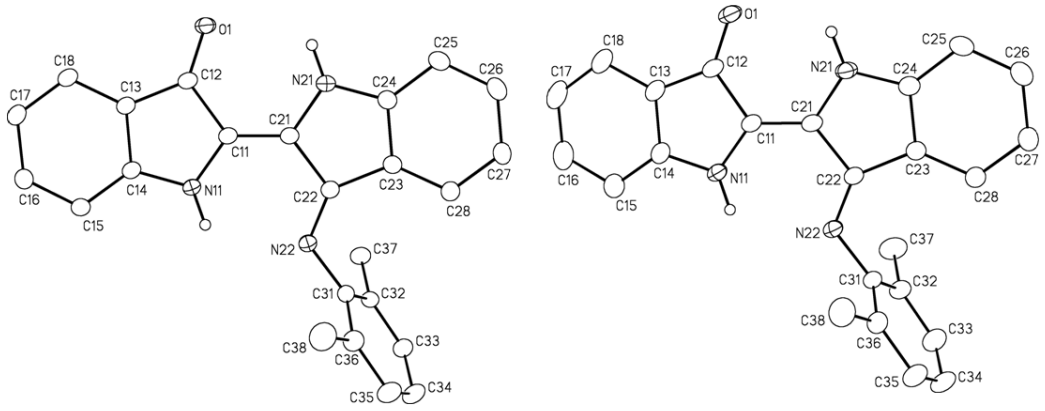

Figure B-2: ORTEP view of two crystallographically independent molecules of **2.1c**, A (left) and B (right). Thermal ellipsoids at the 50% probability level with all hydrogen atoms, with the exception of the N-H atoms, removed for clarity

Table B-2: Bond lengths (Å) and angles (^{o}) for **2.1c**

Molecule A			*Molecule B*		
O1	C12	1.2392(17)	O1	C12	1.2428(19)
N11	C11	1.3798(19)	N11	C11	1.382(2)
N11	C14	1.3754(19)	N11	C14	1.378(2)
N21	C21	1.3753(18)	N21	C21	1.377(2)
N21	C24	1.3848(19)	N21	C24	1.386(2)
N22	C22	1.2905(18)	N22	C22	1.2865(19)
N22	C31	1.4215(18)	N22	C31	1.4200(19)
C11	C12	1.4786(19)	C11	C12	1.467(2)
C11	C21	1.354(2)	C11	C21	1.356(2)
C12	C13	1.458(2)	C12	C13	1.452(2)

C13	C14	1.405(2)		C13	C14	1.406(2)	
C13	C18	1.391(2)		C13	C18	1.393(2)	
C14	C15	1.388(2)		C14	C15	1.388(2)	
C15	C16	1.377(2)		C15	C16	1.387(3)	
C16	C17	1.394(2)		C16	C17	1.393(3)	
C17	C18	1.378(2)		C17	C18	1.370(3)	
C21	C22	1.4765(19)		C21	C22	1.466(2)	
C22	C23	1.469(2)		C22	C23	1.469(2)	
C23	C24	1.404(2)		C23	C24	1.402(2)	
C23	C28	1.394(2)		C23	C28	1.390(2)	
C24	C25	1.387(2)		C24	C25	1.385(2)	
C25	C26	1.384(2)		C25	C26	1.377(2)	
C26	C27	1.391(2)		C26	C27	1.388(2)	
C27	C28	1.381(2)		C27	C28	1.383(2)	
C31	C32	1.405(2)		C31	C32	1.385(2)	
C31	C36	1.398(2)		C31	C36	1.398(2)	
C32	C33	1.386(2)		C32	C33	1.398(2)	
C32	C37	1.503(2)		C32	C37	1.500(3)	
C33	C34	1.380(2)		C33	C34	1.367(3)	
C34	C35	1.375(3)		C34	C35	1.355(3)	
C35	C36	1.387(2)		C35	C36	1.384(2)	
C36	C38	1.499(2)		C36	C38	1.494(3)	

Molecule A				*Molecule B*			
C11	N11	C14	109.65(12)	C11	N11	C14	108.90(13)
C21	N21	C24	110.19(12)	C21	N21	C24	110.18(12)
C22	N22	C31	120.78(13)	C22	N22	C31	120.24(13)
N11	C11	C12	108.18(12)	N11	C11	C12	108.84(13)
N11	C11	C21	125.65(13)	N11	C11	C21	127.01(13)
C12	C11	C21	126.16(13)	C12	C11	C21	124.13(15)
O1	C12	C11	125.25(14)	O1	C12	C11	125.02(15)
O1	C12	C13	130.10(13)	O1	C12	C13	130.35(14)
C11	C12	C13	104.65(12)	C11	C12	C13	104.63(13)
C12	C13	C14	107.31(12)	C12	C13	C14	107.47(13)
C12	C13	C18	132.68(13)	C12	C13	C18	132.12(16)
C14	C13	C18	119.99(14)	C14	C13	C18	120.41(17)
N11	C14	C13	110.19(13)	N11	C14	C13	110.16(15)
N11	C14	C15	128.57(13)	N11	C14	C15	128.45(16)
C13	C14	C15	121.24(14)	C13	C14	C15	121.39(16)
C14	C15	C16	117.59(14)	C14	C15	C16	116.84(19)

C15	C16	C17	121.90(16)	C15	C16	C17	122.1(2)
C16	C17	C18	120.51(15)	C16	C17	C18	120.91(18)
C13	C18	C17	118.77(14)	C13	C18	C17	118.33(18)
N21	C21	C11	124.92(13)	N21	C21	C11	124.62(13)
N21	C21	C22	107.80(12)	N21	C21	C22	107.92(13)
C11	C21	C22	127.28(13)	C11	C21	C22	127.46(14)
N22	C22	C21	120.50(13)	N22	C22	C21	120.21(14)
N22	C22	C23	134.34(13)	N22	C22	C23	134.52(14)
C21	C22	C23	105.16(12)	C21	C22	C23	105.26(13)
C22	C23	C24	106.83(13)	C22	C23	C24	106.98(13)
C22	C23	C28	133.50(14)	C22	C23	C28	133.17(14)
C24	C23	C28	119.67(14)	C24	C23	C28	119.85(14)
N21	C24	C23	109.96(13)	N21	C24	C23	109.66(14)
N21	C24	C25	128.51(14)	N21	C24	C25	128.82(15)
C23	C24	C25	121.52(14)	C23	C24	C25	121.52(15)
C24	C25	C26	117.67(15)	C24	C25	C26	117.50(16)
C25	C26	C27	121.59(15)	C25	C26	C27	122.01(16)
C26	C27	C28	120.63(16)	C26	C27	C28	120.42(16)
C23	C28	C27	118.92(15)	C23	C28	C27	118.69(15)
N22	C31	C32	120.23(14)	N22	C31	C32	120.13(15)
N22	C31	C36	118.56(14)	N22	C31	C36	118.07(15)
C32	C31	C36	121.01(13)	C32	C31	C36	121.60(15)
C31	C32	C33	117.96(15)	C31	C32	C33	117.63(18)
C31	C32	C37	121.67(13)	C31	C32	C37	120.74(16)
C33	C32	C37	120.37(15)	C33	C32	C37	121.62(18)
C32	C33	C34	121.57(16)	C32	C33	C34	121.2(2)
C33	C34	C35	119.58(15)	C33	C34	C35	120.11(18)
C34	C35	C36	121.26(16)	C34	C35	C36	121.6(2)
C31	C36	C35	118.57(16)	C31	C36	C35	117.82(18)
C31	C36	C38	120.67(15)	C31	C36	C38	120.81(16)
C35	C36	C38	120.76(16)	C35	C36	C38	121.37(18)

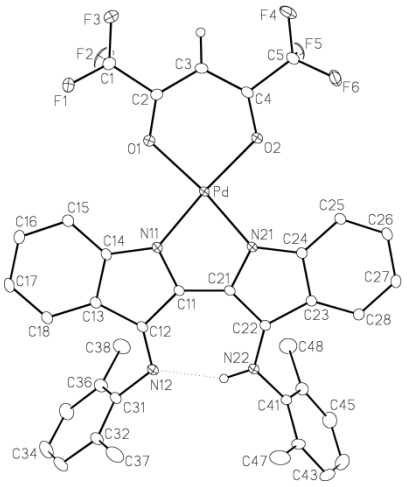

Figure B-3: ORTEP view of **2.2c**. Thermal ellipsoids at the 50% probability level with all hydrogen atoms, with the exception of the imine bridged hydrogen atom, removed for clarity

Table B-3: Bond lengths (Å) and angles (^{o}) for **2.2c**

Pd	O1	2.0182(13)	C13	C14	1.419(2)
Pd	O2	2.0267(12)	C13	C18	1.402(2)
Pd	N11	1.9823(15)	C14	C15	1.391(3)
Pd	N21	1.9911(15)	C15	C16	1.391(3)
F1	C1	1.320(3)	C16	C17	1.397(3)
F2	C1	1.321(3)	C17	C18	1.383(3)
F3	C1	1.328(3)	C21	C22	1.441(2)
F4	C5	1.330(2)	C22	C23	1.446(2)
F5	C5	1.327(2)	C23	C24	1.423(2)
F6	C5	1.320(2)	C23	C28	1.406(2)
O1	C2	1.256(2)	C24	C25	1.400(2)
O2	C4	1.255(2)	C25	C26	1.385(3)
N11	C11	1.361(2)	C26	C27	1.402(3)
N11	C14	1.395(2)	C27	C28	1.379(3)
N12	N22	2.821(2)*a*	C31	C32	1.401(3)
N12	C12	1.310(2)	C31	C36	1.399(3)
N12	C31	1.433(2)	C32	C33	1.392(3)
N12	H22N	2.00*a*	C32	C37	1.503(3)
N21	C21	1.379(2)	C33	C34	1.376(4)
N21	C24	1.381(2)	C34	C35	1.380(4)

N22	C22	1.327(2)	C35	C36	1.387(3)
N22	C41	1.422(2)	C36	C38	1.504(3)
C1	C2	1.537(3)	C41	C42	1.402(3)
C2	C3	1.390(3)	C41	C46	1.399(3)
C3	C4	1.389(3)	C42	C43	1.389(3)
C4	C5	1.539(2)	C42	C47	1.507(4)
C11	C12	1.468(2)	C43	C44	1.374(4)
C11	C21	1.389(2)	C44	C45	1.384(4)
C12	C13	1.455(2)	C45	C46	1.389(3)
			C46	C48	1.504(3)

O1	Pd	O2	92.16(5)	C13	C14	C15	121.07(16)
O1	Pd	N11	92.58(6)	C14	C15	C16	117.76(18)
O1	Pd	N21	172.42(5)	C15	C16	C17	121.70(18)
O2	Pd	N11	174.28(6)	C16	C17	C18	120.89(18)
O2	Pd	N21	94.34(5)	C13	C18	C17	118.59(18)
N11	Pd	N21	80.73(6)	N21	C21	C11	115.29(15)
Pd	O1	C2	123.06(12)	N21	C21	C22	110.76(15)
Pd	O2	C4	122.64(12)	C11	C21	C22	133.89(16)
Pd	N11	C11	113.75(11)	N22	C22	C21	123.35(16)
Pd	N11	C14	137.61(12)	N22	C22	C23	131.70(16)
C11	N11	C14	108.06(14)	C21	C22	C23	104.95(15)
C12	N12	C31	119.05(16)	C22	C23	C24	106.46(15)
Pd	N21	C21	112.97(11)	C22	C23	C28	133.58(17)
Pd	N21	C24	138.08(12)	C24	C23	C28	119.96(16)
C21	N21	C24	107.18(14)	N21	C24	C23	110.65(15)
C22	N22	C41	124.02(15)	N21	C24	C25	128.51(16)
F1	C1	F2	108.4(2)	C23	C24	C25	120.84(16)
F1	C1	F3	107.39(18)	C24	C25	C26	117.70(17)
F1	C1	C2	112.15(17)	C25	C26	C27	121.95(17)
F2	C1	F3	106.53(19)	C26	C27	C28	120.87(18)
F2	C1	C2	109.57(18)	C23	C28	C27	118.68(17)
F3	C1	C2	112.54(18)	N12	C31	C32	119.23(18)
O1	C2	C1	113.37(16)	N12	C31	C36	118.61(18)
O1	C2	C3	129.48(17)	C32	C31	C36	122.15(18)
C1	C2	C3	117.03(17)	C31	C32	C33	117.6(2)
C2	C3	C4	122.49(17)	C31	C32	C37	121.21(18)
O2	C4	C3	129.73(17)	C33	C32	C37	121.1(2)
O2	C4	C5	114.00(16)	C32	C33	C34	121.1(2)

C3	C4	C5	116.14(16)	C33	C34	C35	120.1(2)
F4	C5	F5	107.33(18)	C34	C35	C36	121.3(2)
F4	C5	F6	107.80(18)	C31	C36	C35	117.6(2)
F4	C5	C4	111.90(17)	C31	C36	C38	121.21(19)
F5	C5	F6	107.82(17)	C35	C36	C38	121.2(2)
F5	C5	C4	109.38(16)	N22	C41	C42	117.99(18)
F6	C5	C4	112.39(16)	N22	C41	C46	120.32(17)
N11	C11	C12	110.42(15)	C42	C41	C46	121.51(18)
N11	C11	C21	115.92(15)	C41	C42	C43	118.1(2)
C12	C11	C21	133.63(16)	C41	C42	C47	120.3(2)
N12	C12	C11	123.62(16)	C43	C42	C47	121.6(2)
N12	C12	C13	131.93(16)	C42	C43	C44	121.2(2)
C11	C12	C13	104.45(15)	C43	C44	C45	120.0(2)
C12	C13	C14	106.70(15)	C44	C45	C46	121.1(2)
C12	C13	C18	133.25(17)	C41	C46	C45	118.0(2)
C14	C13	C18	119.99(17)	C41	C46	C48	121.37(19)
N11	C14	C13	110.33(16)	C45	C46	C48	120.6(2)
N11	C14	C15	128.57(17)	N12	H22N	N22	155.1*a*

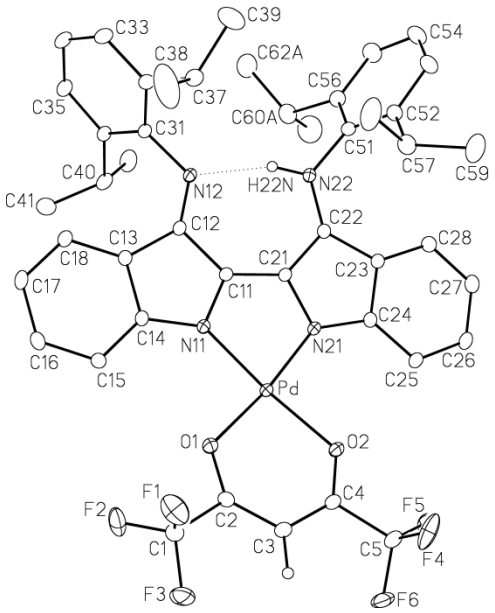

Figure B-4: ORTEP view of **2.2d**. Thermal ellipsoids at the 50% probability level with all hydrogen atoms, with the exception of the N-H atoms, removed for clarity

Table B-4: Bond lengths (Å) and angles (°) for **2.2d**

Pd	O1	2.0142(13)	C21	C22	1.434(2)
Pd	O2	2.0195(12)	C22	C23	1.438(2)
Pd	N11	1.9899(14)	C23	C24	1.426(3)
Pd	N21	1.9878(15)	C23	C28	1.402(3)
F1	C1	1.320(3)	C24	C25	1.401(2)
F2	C1	1.313(3)	C25	C26	1.378(3)
F3	C1	1.320(3)	C26	C27	1.404(3)
F4	C5	1.314(3)	C27	C28	1.376(3)
F5	C5	1.318(2)	C31	C32	1.402(3)
F6	C5	1.333(3)	C31	C36	1.409(3)
O1	C2	1.261(2)	C32	C33	1.391(3)
O2	C4	1.258(2)	C32	C37	1.519(3)
N11	C11	1.353(2)	C33	C34	1.378(3)
N11	C14	1.400(2)	C34	C35	1.378(3)
N12	C12	1.299(2)	C35	C36	1.393(3)
N12	C31	1.432(2)	C36	C40	1.522(3)
N12	N22	2.785(2)*a*	C37	C38	1.506(4)

N12	H22N	1.95*a*	C37	C39	1.502(3)
N21	C21	1.385(2)	C40	C41	1.528(3)
N21	C24	1.377(2)	C40	C42	1.518(3)
N22	C22	1.334(2)	C51	C52	1.404(3)
N22	C51	1.428(2)	C51	C56	1.400(3)
C1	C2	1.528(3)	C52	C53	1.394(3)
C2	C3	1.386(3)	C52	C57	1.525(3)
C3	C4	1.386(3)	C53	C54	1.367(4)
C4	C5	1.531(3)	C54	C55	1.374(4)
C11	C12	1.472(2)	C55	C56	1.394(3)
C11	C21	1.388(2)	C56	C60A	1.525(6)*b*
C12	C13	1.464(2)	C56	C60B	1.519(8)*b*
C13	C14	1.417(3)	C57	C58	1.511(3)
C13	C18	1.395(2)	C57	C59	1.521(3)
C14	C15	1.387(3)	C60A	C61A	1.565(19)
C15	C16	1.387(3)	C60A	C62A	1.52(2)
C16	C17	1.398(3)	C60B	C61B	1.48(3)
C17	C18	1.380(3)	C60B	C62B	1.50(4)

O1	Pd	O2	92.41(5)	N22	C22	C21	123.49(16)
O1	Pd	N11	92.45(6)	N22	C22	C23	130.93(17)
O1	Pd	N21	171.88(6)	C21	C22	C23	105.51(15)
O2	Pd	N11	174.86(6)	C22	C23	C24	106.20(15)
O2	Pd	N21	93.92(6)	C22	C23	C28	133.31(18)
N11	Pd	N21	81.09(6)	C24	C23	C28	120.48(17)
Pd	O1	C2	123.44(12)	N21	C24	C23	110.68(15)
Pd	O2	C4	122.57(12)	N21	C24	C25	129.20(17)
Pd	N11	C11	113.27(11)	C23	C24	C25	120.11(17)
Pd	N11	C14	138.16(13)	C24	C25	C26	117.90(18)
C11	N11	C14	108.24(14)	C25	C26	C27	122.36(18)
C12	N12	C31	121.80(15)	C26	C27	C28	120.50(19)
Pd	N21	C21	112.52(11)	C23	C28	C27	118.64(19)
Pd	N21	C24	139.54(12)	N12	C31	C32	117.45(16)
C21	N21	C24	107.02(15)	N12	C31	C36	120.49(16)
C22	N22	C51	126.09(16)	C32	C31	C36	121.90(17)
F1	C1	F2	106.58(19)	C31	C32	C33	117.98(18)
F1	C1	F3	107.0(2)	C31	C32	C37	121.40(17)
F1	C1	C2	109.97(18)	C33	C32	C37	120.61(18)

F2	C1	F3	107.6(2)	C32	C33	C34	121.1(2)
F2	C1	C2	112.50(17)	C33	C34	C35	120.05(19)
F3	C1	C2	112.90(18)	C34	C35	C36	121.67(19)
O1	C2	C1	112.95(17)	C31	C36	C35	117.24(18)
O1	C2	C3	128.54(18)	C31	C36	C40	122.63(16)
C1	C2	C3	118.41(18)	C35	C36	C40	120.10(17)
C2	C3	C4	123.37(18)	C32	C37	C38	112.2(2)
O2	C4	C3	129.57(18)	C32	C37	C39	112.8(2)
O2	C4	C5	113.72(17)	C38	C37	C39	110.7(3)
C3	C4	C5	116.59(17)	C36	C40	C41	112.73(18)
F4	C5	F5	107.40(19)	C36	C40	C42	110.59(19)
F4	C5	F6	108.2(2)	C41	C40	C42	110.31(18)
F4	C5	C4	110.56(18)	N22	C51	C52	120.12(18)
F5	C5	F6	106.21(18)	N22	C51	C56	117.55(18)
F5	C5	C4	112.63(17)	C52	C51	C56	122.18(19)
F6	C5	C4	111.59(18)	C51	C52	C53	116.9(2)
N11	C11	C12	110.64(15)	C51	C52	C57	122.86(19)
N11	C11	C21	116.41(15)	C53	C52	C57	120.1(2)
C12	C11	C21	132.94(16)	C52	C53	C54	122.0(2)
N12	C12	C11	122.59(16)	C53	C54	C55	120.1(2)
N12	C12	C13	133.29(16)	C54	C55	C56	121.2(2)
C11	C12	C13	104.11(15)	C51	C56	C55	117.6(2)
C12	C13	C14	106.70(15)	C51	C56	C60A	120.8(9)*a*
C12	C13	C18	133.21(17)	C51	C56	C60B	122.4(15)*a*
C14	C13	C18	120.09(17)	C55	C56	C60A	121.5(9)*a*
N11	C14	C13	110.30(16)	C55	C56	C60B	119.4(14)*a*
N11	C14	C15	128.81(17)	C52	C57	C58	110.5(2)
C13	C14	C15	120.89(17)	C52	C57	C59	113.6(2)
C14	C15	C16	117.92(18)	C58	C57	C59	110.4(2)
C15	C16	C17	121.64(19)	C56	C60A	C61A	108.4(11)*a*
C16	C17	C18	120.62(18)	C56	C60A	C62A	111.8(12)*a*
C13	C18	C17	118.82(18)	C61A	C60A	C62A	110.1(12)
N21	C21	C11	115.46(16)	C56	C60B	C61B	113.2(17)*a*
N21	C21	C22	110.51(15)	C56	C60B	C62B	115(2)*a*
C11	C21	C22	134.01(16)	C61B	C60B	C62B	111.9(17)
				N12	H22N	N22	156.6*b*

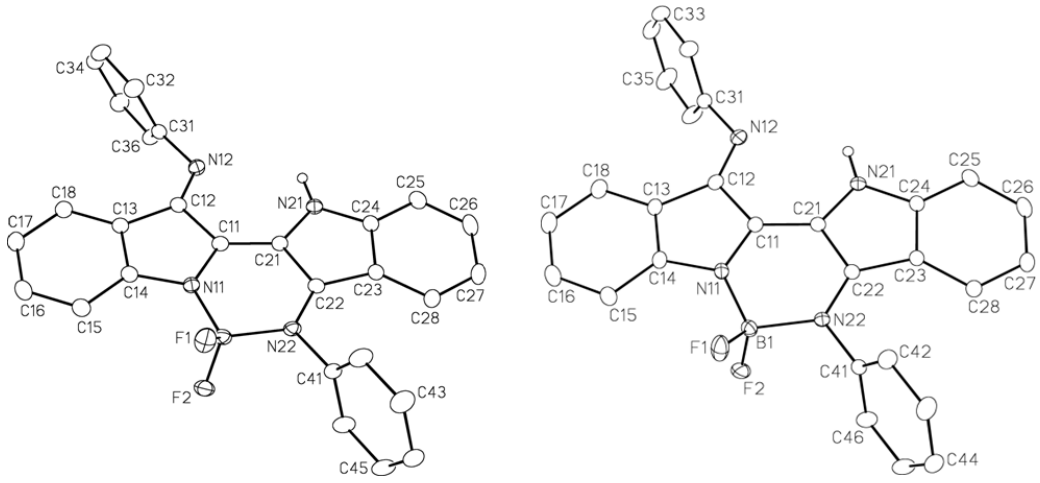

Figure B-5: ORTEP view of the two crystallographically independent molecules of **3.3a**, A (left) and B (right). Thermal ellipsoids at the 50% probability level with all hydrogen atoms, with the exception of the N-H atoms, removed for clarity

Table B-5: Bond lengths (Å) and angles (^{o}) for **3.3a**

Molecule A			*Molecule B*		
F1	B1	1.386(2)	F1	B1	1.382(2)
F2	B1	1.396(2)	F2	B1	1.402(2)
N11	C11	1.358(2)	N11	C11	1.362(2)
N11	C14	1.413(2)	N11	C14	1.413(2)
N11	B1	1.538(2)	N11	B1	1.528(2)
N12	C12	1.279(2)	N12	C12	1.282(2)
N12	C31	1.417(2)	N12	C31	1.419(2)
N21	C21	1.380(2)	N21	C21	1.377(2)
N21	C24	1.369(2)	N21	C24	1.375(2)
N22	C22	1.339(2)	N22	C22	1.341(2)
N22	C41	1.450(2)	N22	C41	1.441(2)
N22	B1	1.555(3)	N22	B1	1.564(2)
C11	C12	1.478(2)	C11	C12	1.474(2)
C11	C21	1.361(2)	C11	C21	1.368(2)
C12	C13	1.473(2)	C12	C13	1.472(2)
C13	C14	1.400(2)	C13	C14	1.400(2)
C13	C18	1.394(2)	C13	C18	1.394(2)

C14	C15	1.381(2)	C14	C15	1.390(2)
C15	C16	1.389(3)	C15	C16	1.386(3)
C16	C17	1.387(3)	C16	C17	1.389(3)
C17	C18	1.382(3)	C17	C18	1.380(3)
C21	C22	1.431(2)	C21	C22	1.421(2)
C22	C23	1.441(2)	C22	C23	1.439(2)
C23	C24	1.415(2)	C23	C24	1.410(2)
C23	C28	1.406(2)	C23	C28	1.410(2)
C24	C25	1.389(3)	C24	C25	1.392(2)
C25	C26	1.371(3)	C25	C26	1.374(3)
C26	C27	1.404(3)	C26	C27	1.400(3)
C27	C28	1.374(3)	C27	C28	1.373(2)
C31	C32	1.381(2)	C31	C32	1.382(2)
C31	C36	1.381(2)	C31	C36	1.377(3)
C32	C33	1.382(3)	C32	C33	1.385(3)
C33	C34	1.377(3)	C33	C34	1.373(3)
C34	C35	1.370(3)	C34	C35	1.373(3)
C35	C36	1.381(3)	C35	C36	1.383(3)
C41	C42	1.374(2)	C41	C42	1.382(2)
C41	C46	1.375(2)	C41	C46	1.375(2)
C42	C43	1.379(3)	C42	C43	1.388(3)
C43	C44	1.370(3)	C43	C44	1.377(3)
C44	C45	1.372(3)	C44	C45	1.372(3)
C45	C46	1.386(3)	C45	C46	1.387(3)

Molecule A				*Molecule B*			
C11	N11	C14	107.52(14)	C11	N11	C14	107.45(14)
C11	N11	B1	125.04(15)	C11	N11	B1	124.48(14)
C14	N11	B1	127.43(15)	C14	N11	B1	127.72(15)
C12	N12	C31	120.75(15)	C12	N12	C31	121.12(15)
C21	N21	C24	108.64(14)	C21	N21	C24	108.13(14)
C22	N22	C41	119.46(15)	C22	N22	C41	119.05(14)
C22	N22	B1	123.79(15)	C22	N22	B1	122.98(14)
C41	N22	B1	116.67(14)	C41	N22	B1	117.96(13)
N11	C11	C12	110.54(15)	N11	C11	C12	110.48(15)
N11	C11	C21	120.65(16)	N11	C11	C21	120.63(15)
C12	C11	C21	128.81(16)	C12	C11	C21	128.77(16)
N12	C12	C11	119.89(16)	N12	C12	C11	119.70(16)
N12	C12	C13	135.85(17)	N12	C12	C13	135.94(16)

C11	C12	C13	104.18(14)	C11	C12	C13	104.35(15)
C12	C13	C14	106.53(15)	C12	C13	C14	106.54(15)
C12	C13	C18	133.69(17)	C12	C13	C18	133.54(17)
C14	C13	C18	119.69(17)	C14	C13	C18	119.90(17)
N11	C14	C13	111.22(15)	N11	C14	C13	111.16(15)
N11	C14	C15	126.94(16)	N11	C14	C15	127.14(17)
C13	C14	C15	121.82(17)	C13	C14	C15	121.68(17)
C14	C15	C16	117.51(18)	C14	C15	C16	117.04(18)
C15	C16	C17	121.50(19)	C15	C16	C17	122.10(19)
C16	C17	C18	120.72(18)	C16	C17	C18	120.43(19)
C13	C18	C17	118.74(17)	C13	C18	C17	118.82(19)
N21	C21	C11	129.47(16)	N21	C21	C11	128.92(16)
N21	C21	C22	108.98(15)	N21	C21	C22	109.28(15)
C11	C21	C22	121.54(16)	C11	C21	C22	121.78(16)
N22	C22	C21	120.70(16)	N22	C22	C21	120.69(15)
N22	C22	C23	133.16(16)	N22	C22	C23	132.88(15)
C21	C22	C23	106.14(15)	C21	C22	C23	106.39(14)
C22	C23	C24	106.14(16)	C22	C23	C24	105.98(14)
C22	C23	C28	134.66(17)	C22	C23	C28	134.76(16)
C24	C23	C28	119.10(17)	C24	C23	C28	119.04(16)
N21	C24	C23	110.05(16)	N21	C24	C23	110.16(15)
N21	C24	C25	128.14(17)	N21	C24	C25	127.69(16)
C23	C24	C25	121.82(17)	C23	C24	C25	122.13(16)
C24	C25	C26	117.64(18)	C24	C25	C26	117.21(17)
C25	C26	C27	121.68(19)	C25	C26	C27	121.93(18)
C26	C27	C28	121.05(19)	C26	C27	C28	121.06(18)
C23	C28	C27	118.66(18)	C23	C28	C27	118.58(17)
N12	C31	C32	121.13(17)	N12	C31	C32	119.75(16)
N12	C31	C36	119.74(16)	N12	C31	C36	120.25(16)
C32	C31	C36	118.92(17)	C32	C31	C36	119.71(17)
C31	C32	C33	120.52(19)	C31	C32	C33	119.83(18)
C32	C33	C34	120.02(19)	C32	C33	C34	120.42(18)
C33	C34	C35	119.80(19)	C33	C34	C35	119.55(19)
C34	C35	C36	120.27(19)	C34	C35	C36	120.5(2)
C31	C36	C35	120.46(19)	C31	C36	C35	119.95(19)
N22	C41	C42	119.81(16)	N22	C41	C42	119.41(15)
N22	C41	C46	120.14(16)	N22	C41	C46	120.42(16)
C42	C41	C46	120.03(17)	C42	C41	C46	120.17(17)
C41	C42	C43	119.93(18)	C41	C42	C43	120.06(18)
C42	C43	C44	120.47(19)	C42	C43	C44	119.93(19)
C43	C44	C45	119.57(19)	C43	C44	C45	119.48(19)

C44	C45	C46	120.48(19)	C44	C45	C46	121.19(19)
C41	C46	C45	119.51(19)	C41	C46	C45	119.16(19)
F1	B1	F2	108.17(16)	F1	B1	F2	108.22(16)
F1	B1	N11	110.19(16)	F1	B1	N11	111.30(16)
F1	B1	N22	110.03(16)	F1	B1	N22	110.13(15)
F2	B1	N11	110.21(16)	F2	B1	N11	109.92(15)
F2	B1	N22	110.08(16)	F2	B1	N22	108.66(15)
N11	B1	N22	108.16(15)	N11	B1	N22	108.59(14)

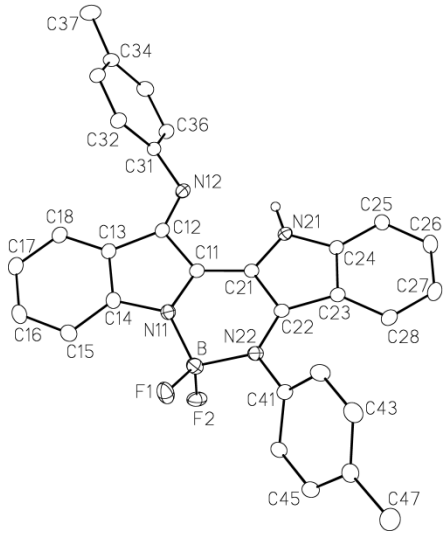

Figure B-6: ORTEP view of **3.3b**. Thermal ellipsoids at the 50% probability level with all hydrogen atoms, with the exception of the N-H atom, removed for clarity

Table B-6: Bond lengths (Å) and angles (^{o}) for **3.3b**

F1	B	1.372(3)	C22	C23	1.448(3)
F2	B	1.413(3)	C23	C24	1.418(3)
N11	C11	1.353(2)	C23	C28	1.411(3)
N11	C14	1.416(2)	C24	C25	1.390(3)
N11	B	1.539(3)	C25	C26	1.370(3)
N12	C12	1.287(2)	C26	C27	1.399(3)

N12	C31	1.413(2)	C27	C28	1.369(3)
N21	C21	1.376(2)	C31	C32	1.392(3)
N21	C24	1.374(2)	C31	C36	1.381(3)
N22	C22	1.349(2)	C32	C33	1.385(3)
N22	C41	1.437(2)	C33	C34	1.385(3)
N22	B	1.571(3)	C34	C35	1.388(3)
C11	C12	1.469(2)	C34	C37	1.504(3)
C11	C21	1.374(3)	C35	C36	1.380(3)
C12	C13	1.469(3)	C41	C42	1.387(3)
C13	C14	1.401(3)	C41	C46	1.388(3)
C13	C18	1.398(3)	C42	C43	1.379(3)
C14	C15	1.386(3)	C43	C44	1.385(3)
C15	C16	1.392(3)	C44	C45	1.385(3)
C16	C17	1.389(3)	C44	C47	1.507(3)
C17	C18	1.381(3)	C45	C46	1.386(3)
C21	C22	1.423(2)			

C11	N11	C14	107.50(16)	N21	C24	C23	109.75(16)
C11	N11	B	122.09(16)	N21	C24	C25	127.74(17)
C14	N11	B	129.40(17)	C23	C24	C25	122.51(17)
C12	N12	C31	123.10(16)	C24	C25	C26	117.49(18)
C21	N21	C24	108.38(15)	C25	C26	C27	121.36(19)
C22	N22	C41	120.50(16)	C26	C27	C28	121.68(19)
C22	N22	B	120.42(15)	C23	C28	C27	118.84(18)
C41	N22	B	118.91(15)	N12	C31	C32	122.86(17)
N11	C11	C12	111.05(16)	N12	C31	C36	117.63(17)
N11	C11	C21	120.09(17)	C32	C31	C36	118.85(18)
C12	C11	C21	128.81(18)	C31	C32	C33	119.93(19)
N12	C12	C11	119.06(17)	C32	C33	C34	121.44(19)
N12	C12	C13	136.91(18)	C33	C34	C35	117.95(18)
C11	C12	C13	103.97(16)	C33	C34	C37	121.2(2)
C12	C13	C14	106.93(16)	C35	C34	C37	120.8(2)
C12	C13	C18	133.39(19)	C34	C35	C36	121.07(19)
C14	C13	C18	119.42(19)	C31	C36	C35	120.74(19)
N11	C14	C13	110.56(17)	N22	C41	C42	120.75(17)
N11	C14	C15	127.34(18)	N22	C41	C46	120.34(16)
C13	C14	C15	122.06(18)	C42	C41	C46	118.90(18)
C14	C15	C16	117.1(2)	C41	C42	C43	120.05(19)
C15	C16	C17	121.8(2)	C42	C43	C44	121.96(19)
C16	C17	C18	120.6(2)	C43	C44	C45	117.24(19)

C13	C18	C17	118.9(2)	C43	C44	C47	121.7(2)
N21	C21	C11	127.38(17)	C45	C44	C47	121.0(2)
N21	C21	C22	109.93(16)	C44	C45	C46	121.74(19)
C11	C21	C22	122.59(18)	C41	C46	C45	119.90(18)
N22	C22	C21	119.70(17)	F1	B	F2	109.23(18)
N22	C22	C23	134.67(17)	F1	B	N11	111.32(19)
C21	C22	C23	105.62(16)	F1	B	N22	111.15(17)
C22	C23	C24	106.30(16)	F2	B	N11	109.08(16)
C22	C23	C28	135.46(18)	F2	B	N22	108.07(18)
C24	C23	C28	118.08(17)	N11	B	N22	107.92(16)

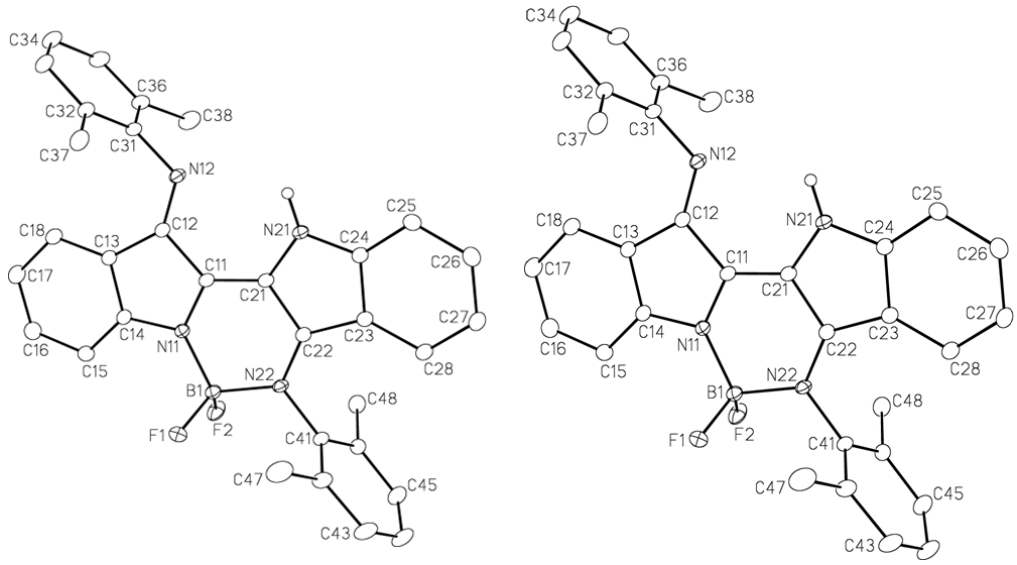

Figure B-7: ORTEP view of the two crystallographically independent molecules of **3.3c**, A (left) and B (right). Thermal ellipsoids at the 50% probability level with all hydrogen atoms, with the exception of the N-H atoms, removed for clarity

Table B-7: Bond lengths (Å) and angles (^{o}) for **3.3c**

Molecule A			*Molecule B*		
F1	B1	1.396(2)	F1	B1	1.385(2)
F2	B1	1.389(2)	F2	B1	1.396(2)
N11	C11	1.3558(19)	N11	C11	1.3566(18)
N11	C14	1.4122(19)	N11	C14	1.4093(19)
N11	B1	1.539(2)	N11	B1	1.533(2)
N12	C12	1.2859(19)	N12	C12	1.2811(19)
N12	C31	1.4245(19)	N12	C31	1.4259(18)
N21	C21	1.3765(19)	N21	C21	1.3790(19)
N21	C24	1.3668(19)	N21	C24	1.3709(19)
N22	C22	1.3421(18)	N22	C22	1.3363(19)
N22	C41	1.4454(18)	N22	C41	1.4468(18)
N22	B1	1.555(2)	N22	B1	1.557(2)
C11	C12	1.485(2)	C11	C12	1.477(2)
C11	C21	1.366(2)	C11	C21	1.366(2)

C12	C13	1.466(2)	C12	C13	1.471(2)
C13	C14	1.407(2)	C13	C14	1.404(2)
C13	C18	1.392(2)	C13	C18	1.390(2)
C14	C15	1.374(2)	C14	C15	1.381(2)
C15	C16	1.389(2)	C15	C16	1.386(2)
C16	C17	1.386(2)	C16	C17	1.385(3)
C17	C18	1.385(2)	C17	C18	1.381(2)
C21	C22	1.425(2)	C21	C22	1.423(2)
C22	C23	1.438(2)	C22	C23	1.441(2)
C23	C24	1.418(2)	C23	C24	1.416(2)
C23	C28	1.406(2)	C23	C28	1.407(2)
C24	C25	1.388(2)	C24	C25	1.393(2)
C25	C26	1.373(2)	C25	C26	1.376(2)
C26	C27	1.400(3)	C26	C27	1.400(2)
C27	C28	1.370(2)	C27	C28	1.367(2)
C31	C32	1.400(2)	C31	C32	1.399(2)
C31	C36	1.401(2)	C31	C36	1.398(2)
C32	C33	1.388(2)	C32	C33	1.388(2)
C32	C37	1.499(2)	C32	C37	1.504(2)
C33	C34	1.373(3)	C33	C34	1.378(2)
C34	C35	1.378(3)	C34	C35	1.379(2)
C35	C36	1.393(2)	C35	C36	1.391(2)
C36	C38	1.503(3)	C36	C38	1.504(2)
C41	C42	1.390(2)	C41	C42	1.396(2)
C41	C46	1.403(3)	C41	C46	1.398(2)
C42	C43	1.414(3)	C42	C43	1.391(2)
C42	C47	1.491(3)	C42	C47	1.503(2)
C43	C44	1.379(4)	C43	C44	1.375(3)
C44	C45	1.356(4)	C44	C45	1.381(3)
C45	C46	1.380(3)	C45	C46	1.391(2)
C46	C48	1.494(3)	C46	C48	1.501(2)

Molecule A				*Molecule B*			
C11	N11	C14	107.95(12)	C11	N11	C14	107.93(12)
C11	N11	B1	124.90(13)	C11	N11	B1	125.43(12)
C14	N11	B1	127.15(12)	C14	N11	B1	126.58(12)
C12	N12	C31	120.86(13)	C12	N12	C31	118.05(13)
C21	N21	C24	108.65(12)	C21	N21	C24	108.20(12)
C22	N22	C41	117.67(12)	C22	N22	C41	117.68(12)

C22	N22	B1	123.12(12)	C22	N22	B1	123.51(12)
C41	N22	B1	118.84(12)	C41	N22	B1	118.65(12)
N11	C11	C12	110.32(13)	N11	C11	C12	110.43(12)
N11	C11	C21	120.33(13)	N11	C11	C21	120.34(13)
C12	C11	C21	129.22(14)	C12	C11	C21	129.23(13)
N12	C12	C11	120.22(13)	N12	C12	C11	120.50(13)
N12	C12	C13	135.63(14)	N12	C12	C13	135.31(14)
C11	C12	C13	104.15(12)	C11	C12	C13	104.16(12)
C12	C13	C14	106.83(13)	C12	C13	C14	106.64(13)
C12	C13	C18	133.55(14)	C12	C13	C18	133.32(14)
C14	C13	C18	119.62(14)	C14	C13	C18	120.04(15)
N11	C14	C13	110.73(13)	N11	C14	C13	110.81(13)
N11	C14	C15	127.41(14)	N11	C14	C15	127.30(14)
C13	C14	C15	121.86(14)	C13	C14	C15	121.89(14)
C14	C15	C16	117.60(15)	C14	C15	C16	116.96(15)
C15	C16	C17	121.51(16)	C15	C16	C17	121.88(17)
C16	C17	C18	120.78(15)	C16	C17	C18	121.08(16)
C13	C18	C17	118.61(15)	C13	C18	C17	118.12(16)
N21	C21	C11	129.27(14)	N21	C21	C11	129.23(13)
N21	C21	C22	109.16(13)	N21	C21	C22	109.46(12)
C11	C21	C22	121.49(13)	C11	C21	C22	121.31(13)
N22	C22	C21	121.10(13)	N22	C22	C21	121.23(13)
N22	C22	C23	132.70(13)	N22	C22	C23	132.64(13)
C21	C22	C23	106.20(12)	C21	C22	C23	106.11(12)
C22	C23	C24	106.07(13)	C22	C23	C24	106.04(13)
C22	C23	C28	135.17(14)	C22	C23	C28	134.77(14)
C24	C23	C28	118.76(14)	C24	C23	C28	119.17(14)
N21	C24	C23	109.90(13)	N21	C24	C23	110.05(13)
N21	C24	C25	128.01(14)	N21	C24	C25	127.91(14)
C23	C24	C25	122.08(14)	C23	C24	C25	122.04(14)
C24	C25	C26	117.48(16)	C24	C25	C26	116.90(15)
C25	C26	C27	121.60(16)	C25	C26	C27	122.00(16)
C26	C27	C28	121.31(16)	C26	C27	C28	121.38(16)
C23	C28	C27	118.75(16)	C23	C28	C27	118.43(15)
N12	C31	C32	120.18(14)	N12	C31	C32	119.19(14)
N12	C31	C36	118.54(15)	N12	C31	C36	118.84(14)
C32	C31	C36	120.96(15)	C32	C31	C36	121.88(14)
C31	C32	C33	118.62(16)	C31	C32	C33	117.80(15)
C31	C32	C37	121.98(15)	C31	C32	C37	120.45(14)
C33	C32	C37	119.40(17)	C33	C32	C37	121.74(15)
C32	C33	C34	121.27(18)	C32	C33	C34	121.24(16)

C33	C34	C35	119.54(17)	C33	C34	C35	120.06(16)
C34	C35	C36	121.63(17)	C34	C35	C36	121.04(16)
C31	C36	C35	117.90(16)	C31	C36	C35	117.88(15)
C31	C36	C38	121.26(15)	C31	C36	C38	121.08(15)
C35	C36	C38	120.84(16)	C35	C36	C38	121.04(15)
N22	C41	C42	119.72(16)	N22	C41	C42	118.91(13)
N22	C41	C46	117.85(15)	N22	C41	C46	118.55(13)
C42	C41	C46	122.40(16)	C42	C41	C46	122.52(14)
C41	C42	C43	116.2(2)	C41	C42	C43	117.39(15)
C41	C42	C47	122.63(16)	C41	C42	C47	122.72(15)
C43	C42	C47	121.2(2)	C43	C42	C47	119.85(16)
C42	C43	C44	121.6(2)	C42	C43	C44	121.40(17)
C43	C44	C45	120.1(2)	C43	C44	C45	120.05(16)
C44	C45	C46	121.4(2)	C44	C45	C46	121.15(16)
C41	C46	C45	118.2(2)	C41	C46	C45	117.48(15)
C41	C46	C48	121.87(17)	C41	C46	C48	121.80(14)
C45	C46	C48	119.9(2)	C45	C46	C48	120.66(15)
F1	B1	F2	107.18(13)	F1	B1	F2	107.53(13)
F1	B1	N11	109.37(14)	F1	B1	N11	110.62(13)
F1	B1	N22	110.49(13)	F1	B1	N22	110.58(14)
F2	B1	N11	111.88(13)	F2	B1	N11	110.02(13)
F2	B1	N22	109.76(14)	F2	B1	N22	110.21(13)
N11	B1	N22	108.18(12)	N11	B1	N22	107.89(12)

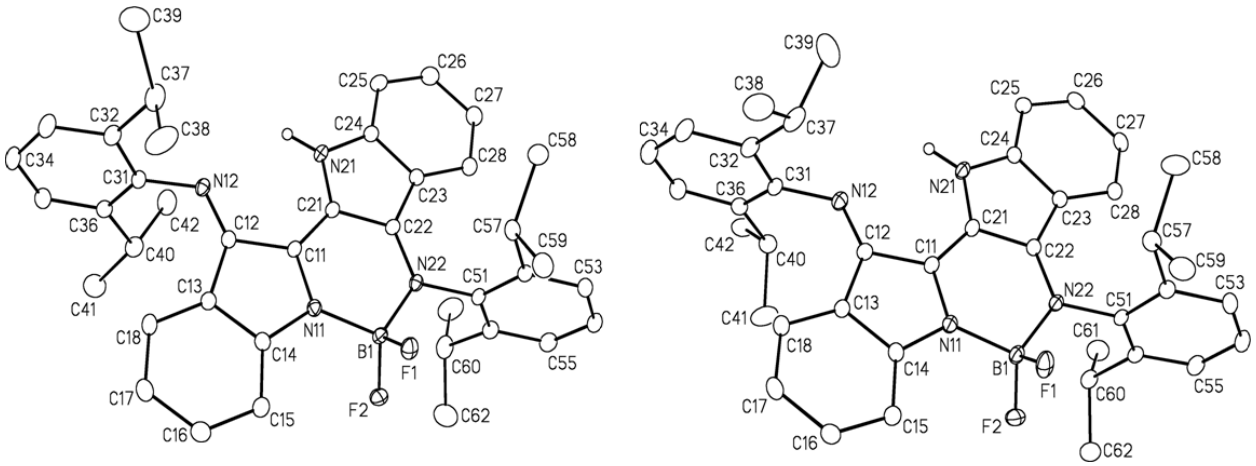

Figure B-8: ORTEP view of the two crystallographically independent molecules of **3.3d**, A (left) and B (right). Thermal ellipsoids at the 50% probability level with all hydrogen atoms, with the exception of the N-H atoms, removed for clarity

Table B-8: Bond lengths (Å) and angles (^{o}) for **3.3d**

Molecule A			*Molecule B*		
F1	B1	1.392(2)	F1	B1	1.399(2)
F2	B1	1.402(2)	F2	B1	1.382(3)
N11	C11	1.357(2)	N11	C11	1.362(2)
N11	C14	1.418(2)	N11	C14	1.412(2)
N11	B1	1.537(3)	N11	B1	1.534(3)
N12	C12	1.280(2)	N12	C12	1.289(2)
N12	C31	1.425(2)	N12	C31	1.428(2)
N21	C21	1.382(2)	N21	C21	1.384(2)
N21	C24	1.375(2)	N21	C24	1.371(2)
N22	C22	1.336(2)	N22	C22	1.337(2)
N22	C51	1.452(2)	N22	C51	1.456(2)
N22	B1	1.559(3)	N22	B1	1.569(3)
C11	C12	1.476(2)	C11	C12	1.469(3)
C11	C21	1.370(3)	C11	C21	1.364(3)
C12	C13	1.474(3)	C12	C13	1.473(2)
C13	C14	1.408(3)	C13	C14	1.405(3)
C13	C18	1.391(3)	C13	C18	1.389(3)
C14	C15	1.382(3)	C14	C15	1.388(3)

C15	C16	1.392(3)		C15	C16	1.385(3)	
C16	C17	1.392(3)		C16	C17	1.389(3)	
C17	C18	1.383(3)		C17	C18	1.385(3)	
C21	C22	1.423(2)		C21	C22	1.420(2)	
C22	C23	1.444(2)		C22	C23	1.446(2)	
C23	C24	1.423(2)		C23	C24	1.418(3)	
C23	C28	1.405(3)		C23	C28	1.408(3)	
C24	C25	1.389(3)		C24	C25	1.396(3)	
C25	C26	1.373(3)		C25	C26	1.368(3)	
C26	C27	1.397(3)		C26	C27	1.410(3)	
C27	C28	1.381(3)		C27	C28	1.377(3)	
C31	C32	1.407(3)		C31	C32	1.406(3)	
C31	C36	1.403(3)		C31	C36	1.405(3)	
C32	C33	1.390(3)		C32	C33	1.388(3)	
C32	C37	1.516(3)		C32	C37	1.519(3)	
C33	C34	1.376(3)		C33	C34	1.375(3)	
C34	C35	1.385(3)		C34	C35	1.382(3)	
C35	C36	1.393(3)		C35	C36	1.391(3)	
C36	C40	1.518(3)		C36	C40	1.519(3)	
C37	C38	1.526(3)		C37	C38	1.514(3)	
C37	C39	1.512(3)		C37	C39	1.526(3)	
C40	C41	1.521(3)		C40	C41	1.528(3)	
C40	C42	1.533(3)		C40	C42	1.518(3)	
C51	C52	1.405(3)		C51	C52	1.398(2)	
C51	C56	1.403(2)		C51	C56	1.399(3)	
C52	C53	1.390(3)		C52	C53	1.393(3)	
C52	C57	1.523(2)		C52	C57	1.521(3)	
C53	C54	1.384(3)		C53	C54	1.380(3)	
C54	C55	1.376(3)		C54	C55	1.378(3)	
C55	C56	1.393(3)		C55	C56	1.394(3)	
C56	C60	1.517(3)		C56	C60	1.524(3)	
C57	C58	1.534(3)		C57	C58	1.530(3)	
C57	C59	1.525(3)		C57	C59	1.519(3)	
C60	C61	1.526(3)		C60	C61	1.532(3)	
C60	C62	1.514(3)		C60	C62	1.533(3)	

Molecule A				*Molecule B*			
C11	N11	C14	108.01(14)	C11	N11	C14	107.61(15)
C11	N11	B1	124.95(15)	C11	N11	B1	125.20(16)

C14	N11	B1	126.98(15)	C14	N11	B1	127.17(15)
C12	N12	C31	119.74(16)	C12	N12	C31	120.64(16)
C21	N21	C24	108.35(15)	C21	N21	C24	108.02(15)
C22	N22	C51	118.44(14)	C22	N22	C51	117.52(15)
C22	N22	B1	123.85(15)	C22	N22	B1	124.06(15)
C51	N22	B1	117.70(14)	C51	N22	B1	118.41(14)
N11	C11	C12	110.54(15)	N11	C11	C12	110.42(16)
N11	C11	C21	120.87(16)	N11	C11	C21	120.85(17)
C12	C11	C21	128.58(16)	C12	C11	C21	128.73(16)
N12	C12	C11	120.18(16)	N12	C12	C11	119.60(17)
N12	C12	C13	135.58(17)	N12	C12	C13	135.75(18)
C11	C12	C13	104.24(15)	C11	C12	C13	104.64(15)
C12	C13	C14	106.78(16)	C12	C13	C14	106.24(16)
C12	C13	C18	133.49(17)	C12	C13	C18	133.67(17)
C14	C13	C18	119.72(17)	C14	C13	C18	120.07(17)
N11	C14	C13	110.41(16)	N11	C14	C13	111.04(16)
N11	C14	C15	127.66(17)	N11	C14	C15	127.40(17)
C13	C14	C15	121.93(17)	C13	C14	C15	121.55(18)
C14	C15	C16	117.11(19)	C14	C15	C16	117.30(18)
C15	C16	C17	121.88(19)	C15	C16	C17	121.76(19)
C16	C17	C18	120.47(19)	C16	C17	C18	120.84(19)
C13	C18	C17	118.89(18)	C13	C18	C17	118.47(18)
N21	C21	C11	129.53(16)	N21	C21	C11	129.10(17)
N21	C21	C22	109.39(15)	N21	C21	C22	109.48(16)
C11	C21	C22	121.08(16)	C11	C21	C22	121.41(16)
N22	C22	C21	121.20(16)	N22	C22	C21	120.92(16)
N22	C22	C23	132.37(16)	N22	C22	C23	132.74(17)
C21	C22	C23	106.43(15)	C21	C22	C23	106.35(15)
C22	C23	C24	105.85(16)	C22	C23	C24	105.71(16)
C22	C23	C28	135.04(17)	C22	C23	C28	134.92(17)
C24	C23	C28	119.10(16)	C24	C23	C28	119.36(17)
N21	C24	C23	109.96(16)	N21	C24	C23	110.40(16)
N21	C24	C25	128.37(17)	N21	C24	C25	127.89(17)
C23	C24	C25	121.65(18)	C23	C24	C25	121.71(18)
C24	C25	C26	117.63(18)	C24	C25	C26	117.54(18)
C25	C26	C27	122.03(19)	C25	C26	C27	121.90(18)
C26	C27	C28	120.96(19)	C26	C27	C28	121.00(18)
C23	C28	C27	118.62(18)	C23	C28	C27	118.48(17)
N12	C31	C32	118.44(16)	N12	C31	C32	119.54(17)
N12	C31	C36	119.11(16)	N12	C31	C36	117.75(17)
C32	C31	C36	122.23(17)	C32	C31	C36	122.49(18)

C31	C32	C33	117.39(18)	C31	C32	C33	117.11(19)
C31	C32	C37	119.92(18)	C31	C32	C37	120.85(18)
C33	C32	C37	122.68(18)	C33	C32	C37	121.99(19)
C32	C33	C34	121.64(19)	C32	C33	C34	121.6(2)
C33	C34	C35	119.9(2)	C33	C34	C35	120.4(2)
C34	C35	C36	121.37(19)	C34	C35	C36	121.0(2)
C31	C36	C35	117.39(18)	C31	C36	C35	117.44(19)
C31	C36	C40	119.92(17)	C31	C36	C40	119.91(17)
C35	C36	C40	122.66(18)	C35	C36	C40	122.64(18)
C32	C37	C38	111.2(2)	C32	C37	C38	113.7(2)
C32	C37	C39	113.54(19)	C32	C37	C39	110.61(19)
C38	C37	C39	110.40(19)	C38	C37	C39	110.8(2)
C36	C40	C41	114.46(19)	C36	C40	C41	110.92(18)
C36	C40	C42	109.96(17)	C36	C40	C42	113.42(18)
C41	C40	C42	109.81(19)	C41	C40	C42	110.04(18)
N22	C51	C52	118.70(15)	N22	C51	C52	118.18(16)
N22	C51	C56	118.77(16)	N22	C51	C56	118.88(16)
C52	C51	C56	122.51(17)	C52	C51	C56	122.91(17)
C51	C52	C53	117.58(17)	C51	C52	C53	117.09(17)
C51	C52	C57	122.44(16)	C51	C52	C57	123.02(17)
C53	C52	C57	119.96(17)	C53	C52	C57	119.86(17)
C52	C53	C54	121.06(19)	C52	C53	C54	121.34(19)
C53	C54	C55	120.10(19)	C53	C54	C55	120.23(19)
C54	C55	C56	121.71(18)	C54	C55	C56	121.14(19)
C51	C56	C55	116.99(18)	C51	C56	C55	117.29(17)
C51	C56	C60	122.74(17)	C51	C56	C60	122.81(17)
C55	C56	C60	120.19(17)	C55	C56	C60	119.88(17)
C52	C57	C58	111.14(15)	C52	C57	C58	111.09(17)
C52	C57	C59	111.06(16)	C52	C57	C59	112.06(17)
C58	C57	C59	110.19(16)	C58	C57	C59	110.15(17)
C56	C60	C61	111.01(19)	C56	C60	C61	111.00(17)
C56	C60	C62	112.26(19)	C56	C60	C62	111.47(16)
C61	C60	C62	110.33(19)	C61	C60	C62	110.58(17)
F1	B1	F2	107.29(15)	F1	B1	F2	108.30(16)
F1	B1	N11	111.03(15)	F1	B1	N11	110.09(16)

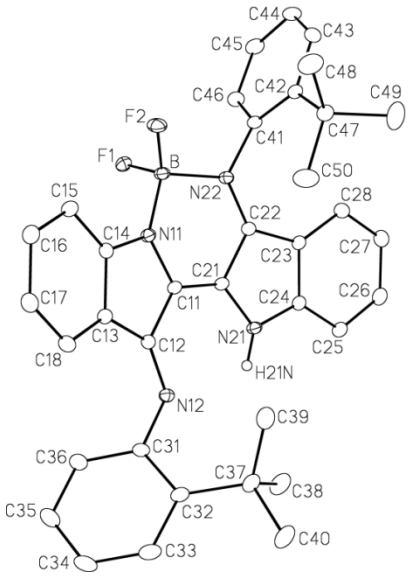

Figure B-9: ORTEP view of **3.3e**. Thermal ellipsoids at the 50% probability level with all hydrogen atoms, with the exception of the N-H atom, removed for clarity

Table B-9: Bond lengths (Å) and angles (^{o}) for **3.3e**

F1	B	1.403(2)	C24	C25	1.396(2)
F2	B	1.3777(19)	C25	C26	1.373(2)
N11	C11	1.3625(18)	C26	C27	1.401(2)
N11	C14	1.4136(19)	C27	C28	1.377(2)
N11	B	1.538(2)	C31	C32	1.411(2)
N12	C12	1.2871(18)	C31	C36	1.393(2)
N12	C31	1.4257(19)	C32	C33	1.399(2)
N21	C21	1.3861(18)	C32	C37	1.535(2)
N21	C24	1.3745(19)	C33	C34	1.383(3)
N22	C22	1.3327(18)	C34	C35	1.378(3)
N22	C41	1.4474(18)	C35	C36	1.381(2)
N22	B	1.562(2)	C37	C38	1.540(2)
C11	C12	1.477(2)	C37	C39	1.540(3)
C11	C21	1.373(2)	C37	C40	1.536(2)
C12	C13	1.476(2)	C41	C42	1.399(2)
C13	C14	1.405(2)	C41	C46	1.396(2)
C13	C18	1.398(2)	C42	C43	1.408(2)
C14	C15	1.384(2)	C42	C47	1.545(2)

C15	C16	1.386(2)	C43	C44	1.377(2)
C16	C17	1.391(2)	C44	C45	1.379(3)
C17	C18	1.385(2)	C45	C46	1.381(2)
C21	C22	1.434(2)	C47	C48	1.528(2)
C22	C23	1.442(2)	C47	C49	1.539(3)
C23	C24	1.417(2)	C47	C50	1.529(2)
C23	C28	1.403(2)			

C11	N11	C14	107.82(12)	C23	C28	C27	118.50(15)
C11	N11	B	123.20(12)	N12	C31	C32	120.28(14)
C14	N11	B	128.97(12)	N12	C31	C36	118.52(14)
C12	N12	C31	119.92(13)	C32	C31	C36	121.02(14)
C21	N21	C24	108.58(12)	C31	C32	C33	115.77(15)
C22	N22	C41	121.44(12)	C31	C32	C37	122.10(14)
C22	N22	B	121.41(12)	C33	C32	C37	122.13(14)
C41	N22	B	116.35(11)	C32	C33	C34	123.10(16)
N11	C11	C12	110.36(12)	C33	C34	C35	119.97(16)
N11	C11	C21	119.51(13)	C34	C35	C36	119.00(17)
C12	C11	C21	129.66(13)	C31	C36	C35	121.13(16)
N12	C12	C11	120.45(13)	C32	C37	C38	109.12(15)
N12	C12	C13	135.23(14)	C32	C37	C39	111.67(13)
C11	C12	C13	104.14(12)	C32	C37	C40	111.76(14)
C12	C13	C14	106.69(13)	C38	C37	C39	110.34(16)
C12	C13	C18	133.69(14)	C38	C37	C40	107.37(14)
C14	C13	C18	119.51(14)	C39	C37	C40	106.48(15)
N11	C14	C13	110.75(13)	N22	C41	C42	123.37(13)
N11	C14	C15	127.23(14)	N22	C41	C46	114.53(13)
C13	C14	C15	121.98(14)	C42	C41	C46	121.93(14)
C14	C15	C16	117.34(15)	C41	C42	C43	115.08(15)
C15	C16	C17	121.79(15)	C41	C42	C47	128.16(14)
C16	C17	C18	120.66(15)	C43	C42	C47	116.75(14)
C13	C18	C17	118.68(15)	C42	C43	C44	123.29(16)
N21	C21	C11	129.43(14)	C43	C44	C45	120.10(15)
N21	C21	C22	108.65(13)	C44	C45	C46	118.84(16)
C11	C21	C22	121.29(13)	C41	C46	C45	120.70(16)
N22	C22	C21	120.57(13)	C42	C47	C48	108.83(13)
N22	C22	C23	132.84(14)	C42	C47	C49	108.04(15)
C21	C22	C23	106.51(12)	C42	C47	C50	116.73(14)
C22	C23	C24	106.05(13)	C48	C47	C49	109.70(16)
C22	C23	C28	134.37(14)	C48	C47	C50	107.33(16)

C24	C23	C28	119.59(14)	C49	C47	C50	106.06(16)
N21	C24	C23	110.13(13)	F1	B	F2	109.47(13)
N21	C24	C25	128.29(14)	F1	B	N11	110.09(13)
C23	C24	C25	121.56(14)	F1	B	N22	108.50(13)
C24	C25	C26	117.26(15)	F2	B	N11	111.48(13)
C25	C26	C27	122.19(15)	F2	B	N22	110.53(13)
C26	C27	C28	120.88(16)	N11	B	N22	106.70(12)

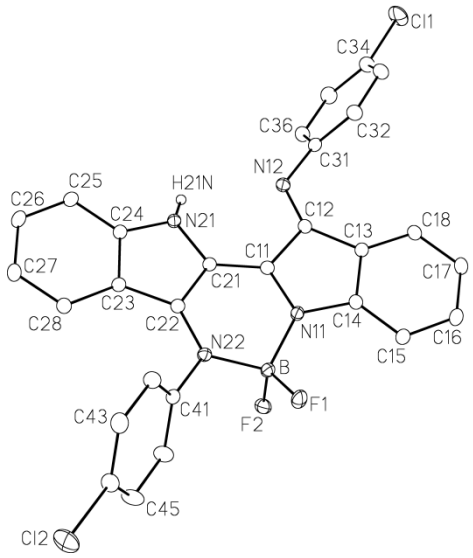

Figure B-10: ORTEP view of **3.3f.** Thermal ellipsoids at the 50% probability level with all hydrogen atoms, with the exception of the N-H atom, removed for clarity

Table B-10: Bond lengths (**Å**) and angles (^{o}) for **3.3f**

Cl1	C34	1.7420(16)	C16	C17	1.390(2)
Cl2	C44	1.7403(16)	C17	C18	1.385(2)
F1	B	1.3721(19)	C21	C22	1.4246(19)
F2	B	1.4157(19)	C22	C23	1.4417(19)
N11	C11	1.3526(18)	C23	C24	1.4200(19)
N11	C14	1.4138(18)	C23	C28	1.407(2)

N11	B	1.5466(19)	C24	C25	1.398(2)
N12	C12	1.2861(19)	C25	C26	1.377(2)
N12	C31	1.4119(18)	C26	C27	1.406(2)
N21	C21	1.3785(18)	C27	C28	1.376(2)
N21	C24	1.3716(18)	C31	C32	1.388(2)
N21	H21N	0.85(2)	C31	C36	1.394(2)
N22	C22	1.3436(18)	C32	C33	1.386(2)
N22	C41	1.4343(17)	C33	C34	1.379(2)
N22	B	1.5610(19)	C34	C35	1.387(2)
C11	C12	1.4776(18)	C35	C36	1.386(2)
C11	C21	1.372(2)	C41	C42	1.381(2)
C12	C13	1.4724(19)	C41	C46	1.381(2)
C13	C14	1.408(2)	C42	C43	1.384(2)
C13	C18	1.397(2)	C43	C44	1.374(3)
C14	C15	1.383(2)	C44	C45	1.382(3)
C15	C16	1.391(2)	C45	C46	1.384(2)

C11	N11	C14	107.72(11)	C24	C23	C28	118.65(13)
C11	N11	B	122.40(11)	N21	C24	C23	110.21(12)
C14	N11	B	129.51(11)	N21	C24	C25	127.85(13)
C12	N12	C31	122.49(12)	C23	C24	C25	121.93(13)
C21	N21	C24	108.20(11)	C24	C25	C26	117.73(13)
C21	N21	H21N	123.9(13)	C25	C26	C27	121.31(14)
C24	N21	H21N	123.8(13)	C26	C27	C28	121.21(14)
C22	N22	C41	119.84(11)	C23	C28	C27	119.10(14)
C22	N22	B	122.15(11)	N12	C31	C32	122.53(13)
C41	N22	B	117.99(11)	N12	C31	C36	117.84(13)
N11	C11	C12	110.84(12)	C32	C31	C36	119.32(14)
N11	C11	C21	120.51(12)	C31	C32	C33	120.68(14)
C12	C11	C21	128.58(13)	C32	C33	C34	119.26(15)
N12	C12	C11	118.88(12)	Cl1	C34	C33	119.18(13)
N12	C12	C13	137.05(13)	Cl1	C34	C35	119.71(13)
C11	C12	C13	103.97(11)	C33	C34	C35	121.10(15)
C12	C13	C14	106.65(12)	C34	C35	C36	119.29(15)
C12	C13	C18	133.85(13)	C31	C36	C35	120.30(15)
C14	C13	C18	119.48(13)	N22	C41	C42	119.78(13)
N11	C14	C13	110.71(12)	N22	C41	C46	120.25(13)
N11	C14	C15	127.31(13)	C42	C41	C46	119.95(14)
C13	C14	C15	121.98(13)	C41	C42	C43	120.75(14)
C14	C15	C16	117.38(14)	C42	C43	C44	118.56(15)

C15	C16	C17	121.57(15)	Cl2	C44	C43	118.62(13)
C16	C17	C18	120.82(14)	Cl2	C44	C45	119.79(14)
C13	C18	C17	118.75(14)	C43	C44	C45	121.59(15)
N21	C21	C11	128.09(13)	C44	C45	C46	119.30(16)
N21	C21	C22	109.49(12)	C41	C46	C45	119.85(15)
C11	C21	C22	122.03(13)	F1	B	F2	108.99(12)
N22	C22	C21	119.95(12)	F1	B	N11	111.87(12)
N22	C22	C23	133.78(13)	F1	B	N22	110.69(12)
C21	C22	C23	106.26(12)	F2	B	N11	109.29(12)
C22	C23	C24	105.82(12)	F2	B	N22	108.07(12)
C22	C23	C28	135.46(13)	N11	B	N22	107.84(11)

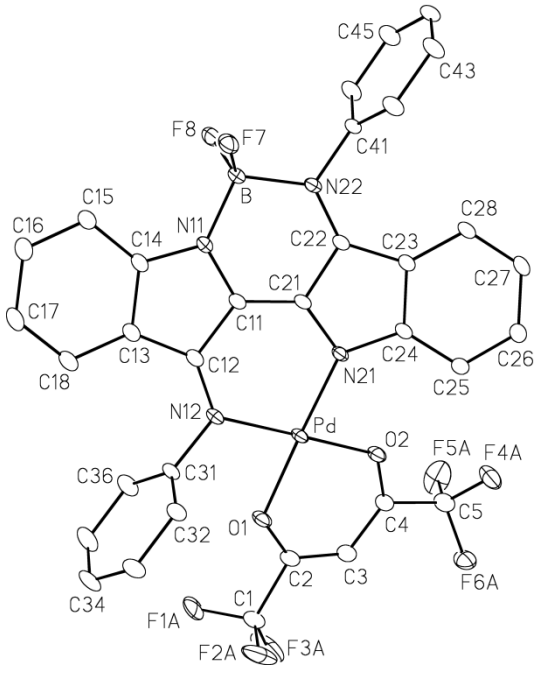

Figure B-11: ORTEP view of **3.6a**. Thermal ellipsoids at the 50% probability level with all hydrogen atoms removed for clarity

Table B-11: Bond lengths (Å) and angles (^{o}) for **3.6a**

Pd	O1	2.0227(18)	C2	C3	1.384(4)
Pd	O2	2.0129(19)	C3	C4	1.392(4)
Pd	N12	2.019(2)	C4	C5	1.531(4)
Pd	N21	1.9969(19)	C11	C12	1.449(3)
F1A	C1	1.341(10)	C11	C21	1.365(3)
F2A	C1	1.270(10)	C12	C13	1.455(4)
F3A	C1	1.250(9)	C13	C14	1.413(4)
F4A	C5	1.316(9)	C13	C18	1.403(4)
F5A	C5	1.250(6)	C14	C15	1.389(4)
F6A	C5	1.371(5)	C15	C16	1.395(4)
F1B	C1	1.291(9)	C16	C17	1.392(5)
F2B	C1	1.374(10)	C17	C18	1.379(4)
F3B	C1	1.236(9)	C21	C22	1.449(3)
F4B	C5	1.275(15)	C22	C23	1.441(3)
F5B	C5	1.423(10)	C23	C24	1.422(3)

F6B	C5	1.268(8)	C23	C28	1.410(3)
F7	B	1.397(4)	C24	C25	1.395(3)
F8	B	1.371(4)	C25	C26	1.385(3)
O1	C2	1.258(3)	C26	C27	1.399(4)
O2	C4	1.260(3)	C27	C28	1.377(4)
N11	C11	1.366(3)	C31	C32	1.379(4)
N11	C14	1.401(3)	C31	C36	1.386(4)
N11	B	1.538(3)	C32	C33	1.392(4)
N12	C12	1.314(3)	C33	C34	1.373(5)
N12	C31	1.448(3)	C34	C35	1.377(5)
N21	C21	1.358(3)	C35	C36	1.396(4)
N21	C24	1.402(3)	C41	C42	1.376(4)
N22	C22	1.323(3)	C41	C46	1.380(4)
N22	C41	1.448(3)	C42	C43	1.391(4)
N22	B	1.588(4)	C43	C44	1.377(5)
C1	C2	1.536(4)	C44	C45	1.372(5)
			C45	C46	1.394(4)

O1	Pd	O2	90.39(8)	N11	C11	C21	121.7(2)
O1	Pd	N12	87.60(8)	C12	C11	C21	126.7(2)
O1	Pd	N21	176.94(8)	N12	C12	C11	122.0(2)
O2	Pd	N12	175.65(8)	N12	C12	C13	133.2(2)
O2	Pd	N21	89.65(8)	C11	C12	C13	104.8(2)
N12	Pd	N21	92.57(8)	C12	C13	C14	106.2(2)
Pd	O1	C2	124.78(18)	C12	C13	C18	134.7(3)
Pd	O2	C4	124.62(18)	C14	C13	C18	119.1(3)
C11	N11	C14	106.7(2)	N11	C14	C13	111.0(2)
C11	N11	B	124.7(2)	N11	C14	C15	126.8(2)
C14	N11	B	128.2(2)	C13	C14	C15	122.2(2)
Pd	N12	C12	125.51(17)	C14	C15	C16	117.3(3)
Pd	N12	C31	116.41(16)	C15	C16	C17	121.1(3)
C12	N12	C31	118.1(2)	C16	C17	C18	121.6(3)
Pd	N21	C21	120.53(16)	C13	C18	C17	118.6(3)
Pd	N21	C24	132.56(17)	N21	C21	C11	127.4(2)
C21	N21	C24	106.13(19)	N21	C21	C22	111.7(2)
C22	N22	C41	118.7(2)	C11	C21	C22	120.8(2)
C22	N22	B	124.5(2)	N22	C22	C21	120.6(2)
C41	N22	B	116.8(2)	N22	C22	C23	134.3(2)
F1A	C1	F2A	103.4(8)	C21	C22	C23	105.1(2)
F1A	C1	F3A	105.7(7)	C22	C23	C24	105.8(2)

F1A	C1	C2	110.2(5)	C22	C23	C28	134.1(2)
F2A	C1	F3A	112.7(9)	C24	C23	C28	120.1(2)
F2A	C1	C2	110.4(6)	N21	C24	C23	111.2(2)
F3A	C1	C2	113.9(6)	N21	C24	C25	128.5(2)
F1B	C1	F2B	100.8(7)	C23	C24	C25	120.2(2)
F1B	C1	F3B	111.6(9)	C24	C25	C26	118.2(2)
F1B	C1	C2	110.9(6)	C25	C26	C27	122.1(2)
F2B	C1	F3B	107.1(7)	C26	C27	C28	120.4(2)
F2B	C1	C2	110.5(5)	C23	C28	C27	118.8(2)
F3B	C1	C2	114.9(5)	N12	C31	C32	118.5(2)
O1	C2	C1	112.3(3)	N12	C31	C36	120.1(2)
O1	C2	C3	129.0(2)	C32	C31	C36	121.3(2)
C1	C2	C3	118.6(3)	C31	C32	C33	119.2(3)
C2	C3	C4	121.6(3)	C32	C33	C34	120.1(3)
O2	C4	C3	129.4(3)	C33	C34	C35	120.6(3)
O2	C4	C5	112.8(2)	C34	C35	C36	120.3(3)
C3	C4	C5	117.9(2)	C31	C36	C35	118.5(3)
F4A	C5	F5A	110.0(6)	N22	C41	C42	120.5(2)
F4A	C5	F6A	102.8(5)	N22	C41	C46	118.9(2)
F4A	C5	C4	112.8(4)	C42	C41	C46	120.6(2)
F5A	C5	F6A	108.2(4)	C41	C42	C43	119.7(3)
F5A	C5	C4	111.1(4)	C42	C43	C44	120.1(3)
F6A	C5	C4	111.6(3)	C43	C44	C45	119.8(3)
F4B	C5	F5B	101.6(8)	C44	C45	C46	120.7(3)
F4B	C5	F6B	117.6(10)	C41	C46	C45	119.0(3)
F4B	C5	C4	109.7(9)	F7	B	F8	109.5(2)
F5B	C5	F6B	101.8(7)	F7	B	N11	110.5(2)
F5B	C5	C4	109.6(5)	F7	B	N22	108.5(2)
F6B	C5	C4	115.0(5)	F8	B	N11	111.7(2)
N11	C11	C12	111.2(2)	F8	B	N22	109.1(2)
				N11	B	N22	107.6(2)

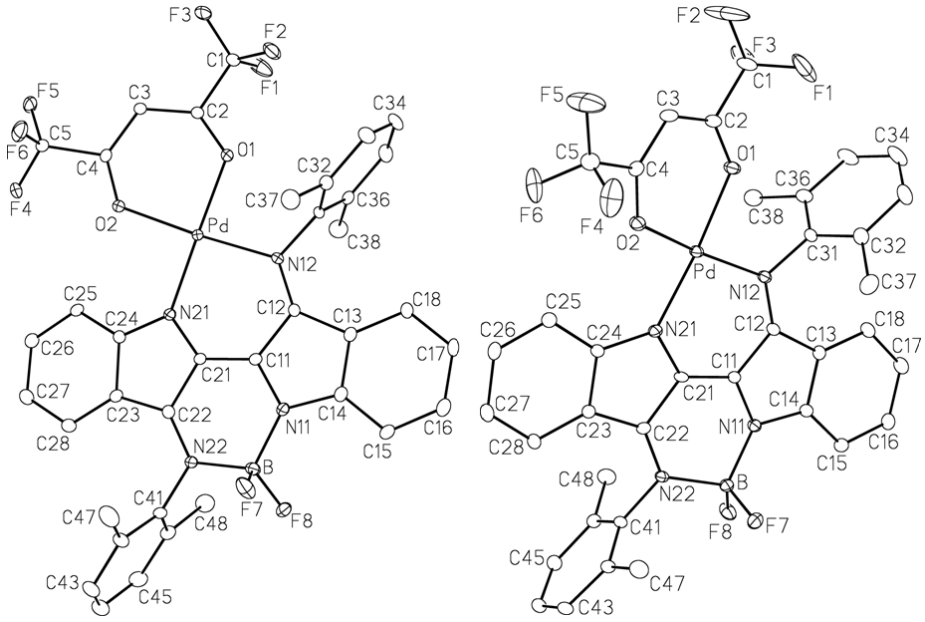

Figure B-12: ORTEP view of the the two crystallographically independent molecules of **3.6c**, A (left) and B (right). Thermal ellipsoids at the 50% probability level with all hydrogen atoms removed for clarity

Table B-12: Bond lengths (Å) and angles (°) for **3.6c**

Molecule A			*Molecule B*		
Pd	O1	2.013(2)	Pd	O1	2.021(2)
Pd	O2	2.0183(19)	Pd	O2	2.029(2)
Pd	N12	2.025(2)	Pd	N12	2.021(2)
Pd	N21	1.998(2)	Pd	N21	2.004(2)
F1	C1	1.318(4)	F1	C1	1.285(4)
F2	C1	1.325(4)	F2	C1	1.279(4)
F3	C1	1.319(4)	F3	C1	1.298(4)
F4	C5	1.319(3)	F4	C5	1.337(4)
F5	C5	1.328(3)	F5	C5	1.283(4)
F6	C5	1.342(4)	F6	C5	1.292(4)
F7	B	1.390(4)	F7	B	1.391(4)
F8	B	1.365(4)	F8	B	1.376(4)
O1	C2	1.264(3)	O1	C2	1.260(4)
O2	C4	1.251(3)	O2	C4	1.255(3)
N11	C11	1.372(4)	N11	C11	1.369(4)

N11	C14	1.394(3)	N11	C14	1.399(3)
N11	B	1.530(4)	N11	B	1.536(4)
N12	C12	1.309(3)	N12	C12	1.316(4)
N12	C31	1.443(3)	N12	C31	1.442(3)
N21	C21	1.356(4)	N21	C21	1.357(4)
N21	C24	1.399(3)	N21	C24	1.396(3)
N22	C22	1.331(4)	N22	C22	1.336(4)
N22	C41	1.439(3)	N22	C41	1.442(3)
N22	B	1.589(4)	N22	B	1.580(4)
C1	C2	1.534(4)	C1	C2	1.525(4)
C2	C3	1.378(4)	C2	C3	1.381(5)
C3	C4	1.389(4)	C3	C4	1.391(4)
C4	C5	1.535(4)	C4	C5	1.540(4)
C11	C12	1.450(4)	C11	C12	1.438(4)
C11	C21	1.370(4)	C11	C21	1.375(4)
C12	C13	1.462(4)	C12	C13	1.462(4)
C13	C14	1.399(4)	C13	C14	1.409(4)
C13	C18	1.408(4)	C13	C18	1.408(4)
C14	C15	1.394(4)	C14	C15	1.391(4)
C15	C16	1.381(4)	C15	C16	1.380(4)
C16	C17	1.392(5)	C16	C17	1.392(4)
C17	C18	1.383(4)	C17	C18	1.381(4)
C21	C22	1.452(4)	C21	C22	1.447(4)
C22	C23	1.436(4)	C22	C23	1.431(4)
C23	C24	1.427(4)	C23	C24	1.435(4)
C23	C28	1.400(4)	C23	C28	1.399(4)
C24	C25	1.395(4)	C24	C25	1.394(4)
C25	C26	1.382(4)	C25	C26	1.379(4)
C26	C27	1.397(4)	C26	C27	1.412(5)
C27	C28	1.380(4)	C27	C28	1.368(4)
C31	C32	1.384(4)	C31	C32	1.401(4)
C31	C36	1.395(4)	C31	C36	1.402(4)
C32	C33	1.396(4)	C32	C33	1.386(4)
C32	C37	1.507(4)	C32	C37	1.516(5)
C33	C34	1.376(5)	C33	C34	1.369(6)
C34	C35	1.369(5)	C34	C35	1.381(6)
C35	C36	1.380(4)	C35	C36	1.391(4)
C36	C38	1.499(4)	C36	C38	1.490(4)
C41	C42	1.396(4)	C41	C42	1.404(4)
C41	C46	1.403(4)	C41	C46	1.398(4)
C42	C43	1.393(4)	C42	C43	1.390(4)

	C42	C47	1.517(4)		C42	C47	1.500(4)
	C43	C44	1.366(5)		C43	C44	1.363(4)
	C44	C45	1.391(5)		C44	C45	1.386(5)
	C45	C46	1.387(4)		C45	C46	1.391(4)
	C46	C48	1.506(5)		C46	C48	1.503(4)

Molecule A				*Molecule B*			
O1	Pd	O2	90.09(8)	O1	Pd	O2	89.70(8)
O1	Pd	N12	86.77(8)	O1	Pd	N12	86.70(9)
O1	Pd	N21	174.79(9)	O1	Pd	N21	172.84(9)
O2	Pd	N12	170.82(8)	O2	Pd	N12	167.96(9)
O2	Pd	N21	90.32(8)	O2	Pd	N21	91.25(9)
N12	Pd	N21	93.59(9)	N12	Pd	N21	93.75(9)
Pd	O1	C2	124.86(18)	Pd	O1	C2	125.2(2)
Pd	O2	C4	124.68(18)	Pd	O2	C4	124.32(19)
C11	N11	C14	106.5(2)	C11	N11	C14	106.9(2)
C11	N11	B	124.1(2)	C11	N11	B	123.4(2)
C14	N11	B	129.4(2)	C14	N11	B	129.0(2)
Pd	N12	C12	125.91(18)	Pd	N12	C12	126.17(19)
Pd	N12	C31	116.34(16)	Pd	N12	C31	117.27(17)
C12	N12	C31	117.3(2)	C12	N12	C31	116.0(2)
Pd	N21	C21	121.27(19)	Pd	N21	C21	121.82(19)
Pd	N21	C24	132.22(18)	Pd	N21	C24	132.54(19)
C21	N21	C24	106.2(2)	C21	N21	C24	105.5(2)
C22	N22	C41	117.6(2)	C22	N22	C41	118.3(2)
C22	N22	B	123.6(2)	C22	N22	B	122.4(2)
C41	N22	B	118.8(2)	C41	N22	B	119.2(2)
F1	C1	F2	106.7(3)	F1	C1	F2	108.4(4)
F1	C1	F3	109.3(3)	F1	C1	F3	105.1(3)
F1	C1	C2	110.1(2)	F1	C1	C2	110.9(3)
F2	C1	F3	106.2(3)	F2	C1	F3	106.3(3)
F2	C1	C2	111.4(3)	F2	C1	C2	113.3(3)
F3	C1	C2	112.8(2)	F3	C1	C2	112.5(3)
O1	C2	C1	112.0(2)	O1	C2	C1	111.9(3)
O1	C2	C3	129.2(3)	O1	C2	C3	129.3(3)
C1	C2	C3	118.8(3)	C1	C2	C3	118.8(3)
C2	C3	C4	121.3(3)	C2	C3	C4	120.8(3)
O2	C4	C3	129.7(3)	O2	C4	C3	130.1(3)
O2	C4	C5	113.1(2)	O2	C4	C5	112.2(3)

C3	C4	C5	117.2(2)	C3	C4	C5	117.7(3)
F4	C5	F5	107.5(2)	F4	C5	F5	103.8(3)
F4	C5	F6	107.5(2)	F4	C5	F6	103.6(3)
F4	C5	C4	112.3(2)	F4	C5	C4	109.6(3)
F5	C5	F6	107.3(2)	F5	C5	F6	111.8(3)
F5	C5	C4	113.0(2)	F5	C5	C4	114.2(3)
F6	C5	C4	109.0(2)	F6	C5	C4	112.9(3)
N11	C11	C12	111.1(2)	N11	C11	C12	111.0(2)
N11	C11	C21	122.3(3)	N11	C11	C21	121.6(2)
C12	C11	C21	126.6(3)	C12	C11	C21	127.4(3)
N12	C12	C11	122.8(2)	N12	C12	C11	122.7(3)
N12	C12	C13	132.8(2)	N12	C12	C13	132.2(2)
C11	C12	C13	104.3(2)	C11	C12	C13	105.1(2)
C12	C13	C14	106.3(2)	C12	C13	C14	105.9(2)
C12	C13	C18	133.2(3)	C12	C13	C18	134.5(3)
C14	C13	C18	120.5(3)	C14	C13	C18	119.6(2)
N11	C14	C13	111.6(2)	N11	C14	C13	111.0(2)
N11	C14	C15	127.2(3)	N11	C14	C15	127.4(2)
C13	C14	C15	121.2(3)	C13	C14	C15	121.6(3)
C14	C15	C16	117.4(3)	C14	C15	C16	117.6(3)
C15	C16	C17	122.2(3)	C15	C16	C17	121.7(3)
C16	C17	C18	120.8(3)	C16	C17	C18	121.3(3)
C13	C18	C17	117.9(3)	C13	C18	C17	118.2(3)
N21	C21	C11	128.2(3)	N21	C21	C11	127.7(3)
N21	C21	C22	111.7(2)	N21	C21	C22	112.3(3)
C11	C21	C22	120.0(3)	C11	C21	C22	119.9(3)
N22	C22	C21	121.1(2)	N22	C22	C21	121.1(3)
N22	C22	C23	133.8(3)	N22	C22	C23	133.7(3)
C21	C22	C23	105.1(2)	C21	C22	C23	105.2(2)
C22	C23	C24	105.8(2)	C22	C23	C24	105.4(2)
C22	C23	C28	133.9(3)	C22	C23	C28	134.0(3)
C24	C23	C28	120.3(3)	C24	C23	C28	120.5(3)
N21	C24	C23	111.2(2)	N21	C24	C23	111.6(2)
N21	C24	C25	128.8(3)	N21	C24	C25	129.6(3)
C23	C24	C25	120.0(2)	C23	C24	C25	118.9(2)
C24	C25	C26	117.9(3)	C24	C25	C26	119.2(3)
C25	C26	C27	122.9(3)	C25	C26	C27	121.9(3)
C26	C27	C28	119.7(3)	C26	C27	C28	119.7(3)
C23	C28	C27	119.2(3)	C23	C28	C27	119.6(3)
N12	C31	C32	118.5(2)	N12	C31	C32	118.5(2)
N12	C31	C36	118.9(2)	N12	C31	C36	118.9(2)

C32	C31	C36	122.6(3)	C32	C31	C36	122.6(3)
C31	C32	C33	117.4(3)	C31	C32	C33	117.3(3)
C31	C32	C37	121.2(3)	C31	C32	C37	120.8(3)
C33	C32	C37	121.5(3)	C33	C32	C37	121.8(3)
C32	C33	C34	120.9(3)	C32	C33	C34	121.3(3)
C33	C34	C35	120.2(3)	C33	C34	C35	120.6(3)
C34	C35	C36	121.2(3)	C34	C35	C36	120.9(3)
C31	C36	C35	117.7(3)	C31	C36	C35	117.2(3)
C31	C36	C38	120.4(3)	C31	C36	C38	120.3(3)
C35	C36	C38	121.9(3)	C35	C36	C38	122.6(3)
N22	C41	C42	120.0(2)	N22	C41	C42	119.8(2)
N22	C41	C46	118.1(3)	N22	C41	C46	118.3(2)
C42	C41	C46	121.9(3)	C42	C41	C46	121.9(2)
C41	C42	C43	118.0(3)	C41	C42	C43	117.3(3)
C41	C42	C47	121.6(3)	C41	C42	C47	121.8(3)
C43	C42	C47	120.4(3)	C43	C42	C47	120.9(3)
C42	C43	C44	121.4(3)	C42	C43	C44	121.9(3)
C43	C44	C45	119.8(3)	C43	C44	C45	119.9(3)
C44	C45	C46	121.4(3)	C44	C45	C46	120.9(3)
C41	C46	C45	117.6(3)	C41	C46	C45	117.9(3)
C41	C46	C48	121.4(3)	C41	C46	C48	122.0(3)
C45	C46	C48	121.0(3)	C45	C46	C48	120.1(3)
F7	B	F8	109.0(3)	F7	B	F8	109.5(2)
F7	B	N11	110.4(2)	F7	B	N11	110.7(2)
F7	B	N22	108.6(3)	F7	B	N22	108.3(2)
F8	B	N11	111.3(3)	F8	B	N11	110.8(3)
F8	B	N22	109.6(2)	F8	B	N22	110.1(2)
N11	B	N22	108.0(2)	N11	B	N22	107.3(2)

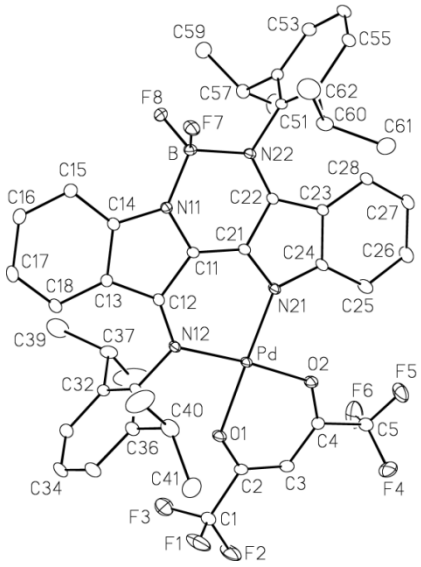

Figure B-13: ORTEP view of **3.6d**, A (left) and B (right). Thermal ellipsoids at the 50% probability level with all hydrogen atoms removed for clarity

Table B-13: Bond lengths (Å) and angles (°) for **3.6d**

Pd	O1	2.025(2)	C15	C16	1.383(4)
Pd	O2	2.021(2)	C16	C17	1.402(5)
Pd	N12	2.034(2)	C17	C18	1.377(4)
Pd	N21	2.013(2)	C21	C22	1.450(4)
F1	C1	1.318(5)	C22	C23	1.431(4)
F2	C1	1.315(4)	C23	C24	1.426(4)
F3	C1	1.307(5)	C23	C28	1.410(4)
F4	C5	1.330(4)	C24	C25	1.397(4)
F5	C5	1.310(4)	C25	C26	1.386(5)
F6	C5	1.293(5)	C26	C27	1.387(5)
F7	B	1.388(4)	C27	C28	1.377(4)
F8	B	1.391(4)	C31	C32	1.396(4)
O1	C2	1.257(4)	C31	C36	1.407(4)
O2	C4	1.260(4)	C32	C33	1.403(4)
N11	C11	1.363(3)	C32	C37	1.516(5)
N11	C14	1.395(3)	C33	C34	1.373(5)
N11	B	1.528(4)	C34	C35	1.384(5)
N12	C12	1.316(4)	C35	C36	1.396(4)

N12	C31	1.442(3)	C36	C40	1.514(5)
N21	C21	1.365(3)	C37	C38	1.510(6)
N21	C24	1.400(3)	C37	C39	1.523(6)
N22	C22	1.323(3)	C40	C41	1.529(5)
N22	C51	1.450(3)	C40	C42	1.514(6)
N22	B	1.580(4)	C51	C52	1.404(4)
C1	C2	1.540(4)	C51	C56	1.401(4)
C2	C3	1.382(4)	C52	C53	1.395(4)
C3	C4	1.395(4)	C52	C57	1.521(4)
C4	C5	1.541(4)	C53	C54	1.381(5)
C11	C12	1.446(4)	C54	C55	1.388(5)
C11	C21	1.369(4)	C55	C56	1.400(4)
C12	C13	1.458(4)	C56	C60	1.513(4)
C13	C14	1.408(4)	C57	C58	1.521(5)
C13	C18	1.412(4)	C57	C59	1.527(5)
C14	C15	1.392(4)	C60	C61	1.527(5)
			C60	C62	1.529(5)

O1	Pd	O2	89.15(8)	N21	C21	C22	111.8(2)
O1	Pd	N12	86.15(9)	C11	C21	C22	119.8(2)
O1	Pd	N21	178.80(10)	N22	C22	C21	121.4(2)
O2	Pd	N12	174.41(9)	N22	C22	C23	133.4(2)
O2	Pd	N21	90.49(9)	C21	C22	C23	105.2(2)
N12	Pd	N21	94.27(9)	C22	C23	C24	105.9(2)
Pd	O1	C2	125.5(2)	C22	C23	C28	133.3(3)
Pd	O2	C4	125.8(2)	C24	C23	C28	120.8(3)
C11	N11	C14	107.3(2)	N21	C24	C23	111.4(2)
C11	N11	B	125.8(2)	N21	C24	C25	129.8(3)
C14	N11	B	126.9(2)	C23	C24	C25	118.8(3)
Pd	N12	C12	125.91(18)	C24	C25	C26	118.7(3)
Pd	N12	C31	116.82(17)	C25	C26	C27	122.8(3)
C12	N12	C31	117.0(2)	C26	C27	C28	119.7(3)
Pd	N21	C21	121.02(18)	C23	C28	C27	119.1(3)
Pd	N21	C24	133.33(19)	N12	C31	C32	118.4(2)
C21	N21	C24	105.6(2)	N12	C31	C36	119.2(3)
C22	N22	C51	117.9(2)	C32	C31	C36	122.4(3)
C22	N22	B	124.4(2)	C31	C32	C33	117.6(3)
C51	N22	B	117.7(2)	C31	C32	C37	122.9(3)
F1	C1	F2	106.7(3)	C33	C32	C37	119.5(3)
F1	C1	F3	106.2(3)	C32	C33	C34	121.2(3)

F1	C1	C2	111.2(3)
F2	C1	F3	109.1(4)
F2	C1	C2	113.0(3)
F3	C1	C2	110.4(3)
O1	C2	C1	112.1(3)
O1	C2	C3	129.2(3)
C1	C2	C3	118.7(3)
C2	C3	C4	121.4(3)
O2	C4	C3	128.5(3)
O2	C4	C5	114.5(3)
C3	C4	C5	117.0(3)
F4	C5	F5	105.4(3)
F4	C5	F6	107.8(3)
F4	C5	C4	111.4(3)
F5	C5	F6	109.1(3)
F5	C5	C4	112.4(3)
F6	C5	C4	110.4(3)
N11	C11	C12	110.9(2)
N11	C11	C21	121.5(2)
C12	C11	C21	127.7(2)
N12	C12	C11	122.7(2)
N12	C12	C13	132.6(2)
C11	C12	C13	104.8(2)
C12	C13	C14	106.3(2)
C12	C13	C18	134.5(3)
C14	C13	C18	119.2(3)
N11	C14	C13	110.7(2)
N11	C14	C15	127.0(3)
C13	C14	C15	122.2(3)
C14	C15	C16	117.4(3)
C15	C16	C17	121.4(3)
C16	C17	C18	121.4(3)
C13	C18	C17	118.4(3)
N21	C21	C11	128.4(2)

C33	C34	C35	120.1(3)
C34	C35	C36	121.4(3)
C31	C36	C35	117.2(3)
C31	C36	C40	122.2(3)
C35	C36	C40	120.5(3)
C32	C37	C38	110.5(3)
C32	C37	C39	110.9(4)
C38	C37	C39	111.4(5)
C36	C40	C41	112.6(3)
C36	C40	C42	110.9(3)
C41	C40	C42	109.6(3)
N22	C51	C52	118.7(2)
N22	C51	C56	118.5(2)
C52	C51	C56	122.8(3)
C51	C52	C53	117.0(3)
C51	C52	C57	123.1(3)
C53	C52	C57	119.9(3)
C52	C53	C54	121.9(3)
C53	C54	C55	119.9(3)
C54	C55	C56	121.0(3)
C51	C56	C55	117.5(3)
C51	C56	C60	123.2(2)
C55	C56	C60	119.3(3)
C52	C57	C58	111.3(3)
C52	C57	C59	111.8(3)
C58	C57	C59	110.8(3)
C56	C60	C61	110.9(3)
C56	C60	C62	111.1(3)
C61	C60	C62	110.9(3)
F7	B	F8	108.5(2)
F7	B	N11	111.6(2)
F7	B	N22	109.0(2)
F8	B	N11	111.4(2)
F8	B	N22	109.0(2)
N11	B	N22	107.1(2)

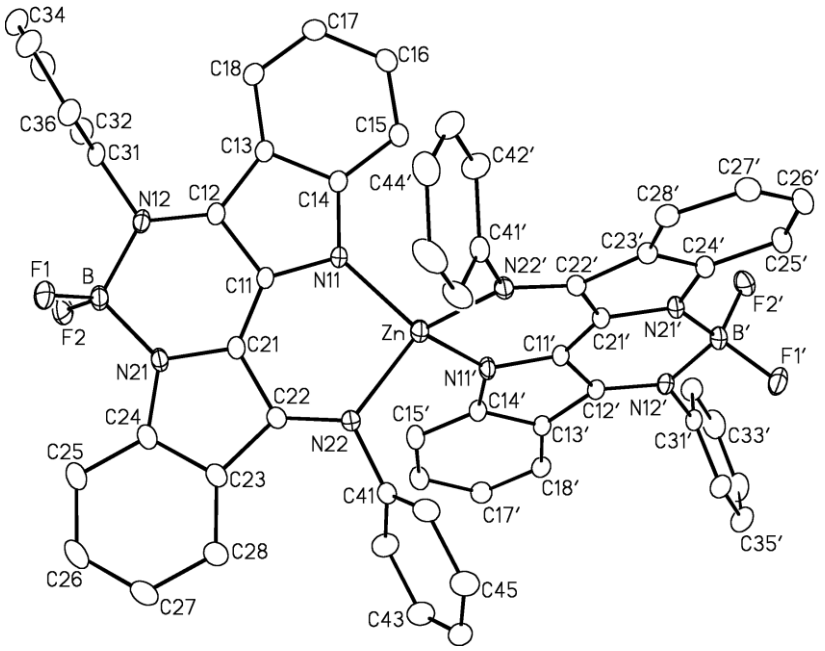

Figure B-14: ORTEP view of **4.1**. Thermal ellipsoids at the 50% probability level with all hydrogen atoms removed for clarity

Table B-14: Bond lengths (Å) and angles (^{o}) for **4.1**

Zn	N11	1.965(2)	C15	C16	1.375(4)
Zn	N11’	1.965(2)	C16	C17	1.414(4)
Zn	N22	2.076(2)	C17	C18	1.371(4)
Zn	N22’	2.076(2)	C21	C22	1.457(3)
F1	B	1.392(3)	C22	C23	1.465(3)
F2	B	1.392(4)	C23	C24	1.408(4)
N11	C11	1.376(3)	C23	C28	1.397(4)
N11	C14	1.376(3)	C24	C25	1.403(4)
N12	C12	1.331(3)	C25	C26	1.381(5)
N12	C31	1.441(3)	C26	C27	1.382(5)
N12	B	1.558(4)	C27	C28	1.389(4)
N21	C21	1.368(3)	C31	C32	1.383(4)
N21	C24	1.396(3)	C31	C36	1.383(4)
N21	B	1.544(4)	C32	C33	1.388(5)
N22	C22	1.307(3)	C33	C34	1.370(5)
N22	C41	1.432(3)	C34	C35	1.381(5)

C11	C12	1.449(3)	C35	C36	1.385(4)
C11	C21	1.370(4)	C41	C42	1.390(4)
C12	C13	1.432(3)	C41	C46	1.370(4)
C13	C14	1.430(3)	C42	C43	1.377(4)
C13	C18	1.406(3)	C43	C44	1.374(5)
C14	C15	1.398(4)	C44	C45	1.371(5)
			C45	C46	1.396(4)

N11	Zn	N11’	132.25(13)	C11	C21	C22	128.7(2)
N11	Zn	N22	95.71(8)	N22	C22	C21	121.9(2)
N11	Zn	N22’	107.64(8)	N22	C22	C23	133.0(2)
N11’	Zn	N22	107.64(8)	C21	C22	C23	105.1(2)
N11’	Zn	N22’	95.71(8)	C22	C23	C24	105.6(2)
N22	Zn	N22’	120.37(12)	C22	C23	C28	134.2(3)
Zn	N11	C11	120.47(16)	C24	C23	C28	120.1(2)
Zn	N11	C14	133.50(16)	N21	C24	C23	111.6(2)
C11	N11	C14	105.84(19)	N21	C24	C25	127.2(3)
C12	N12	C31	117.7(2)	C23	C24	C25	121.2(3)
C12	N12	B	124.5(2)	C24	C25	C26	117.1(3)
C31	N12	B	117.82(19)	C25	C26	C27	122.3(3)
C21	N21	C24	107.2(2)	C26	C27	C28	121.0(3)
C21	N21	B	125.1(2)	C23	C28	C27	118.2(3)
C24	N21	B	127.6(2)	N12	C31	C32	119.8(2)
Zn	N22	C22	124.23(17)	N12	C31	C36	119.4(2)
Zn	N22	C41	117.06(15)	C32	C31	C36	120.8(3)
C22	N22	C41	118.4(2)	C31	C32	C33	119.1(3)
N11	C11	C12	111.1(2)	C32	C33	C34	120.6(3)
N11	C11	C21	128.4(2)	C33	C34	C35	120.1(3)
C12	C11	C21	120.4(2)	C34	C35	C36	120.3(3)
N12	C12	C11	121.0(2)	C31	C36	C35	119.2(3)
N12	C12	C13	133.4(2)	N22	C41	C42	120.8(3)
C11	C12	C13	105.6(2)	N22	C41	C46	119.3(2)
C12	C13	C14	105.1(2)	C42	C41	C46	119.9(3)
C12	C13	C18	134.9(2)	C41	C42	C43	119.6(3)
C14	C13	C18	119.9(2)	C42	C43	C44	120.4(3)
N11	C14	C13	112.3(2)	C43	C44	C45	120.4(3)
N11	C14	C15	127.6(2)	C44	C45	C46	119.5(3)
C13	C14	C15	120.1(2)	C41	C46	C45	120.2(3)
C14	C15	C16	118.7(2)	F1	B	F2	108.8(2)
C15	C16	C17	121.4(2)	F1	B	N12	109.3(2)

C16	C17	C18	120.8(2)	F1	B	N21	110.6(2)
C13	C18	C17	119.0(2)	F2	B	N12	109.5(2)
N21	C21	C11	120.9(2)	F2	B	N21	111.0(2)
N21	C21	C22	110.4(2)	N12	B	N21	107.69(19)

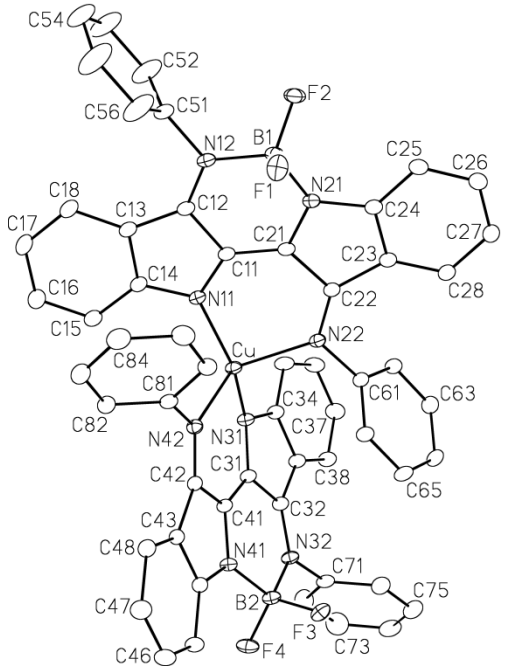

Figure B-15: ORTEP view of **4.2a**. Thermal ellipsoids at the 50% probability level with all hydrogen atoms removed for clarity

Table B-15: Bond lengths (Å) and angles (^{o}) for **4.2a**

Cu	N11	1.8913(15)	C26	C27	1.394(3)
Cu	N22	2.0690(16)	C27	C28	1.380(3)
Cu	N31	1.8974(15)	C31	C32	1.445(2)
Cu	N42	2.0633(15)	C31	C41	1.367(3)
F1	B1	1.393(3)	C32	C33	1.441(3)
F2	B1	1.372(3)	C33	C34	1.418(3)

F3	B2	1.393(3)	C33	C38	1.402(3)
F4	B2	1.378(3)	C34	C35	1.398(3)
N11	C11	1.367(2)	C35	C36	1.381(3)
N11	C14	1.383(2)	C36	C37	1.396(3)
N12	C12	1.321(3)	C37	C38	1.390(3)
N12	C51	1.445(2)	C41	C42	1.463(2)
N12	B1	1.576(3)	C42	C43	1.464(2)
N21	C21	1.362(2)	C43	C44	1.412(3)
N21	C24	1.399(2)	C43	C48	1.396(3)
N21	B1	1.537(2)	C44	C45	1.393(3)
N22	C22	1.307(3)	C45	C46	1.380(3)
N22	C61	1.435(2)	C46	C47	1.398(3)
N31	C31	1.374(2)	C47	C48	1.384(3)
N31	C34	1.381(2)	C51	C52	1.360(3)
N32	C32	1.326(2)	C51	C56	1.364(3)
N32	C71	1.442(2)	C52	C53	1.387(4)
N32	B2	1.585(3)	C53	C54	1.350(4)
N41	C41	1.365(2)	C54	C55	1.377(4)
N41	C44	1.394(2)	C55	C56	1.391(4)
N41	B2	1.537(2)	C61	C62	1.392(3)
N42	C42	1.307(2)	C61	C66	1.384(3)
N42	C81	1.429(2)	C62	C63	1.382(3)
C11	C12	1.451(2)	C63	C64	1.386(3)
C11	C21	1.367(3)	C64	C65	1.380(3)
C12	C13	1.441(3)	C65	C66	1.393(3)
C13	C14	1.421(3)	C71	C72	1.369(3)
C13	C18	1.405(3)	C71	C76	1.378(3)
C14	C15	1.395(3)	C72	C73	1.397(3)
C15	C16	1.378(3)	C73	C74	1.370(4)
C16	C17	1.402(3)	C74	C75	1.375(4)
C17	C18	1.376(3)	C75	C76	1.389(3)
C21	C22	1.465(2)	C81	C82	1.388(3)
C22	C23	1.471(3)	C81	C86	1.392(3)
C23	C24	1.412(3)	C82	C83	1.392(3)
C23	C28	1.397(3)	C83	C84	1.379(3)
C24	C25	1.388(3)	C84	C85	1.382(3)
C25	C26	1.388(3)	C85	C86	1.388(3)

C11	N11	C14	107.50(16)	N21	C24	C23	109.75(16)
C11	N11	B	122.09(16)	N21	C24	C25	127.74(17)

C14	N11	B	129.40(17)	C23	C24	C25	122.51(17)
C12	N12	C31	123.10(16)	C24	C25	C26	117.49(18)
C21	N21	C24	108.38(15)	C25	C26	C27	121.36(19)
C22	N22	C41	120.50(16)	C26	C27	C28	121.68(19)
C22	N22	B	120.42(15)	C23	C28	C27	118.84(18)
C41	N22	B	118.91(15)	N12	C31	C32	122.86(17)
N11	C11	C12	111.05(16)	N12	C31	C36	117.63(17)
N11	C11	C21	120.09(17)	C32	C31	C36	118.85(18)
C12	C11	C21	128.81(18)	C31	C32	C33	119.93(19)
N12	C12	C11	119.06(17)	C32	C33	C34	121.44(19)
N12	C12	C13	136.91(18)	C33	C34	C35	117.95(18)
C11	C12	C13	103.97(16)	C33	C34	C37	121.2(2)
C12	C13	C14	106.93(16)	C35	C34	C37	120.8(2)
C12	C13	C18	133.39(19)	C34	C35	C36	121.07(19)
C14	C13	C18	119.42(19)	C31	C36	C35	120.74(19)
N11	C14	C13	110.56(17)	N22	C41	C42	120.75(17)
N11	C14	C15	127.34(18)	N22	C41	C46	120.34(16)
C13	C14	C15	122.06(18)	C42	C41	C46	118.90(18)
C14	C15	C16	117.1(2)	C41	C42	C43	120.05(19)
C15	C16	C17	121.8(2)	C42	C43	C44	121.96(19)
C16	C17	C18	120.6(2)	C43	C44	C45	117.24(19)
C13	C18	C17	118.9(2)	C43	C44	C47	121.7(2)
N21	C21	C11	127.38(17)	C45	C44	C47	121.0(2)
N21	C21	C22	109.93(16)	C44	C45	C46	121.74(19)
C11	C21	C22	122.59(18)	C41	C46	C45	119.90(18)
N22	C22	C21	119.70(17)	F1	B	F2	109.23(18)
N22	C22	C23	134.67(17)	F1	B	N11	111.32(19)
C21	C22	C23	105.62(16)	F1	B	N22	111.15(17)
C22	C23	C24	106.30(16)	F2	B	N11	109.08(16)
C22	C23	C28	135.46(18)	F2	B	N22	108.07(18)
C24	C23	C28	118.08(17)	N11	B	N22	107.92(16)

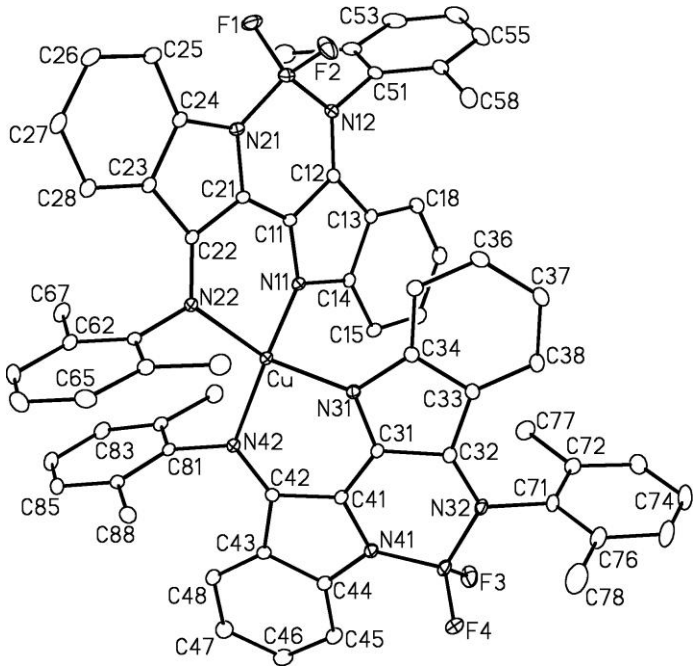

Figure B-16: ORTEP view of **4.2c**. Thermal ellipsoids at the 50% probability level with all hydrogen atoms removed for clarity

Table B-16: Bond lengths (Å) and angles (^{o}) for **4.2c**

Cu	N11	1.9306(17)	C32	C33	1.442(3)
Cu	N22	2.0354(17)	C33	C34	1.426(3)
Cu	N31	1.9387(18)	C33	C38	1.403(3)
Cu	N42	2.0348(17)	C34	C35	1.392(3)
F1	B1	1.390(3)	C35	C36	1.381(3)
F2	B1	1.387(3)	C36	C37	1.405(3)
F3	B2	1.383(3)	C37	C38	1.379(3)
F4	B2	1.385(3)	C41	C42	1.464(3)
N11	C11	1.366(3)	C42	C43	1.466(3)
N11	C14	1.391(3)	C43	C44	1.411(3)
N12	C12	1.332(3)	C43	C48	1.398(3)
N12	C51	1.451(3)	C44	C45	1.385(3)
N12	B1	1.583(3)	C45	C46	1.382(3)
N21	C21	1.366(3)	C46	C47	1.391(4)
N21	C24	1.402(3)	C47	C48	1.386(3)

N21	B1	1.539(3)	C51	C52	1.399(3)
N22	C22	1.314(3)	C51	C56	1.396(3)
N22	C61	1.442(3)	C52	C53	1.396(4)
N31	C31	1.368(3)	C52	C57	1.502(4)
N31	C34	1.394(3)	C53	C54	1.376(4)
N32	C32	1.325(3)	C54	C55	1.378(4)
N32	C71	1.454(3)	C55	C56	1.393(3)
N32	B2	1.580(3)	C56	C58	1.504(3)
N41	C41	1.366(3)	C61	C62	1.403(3)
N41	C44	1.402(3)	C61	C66	1.400(3)
N41	B2	1.539(3)	C62	C63	1.387(3)
N42	C42	1.309(3)	C62	C67	1.508(3)
N42	C81	1.446(3)	C63	C64	1.382(4)
C11	C12	1.439(3)	C64	C65	1.373(4)
C11	C21	1.368(3)	C65	C66	1.396(3)
C12	C13	1.438(3)	C66	C68	1.502(3)
C13	C14	1.427(3)	C71	C72	1.392(3)
C13	C18	1.403(3)	C71	C76	1.391(3)
C14	C15	1.395(3)	C72	C73	1.388(3)
C15	C16	1.378(3)	C72	C77	1.505(3)
C16	C17	1.399(3)	C73	C74	1.376(4)
C17	C18	1.380(3)	C74	C75	1.373(4)
C21	C22	1.453(3)	C75	C76	1.398(4)
C22	C23	1.468(3)	C76	C78	1.503(4)
C23	C24	1.412(3)	C81	C82	1.399(3)
C23	C28	1.402(3)	C81	C86	1.399(3)
C24	C25	1.389(3)	C82	C83	1.389(3)
C25	C26	1.387(3)	C82	C87	1.507(3)
C26	C27	1.391(3)	C83	C84	1.389(3)
C27	C28	1.382(3)	C84	C85	1.384(3)
C31	C32	1.446(3)	C85	C86	1.392(3)
C31	C41	1.371(3)	C86	C88	1.501(3)

N11	Cu	N22	94.99(7)	C33	C38	C37	118.7(2)
N11	Cu	N31	97.31(7)	N41	C41	C31	120.93(19)
N11	Cu	N42	127.03(7)	N41	C41	C42	110.34(18)
N22	Cu	N31	131.43(7)	C31	C41	C42	128.51(19)
N22	Cu	N42	112.62(7)	N42	C42	C41	122.15(19)
N31	Cu	N42	96.42(7)	N42	C42	C43	133.0(2)
Cu	N11	C11	120.33(14)	C41	C42	C43	104.72(18)

Cu	N11	C14	130.53(14)	C42	C43	C44	106.32(19)
C11	N11	C14	104.78(17)	C42	C43	C48	134.0(2)
C12	N12	C51	116.51(18)	C44	C43	C48	119.6(2)
C12	N12	B1	123.17(18)	N41	C44	C43	110.81(19)
C51	N12	B1	120.20(17)	N41	C44	C45	127.2(2)
C21	N21	C24	107.00(17)	C43	C44	C45	121.9(2)
C21	N21	B1	124.42(18)	C44	C45	C46	117.3(2)
C24	N21	B1	128.37(18)	C45	C46	C47	122.0(2)
Cu	N22	C22	122.66(14)	C46	C47	C48	120.9(2)
Cu	N22	C61	121.69(13)	C43	C48	C47	118.4(2)
C22	N22	C61	115.33(17)	N12	C51	C52	118.8(2)
Cu	N31	C31	120.31(14)	N12	C51	C56	118.6(2)
Cu	N31	C34	128.38(14)	C52	C51	C56	122.4(2)
C31	N31	C34	104.92(17)	C51	C52	C53	117.4(2)
C32	N32	C71	118.98(18)	C51	C52	C57	122.5(2)
C32	N32	B2	123.27(18)	C53	C52	C57	120.1(2)
C71	N32	B2	117.19(17)	C52	C53	C54	121.0(3)
C41	N41	C44	107.76(18)	C53	C54	C55	120.5(2)
C41	N41	B2	125.02(19)	C54	C55	C56	120.9(3)
C44	N41	B2	127.19(18)	C51	C56	C55	117.7(2)
Cu	N42	C42	123.06(14)	C51	C56	C58	121.7(2)
Cu	N42	C81	120.47(13)	C55	C56	C58	120.5(2)
C42	N42	C81	115.56(17)	N22	C61	C62	119.27(19)
N11	C11	C12	112.46(18)	N22	C61	C66	118.38(19)
N11	C11	C21	126.27(19)	C62	C61	C66	122.3(2)
C12	C11	C21	121.27(19)	C61	C62	C63	117.5(2)
N12	C12	C11	121.10(19)	C61	C62	C67	121.1(2)
N12	C12	C13	133.60(19)	C63	C62	C67	121.4(2)
C11	C12	C13	105.30(18)	C62	C63	C64	121.1(2)
C12	C13	C14	104.89(18)	C63	C64	C65	120.6(2)
C12	C13	C18	135.2(2)	C64	C65	C66	120.9(2)
C14	C13	C18	119.9(2)	C61	C66	C65	117.5(2)
N11	C14	C13	112.52(18)	C61	C66	C68	121.5(2)
N11	C14	C15	126.60(19)	C65	C66	C68	120.9(2)
C13	C14	C15	120.79(19)	N32	C71	C72	117.67(19)
C14	C15	C16	117.9(2)	N32	C71	C76	120.0(2)
C15	C16	C17	122.0(2)	C72	C71	C76	122.3(2)
C16	C17	C18	121.0(2)	C71	C72	C73	118.0(2)
C13	C18	C17	118.5(2)	C71	C72	C77	121.5(2)
N21	C21	C11	120.96(19)	C73	C72	C77	120.5(2)
N21	C21	C22	111.25(18)	C72	C73	C74	121.1(2)

C11	C21	C22	127.78(19)	C73	C74	C75	119.9(2)
N22	C22	C21	122.44(18)	C74	C75	C76	121.5(3)
N22	C22	C23	133.06(19)	C71	C76	C75	117.2(2)
C21	C22	C23	104.44(17)	C71	C76	C78	122.4(2)
C22	C23	C24	106.22(18)	C75	C76	C78	120.4(2)
C22	C23	C28	134.0(2)	N42	C81	C82	118.39(18)
C24	C23	C28	119.8(2)	N42	C81	C86	119.03(18)
N21	C24	C23	111.03(18)	C82	C81	C86	122.6(2)
N21	C24	C25	127.4(2)	C81	C82	C83	117.9(2)
C23	C24	C25	121.6(2)	C81	C82	C87	120.8(2)
C24	C25	C26	117.6(2)	C83	C82	C87	121.2(2)
C25	C26	C27	121.4(2)	C82	C83	C84	120.7(2)
C26	C27	C28	121.5(2)	C83	C84	C85	120.2(2)
C23	C28	C27	118.2(2)	C84	C85	C86	121.1(2)
N31	C31	C32	112.51(18)	C81	C86	C85	117.5(2)
N31	C31	C41	126.80(19)	C81	C86	C88	121.03(19)
C32	C31	C41	120.16(19)	C85	C86	C88	121.4(2)
N32	C32	C31	121.79(19)	F1	B1	F2	108.5(2)
N32	C32	C33	133.3(2)	F1	B1	N12	109.7(2)
C31	C32	C33	104.79(18)	F1	B1	N21	110.8(2)
C32	C33	C34	105.41(18)	F2	B1	N12	109.4(2)
C32	C33	C38	134.4(2)	F2	B1	N21	110.5(2)
C34	C33	C38	120.2(2)	N12	B1	N21	107.94(18)
N31	C34	C33	112.31(18)	F3	B2	F4	109.2(2)
N31	C34	C35	127.4(2)	F3	B2	N32	108.55(19)
C33	C34	C35	120.2(2)	F3	B2	N41	110.6(2)
C34	C35	C36	118.5(2)	F4	B2	N32	110.1(2)
C35	C36	C37	121.7(2)	F4	B2	N41	110.7(2)
C36	C37	C38	120.7(2)	N32	B2	N41	107.65(18)

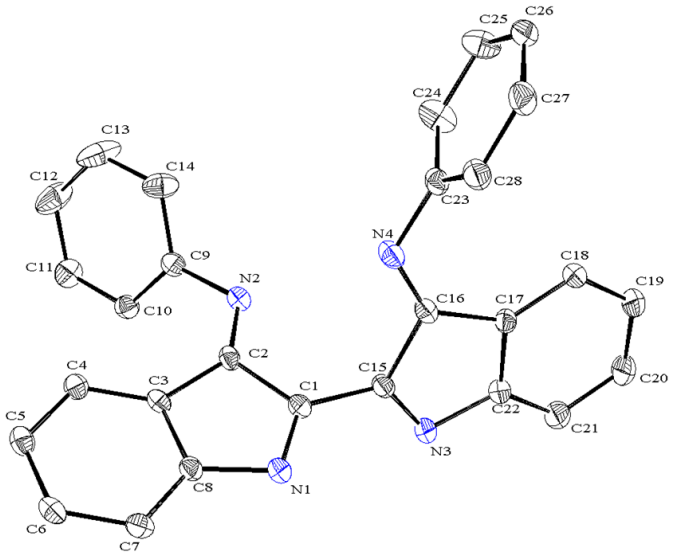

Figure B-17: ORTEP view of **5.1a**. Thermal ellipsoids at the 50% probability level with all hydrogen atoms removed for clarity

Table B-17: Bond lengths (Å) and angles (°) for **5.1a**

C1	N1	1.2933 (17)	C15	N3	1.2879 (17)
C1	C15	1.4747 (18)	C15	C16	1.5021 (18)
C2	C2	1.5003 (18)	C16	N4	1.2714 (17)
C2	N2	1.2773 (17)	C16	C17	1.4788 (18)
C2	C3	1.4790 (18)	C17	C18	1.3850 (18)
C3	C4	1.3816 (18)	C17	C22	1.4003 (19)
C3	C8	1.4034 (18)	C18	C19	1.395 (2)
C4	C5	1.3952 (18)	C18	H18	0.9500
C4	H4	0.9500	C19	C20	1.384 (2)
C5	C6	1.3843 (19)	C19	H19	0.9500
C5	H5	0.9500	C20	C21	1.397 (2)
C6	C7	1.3952 (19)	C20	H20	0.9500
C6	H6	0.9500	C21	C22	1.377 (2)
C7	C8	1.3817 (18)	C21	H21	0.9500
C7	H7	0.9500	C22	N3	1.4429 (17)
C8	N1	1.4371 (17)	C23	C28	1.384 (2)
C9	C14	1.3898 (19)	C23	C23	1.284 (2)
C9	C10	1.3926 (19)	C23	N4	1.4250 (17)

C9	N2	1.4216 (17)	C24	C25	1.388 (2)
C10	C11	1.3813 (19)	C24	H24	0.9500
C10	H10	0.9500	C25	C26	1.380 (2)
C11	C12	1.381 (2)	C25	H25	0.9500
C11	H11	0.9500	C26	C27	1.379 (2)
C12	C13	1.384 (2)	C26	H26	0.9500
C12	H12	0.9500	C27	C28	1.385 (2)
C13	C14	1.382 (2)	C27	H27	0.9500
C13	H13	0.9500	C28	H28	0.9500
C14	H14	0.9500			

N1	C1	C15	122.91 (12)	C1	C16	C16	123.53 (11)
N1	C1	C2	113.33 (11)	N4	C16	C17	134.83 (12)
C15	C1	C2	123.74 (11)	N4	C16	C15	122.01 (12)
N2	C2	C3	135.03 (12)	C17	C16	C15	103.14 (11)
N2	C2	C15	121.94 (12)	C18	C17	C22	120.50 (12)
C3	C2	C15	103.02 (11)	C18	C17	C16	134.57 (13)
C4	C3	C8	120.26 (12)	C22	C17	C16	104.88 (11)
C4	C3	C2	134.47 (12)	C17	C18	C19	117.82 (13)
C8	C3	C2	105.08 (11)	C17	C18	H18	121.1
C3	C4	C5	118.31 (12)	C19	C18	H18	121.1
C3	C4	H4	120.8	C20	C19	C18	121.26 (13)
C5	C4	H4	120.8	C20	C19	H19	119.4
C6	C5	C4	120.89 (13)	C18	C19	H19	119.4
C6	C5	H5	119.6	C19	C20	C21	121.06 (14)
C4	C5	H5	119.6	C19	C20	H20	119.5
C5	C6	C7	121.44 (12)	C21	C20	H20	119.5
C5	C6	H6	119.3	C22	C21	C20	117.49 (14)
C7	C6	H6	119.3	C22	C21	H21	121.3
C8	C7	C6	117.26 (12)	C20	C21	H21	121.3
C8	C7	H7	121.4	C21	C22	C17	121.79 (13)
C6	C7	H7	121.4	C21	C22	N3	125.76 (13
C7	C8	C3	121.83 (12)	C17	C22	N3	112.42 (12)
C7	C8	N1	125.75 (12)	C28	C23	C24	120.01 (13)
C3	C8	N1	112.35 (11)	C28	C23	N4	118.85 (12)
C14	C9	C10	119.93 (13)	C24	C23	N4	120.99 (13)
C14	C9	N2	119.27 (12)	C23	C24	C25	119.61 (14)
C10	C9	N2	120.64 (12)	C23	C24	H24	120.2
C11	C10	C9	120.12 (13)	C25	C24	H24	120.2
C11	C10	H10	119.9	C26	C25	C24	120.39 (14)

C9	C10	H10	119.9	C26	C25	H25	119.8
C10	C11	C12	119.80 (14)	C24	C25	H25	119.8
C10	C11	H11	120.1	C27	C26	C25	119.76 (13)
C12	C11	H11	120.1	C27	C26	H26	120.1
C11	C12	C13	120.18 (15)	C25	C26	H26	120.1
C11	C12	H12	119.9	C26	C27	C28	120.29 (14)
C13	C12	H12	119.9	C26	C27	H27	119.9
C14	C13	C12	120.47 (15)	C28	C27	H27	119.9
C14	C13	H13	119.8	C23	C28	C27	119.85 (13)
C12	C13	H13	119.8	C23	C28	H28	120.1
C13	C14	C9	119.39 (14)	C27	C28	H28	120.1
C13	C14	H14	120.3	C1	N1	C8	106.17 (11)
C9	C14	H14	120.3	C2	N2	C9	119.09 (11)
N3	C15	C1	123.12 (12	C15	N3	C22	106.08 (11)
N3	C15	C16	113.35 (11)	C16	N4	C23	119.93 (11)

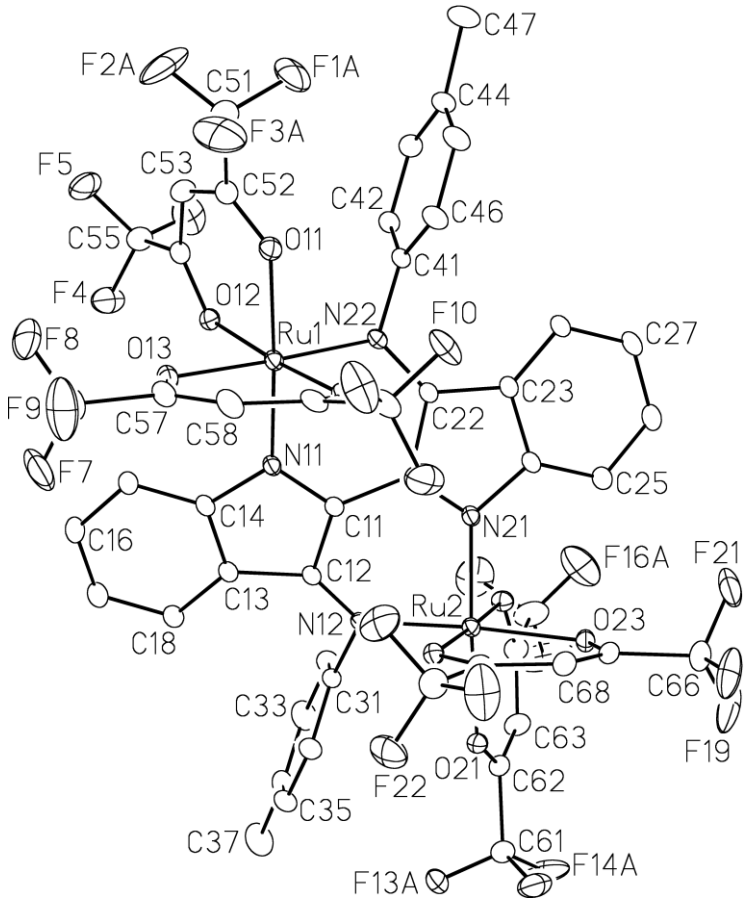

Figure B-18: ORTEP view of **5.2b-trans**. Thermal ellipsoids at the 50% probability level with all hydrogen atoms removed for clarity. **5.2b-trans** presents as a racemate of ΛΛ and ΔΔ isomers

Table B-18: Bond lengths (Å) and angles (°) for **5.2b-trans**

Ru1	O11	2.0717(19)	N11	C14	1.429(3)
Ru1	O12	2.0229(19)	N12	C12	1.302(3)
Ru1	O13	2.0516(19)	N12	C31	1.444(3)
Ru1	O14	2.0165(19)	N21	C21	1.337(3)
Ru1	N11	1.981(2)	N21	C24	1.427(3)
Ru1	N22	1.992(2)	N22	C22	1.304(3)
Ru2	O21	2.0746(18)	N22	C41	1.444(3)
Ru2	O22	2.0266(19)	C11	C12	1.467(3)
Ru2	O23	2.0530(18)	C11	C21	1.409(3)
Ru2	O24	2.0102(18)	C12	C13	1.457(3)

Ru2	N12	1.991(2)	C13	C14	1.405(4)
Ru2	N21	1.974(2)	C13	C18	1.395(4)
F1A	C51	1.278(6)	C14	C15	1.380(4)
F2A	C51	1.277(7)	C15	C16	1.385(4)
F3A	C51	1.385(8)	C16	C17	1.382(4)
F1B	C51	1.246(13)	C17	C18	1.383(4)
F2B	C51	1.151(13)	C21	C22	1.461(3)
F3B	C51	1.412(11)	C22	C23	1.468(3)
F4	C55	1.311(4)	C23	C24	1.399(4)
F5	C55	1.330(4)	C23	C28	1.397(3)
F6	C55	1.325(5)	C24	C25	1.386(4)
F7	C56	1.296(4)	C25	C26	1.389(4)
F8	C56	1.310(5)	C26	C27	1.383(4)
F9	C56	1.302(5)	C27	C28	1.386(4)
F10	C60	1.320(3)	C31	C32	1.376(4)
F11	C60	1.321(4)	C31	C36	1.386(4)
F12	C60	1.314(4)	C32	C33	1.388(4)
F13A	C61	1.298(6)	C33	C34	1.377(5)
F14A	C61	1.325(7)	C34	C35	1.383(5)
F15A	C61	1.321(7)	C34	C37	1.514(4)
F16A	C65	1.293(7)	C35	C36	1.387(4)
F17A	C65	1.339(7)	C41	C42	1.375(4)
F18A	C65	1.284(7)	C41	C46	1.385(4)
F13B	C61	1.291(10)	C42	C43	1.390(4)
F14B	C61	1.234(9)	C43	C44	1.385(4)
F15B	C61	1.287(9)	C44	C45	1.377(5)
F16B	C65	1.284(16)	C44	C47	1.511(4)
F17B	C65	1.329(12)	C45	C46	1.382(4)
F18B	C65	1.167(12)	C51	C52	1.528(5)
F19	C66	1.282(4)	C52	C53	1.380(5)
F20	C66	1.324(4)	C53	C54	1.392(4)
F21	C66	1.294(4)	C54	C55	1.528(5)
F22	C70	1.320(4)	C56	C57	1.535(4)
F23	C70	1.320(4)	C57	C58	1.389(5)
F24	C70	1.318(4)	C58	C59	1.389(4)
O11	C52	1.257(4)	C59	C60	1.523(4)
O12	C54	1.257(3)	C61	C62	1.539(4)
O13	C57	1.256(4)	C62	C63	1.383(4)
O14	C59	1.265(3)	C63	C64	1.383(4)
O21	C62	1.258(3)	C64	C65	1.519(5)
O22	C64	1.263(3)	C66	C67	1.532(4)

	O23	C67	1.258(3)	C67	C68	1.383(4)	
	O24	C69	1.262(3)	C68	C69	1.390(4)	
	N11	C11	1.333(3)	C69	C70	1.515(4)	

O11	Ru1	O12	91.76(8)	C43	C44	C47	121.1(3)
O11	Ru1	O13	82.20(8)	C45	C44	C47	120.5(3)
O11	Ru1	O14	84.06(8)	C44	C45	C46	121.7(3)
O11	Ru1	N11	176.36(8)	C41	C46	C45	118.8(3)
O11	Ru1	N22	93.53(8)	F1A	C51	F2A	110.7(5)
O12	Ru1	O13	88.20(8)	F1A	C51	F3A	100.3(5)
O12	Ru1	O14	175.73(7)	F1A	C51	C52	113.1(4)
O12	Ru1	N11	88.91(8)	F2A	C51	F3A	106.5(6)
O12	Ru1	N22	95.50(8)	F2A	C51	C52	115.0(4)
O13	Ru1	O14	92.05(8)	F3A	C51	C52	110.1(4)
O13	Ru1	N11	94.25(8)	F1B	C51	F2B	108.3(11)
O13	Ru1	N22	174.46(8)	F1B	C51	F3B	100.0(8)
O14	Ru1	N11	95.32(8)	F1B	C51	C52	112.3(6)
O14	Ru1	N22	83.95(8)	F2B	C51	F3B	110.0(11)
N11	Ru1	N22	89.96(8)	F2B	C51	C52	118.6(6)
O21	Ru2	O22	91.65(7)	F3B	C51	C52	105.9(5)
O21	Ru2	O23	83.69(7)	O11	C52	C51	113.6(3)
O21	Ru2	O24	88.85(7)	O11	C52	C53	129.2(3)
O21	Ru2	N12	93.25(8)	C51	C52	C53	117.2(3)
O21	Ru2	N21	176.82(8)	C52	C53	C54	124.3(3)
O22	Ru2	O23	89.78(8)	O12	C54	C53	128.8(3)
O22	Ru2	O24	177.92(7)	O12	C54	C55	112.4(3)
O22	Ru2	N12	93.98(8)	C53	C54	C55	118.7(3)
O22	Ru2	N21	88.82(8)	F4	C55	F5	106.6(3)
O23	Ru2	O24	92.28(7)	F4	C55	F6	108.8(4)
O23	Ru2	N12	175.22(8)	F4	C55	C54	111.6(3)
O23	Ru2	N21	93.16(8)	F5	C55	F6	107.0(3)
O24	Ru2	N12	83.97(8)	F5	C55	C54	112.3(3)
O24	Ru2	N21	90.78(8)	F6	C55	C54	110.3(3)
N12	Ru2	N21	89.86(8)	F7	C56	F8	107.0(4)
Ru1	O11	C52	121.87(19)	F7	C56	F9	109.1(4)
Ru1	O12	C54	123.42(19)	F7	C56	C57	110.8(3)
Ru1	O13	C57	122.24(19)	F8	C56	F9	105.1(3)
Ru1	O14	C59	122.01(19)	F8	C56	C57	111.1(3)
Ru2	O21	C62	122.19(18)	F9	C56	C57	113.4(3)
Ru2	O22	C64	123.20(18)	O13	C57	C56	111.6(3)

Ru2	O23	C67	121.91(17)	O13	C57	C58	129.2(3)
Ru2	O24	C69	123.45(17)	C56	C57	C58	119.2(3)
Ru1	N11	C11	125.51(16)	C57	C58	C59	123.3(3)
Ru1	N11	C14	127.13(17)	O14	C59	C58	129.2(3)
C11	N11	C14	107.1(2)	O14	C59	C60	111.7(3)
Ru2	N12	C12	123.99(17)	C58	C59	C60	119.2(3)
Ru2	N12	C31	117.51(16)	F10	C60	F11	106.0(3)
C12	N12	C31	117.9(2)	F10	C60	F12	107.3(3)
Ru2	N21	C21	125.11(17)	F10	C60	C59	110.8(2)
Ru2	N21	C24	127.65(17)	F11	C60	F12	107.0(3)
C21	N21	C24	107.2(2)	F11	C60	C59	111.9(3)
Ru1	N22	C22	124.20(17)	F12	C60	C59	113.4(3)
Ru1	N22	C41	117.28(16)	F13A	C61	F14A	110.2(5)
C22	N22	C41	117.6(2)	F13A	C61	F15A	106.6(4)
N11	C11	C12	111.4(2)	F13A	C61	C62	112.4(3)
N11	C11	C21	122.7(2)	F14A	C61	F15A	104.0(4)
C12	C11	C21	124.0(2)	F14A	C61	C62	111.9(4)
N12	C12	C11	123.2(2)	F15A	C61	C62	111.3(4)
N12	C12	C13	131.9(2)	F13B	C61	F14B	106.7(7)
C11	C12	C13	104.8(2)	F13B	C61	F15B	98.5(6)
C12	C13	C14	106.1(2)	F13B	C61	C62	113.9(5)
C12	C13	C18	134.2(2)	F14B	C61	F15B	113.0(7)
C14	C13	C18	119.7(2)	F14B	C61	C62	114.0(5)
N11	C14	C13	110.7(2)	F15B	C61	C62	109.7(5)
N11	C14	C15	127.3(2)	O21	C62	C61	113.5(3)
C13	C14	C15	122.0(2)	O21	C62	C63	129.3(3)
C14	C15	C16	117.3(3)	C61	C62	C63	117.2(3)
C15	C16	C17	121.6(3)	C62	C63	C64	124.1(3)
C16	C17	C18	121.4(3)	O22	C64	C63	129.4(3)
C13	C18	C17	118.1(3)	O22	C64	C65	111.4(3)
N21	C21	C11	122.7(2)	C63	C64	C65	119.1(3)
N21	C21	C22	111.2(2)	F16A	C65	F17A	102.4(5)
C11	C21	C22	124.4(2)	F16A	C65	F18A	109.3(6)
N22	C22	C21	123.4(2)	F16A	C65	C64	113.5(4)
N22	C22	C23	131.6(2)	F17A	C65	F18A	105.0(6)
C21	C22	C23	104.8(2)	F17A	C65	C64	110.4(4)
C22	C23	C24	105.8(2)	F18A	C65	C64	115.2(4)
C22	C23	C28	134.3(2)	F16B	C65	F17B	98.4(9)
C24	C23	C28	119.9(2)	F16B	C65	F18B	109.6(10)
N21	C24	C23	110.9(2)	F16B	C65	C64	112.4(7)
N21	C24	C25	127.1(2)	F17B	C65	F18B	109.6(11)

C23	C24	C25	122.0(2)	F17B	C65	C64	108.2(5)
C24	C25	C26	117.1(3)	F18B	C65	C64	116.9(6)
C25	C26	C27	121.6(3)	F19	C66	F20	106.6(3)
C26	C27	C28	121.3(3)	F19	C66	F21	108.9(4)
C23	C28	C27	118.0(3)	F19	C66	C67	112.2(3)
N12	C31	C32	119.6(2)	F20	C66	F21	105.1(3)
N12	C31	C36	119.3(2)	F20	C66	C67	112.8(3)
C32	C31	C36	121.1(3)	F21	C66	C67	110.9(3)
C31	C32	C33	118.7(3)	O23	C67	C66	112.3(3)
C32	C33	C34	121.8(3)	O23	C67	C68	129.2(3)
C33	C34	C35	118.2(3)	C66	C67	C68	118.5(3)
C33	C34	C37	121.0(3)	C67	C68	C69	124.2(3)
C35	C34	C37	120.7(3)	O24	C69	C68	128.5(3)
C34	C35	C36	121.5(3)	O24	C69	C70	111.9(2)
C31	C36	C35	118.7(3)	C68	C69	C70	119.6(3)
N22	C41	C42	119.7(2)	F22	C70	F23	105.6(3)
N22	C41	C46	119.2(2)	F22	C70	F24	107.8(3)
C42	C41	C46	121.0(2)	F22	C70	C69	111.5(3)
C41	C42	C43	119.0(3)	F23	C70	F24	106.8(3)
C42	C43	C44	121.1(3)	F23	C70	C69	111.0(3)
C43	C44	C45	118.5(3)	F24	C70	C69	113.7(3)

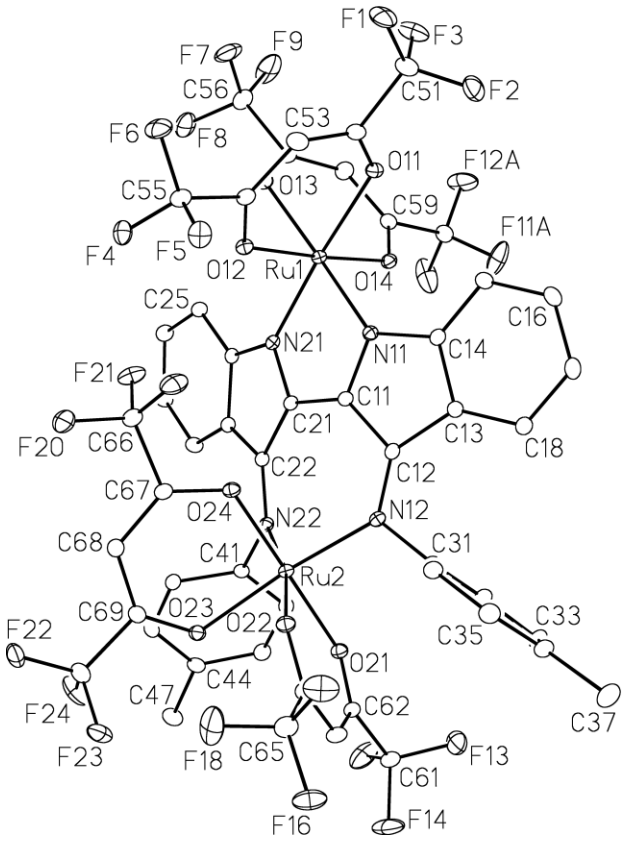

Figure B-19: ORTEP view of **5.2b-cis**. Thermal ellipsoids at the 50% probability level with all hydrogen atoms removed for clarity. **5.2b-cis** present as a racemate of ΛΛ and ΔΔ isomers

Table B-19: Bond lengths (Å) and angles (^{o}) for **5.2b-cis**

Ru1	O11	2.0575(16)	N21	C21	1.334(3)
Ru1	O12	2.0315(15)	N21	C24	1.411(3)
Ru1	O13	2.0676(15)	N22	C22	1.313(3)
Ru1	O14	2.0394(16)	N22	C41	1.454(3)
Ru1	N11	1.9805(18)	C11	C12	1.464(3)
Ru1	N21	2.0030(18)	C11	C21	1.415(3)
Ru2	O21	2.0391(15)	C12	C13	1.477(3)
Ru2	O22	2.0556(16)	C13	C14	1.405(3)
Ru2	O23	2.0550(15)	C13	C18	1.393(3)
Ru2	O24	2.0137(15)	C14	C15	1.376(3)
Ru2	N12	2.0154(18)	C15	C16	1.389(3)

Ru2	N22	2.0063(18)	C16	C17	1.384(4)
F1	C51	1.334(3)	C17	C18	1.389(3)
F2	C51	1.331(3)	C21	C22	1.465(3)
F3	C51	1.329(3)	C22	C23	1.469(3)
F4	C55	1.322(3)	C23	C24	1.406(3)
F5	C55	1.339(3)	C23	C28	1.400(3)
F6	C55	1.331(3)	C24	C25	1.382(3)
F7	C56	1.330(4)	C25	C26	1.391(3)
F8	C56	1.331(4)	C26	C27	1.386(3)
F9	C56	1.320(3)	C27	C28	1.387(3)
F10A	C60	1.294(4)	C31	C32	1.385(3)
F11A	C60	1.309(4)	C31	C36	1.385(3)
F12A	C60	1.287(4)	C32	C33	1.388(3)
F10B	C60	1.256(8)	C33	C34	1.387(4)
F11B	C60	1.300(9)	C34	C35	1.393(4)
F12B	C60	1.246(8)	C34	C37	1.513(3)
F13	C61	1.320(3)	C35	C36	1.382(3)
F14	C61	1.321(3)	C41	C42	1.382(3)
F15	C61	1.313(3)	C41	C46	1.387(3)
F16	C65	1.328(3)	C42	C43	1.388(3)
F17	C65	1.326(4)	C43	C44	1.386(3)
F18	C65	1.308(3)	C44	C45	1.394(3)
F19	C66	1.325(3)	C44	C47	1.511(3)
F20	C66	1.328(3)	C45	C46	1.384(3)
F21	C66	1.326(3)	C51	C52	1.528(3)
F22	C70	1.323(3)	C52	C53	1.384(4)
F23	C70	1.337(3)	C53	C54	1.388(3)
F24	C70	1.326(3)	C54	C55	1.532(3)
O11	C52	1.263(3)	C56	C57	1.533(3)
O12	C54	1.264(3)	C57	C58	1.388(4)
O13	C57	1.255(3)	C58	C59	1.394(3)
O14	C59	1.257(3)	C59	C60	1.536(3)
O21	C62	1.254(3)	C61	C62	1.535(3)
O22	C64	1.260(3)	C62	C63	1.396(4)
O23	C69	1.256(3)	C63	C64	1.391(4)
O24	C67	1.262(3)	C64	C65	1.533(3)
N11	C11	1.337(3)	C66	C67	1.523(3)
N11	C14	1.415(3)	C67	C68	1.392(3)
N12	C12	1.302(3)	C68	C69	1.394(3)
N12	C31	1.451(3)	C69	C70	1.527(3)

O11	Ru1	O12	92.17(6)	N22	C41	C42	119.52(19)
O11	Ru1	O13	81.68(6)	N22	C41	C46	119.61(19)
O11	Ru1	O14	85.69(6)	C42	C41	C46	120.7(2)
O11	Ru1	N11	99.61(7)	C41	C42	C43	118.9(2)
O11	Ru1	N21	176.15(7)	C42	C43	C44	121.7(2)
O12	Ru1	O13	86.20(6)	C43	C44	C45	118.2(2)
O12	Ru1	O14	176.88(6)	C43	C44	C47	121.4(2)
O12	Ru1	N11	93.00(7)	C45	C44	C47	120.4(2)
O12	Ru1	N21	90.22(7)	C44	C45	C46	121.0(2)
O13	Ru1	O14	91.24(6)	C41	C46	C45	119.5(2)
O13	Ru1	N11	178.51(7)	F1	C51	F2	107.9(2)
O13	Ru1	N21	101.50(7)	F1	C51	F3	107.2(2)
O14	Ru1	N11	89.60(7)	F1	C51	C52	112.9(2)
O14	Ru1	N21	92.04(7)	F2	C51	F3	107.5(2)
N11	Ru1	N21	77.24(7)	F2	C51	C52	110.7(2)
O21	Ru2	O22	92.03(6)	F3	C51	C52	110.4(2)
O21	Ru2	O23	86.48(6)	O11	C52	C51	112.4(2)
O21	Ru2	O24	179.50(6)	O11	C52	C53	128.9(2)
O21	Ru2	N12	92.23(7)	C51	C52	C53	118.7(2)
O21	Ru2	N22	93.28(7)	C52	C53	C54	124.1(2)
O22	Ru2	O23	79.72(6)	O12	C54	C53	129.5(2)
O22	Ru2	O24	87.50(6)	O12	C54	C55	114.3(2)
O22	Ru2	N12	91.04(7)	C53	C54	C55	116.2(2)
O22	Ru2	N22	168.78(7)	F4	C55	F5	107.0(2)
O23	Ru2	O24	93.26(6)	F4	C55	F6	107.5(2)
O23	Ru2	N12	170.61(7)	F4	C55	C54	112.95(19)
O23	Ru2	N22	90.74(7)	F5	C55	F6	106.72(19)
O24	Ru2	N12	87.95(7)	F5	C55	C54	110.2(2)
O24	Ru2	N22	87.15(7)	F6	C55	C54	112.1(2)
N12	Ru2	N22	98.62(7)	F7	C56	F8	106.3(2)
Ru1	O11	C52	122.51(15)	F7	C56	F9	107.9(3)
Ru1	O12	C54	122.65(15)	F7	C56	C57	111.1(2)
Ru1	O13	C57	122.59(15)	F8	C56	F9	107.2(3)
Ru1	O14	C59	123.28(15)	F8	C56	C57	110.4(2)
Ru2	O21	C62	122.75(15)	F9	C56	C57	113.5(2)
Ru2	O22	C64	121.79(15)	O13	C57	C56	112.4(2)
Ru2	O23	C69	121.44(14)	O13	C57	C58	129.4(2)
Ru2	O24	C67	122.12(14)	C56	C57	C58	118.2(2)
Ru1	N11	C11	117.69(14)	C57	C58	C59	123.4(2)
Ru1	N11	C14	133.77(15)	O14	C59	C58	129.4(2)
C11	N11	C14	107.96(17)	O14	C59	C60	113.2(2)

Ru2	N12	C12	129.87(15)	C58	C59	C60	117.4(2)
Ru2	N12	C31	114.18(13)	F10A	C60	F11A	104.7(4)
C12	N12	C31	115.32(18)	F10A	C60	F12A	109.1(4)
Ru1	N21	C21	117.19(14)	F10A	C60	C59	110.4(3)
Ru1	N21	C24	134.43(14)	F11A	C60	F12A	105.8(4)
C21	N21	C24	107.69(17)	F11A	C60	C59	113.4(2)
Ru2	N22	C22	128.30(14)	F12A	C60	C59	113.1(3)
Ru2	N22	C41	113.04(13)	F10B	C60	F11B	103.6(6)
C22	N22	C41	117.27(17)	F10B	C60	F12B	107.6(7)
N11	C11	C12	110.94(18)	F10B	C60	C59	110.4(4)
N11	C11	C21	113.69(18)	F11B	C60	F12B	106.0(6)
C12	C11	C21	134.18(19)	F11B	C60	C59	114.3(4)
N12	C12	C11	124.97(19)	F12B	C60	C59	114.3(4)
N12	C12	C13	130.60(19)	F13	C61	F14	106.5(2)
C11	C12	C13	104.33(17)	F13	C61	F15	107.7(2)
C12	C13	C14	105.83(18)	F13	C61	C62	110.8(2)
C12	C13	C18	135.1(2)	F14	C61	F15	107.3(2)
C14	C13	C18	119.1(2)	F14	C61	C62	112.9(2)
N11	C14	C13	110.60(19)	F15	C61	C62	111.4(2)
N11	C14	C15	126.8(2)	O21	C62	C61	112.8(2)
C13	C14	C15	122.5(2)	O21	C62	C63	129.2(2)
C14	C15	C16	117.6(2)	C61	C62	C63	117.9(2)
C15	C16	C17	120.9(2)	C62	C63	C64	123.8(2)
C16	C17	C18	121.4(2)	O22	C64	C63	129.2(2)
C13	C18	C17	118.5(2)	O22	C64	C65	111.7(2)
N21	C21	C11	113.57(18)	C63	C64	C65	119.0(2)
N21	C21	C22	111.18(17)	F16	C65	F17	106.1(2)
C11	C21	C22	133.48(19)	F16	C65	F18	107.9(3)
N22	C22	C21	124.40(18)	F16	C65	C64	112.9(2)
N22	C22	C23	131.25(19)	F17	C65	F18	108.2(3)
C21	C22	C23	104.27(17)	F17	C65	C64	110.9(2)
C22	C23	C24	105.75(18)	F18	C65	C64	110.6(2)
C22	C23	C28	135.4(2)	F19	C66	F20	107.2(2)
C24	C23	C28	118.75(19)	F19	C66	F21	107.2(2)
N21	C24	C23	110.70(18)	F19	C66	C67	111.6(2)
N21	C24	C25	126.4(2)	F20	C66	F21	108.0(2)
C23	C24	C25	122.86(19)	F20	C66	C67	113.1(2)
C24	C25	C26	117.4(2)	F21	C66	C67	109.5(2)
C25	C26	C27	120.6(2)	O24	C67	C66	111.8(2)
C26	C27	C28	122.1(2)	O24	C67	C68	129.5(2)
C23	C28	C27	118.2(2)	C66	C67	C68	118.7(2)

N12	C31	C32	119.93(19)	C67	C68	C69	123.9(2)
N12	C31	C36	119.42(19)	O23	C69	C68	129.0(2)
C32	C31	C36	120.6(2)	O23	C69	C70	112.6(2)
C31	C32	C33	119.1(2)	C68	C69	C70	118.4(2)
C32	C33	C34	121.5(2)	F22	C70	F23	106.4(2)
C33	C34	C35	117.9(2)	F22	C70	F24	108.6(2)
C33	C34	C37	121.1(2)	F22	C70	C69	113.6(2)
C35	C34	C37	121.0(2)	F23	C70	F24	106.4(2)
C34	C35	C36	121.6(2)	F23	C70	C69	110.0(2)
C31	C36	C35	119.2(2)	F24	C70	C69	111.6(2)

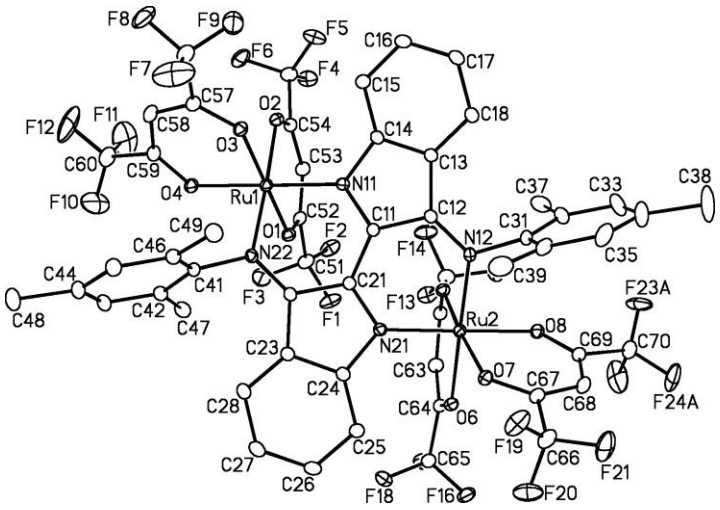

Figure B-20: ORTEP view of **5.2h-trans**. Thermal ellipsoids at the 50% probability level with all hydrogen atoms removed for clarity. **5.2h-trans** presents as a racemate of ΛΛ and ΔΔ isomers

Table B-20: Bond lengths (Å) and angles (°) for **5.2h-trans**

Ru1	O1	2.0119(16)	N22	C22	1.307(3)
Ru1	O2	2.0456(16)	N22	C41	1.450(3)
Ru1	O3	2.0366(16)	C11	C12	1.465(3)
Ru1	O4	2.0639(16)	C11	C21	1.408(3)
Ru1	N11	1.9741(18)	C12	C13	1.461(3)
Ru1	N22	2.0047(18)	C13	C14	1.404(3)
Ru2	O5	2.0168(15)	C13	C18	1.394(3)
Ru2	O6	2.0477(16)	C14	C15	1.379(3)
Ru2	O7	2.0416(16)	C15	C16	1.388(3)
Ru2	O8	2.0584(16)	C16	C17	1.390(4)
Ru2	N12	2.0059(19)	C17	C18	1.387(3)
Ru2	N21	1.9840(18)	C21	C22	1.464(3)
F1	C51	1.334(3)	C22	C23	1.462(3)
F2	C51	1.323(3)	C23	C24	1.406(3)
F3	C51	1.329(3)	C23	C28	1.391(3)
F4	C55	1.329(3)	C24	C25	1.383(3)
F5	C55	1.322(3)	C25	C26	1.391(3)
F6	C55	1.338(3)	C26	C27	1.383(4)
F7	C56	1.295(4)	C27	C28	1.388(3)

F8	C56	1.316(3)	C31	C32	1.396(4)
F9	C56	1.303(4)	C31	C36	1.391(4)
F10	C60	1.253(4)	C32	C33	1.394(4)
F11	C60	1.357(5)	C32	C37	1.498(5)
F12	C60	1.262(4)	C33	C34	1.370(7)
F13	C61	1.326(3)	C34	C35	1.388(6)
F14	C61	1.325(3)	C34	C38	1.514(5)
F15	C61	1.331(3)	C35	C36	1.394(4)
F16	C65	1.325(3)	C36	C39	1.495(5)
F17	C65	1.336(3)	C41	C42	1.399(3)
F18	C65	1.326(3)	C41	C46	1.393(3)
F19	C66	1.315(3)	C42	C43	1.394(3)
F20	C66	1.326(4)	C42	C47	1.500(3)
F21	C66	1.324(3)	C43	C44	1.381(4)
F22A	C70	1.357(8)	C44	C45	1.385(4)
F23A	C70	1.221(9)	C44	C48	1.511(4)
F24A	C70	1.300(5)	C45	C46	1.391(3)
F22B	C70	1.215(7)	C46	C49	1.507(3)
F23B	C70	1.288(12)	C51	C52	1.527(3)
F24B	C70	1.367(6)	C52	C53	1.391(3)
O1	C52	1.256(3)	C53	C54	1.385(3)
O2	C54	1.266(3)	C54	C55	1.529(3)
O3	C57	1.263(3)	C56	C57	1.529(4)
O4	C59	1.254(3)	C57	C58	1.387(4)
O5	C62	1.259(3)	C58	C59	1.390(4)
O6	C64	1.265(3)	C59	C60	1.528(4)
O7	C67	1.260(3)	C61	C62	1.529(3)
O8	C69	1.259(3)	C62	C63	1.392(3)
N11	C11	1.334(3)	C63	C64	1.390(3)
N11	C14	1.424(3)	C64	C65	1.523(3)
N12	C12	1.303(3)	C66	C67	1.533(3)
N12	C31	1.448(3)	C67	C68	1.391(3)
N21	C21	1.335(3)	C68	C69	1.388(3)
N21	C24	1.424(3)	C69	C70	1.527(3)

O1	Ru1	O2	92.74(6)	N22	C41	C42	119.3(2)
O1	Ru1	O3	177.41(6)	N22	C41	C46	118.1(2)
O1	Ru1	O4	86.68(6)	C42	C41	C46	122.6(2)
O1	Ru1	N11	90.05(7)	C41	C42	C43	116.7(2)
O1	Ru1	N22	84.04(7)	C41	C42	C47	123.1(2)

O2	Ru1	O3	84.99(6)	C43	C42	C47	120.2(2)
O2	Ru1	O4	82.90(7)	C42	C43	C44	122.8(2)
O2	Ru1	N11	93.85(7)	C43	C44	C45	118.2(2)
O2	Ru1	N22	175.00(7)	C43	C44	C48	120.5(3)
O3	Ru1	O4	91.78(6)	C45	C44	C48	121.3(3)
O3	Ru1	N11	91.35(7)	C44	C45	C46	122.0(2)
O3	Ru1	N22	98.13(7)	C41	C46	C45	117.6(2)
O4	Ru1	N11	175.27(7)	C41	C46	C49	121.6(2)
O4	Ru1	N22	93.08(7)	C45	C46	C49	120.8(2)
N11	Ru1	N22	89.98(7)	F1	C51	F2	107.6(2)
O5	Ru2	O6	93.11(6)	F1	C51	F3	107.3(2)
O5	Ru2	O7	174.55(6)	F1	C51	C52	111.3(2)
O5	Ru2	O8	83.05(6)	F2	C51	F3	107.2(2)
O5	Ru2	N12	84.74(7)	F2	C51	C52	113.8(2)
O5	Ru2	N21	90.96(7)	F3	C51	C52	109.4(2)
O6	Ru2	O7	85.11(6)	O1	C52	C51	112.1(2)
O6	Ru2	O8	85.42(6)	O1	C52	C53	129.2(2)
O6	Ru2	N12	177.42(7)	C51	C52	C53	118.5(2)
O6	Ru2	N21	92.05(7)	C52	C53	C54	123.6(2)
O7	Ru2	O8	91.67(6)	O2	C54	C53	129.5(2)
O7	Ru2	N12	96.91(7)	O2	C54	C55	111.9(2)
O7	Ru2	N21	94.25(7)	C53	C54	C55	118.6(2)
O8	Ru2	N12	92.89(7)	F4	C55	F5	108.1(2)
O8	Ru2	N21	173.35(7)	F4	C55	F6	107.7(2)
N12	Ru2	N21	89.42(7)	F4	C55	C54	113.4(2)
Ru1	O1	C52	123.07(15)	F5	C55	F6	106.9(2)
Ru1	O2	C54	121.72(15)	F5	C55	C54	111.2(2)
Ru1	O3	C57	122.50(15)	F6	C55	C54	109.2(2)
Ru1	O4	C59	122.22(16)	F7	C56	F8	108.2(3)
Ru2	O5	C62	121.63(14)	F7	C56	F9	107.1(3)
Ru2	O6	C64	121.57(14)	F7	C56	C57	110.6(2)
Ru2	O7	C67	122.41(15)	F8	C56	F9	106.0(3)
Ru2	O8	C69	123.42(15)	F8	C56	C57	113.2(2)
Ru1	N11	C11	123.41(15)	F9	C56	C57	111.5(2)
Ru1	N11	C14	129.29(15)	O3	C57	C56	112.1(2)
C11	N11	C14	107.29(18)	O3	C57	C58	129.4(2)
Ru2	N12	C12	122.68(15)	C56	C57	C58	118.5(2)
Ru2	N12	C31	118.09(14)	C57	C58	C59	123.8(2)
C12	N12	C31	118.50(19)	O4	C59	C58	129.4(2)
Ru2	N21	C21	122.56(15)	O4	C59	C60	112.6(2)
Ru2	N21	C24	130.36(14)	C58	C59	C60	118.0(2)

C21	N21	C24	107.02(18)	F10	C60	F11	101.1(3)
Ru1	N22	C22	122.63(15)	F10	C60	F12	116.1(3)
Ru1	N22	C41	118.64(14)	F10	C60	C59	113.9(3)
C22	N22	C41	118.21(18)	F11	C60	F12	99.1(3)
N11	C11	C12	111.23(18)	F11	C60	C59	108.7(3)
N11	C11	C21	122.75(19)	F12	C60	C59	115.5(3)
C12	C11	C21	124.27(19)	F13	C61	F14	107.7(2)
N12	C12	C11	122.62(19)	F13	C61	F15	107.3(2)
N12	C12	C13	132.8(2)	F13	C61	C62	113.3(2)
C11	C12	C13	104.57(18)	F14	C61	F15	108.3(2)
C12	C13	C14	106.03(19)	F14	C61	C62	111.8(2)
C12	C13	C18	134.1(2)	F15	C61	C62	108.2(2)
C14	C13	C18	119.8(2)	O5	C62	C61	112.7(2)
N11	C14	C13	110.59(19)	O5	C62	C63	129.5(2)
N11	C14	C15	127.5(2)	C61	C62	C63	117.6(2)
C13	C14	C15	121.9(2)	C62	C63	C64	123.6(2)
C14	C15	C16	117.7(2)	O6	C64	C63	129.1(2)
C15	C16	C17	121.1(2)	O6	C64	C65	112.7(2)
C16	C17	C18	121.3(2)	C63	C64	C65	118.3(2)
C13	C18	C17	118.1(2)	F16	C65	F17	107.7(2)
N21	C21	C11	122.52(19)	F16	C65	F18	107.6(2)
N21	C21	C22	111.50(18)	F16	C65	C64	111.8(2)
C11	C21	C22	124.2(2)	F17	C65	F18	107.0(2)
N22	C22	C21	123.00(19)	F17	C65	C64	112.6(2)
N22	C22	C23	132.4(2)	F18	C65	C64	109.8(2)
C21	C22	C23	104.62(18)	F19	C66	F20	107.3(2)
C22	C23	C24	105.89(19)	F19	C66	F21	108.0(2)
C22	C23	C28	134.2(2)	F19	C66	C67	112.5(2)
C24	C23	C28	119.9(2)	F20	C66	F21	106.0(2)
N21	C24	C23	110.83(19)	F20	C66	C67	109.7(2)
N21	C24	C25	127.2(2)	F21	C66	C67	113.0(2)
C23	C24	C25	122.0(2)	O7	C67	C66	112.6(2)
C24	C25	C26	117.1(2)	O7	C67	C68	130.1(2)
C25	C26	C27	121.6(2)	C66	C67	C68	117.2(2)
C26	C27	C28	121.2(2)	C67	C68	C69	123.8(2)
C23	C28	C27	118.2(2)	O8	C69	C68	128.5(2)
N12	C31	C32	118.6(2)	O8	C69	C70	113.2(2)
N12	C31	C36	118.3(2)	C68	C69	C70	118.2(2)
C32	C31	C36	123.1(3)	F22A	C70	F23A	105.2(8)
C31	C32	C33	116.4(3)	F22A	C70	F24A	100.3(5)
C31	C32	C37	122.1(3)	F22A	C70	C69	106.7(4)

C33	C32	C37	121.5(3)	F23A	C70	F24A	114.3(7)
C32	C33	C34	123.0(4)	F23A	C70	C69	114.6(6)
C33	C34	C35	118.2(3)	F24A	C70	C69	113.9(3)
C33	C34	C38	120.9(5)	F22B	C70	F23B	109.3(8)
C35	C34	C38	120.9(5)	F22B	C70	F24B	108.3(6)
C34	C35	C36	122.2(4)	F22B	C70	C69	115.5(4)
C31	C36	C35	116.9(3)	F23B	C70	F24B	98.9(8)
C31	C36	C39	122.1(2)	F23B	C70	C69	113.2(6)
C35	C36	C39	121.0(3)	F24B	C70	C69	110.2(3)

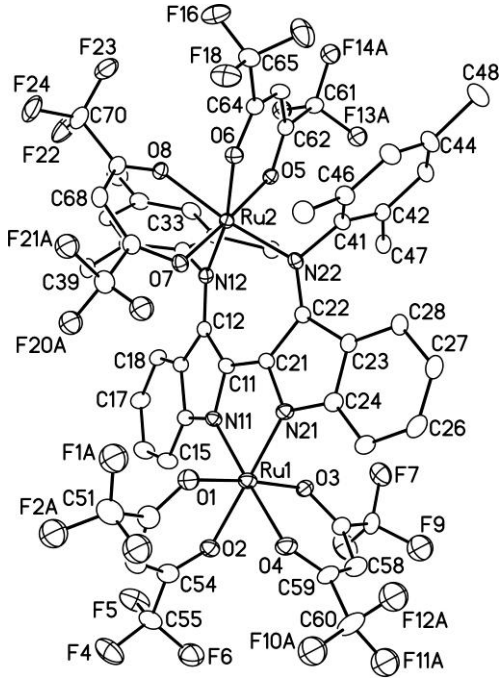

Figure B-21: ORTEP view of **5.2h-cis**. Thermal ellipsoids at the 50% probability level with all hydrogen atoms removed for clarity. **5.2h-cis** presents as a racemate of ΛΔ and ΔΛ isomers

Table B-21: Bond lengths (Å) and angles (^{o}) for **5.2h-cis**

Ru1	O1	1.994(5)	N11	C14	1.418(8)
Ru1	O2	2.073(5)	N12	C12	1.319(7)
Ru1	O3	2.034(4)	N12	C31	1.459(7)

Ru1	O4	2.070(5)	N21	C21	1.344(7)
Ru1	N11	1.989(5)	N21	C24	1.410(8)
Ru1	N21	1.995(5)	N22	C22	1.308(7)
Ru2	O5	2.038(4)	N22	C41	1.463(7)
Ru2	O6	2.076(4)	C11	C12	1.457(8)
Ru2	O7	2.027(4)	C11	C21	1.417(8)
Ru2	O8	2.052(4)	C12	C13	1.458(8)
Ru2	N12	2.022(5)	C13	C14	1.413(8)
Ru2	N22	2.020(5)	C13	C18	1.388(8)
F1A	C51	1.317(17)	C14	C15	1.370(9)
F2A	C51	1.352(18)	C15	C16	1.375(10)
F3A	C51	1.420(19)	C16	C17	1.381(10)
F1B	C51	1.280(17)	C17	C18	1.379(9)
F2B	C51	1.323(18)	C21	C22	1.452(8)
F3B	C51	1.373(19)	C22	C23	1.477(8)
F4	C55	1.319(9)	C23	C24	1.394(9)
F5	C55	1.310(10)	C23	C28	1.394(8)
F6	C55	1.327(10)	C24	C25	1.381(9)
F7	C56	1.315(9)	C25	C26	1.388(10)
F8	C56	1.307(9)	C26	C27	1.372(11)
F9	C56	1.347(9)	C27	C28	1.396(9)
F10A	C60	1.227(17)	C31	C32	1.382(8)
F11A	C60	1.345(17)	C31	C36	1.406(8)
F12A	C60	1.459(19)	C32	C33	1.398(9)
F10B	C60	1.262(17)	C32	C37	1.506(9)
F11B	C60	1.292(18)	C33	C34	1.378(10)
F12B	C60	1.576(19)	C34	C35	1.375(10)
F13A	C61	1.360(11)	C34	C38	1.506(9)
F14A	C61	1.322(11)	C35	C36	1.386(9)
F15A	C61	1.325(12)	C36	C39	1.505(9)
F13B	C61	1.305(11)	C41	C42	1.384(8)
F14B	C61	1.352(11)	C41	C46	1.402(9)
F15B	C61	1.328(12)	C42	C43	1.396(9)
F16	C65	1.320(9)	C42	C47	1.499(9)
F17	C65	1.337(9)	C43	C44	1.377(10)
F18	C65	1.313(9)	C44	C45	1.391(10)
F19A	C66	1.253(13)	C44	C48	1.516(9)
F20A	C66	1.331(13)	C45	C46	1.384(9)
F21A	C66	1.408(13)	C46	C49	1.509(9)
F19B	C66	1.395(14)	C51	C52	1.528(12)
F20B	C66	1.338(13)	C52	C53	1.389(12)
F21B	C66	1.288(13)	C53	C54	1.412(11)
F22	C70	1.305(10)	C54	C55	1.509(11)

F23	C70	1.331(10)	C56	C57	1.491(10)
F24	C70	1.326(8)	C57	C58	1.371(10)
O1	C52	1.249(9)	C58	C59	1.408(11)
O2	C54	1.235(9)	C59	C60	1.541(12)
O3	C57	1.276(8)	C61	C62	1.534(9)
O4	C59	1.272(9)	C62	C63	1.376(9)
O5	C62	1.258(7)	C63	C64	1.383(9)
O6	C64	1.271(7)	C64	C65	1.527(9)
O7	C67	1.257(7)	C66	C67	1.525(9)
O8	C69	1.256(7)	C67	C68	1.390(9)
N11	C11	1.350(7)	C68	C69	1.393(9)
			C69	C70	1.534(9)

O1	Ru1	O2	92.2(2)	C45	C44	C48	120.0(7)
O1	Ru1	O3	175.38(19)	C44	C45	C46	121.7(6)
O1	Ru1	O4	84.9(2)	C41	C46	C45	117.2(6)
O1	Ru1	N11	95.1(2)	C41	C46	C49	123.2(6)
O1	Ru1	N21	89.5(2)	C45	C46	C49	119.4(6)
O2	Ru1	O3	84.65(18)	F1A	C51	F2A	115.0(12)
O2	Ru1	O4	81.6(2)	F1A	C51	F3A	98.7(12)
O2	Ru1	N11	100.33(19)	F1A	C51	C52	114.1(10)
O2	Ru1	N21	177.25(19)	F2A	C51	F3A	106.0(11)
O3	Ru1	O4	91.36(19)	F2A	C51	C52	113.8(11)
O3	Ru1	N11	88.82(19)	F3A	C51	C52	107.4(10)
O3	Ru1	N21	93.8(2)	F1B	C51	F2B	107.5(12)
O4	Ru1	N11	178.0(2)	F1B	C51	F3B	108.5(12)
O4	Ru1	N21	100.7(2)	F1B	C51	C52	112.9(11)
N11	Ru1	N21	77.32(19)	F2B	C51	F3B	104.3(12)
O5	Ru2	O6	91.41(15)	F2B	C51	C52	113.8(11)
O5	Ru2	O7	176.80(16)	F3B	C51	C52	109.4(11)
O5	Ru2	O8	86.41(15)	O1	C52	C51	112.8(8)
O5	Ru2	N12	90.82(17)	O1	C52	C53	130.0(8)
O5	Ru2	N22	94.77(16)	C51	C52	C53	117.2(8)
O6	Ru2	O7	85.49(16)	C52	C53	C54	123.7(7)
O6	Ru2	O8	78.77(16)	O2	C54	C53	127.7(8)
O6	Ru2	N12	169.54(17)	O2	C54	C55	112.6(7)
O6	Ru2	N22	90.45(18)	C53	C54	C55	119.8(7)
O7	Ru2	O8	92.17(16)	F4	C55	F5	108.4(7)
O7	Ru2	N12	92.08(17)	F4	C55	F6	105.5(7)
O7	Ru2	N22	86.09(17)	F4	C55	C54	111.8(7)
O8	Ru2	N12	91.18(17)	F5	C55	F6	106.3(7)

O8	Ru2	N22	169.19(18)	F5	C55	C54	111.6(6)
N12	Ru2	N22	99.54(19)	F6	C55	C54	112.7(7)
Ru1	O1	C52	123.2(5)	F7	C56	F8	107.1(7)
Ru1	O2	C54	123.2(5)	F7	C56	F9	106.1(6)
Ru1	O3	C57	124.0(4)	F7	C56	C57	113.3(6)
Ru1	O4	C59	122.1(5)	F8	C56	F9	106.2(7)
Ru2	O5	C62	123.3(4)	F8	C56	C57	111.1(6)
Ru2	O6	C64	121.7(4)	F9	C56	C57	112.6(6)
Ru2	O7	C67	121.8(4)	O3	C57	C56	112.2(6)
Ru2	O8	C69	120.7(4)	O3	C57	C58	129.0(7)
Ru1	N11	C11	117.9(4)	C56	C57	C58	118.8(7)
Ru1	N11	C14	133.2(4)	C57	C58	C59	123.6(7)
C11	N11	C14	108.1(5)	O4	C59	C58	129.5(7)
Ru2	N12	C12	130.9(4)	O4	C59	C60	112.2(7)
Ru2	N12	C31	113.5(3)	C58	C59	C60	118.2(7)
C12	N12	C31	114.9(5)	F10A	C60	F11A	110.1(13)
Ru1	N21	C21	117.6(4)	F10A	C60	F12A	109.4(14)
Ru1	N21	C24	133.9(4)	F10A	C60	C59	115.0(11)
C21	N21	C24	108.1(5)	F11A	C60	F12A	102.1(12)
Ru2	N22	C22	130.0(4)	F11A	C60	C59	112.6(11)
Ru2	N22	C41	113.4(3)	F12A	C60	C59	106.8(10)
C22	N22	C41	115.9(5)	F10B	C60	F11B	125.9(14)
N11	C11	C12	110.5(5)	F10B	C60	F12B	96.4(11)
N11	C11	C21	113.2(5)	F10B	C60	C59	115.6(11)
C12	C11	C21	135.2(5)	F11B	C60	F12B	90.1(11)
N12	C12	C11	125.0(5)	F11B	C60	C59	115.5(10)
N12	C12	C13	129.9(5)	F12B	C60	C59	101.0(11)
C11	C12	C13	105.1(5)	F13A	C61	F14A	109.3(7)
C12	C13	C14	106.5(5)	F13A	C61	F15A	105.7(7)
C12	C13	C18	135.8(5)	F13A	C61	C62	109.9(6)
C14	C13	C18	117.7(5)	F14A	C61	F15A	109.4(7)
N11	C14	C13	109.7(5)	F14A	C61	C62	113.3(7)
N11	C14	C15	126.8(6)	F15A	C61	C62	109.1(7)
C13	C14	C15	123.4(6)	F13B	C61	F14B	110.9(7)
C14	C15	C16	117.2(6)	F13B	C61	F15B	107.8(7)
C15	C16	C17	120.9(6)	F13B	C61	C62	109.6(6)
C16	C17	C18	121.9(6)	F14B	C61	F15B	102.8(7)
C13	C18	C17	118.8(6)	F14B	C61	C62	112.6(6)
N21	C21	C11	113.7(5)	F15B	C61	C62	112.8(7)
N21	C21	C22	110.6(5)	O5	C62	C61	112.7(5)
C11	C21	C22	134.4(5)	O5	C62	C63	129.4(6)

N22	C22	C21	125.6(5)	C61	C62	C63	117.9(6)
N22	C22	C23	129.8(5)	C62	C63	C64	124.4(6)
C21	C22	C23	104.5(5)	O6	C64	C63	129.1(6)
C22	C23	C24	106.1(5)	O6	C64	C65	113.6(5)
C22	C23	C28	135.6(6)	C63	C64	C65	117.3(6)
C24	C23	C28	118.3(6)	F16	C65	F17	106.2(6)
N21	C24	C23	110.4(5)	F16	C65	F18	107.4(6)
N21	C24	C25	126.1(6)	F16	C65	C64	110.8(6)
C23	C24	C25	123.5(6)	F17	C65	F18	107.5(7)
C24	C25	C26	116.8(7)	F17	C65	C64	110.9(6)
C25	C26	C27	121.3(6)	F18	C65	C64	113.6(6)
C26	C27	C28	121.2(6)	F19A	C66	F20A	107.9(9)
C23	C28	C27	118.7(6)	F19A	C66	F21A	105.9(9)
N12	C31	C32	119.9(5)	F19A	C66	C67	115.7(8)
N12	C31	C36	118.4(5)	F20A	C66	F21A	108.3(8)
C32	C31	C36	121.7(5)	F20A	C66	C67	108.1(8)
C31	C32	C33	117.7(6)	F21A	C66	C67	110.6(7)
C31	C32	C37	122.7(5)	F19B	C66	F20B	104.4(8)
C33	C32	C37	119.4(6)	F19B	C66	F21B	106.8(9)
C32	C33	C34	122.2(6)	F19B	C66	C67	109.2(7)
C33	C34	C35	118.1(6)	F20B	C66	F21B	108.0(8)
C33	C34	C38	121.3(7)	F20B	C66	C67	111.4(8)
C35	C34	C38	120.6(7)	F21B	C66	C67	116.4(8)
C34	C35	C36	122.7(6)	O7	C67	C66	112.3(6)
C31	C36	C35	117.3(6)	O7	C67	C68	130.0(6)
C31	C36	C39	122.7(5)	C66	C67	C68	117.7(6)
C35	C36	C39	119.9(6)	C67	C68	C69	122.7(6)
N22	C41	C42	116.5(5)	O8	C69	C68	130.0(6)
N22	C41	C46	120.7(5)	O8	C69	C70	111.0(6)
C42	C41	C46	122.7(5)	C68	C69	C70	119.0(6)
C41	C42	C43	117.3(6)	F22	C70	F23	106.9(7)
C41	C42	C47	123.0(5)	F22	C70	F24	108.5(7)
C43	C42	C47	119.6(6)	F22	C70	C69	111.0(6)
C42	C43	C44	121.8(6)	F23	C70	F24	106.2(7)
C43	C44	C45	118.9(6)	F23	C70	C69	110.9(6)
C43	C44	C48	121.1(7)	F24	C70	C69	113.1(6)

Appendix C: Electrochemical Data

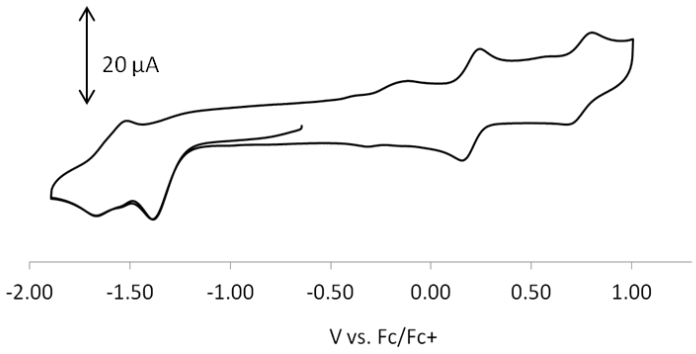

Figure C-1: Cyclic voltammogram of **2.2d** (CH_2Cl_2 solution, 0.1 mM Bu_4NBF_4 electrolyte and scan rate 100 mVs^{-1})

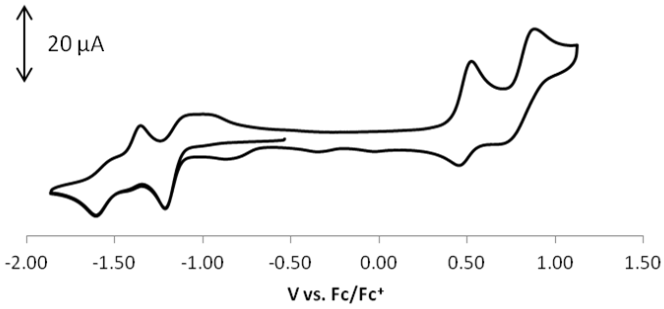

Figure C-2: Cyclic voltammogram of **3.3b** (CH_2Cl_2 solution, 0.1 mM Bu_4NBF_4 electrolyte and scan rate 100 mV^{s-1})

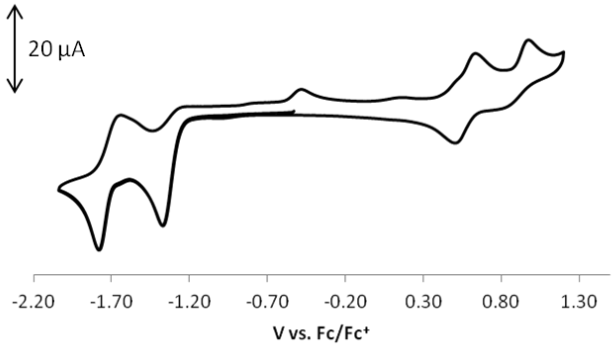

Figure C-3: Cyclic voltammogram of **3.3d** (CH_2Cl_2 solution, 0.1 mM Bu_4NBF_4 electrolyte and scan rate 100 mVs^{-1})

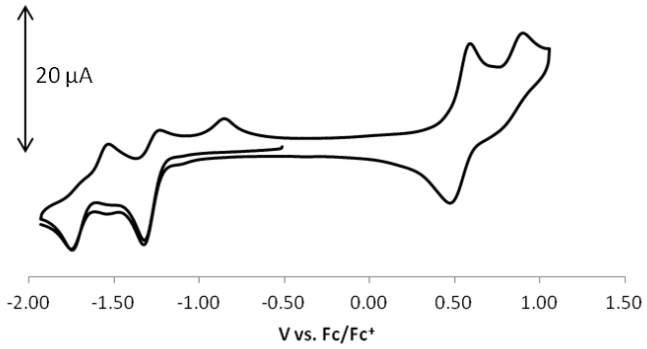

Figure C-4: Cyclic voltammogram of **3.3e** (CH_2Cl_2 solution, 0.1 mM Bu_4NBF_4 electrolyte and scan rate 100 mVs^{-1})

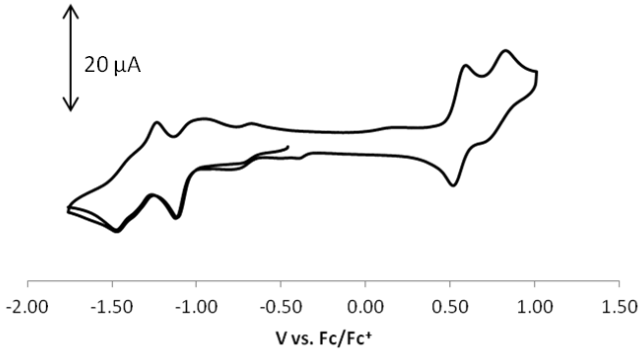

Figure C-5: Cyclic voltammogram of **3.3f** (CH_2Cl_2 solution, 0.1 mM Bu_4NBF_4 electrolyte and scan rate 100 mVs^{-1})

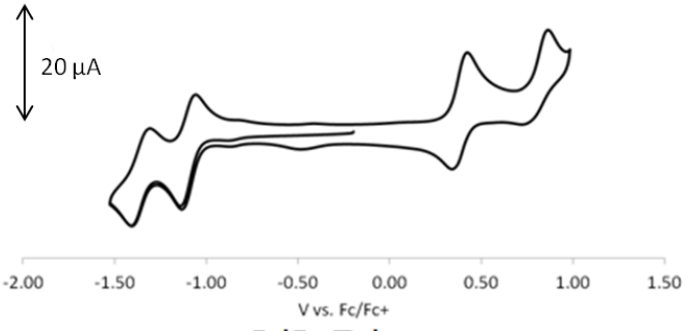

Figure C-6: Cyclic voltammogram of **3.6b** (CH_2Cl_2 solution, 0.1 mM Bu_4NBF_4 electrolyte and scan rate 100 mVs^{-1})

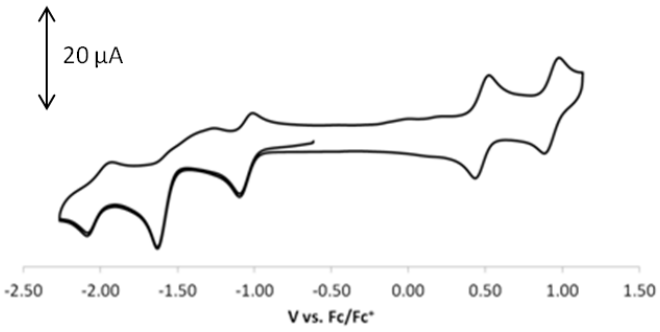

Figure C-7: Cyclic voltammogram of **3.6c** (CH_2Cl_2 solution, 0.1 mM Bu_4NBF_4 electrolyte and scan rate 100 mVs^{-1})

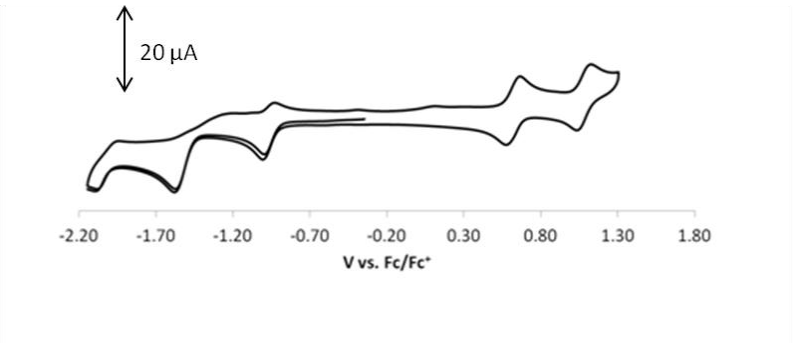

Figure C-8: Cyclic voltammogram of **3.6d** (CH_2Cl_2 solution, 0.1 mM Bu_4NBF_4 electrolyte and scan rate 100 mVs^{-1})

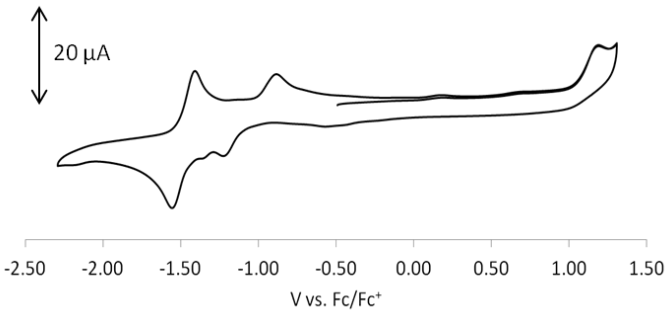

Figure C-9: Cyclic voltammogram of **5.1a** (CH_2Cl_2 solution, 0.1 mM Bu_4NBF_4 electrolyte and scan rate 100 mVs^{-1})

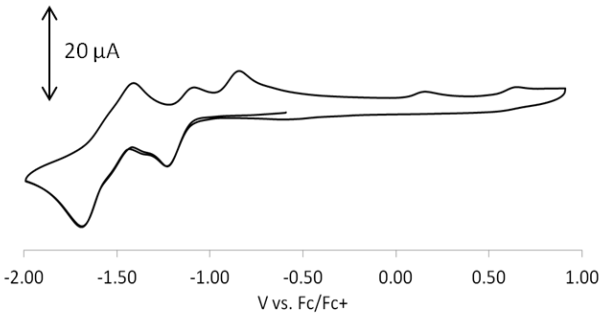

Figure C-10: Cyclic voltammogram of **5.1b** (CH_2Cl_2 solution, 0.1 mM Bu_4NBF_4 electrolyte and scan rate 100 mVs^{-1})

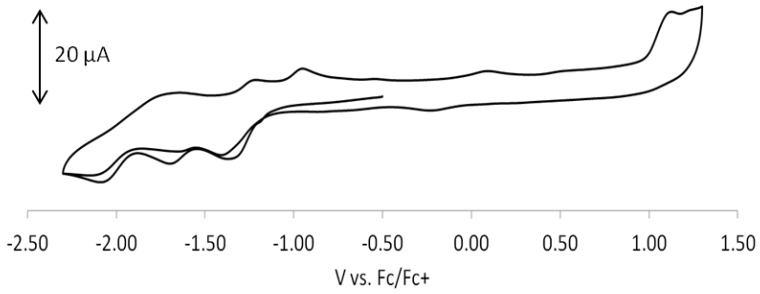

Figure C-11: Cyclic voltammogram of **5.1c** (CH_2Cl_2 solution, 0.1 mM Bu_4NBF_4 electrolyte and scan rate 100 mVs^{-1})

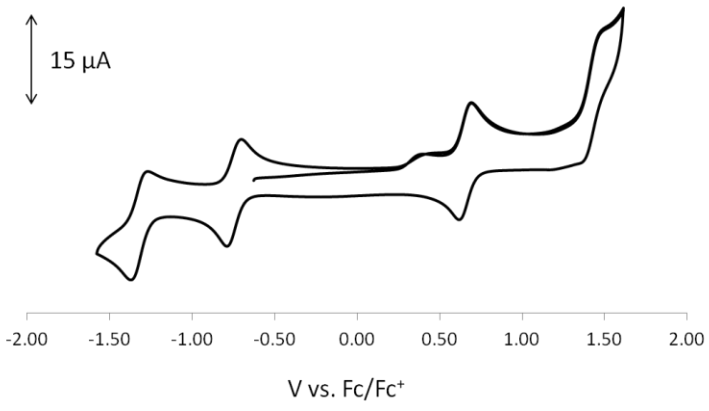

Figure C-12: Cyclic voltammogram of **5.2b-trans** (CH_2Cl_2 solution, 0.1 mM Bu_4NBF_4 electrolyte and scan rate 100 mVs^{-1})

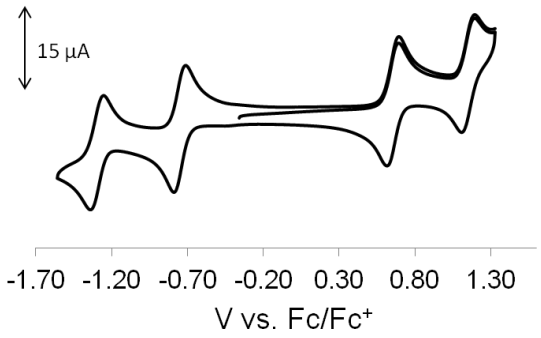

Figure C-13: Cyclic voltammogram of **5.2b-cis** (CH_2Cl_2 solution, 0.1 mM Bu_4NBF_4 electrolyte and scan rate 100 mVs^{-1}

Appendix D: NMR spectra

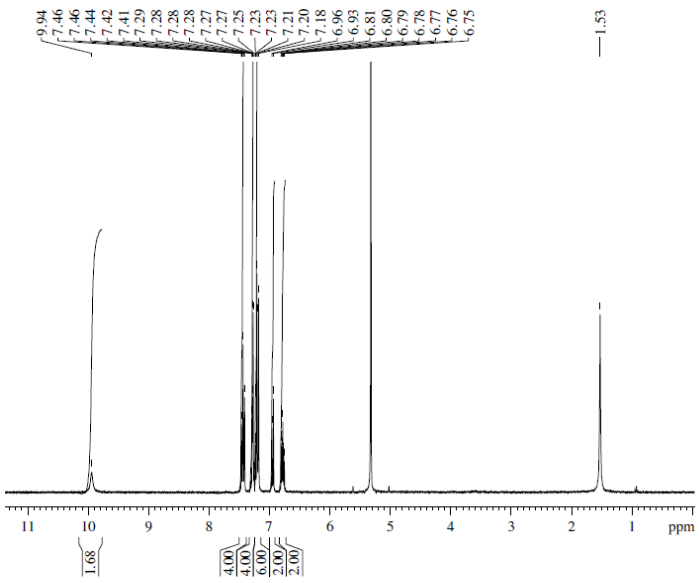

Figure D-1: ^{1}H NMR of **1.32a**. Peaks at 5.32 ppm due to solvent and 1.53 ppm due to residual water (Expected elemental analysis C 81.53 %, H 4.89 %, N 13.58 %; experimental C 77.04 %, H 4.58 %, 12.87 %

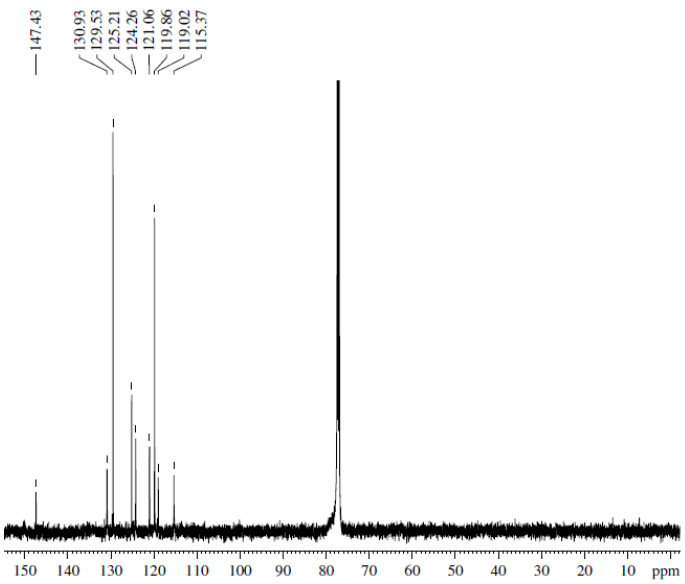

Figure D-2: ^{13}C NMR of **1.32a**

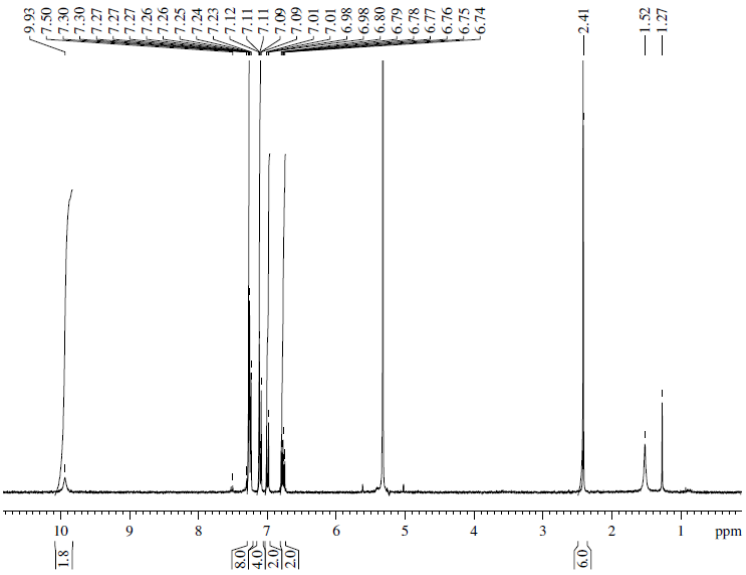

Figure D-3: ^{1}H NMR of **1.32b**. Peaks at 5.32 ppm due to solvent and 1.52 ppm due to residual water

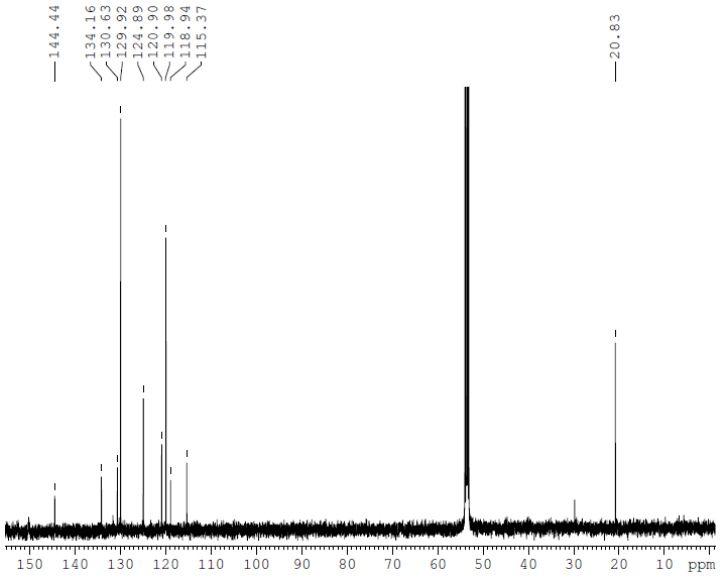

Figure D-4: ^{13}C NMR of **1.32b**

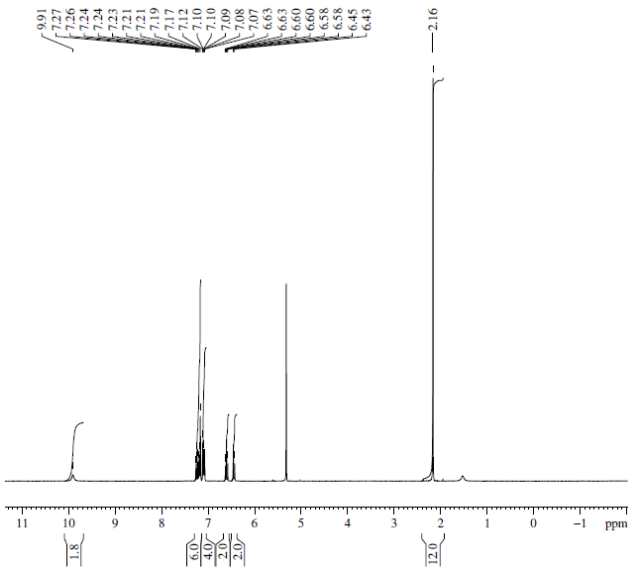

Figure D-5: ^{1}H NMR of **1.32c**. Peaks at 5.32 ppm due to solvent

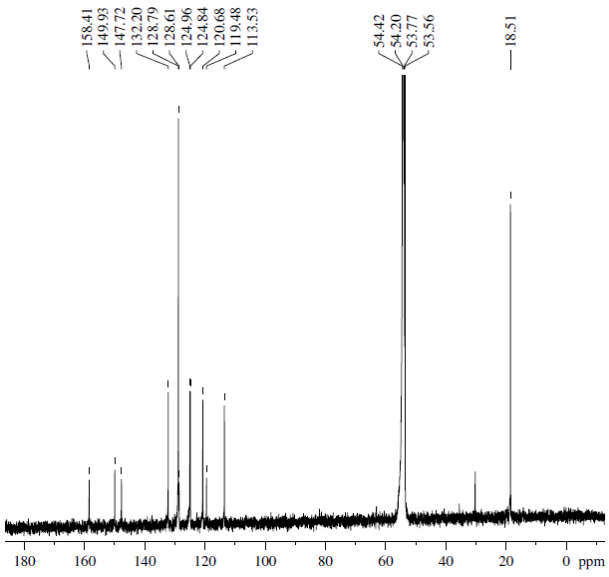

Figure D-6: ^{13}C NMR of **1.32c**

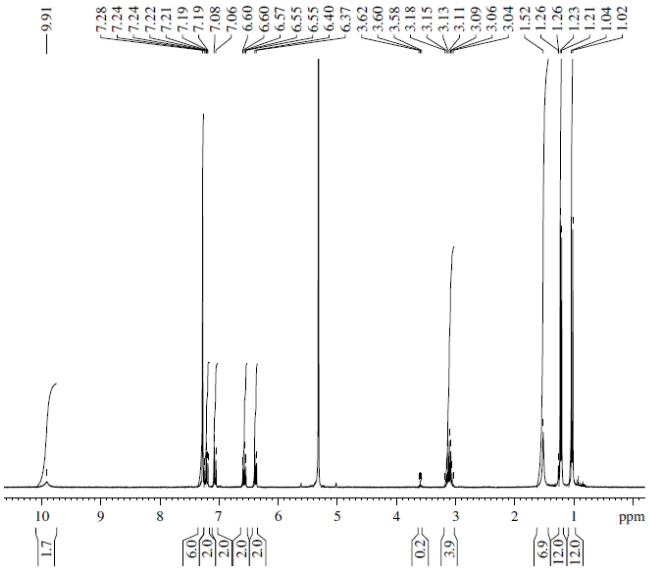

Figure D-7: ^{1}H NMR of **1.32d**. Peaks at 5.32 ppm due to solvent and 1.52 ppm due to residual water

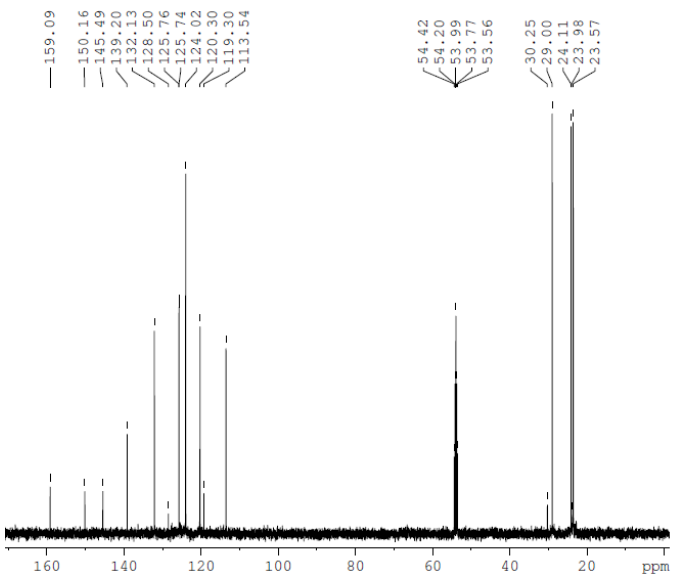

Figure D-8: ^{13}C NMR of **1.32d**

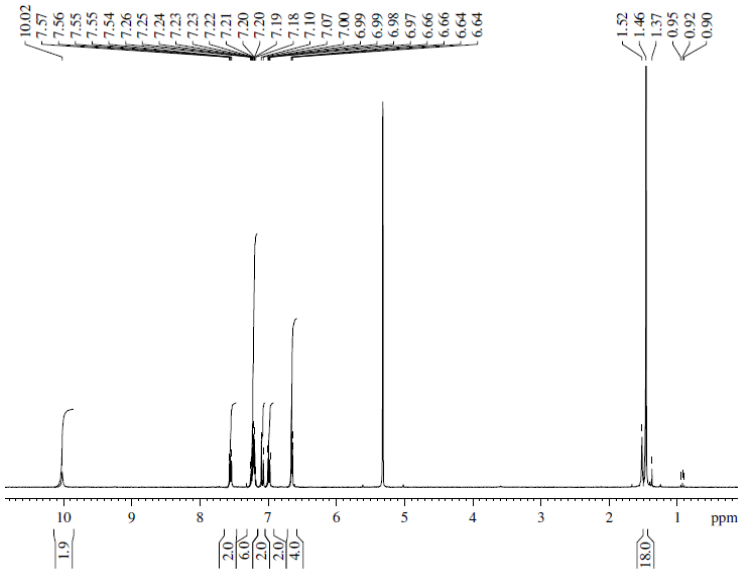

Figure D-9: ^{1}H NMR of **1.32e**. Peaks at 5.32 ppm due to solvent and 1.52 ppm due to residual water

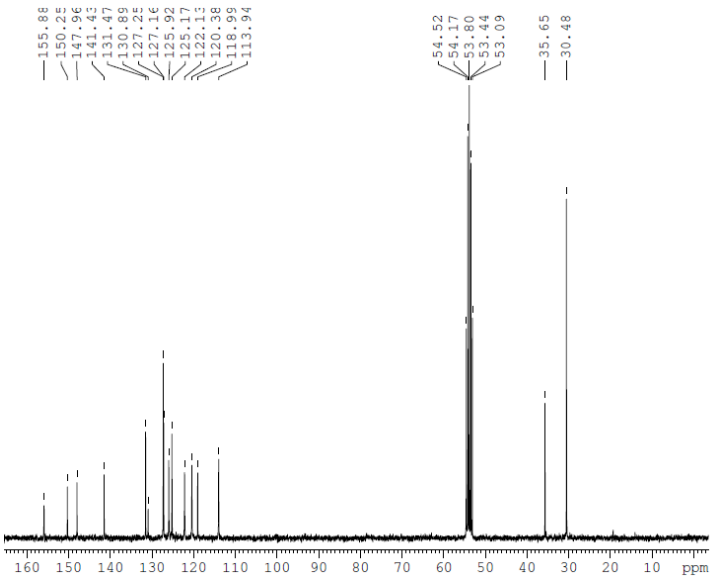

Figure D-10: ^{13}C NMR of **1.32e**

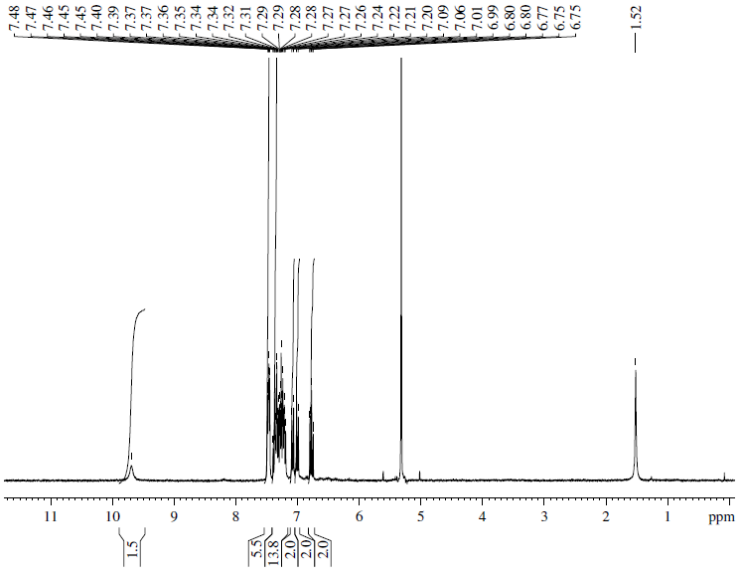

Figure D-11: ^{1}H NMR of **1.32g**. Peaks at 5.32 ppm due to solvent and 1.52 ppm due to residual water

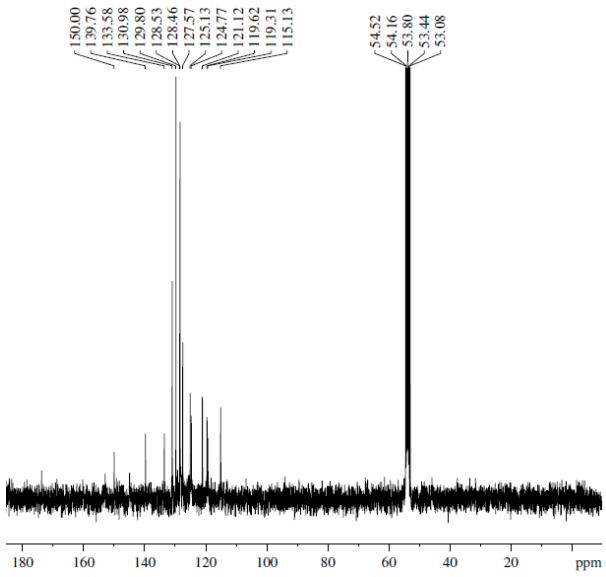

Figure D-12: ^{13}C NMR of **1.32g**

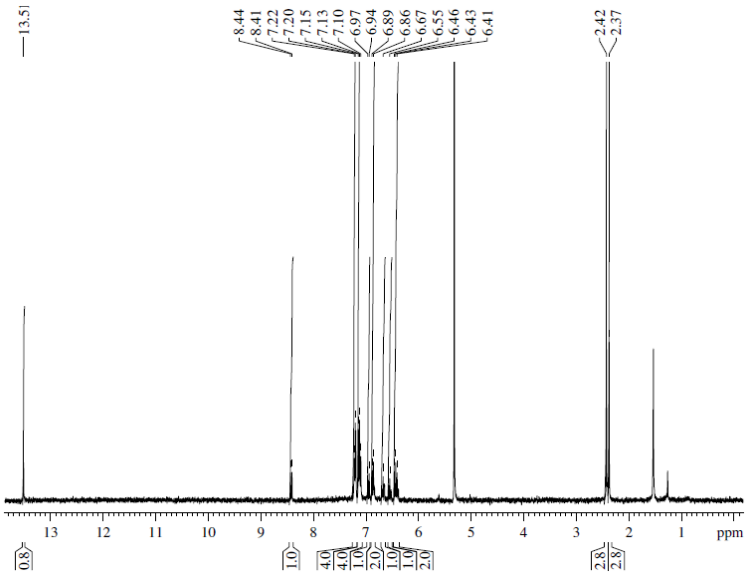

Figure D-13: ^{1}H NMR of **1.32b'**. Peaks at 5.32 ppm due to solvent and 1.52 ppm due to residual water

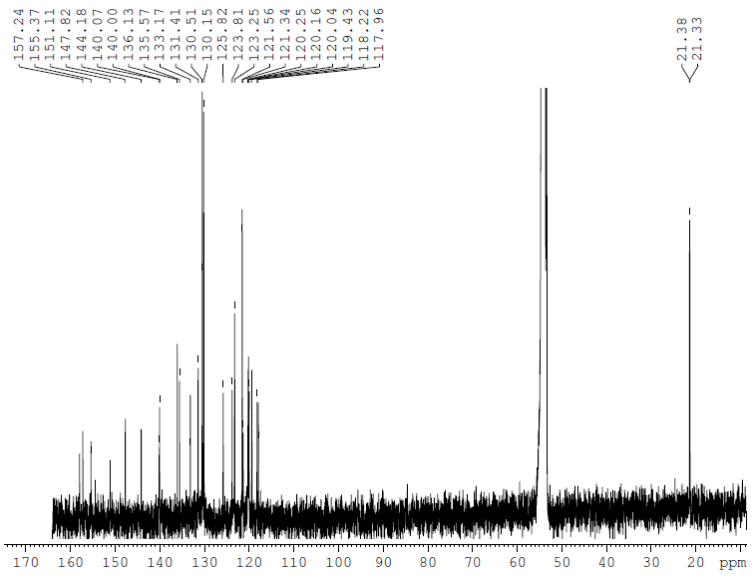

Figure D-14: ^{13}C NMR of **1.32b'**

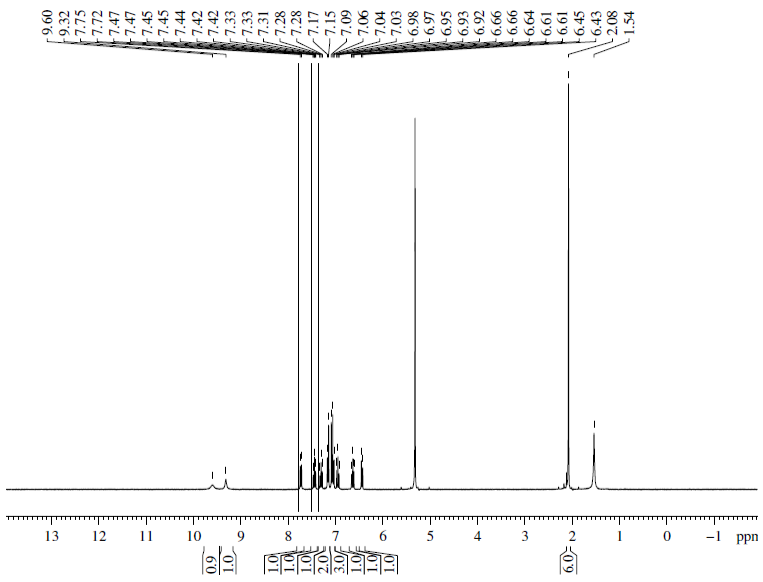

Figure D-15: ^{1}H NMR of **2.1c**. Peaks at 5.32 ppm due to solvent and 1.54 ppm due to residual water

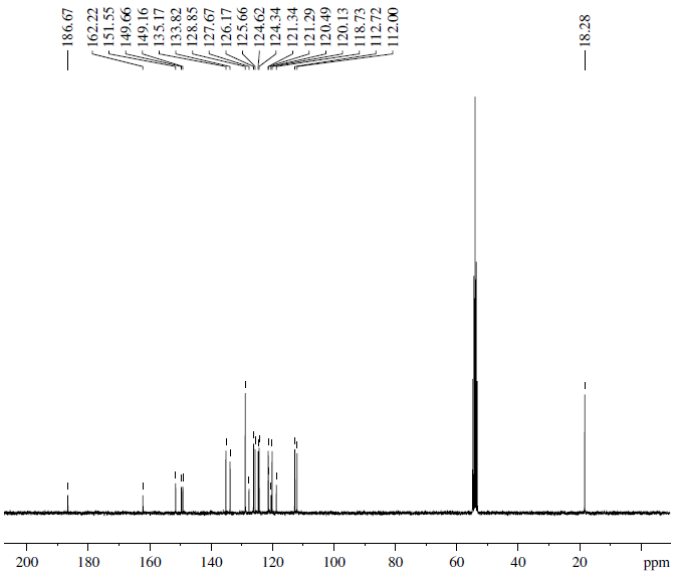

Figure D-16: ^{13}C NMR of **2.1c**

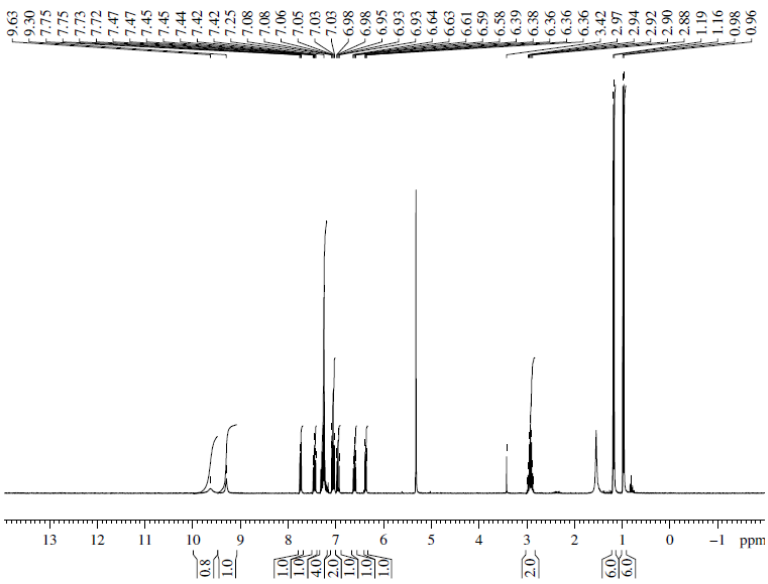

Figure D-17: ^{1}H NMR of **2.1d**. Peaks at 5.32 ppm due to solvent and 1.54 ppm due to residual water

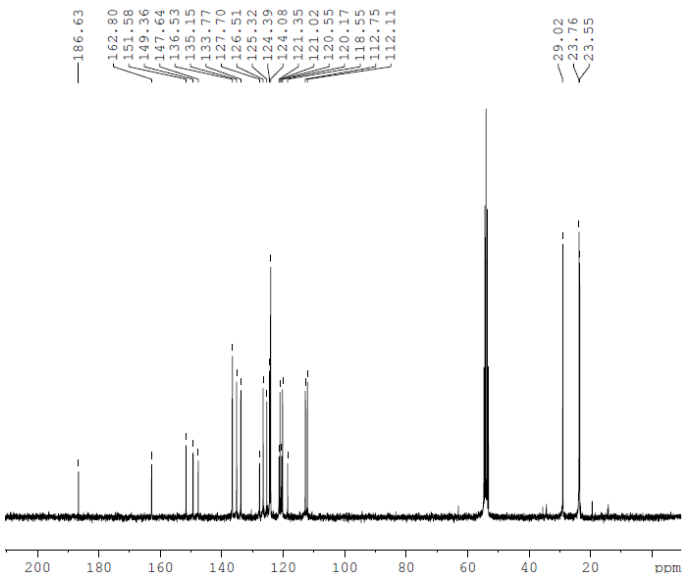

Figure D-18: ^{13}C NMR of **2.1d**

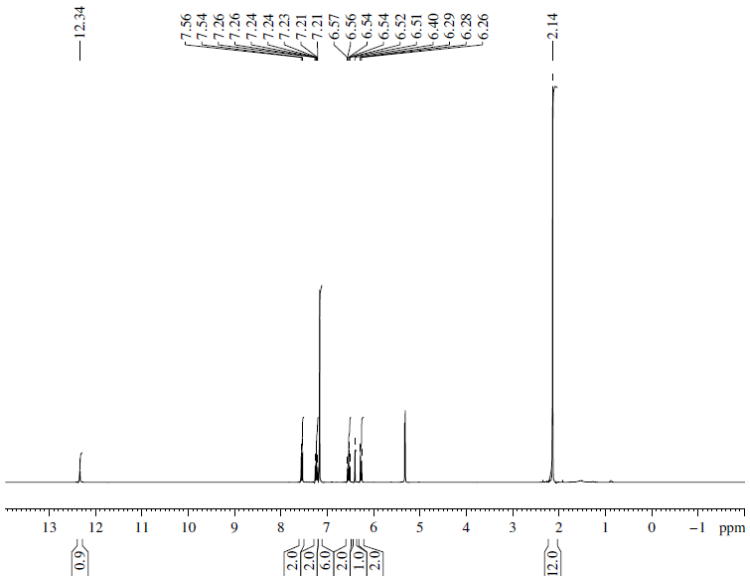

Figure D-19: ^{1}H NMR of **2.2c**. Peak at 5.32 ppm due to solvent

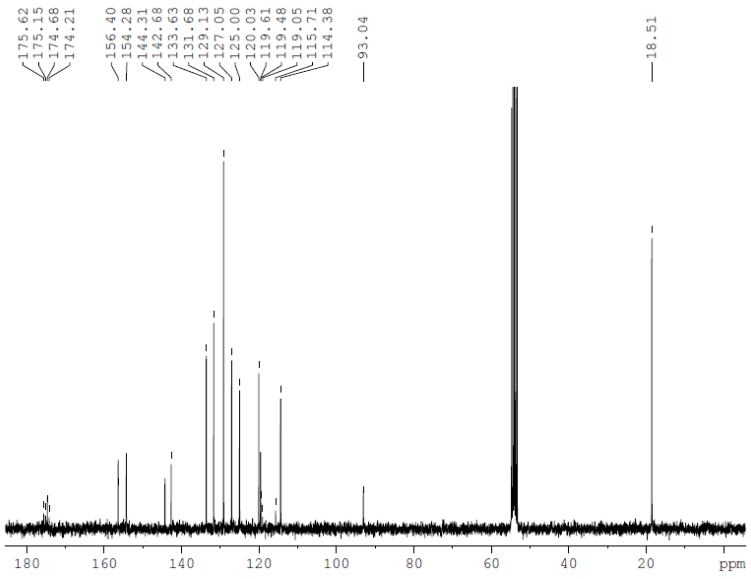

Figure D-20: ^{13}C NMR of **2.2c**

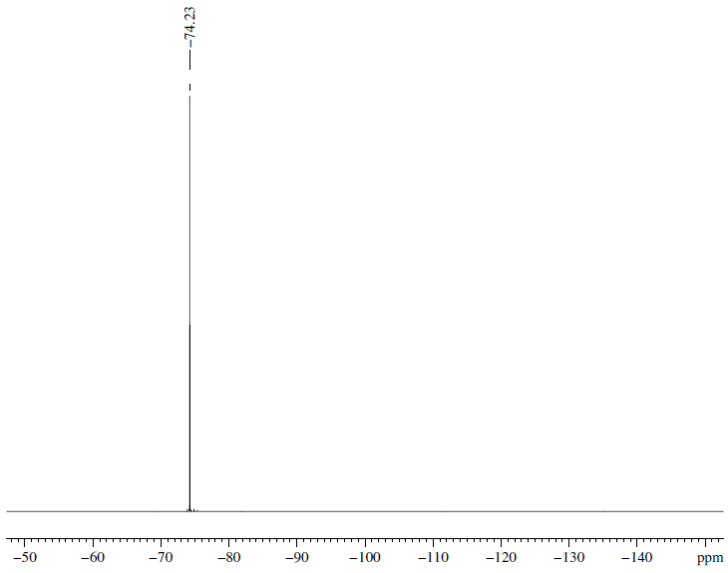

Figure D-21: $^{19}F\{^{1}H\}$ NMR of **2.2c**

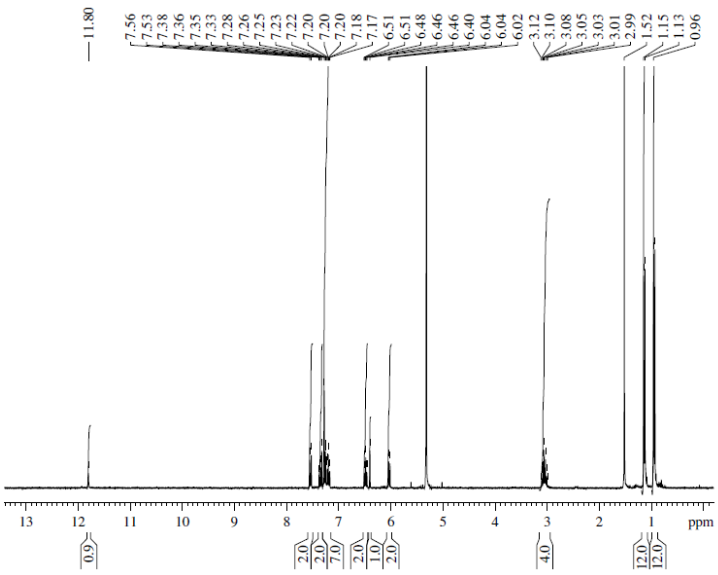

Figure D-22: ^{1}H NMR of **2.2d**. Peaks at 5.32 ppm due to solvent and 1.52 ppm due to residual water

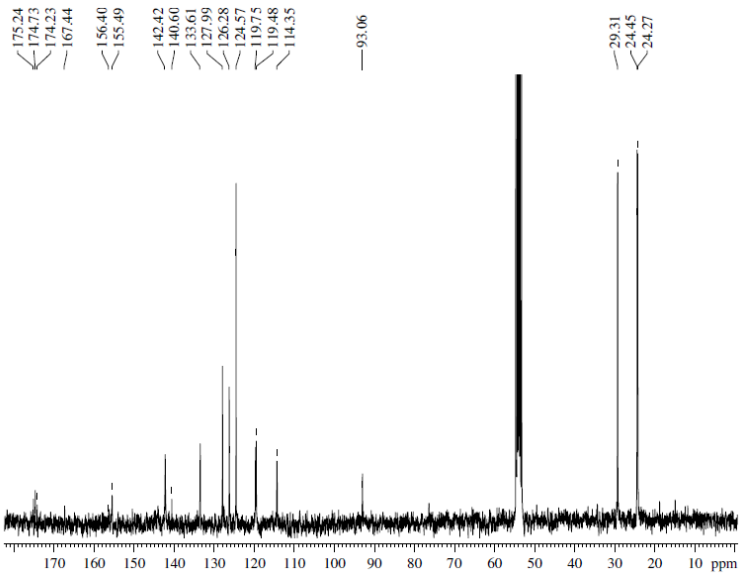

Figure D-23: ^{13}C NMR of **2.2d**

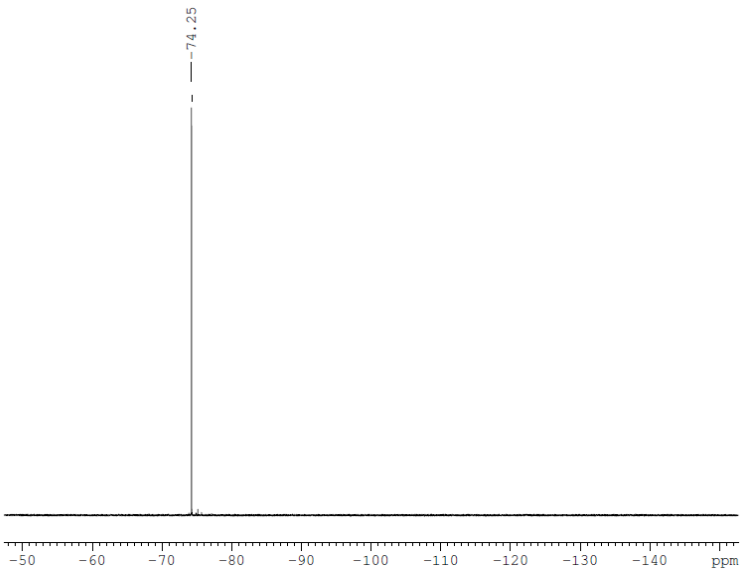

Figure D-24: $^{19}F\{^{1}H\}$ NMR of **2.2d**

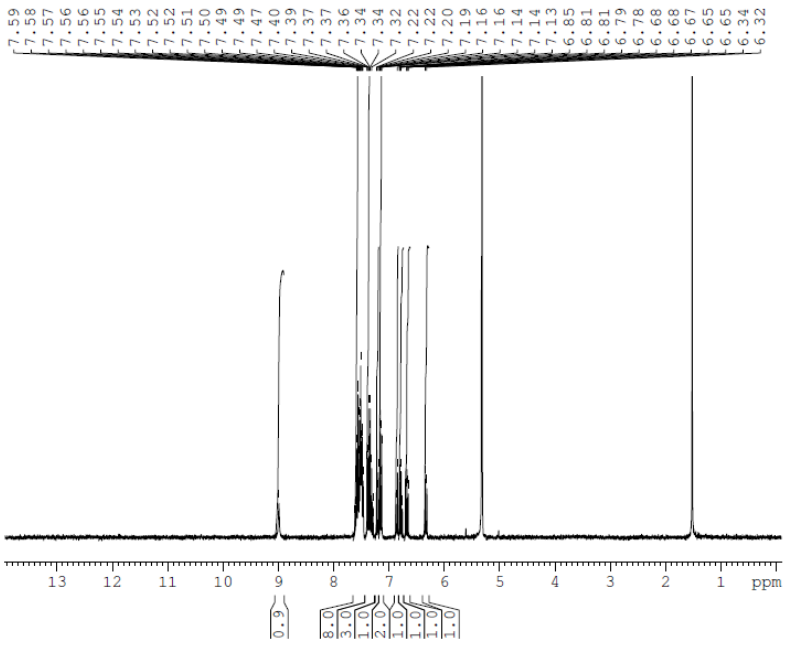

Figure D-25: ^{1}H NMR of **3.3a**. Peaks at 5.32 ppm due to solvent and 1.54 ppm due to residual water

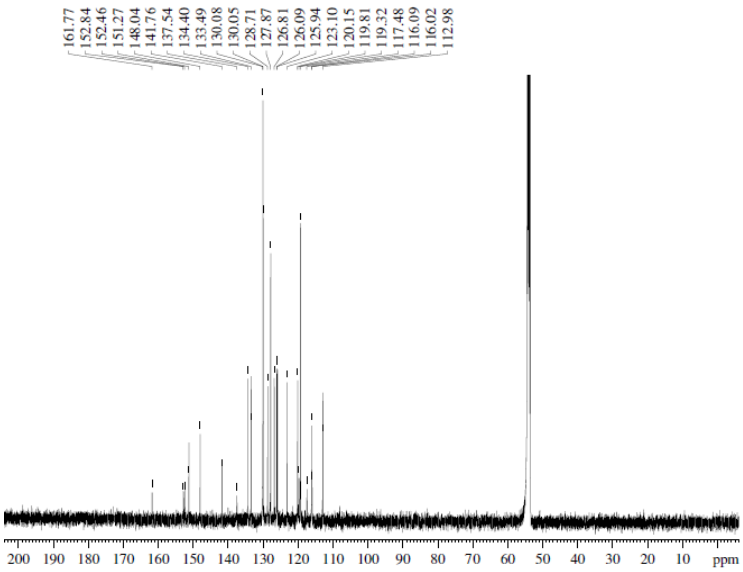

Figure D-26: ^{13}C NMR of **3.3a**

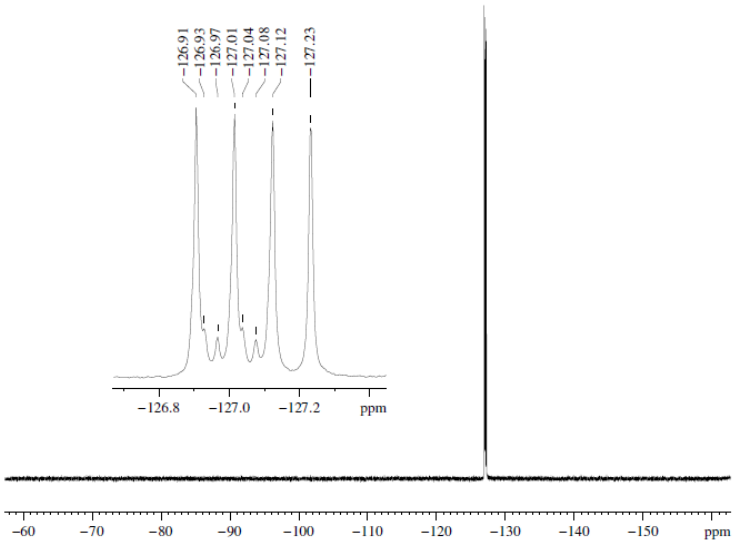

Figure D-217: $^{19}F\{^{1}H\}$ NMR of **3.3a**

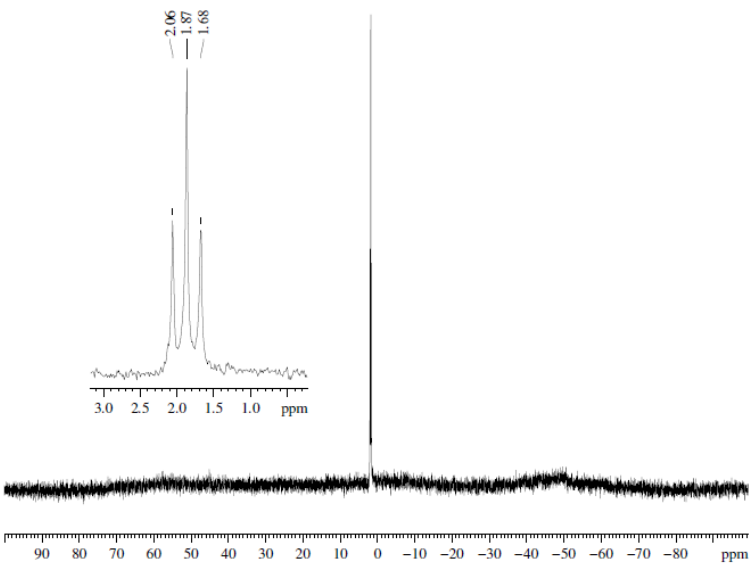

Figure D-28: ^{11}B NMR of **3.3a**

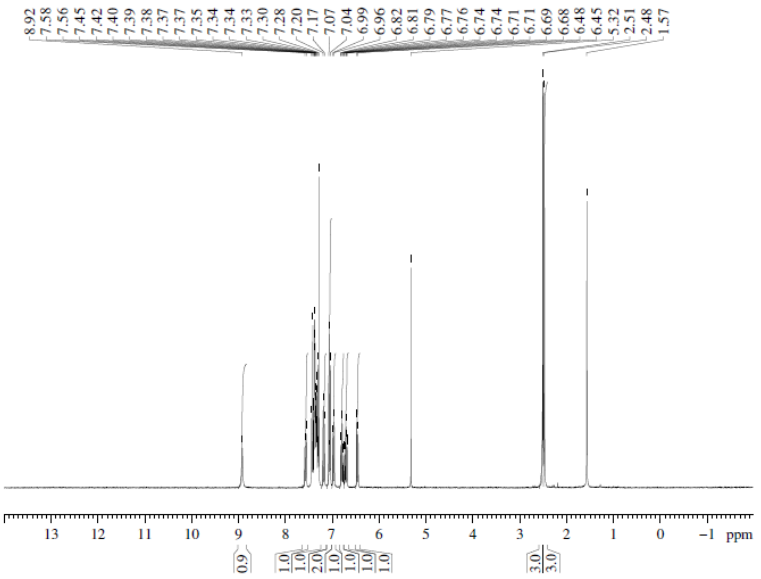

Figure D-239: ^{1}H NMR of **3.3b**. Peaks at 5.32 ppm due to solvent and 1.57 ppm due to residual water

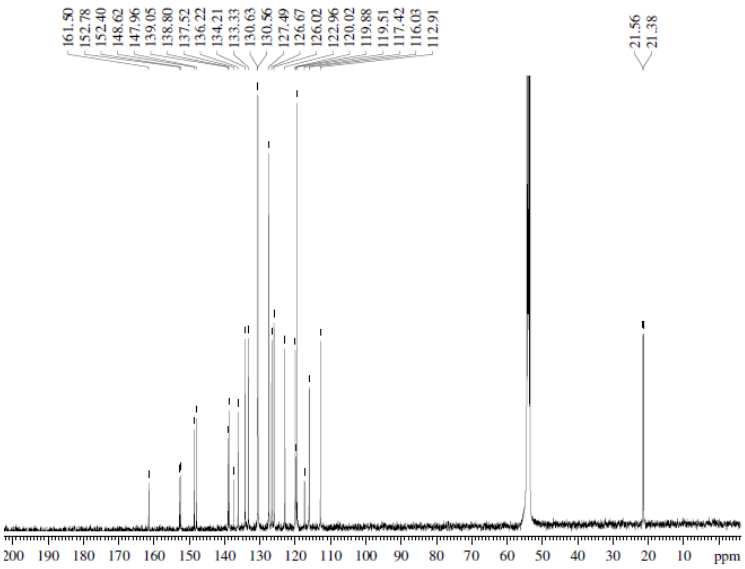

Figure D-30: ^{13}C NMR of **3.3b**

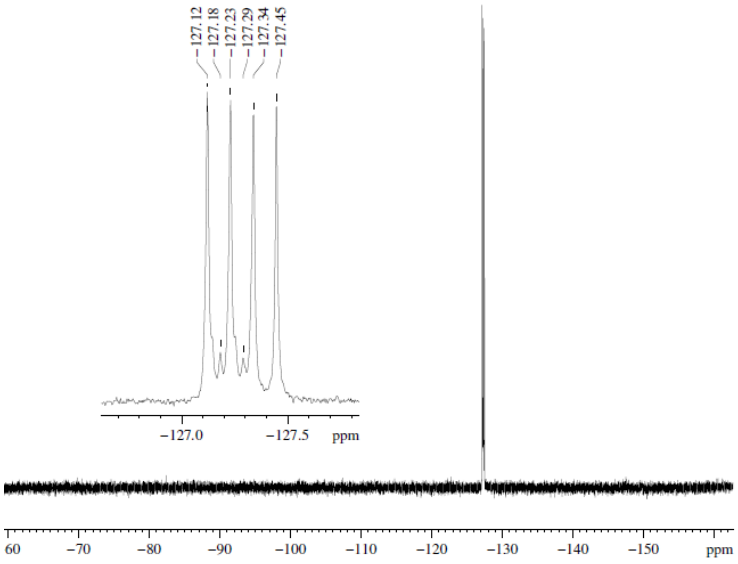

Figure D-31: $^{19}F\{^{1}H\}$ NMR of **3.3b**

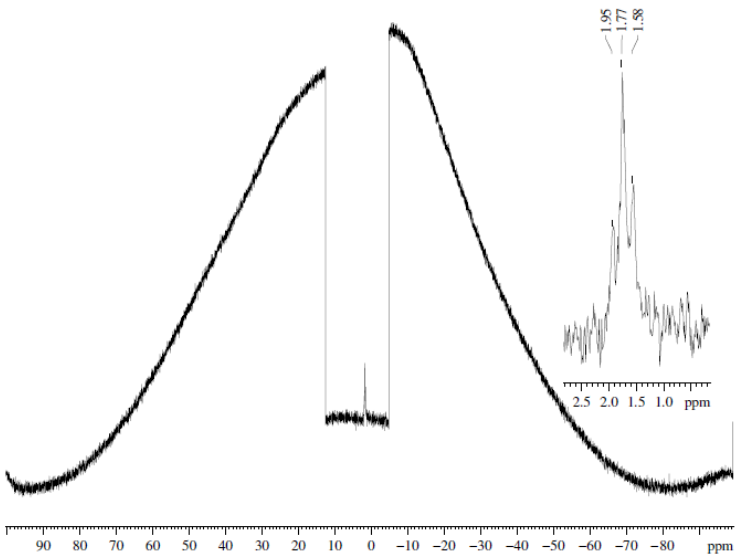

Figure D-32: ^{11}B NMR of **3.3b**

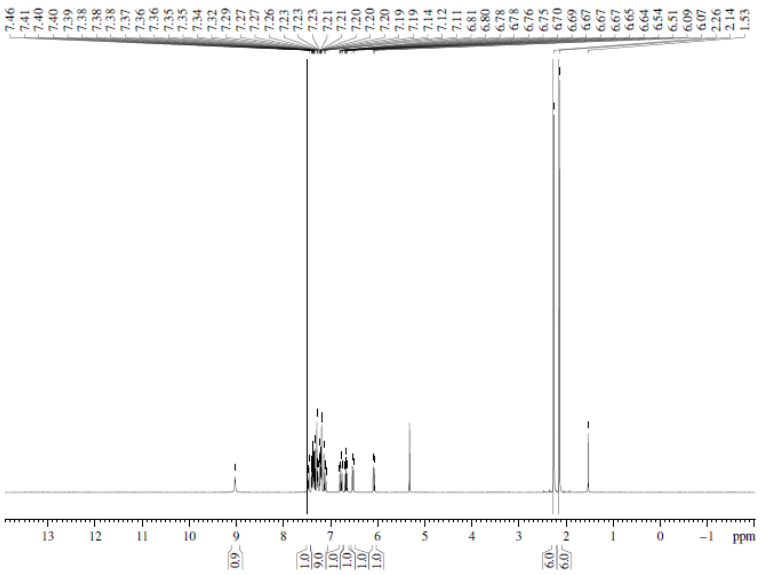

Figure D-33: ^{1}H NMR of **3.3c**. Peaks at 5.32 ppm due to solvent and 1.53 ppm due to residual water

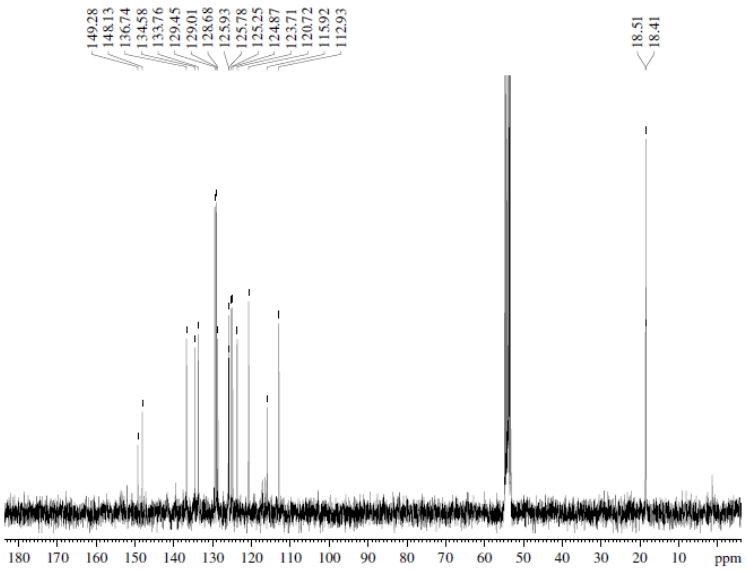

Figure D-344: ^{13}C NMR of **3.3c**

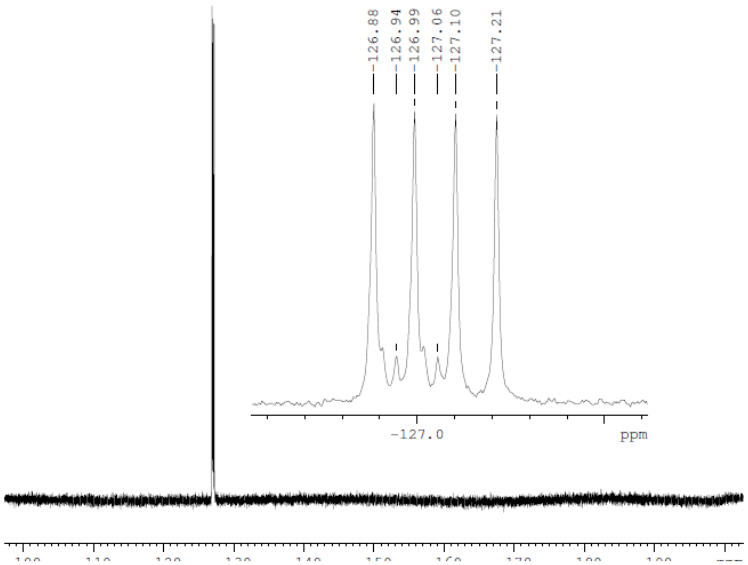

Figure D-35: $^{19}F\{^{1}H\}$ NMR of **3.3c**

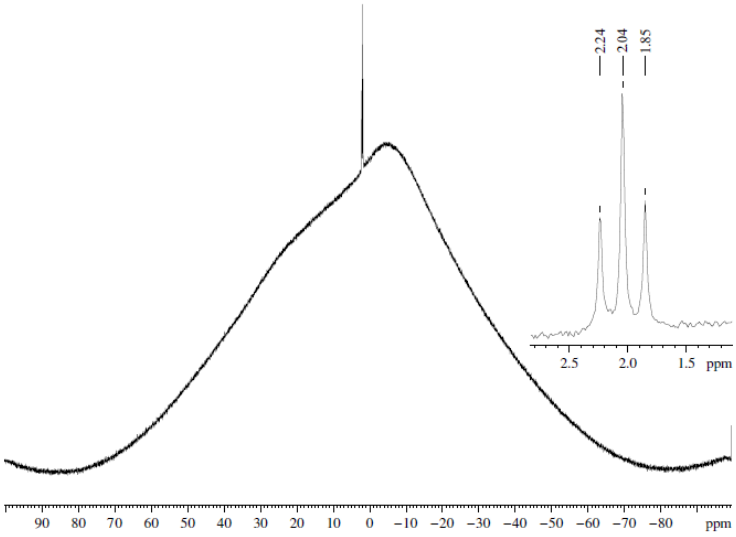

Figure D-36: ^{11}B NMR of **3.3c**

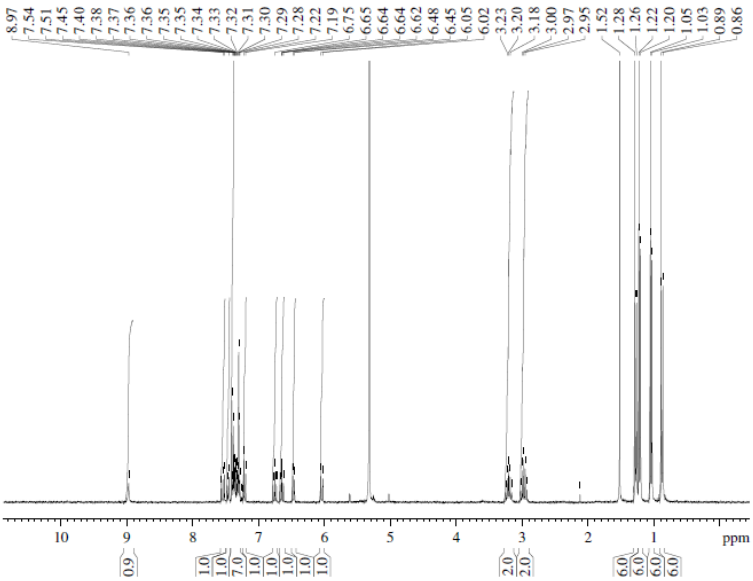

Figure D-37: ^{1}H NMR of **3.3d**. Peaks at 5.32 ppm due to solvent and 1.52 ppm due to residual water

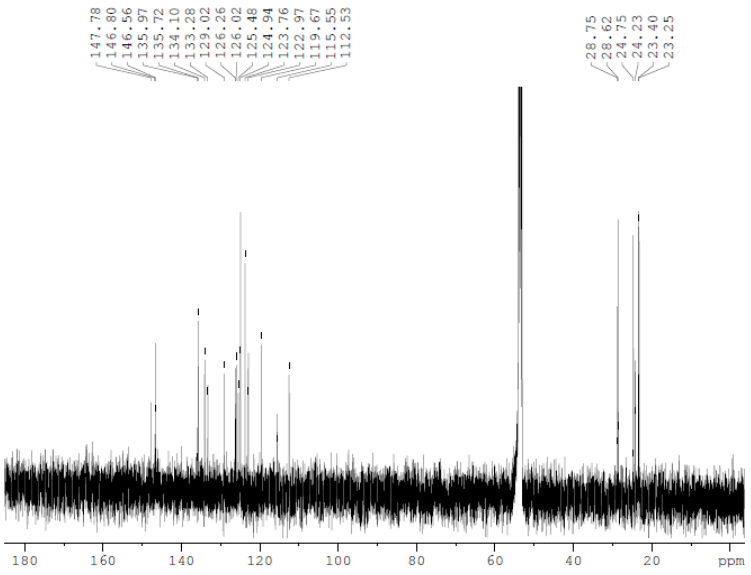

Figure D-38: ^{13}C NMR of **3.3d**

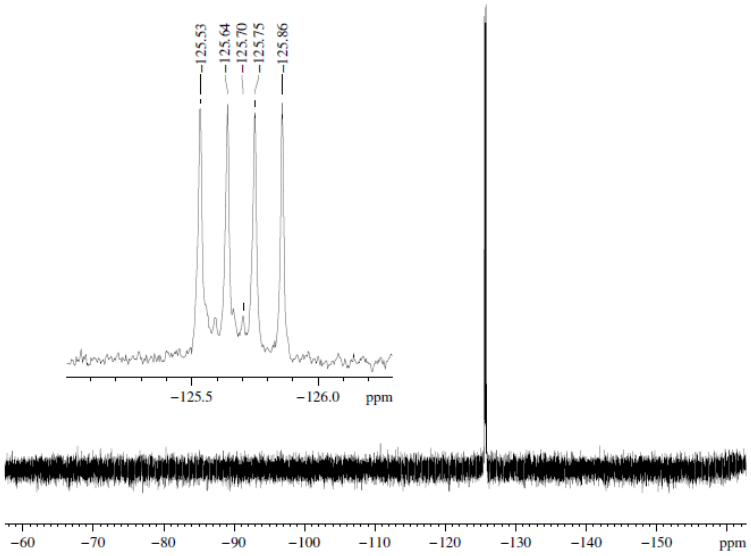

Figure D-39: $^{19}F\{^{1}H\}$ NMR of **3.3d**

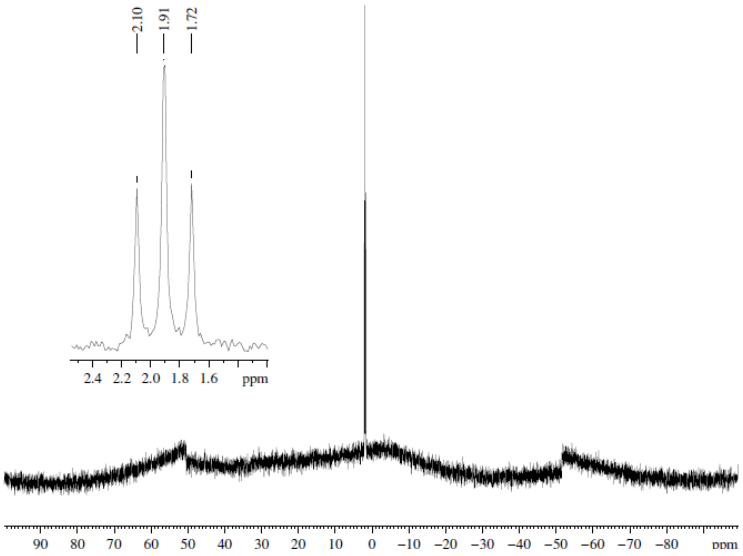

Figure D-405: ^{11}B NMR of **3.3d**

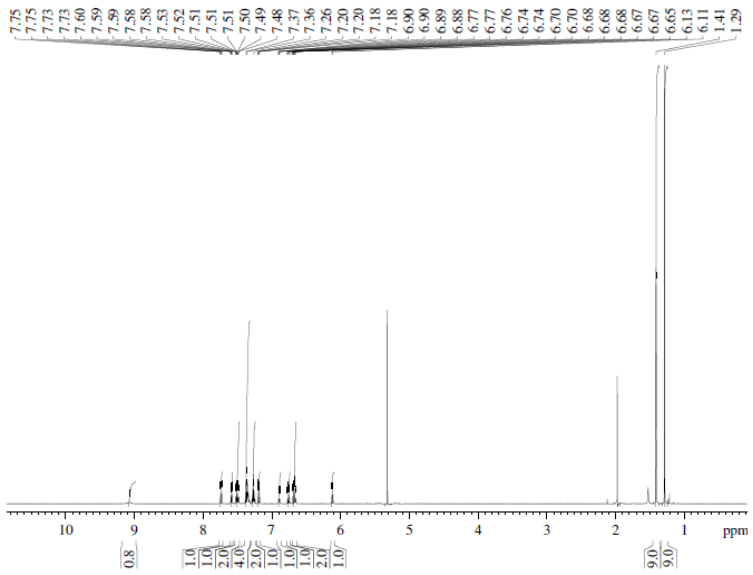

Figure D-41: ^{1}H NMR of **3.3e**. Peaks at 5.32 ppm due to solvent and 1.52 ppm due to residual water

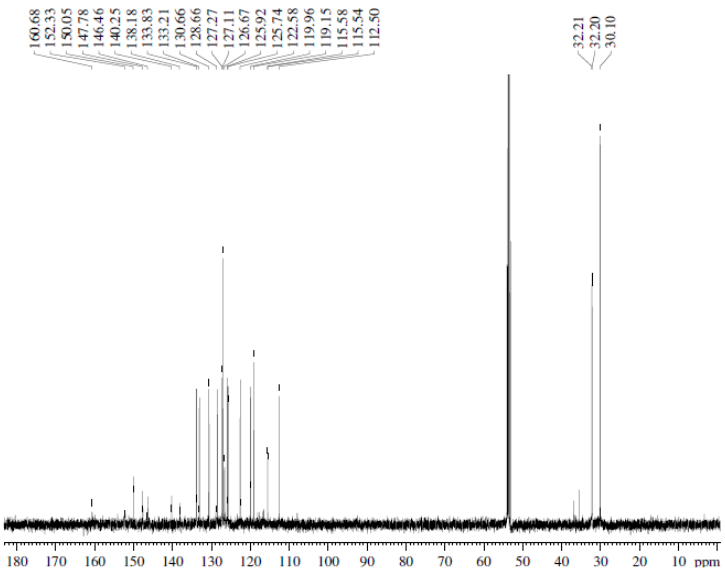

Figure D-426: ^{13}C NMR of **3.3e**

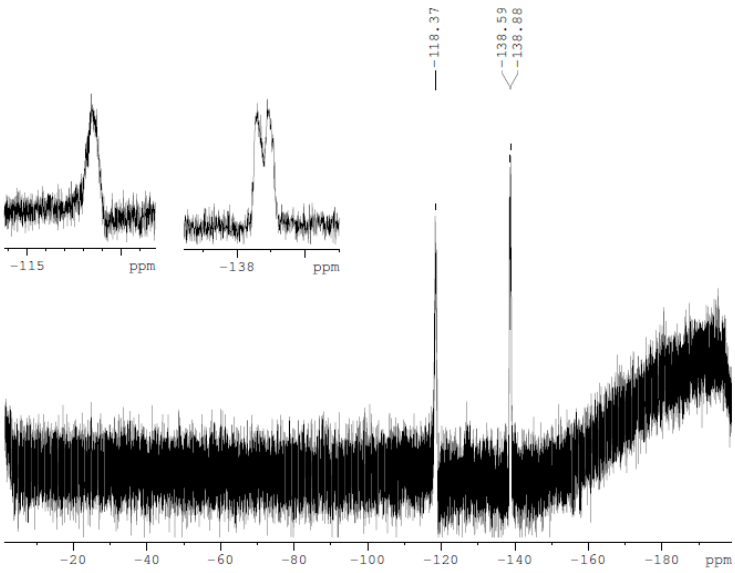

Figure D-43: $^{19}F\{^{1}H\}$ NMR of **3.3e**

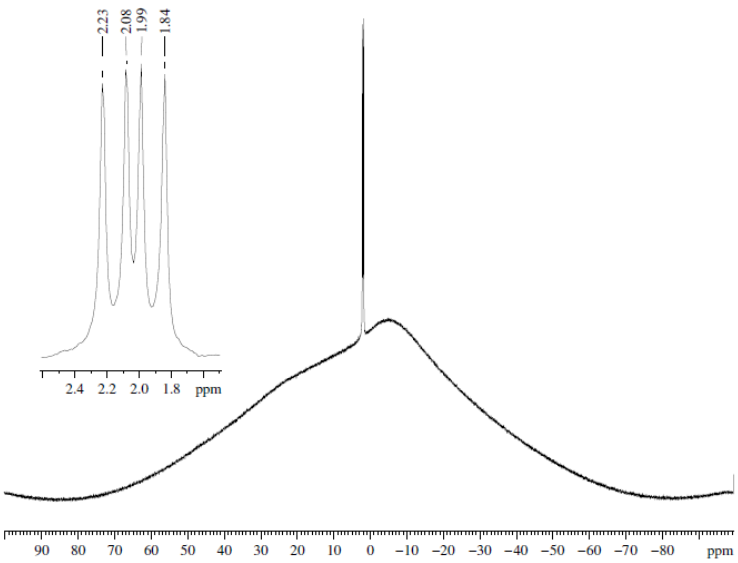

Figure D-44: ^{11}B NMR of **3.3e**

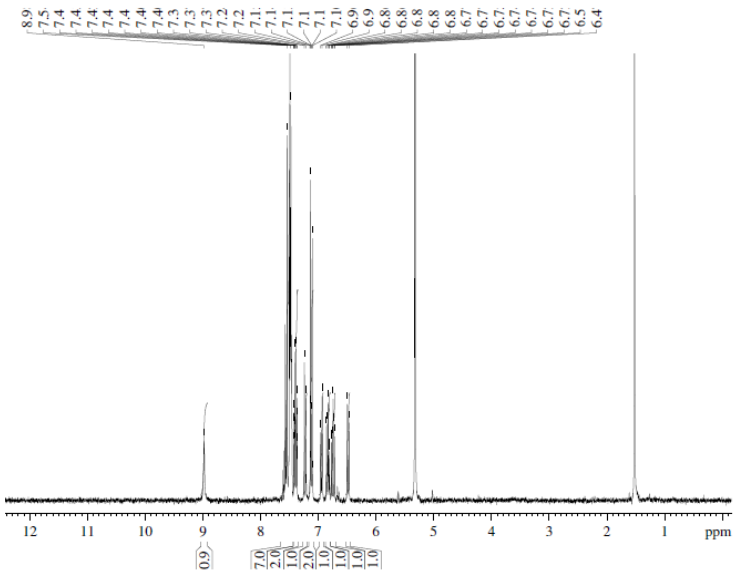

Figure D-45: ^{1}H NMR of **3.3f**. Peaks at 5.32 ppm due to solvent and 1.52 ppm due to residual water

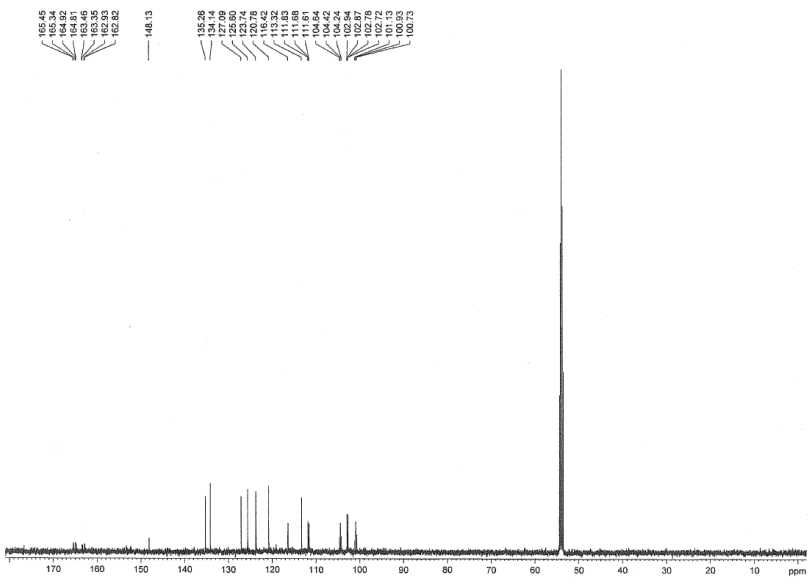

Figure D-46: ^{13}C NMR of **3.3f**

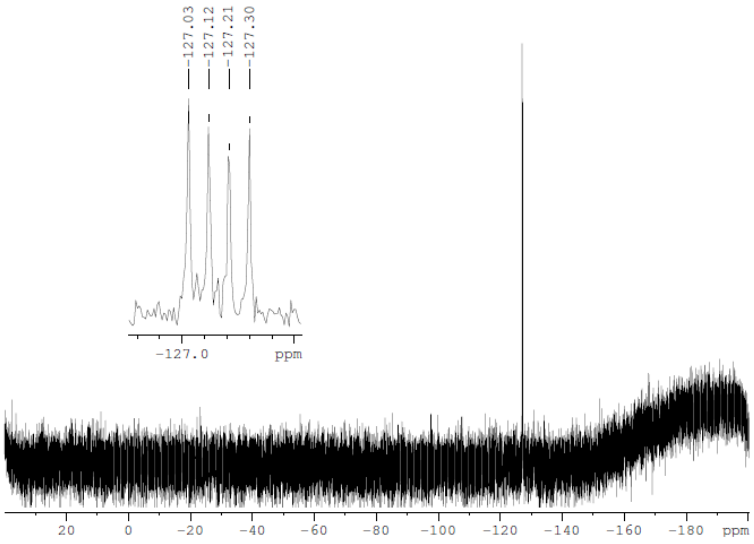

Figure D-47: $^{19}F\{^{1}H\}$ NMR of **3.3f**

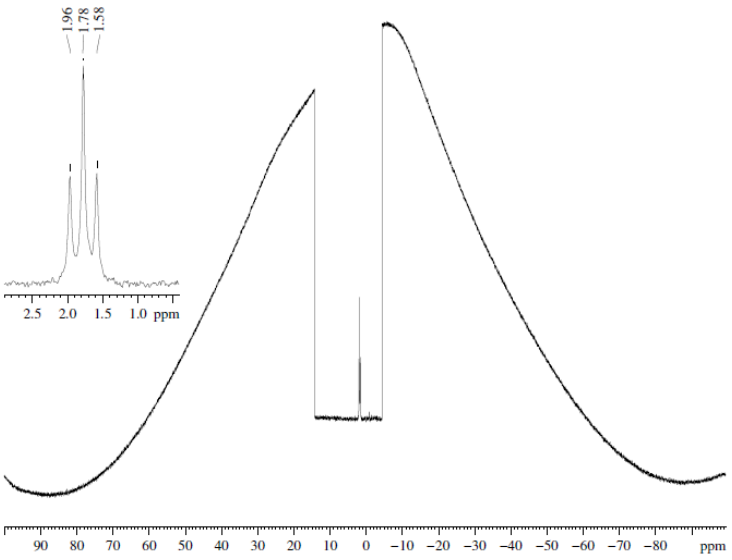

Figure D-48: ^{11}B NMR of **3.3f**

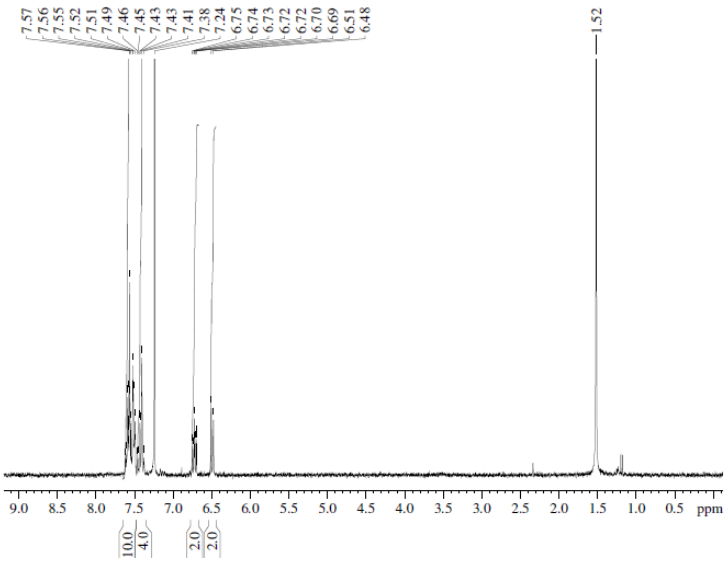

Figure D-49: ^{1}H NMR of **3.5a**. Peaks at 7.24 ppm due to solvent and 1.52 ppm due to residual water

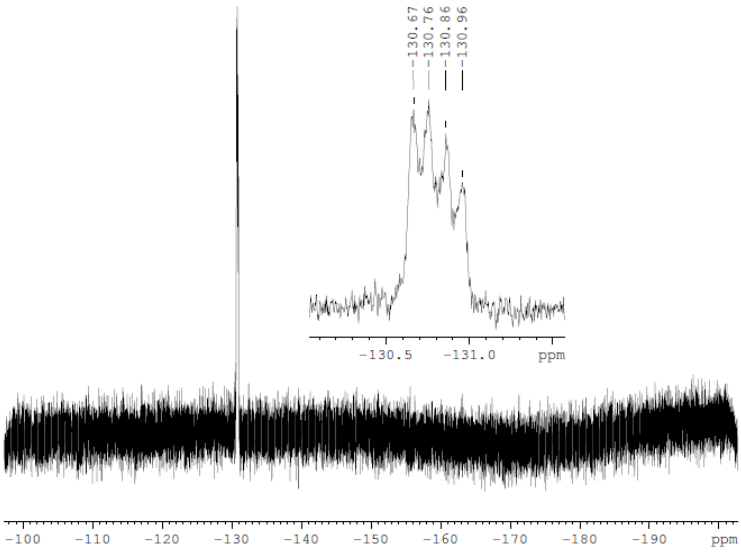

Figure D-50: $^{19}F\{^{1}H\}$ NMR of **3.3f**

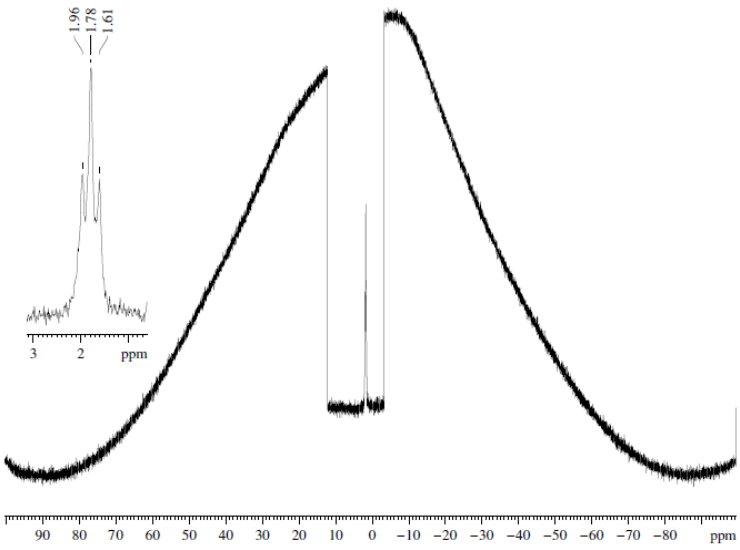

Figure D-51: ^{11}B NMR of **3.5a**

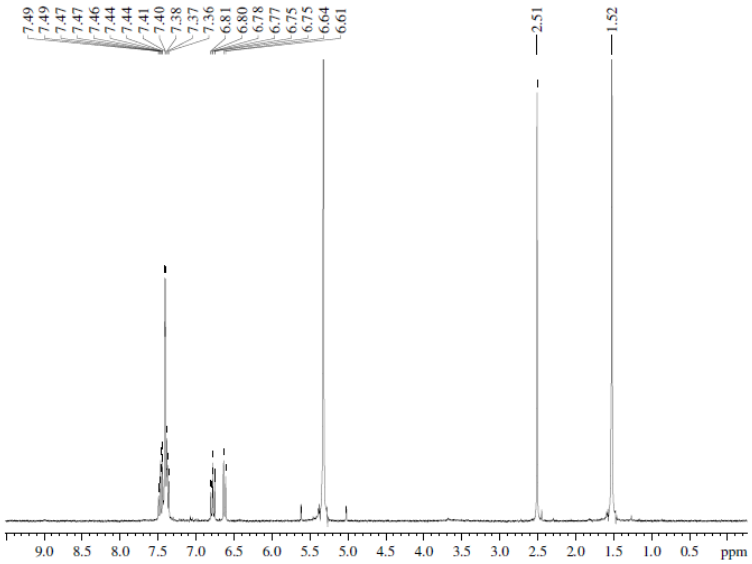

Figure D-52: ^{1}H NMR of **3.5b**. Peaks at 5.32 ppm due to solvent and 1.52 ppm due to residual water

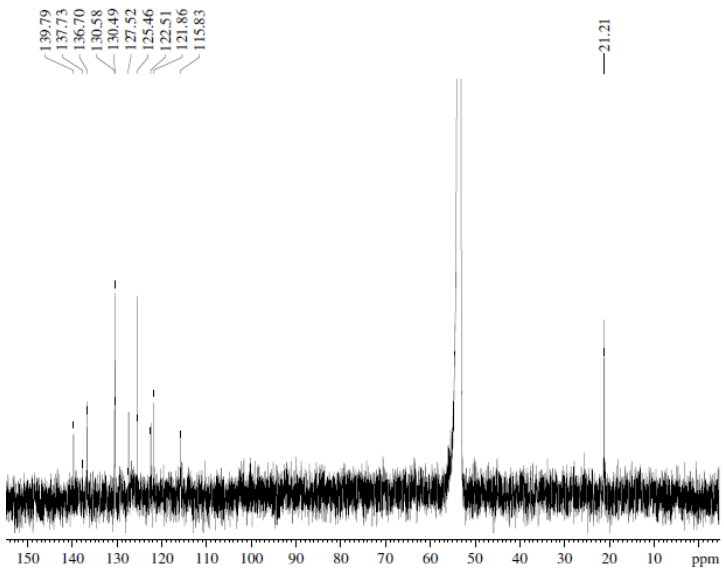

Figure D-53: ^{13}C NMR of **3.5b**

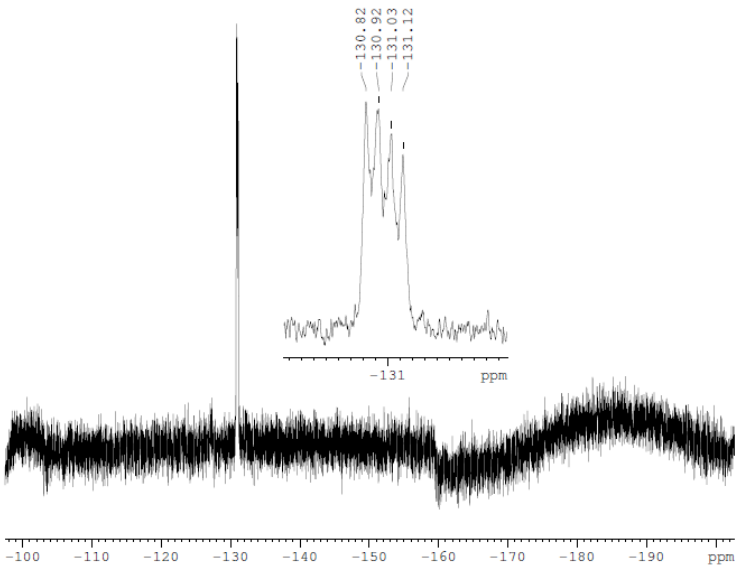

Figure D-54: $^{19}F\{^{1}H\}$ NMR of **3.5b**

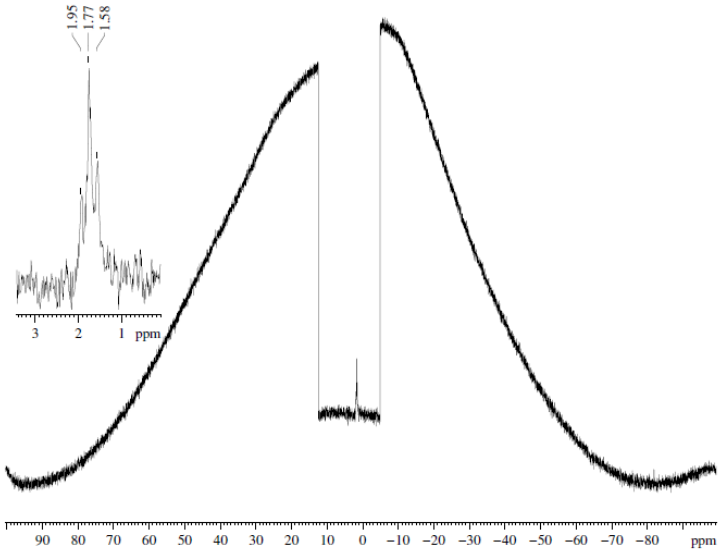

Figure D-55: ^{11}B NMR of **3.5**

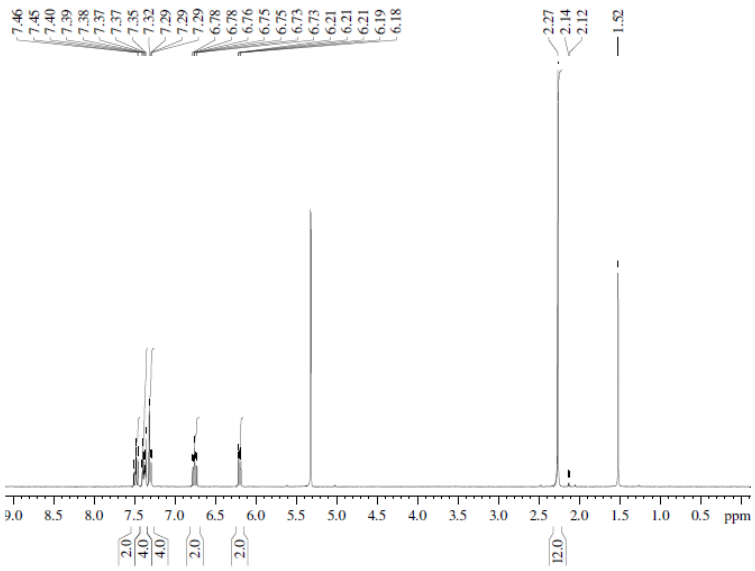

Figure D-56: ^{1}H NMR of **3.5c**. Peaks at 5.32 ppm due to solvent and 1.52 ppm due to residual water

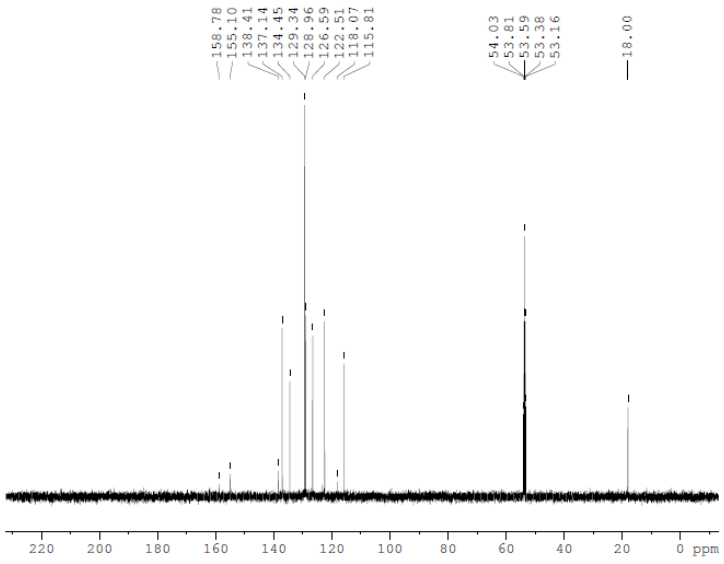

Figure D-57: ^{13}C NMR of **3.5c**

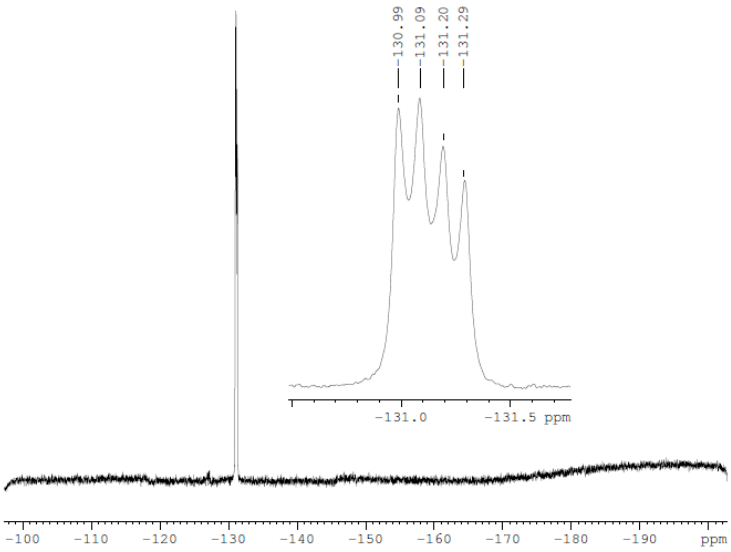

Figure D-58: $^{19}F\{^{1}H\}$ NMR of **3.5c**

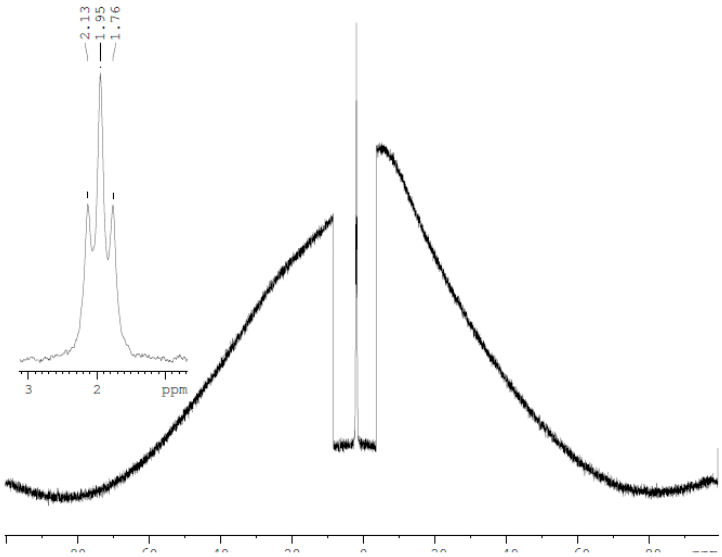

Figure D-59: ^{11}B NMR of **3.5c**

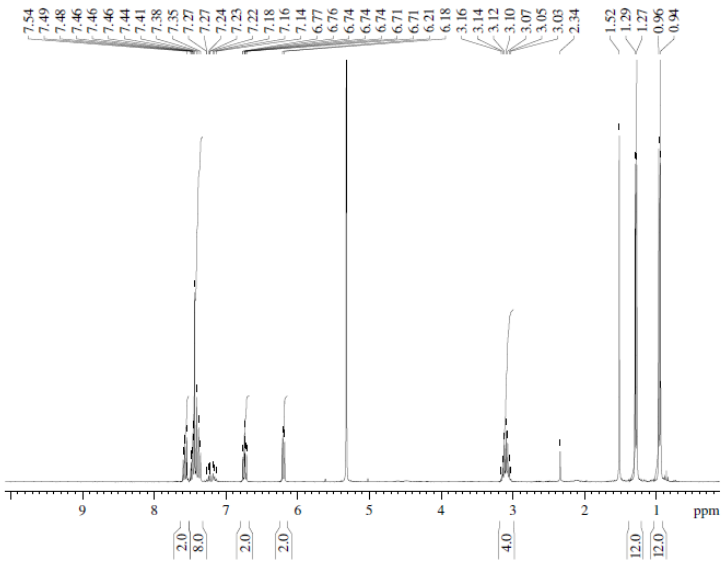

Figure D-60: ^{1}H NMR of **3.5d**. Peaks at 5.32 ppm due to solvent and 1.52 ppm due to residual water

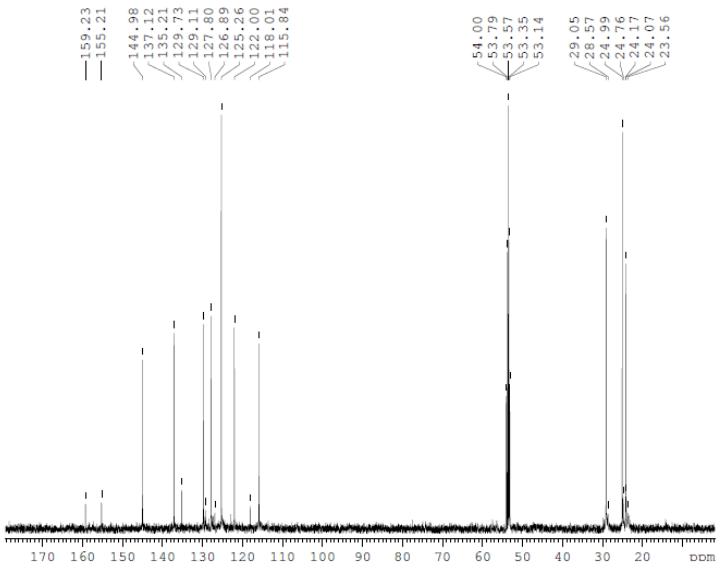

Figure D-61: ^{13}C NMR of **3.5d**

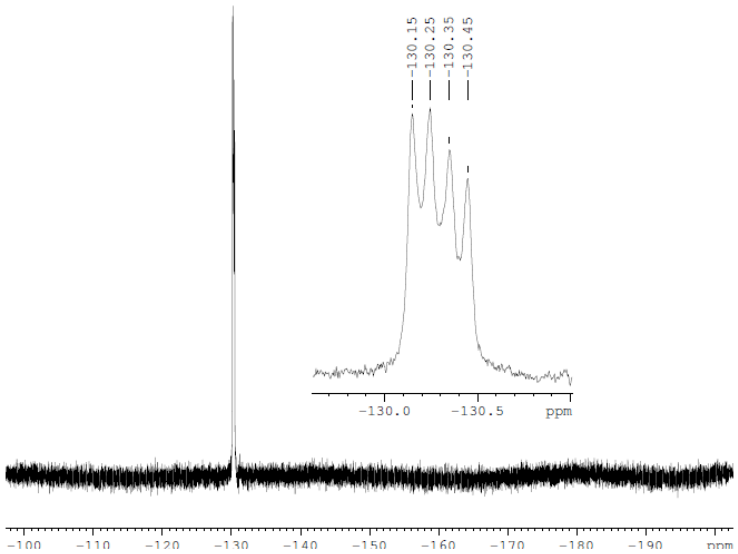

Figure D-62: $^{19}F\{^{1}H\}$ NMR of **3.5c**

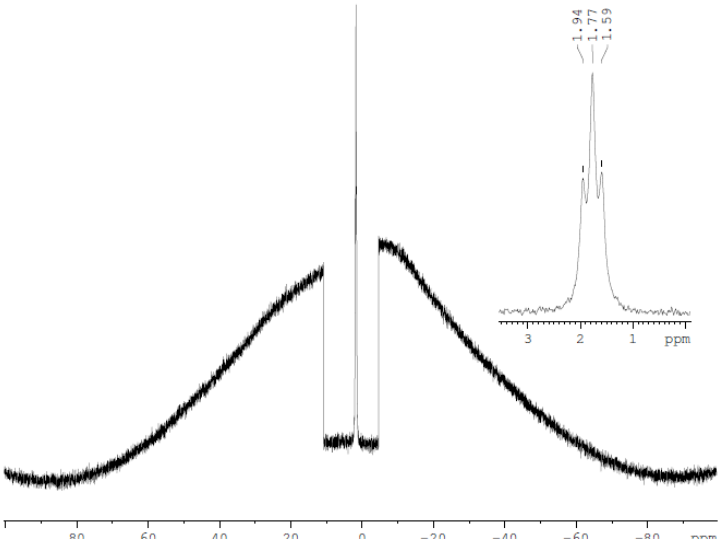

Figure D-63: ^{11}B NMR of **3.5d**

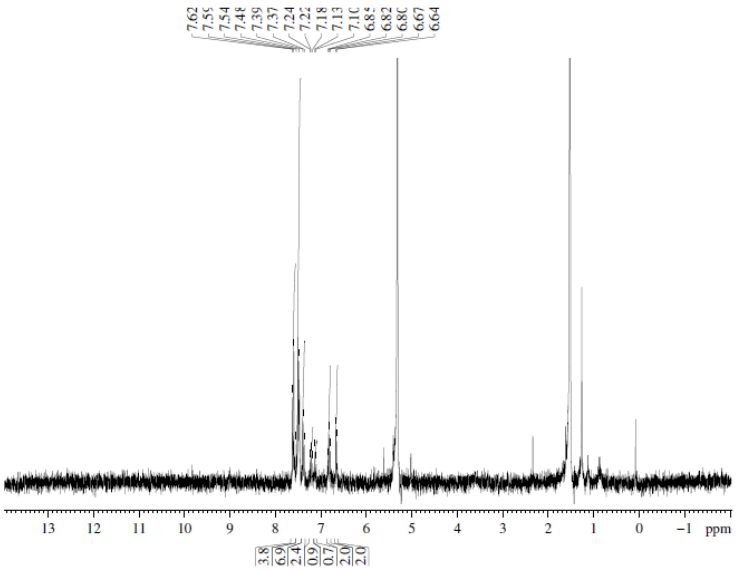

Figure D-64: ^{1}H NMR of **3.5f**. Peaks at 5.32 ppm due to solvent and 1.52 ppm due to residual water

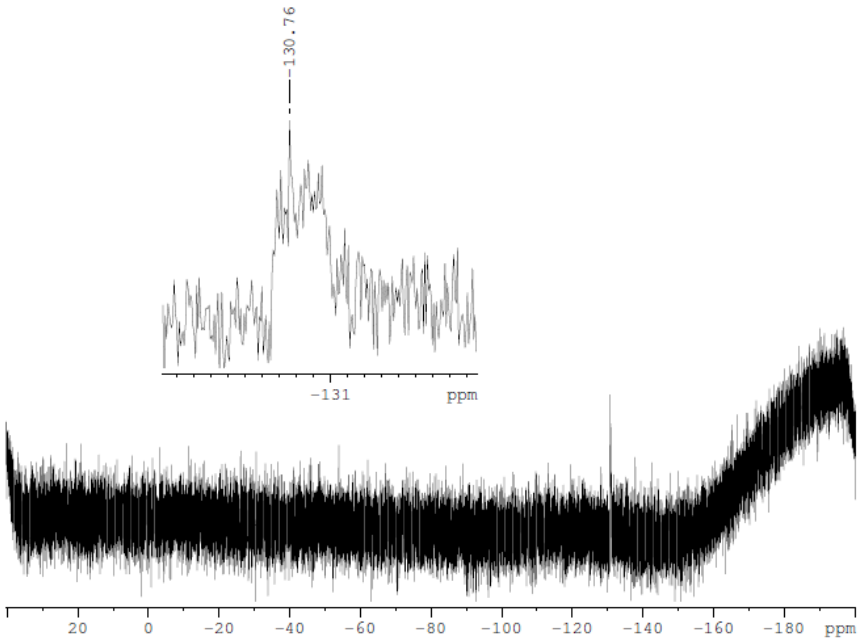

Figure D-65: ^{19}F{^{1}H} NMR of **3.5f**

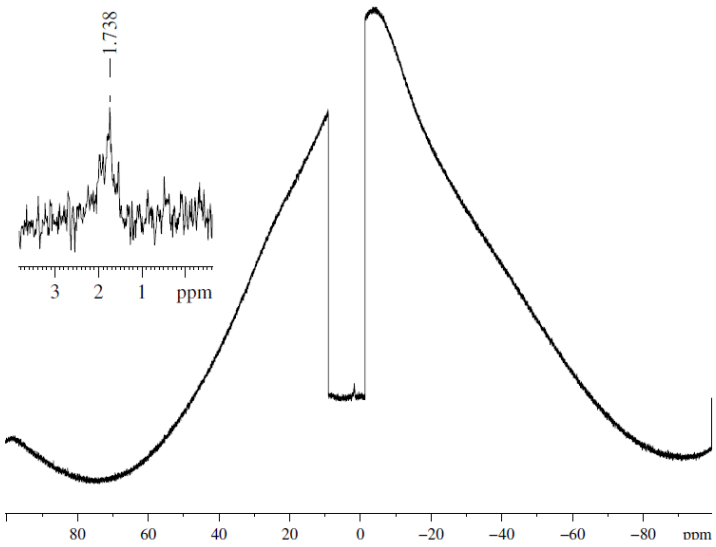

Figure D-66: ^{11}B NMR of **3.5f**

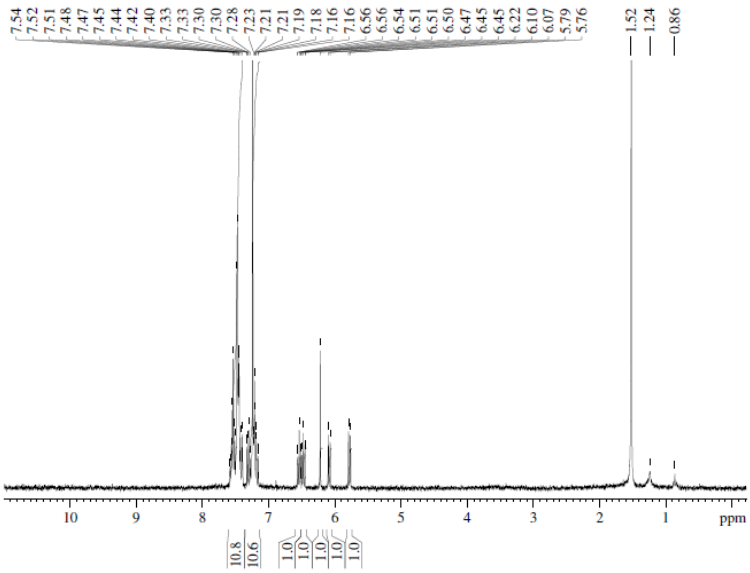

Figure D-67: ^{1}H NMR of **3.6a**. Peaks at 7.24 ppm due to solvent and 1.52 ppm due to residual water

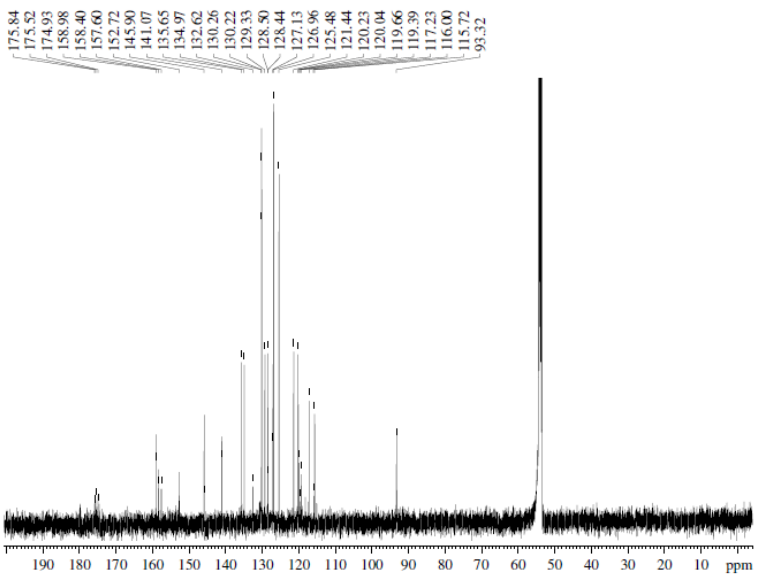

Figure D-68: ^{13}C NMR of **3.6a**

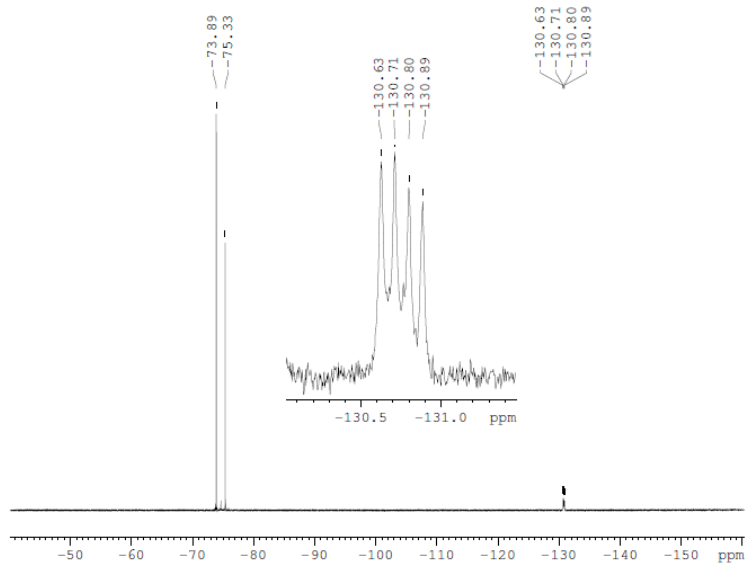

Figure D-69: $^{19}F\{^{1}H\}$ NMR of **3.6a**

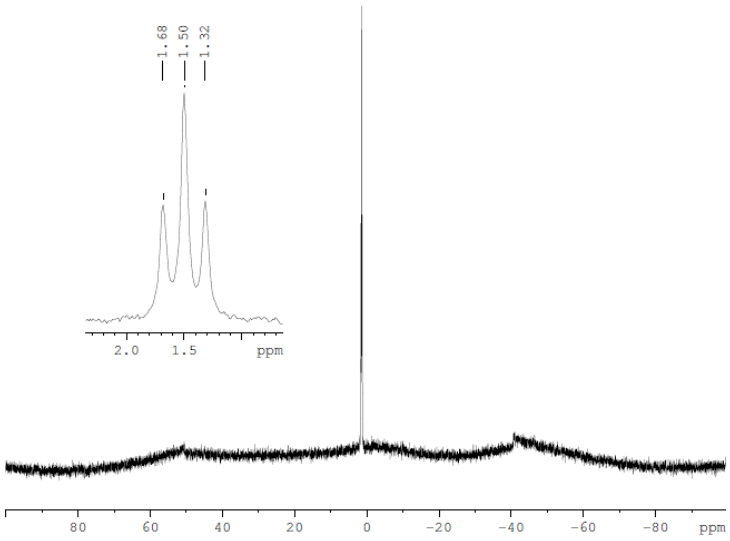

Figure D-70: ^{11}B NMR of **3.6a**

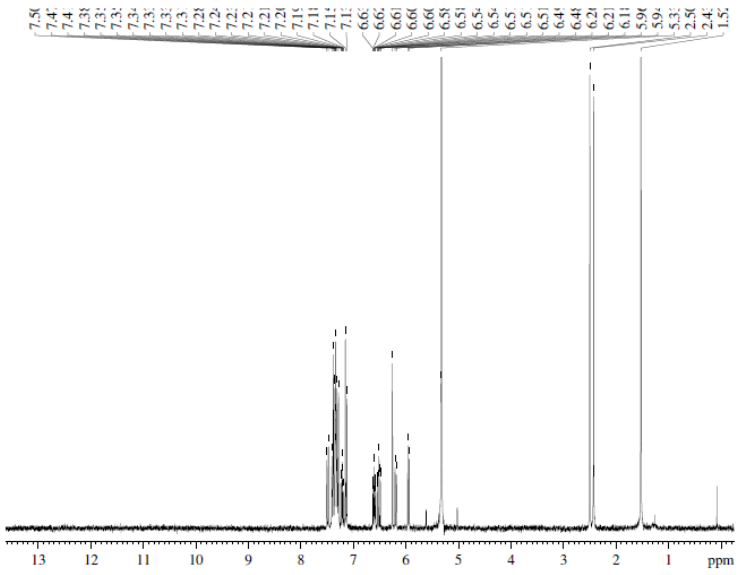

Figure D-71: ^{1}H NMR of **3.6b**. Peaks at 5.32 ppm due to solvent and 1.52 ppm due to residual water

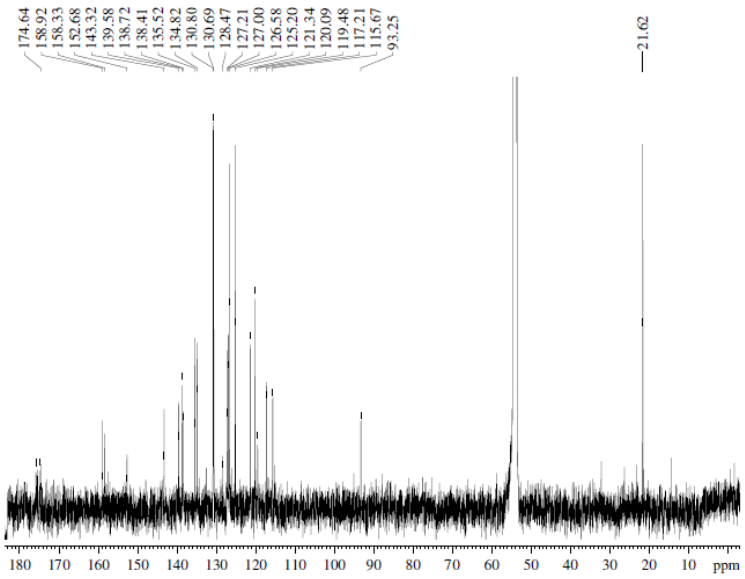

Figure D-72: ^{13}C NMR of **3.6b**

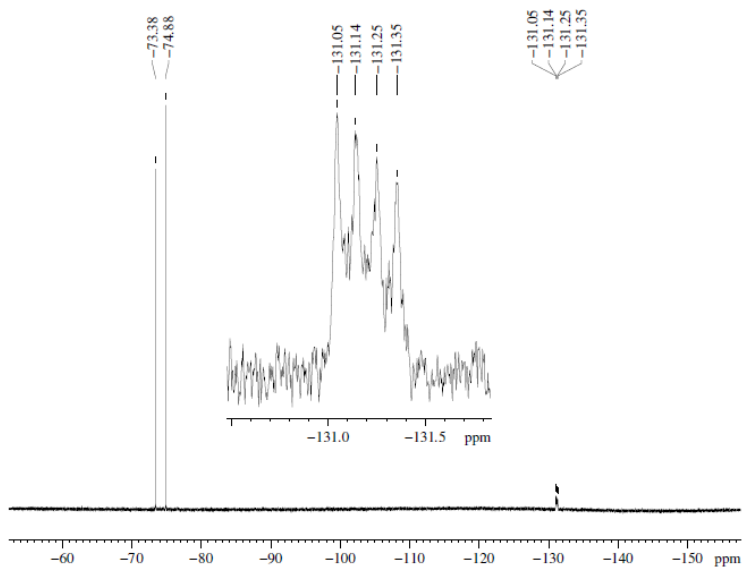

Figure D-73: $^{19}F\{^{1}H\}$ NMR of **3.6b**

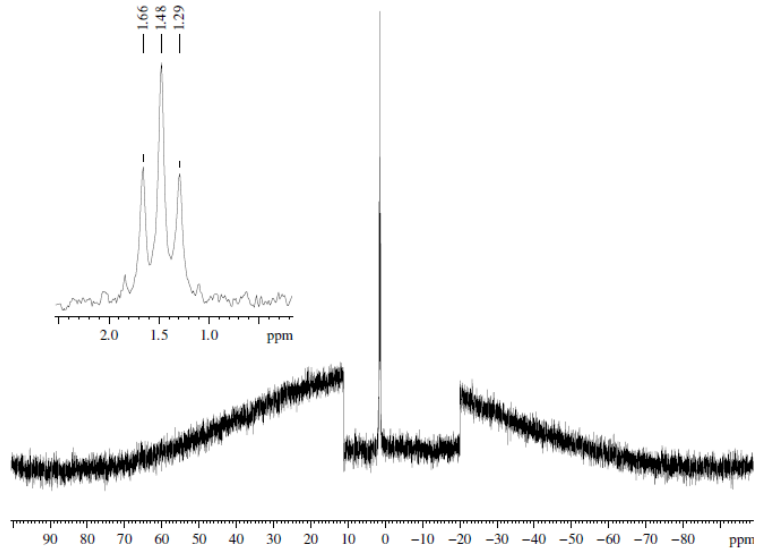

Figure D-74: ^{11}B NMR of **3.6b**

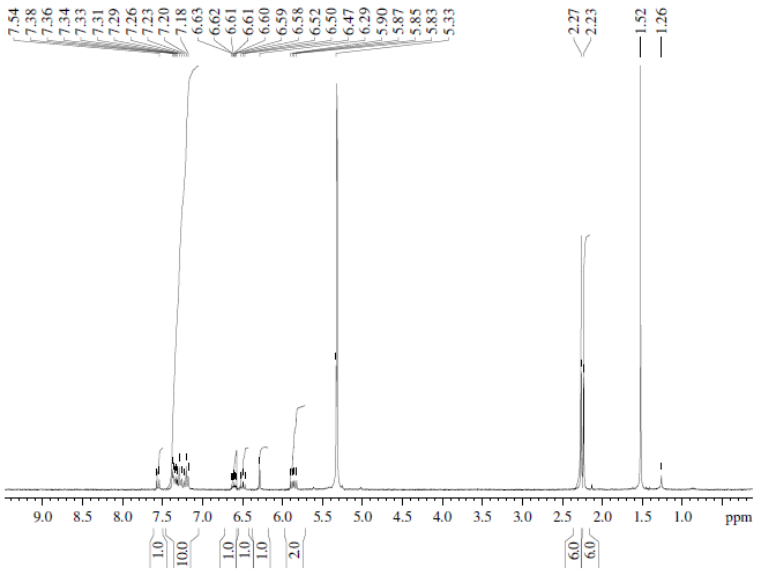

Figure D-75: ^{1}H NMR of **3.6c**. Peaks at 5.32 ppm due to solvent and 1.52 ppm due to residual water

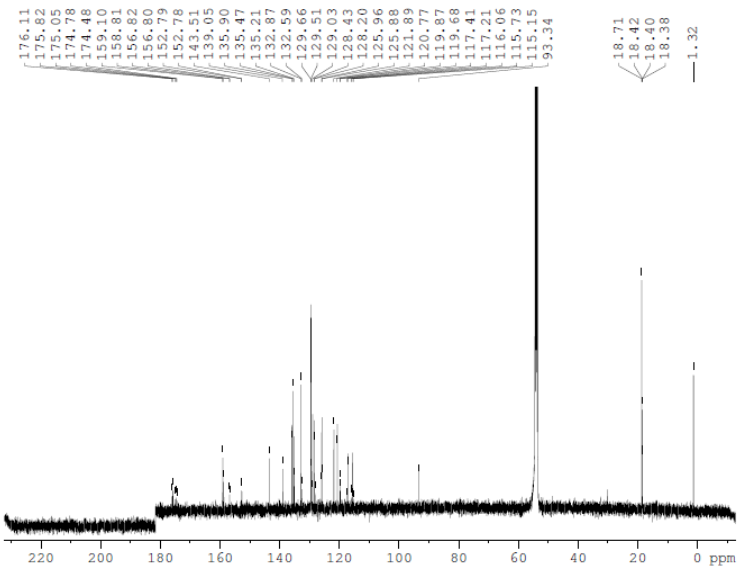

Figure D-76: ^{13}C NMR of **3.6c**

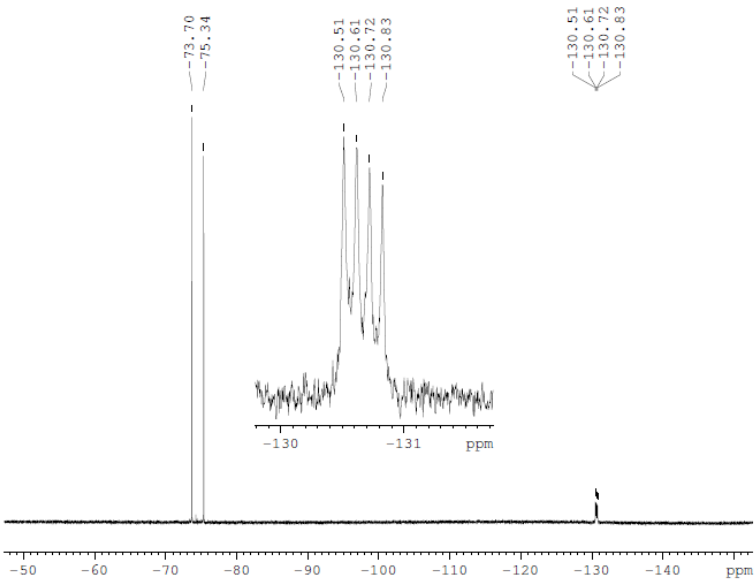

Figure D-77: $^{19}F\{^{1}H\}$ NMR of **3.6c**

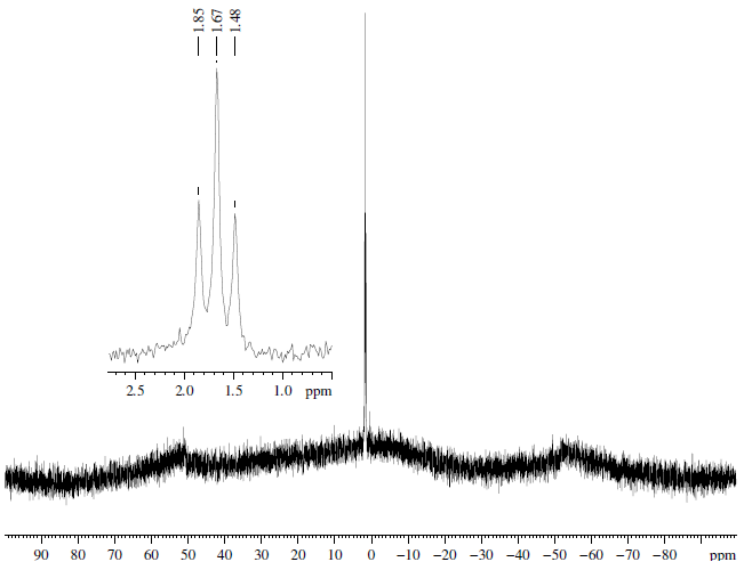

Figure D-78: ^{11}B NMR of **3.6c**

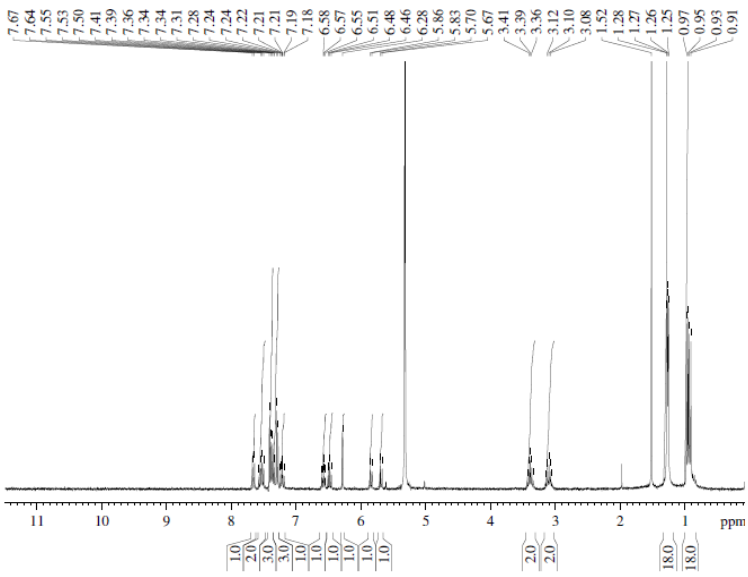

Figure D-79: ^{1}H NMR of **3.6d**. Peaks at 5.32 ppm due to solvent and 1.52 ppm due to residual water

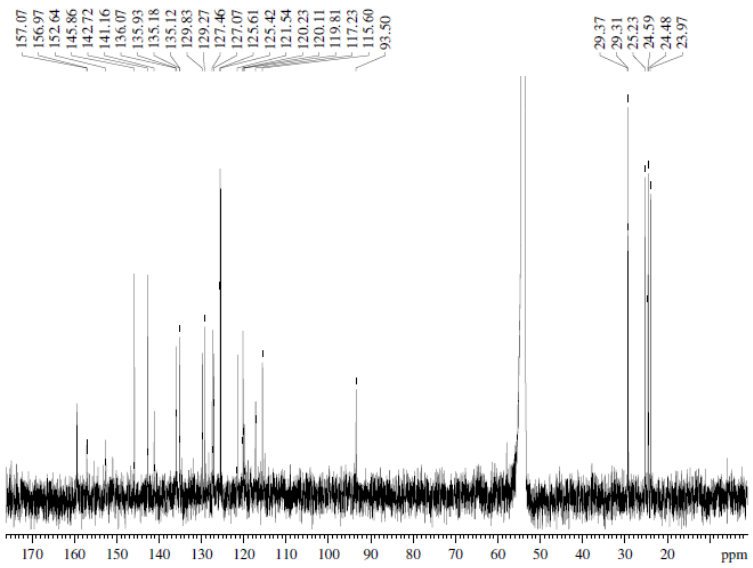

Figure D-80: ^{13}C NMR of **3.6d**

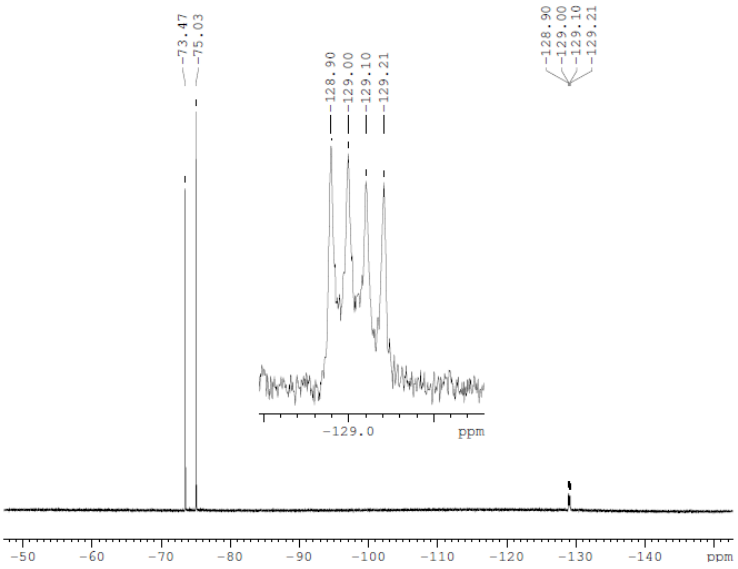

Figure D-81: $^{19}F\{^{1}H\}$ NMR of **3.6d**

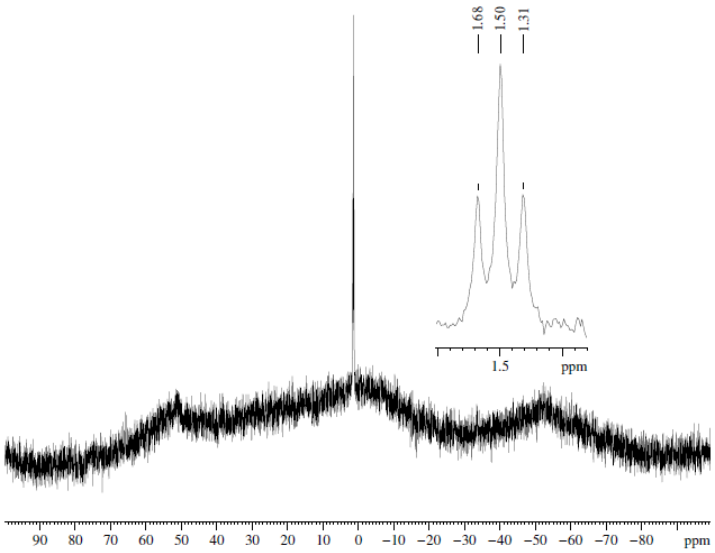

Figure D-82: ^{11}B NMR of **3.6d**

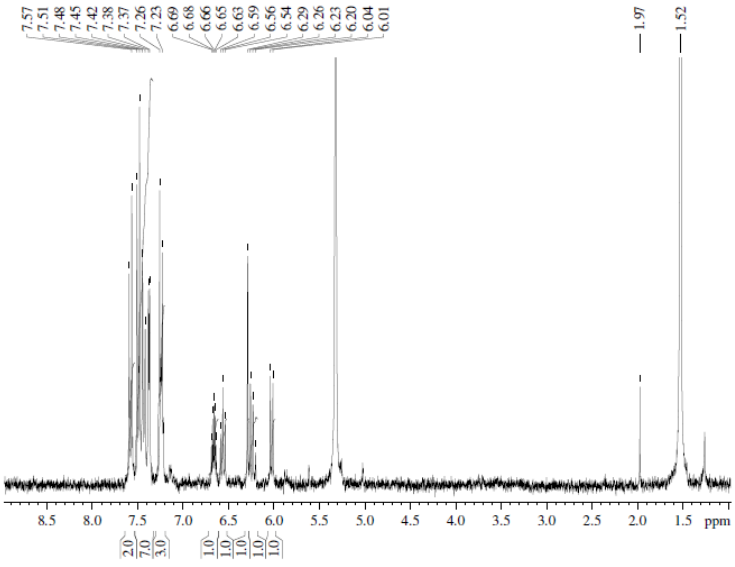

Figure D-83: ^{1}H NMR of **3.6f**. Peaks at 5.32 ppm due to solvent, 1.97ppm due to MeCN and 1.52 ppm due to residual water

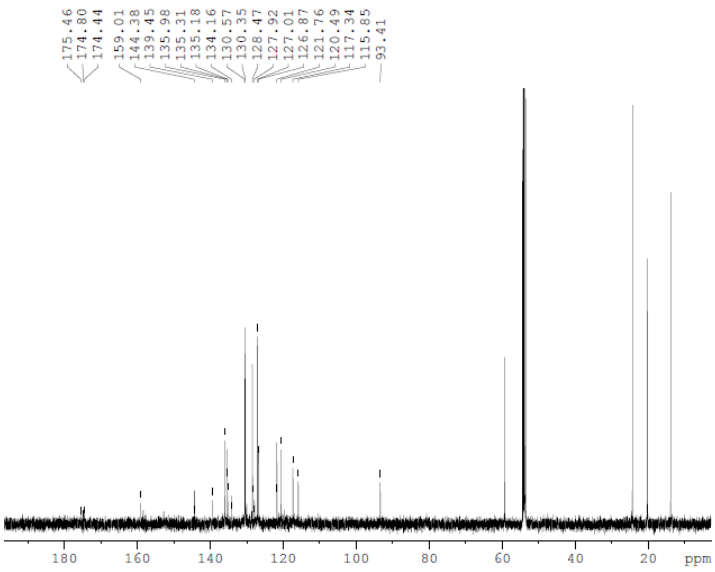

Figure D-84: ^{13}C NMR of **3.6f**

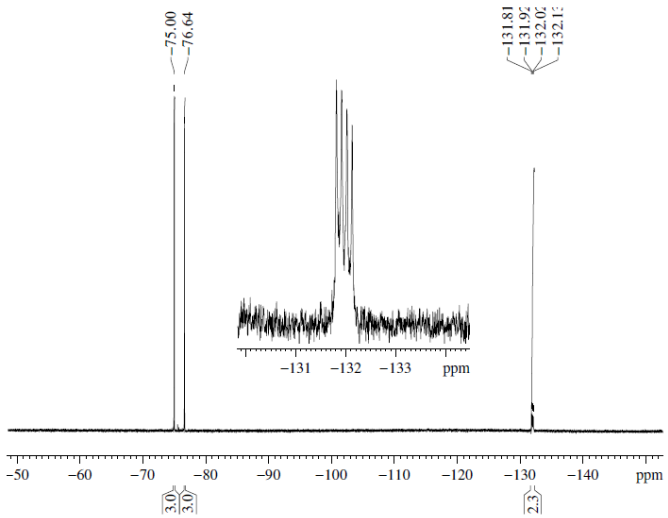

Figure D-85: $^{19}F\{^{1}H\}$ NMR of **3.6f**

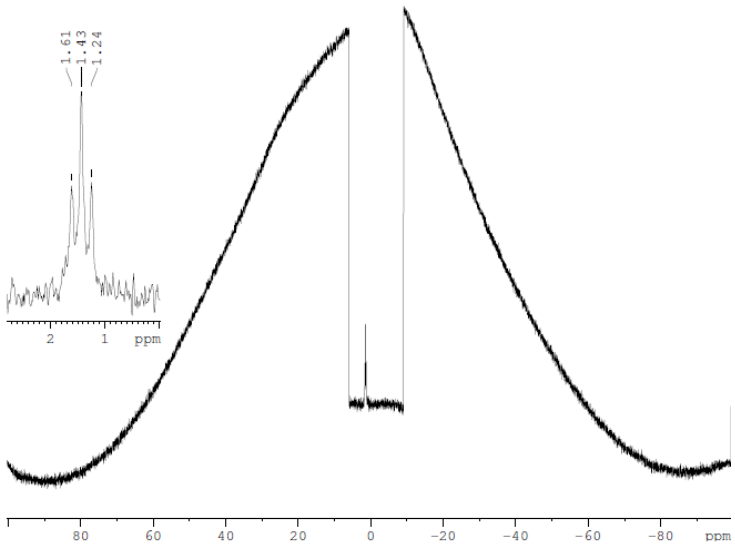

Figure D-86: ^{11}B NMR of **3.6f**

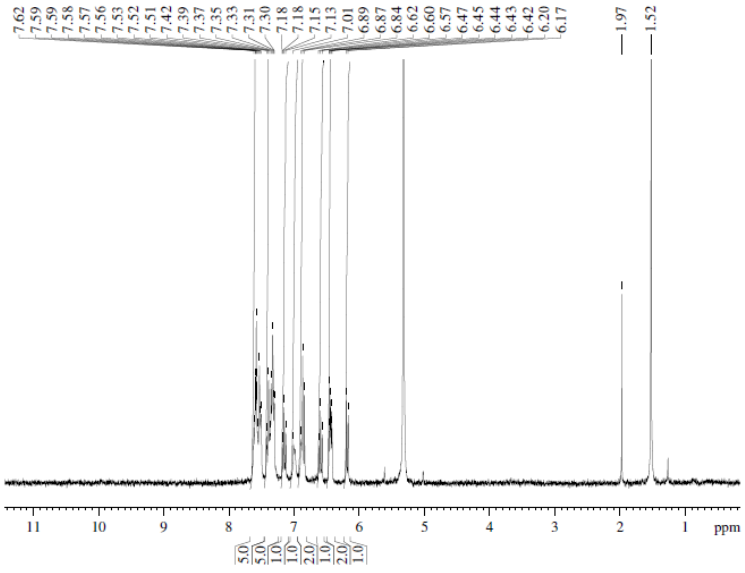

Figure D-87: ^{1}H NMR of **4.1**. Peaks at 5.32 ppm due to solvent and 1.52 ppm due to residual water

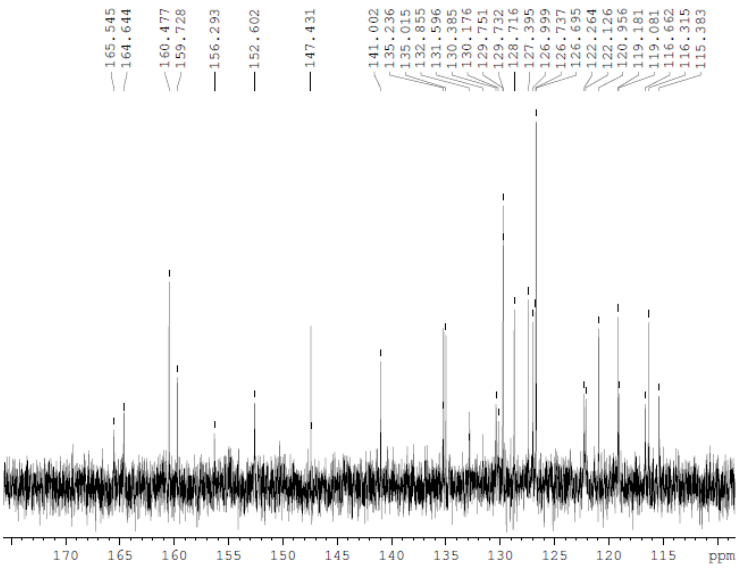

Figure D-88: ^{13}C NMR of **4.1**

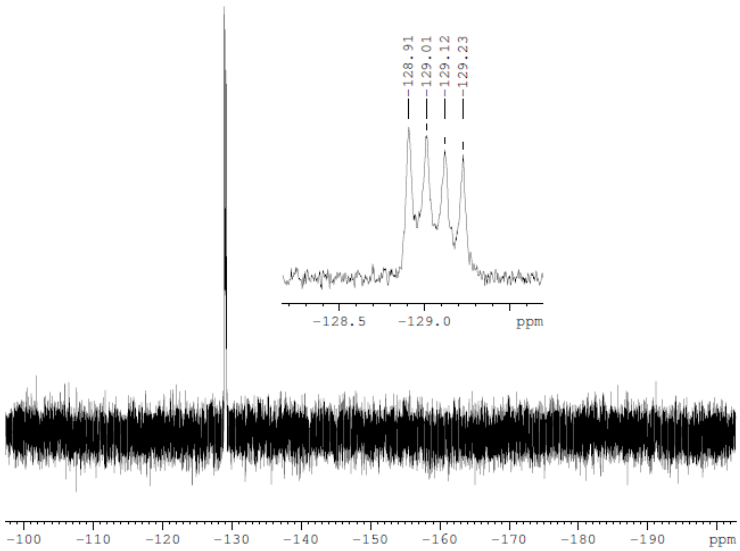

Figure D-89: $^{19}F\{^{1}H\}$ NMR of **4.1**

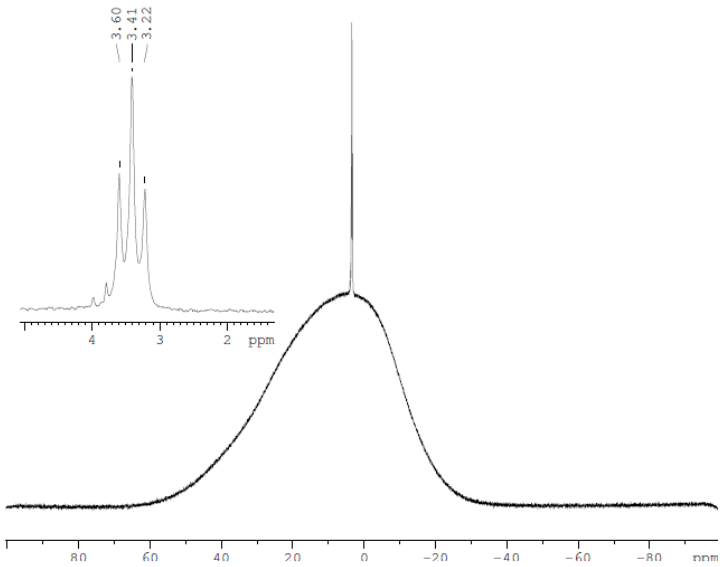

Figure D-90: ^{11}B NMR of **4.1**

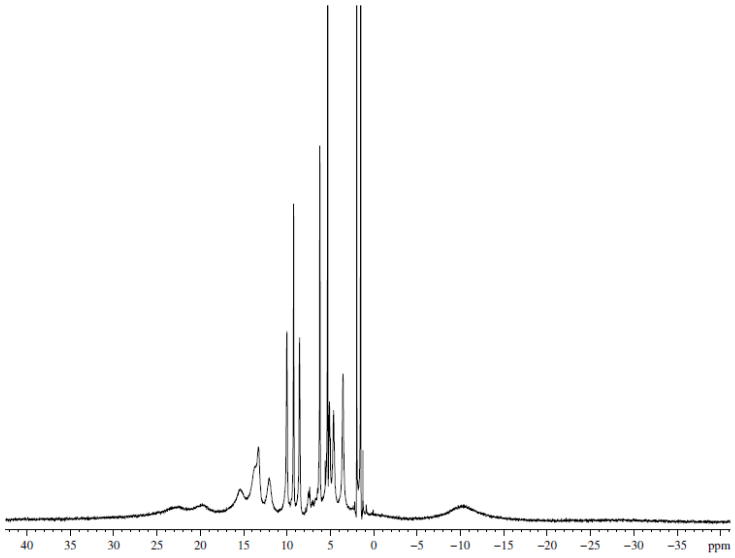

Figure D-91: ^{1}H NMR paramagnetic of **4.2a**. Peaks at 5.32 ppm due to solvent and 1.52 ppm due to residual water

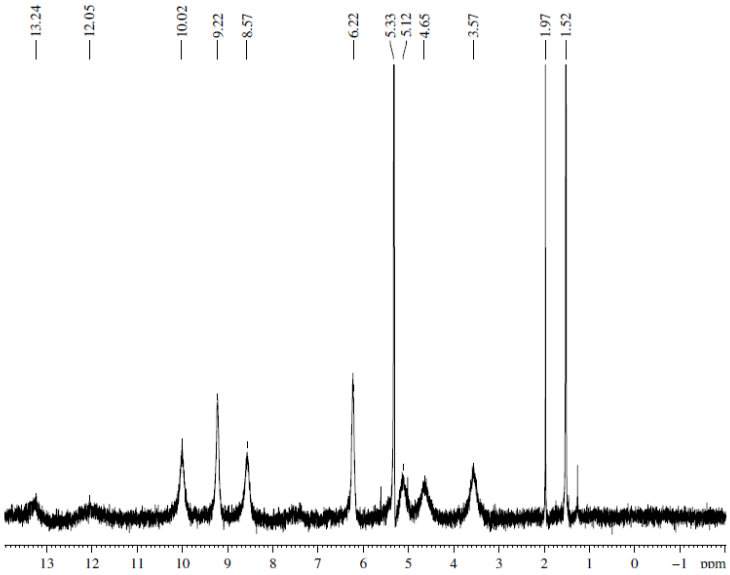

Figure D-92: ^{1}H NMR paramagnetic (zoom) of **4.2a**. Peaks at 5.32 ppm due to solvent and 1.52 ppm due to residual water

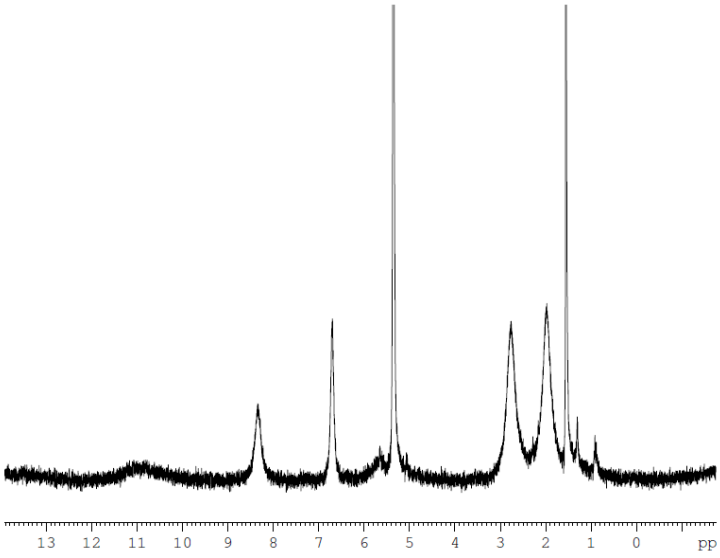

Figure D-93: ^{1}H NMR of **4.2c**. Peaks at 5.32 ppm due to solvent and 1.52 ppm due to residual water

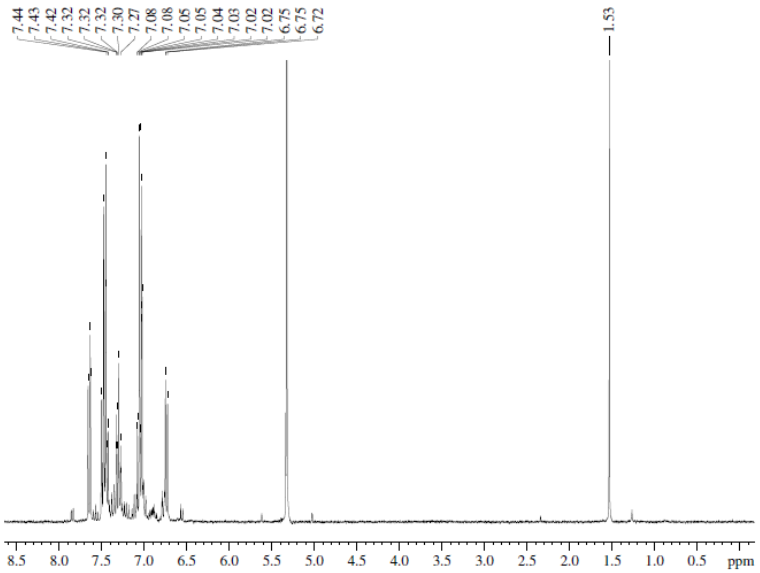

Figure D-94: ^{1}H NMR of **5.1a**. Peaks at 5.32 ppm due to solvent and 1.52 ppm due to residual water

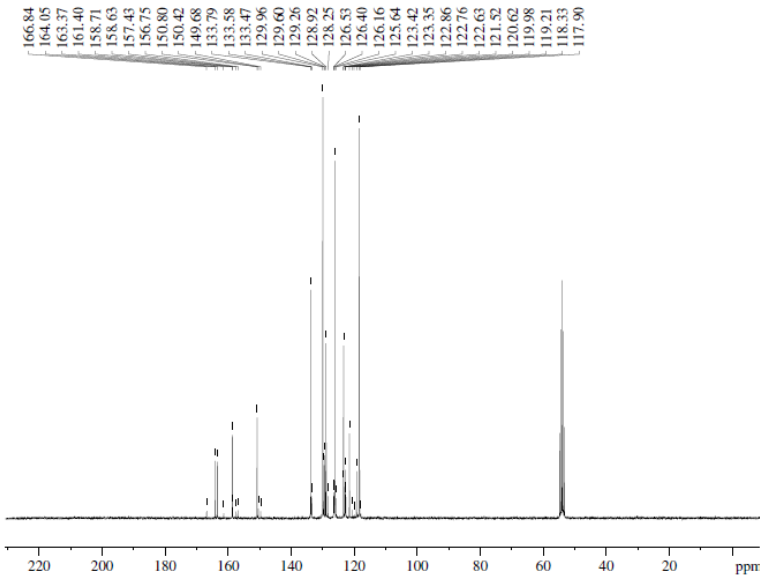

Figure D-95: ^{13}C NMR of **5.1a**

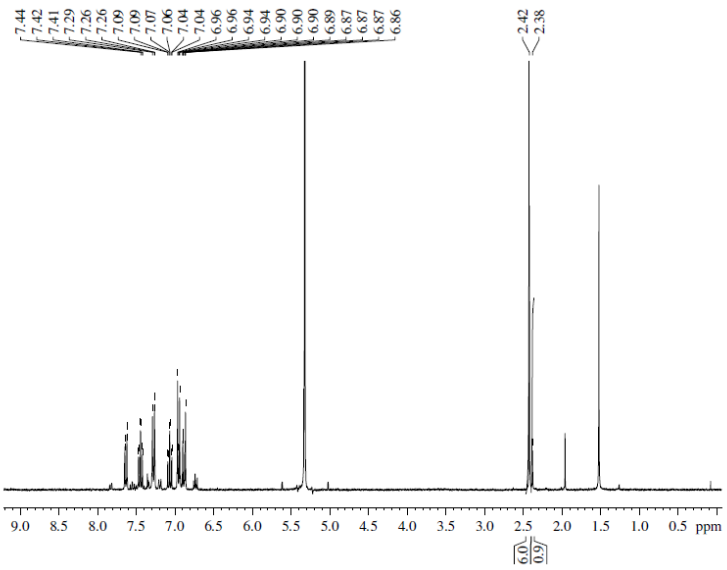

Figure D-96: ^{1}H NMR of **5.1b**. Peaks at 5.32 ppm due to solvent and 1.54 ppm due to residual water

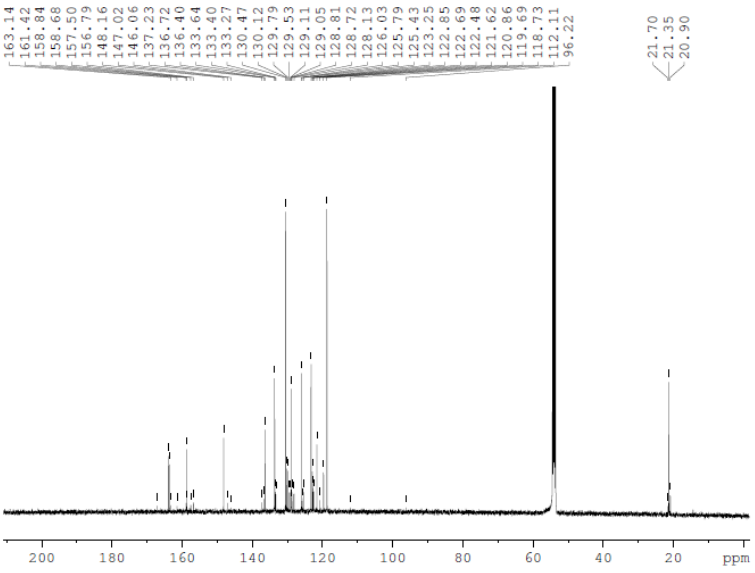

Figure D-97: ^{13}C NMR of **5.1b**

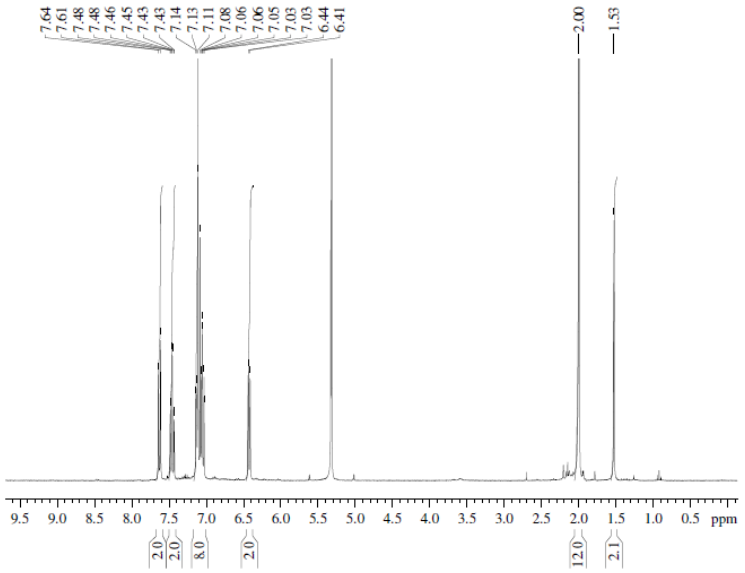

Figure D-98: ^{1}H NMR of **5.1c**. Peaks at 5.32 ppm due to solvent and 1.53 ppm due to residual water

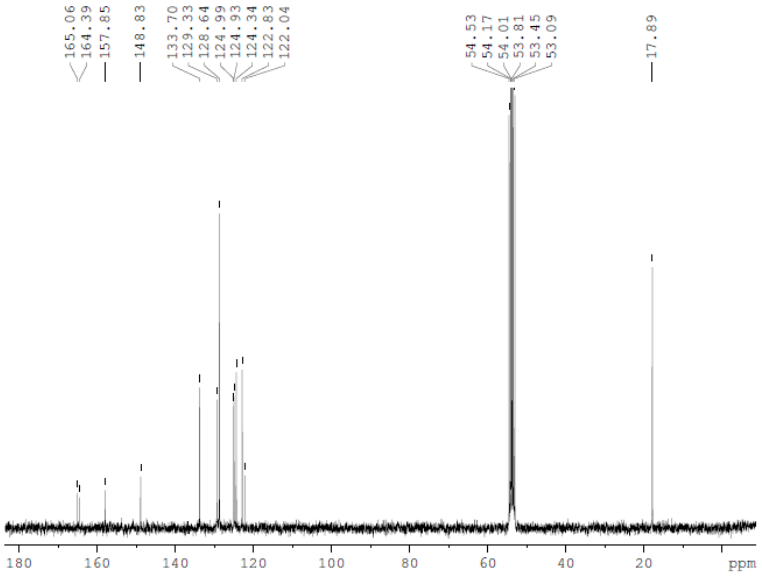

Figure D-99: ^{13}C NMR of **5.1c**

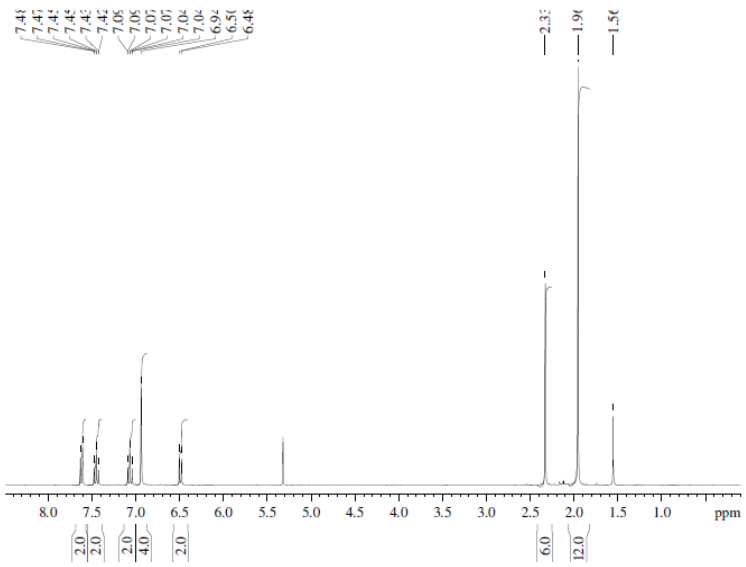

Figure D-100: ^{1}H NMR of **5.1h**. Peaks at 5.32 ppm due to solvent and 1.53 ppm due to residual water

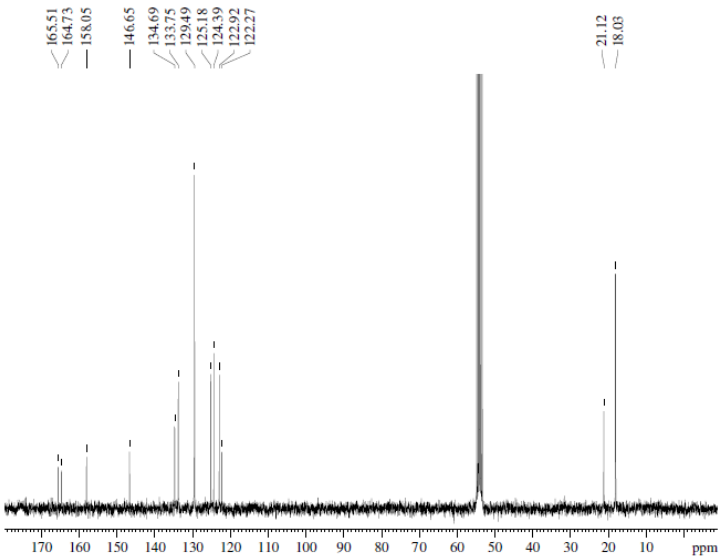

Figure D-101: ^{13}C NMR of **5.1h**

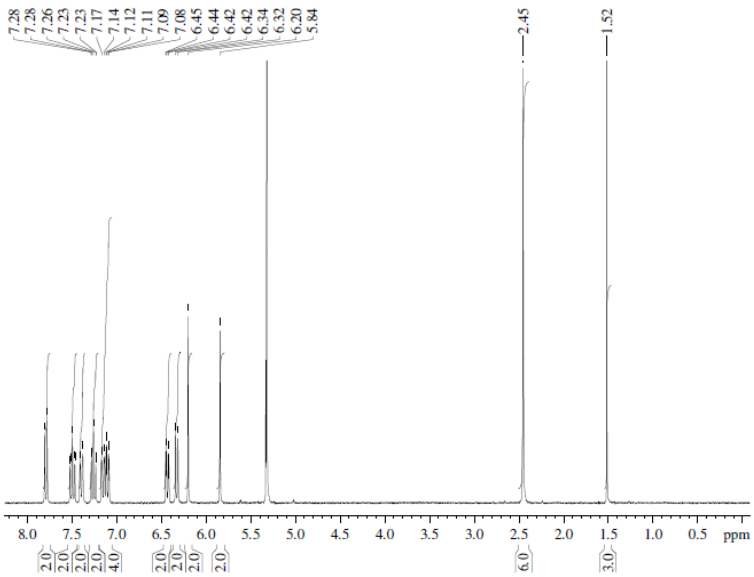

Figure D-102: ^{1}H NMR of **5.2b-trans**. Peaks at 5.32 ppm due to solvent and 1.52 ppm due to residual water

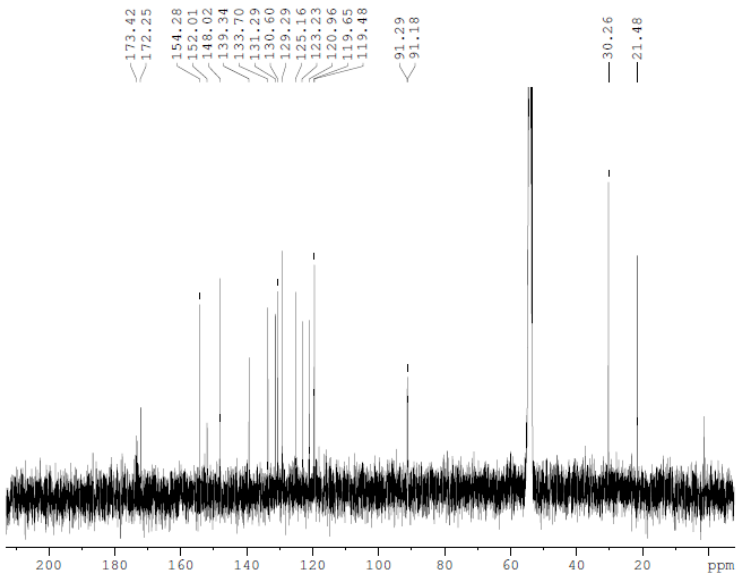

Figure D-103: ^{13}C NMR of **5.2b-trans**

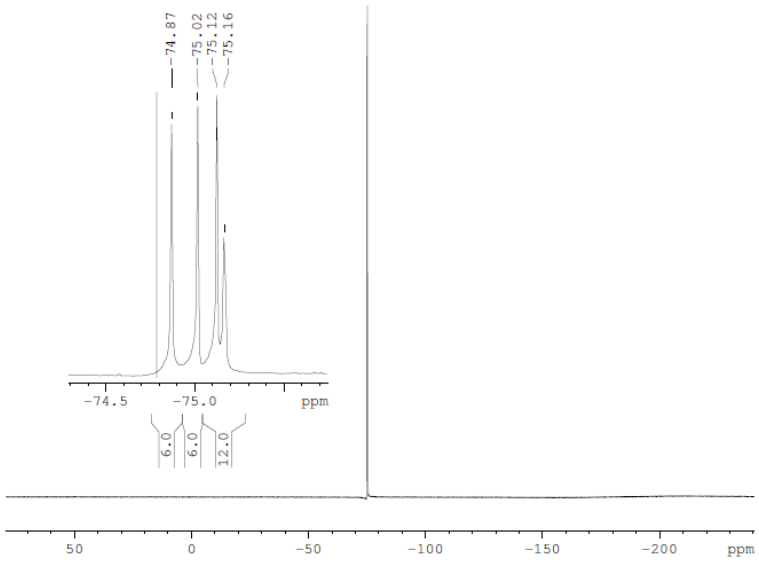

Figure D-104: $^{19}F\{^{1}H\}$ NMR of **5.2b-trans**

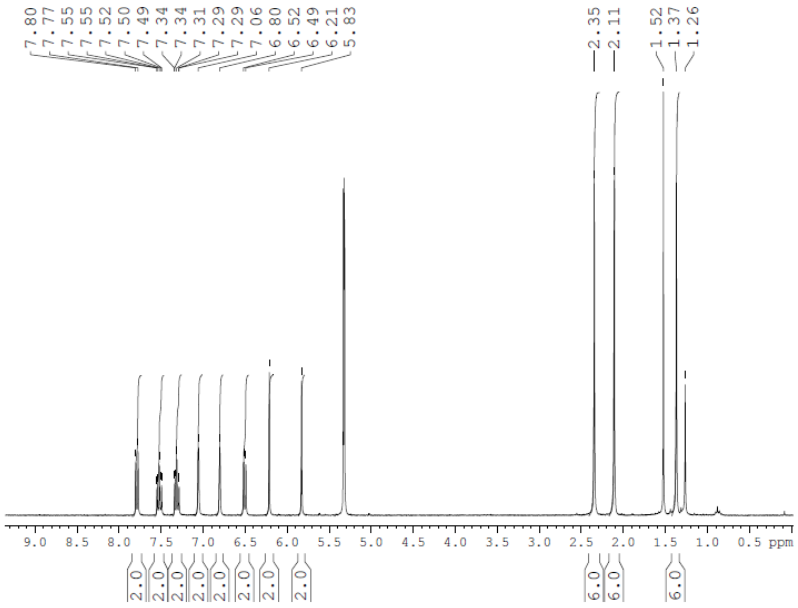

Figure D-105: ^{1}H NMR of **5.2h-trans**. Peaks at 5.32 ppm due to solvent and 1.53 ppm due to residual water

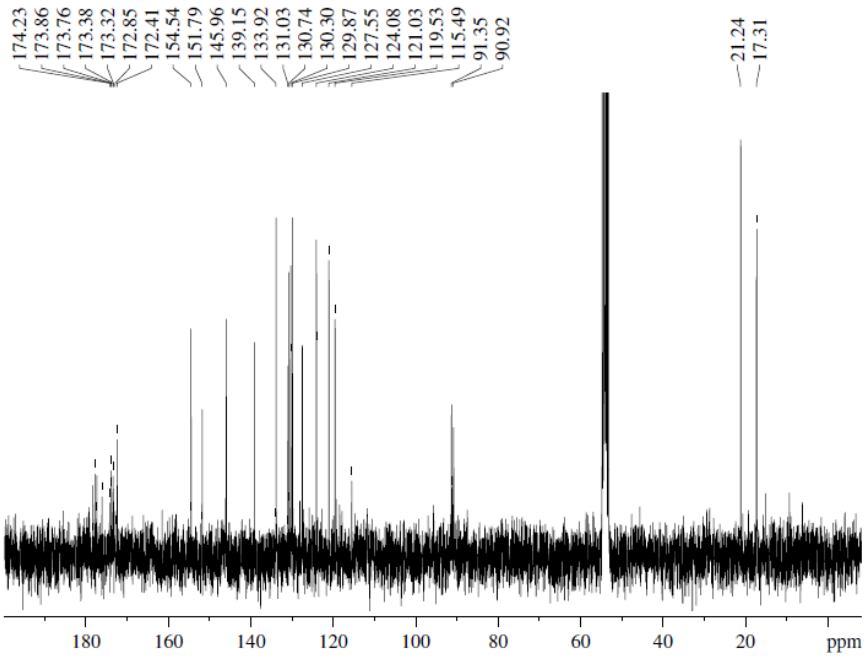

Figure D-106: ^{13}C NMR of **5.2h-trans**

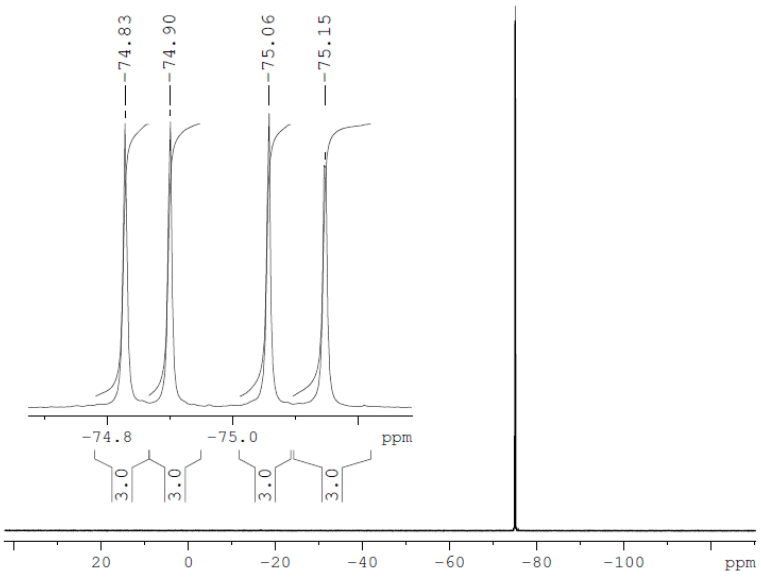

Figure D-107: $^{19}F\{^{1}H\}$ NMR of **5.2h-trans**

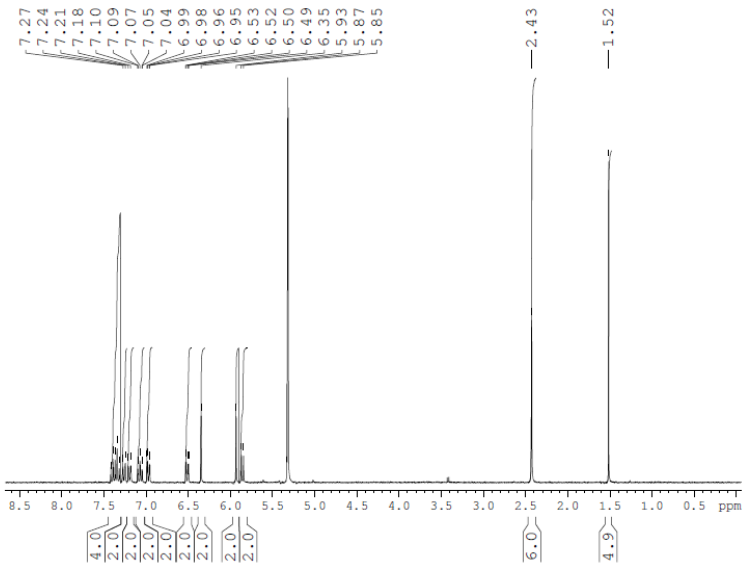

Figure D-108: ^{1}H NMR of **5.2b-cis**. Peaks at 5.32 ppm due to solvent and 1.52 ppm due to residual water

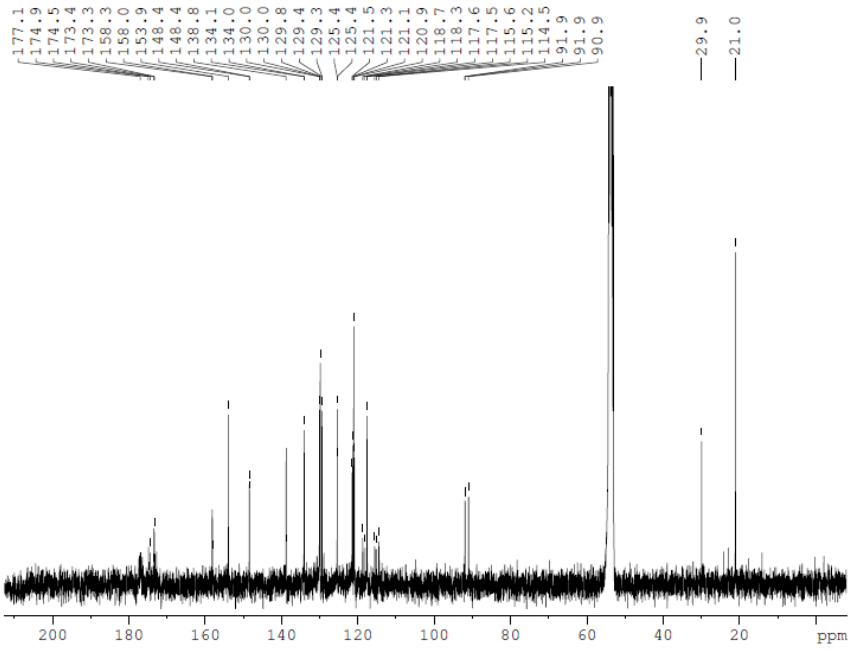

Figure D-109: ^{13}C NMR of **5.2b-cis**

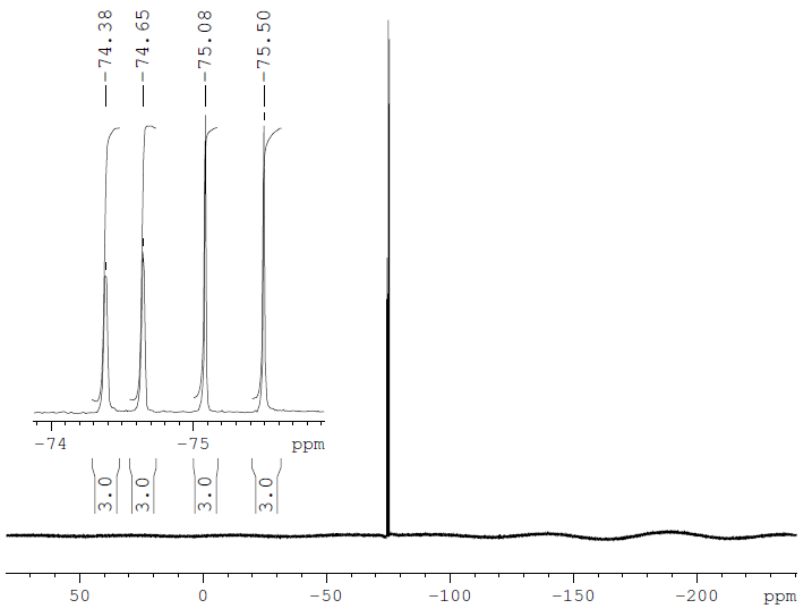

Figure D-110: $^{19}F\{^{1}H\}$ NMR of **5.2b-cis**

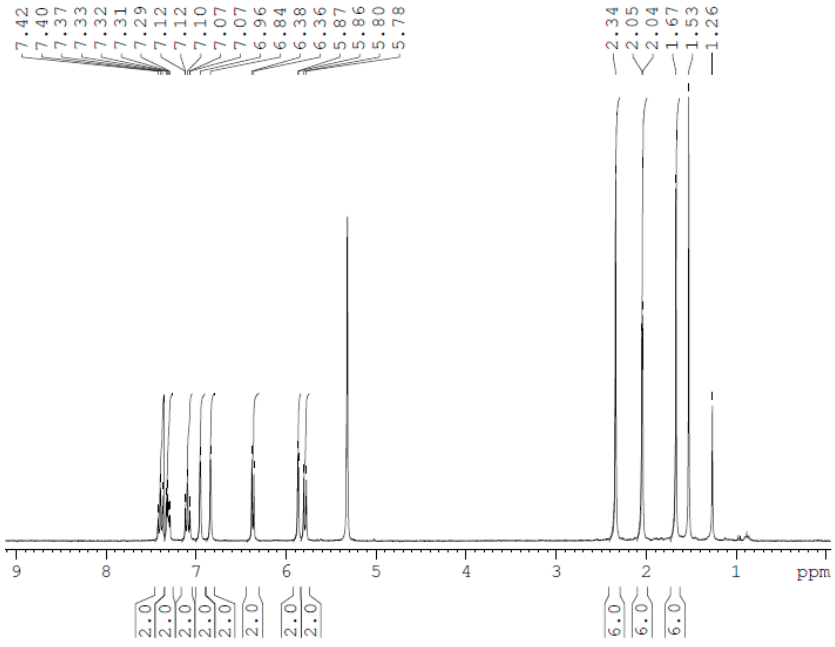

Figure D-111: ^{1}H NMR of **5.2h-cis**. Peaks at 5.32 ppm due to solvent and 1.52 ppm due to residual water

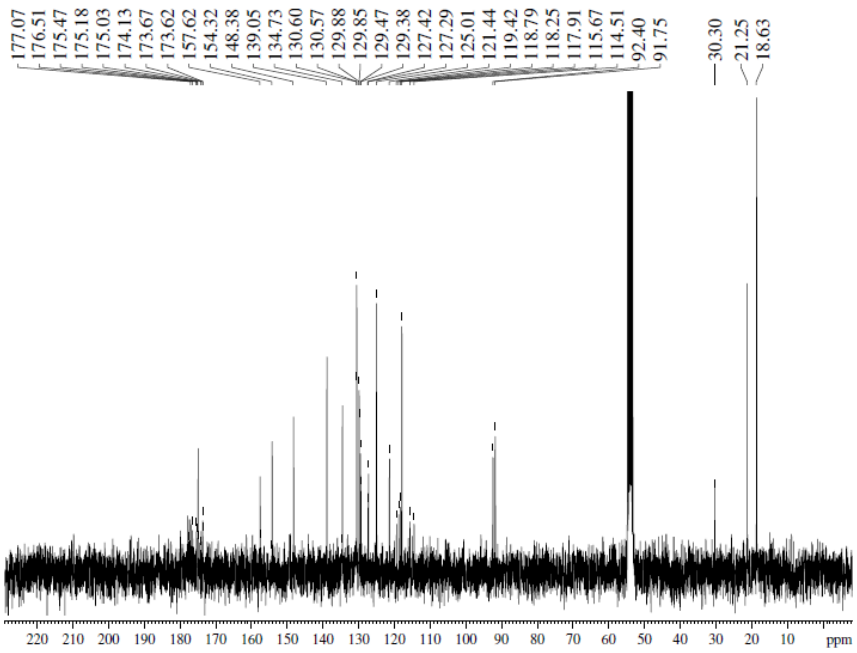

Figure D-112: ^{13}C NMR of **5.2h-cis**

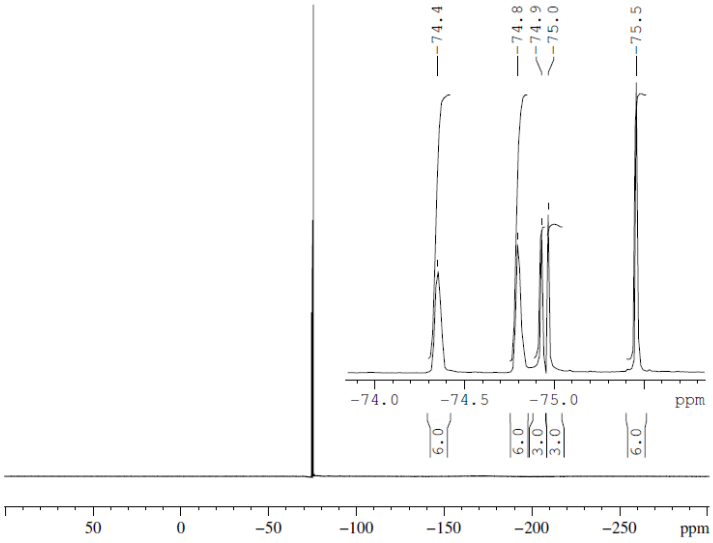

Figure D-113: $^{19}F\{^{1}H\}$ NMR of **5.2h-cis**

Appendix E: HRMS Data (specifications can be found in section 2.4.1)

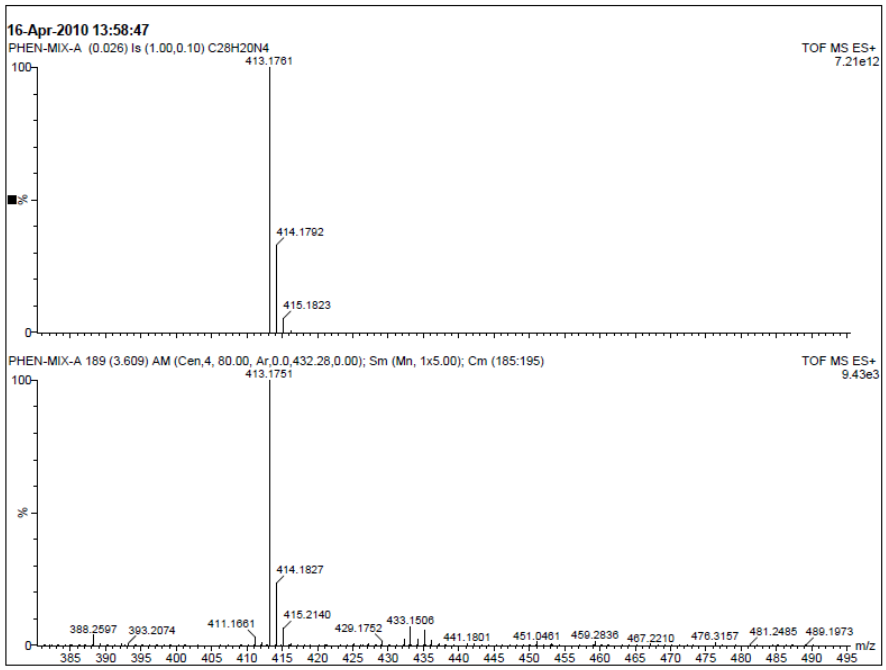

Figure E-1: HRMS of **1.32a** [theoretical (top), experimental (bottom)]

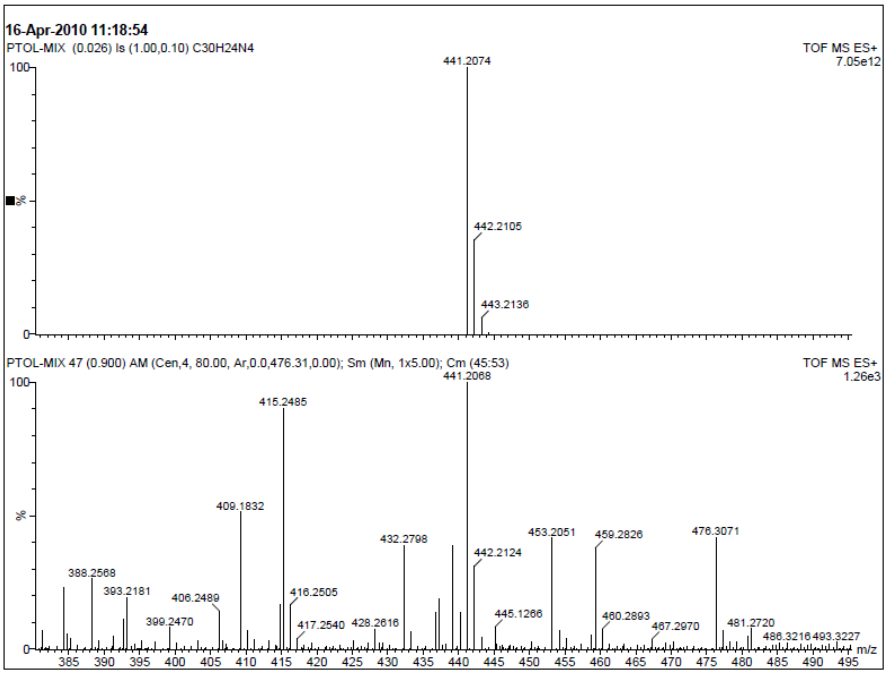

Figure E-2: HRMS of **1.32b** [theoretical (top), experimental (bottom)]

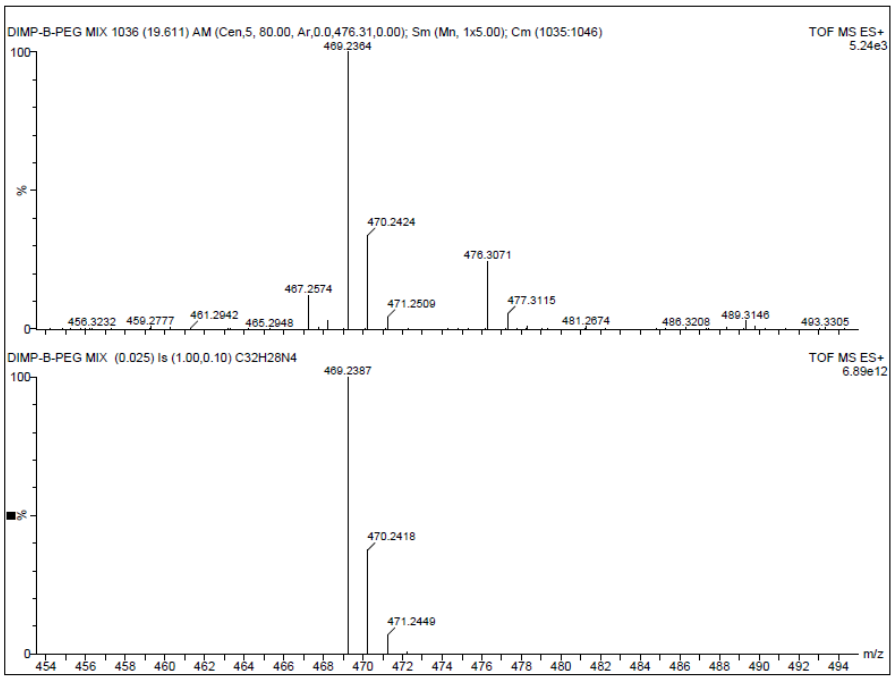

Figure E-3: HRMS of **1.32c** [theoretical (bottom), experimental (top)]

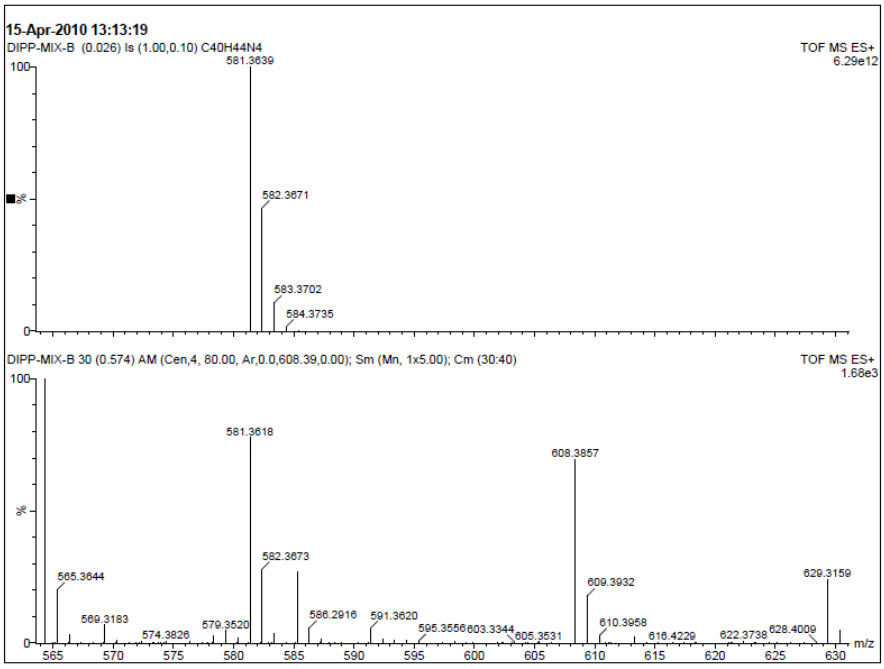

Figure E-4: HRMS of **1.32d** [theoretical (top), experimental (bottom)]

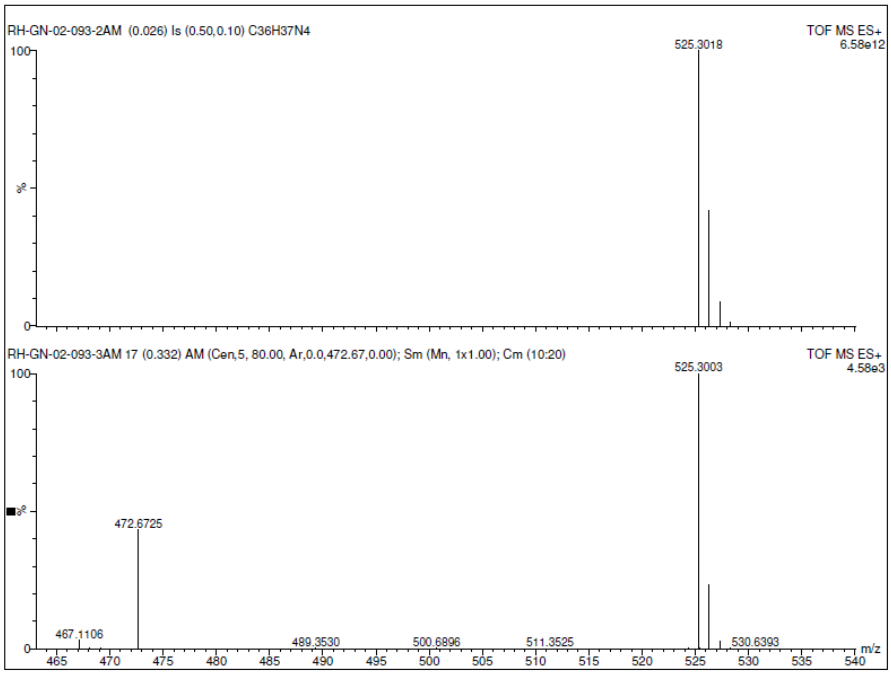

Figure E-5: HRMS of **1.32e** [theoretical (top), experimental (bottom)]

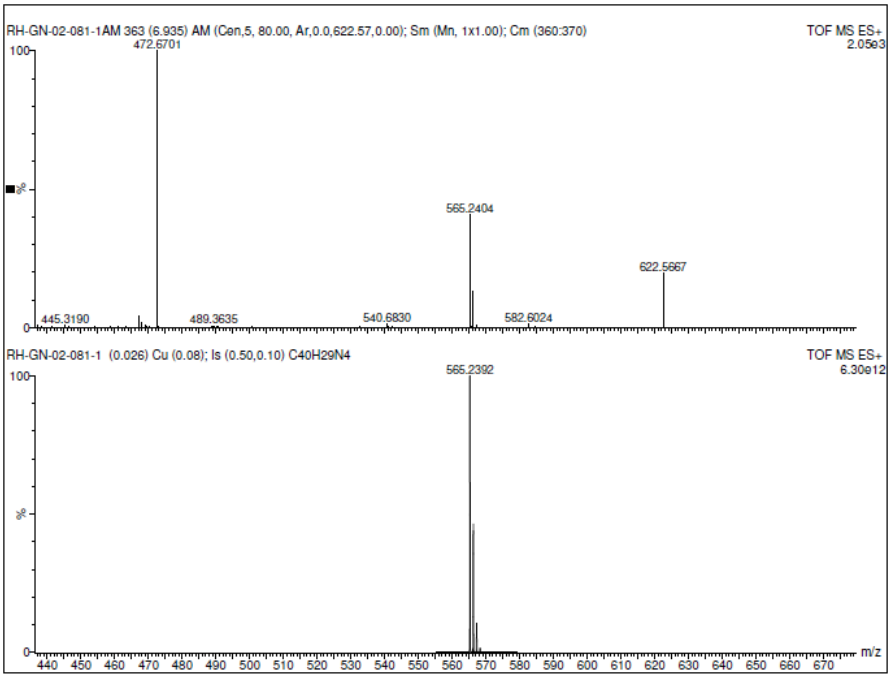

Figure E-6: HRMS of **1.32g** [theoretical (bottom), experimental (top)]

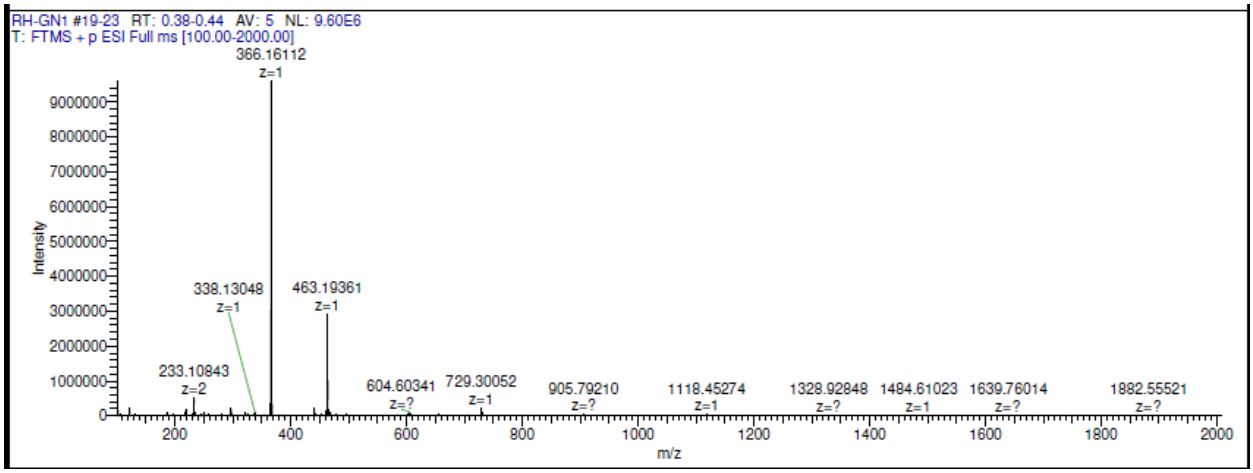

Figure E-7: HRMS of **2.1c** [experimental]

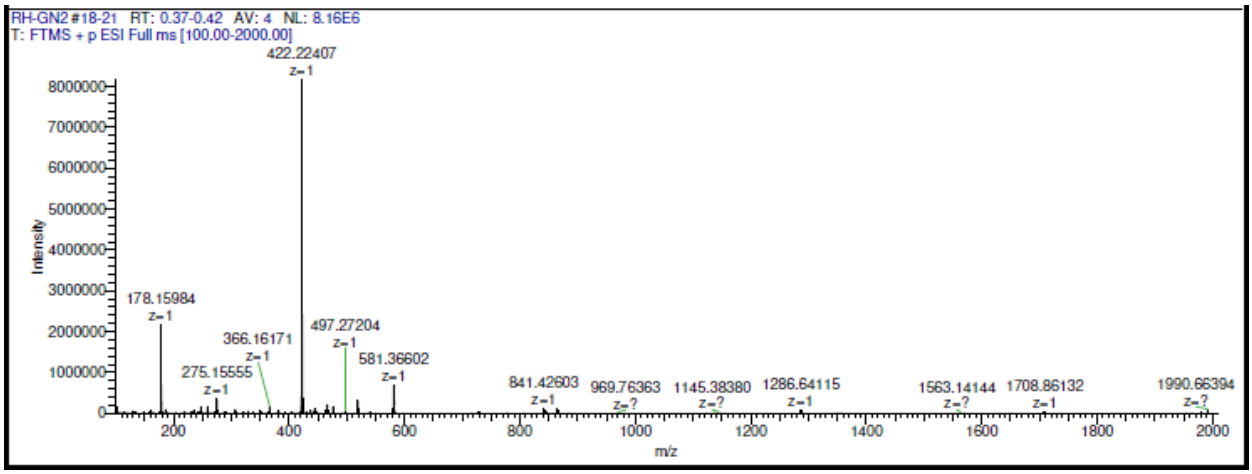

Figure E-8: HRMS of **2.1d** [experimental]

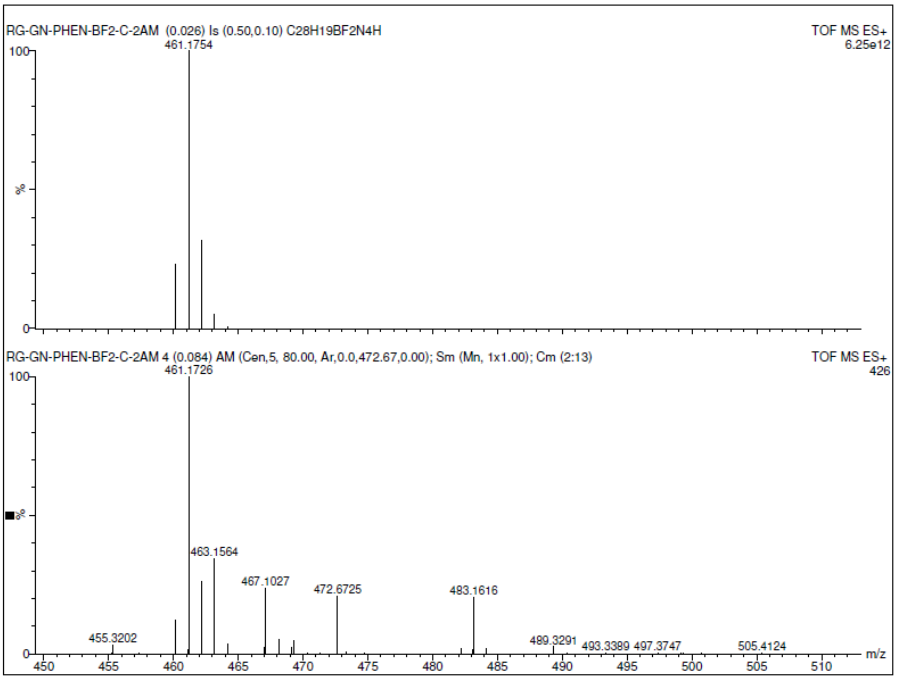

Figure E-9: HRMS of **3.3**a [theoretical (top) experimental (bottom)]

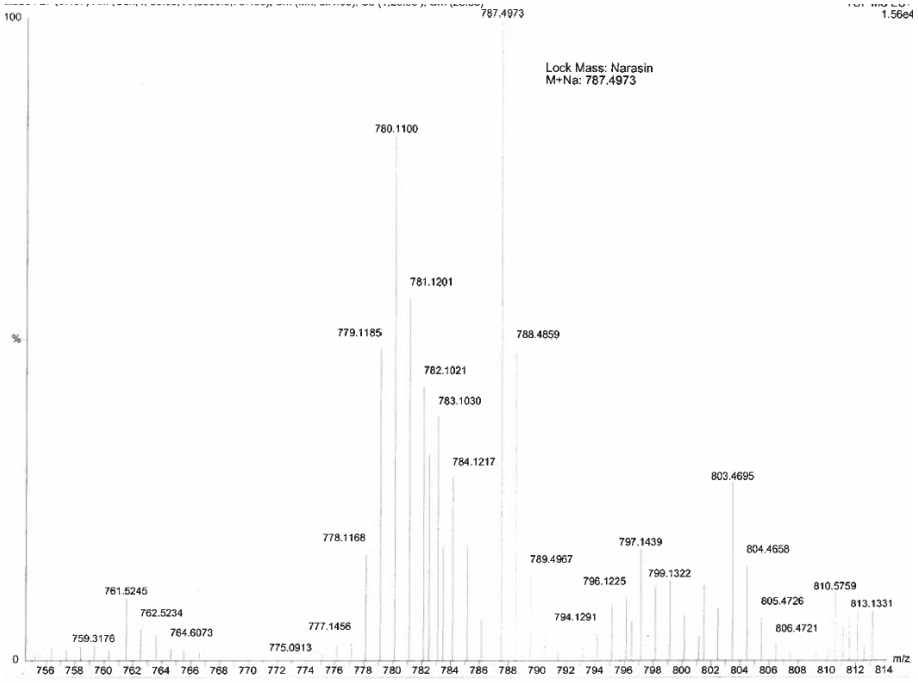

Figure E-10: HRMS of **2.2c** (experimental)

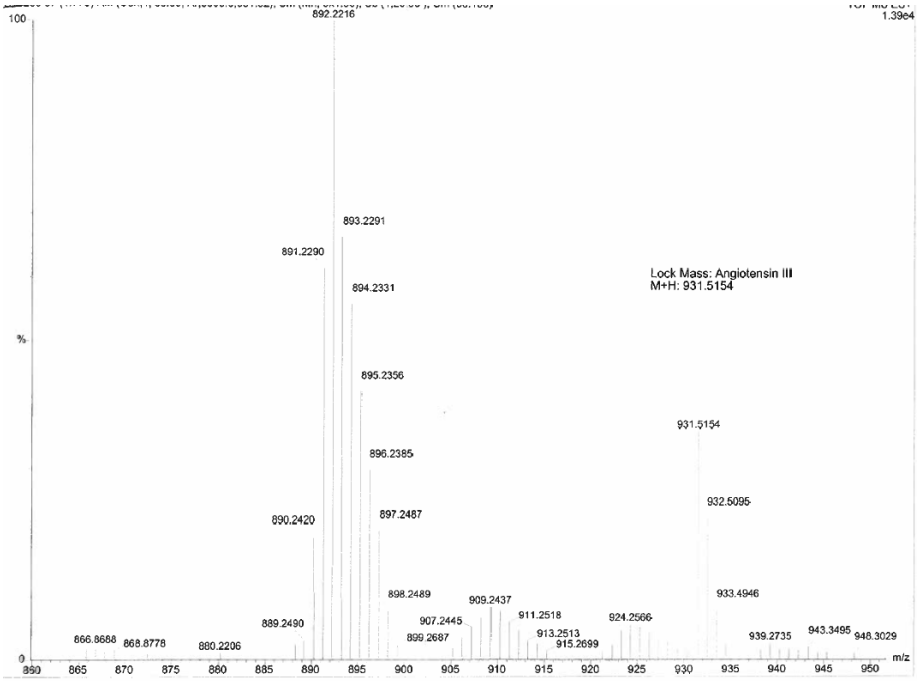

Figure E-11: HRMS of **2.2d** (experimental)

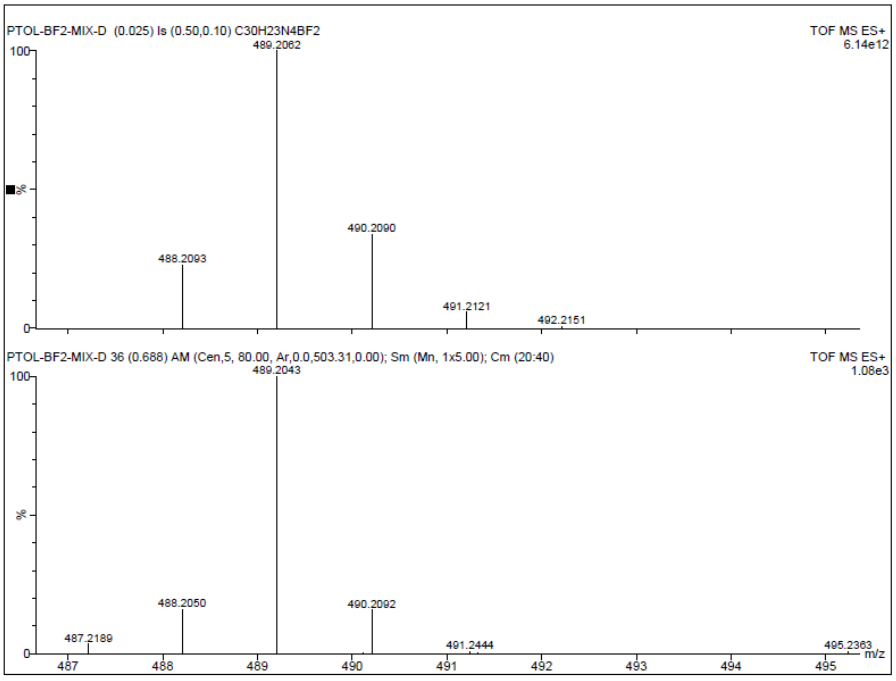

Figure E-12: HRMS of **3.3b** [theoretical (bottom) experimental (top)]

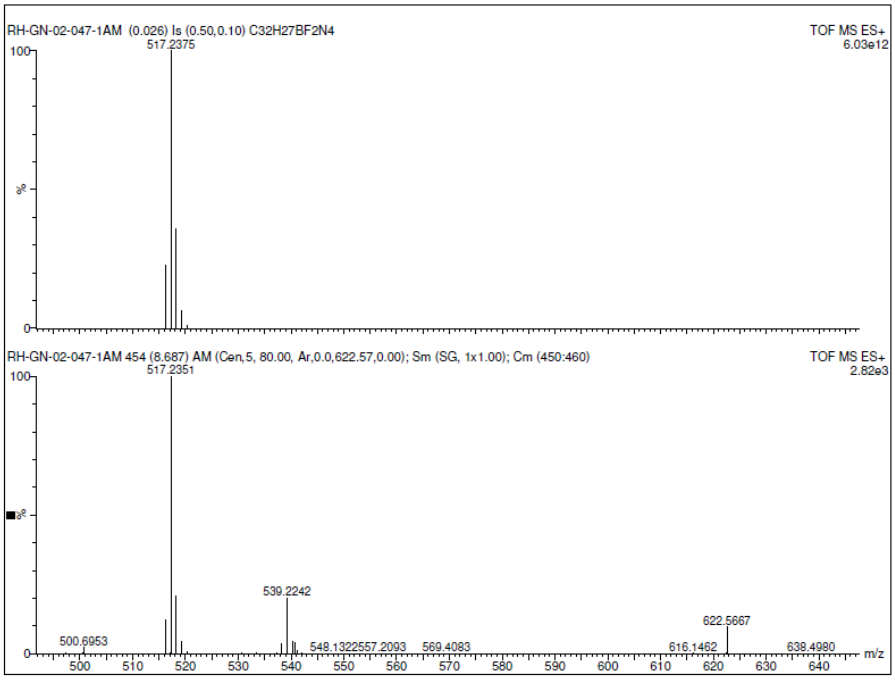

Figure E-13: HRMS of **3.3c** [theoretical (top) experimental (bottom)]

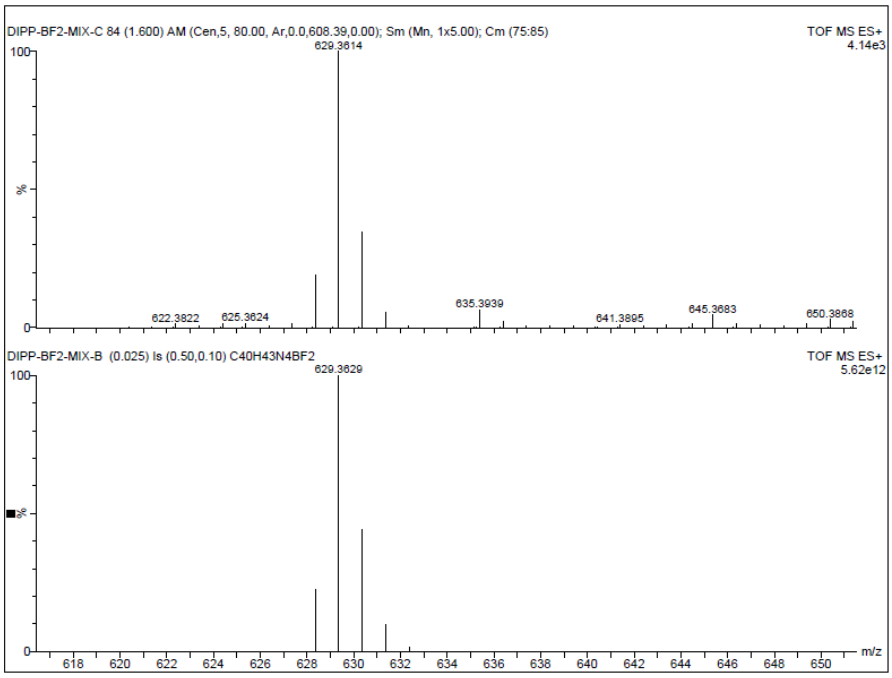

Figure E-14: HRMS of **3.3d** [theoretical (bottom) experimental (top)]

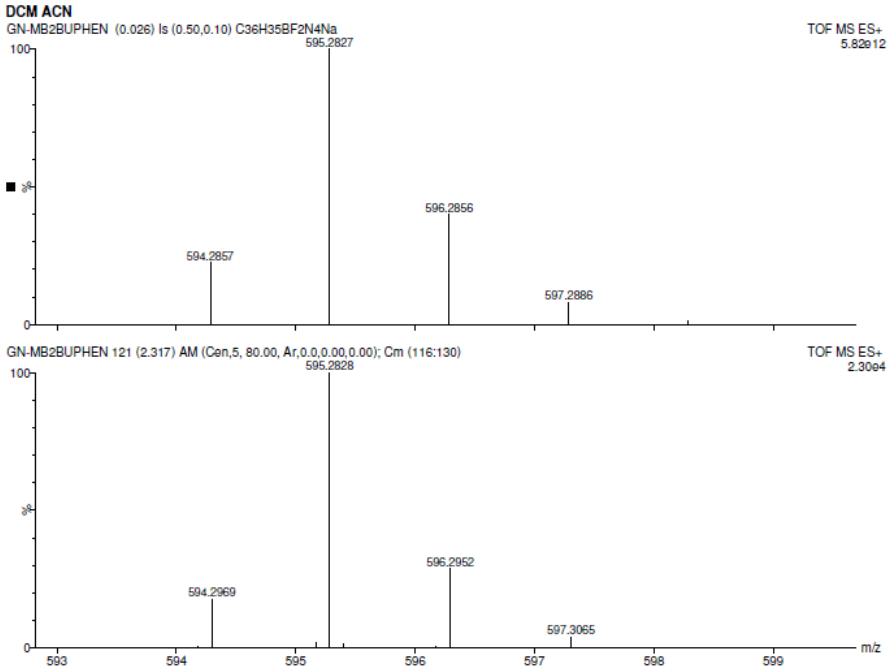

Figure E-15: HRMS of **3.3e** [theoretical (bottom) experimental (top)]

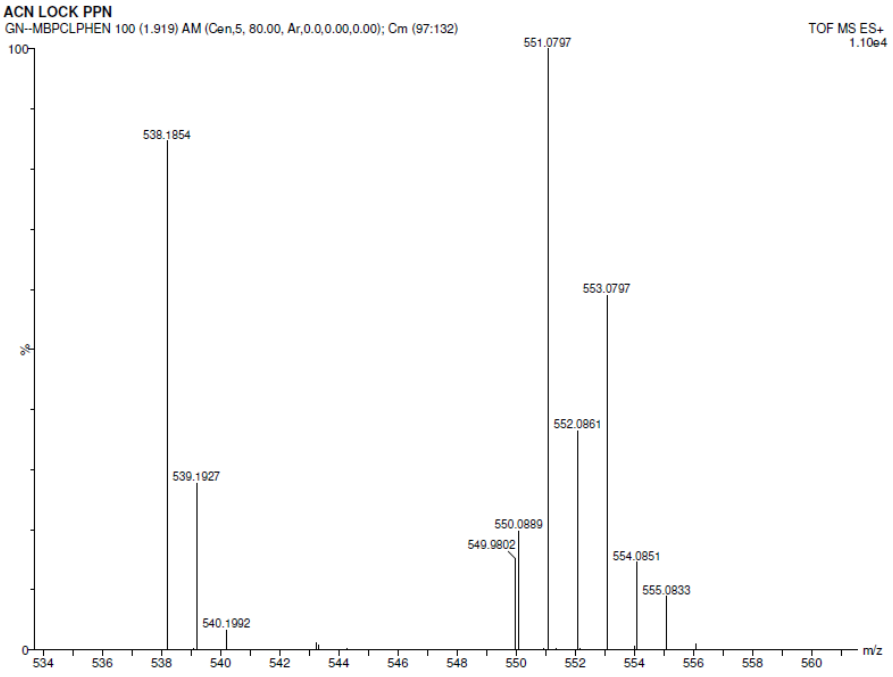

Figure E-16: HRMS of **3.3f** experimental

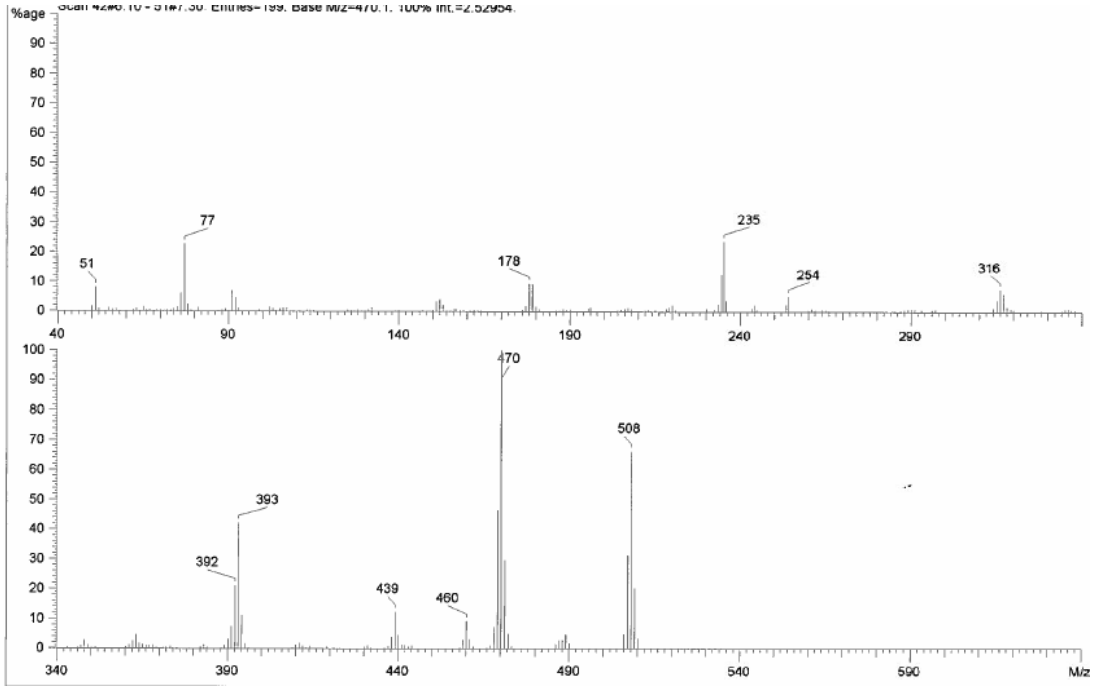

Figure E-17: HRMS of **3.5a** [experimental]

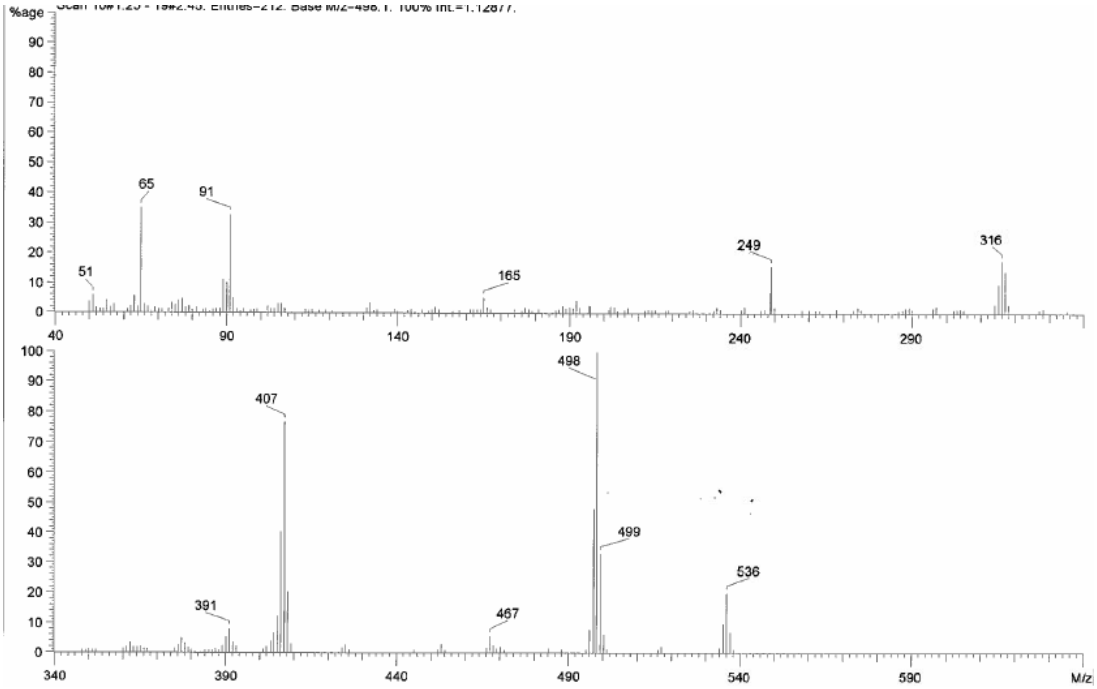

Figure E-18: HRMS of **3.5b** [experimental]

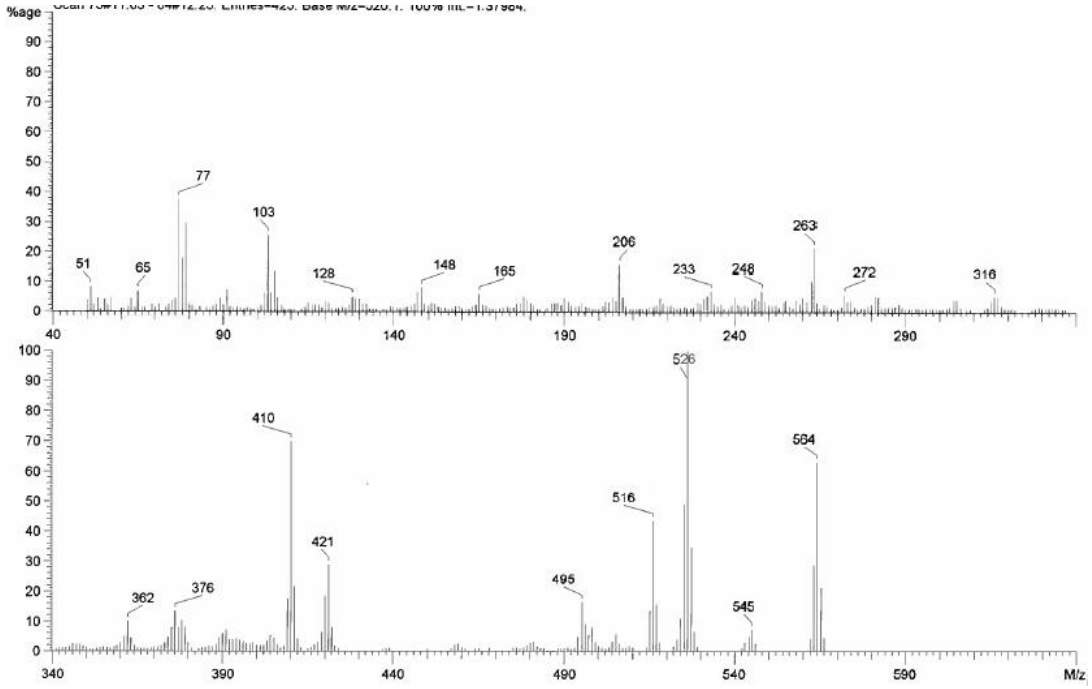

Figure E-19: HRMS of **3.5c** [experimental]

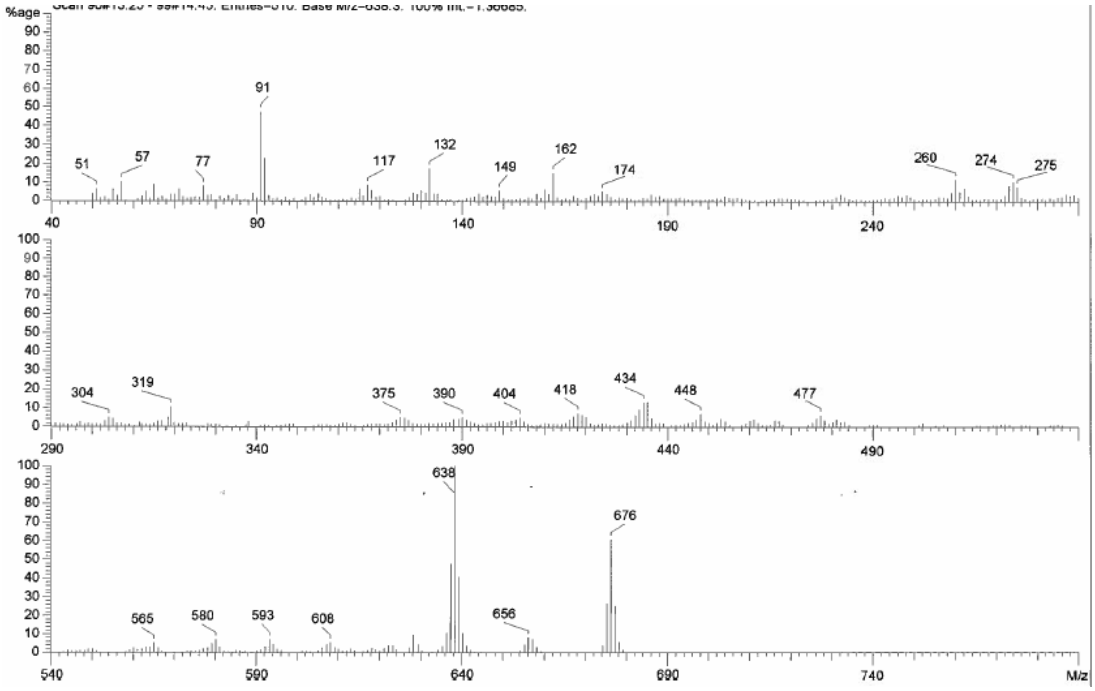

Figure E-20: HRMS of **3.5d** [experimental]

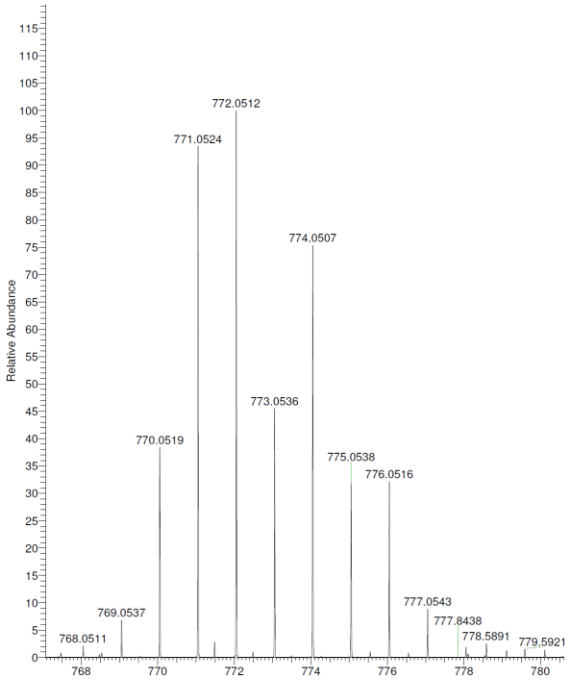

Figure E-21: HRMS of **3.6a** [experimental]

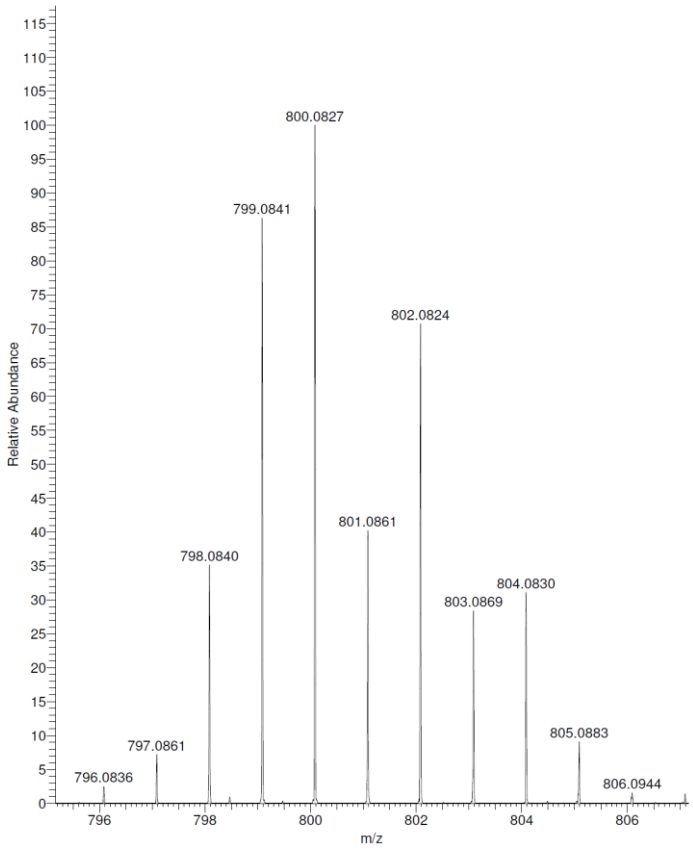

Figure E-22: HRMS of **3.6b** [experimental]

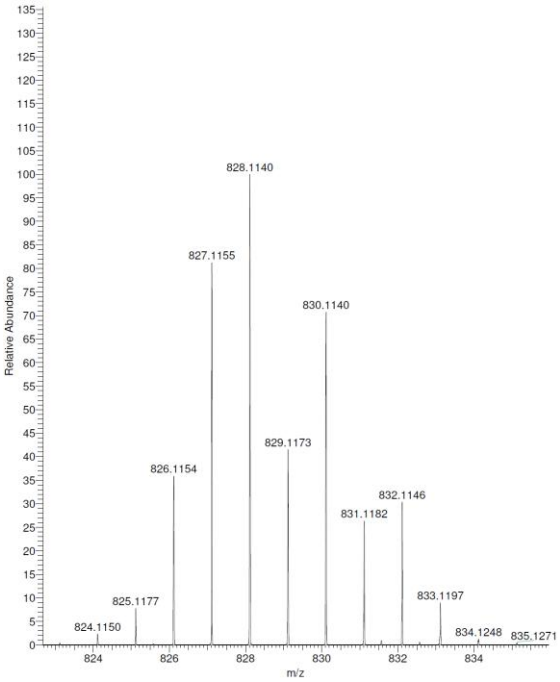

Figure E-23: HRMS of **3.6c** [experimental]

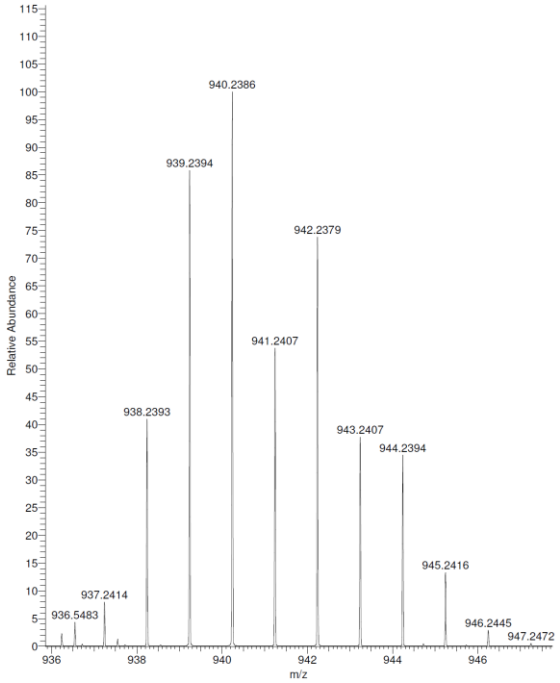

Figure E-24: HRMS of **3.6d** [experimental]

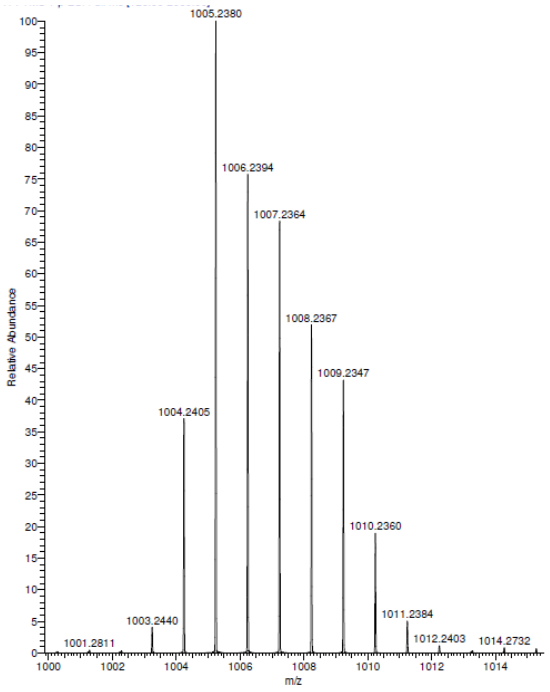

Figure E-25: HRMS of **4.1** [experimental]

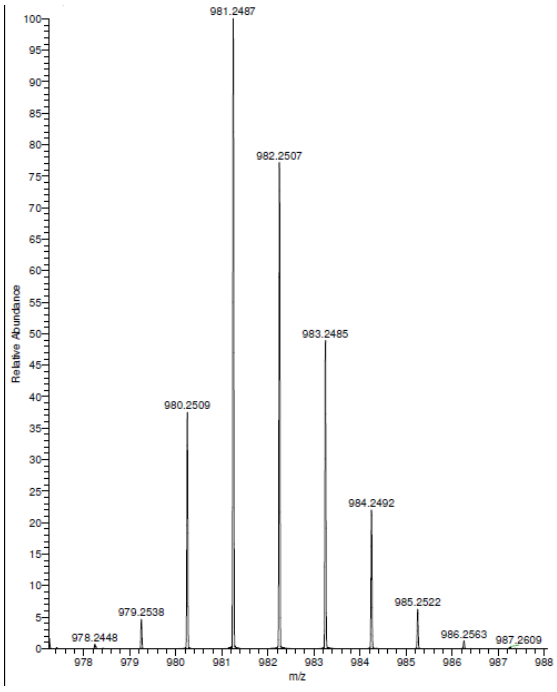

Figure E-26: HRMS of **4.2a** [experimental]

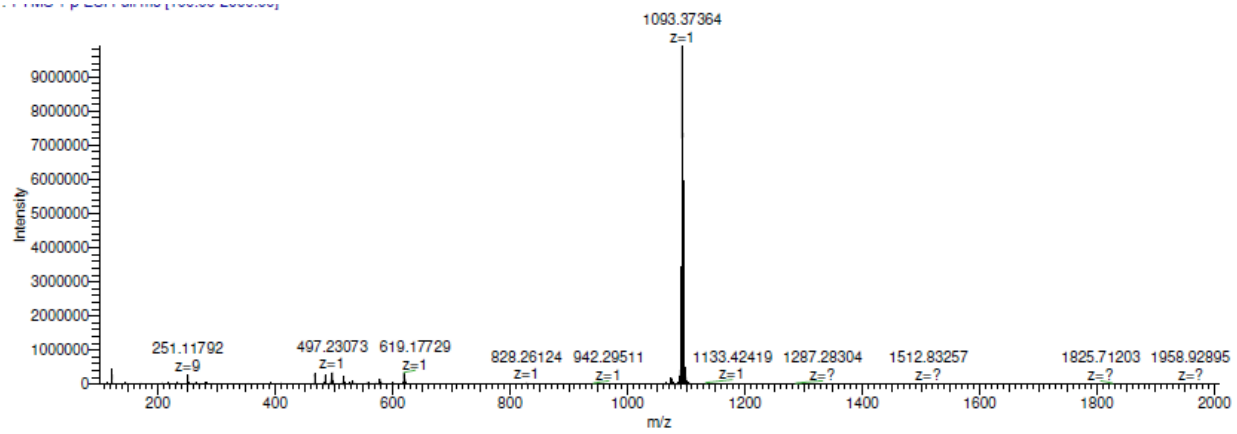

Figure E-27: HRMS of **4.2c** [experimental]

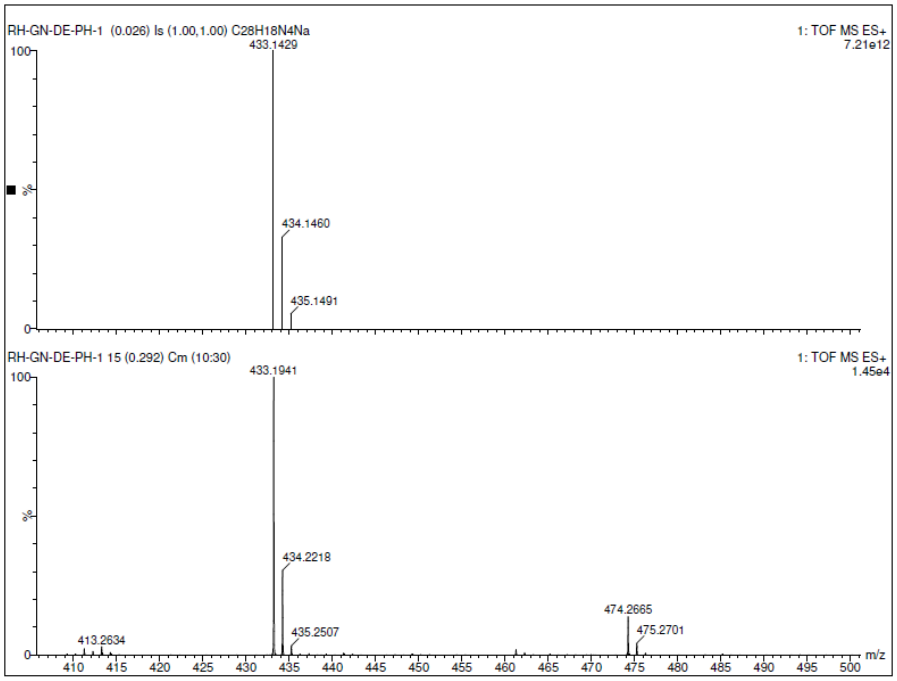

Figure E-28: HRMS of **5.1a** [theoretical (top), experimental (bottom)]

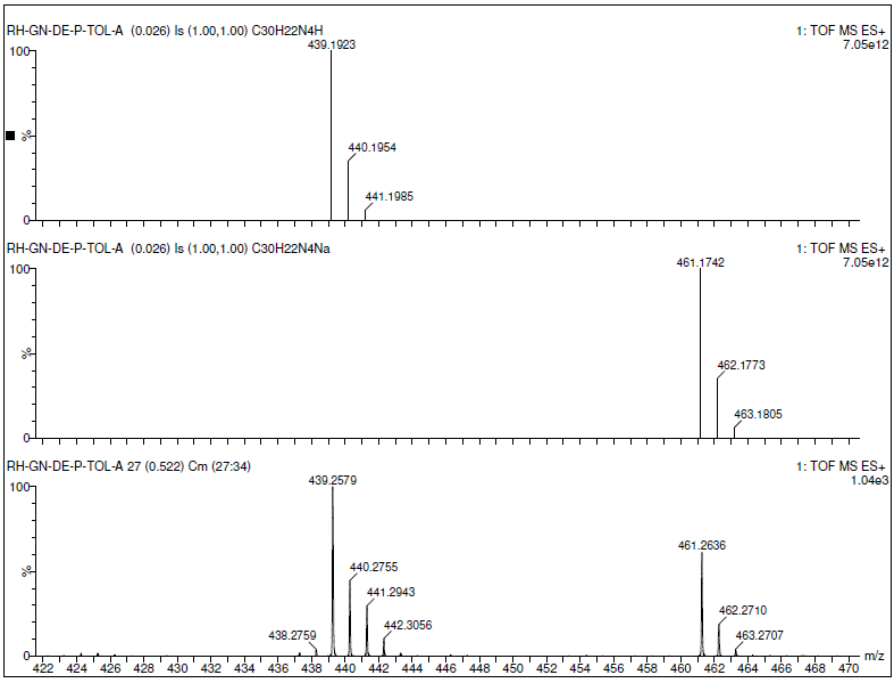

Figure E-29: HRMS of **5.1b** [theoretical (top and middle), experimental (bottom)]

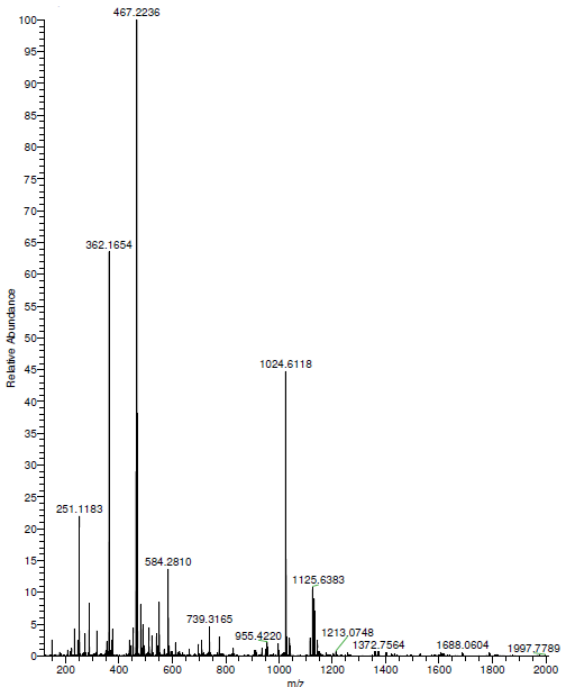

Figure E-30: HRMS of **5.1c** [experimental]

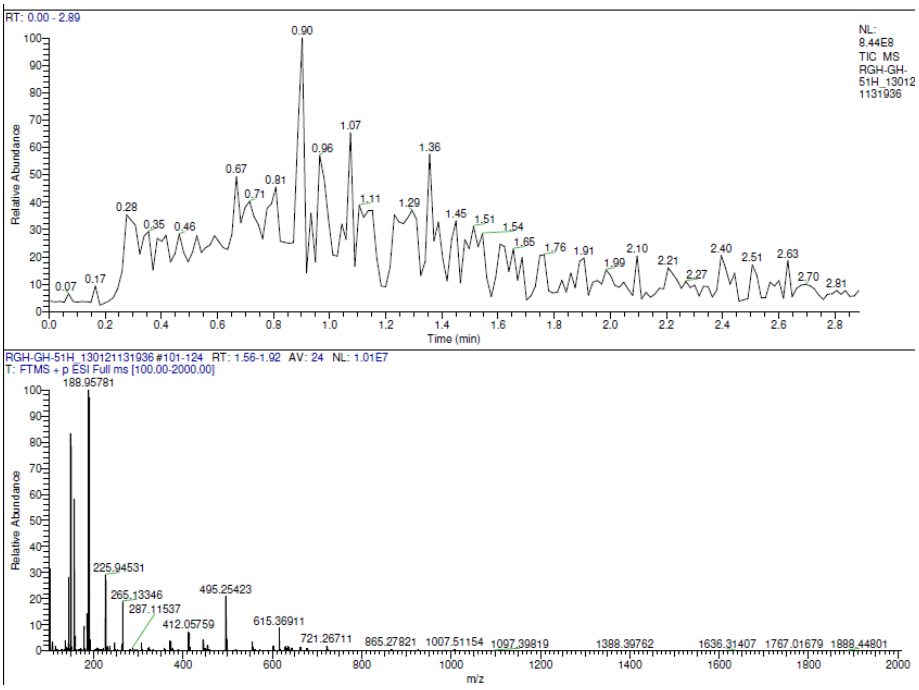

Figure E-31: HRMS of **5.1h** [experimental]

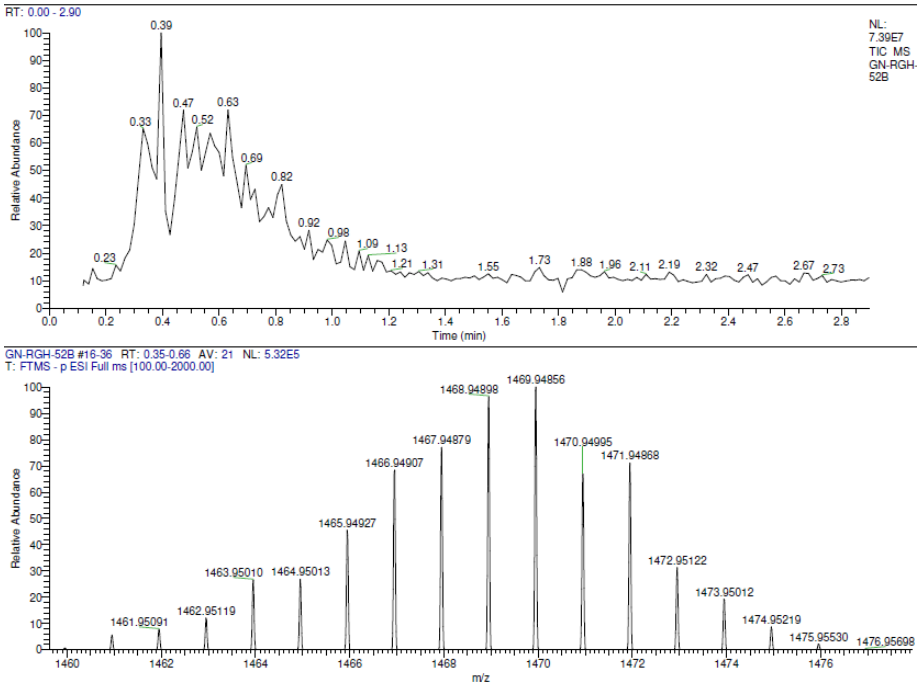

Figure E-32: HRMS of **5.2b-trans** [experimental]

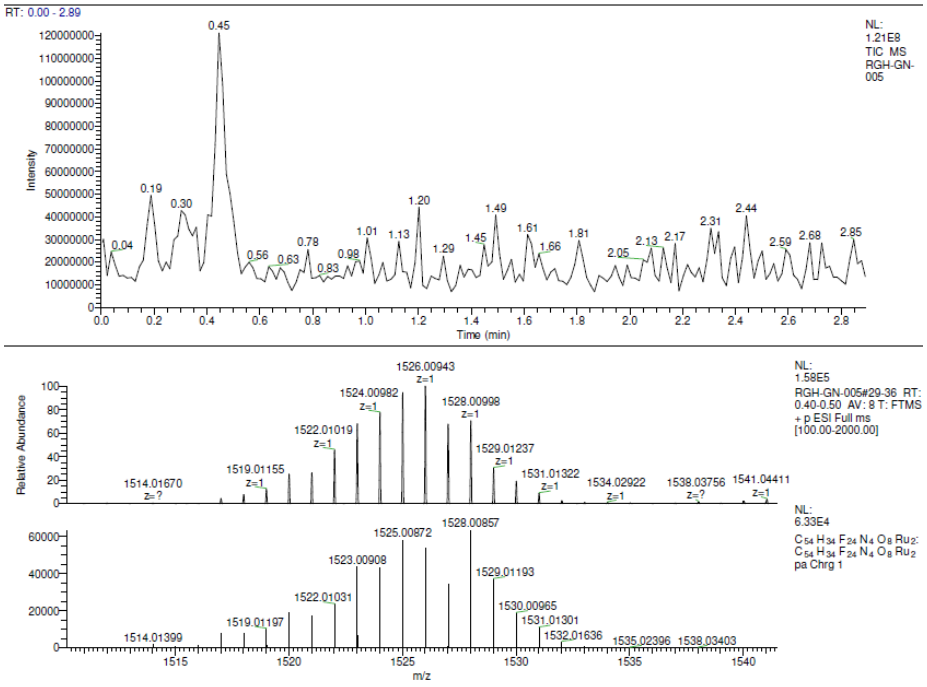

Figure E-331: HRMS of **5.2h-trans** [experimental (bottom), theoretical (middle)]

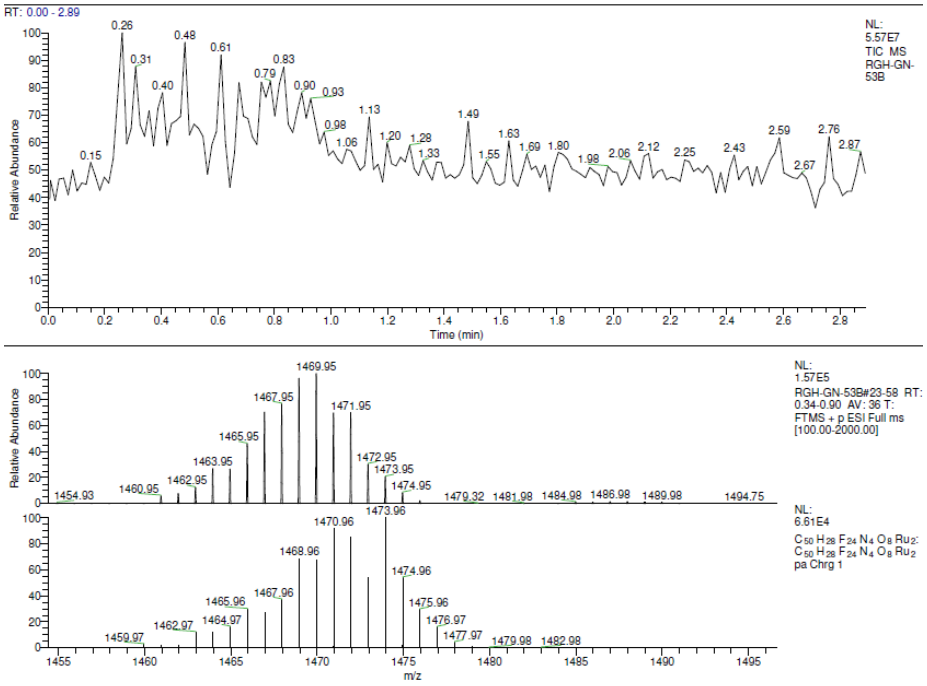

Figure E-34: HRMS of **5.2b-cis** [experimental (bottom), theoretical (middle)]

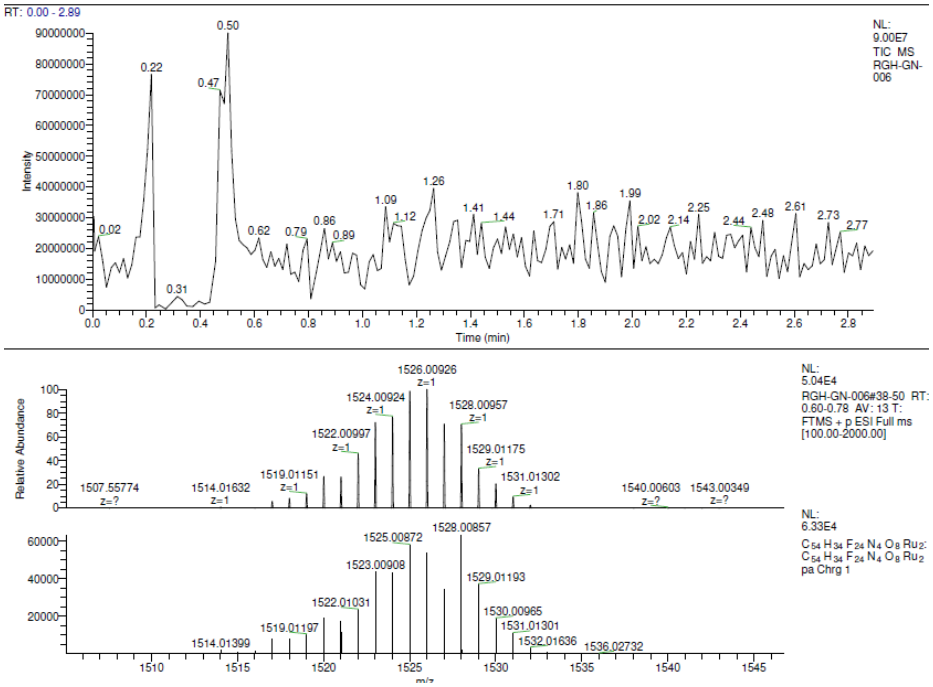

Figure E-35: HRMS of **5.2h-cis** [experimental (top), theoretical (bottom)]

Appendix F: UV-vis-NIR Data (all solutions 1.25 x 10^{-5} M)

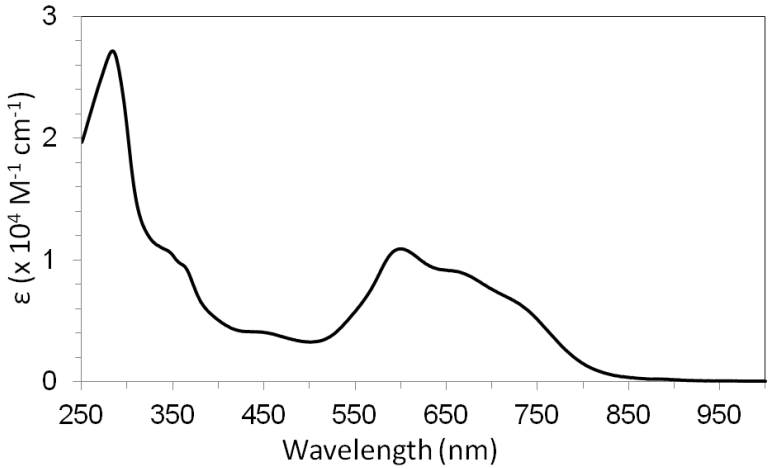

Figure F-1 UV/vis/NIR spectrum of **1.32b**

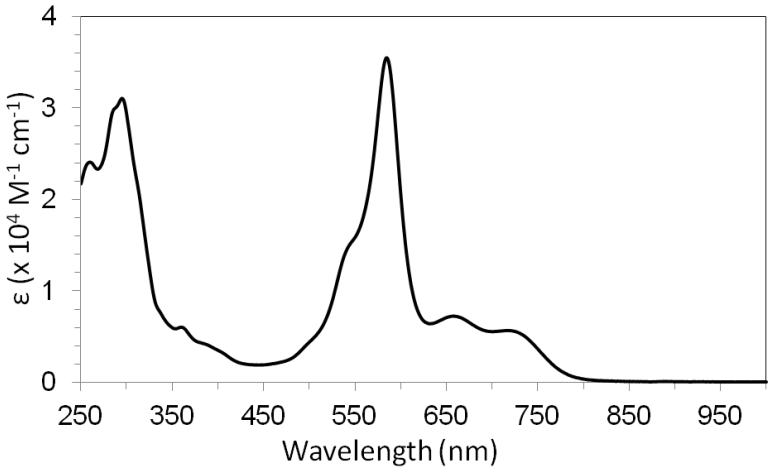

Figure F-2 UV/vis/NIR spectrum of **1.32c**

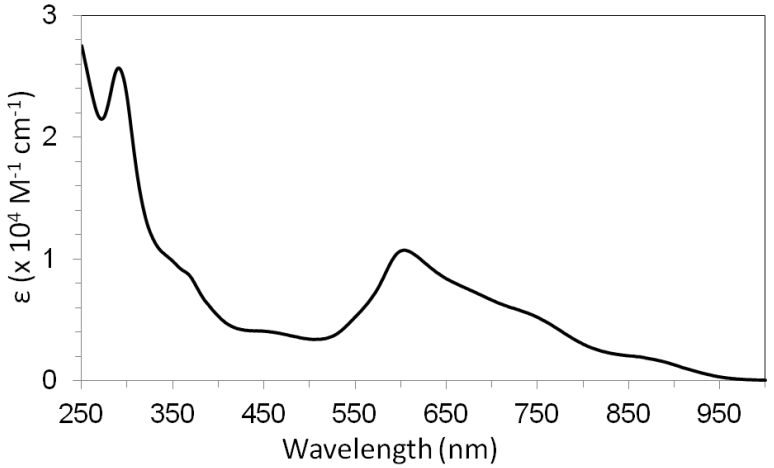

Figure F-3: UV/vis/NIR spectrum of **1.32g**

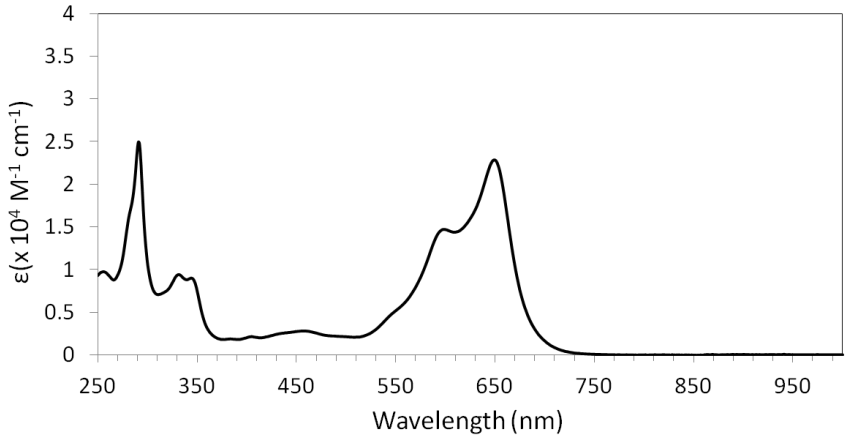

Figure F-4: UV/vis/NIR spectrum of **3.3a**

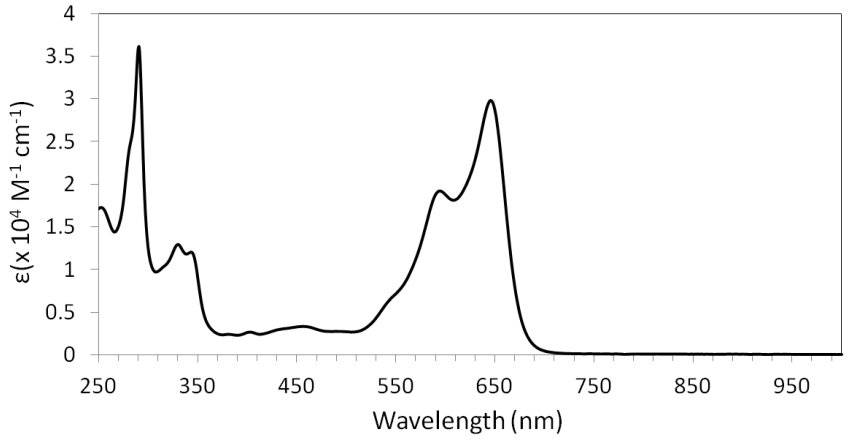

Figure F-5: UV/vis/NIR spectrum of **3.3c**

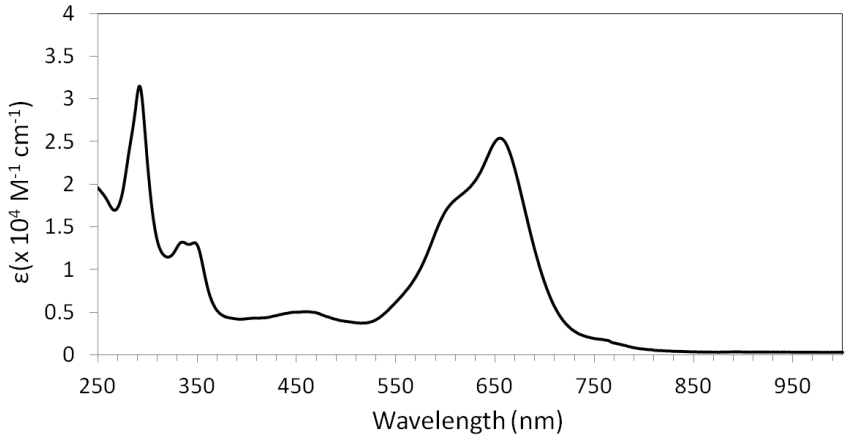

Figure F-6: UV/vis/NIR spectrum s of **3.3f**

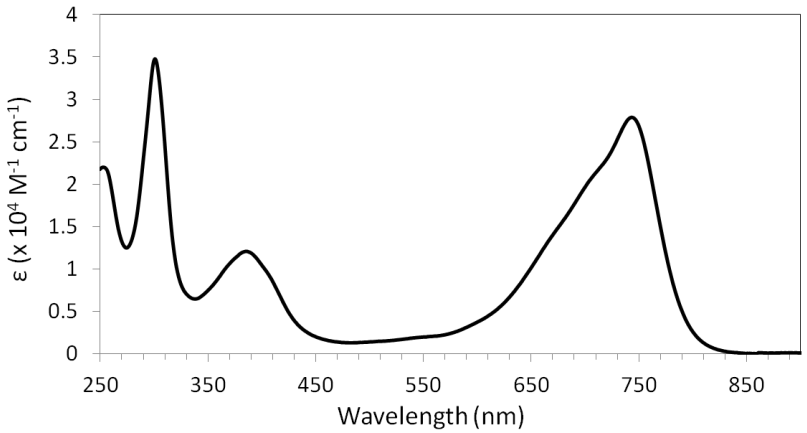

Figure F-7: UV/vis/NIR spectrum of **3.5a**

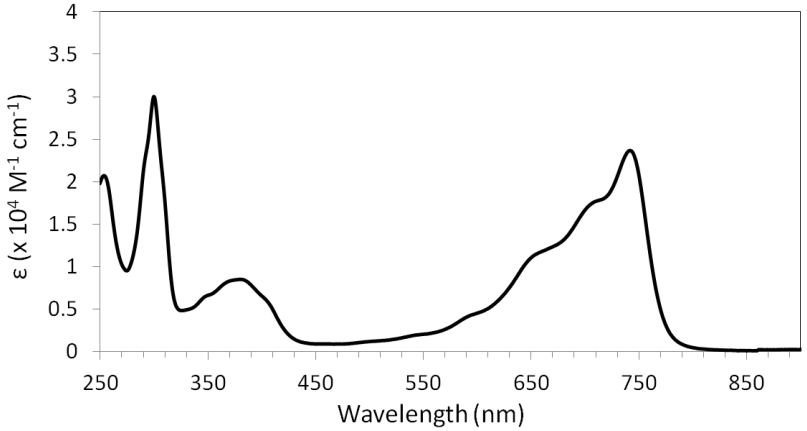

Figure F-8: UV/vis/NIR spectrum of **3.5c**

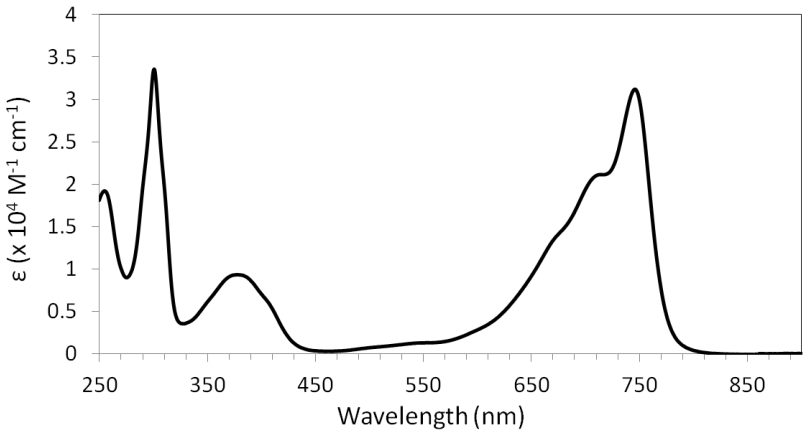

Figure F-9: UV/vis/NIR spectrum of **3.5d**

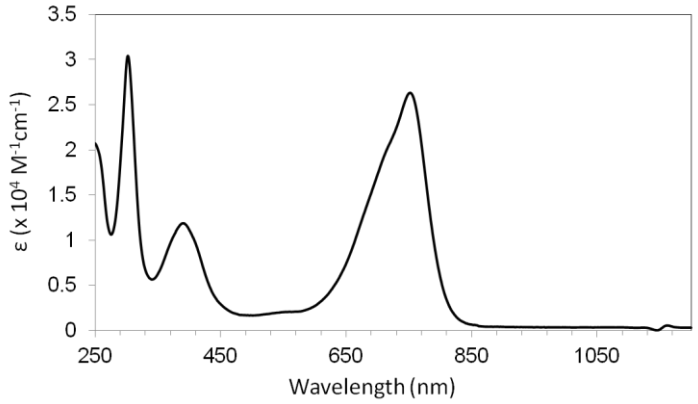

Figure F-10: UV/vis/NIR spectrum of **3.5f**

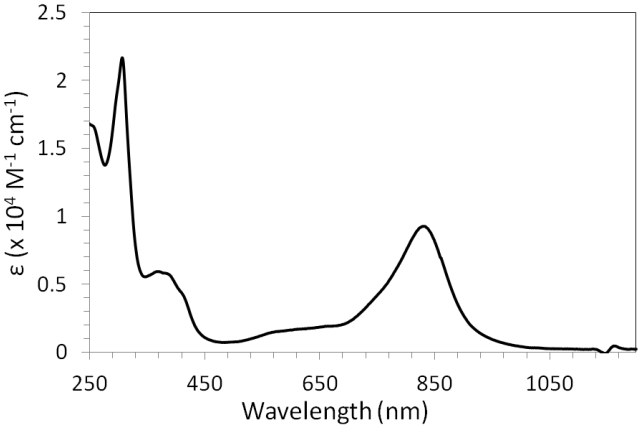

Figure F-11: UV/vis/NIR spectrum of **3.6f**

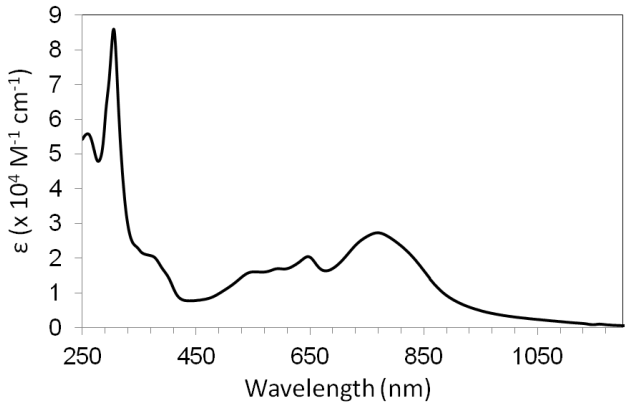

Figure F-12: UV/vis/NIR spectrum of **4.2c**

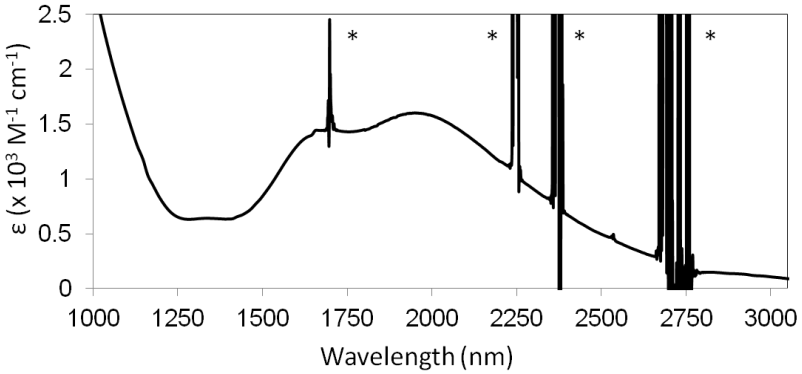

Figure F-13: UV/vis/NIR spectrum of **4.2c** (* spectrometer artifacts)

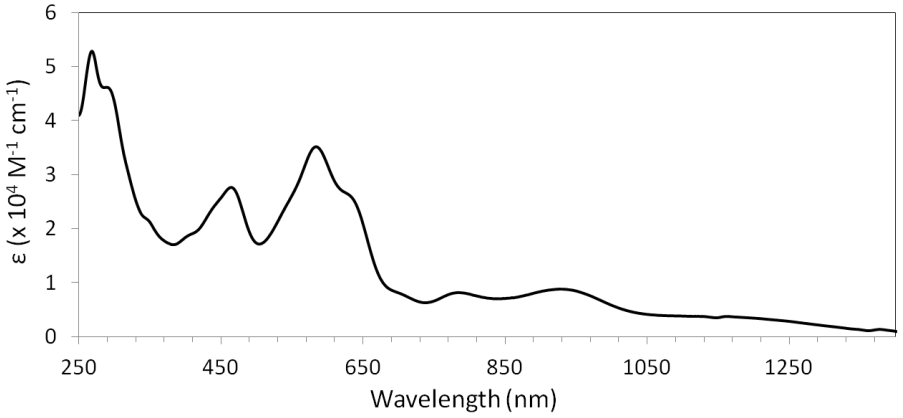

Figure F-14: UV/vis/NIR spectrum of **5.2b-trans**

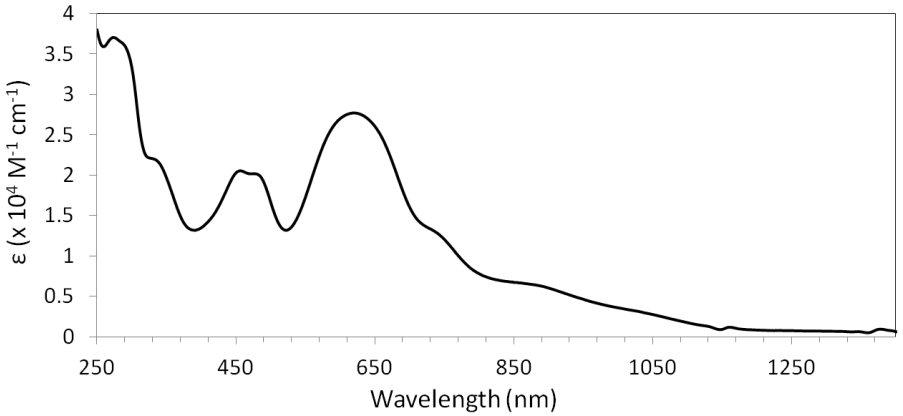

Figure F-15: UV/vis/NIR spectrum of **5.2b-cis**

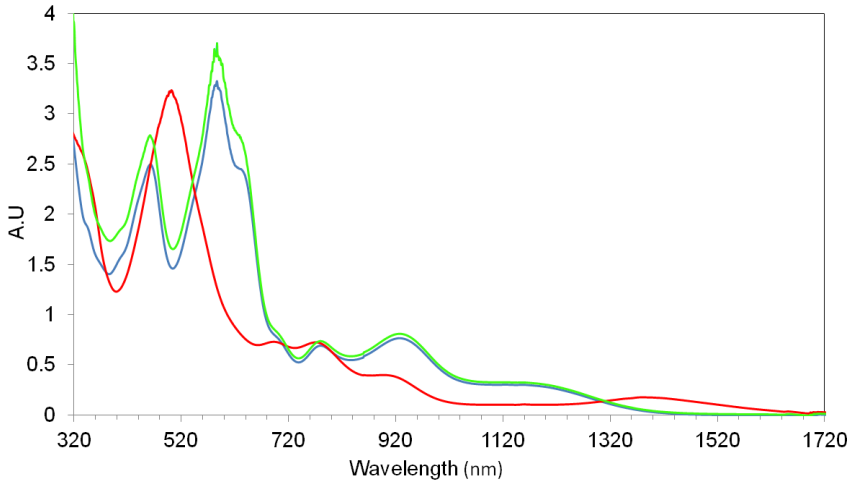

Figure F-16: UV/vis/NIR spectrum of **5.2h-trans** (blue), **[5.2h-trans]**$^{+}$ (red) and that obtained from the reduction of **[5.2h-trans]**$^{+}$ (green)

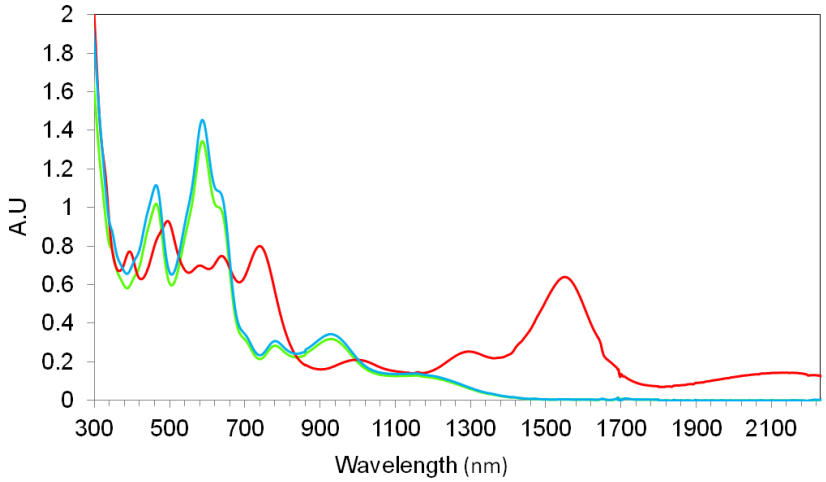

Figure F-17: UV/vis/NIR spectrum of **5.2h-trans** (blue), **[5.2h-trans]**$^{-}$ (red) and that obtained from the oxidation of **[5.2h-trans]**$^{+}$ (green)

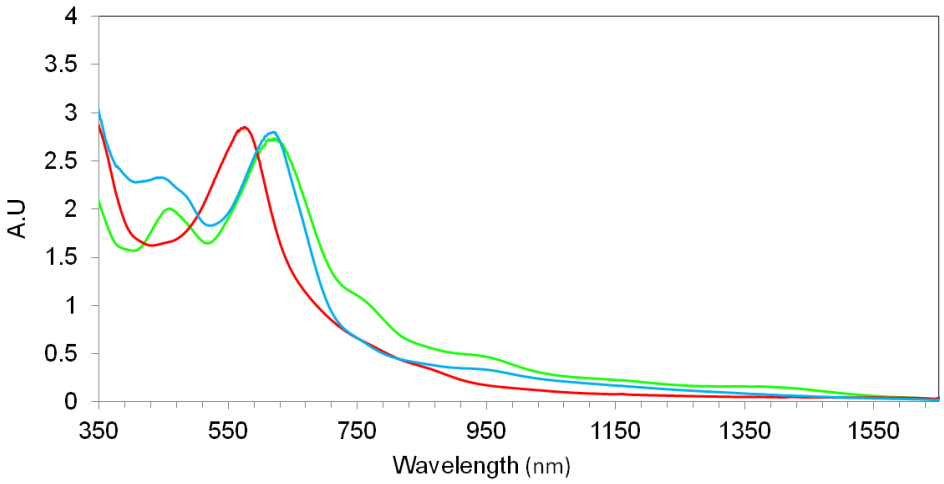

Figure F-18: UV/vis/NIR spectrum of **5.2h-cis** (blue), **[5.2h-cis]**$^{+}$ (red) and that obtained from the reduction of **[5.2h-cis]**$^{+}$ (green)

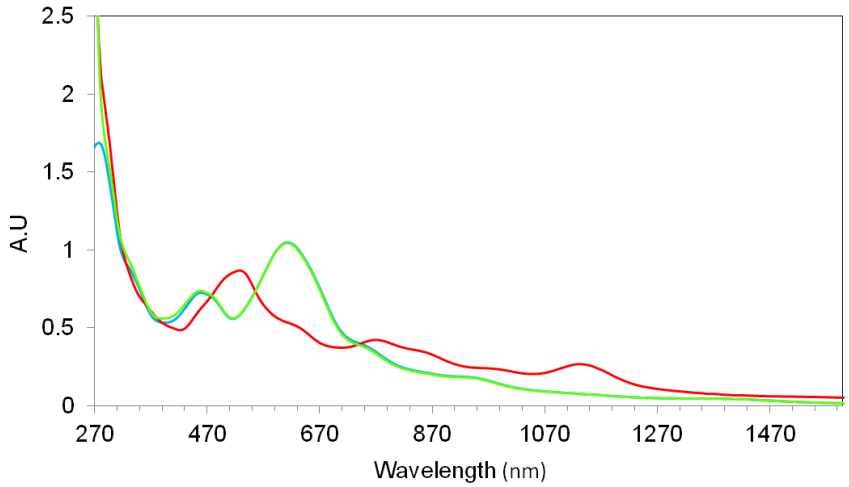

Figure F-19: UV/vis/NIR spectrum of **5.2h-cis** (blue), **[5.2h-cis]**$^{-}$ (red) and that obtained from the oxidation of **[5.2h-cis]**$^{-}$ (green)

Appendix G: Computations

Density functional theory (DFT) calculations employed the Gaussian 09 (Revision C.01) program[159] and the B3LYP[160] functional. Optimized geometries were calculated using the 6-31G* basis set on all light element and the LANL2DZ set 161 was employed for palladium. Frequency calculations (same level of theory) confirmed that the optimized structures were potential energy surface minima Single point calculations were performed using the TZVP basis set[162] on all light atoms and LANL2DZ for Pd. The 30 lowest energy electronic transitions were calculated using time-dependent DFT[163] (TZVP and LANL2DZ as above) and the polarized continuum model (PCM) was employed to model solvation (solvent = CH_2Cl_2, dielectric $\varepsilon = 8.94$).[164]

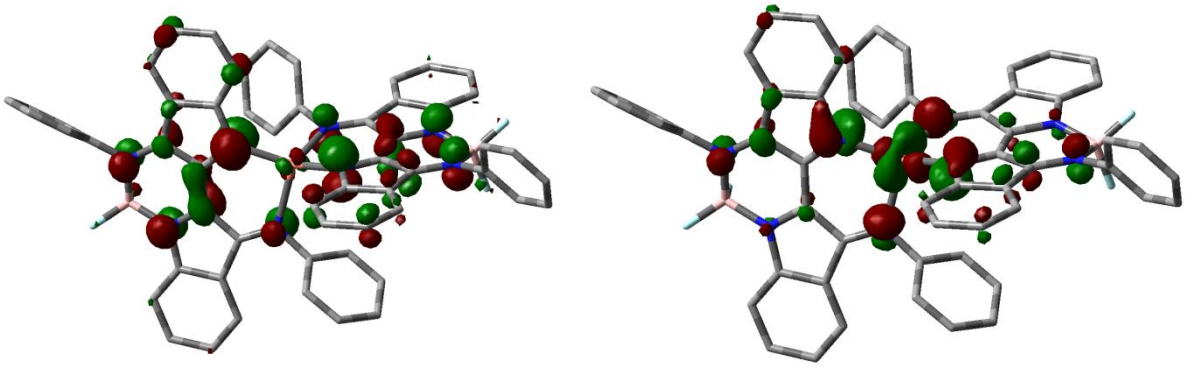

Figure G-1: Time dependant DFT calculations of **4.2a** HOMO (left) and LUMO (right)